*NASA Conference Publication 3015*

# 15th Space Simulation Conference

*Support the Highway to Space Through Testing*

Joseph Stecher, *Editor*
*NASA Goddard Space Flight Center*
*Greenbelt, Maryland*

**NASA**

National Aeronautics and
Space Administration

Office of Management

Scientific and Technical
Information Division

**1989**

# PREFACE

The Fifteenth Space Simulation Conference, held at the Williamsburg Hilton and National Conference Center, Williamsburg, Virginia, October 31 to November 3, 1988, is hosted by the Institute of Environmental Sciences (IES) and supported by the American Institute of Aeronautics and Astronautics (AIAA) and the American Society for Testing Materials (ASTM). The conference is further supported by the National Aeronautics and Space Administration (NASA) by their publication of these proceedings.

Some thirty years ago, man was able to reach out and touch space for the first time using the tools of technology to understand this new frontier. Soon after, the first meeting of the Space Simulation Conference, or the Tri-Society as it was initially referred, came into existence. Today, the Fifteenth Space Simulation Conference represents a gathering of respected individuals presenting papers to "Support the Highway to Space Through Testing." And the papers presented at this conference and the resulting discussions again will continue to carry on our ability for a permanent presence in space.

I would like to take this opportunity to publicly thank a few of those people whose efforts have made this conference and the publication of this document possible. Thanks go to Richard (Dick) Hartenbaum, Technical Program Chairman, GE Astro Space Division, and his people on the technical committee; Joseph (Joe) Stecher III, Publication Chairman, NASA Goddard Space Flight Center; and John D. Campbell, IES Meeting Manager, for bringing us to Williamsburg. In addition, the program committee would like to express our special thanks to Janet A. Ehmann, Executive Director, Institute of Environmental Sciences, and her staff for handling all the details which ensured a successful conference.

I wish all of you success and hope this conference will become as valued an experience as it has for me.


Albert R. Lunde
General Chairman


iii

# COMMITTEES FOR

# 15TH SPACE SIMULATION CONFERENCE

## MEETING MANAGEMENT COMMITTEE

General Chairman:         Albert R. Lunde, Boeing Aerospace Company
Technical Program:        Richard Hartenbaum, GE Astro Space Dividion
IES Meeting Manager:      John D. Campbell, Consultant
Publication Chairman:     Joseph L. Stecher III, NASA Goddard Space Flight Center
Facilities Chairman:      Russell T. Hollingsworth, Consultant
IES Executive Director:   Janet A. Ehmann, Institute of Environmental Sciences

## TECHNICAL PROGRAM COMMITTEE

Eugene N. Borson, The Aerospace Corporation
Peter W. Brinkman, ESA/ESTEC
John W. Harrell, Jet Propulsion Laboratory
Raymond D. Rempt, Boeing Aerospace Company
George F. Wright, Jr., Sandia National Laboratories
George Mikk, Perkin-Elmer Corporation
Robert P. Parrish, Jr., Martin Marietta Corporation
Richard Shoulberg, GE Astro Space Division

## JOINT POLICY COMMITTEE

### IES

John D. Campbell, Consultant
George Frankel, Grumman Aerospace

### ASTM

Eugene N. Borson, The Aerospace Corporation
George F. Wright, Jr., Sandia National Laboratories

### AIAA

George Mikk, Perkin-Elmer Corporation
Doug McKenney, Boeing Aerospace Company

# CONTENTS

## SESSION IV: DYNAMIC TESTING

Chairman: Richard Shoulberg, GE Astro Space Division
Co-Chairman: Charles G. Krisch, GE Astro Space Division

## SESSION V: SPACE SIMULATION I

Chairman: Robert Parrish, Martin Marietta Corporation
Co-Chairman: Dean Chambers, Martin Marietta Corporation

ix

## SESSION VIII: ANALYTICAL EXPERIMENTAL HEAT TRANSFER

Chairman: George F. Wright, Jr., Sandia National Laboratories
Co-Chairman: R. E. Sheldahl, Sandia National Laboratories

## SESSION IX: THERMAL CONTROL COATINGS AND MEASUREMENTS

Chairman: George Mikk, Perkin-Elmer Corporation
Co-Chairman: Thomas J. Best, U.S.A.F. – Arnold A.F.S.

Session I

# CONTAMINATION I

# WF/PC INTERNAL MOLECULAR CONTAMINATION DURING SYSTEM THERMAL-VACUUM TEST

D. Taylor, J. Barengoltz, T. Jenkins, K. Leschly, and J. Triolo
Jet Propulsion Laboratory
California Institute of Technology

## ABSTRACT

The Wide-Field/Planetary Camera (WF/PC) uses eight Charge Coupled Devices (CCDs) as imaging sensors in the wavelength region from 1200 to 11,000 angstroms. The CCDs are operated at temperatures below $-80°C$ for noise reduction and quantum efficiency stability. As a consequence, the CCDs are susceptible to very low levels of internal contaminants which affect the far ultra-violet (FUV) instrument performance. This concern is further magnified by the limited venting paths to the external environment.

During the recent system thermal-vacuum test of the WF/PC (February–March 1988), instrumentation was added to the WF/PC to characterize the internal molecular contamination and verify the instrument throughput down to 1470 angstrom. The following instruments were mounted on an access plate with view of the inside of WF/PC: A 15 MHz temperature controlled quartz crystal microbalance (TQCM), a thermocouple pressure gauge, and an optical witness mirror. Four UV-sources were added to the Optical Stimulus used to verify the optical performance of the WF/PC. The optical stimulus simulates the F/24 beam provided by the Hubble Space Telescope (HST) to the WF/PC pick-off mirror mounted external to the camera.

Throughout the system thermal-vacuum test (37 days) the following data was collected of relevance to contamination:

- Temperature data for the WF/PC optical bench, internal electronic assemblies, CCDs, heat-pipe system, radiator, and the external thermal shrouds.

- TQCM data, with the crystal temperature set at $-20°C$ during most of the test.

- Pressure data for the vacuum chamber and the internal WF/PC environment.

- WF/PC thruput data at 1470A, 2500A, and 4100A during each of the CCD cooldown cycles.

Analysis of the above data elements revealed the presence of two contaminants affecting the FUV performance of the WF/PC. The one contaminant (heavy volatile), is correlated with the electronic and housing temperature, and the contamination was significantly reduced when the electronics were operated below +8 to $+10°C$. The other contaminant (light volatile), was controlled by the heat-pipe temperature and was significantly reduced when the Thermal Electric Cooler (TEC) hot-junction temperature is below $-40$ to $-50°C$. These conclusions are supported both by TQCM data and WF/PC thruput measurements at 1470A.

The utility of contamination sensors located inside instruments during system tests was demonstrated. Vacuum chamber background readings could not reflect the internal conditions of interest because WF/PC is almost sealed, the background followed shroud and WF/PC external surface temperatures, and these external surface emissions would swamp the relatively low internal fluxes. The TQCM data internal to WF/PC provided information on the physical sources of contamination and possible contaminant species that affected instrument performance. The entire data set also guided remedial measures.

1

After the thermal-vacuum test and prior to final installation of the WF/PC into the HST, the WF/PC was modified in two areas:

- To enable on-orbit decontamination of the CCDs, heaters (66W total), were added to the eight heat-pipe/radiator saddles. This change provides a capability to boil-off the CCDs at temperatures above +10°C.

- To reduce the on-orbit outgassing rate of the high temperature volatile, patches were removed from the thermal blankets covering the electronic bays. This change reduces the expected operating temperature of the electronics by 2 to 3°C (down to between 0 to 5°C nominal).

# Wide Field/Planetary Camera

- TWO CAMERA SYSTEMS

|  | WIDE FIELD | PLANETARY |
|---|---|---|
| FOCAL RATIO | f/12.9 | f/30 |
| COMPOSITE ANGULAR FOV | 2.67 x 2.67 arcmin | 68.7 x 68.7 arcsec |
| NUMBER OF CCD CAMERAS | 4 (2 x 2) | 4 (2 x 2) |
| NUMBER OF PIXELS | 1600 x 1600 | 1600 x 1600 |
| WAVELENGTH COVERAGE | 1200Å TO 10,000Å | 1200Å TO 10,000 |
| NUMBER OF FILTERS | 48 | 48 |

- SCIENCE OBJECTIVES -

• DETERMINATION OF COSMIC DISTANCE SCALE (7x IMPROVEMENT)
• TESTS OF WORLD MODELS AND COSMIC EVOLUTION
• COMPARATIVE EVOLUTIONARY STUDIES OF DISTANT AND LOCAL GALAXIES
• STELLAR POPULATION STUDIES TO VERY FAINT LEVELS
• HIGH-RESOLUTION LUMINOSITY PROFILES OF GALACTIC NUCLEI
• ENERGY DISTRIBUTION OF STARS AND COMPACT SOURCES
• DYNAMIC MOTIONS IN SUPERNOVAE REMNANTS AND PROTO-STARS
• SEARCH FOR EXTRA-SOLAR PLANETS
• DETERMINATION OF CLOUD MOTIONS AND COMPOSITION OF PLANETARY
  ATMOSPHERES, THE DYNAMICAL FIGURES OF PLANETS, THE CARTOGRAPHY
  OF ASTERIODS AND SATELLITES, AND THE STRUCTURE OF COMETS

Figure 1

3

**Wide Field/Planetary Camera**

Figure 2

Figure 3

5
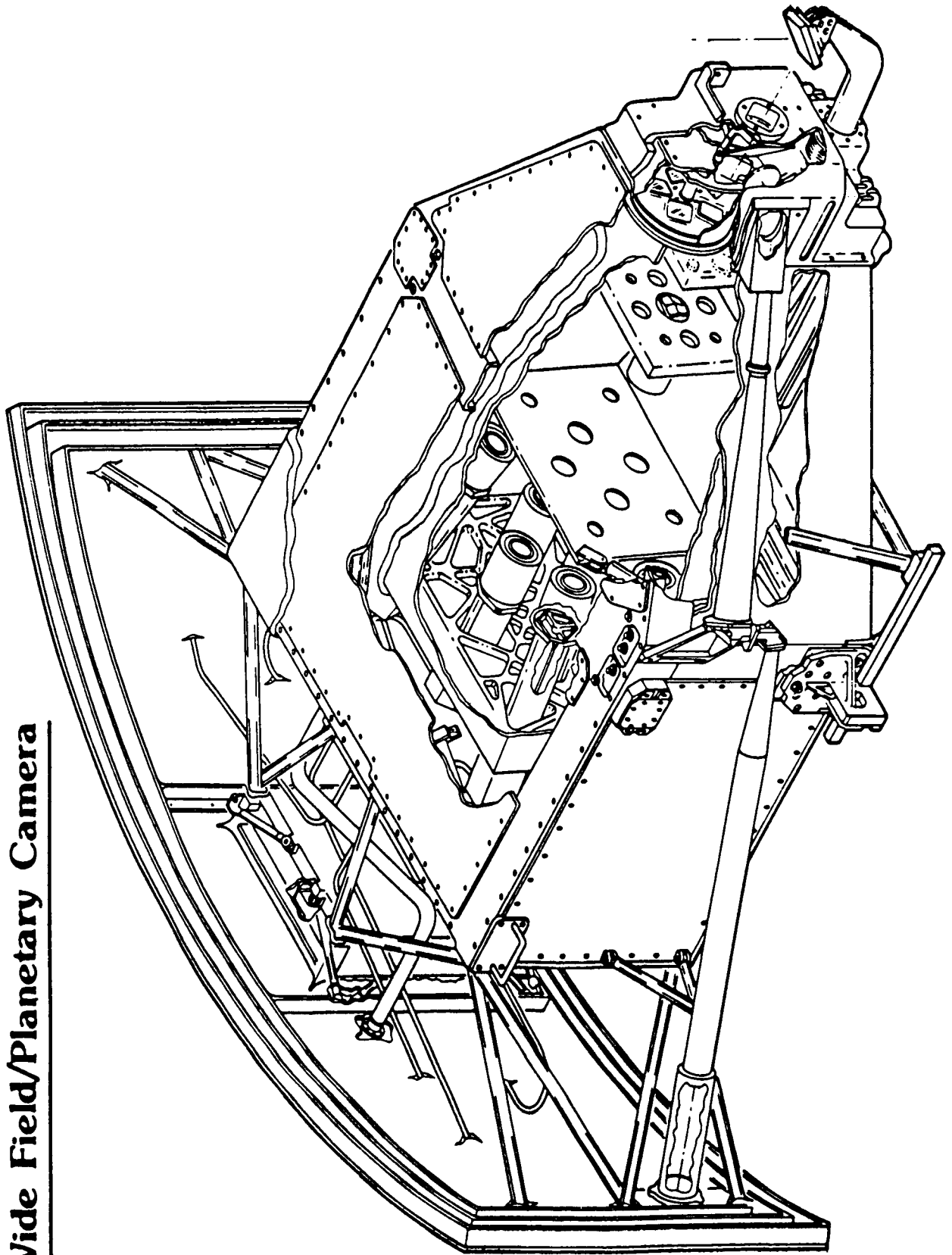
# Wide Field/Planetary Camera
## WF/PC OPTICAL SYSTEM
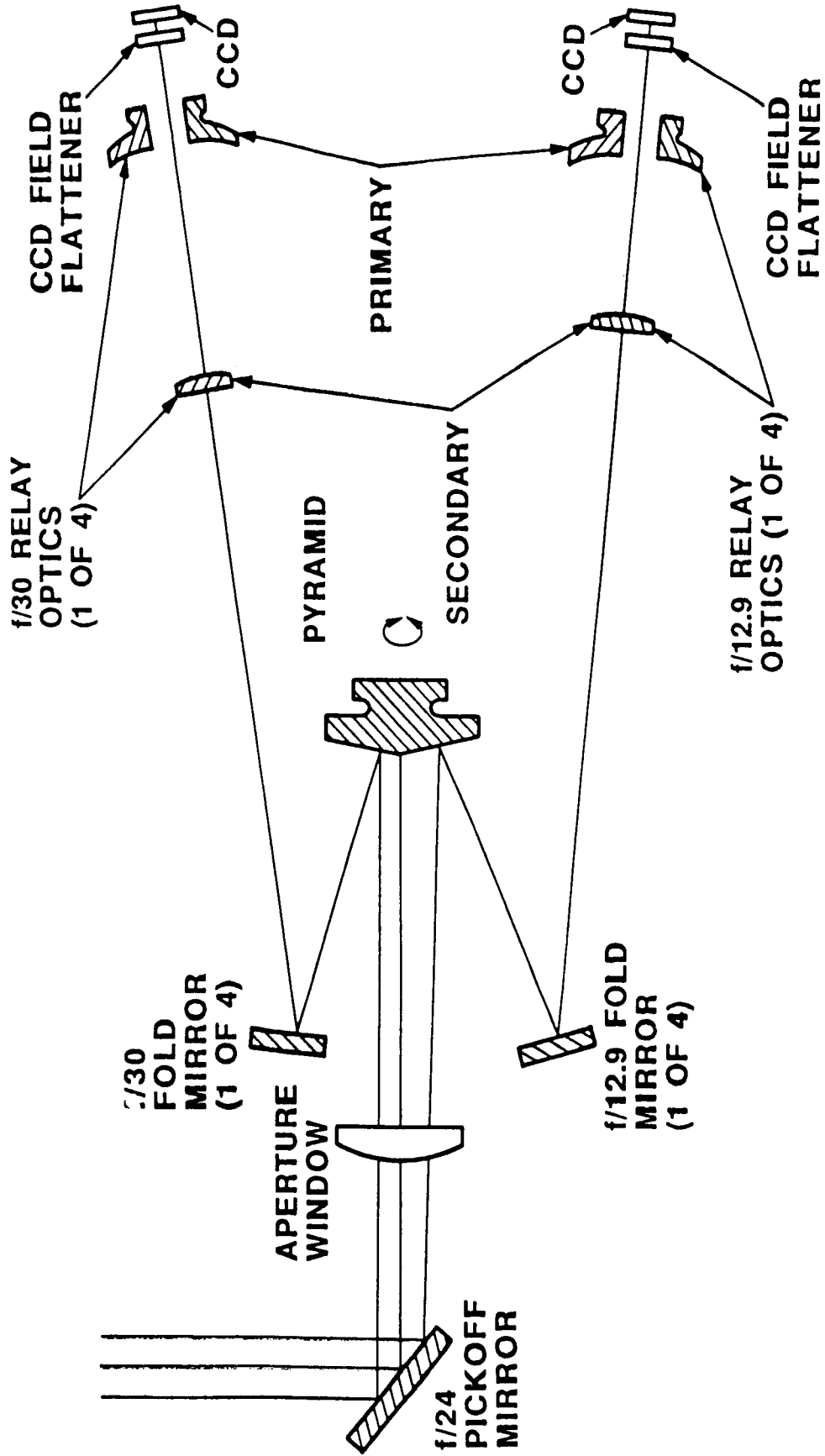
CCD FIELD FLATTENER

CCD

CCD

CCD FIELD FLATTENER

PRIMARY

f/30 RELAY OPTICS (1 OF 4)

f/12.9 RELAY OPTICS (1 OF 4)

PYRAMID

SECONDARY

f/30 FOLD MIRROR (1 OF 4)

f/12.9 FOLD MIRROR (1 OF 4)

APERTURE WINDOW

f/24 PICKOFF MIRROR

Figure 4

6

Figure 5

7

Figure 6

8

Figure 7

9

QE COOL DOWN DATA FROM TVT-6

WF2 (W/DIODE)

#: COOLDOWN CYCLE

Figure 8

10
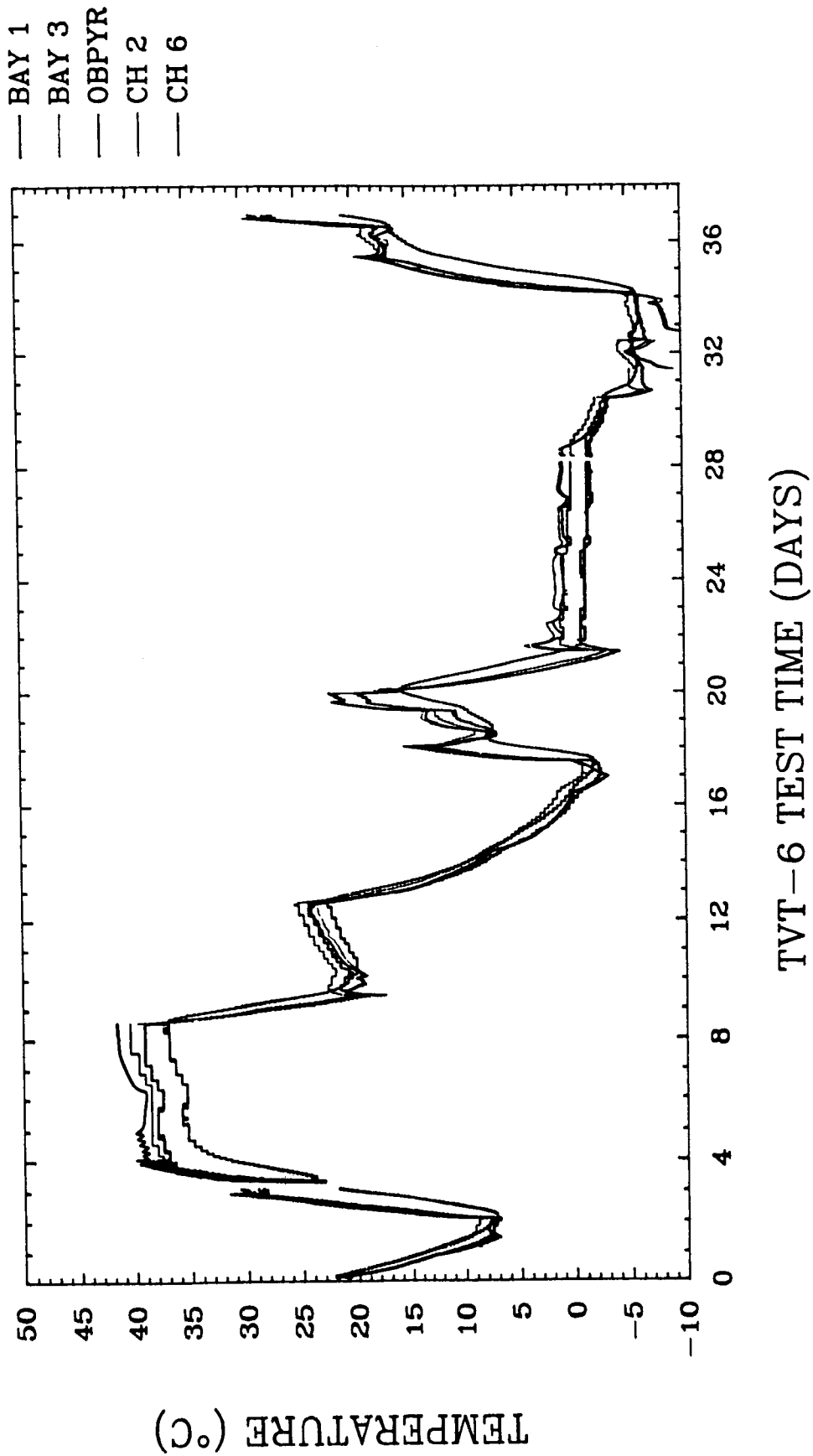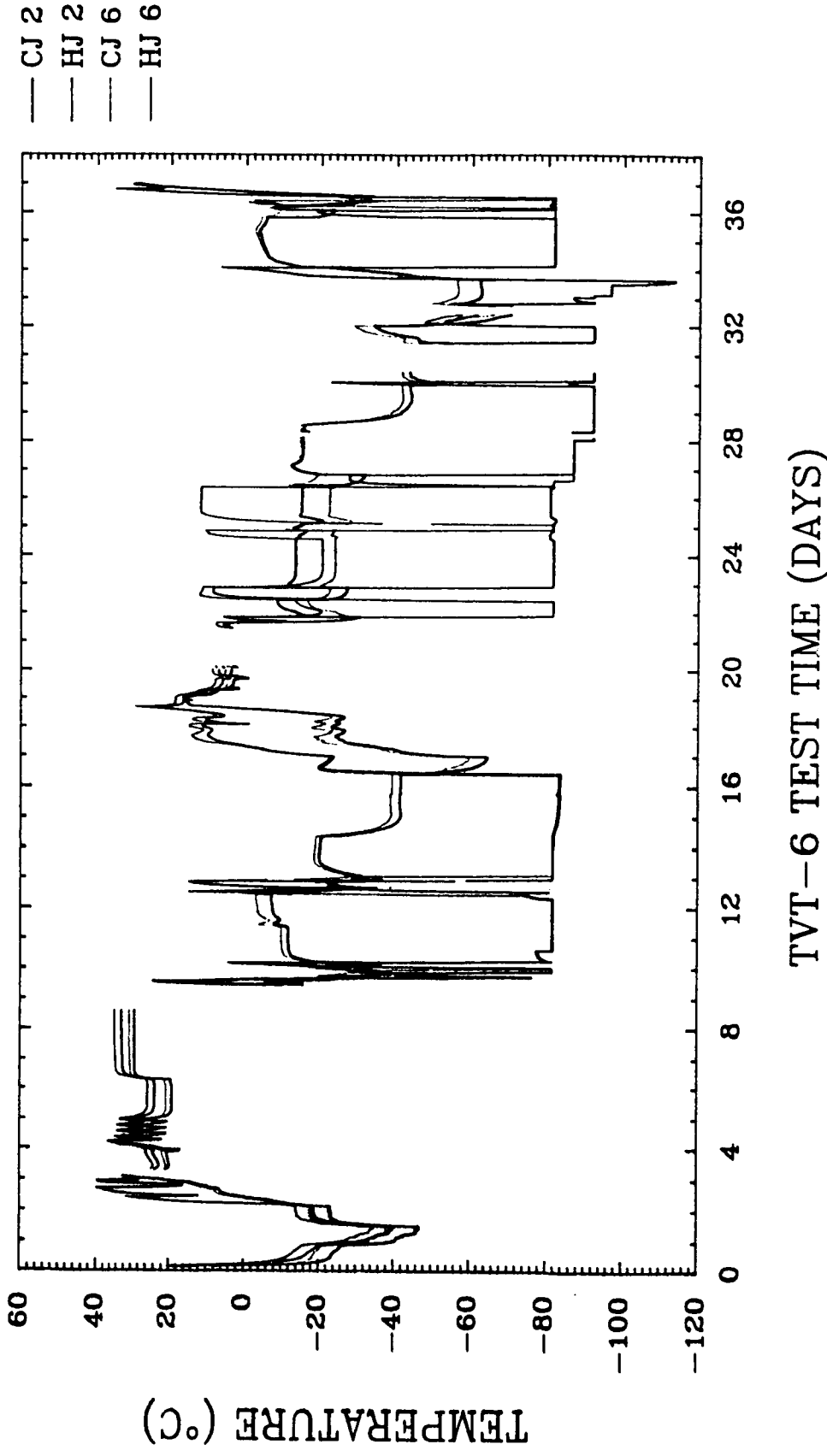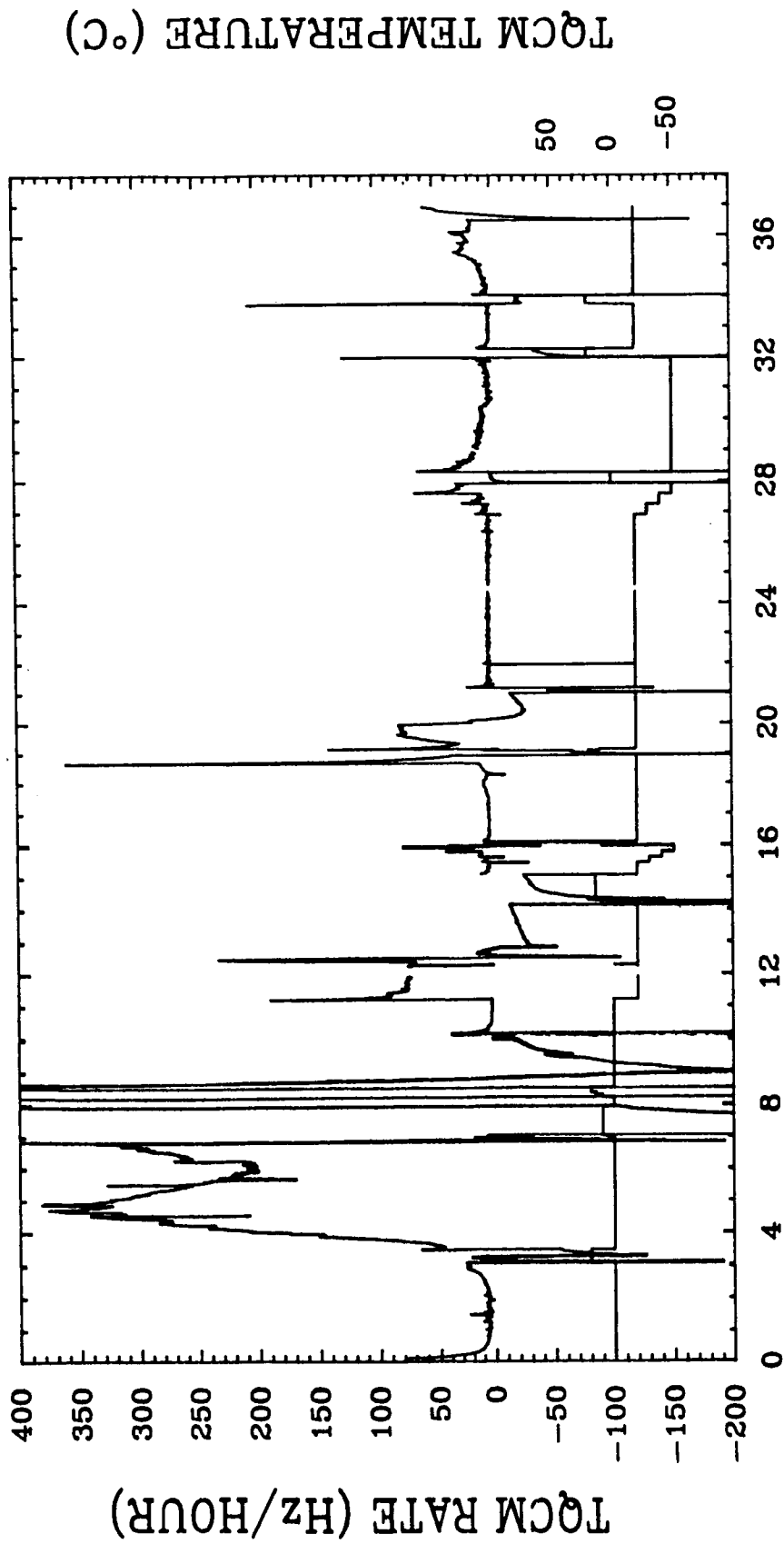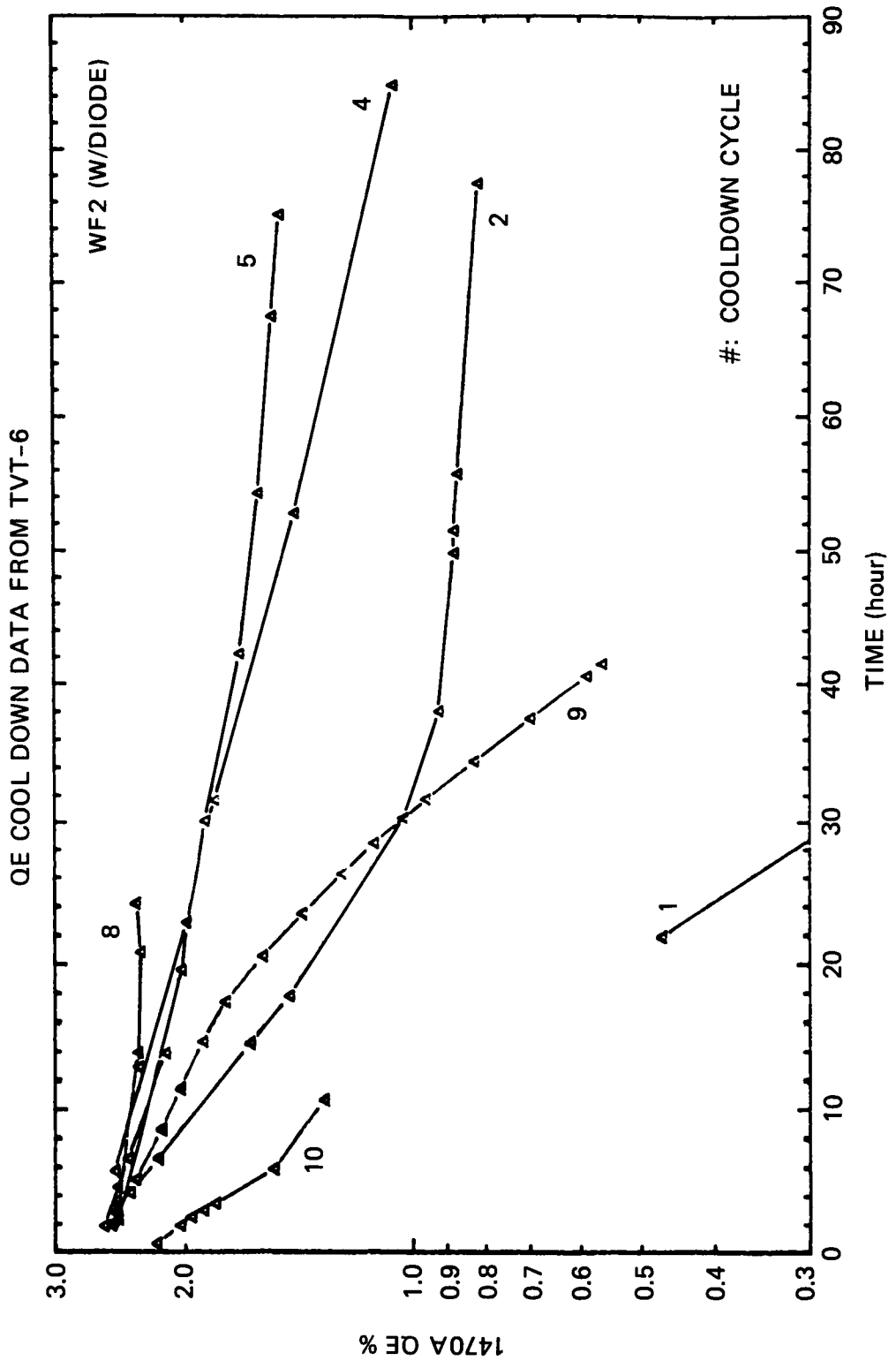
# WIDE FIELD/PLANETARY CAMERA (WF/PC)
# CONTAMINATION CONTROL ASSESSMENT

C. Maag, J. Millard, and M. Anderson
California Institute of Technology, Pasadena, CA 91109

## ABSTRACT

The Jet Propulsion Laboratory (JPL) has conducted an in depth contamination study of the Wide Field/ Planetary Camera (WF/PC).* The WF/PC is one of five science instruments on the Hubble Space Telescope (HST). The WF/PC provides a viewing capability for far ultraviolet, optical and near infrared astronomy. The WF/PC has a graphite epoxy optical bench with cooled detectors and an aperture window through which stellar energy is transmitted.

The major concern of this study was the formation of a haze on the transmissive optics when exposed to a vacuum environment. The phenomena was determined to be a result of molecular transport from a low outgassing structural adhesive. Detailed analyses, both chemical and analytical were conducted to assess the formation of the haze. This paper will relate the findings of this contamination study.

Detailed spectral and chemical analyses were conducted on the aperture window to determine the source of the haze. Results of size exclusion chromatography, atomic absorption spectroscopy, Fourier Infrared Transmission and Fourier Transform Diffuse IR Reflectance of the haze and molecular films from surrounding areas will be discussed. In addition, special tests were developed to recreate the formation of the haze on a similar aperture window. Results of these tests will also be discussed.

Since the chemical and spectral analyses provided results which propagated many emotional responses, an additional study was conducted. The purpose of the study was to determine quantitatively if the adhesive or any other material could be responsible for the molecular contamination pattern found on the aperture window. This would be determined by comparison of the contamination distribution on the window, as evidenced by photographs, with the analytical distribution computed, assuming these materials were the sole source of the contamination by means of outgassing.

The approach taken was to perform a simplified computer simulation of the outgassing of each of these materials and record the mass distribution created by each material on the aperture window. A detailed geometric computer model of the pertinent interior surfaces of the housing was created. The JPL mass transport program was then used to perform an outgassing simulation for each material in order to determine the results.

Each material was considered individually, as it was not known if the actual contamination was a result of one, many, or possibly none of the materials considered.

Results of this assessment and the comparison with the aforementioned chemical analyses provided incontrovertible evidence as to the cause of the window haze. The resultant clean-up and subsequent elimination of the problem will also be addressed.

---

*Maag, C. R., *Results/Findings of the WF/PC Contamination Team*, Draft, JPL Internal Document, May 1987.

# CHARACTERIZATION OF A GRAPHITE EPOXY OPTICAL BENCH DURING THERMAL VACUUM CYCLING[1]

Patricia A.Hansen, Teresa K. Jenkins,
Carl R. Maag, and Daniel M. Taylor
Jet Propulsion Laboratory
California Institute of Technology

## ABSTRACT

In-situ monitoring of the Wide-Field/Planetary Camera, a Hubble Space Telescope science instrument, was performed in a vacuum environment to better understand the formation of ice on cooled optical detectors. Several diagnostic instruments were mounted on an access plate and viewed the interior of the instrument housing and the graphite epoxy optical bench. The diagnostic instruments were comprised of the following: a TQCM (Temperature-Controlled Quartz Crystal Microbalance), a Pressure Gauge and an Optical Witness Sample. This paper describes the instrumentation and the rationale for choosing this instrumentation. In addition, the performance of the instrumentation during monitoring operations will be presented.

## INTRODUCTION

An in-depth contamination study of the Wide-Field/Planetary Camera (WF/PC) was conducted by the Jet Propulsion Laboratory (JPL).[2] As part of this study the formation of ice on the cooled detectors was investigated. During previous system thermal vacuum tests, a contaminant, thought to be ice, was observed on the detectors. This contaminant was easily removed when the detectors were warmed up while under vacuum. After this period, the detectors were cooled and no contaminant, or ice, was seen on the detectors during imaging.

This phenomena was thought to be the result of water desorption from the graphite epoxy optical bench material (ref. 1). To better understand this phenomena, several diagnostic instruments were proposed for in-situ monitoring

---

[2] Carl R. Maag: Results/Findings of the WF/PC Contamination Team, Draft. JPL Internal Document, Jet Propulsion Laboratory, Pasadena, CA, May 1987.

of the WF/PC during a system thermal vacuum test. The diagnostic instruments
included a Temperature-Controlled Quartz Crystal Microbalance (TQCM), a
Pressure Gauge and an Optical Witness Sample (OWS). These instruments were
mounted on an access plate and viewed the interior of the instrument housing
and the thermally blanketed graphite epoxy optical bench.

One of the principal ground rules was that the diagnostic instrumentation
could not introduce contaminants into the WF/PC housing and could not change
the existing heat flow paths. Thus the instrumentation was subjected to
rigorous preconditioning prior to installation on the WF/PC housing. In
addition, only low outgassing materials were used on the access plate.

During the system thermal vacuum test additional diagnostic
instrumentation and contamination monitoring devices were used to measure the
test environment. Only the access plate instrumentation will be discussed in
this paper. A summary of the access plate instrumentation results is also
presented. An in-depth discussion of the TQCM measurement techniques and data
reduction is the subject of another paper included in this conference
(ref. 2).


## WIDE-FIELD/PLANETARY CAMERA


The WF/PC is the radial science instrument on the Hubble Space Telescope
(HST) developed and built by the JPL and the California Institute of
Technology. The scientific objectives of the WF/PC are to provide
photometrically and geometrically accurate, multiband observations of stars
and extended sources over a wide field-of-view (FOV) on the HST, and to
provide very high angular resolution photometrically and geometrically
accurate, multiband images of the solar system and its astronomical objects.

The WF/PC contains two complete optical relay and detector systems as
shown in Figure 1. Each system is capable of producing a four-part image
mosaic. One relay system operates for wide-field work and the other operates
for planetary or high resolution work. Only one optical system provides
images at any given time.

Once the relay optics intercept the light, they reflect it through the
primary and secondary optics to the detectors located in the rear of the
optical assemblies (in the camera heads). The eight (8) detectors (one in
each of the four camera heads for either the wide-field or planetary system)
contain charge coupled devices (CCDs). The CCDs are cooled to a nominal
temperature of -90°C to suppress their dark current and to improve their
performance.


## WF/PC CONTAMINATION STUDY


The WF/PC contamination study investigated the formation of ice on
critical surfaces such as the CCD windows and the Thermoelectric Coolers

(TEC).  The goal of this investigation was to prevent the formation of ice on optical surfaces and to develop operational strategies to respond to ice formation if it reoccurred during flight operations.

Models predicting the formation of ice were developed to define and quantify the parameters associated with this phenomena.  As this phenomena was thought to be the result of water desorption from the graphite epoxy optical bench material, a model of the dew point inside the housing was derived for external vacuum conditions.[3]  When the temperature of a surface such as the CCD windows or TECs are below the dew point temperature (and below the freezing point of water) ice will form on these surfaces.  This dew point model was then used to develop operational strategies for cooling the detectors.

Several layers of MLI (multilayer insulation) blanket were removed from the housing to decrease the nominal operating temperature of the WF/PC by several degrees.  Scenarios were developed to predict the time delay after launch for the dew point temperature of the outgassing water, or contaminant, to be below the temperature of the CCD windows.[4]  The operating temperature of the detectors was raised ten degrees to allow early operation of the detectors.  It is believed that these changes will result in ice free operation of the cooled detectors 30 days after launch.

The diagnostic instrumentation was proposed for in-situ monitoring of the optical bench and housing to quantify the initial parameters of the derived models.  A TQCM was employed to measure the adsorption and desorption of volatile condensible material (VCM) on the surfaces in the WF/PC, primarily the graphite epoxy optical bench and the electronics.  The pressure gauge was employed to measure the initial water content of the optical bench (i.e. the partial pressure of water).  The OWS was used to measure any change in reflectance of an optical surface due to the deposition of outgassed material on that surface.  The access plate was a structural member only.

DIAGNOSTIC INSTRUMENTATION

INSTRUMENT CONFIGURATION

The diagnostic instrumentation was mounted on the access plate as shown in Figure 2.  The operational constraints of the pressure gauge required it be mounted on an extended inlet tube outside the WF/PC shrouds.  The inlet tube

---

[3]  Jack B. Barengoltz: A Model of the WF/PC Dew Point.  JPL Interoffice Memorandum No. 3543:87:0010, Jet Propulsion Laboratory, Pasadena, CA, January 15, 1987.

[4]  Jack B. Barengoltz: WF/PC Thermal Blankets Revisited.  JPL Interoffice Memorandum No. 3543:87:0084, Jet Propulsion Laboratory, Pasadena, CA, May 14, 1987.

was mounted on the access plate as shown in Figure 2. The access plate was mounted on the WF/PC housing as shown in Figures 3 and 4.


ACCESS PLATE


The goal of the monitoring was to better understand the formation of ice on the detectors using "passive" measurement techniques. As such, it was imperative that the access plate and diagnostic instrumentation did not change the existing WF/PC heat flow paths or introduce volatile condensible material (VCM) into the housing.

VESPEL (SP-1) was chosen as the material for the access plate as it provided good thermal isolation from the WF/PC housing and the vacuum chamber shrouds, was easily machined and was a low outgassing material. The access plate was subjected to a 80°C ± 2°C vacuum bakeout for 36 hours at 1 x 10$^{-6}$ torr prior to installation onto the WF/PC housing. Swab sampling was performed prior to installation to verify that the access plate would not contaminate the interior housing of the WF/PC during test.[5]

Freon TF (Burdick-Jackson HPLC purity 1,1,2-Trifluorotrichloroethane) was used to clean the access plate and the external surfaces of the diagnostic instrumentation prior to installation onto the WF/PC housing. The NVR (nonvolatile residue) was removed from these surfaces and thus prevented the introduction of organic contaminants into the WF/PC housing.


TEMPERATURE-CONTROLLED QUARTZ CRYSTAL MICROBALANCE


A temperature-controlled quartz crystal microbalance (TQCM) performed in-situ measurements of adsorbed and desorbed VCM on surfaces in the WF/PC, primarily the graphite epoxy optical bench and electronics. The TQCM was instrumented with 15 MHz optically polished crystals (ref. 3). The crystals were coated with aluminum to be representative of a reflective optical surface.

The heat generated by the TQCM electronics was removed by a gold plated copper heat sink which was thermally coupled to a heat exchanger maintained at 10°C ± 5°C. This provision, suggested by the manufacturer, provided increased accuracy of the TQCM measurements (ref. 3). In addition, this provision allowed the contamination loading from the WF/PC optical bench and housing to be monitored without changing the existing heat flow paths.

The TQCM monitored the access plate vacuum bakeout. As a monitoring device, the TQCM was subjected to a 80°C ± 2°C vacuum bakeout for 36 hours.

---

[5] Patricia A. Hansen: Results of the WF/PC Access Plate Bakeout. JPL Interoffice Memorandum No. 354C:88:0012 (ST-DFM 1140), Jet Propulsion Laboratory, Pasadena, CA, January 21. 1988.

Prior to installation on the access plate, the exterior surfaces of the TQCM were cleaned.

PRESSURE GAUGE

The pressure gauge was a Series 275 Convectron gauge from Granville-Phillips Company (ref. 4). It was capable of providing a pressure measurement from 1000 torr to $10^{-3}$ torr. The gauge tube contained a temperature compensated heat loss sensor which utilized conduction cooling to sense pressure at lower pressures. At higher pressures, it utilized convection cooling in which gas molecules were circulated through the gauge tube by gravitational force.

Prior to installation on the access plate, the pressure gauge was calibrated to extend the nominal useful range from $1 \times 10^{-3}$ torr to $2 \times 10^{-4}$ torr. The pressure gauge was also subjected to a 80°C ± 2°C vacuum bakeout for 24 hours at $1 \times 10^{-6}$ torr. The exterior surfaces of the pressure gauge were cleaned prior to installation on the access plate.

The pressure gauge inlet tube was extended to allow the pressure gauge to be mounted on the access plate but reside several inches away from the access plate due to operational constraints. During operation, the pressure gauge was mounted to remain in a horizontal position and at ambient temperatures. Although not shown mounted on the access plate in Figure 4, the pressure gauge is presented in Figure 5.

OPTICAL WITNESS SAMPLE

The optical witness sample (OWS) was an optically polished aluminum sample. The sample was coated with $MgF_2$ to simulate an optical surface. The OWS was installed in a holder for ease of handling prior to installation. An example of the OWS installed in a holder is shown mounted on the external test fixture in Figure 6.

The reflectance of the OWS was measured at several wavelengths (1216 Å, 1608 Å, 2200 Å, 2537 Å and 3130 Å) prior to installation on the access plate. The OWS holder was vacuum baked with the access plate.[5] The exterior surfaces of the holder were cleaned prior to the OWS installation.

THERMAL VACUUM TEST MONITORING

The TQCM and pressure gauge continuously monitored the WF/PC optical bench and housing during the system thermal vacuum test. The WF/PC test profile simulated three flight operational conditions: nominal operational conditions, a flight hot case and a flight cold case. During these profiles

16

the temperature of the TQCM was varied to measure the relative volatility of the surface contamination from the optical bench and housing.

The OWS was continuously exposed to the WF/PC housing and optical bench. The OWS was not temperature controlled and was coupled by radiation to the housing and optical bench. Thus the OWS followed the temperature profile of the housing and optical bench and varied from approximately 35°C to -5°C.

RESULTS

The temperature of the TQCM was varied to measure the relative volatility of the surface contamination from the optical bench and housing which was held at a constant temperature during the test profiles. Self-contamination of the TQCM was considered highly improbable due to the rigorous preconditioning program of the access plate and diagnostic instrumentation. Therefore, the contamination source was internal to the WF/PC. The TQCM measured two groups of contaminants as a result of varying its temperature and the optical bench and housing temperature. As a result of these measurements, it was concluded that the TQCM collected an organic contaminant, not ice, when cold. The source of this contamination was not identified as the optical bench and housing are composed of many subassemblies (e.g. electronics, camera head, mechanisms, etc). However, additional measurements indicated the contamination source was strongly correlated to the operation of the electronics bays. Although surface contamination was detected by the TQCM, additional temperature cases showed that the detectors could be outgassed without detector performance loss. An in-depth discussion of the TQCM results is the subject of another paper included in this conference (ref. 2).

During operation, the TQCM was not operated at a temperature cold enough to collect ice. For operational temperatures below -60°C, the manufacturer suggests using a CQCM (Cryogenic Quartz Crystal Microbalance) (ref. 3). However, ice formation on the detectors (i.e. the CCD windows) was not expected as the amount of adsorbed water in the graphite epoxy optical bench and housing had been limited by the use of an ultradry nitrogen purge prior to test and the use of operational strategies during the test. The ultra-dry nitrogen purge system and the operational strategies are the subject of another paper included in this conference (ref. 5).

The TQCM measurements identified that water (ice) was not the only contaminant inside the WF/PC housing and optical bench. Flat field imaging was performed to verify that the operational strategies did indeed result in ice free operation of the cooled detectors (ref. 6). These images were not obscured as in previous tests. Therefore, these operational strategies resulted in ice free operation of the cooled detectors.

The pressure gauge was initially recommended so that its measurements could be used to derive the partial pressure of water inside the WF/PC, it was found that these measurements needed to be extended into the $10^{-5}$ torr range. In the event of ice formation on the CCDs, the pressure gauge would have been used to determine the actual vapor pressure of the ice, or contaminant. In

addition, the pressure gauge would have been used to determine the vapor pressure of the ice during the detector warmup/ice removal sequences.

As the detectors did not collect ice, the pressure gauge was only used to measure the pressure differential between the WF/PC housing and the vacuum chamber during chamber pump down and purging sequences. The rate of diffusion of the purge gas out of the camera and the effectiveness of the vent tube were measured. These measurements were correlated with the previous predictions.[6]

The OWS was measured immediately after test. The results of these measurements showed the reflectance of the OWS did not degrade beyond three (3) percent at Lyman-Alpha wavelengths. The OWS reflectance measurements indicated that if warmed to room temperature and atmospheric pressure, the contaminant did not cause a loss in reflectance on an optical surface (i.e. the CCD windows).

CONCLUSIONS

Significant information was obtained with in-situ monitoring of the WF/PC optical bench and housing during a system thermal vacuum test. The diagnostic instrumentation was an invaluable tool in monitoring the internal contamination. The instrumentation allowed the internal environment of the WF/PC to be monitored without altering the functional requirements or nominal operating requirements of the WF/PC.

The TQCM performed in-situ measurements of adsorbed and desorbed VCM on the internal surfaces of the WF/PC. The TQCM measured an organic contaminant, less volatile than water, correlated to the operation of the electronics bays within the WF/PC. The OWS reflectance measurements indicated that if warmed to room temperature and atmospheric pressure, the contaminant did not cause a loss in reflectance on an optical surface.

Although the TQCM temperature was not cold enough to simulate the cooled detectors, verification of ice free operation of the cooled detectors was performed with flat field imaging. The flat field images were not obscured, thus verifying ice free operation of the cooled detectors.

---

[6] Jack B. Barengoltz: Actual WF/PC Venting and Implications for Water Modeling. JPL Interoffice Memorandum No. 354:JB:88:0129, Jet Propulsion Laboratory, Pasadena, CA, May 2, 1988.

REFERENCES

1.  Springer, G. S.; et. al.: Environmental Effects on Composite Materials. Westport, CT:Technomic, 1981.

2.  Taylor, D.; Barengoltz, J; Jenkins, T.; Leschly, K.; and Triolo, J.: WF/PC Internal Molecular Contamination During System Thermal-Vacuum Test. 15th Space Simulation Conference, NASA CP-____, 1988. (Paper ____ of this compilation.)

3.  Extended Range TQCM Engineering Report, Revision C. FAR-78-012, Faraday Laboratories Inc., La Jolla, CA, April 24, 1986.

4.  Wide Range Convectron Vacuum Gauges from Granville-Phillips. Product Literature No. 275 177 100, Granville-Phillips Co., Boulder, CO, February 1987.

5.  Hansen, P.; Maag, C.; Argoud, M.; Barengoltz, J.; and Taylor, D.: Wide-Field/Planetary Camera Contamination Control Assessment. 15th Space Simulation Conference, NASA CP-____, 1988. (Paper ____ of this compilation.)

6.  Westphal, J.: Science Performance Summary. JPL Document No. D-5322 (CM-02), WF/PC I Delta Pre-Ship Review, April 6, 1988.
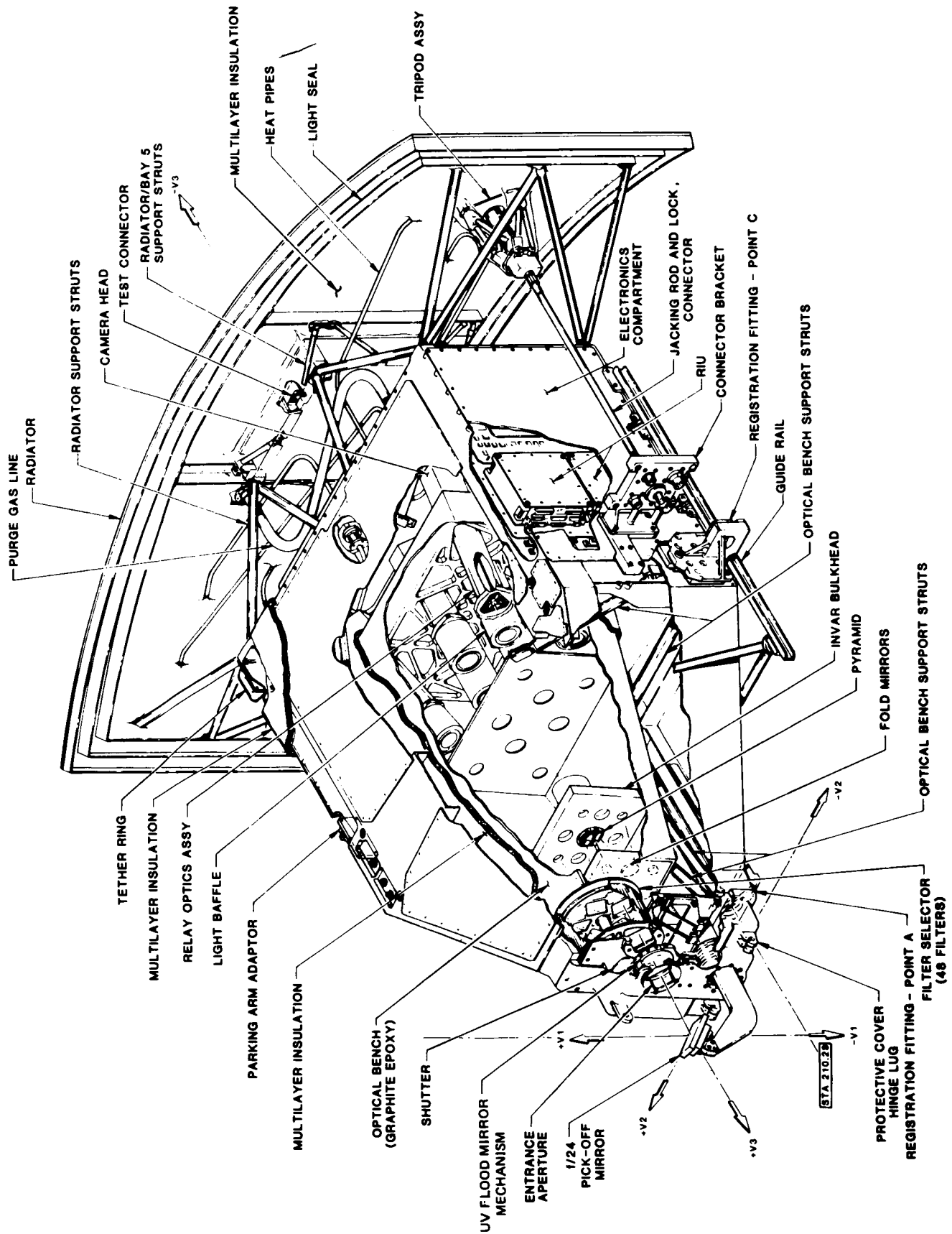
Figure 1. Wide Field/Planetary Camera Cutaway View

WITNESS MIRROR

THERMOCOUPLE
VACUUM
GAUGE

TQCM

10.1 in.

9.9 in.
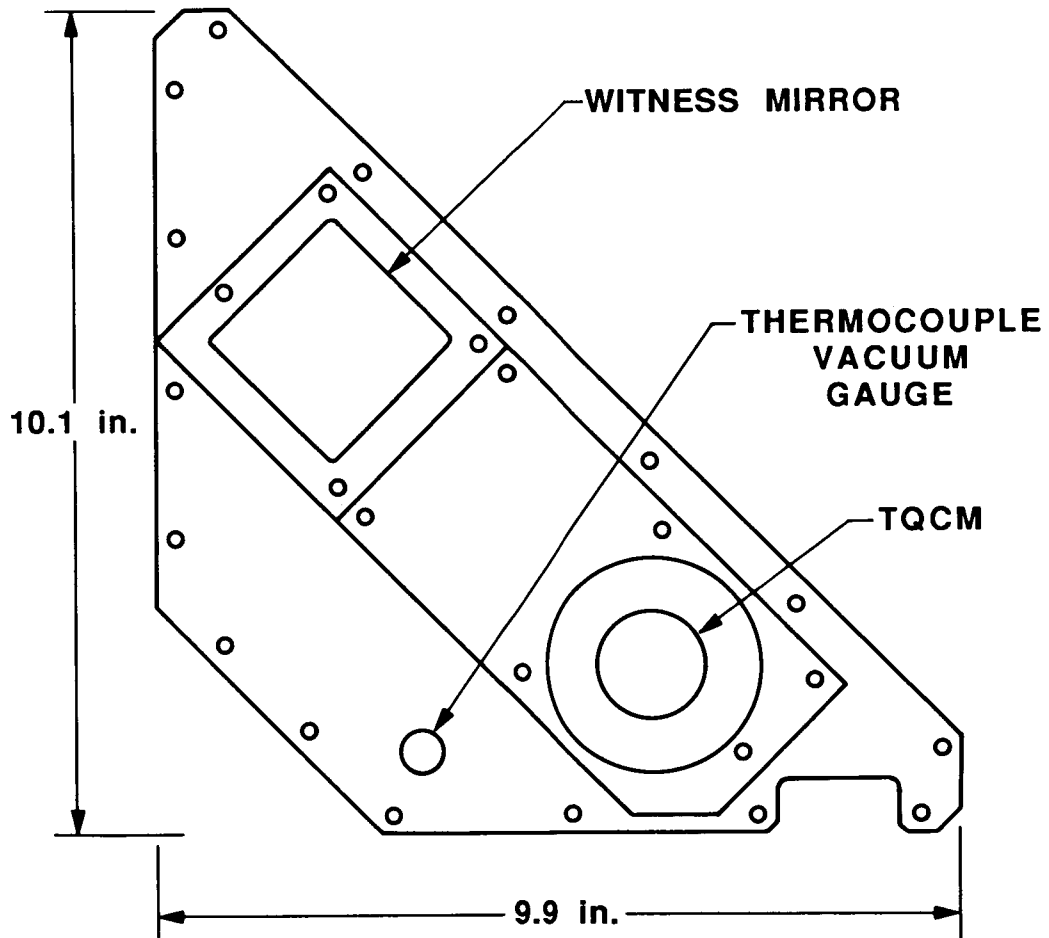
Figure 2.  WF/PC Access Plate

-V3

+V1

-V2

+V3

+V2

-V1
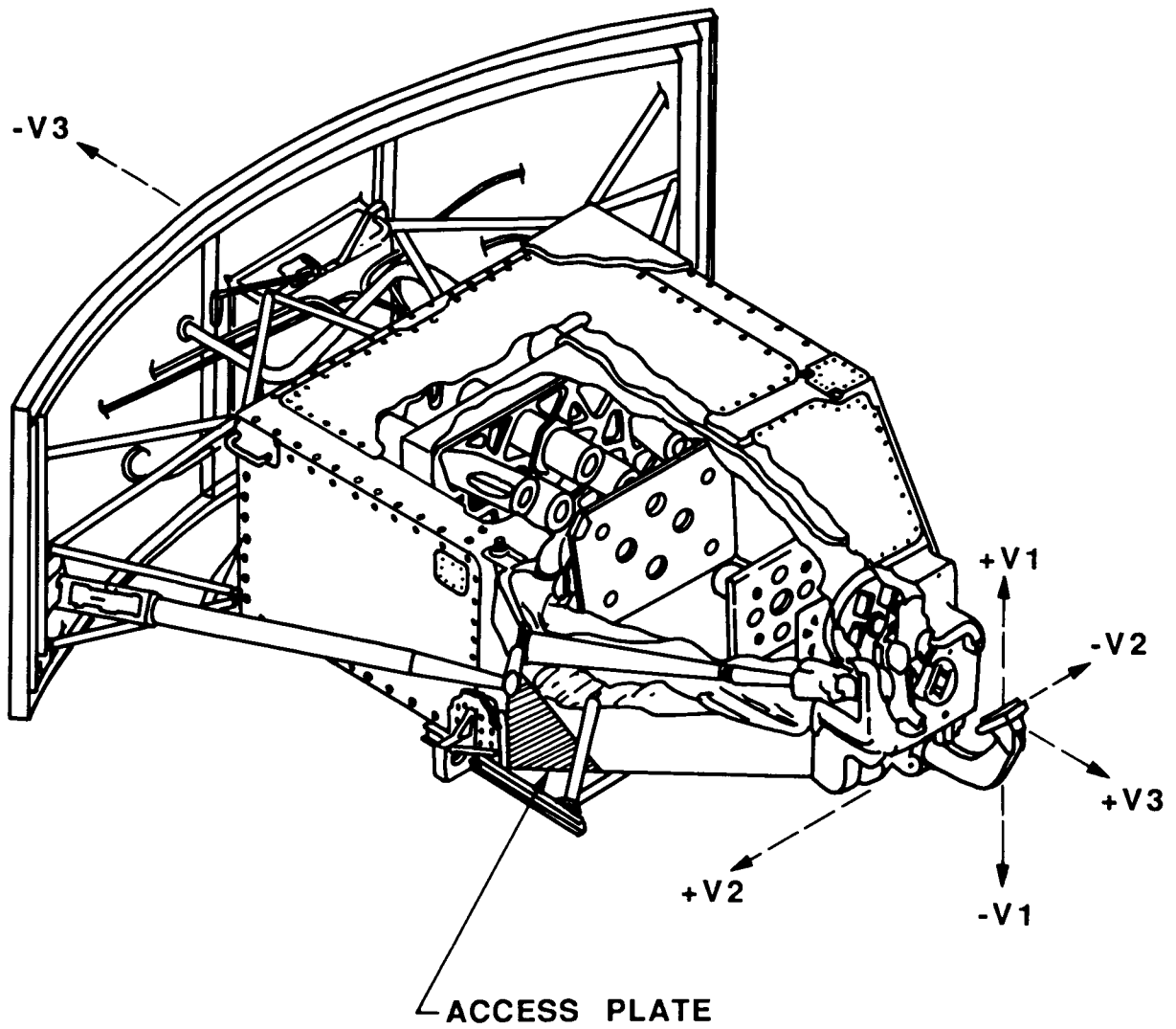
ACCESS PLATE

Figure 3.  Wide Field/Planetary Camera with Access Plate
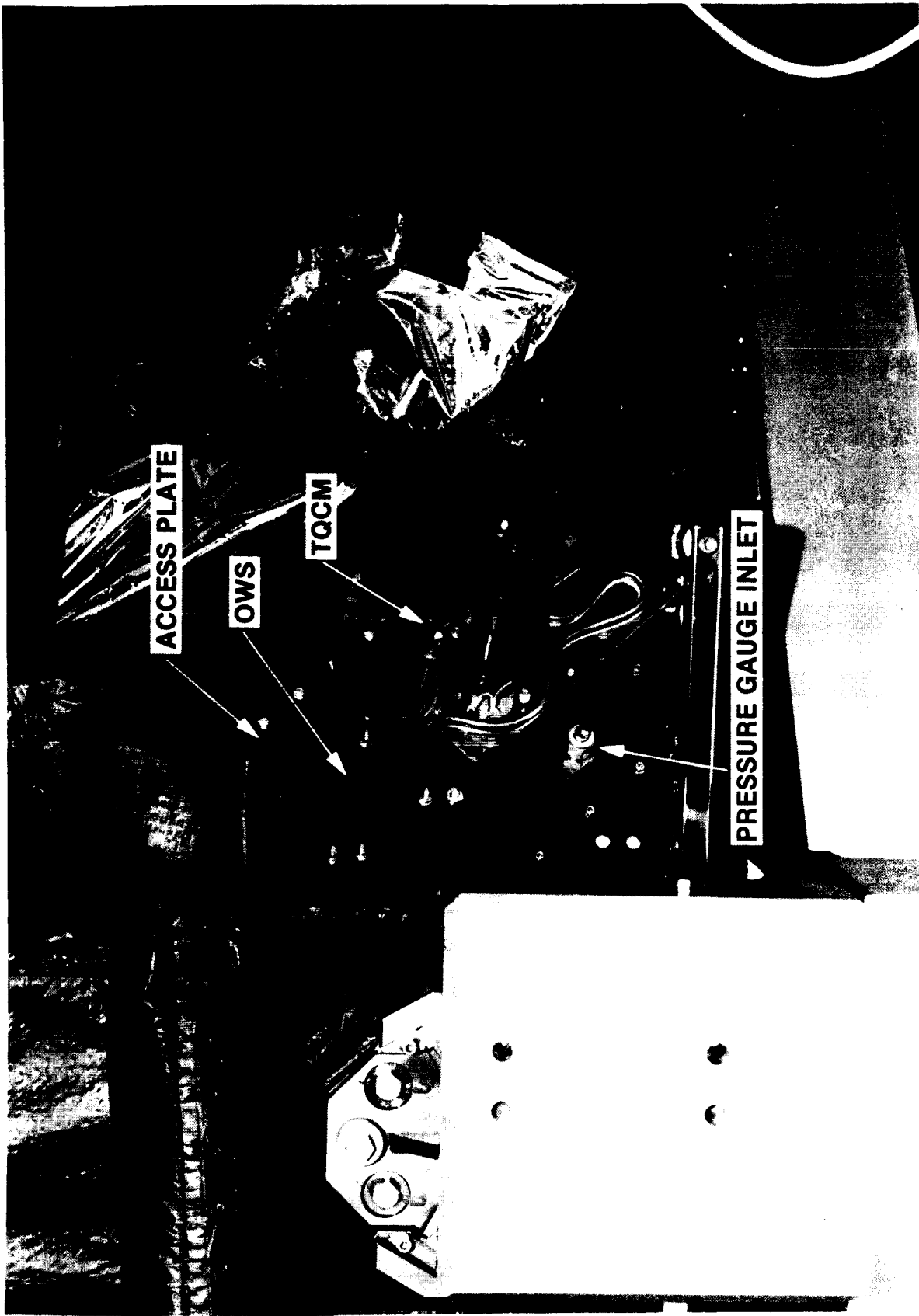
Figure 4. Access Plate Mounted on the Wide Field/Planetary Camera
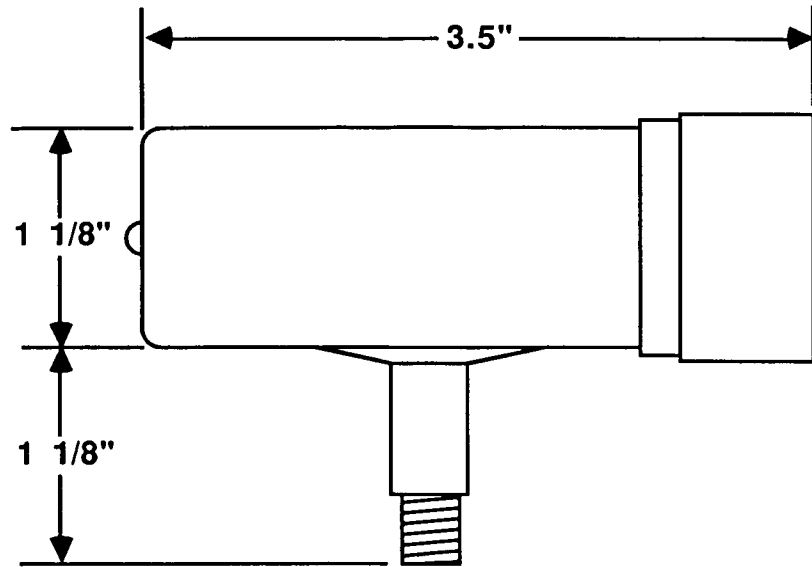
Figure 5.   Pressure Gauge
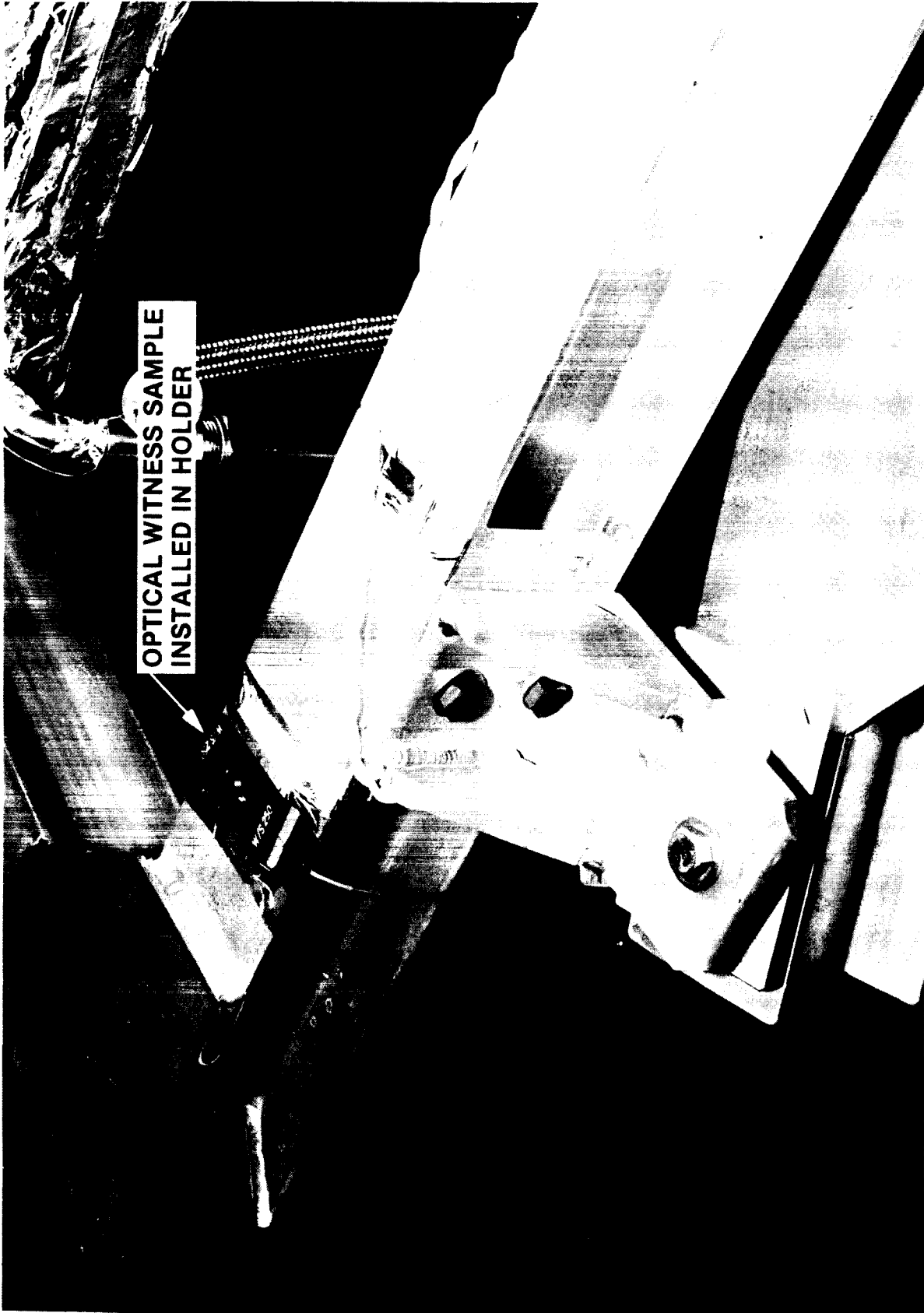
OPTICAL WITNESS SAMPLE
INSTALLED IN HOLDER

Figure 6. Wide Field/Planetary Camera Optical Witness Sample

25

Session II

# CONTAMINATION II

# CLASS 100 LARGE SPACECRAFT FACILITY

L.E. Ryan
TRW Operations & Support Group

## ABSTRACT

A new, large spacecraft dedicated clean facility has been built and is operating at TRW Space & Defense, Redondo Beach, California. The facility includes typical integration and test (I&T) and laboratory capabilities. Over 4500 square feet of HEPA filtered, air conditioned, hydrocarbon monitored, and personnel controlled working area is currently being used in state-of-the-art aerospace applications.

Design and construction of the facility, known as TF2 (for Test Facility #2), was sponsored by TRW's Space & Technology Group (S&TG). From the beginning, the purpose of the facility was to provide the company with the flexibility of providing very high levels of contamination control for its present and forthcoming contamination sensitive programs. To accomplish this goal, providing the necessary detail for the planning stages all the way through to present operating procedures and future enhancements were emphasized.

A private consultant was hired to assist in the preliminary design of the TF2 Clean Rooms (CR's). Because of energy requirements and space efficiency, HEPA filtered ceilings and side wall air returns — hence constituting a downflow — were selected. Large horizontal obstructions were projected as fixtures in these rooms and resultant eddy currents were computed as worse in a horizontal flow arrangement. Drawings were released ensuring proper materials and construction practices were applied. Upon completion, the consultant performed preoperation characterization of airflow and airborne particulate concentrations.

An automated Clean Room Monitoring System (CRMS) was purchased and set up to provide continuous monitoring of several environmental parameters of interest. Among these are airborne particulate concentrations (0.01 and 0.5 micron sensitivities), temperature, relative humidity, airborne hydrocrabons, and air (downflow) velocity. Parameters are measured 24 hours a day and recorded on a storage device for up to 4 months at a time.

Personnel entering these CR's have undergone training and contamination awareness sessions. Full Class 100 clean room outfits — hoods, coveralls, high boots, gloves, and facemasks — are required for entry. Paper, wood, painted surfaces, or other potential particle generating material is not allowed in the CR's. Anterooms and staging areas are provided to change garments and clean hardware for entry. Quarterly monitoring reports are submitted to program offices to ensure proper clean room maintenance and personnel procedures are implemented.

# CORRELATION STUDIES ON SURFACE
# PARTICLE DETECTION METHODS*

Ronald V. Peterson and James C. White
Hughes Aircraft Company

ABSTRACT

The accurate determination of dust levels on optical surfaces is necessary to assess sensor system performance. A comparison study was made on several particle measurement methods including those based on direct imaging and light scattering. The effectiveness of removing the particles from the surface prior to determining particle size distributions was also assessed.

These studies revealed that some methods, especially those requiring particle removal before analysis, are subject to large systematic errors affecting particle size distributions. Thus, an understanding of the particle measurement methods employed is necessary before any surface cleanliness or obstruction value assignments are accepted as true representation of an optical surface contamination condition.

## INTRODUCTION

Since the advent of optical and other contamination sensitive systems on board spacecraft, there has been a concern that particulate and molecular contamination would compromise the performance during the lifetime of the spacecraft. These concerns are not unfounded as decreased performance in some recent spacecraft has been attributed to contamination.

As the demand for greater cleanliness levels increases due to the higher performance requirements, so does the need to develop more sensitive, reliable methods for the measurement of surface particlate contamination.

In a previous SPIE paper[1] the current particle detection/analysis methods for spacecraft surfaces were discussed. Methods included detection and analysis of

30

particles directly on a surface, as well as those that require the removal of particles from the surface in order to perform the analysis. In certain instances the goemetry of the hardware may dictate that particles be removed for effective particle measurement.

In this paper, correlation studies will be discussed on work performed on some of these methods. The correlations were done by analyzing the same or similar sample populations with the different methods. Particle distributions were obtained and plotted in terms of cleanliness levels and obscuration or covering fraction (CF) values. Bidirectional reflectance distribution function (BRDF) scatter was also measured on some samples and compared with particle counting methods.

## SAMPLE WITNESS PLATES

Several sample witness plates were selected for use in the correlation study. These are listed in Table I. They were selected on the basis of optical materials used in spacecraft and witness samples typically used in monitoring cleanliness levels during spacecraft ground operations.

Table I    Sample Witness Plates for Dust Fallout

| | |
|---|---|
| Aluminum Mirrors on Glass Substrate with SiOx Overcoat   (CLM) | 1 x 1 inch<br>6 x 6 inch |
| Polished Glass<br>(CLBG)<br>(DMC) | 1 x 1 inch black<br>6 x 6 inch black<br>3 x 3 inch clear |
| Filter Paper<br>(CLF) | 47mm Diameter Millipore<br>Grided |

## PARTICLE POPULATION MEDIA

The sample witness plates were populated with particle fallout from a laboratory environment. The laboratory fallout, collected over a period of days, roughly followed a Mil-Std 1246A[2] distribution with fewer particles detected below 10μm and more detected above 50μm  than would be expected from the 1246A idealized distribution.

## DETECTION/ANALYSIS METHODS

The particle detection/analysis methods listed in Table II were used in the correlation study. The methods tested included direct measurement of the witness samples such as photography, microscopy, and light scattering and an indirect method which involved a solvent flush of the surface to remove the particles with subsequent particle analysis by microscopy or automatic particle counting.

TABLE II  Particle Detection/Analysis Methods Used in Correlation Study

|  | SAMPLE TYPE |
| --- | --- |
| Stereo Optical Microscopy | Fallout and rinses collected on Filter Paper |
| Optical Microscopy | Fallout and rinses collected on Filter Paper |
| Photography | Mirror and Glass Samples |
| BRDF Scatter | Mirror and Glass Samples |
| Automatic Particle Counter | Rinses from Mirror & Glass Samples |

Following population of the witness sample with laboratory fallout, the samples were analyzed utilizing the scheme in Table III.

## DESCRIPTION OF METHODS

### OPTICAL MICROSCOPY

Optical microscopy is a standard method used to count particles on substrates. It is most effective on grided filter paper where particle populations can be counted within defined areas. Two optical microscopy methods were used to count particles. One, using a light microscope with oblique lighting, follows the ASTM F312 method. Particles are observed at 100x for the smaller size particles and 40x for the larger ones. The second method, developed in the Hughes Contamination Physics Laboratory of the Optical Technology Department, uses a stereo microscope with grazing incident lighting of the sample surface. Magnification is about 70.

The two microscope methods were compared as part of this correlation study.

TABLE III          Particle Detection Correlation Scheme

Particle Fallout

```
    Mirror              Black              Clear              Filter
                        Glass              Glass              Paper
      |                   |                  |                  |
      v                   v                  v                  v
  Photography ────────Photography       Photography         Microscopy
      |           |
      |           |
      v           v
  Light Scatter   Light Scatter         Flush Filter
  Measurements    Measurements          Microscopy
                  |
                  |
                  v
```

Flush, Filter Microscopy

        or

Flush, Automatic Particle
        Counting

33
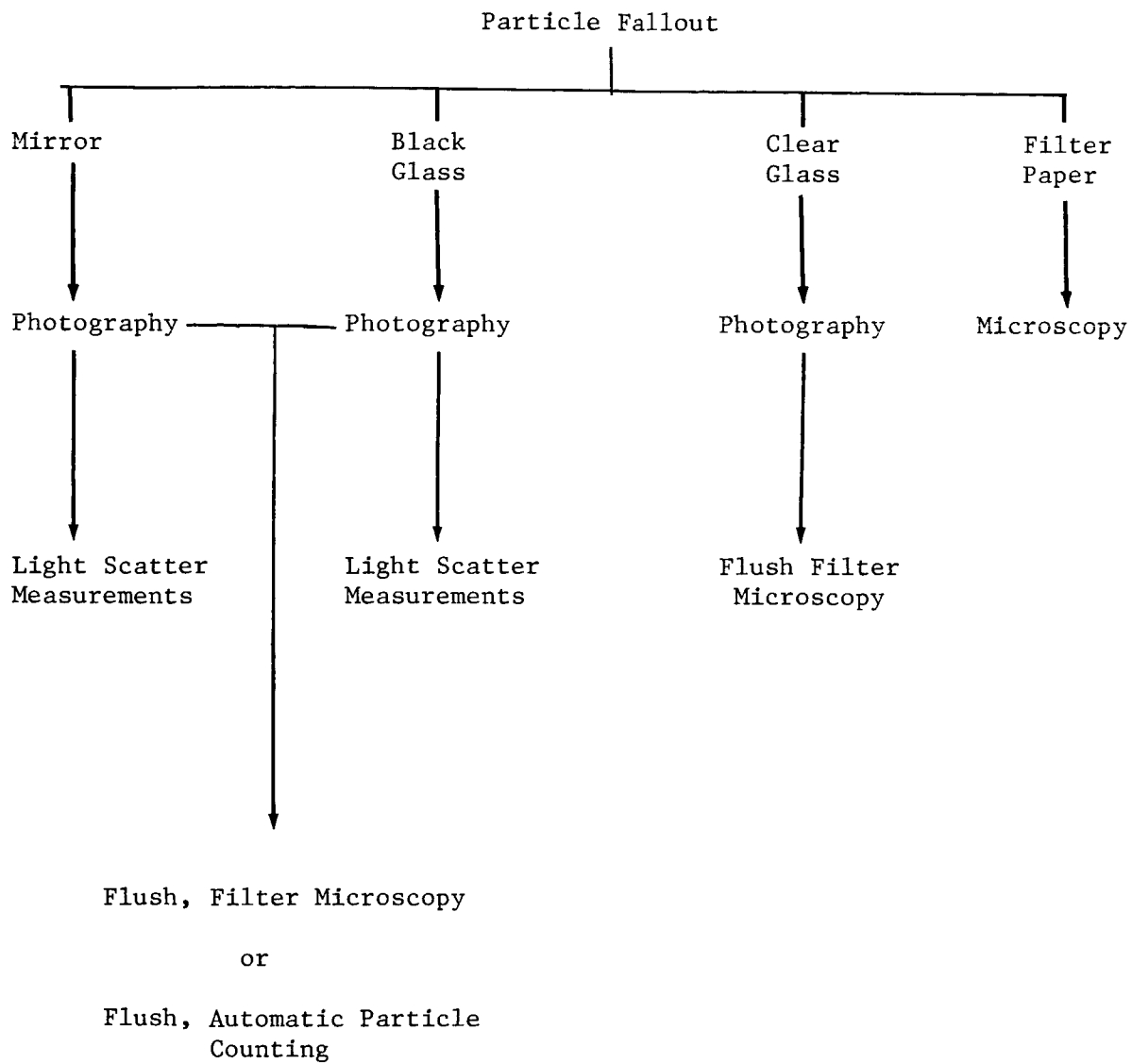
## PHOTOGRAPHIC/CAMERA METHOD

The photographic/camera system used in the Hughes contamination Physics Laboratory has a Polaroid enlargement camera equipped with a MD-4 shutter and a Nikkon 55MM macrolens. Photographs of particles on mirror or glass surfaces are taken at a magnification of 10 on Polaroid type 55 film giving a 0.4 by 0.45 inch frame. The developed negative is projected onto a grided surface and the particles sized and counted at an overall magnification of 100.

## BIDIRECTIONAL REFLECTANCE DISTRIBUTION FUNCTION (BRDF) SCATTER

BRDF is an optical function which describes the scattering properties of a surface. Scattering is due to surface irregularities or imperfections as well as contamination. Contamination will scatter part of the incident radiation with an intensity which depends on direction. BRDF is obtained from the quantification of the spatial distribution of the scattered energy.

The Hughes Optical Technology Scatterometer Laboratory has the capability of measuring BRDF on various size and configured mirror and glass witness plates and optical components at several wavelengths including 351.1, 514.5, 632.8nm and 1.06, 3.39 and 10.6μm. Surface cleanliness levels and covering fraction or obscuration values are related to the BRDF measurements and the particle measurements were used to study and correlate the relationship.

## SURFACE FLUSH METHODS

A standard method for evaluating hardware cleanliness calls for flushing the surface with solvent to remove the particles, then filtering and counting the particles on the filter paper using a light microscope. This method is widely used in the spacecraft contamination community to ascertain and monitor hardware cleanliness levels. This method was followed to provide data on particle populations on glass and mirror surfaces following flushing.

The surface flush method is also used to obtain samples for measurement in the liquid particle counter. In this case the solvent flush is directly measured in the automatic counter.

Approximately 100 ml of filtered IPA solvent under 25 PSI pressure was directed onto the sample surface and thoroughly flushed. The collected solvent flush was filtered for microscopic analysis of the particles on the filter or measured directly in the liquid particle counter/analyzer.

## LIQUID PARTICLE COUNTER

The liquid particle counter works on the principle of light scattering from particles. Light from a source (generally a laser) passes through a known volume of liquid and the scattered light from the particles in the moving fluid are collected on a detector and recorded in intensity bins which relate to particle size (area).

A serious problem with these instruments is that of diminishing sensitivity to larger particles ($>25\mu m$) and those that have similar indices of refraction as the

fluid system.

Bubbles in the sample fluid are also a problem in that they are counted as particles. A pure prefiltered bubble-free fluid must be used as a carrier, otherwise very high particle backgrounds will be encountered.

The automatic counter used in this study was a HiAC/Rayco model 4100.


## CONTAMINATION OF WITNESS SAMPLES

Three experiments were performed for the purpose of collecting laboratory fallout samples.

The experimental conditions, witness sample types and particle analysis methods used are shown in Table IV.

The three experiments or data sets from laboratory fallout were taken by placing the witness samples plates and filter papers on top of a wall cabinet in one of our laboratories. The 400 square foot room has filtered inlet air flowing from ceiling ducts. The working laboratory is not classified as a clean room.


## PRESENTATION OF DATA

The particles imaged using the photography and microscopy methods were manually counted and placed into size bins according to their particle diameter. The size bins chosen were 5-10, 11-25, 26-50, 51-100, 100 and 200 (fibers) $\mu$m. The counting procedure for the two methods was thus standardized and the obscuration or covering fraction values and cleanliness levels were calculated from this data.

This obscuration or covering fraction data were obtained from the particle size distributions by multiplying the average area (from the mean diameter in the bin) by the total number of particles in a bin. All the particle areas in the bins were summed to give a total particle area which is then expressed as a fraction of the total area sampled.

Mil-Std 1246A defines the product cleanliness levels on the basis of the number of particles of given size on a surface per square foot. The number of particles per square foot of surface, for all particles of the specified size and larger, plot as a straight line on the log vs. log$^2$ scales as shown in Figure 1. The particulate cleanliness level is defined by the line crossing the abscissa.

The particle size data from microscopy and photography were plotted on the 1246A format to compare cleanliness level for the different fallouts and analysis methods. Data from the surface flushed samples were treated in an identical manner as the photography and microscopy data.

The light scatter data is reported as total integrated scatter (TIS) over a 2 to 60$^o$ scattering angle. Laser light (514.5nm) is incident upon the sample at 5$^o$ off the normal. The BRDF data is discussed in a later section.

TABLE IV          Contamination Experiments Laboratory Particle Fallout

| Exposure Time | Sample No. | Substrate | Analyses |
|---|---|---|---|
| **Experiment No. 1** | | | |
| 10 Days | CL1 | Al Mirror | P, LS |
| | CL2 | Black Glass | P, LS |
| | CL6M1 | 6 x 6" Al Mirror | FFLM, FPC |
| **Experiment No. 2A** | | | |
| 7 Days | CLM3 | Al Mirror | P |
| | CLBG3 | Black Glass | P |
| | DMC | 3 x 3" Clear Glass | P |
| **Experiment No. 2B** | | | |
| 12 Days | CLM3 | Al Mirror | P |
| | CLBG3 | Black Glass | P |
| | DMC | 3 x 3" Clear Glass | P |
| **Experiment No. 2C** | | | |
| 15 Days | CLM3 | Al Mirror | P, LS |
| | CLM4 | Al Mirror | P, LS |
| | CLBG3 | Black Glass | P, LS |
| | CL6BG1 | 6 x 6" Black Glass | P,FFLM,FPC |
| | DMC | 3 x 3" Clear Glass | P, FPC |
| | CLF2 | Filter Paper | LM |
| | CLF3 | Filter Paper | LM, SM |
| **Experiment No. 3** | | | |
| 7 Days | CL2M1 | 2 x 2" Al Mirror | P, LS |
| | CL2BG1 | 2 x 2" Black Glass | P, LS |
| | DMC | 3 x 3" Clear Glass | P |
| | CLF20 | Filter Paper | SM |

Analysis Symbols

   P – Photography
  LS – Light Scattering
  IM – Light Microscope
  SM – Stereo Microscope
FFLM – Flush, Filter, Light Microscope
 FPC – Flush, Particle Counter

## RESULTS

### LABORATORY FALLOUT

The initial laboratory fallout experiment consisted of exposure of two mirrors and a black glass substrate to 10 days fallout. The results of the particle analyses are shown in Table V where the obscuration or covering fraction (CF) values have been calculated from the particle size distributions. Light scatter (TIS) data was obtained on one sample. It can be immediately seen that the flush, filter, microscopy and the flush, automatic particle counter methods give dramatically lower CF values that those obtained by the photography method.

| TABLE V | Laboratory Fallout – Experiment 1 – 10 days | | |
|---------|-------------------|------------------|-------------------|
| Sample | Method of Analysis | % Covering Fraction | Total Integrated Scatter |
| CL1AL | Photography | 0.18 | 2.65 X $10^{-3}$ |
| CL1BG | Photography | 0.2 | |
| CL6M1 | Photography | 0.35 | |
| | Flush, Filter, Microscopy | 0.012 | |
| | Flush, Automatic Particle Counter | 0.008 | |

Figure 2 shows plots of cleanliness levels obtained from the particle analysis data. The top curve is from the photography measurements on the 6 x 6 inch aluminum mirror. The other two curves represent data obtained from flushing and analyzing the particles from the surface of the mirror following photography. Half of the flush was filtered and the particle counted using optical microscopy. The other half of the flush was analyzed using the liquid automatic particle counter. All particle distributions were normalized to a one square foot area for presentation with the 1246A curves. The brackets represent photographic data from a 1 x 1 inch mirror and a 1 x 1 inch black glass sample that were exposed simultaneously with the large mirror.

While the photographic method gives reasonable correlation with the idealized 1246A curves in the mid particle sizes, the flush and analysis methods give large departures from the idealized curves and, of course, the photography measurements.

The photography method shows the cleanliness level at about 600-700 and CF (covering fraction) of about 0.2 to 0.3%. The flush/microscopy method gave a cleanliness level of about 300 and only about 0.01% CF. Thus, if the flush data were to be believed, a component or the optical sample would pass as clean

when, in fact, the samples even appear dirty.

The CF and TIS data obtained from particle analysis samples exposed in experiment 2 is shown in Table VI. The data shows an increase in the number of particles (CF) with lengthening exposure to the lab environment as would be expected.

The total integrated scatter (TIS) and the covering fraction data show good agreement for laboratory fallout. The black glass data, however, reveal about an order of magnitude less TIS for a given covering fraction, due to absorption of scattered light by the black glass. Figure 3 is the cleanliness data from the 15 day experiment (Exp. 2C). The data show an increase in the number of particles (CF) with lenthening exposure to the lab environment as would be expected. There is good agreement between particle distribution obtained on the mirror and the black glass samples. The photographic results results from the glass plate (DMC) showed fewer particles but were in reasonable agreement with the CLM3 and CLBG3 particle size distributions.

The cleanliness levels plots of microscopy measurements from the filter paper exposed to the fallout are shown in Figure 4. The CF and cleanliness levels show that fewer particles were collected or observed on the filter papers than on the mirrors and blackglass. It can be seen from Figure 4 that the light microscope (ASTM methods)cleanliness level was lower (showed fewer particles) than the stereo method with grazing incident light. This was especially evident at the smaller particle region of the graph. This difference was attributed to the difficulty associated with seeing particles that are not properly illuminated. Grazing incident light is much superior to light illumination at $45^{o}$ to the surface when observing small particles on a surface because it results in better optical contrast.

Even with grazing incident light (and also the photographic method) the particle population drops off from the 1246A idealized curve as the particle size drops below 25um. While it may be true that there are fewer particles falling out below 25um than would be suggested by the idealized curves, some or most of the tail-off is probably due to increasing difficulty in observing smaller particles.

The increase in particle population in the large particle sized that would be expected (from 1246A) is likely a result of man-generated particles and fibers from activities inside the room that are not expected in idealized situations but very much expected in real situations! Few particles are counted in the large-size region (above 100$\mu$m) and, therefore, are not considered to be statistically representative.

When the method of particle analysis involved the removal of particles using a solvent flush an even more dramatic decrease in particle population was noted as can be seen in Table VI and Figure 5. These results corroborate the results obtained from Experiment 1 where the solvent flush method also gave unreasonable CF and cleanliness levels from the contaminated samples.

The data showed that rinsing does not effectively remove all particles from a surface and that low values of particle concentration can be expected when this method is employed. It appears from the data that the larger particles are more efficiently removed by flushing that the smaller particles. Rinsing a surface, filtering the rinse and microscopic evaluation does not give good results, however, rinsing, followed by liquid particle counting is even worse as the results in Figures 2 and 5 reveal.

TABLE VI          Laboratory Fallout - Experiment 2

| Sample | Method of Analysis | % Covering Fraction | Total Integrated Scatter |
|---|---|---|---|
| **Experiment 2A (7 Days)** | | | |
| CLM-3 | Photography | 0.25 | |
| CLBG-3 | Photography | 0.20 | |
| DMC | Photography | 0.10 | |
| **Experiment 2B (12 Days)** | | | |
| CLM-3 | Photography | 0.41 | |
| CLBG-3 | Photography | 0.34 | |
| DMC | Photography | 0.26 | |
| **Experiment 2C (15 Days)** | | | |
| CLM-3 | Photography | 0.54 | |
| CLBG-3 | Photography | 0.46 | $4.03 \times 10^{-4}$ |
| DMC | Photography | 0.39 | |
| DMC | Flush, Filter, Microscopy | 0.2 | |
| CL6BG--1 | Photography | 0.53 | $2.83 \times 10^{-4}$ |
| CL6BG-1 | Flush, Filter Microscopy | 0.02 | |
| CL6BG-1 | Flush, Filter Microscopy | 0.02 | |
| CL6BG-1 | Flush, Filter Auto Particle Counter | 0.004 | |
| CLF-3 | Stereo Microscope | 0.29 | |
| CLF-3 | Stereo Microscope | 0.14 | |

A Hiac/Royco automatic particle counter was used to measure the particle size distribution in one-half the rinse from CL6BG1. The small and large particle sizes are extremely low compared to the photographic and microscopic methods. This is attributed to the rinse not efficiently removing the small particles and the analyzer being insensitive to the larger ($>20\mu m$) particles.

Data from experiment 3 is shown in TABLE VII.

These data verify what was found in the first and second experiment, namely that:

1) Photography gives particle distribution that are reasonable for the type and length of fallout.

2) The mirror and black glass samples give similar results.

3) The cleanliness level plots follow the Mil-Std 1246A in the mid particle range (25 - 100$\mu m$) but are lower in population in the smaller and higher in the larger particle regions than predicted in 1246A.

TABLE VII          Laboratory Fallout - Experiment 3, 7 Days

| Sample | Method Analysis | % Covering Fraction | Total Integrated Scatter |
|--------|-----------------|---------------------|--------------------------|
| CL2M1 | Photography | 0.31 | $1.67 \times 10^{-3}$ |
| CL2BG1 | Photography | 0.23 | $1.6 \times 10^{-4}$ |

LIGHT SCATTERING

The results of the BFDF scatter measurements on the laboratory fallout samples are shown in Figures 6 - 8. Figure 6 is the data from the CL2M1 and CL2BG1 samples from Experiment 3. Clean black glass and mirror samples are shown for comparison.

Black glass gives about an order magnitude less scatter than the mirror samples that were used in this study. It is interesting to see that the increase in scatter is greater at the larger scatter angles for all the contaminated samples, i.e., smaller particles are greater contributors to scatter at the larger angles.

Two samples, CLM-3 and CLBG-3 were scanned in five wavelength region for BRDF scatter. The BRDF data is presented in Figures 7 and 8. The visible and near IR curves are similar while the mid-IR curves (3.39 and 10.6$\mu m$) deviate by scattering relatively less in the high scatter angles and more in the mid-angle regions. It would be expected that the small particles would affect the high angle scatter less in the infrared due to the longer wavelength. A clean substrate background is also presented in the 15 day laboratory fallout curves.

## SUMMARY AND CONCLUSIONS

Several method of paritcle detection and analysis have been tested and correlated using particles from laboratory fallout. The methods included microscopy, photography, surface flush with microscopy, surface flush with liquid particle counting and BRDF scattering.

In comparing the microscopy and photographic technique it was found that photography gave somewhat higher particle counts.

The microscopy method, which generally gave lower counts in the less than 25um region, was improved when a stereo microscope with grazing incident light was used to illuminate the particles for viewing.

Flushing of the surface with a solvent gave lower particle populations when the filter/microscopy method was used for counting and very much lower results when automatic particle counting methods were used. Flushing does not appear to effectively remove the smaller lower particle sizes and skewed the results when plotted on a Mil-Std-1246A curve.

Laboratory fallout generally followed the 1246A curve between 10 and 50μm with lower populations detected at the smaller (below 10μm) particle sizes.

The fewer smaller particles was partially attributed to difficulty in detection of smaller particles while the higher population of large particles was attributed to normal activity in an uncontrolled (cleanliness speaking) laboratory environment.

BRFD is an effective way of detecting contamination on optical surfaces, however, the particle size distributions cannot be generated from BRDF data. The increases in BRDF were generally what was expected for the laboratory fallout. Hughes, however does have a computer program based on Mie scattering that calculates BRDF from particle populations. The predictions from this program closely matched the measured BRDF values for laboratory fallout in the visible region of the spectrum.

REFERENCES

1.    Peterson, R.V.:  Detection Methods for Particles on Optical Surfaces.
      SPIE  30th Annual International Technical Symposium on Optical and Opto-
      Electronic Engineering,  San Diego, CA.  17-22 August 1986.

2.    Mil-STD-1246A:  Military Standard Product Cleanliness Levels and Contamination
      Control Program.  18 August 1967.
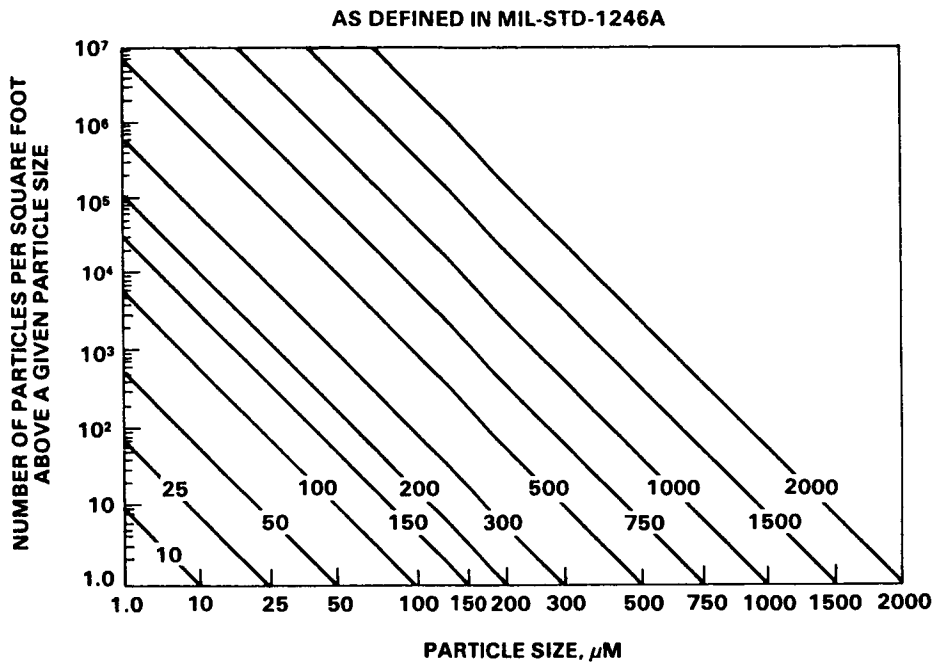
Figure 1.  Product Cleanliness Levels

COMPARISON OF PHOTOGRAPHY WITH SOLVENT FLUSH METHODS

AS DEFINED IN MIL-STD-1246A



A — PHOTOGRAPHY
B — FLUSH, FILTER MICROSCOPY
C — FLUSH, LIQUID PARTICLE COUNTER
I — OTHER SAMPLES (2) PHOTOGRAPHY
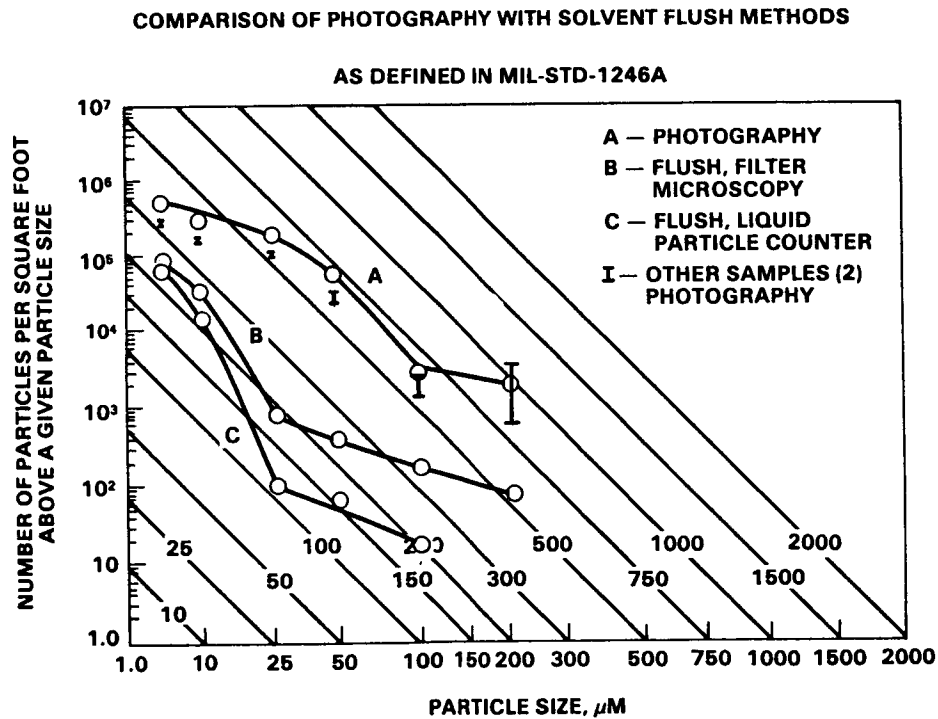
Figure 2.  10 Day Fallout Data

**PHOTOGRAPHY MEASURES LEVEL 600-700 FOR 15 DAY FALLOUT SLIGHTLY HIGHER FOR MIRRORS THAN GLASS SAMPLES**
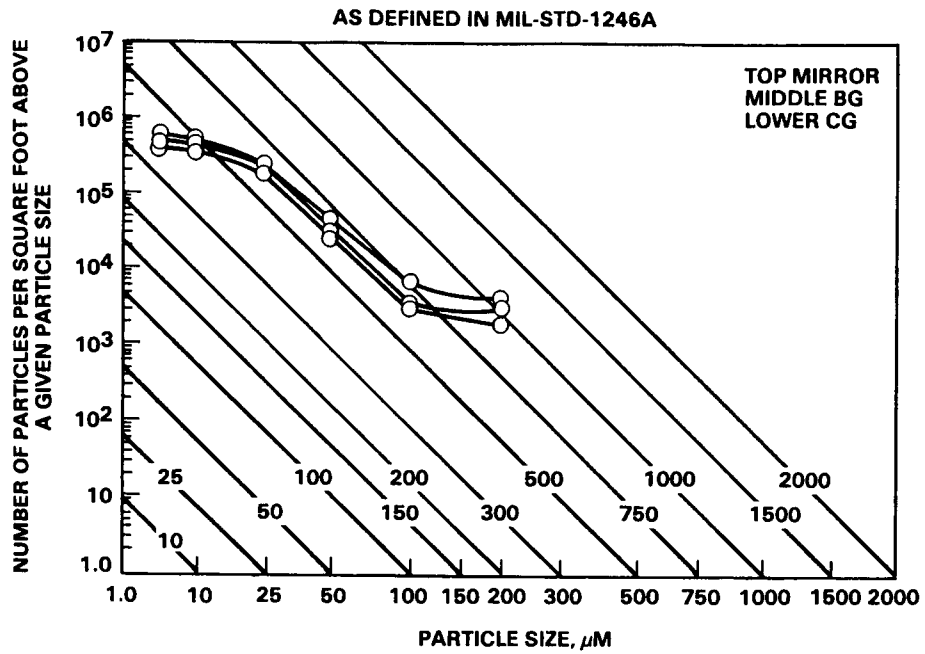


Figure 3. 15 Day Fallout Data

**LIGHT MICROSCOPE NOT AS EFFECTIVE AS STEREO MICROSCOPE OR PHOTOGRAPHY IN DETECTING SMALL PARTICLES**
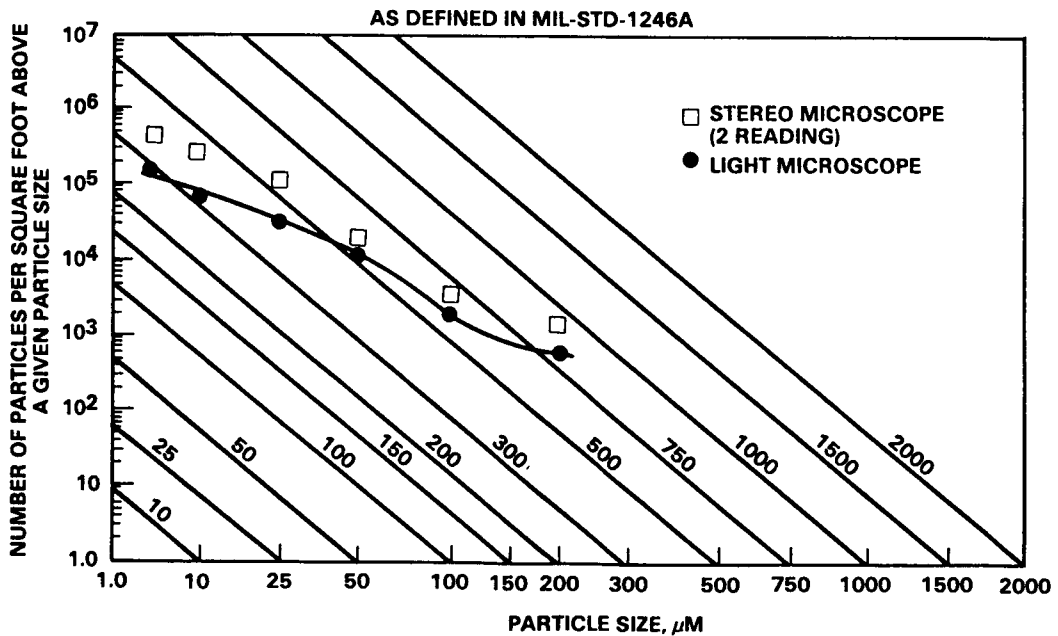


Figure 4. Comparison of Light Microscope and Stereo Microscope Particle Measurements

44

COMPARISON OF PHOTOGRAPHY WITH SOLVENT FLUSH METHODS
AS DEFINED IN MIL-STD-1246A
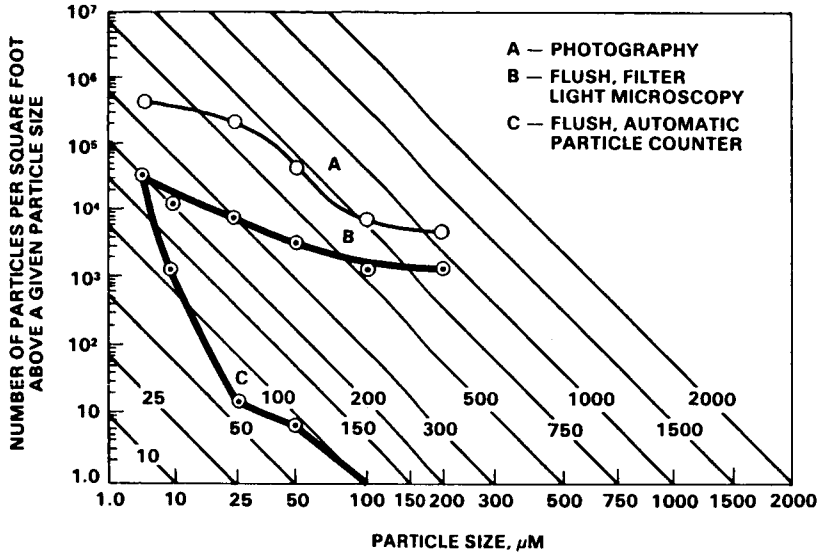
Figure 5.   15 Day Fallout Solvent Flush Data
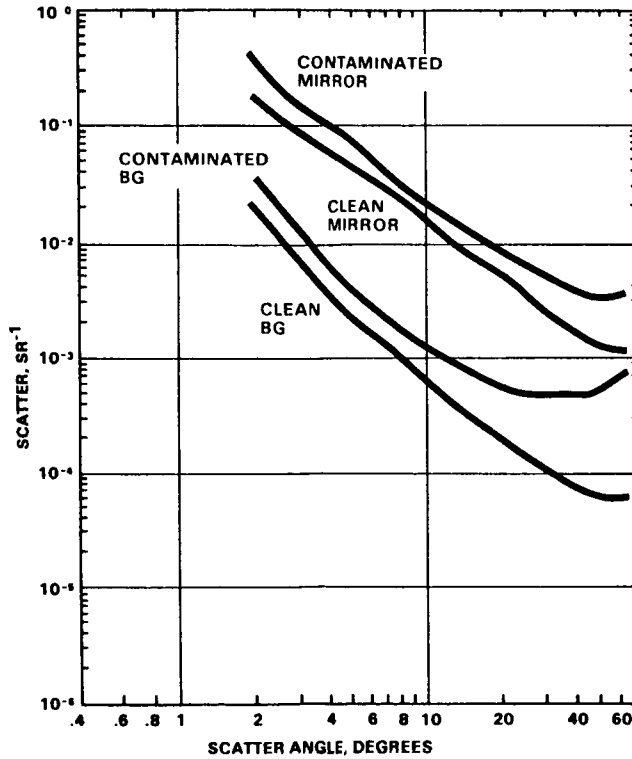
Figure 6.   BRDF on CL2M1 and CL2BG1   (Exp. 3)
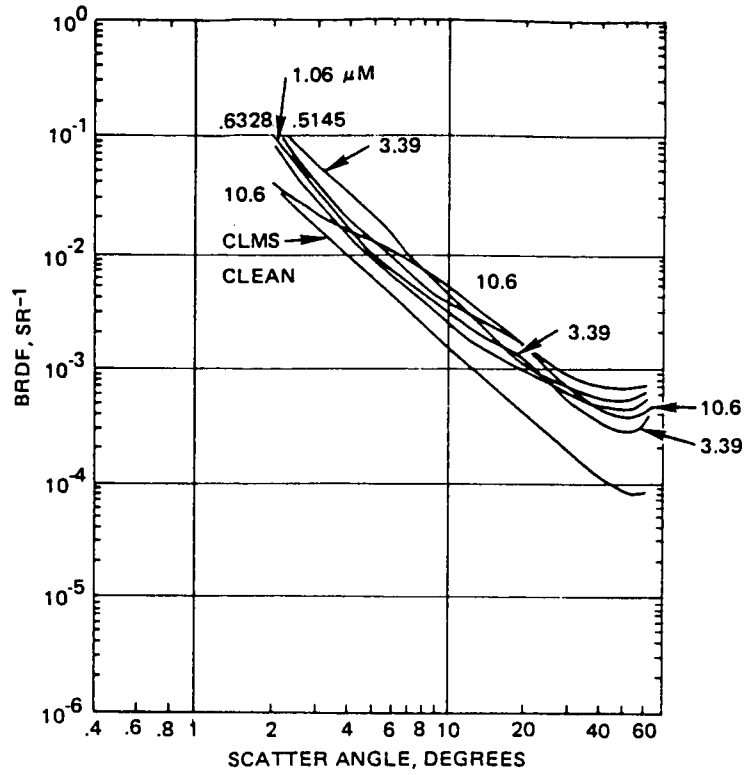
Figure 7. BRDF Measurements of CLM-3 for 5 Wavelengths
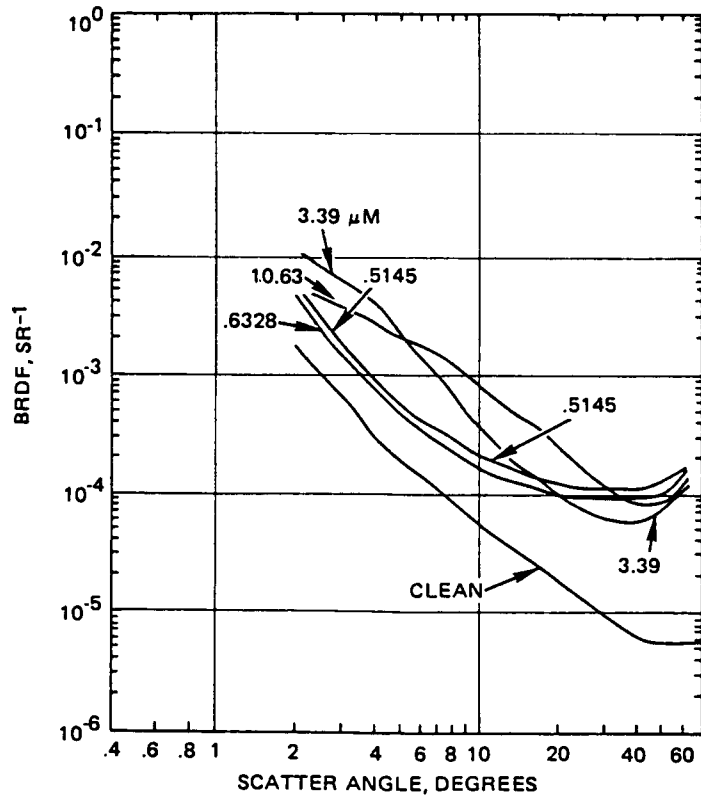


Figure 8. BRDF Measurements on CLBG-3 for 5 Wavelengths

46

# PRECISION CLEANING METHODS FOR SPACECRAFT APPLICATIONS

L. E. Ryan and H. Lindewall
TRW Operations & Support Group

## ABSTRACT

Carbon dioxide ($CO_2$) snow is being heralded as the latest innovative technology for cleaning micro and macro contamination from highly sensitive components as well as very fragile surfaces. TRW's Materials Engineering Department has constructed a small scale $CO_2$ snow cleaning apparatus to clean both molecular films and particles from small and large components and surfaces.

With assistance from Dr. Stuart Hoenig of the University of Arizona and Mr. William Weltmer of AIRCO Specialty Gases, the authors have developed a simple, low cost method of precision cleaning surfaces which may have been damaged or not cleaned well by other precision cleaning techniques (e.g., solvent wash, uv/ozone, oxygen ion/plasma, inert gas blowing).

Various types of surfaces were cleaned using the $CO_2$ snow technique. Vacuum deposited and sputtered metallic coatings such as germanium (Ge), aluminum (Al), and silver (Ag), silicon (Si) wafers, and polished copper (Cu) conical mirrors were purposely contaminated with everyday aerospace (manufacturing/laboratory facility) contaminants, including particle fallout and fingerprints. Precleaning characterization by Bidirectional Reflectance Distribution Function (BRDF), ellipsometry, nonvolatile residue, and microscopic particle evaluation served as evaluation of cleaning efficiency.

After initial characterization, contamination, and 2nd measurement, the samples were cleaned with $CO_2$ varying parameters such as stream length (exposure time) angle of incidence, and orientation of the sample. Post characterization followed by the aforementioned methods along with surface microanalysis by Scanning Auger Microscopy/X-ray Photoelectron Spectroscopy (SAM/XPS) and Scanning Electron Microscopy (SEM).

Good results have been obtained with this trial application. Feedback from several program offices which MED supports has been promising. The $CO_2$ cleaning process lends itself to application on small or large scales.

Session III

# ATOMIC OXYGEN

# THE NASA ATOMIC OXYGEN EFFECTS TEST PROGRAM

Bruce A. Banks, Sharon K. Rutledge, and Joyce A. Brady
NASA Lewis Research Center

## ABSTRACT

The NASA Atomic Oxygen Effects Test Program has been established to compare the low earth orbital simulation characteristics of existing atomic oxygen test facilities and utilize the collective data from a multitude of simulation facilities to promote understanding of mechanisms and erosion yield dependence upon energy, flux, metastables, charge, and environmental species. Program participants received characterized materials from a common source for evaluation in their atomic oxygen test facilities. Four materials chosen for this evaluation include Kapton HN polyimide, FEP Teflon, polyethylene, and graphite single crystals. The conditions and results of atomic oxygen exposure of these materials is reported by the participating organizations and then assembled to identify degrees of dependency of erosion yields that may not be observable from any single atomic oxygen low earth orbital simulation facility. To date, the program includes 30 test facilities. Characteristics of the participating test facilities and results to date are reported.

## INTRODUCTION

The long-term durability of low earth orbital (LEO) space systems will require the utilization of spacecraft materials which are compatible with the orbital environment. Atomic oxygen is one of the most threatening natural species in the LEO environment. Solar ultraviolet light of wavelengths shorter than 2,430 Å causes photodissociation of the diatomic oxygen present in the earth's upper atmosphere to produce atomic oxygen. Photodissociated atomic oxygen has a high probability of long-term survival between the altitutes of approximately 180 km and 650 km because there is an appropriate $O_2$ density here to facilitate reasonable atomic oxygen production and a low probability of interaction with neighboring atoms or molecules (fig. 1, ref. 1). Spacecraft orbiting the earth in near equatorial orbits ram into atomic oxygen atoms producing relative impact energies between 4.1 and 4.5 eV (fig. 2), which are high enough to break many chemical bonds of materials frequently used on spacecraft. Typical spacecraft materials such as Kapton polyimide, epoxy composites, organic paints, and silver are readily oxidized as a result of atomic oxygen exposure (table I, ref. 2). The identification and verification of atomic oxygen durable alternative materials or protective coatings for vulnerable materials for long-duration use in the LEO environment will require the development of atomic oxygen LEO simulation facilities to ensure environmental compatibility. As a result of the growing need for long-term space system durability in the LEO environment, numerous atomic oxygen LEO ground simulation facilities have been and continue to be developed.

The current level of understanding of atomic oxygen interaction mechanisms is significantly limited by the inability of any single test facility to produce the varied exposure conditions necessary to determine which

factors are important in the simulation of the LEO atomic oxygen environment to obtain results identical to those observed in space. As a result of the NASA Workshop on Atomic Oxygen Effects held November 10-11, 1986 in Pasadena, California, an atomic oxygen effects test program was initiated to improve this state of understanding in a coordinated manner (ref. 3).


ATOMIC OXYGEN EFFECTS TEST PROGRAM

The objectives of the NASA Atomic Oxygen Effects Test Program are:

O   to compare the LEO simulation characteristics of existing atomic oxygen facilities; and

O   to utilize collective data from a multitude of simulation facilities to promote understanding of mechanisms and erosion yield dependence upon energy, flux, metastables, charge, and environmental species.

This program is intended to further the understanding of atomic oxygen interaction mechanisms and simulation phenomena through collective information gathered from numerous simulation facilities and space test results. The wide variety of operating and environmental test conditions in LEO simulation facilities throughout the world may enable interaction dependencies to be more easily and economically understood than may be possible through the limited range of capabilities within any single test facility. This program is not intended to be a means for ranking simulation facilities, but instead is a means for collective information exchange and identification of simulation parameters which play a role in atomic oxygen interaction with materials. It is hoped that as a result of information exchanged through this program, that individual LEO simulation researchers will be able to more clearly identify the operating conditions which most closely simulate results obtained in space and will be able to accurately correlate ground test results with space test results.

The test program is open to all interested participants. Samples of characterized materials from common sources have been provided at no cost to the participants. Four materials were selected for evaluation:

O   Kapton HN polyimide, 0.002 inch (0.05 mm) thick

O   Fluorinated ethylene propylene (FEP Teflon), 0.002 inch (0.05 mm) thick

O   Polyethylene, low oxygen content, 0.002 inch (0.05 mm) thick

O   Graphite, single crystal

-   Highly oriented pyrolytic graphite (HOPG), monochrometer grade, 10 mm x 10 mm x 2 mm

-   Pyrolytic graphite, 25 mm x 25 mm x 2 mm

These materials were selected as a result of panel discussions held at the NASA Workshop on Atomic Oxygen Effects, November 10-11, 1986. The basis for selecting these materials was that erosion yield quantification data already exists for Kapton H, FEP Teflon, polyethylene, and graphite from STS-8 and earlier shuttle flights. Kapton HN polyimide was selected instead of Kapton H because Kapton H is no longer readily available, and plans have been made to use Kapton HN for Space Station photovoltaic array blankets. In answer to the question of whether or not the erosion yield of Kapton H is identical to that of Kapton HN, the supplier of these materials, E. I. du Pont de Nemours & Co., Inc., has indicated that these two materials are chemically identical in spite of slight differences in optical properties. Two forms of graphite were chosen so that both surface profilimetry and weight loss could be used for erosion yield calculations. HOPG is more ideal for surface profilimetry, and pyrolytic graphite is best suited for weight loss measurements. Chemically characterized samples of the test materials have been supplied to approximately 30 participating facilities since February 10, 1988. Additional samples will be provided as requested to existing and new participants. The test materials are exposed in the participant's facility, and erosion yield and sample exposure information is then returned to the authors at NASA Lewis Research Center. The following list of information was solicited:

O    Flux, atomic oxygen atoms/($cm^2$ sec)

O    Fluence, total number of incident atomic oxygen atoms/$cm^2$

O    Energy, eV

O    Metastable state distribution, fraction of total incident atomic oxygen atoms in each state

O    Charged species population, such as flux of $O^+$ and $O_2^+$, etc.

O    Environmental gas species, such as $O_2$, $N_2$, He, Ar, etc.

O    Species partial pressure

O    Peak flux, for pulsed exposure systems

O    Energy distribution

O    Sample temperature

O    UV environment, wavelength versus intensity distribution

O    Sample surface preparation, if altered from "as received"

O    Oxygen purity, parts per million of contaminant gases

In addition to the sample exposure information, each participant was asked to provide any information concerning the effects of atomic oxygen exposure on the samples provided to them which they found through exposure in their

facilities or through post-exposure characterization. The information requested includes:

O    Erosion yield ($cm^3$ or grams)/(atom or ion)

O    Method of erosion yield measurement

O    Surface morphology: scanning electron microscopy (SEM)

O    Surface chemistry:

-    ESCA, EDAX, FTIR, and IR (and duration between atomic oxygen exposure and the specific characterization)

-    Ejected species (energy, etc.)

-    Surface energy

-    Dry run characterization (sample analysis before and after exposure in chamber without atomic oxygen exposure)

-    In situ characterization, such as AUGER

O    Mechanical properties: stress versus strain

O    Optical properties: reflectance, transmittance, absorptance, and emittance

Participants in the test program were also asked to provide information describing and characterizing their atomic oxygen exposure facilities. Submittal of data from exposure tests is intended to be an ongoing activity throughout 1988 and 1989. Facility characteristic and erosion dependence information will be sent to all contributing participants on a periodic basis. Thus, all participants will receive facility information and results of materials exposure that was provided from all the participating organizations.


## ATOMIC OXYGEN TEST FACILITIES

The NASA Atomic Oxygen Effects Test Program currently encompasses 30 atomic oxygen test facilities representing 22 organizations. A list of the facilities and participants can be found in table II. Figure 3 summarizes the generic types of simulation facilities which produce atomic oxygen in neutral ground or exited states. Figure 4 portrays the atomic oxygen flux and energy associated with test facilities listed in table II.


## CURRENT RESULTS

Although test results are just beginning to arrive, it is appropriate to summarize the results currently available. Sample exposure data has been received from six different atomic oxygen simulation facilities, including

four thermal energy facilities and two more energetic beam facilities. Because of the difficulty in quantifying atomic oxygen flux, erosion yields were compared to those of Kapton HN to extract some information about erosion yield dependencies for the various materials. Since most of the results to date are from asher or discharge type facilities, erosion yield dependence relative to Kapton for the various materials can be plotted as a function of environmental pressure for the asher or flowing afterglow facilities, as shown in figure 5.

To illustrate the comparison between space test and ground simulation results, horizontal lines have been drawn in figure 5 which represent the most commonly agreed upon space test results for erosion yields of the various materials relative to Kapton H (see table III). As can be seen from the data, all the facilities (thermal as well as energetic) report relative erosion yields of polyethylene which are substantially greater than those observed in space. The relative erosion yields of FEP Teflon compared to Kapton are also generally higher than those observed in space. However, the laboratory simulation results for pyrolytic graphite indicate slightly lower relative rates and one instance of near agreement. One might be inclined to propose that lower plasma asher operating pressures or lower power densities in plasma ashers more closely simulate space conditions with less proability of relative rate anomalies caused by the accelerated flux. However, as can be seen from the data, there is no clear trend indicating more agreement with space results as the operating pressure is reduced or RF power lowered.

It would be desirable to examine the dependence of erosion yields relative to Kapton as a function of flux for both ashers and directed beam facilities. However, because quantification of flux is very difficult in plasma ashers and neutral beam systems, another measure of flux which can be used is the erosion rate of Kapton HN per unit area. Although the erosion rate of Kapton HN per unit area may not necessarily be a linear indicator of atomic oxygen flux, it should at least be a monotonically increasing function of the flux. Figure 6 shows plots of erosion yields relative to Kapton versus Kapton HN mass loss rate per unit area. They depict both asher and directed beam results on one plot for each material. These plots indicate the relative erosion yields as a function of effective atomic oxygen flux as opposed to actual flux. If the actual erosion yield of Kapton HN increases with energy to the 0.68 power, as indicated by Ferguson (refs. 4 and 5), then the Kapton erosion yields in ashers (operated at 0.1 - 0.2 eV) would be reduced by a factor of 10 from those yields measured from space tests on STS-8 (4.4 eV). Kapton erosion yields of $0.3 \times 10^{-24}$ $cm^3$/atom in ashers would require an order of magnitude higher fluxes than in space to obtain the same recession rates as observed in space.

For comparative purposes, the results from the most commonly agreed upon space test results from table III are shown in the plot, not as a horizontal line, but as a data point at the actual STS-8 Kapton H mass loss rate per unit area. As can be seen in all the plots, there is no clear indication that decreasing erosion rate or flux tends to give any greater agreement with space results for the relative rates of various materials. As can be seen from the three plots in figure 6, polyethylene and FEP Teflon show erosion yields relative to Kapton that are generally higher than those

observed in space, and the relative erosion yields of graphite are lower than those observed in space. It is interesting to note that although some facilities are in near agreement with the space results for each material, no single facility is in near agreement for all materials.

Figure 7 shows the erosion yields of polyethylene, FEP Teflon, and pyrolytic graphite as a function of atomic oxygen energy. Because a limited number of types of facilities contributed to this data, the data points tend to cluster around the thermal energies of RF plasma ashers with limited energetic beam facility results. Space test results are also shown on these plots. As atomic oxygen beam facilities become operational, greater insight as to the dependencies upon atomic oxygen energy may be resolved. In addition, clarification of the relevance of charged or neutral oxygen might become discernable.

## CONCLUSIONS

The NASA Atomic Oxygen Effects Test Program has been established to compare the low earth orbital simulation characteristics of existing atomic oxygen test facilities and to utilize the collective data from a multitude of simulation facilities to promote understanding of mechanism and erosion yield dependence upon energy, flux, metastables, charge, and environmental species. To date, 46 participants representing 30 different atomic oxygen test facilities and 22 organizations are participating in this program. Although data has not yet been received from most of the program participants, preliminary results from two energetic beam facilities and four low energy thermal (or asher) facilities indicate no clear dependence of atomic oxygen erosion yield upon plasma asher operating pressure, effective atomic oxygen flux, or atomic oxygen energy.

## ACKNOWLEDGEMENTS

# REFERENCES

1. Banks, B. A., Mirtich, M. J., Rutledge, S. R., and Nahra, H. K.: Protection of Solar Array Blankets from Attack by Low Earth Orbital Atomic Oxygen. Paper presented at the 18th IEEE Photovoltaic Specialists Conference, October 21-25, 1985, Las Vegas, NV.

2. Banks, B. A., Rutledge, S. K., Merrow, J. E., and Brady, J. A.: Atomic Oxygen Effects on Materials. In the proceedings of the NASA/SDIO Spacecraft Environment Effects on Materials, Langley Research Center, June 28-30, 1988.

3. Brinza, D. E., Ed.: Proceedings of the NASA Workshop on Atomic Oxygen Effects, November 10-11, 1986, Pasadena, CA.

4. Ferguson, D. C.: The Energy Dependence of Surface Morphology of Kapton Degradation Under Atomic Oxygen Bombardment. In the proceedings of the 13th Space Simulation Conference, October 8-11, 1984, Orlando, FL.

5. Purvis, C. K., Ferguson, D. C., Snyder, D. B., Grier, N. T., Stastus, J. V., and Roche, J. C.: Environmental Interactions Considerations for Space Station and Solar Array Design, Preliminary, July, 1988.

## TABLE I. - ATOMIC OXYGEN EROSION YIELDS OF VARIOUS MATERIALS

| MATERIAL | EROSION YIELD, $10^{-24}$ $CM^3$/ATOM |
|---|---|
| Kapton H polyimide | 3.0 |
| Mylar polyester | 2.7 - 3.9 |
| Polyethylene | 3.3 - 3.7 |
| Epoxy | 1.7 |
| Polycarbonate | 2.9 - 6.0 |
| Polystyrene | 1.7 |
| Polysulfone | 2.4 |
| Urethane (black, conductive) | 0.3 |
| Silver | 10.5 |
| Carbon | 0.9 - 1.7 |
| Chemglaze Z306 (flat, black) | 0.35 |
| FEP Teflon | 0.037 |
| Aluminum | 0.0 |
| Copper | 0.0 |
| Gold | 0.0 |
| Platinum | 0.0 |
| $SiO_2$ | 0.0 |

# TABLE II. - ATOMIC OXYGEN TEST FACILITIES

| | ORGANIZATION | LOCATION | FACILITY DESCRIPTION | TEST PROGRAM PARTICIPANT |
|---|---|---|---|---|
| 1. | Alabama, University of | Huntsville, AL | Thermal A/O source | John Gregory |
| 2. | Auburn University | Auburn, AL | RF plasma excited N is reacted with NO gas to produce thermal ground state A/O | Charles Neely |
| 3. | Auburn University | Auburn, AL | RF plasma asher | Bruce Tatarchuk |
| 4. | Boeing Aerospace Co. | Seattle, WA | Low frequency RF plasma; samples located downstream from glow | Gary Pippin / Roger Bourassa |
| 5. | Case Western Reserve University | Cleveland, OH | Variable energy ion gun | T. G. Eck / Dick Hoffman |
| 6. | David Sarnoff Research Center | Princeton, NJ | Single grid, low energy ion source | Bawa Singh |
| 7. | General Electric - Space Division | Philadelphia, PA | Single grid ion source with charge exchange | Leo Amore / James Lloyd |
| 8. | Jet Propulsion Lab | Pasadena, CA | Formation of O⁻ by dissociative attachment. Electrostatic acceleration of ions to final energy, then photo-detachment of electrons from ions with a laser | Ara Chutjian / Otto Orient |
| 9. | Jet Propulsion Lab | Pasadena, CA | Pulsed laser induced breakdown followed by expansion through a nozzle | David Brinza / Ranty Liang |
| 10. | Lockheed Palo Alto Research | Palo Alto, CA | RF plasma asher | Matt McCargo |
| 11. | Los Alamos National Laboratory | Los Alamos, NM | Continuous laser heated discharge | Jon B. Cross |
| 12. | Martin Marietta Denver Aerospace | Denver, CO | Ion gun; magnet for charge/mass selection; multi stage aperture for beam deceleration; deflection | Gary W. Sjolander |
| 13. | McDonnell Douglas Astronautics Co. | Huntington Beach, CA | RF plasma system with Faraday cage | Esther H. Lan / C. A. Smith |
| 14. | NASA - Ames Research Center | Moffett Field, CA | Microwave discharge, multisample chamber | Larry L. Fewell |
| 15. | NASA - Ames Research Center | Moffett Field, CA | RF O₂ plasma; samples downstream from plasma glow | Morton Golub / Ted Wydevan |
| 16. | NASA - Ames Research Center | Moffett Field, CA | RF plasma with sample downstream from glow; sample is UV shielded | Narcinda R. Lerner |
| 17. | NASA - Johnson Space Center | Houston, TX | Flowing afterglow | Steven L. Koontz |
| 18. | NASA - Johnson Space Center | Houston, TX | RF plasma asher | Steven L. Koontz |
| 19. | NASA - Langley Research Center | Hampton, VA | RF plasma asher | Carmen E. Batten |
| 20. | NASA - Langley Research Center | Hampton, VA | Electron stimulated desorption from mesh | R. A. Outlaw |
| 21. | NASA - Lewis Research Center | Cleveland, OH | Electron bombardment gridless ion source | Bruce A. Banks / Sharon K. Rutledge |
| 22. | NASA - Lewis Research Center | Cleveland, OH | RF plasma asher run on air | Bruce A. Banks / Sharon K. Rutledge |
| 23. | NASA - Lewis Research Center | Cleveland, OH | Dissociation and ionization in tunable microwave cavity followed by electro-static acceleration | Dale C. Ferguson |
| 24. | NASA - Marshall Space Flight Center | MSFC, AL | Electron bombardment ion source with electromagnetic charge/mass selection downstream, then deceleration with charge neutralization and deflection of non-neutralized ions | Ralph Carruth / Jill Carhorl |
| 25. | Nebraska, University of | Lincoln, NE | RF plasma asher | John A. Woollam |
| 26. | Physical Sciences, Inc. | Andover, MA | Pulsed laser induced breakdown followed by expansion through a nozzle | George Caledonia / Robert Krech |
| 27. | Princeton Plasma Physics Laboratory | Princeton, NJ | Neutralization of ions formed in plasma by biased plate | William Langer / S. A. Cohen / D. M. Manos / R. W. Motley / M. Ono / S. Paul / D. Roberts / H. Selberg |
| 28. | Texas, University of | Austin, TX | Ion beam with charge exchange | Dennis Kohl |
| 29. | Toronto, University of (Aerospace Institute) | Downsview, Ontario Canada | Microwave generated plasma. Noble gas carrier transports A/O through skimmer to produce high flux density | Rod C. Tennyson |
| 30. | Vanderbilt University | Nashville, TN | Ion gun. Wein filter for charge state selection; deceleration of ions through system of grids; grazing incidence impact with polished nickel surface to neutralize ions. Electrostatic deflec-tion of non-neutralized ions | Royal Albridge / N. Tolk |

## TABLE III. – COMPARISON OF ATOMIC OXYGEN TEST PROGRAM MATERIALS PROPERTIES AND SPACE TEST RESULTS

| Material | Density, gm/cm$^3$ | Range of Erosion Yields from Space Tests, cm$^3$/atom 10$^{-24}$ cm$^3$/atom | Erosion Yield Most Commonly Agreed Upon from Space Tests 10$^{-24}$ cm$^3$/atom | Ratio Relative to Kapton H | Mass Loss Rate per Area on STS-8*, 10$^{-8}$ gm/(cm$^2$sec) |
|---|---|---|---|---|---|
| Kapton H or HN | 1.42 | 1.5 – 3.1 | 3.0 | 1.0 | 1.01 |
| Polyethylene | 0.918 | 3.3 – 3.7 | 3.3 | 1.1 | 0.715 |
| FEP Teflon | 2.15 | 0.0 – 0.5 | 0.037 | 0.012 | 0.0188 |
| Pyrolytic graphite | 2.2 | 0.9 – 1.7 | 1.2 | 0.40 | 0.623 |
| Highly oriented pyrolytic graphite | 2.26 | 0.9 – 1.7 | 1.2 | 0.40 | 0.640 |

\* Assuming STS-8 flux = 2.36 x 10$^{15}$ atoms/(cm$^2$sec)
or fluence = 3.5 x 10$^{20}$ atoms/cm$^2$
and exposure duration = 41.17 hours
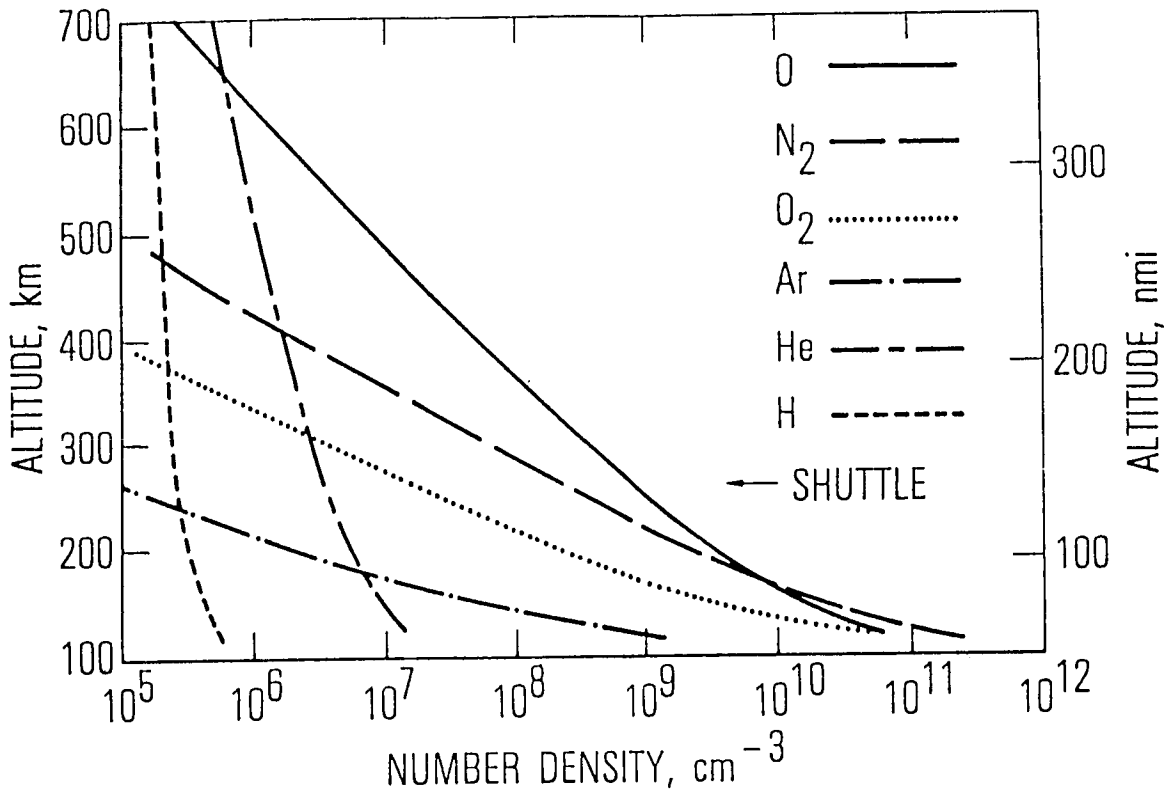
**FIGURE 1 – LOW EARTH ORBITAL ENVIRONMENT**
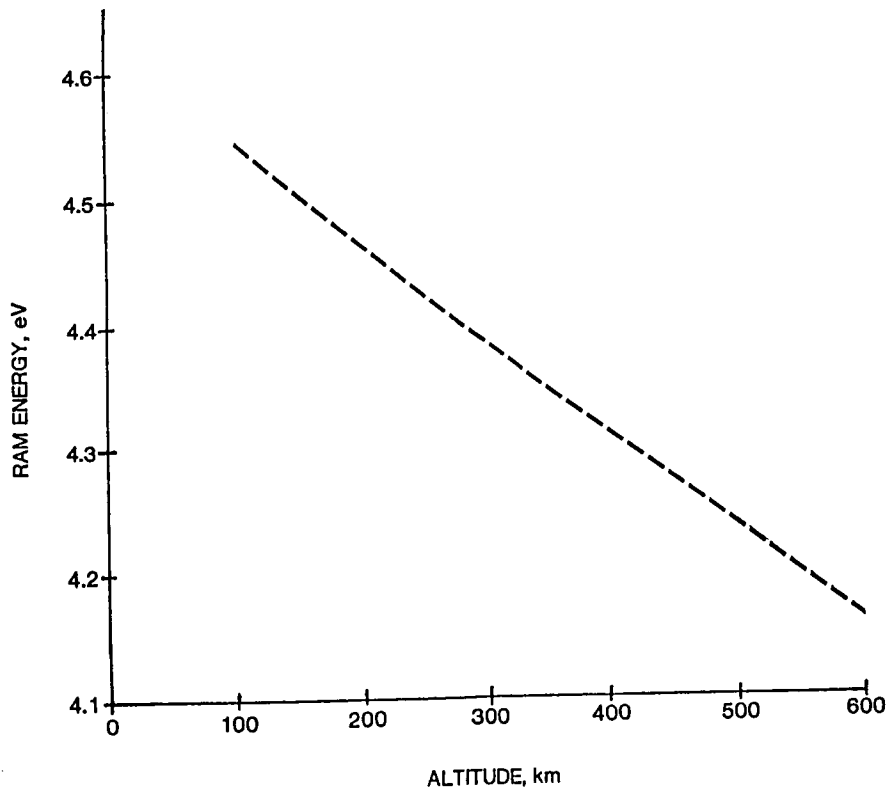


**FIGURE 2 – ATOMIC OXYGEN RAM ENERGY DEPENDENCE UPON ALTITUDE**
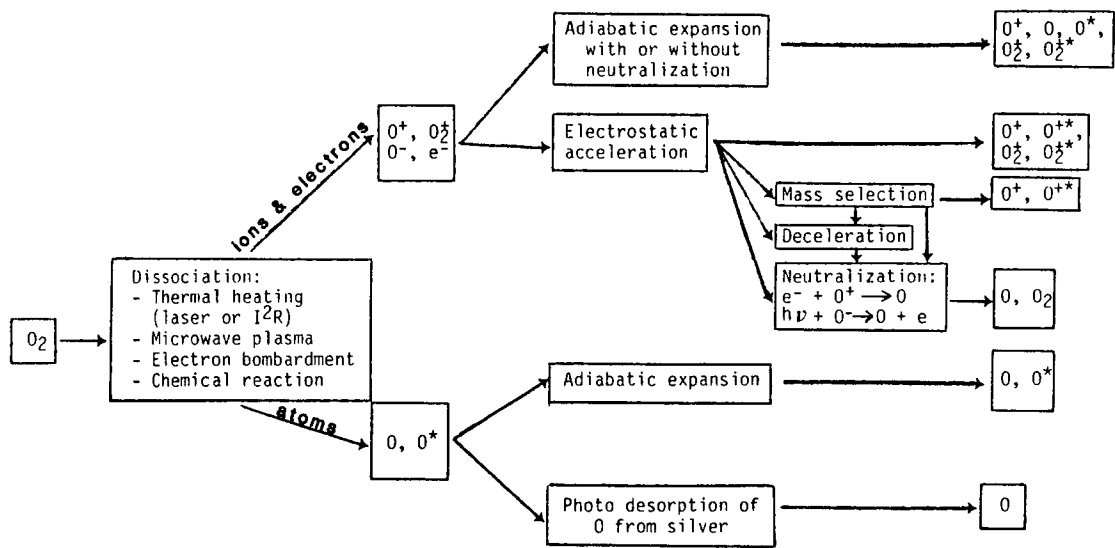
FIGURE 3. - PROCESSES USED FOR SIMULATION OF LOW EARTH ORBITAL ATOMIC OXYGEN
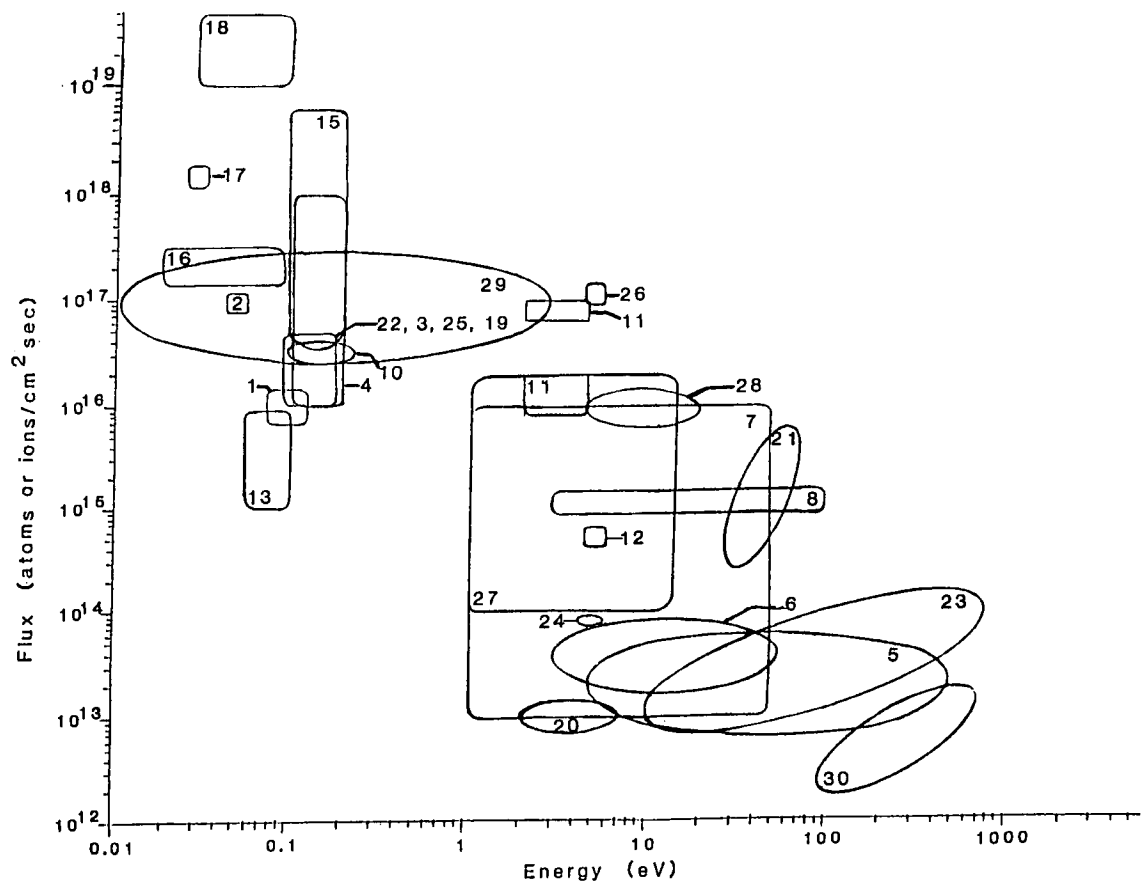


FIGURE 4. - ATOMIC OXYGEN TEST FACILITY FLUX ENERGY DOMAINS

62
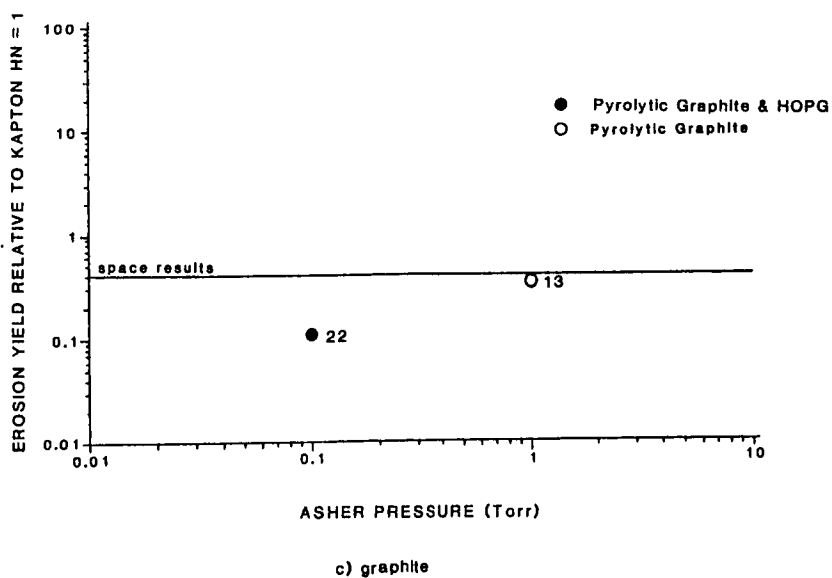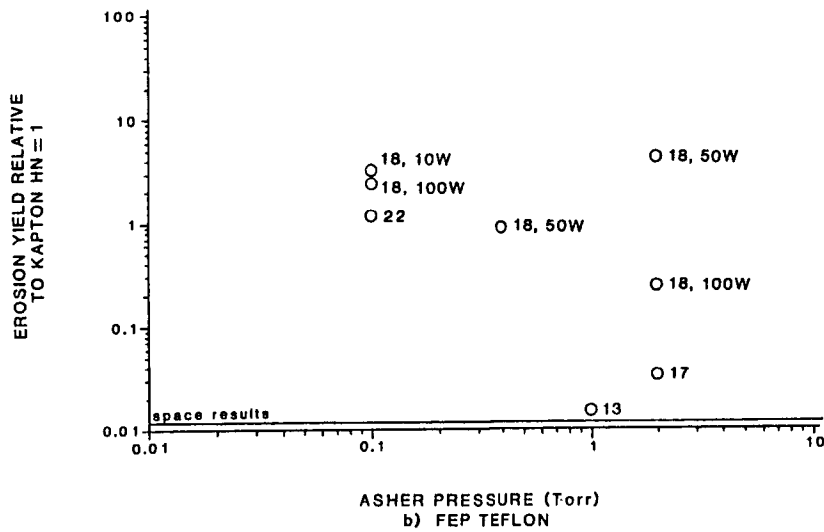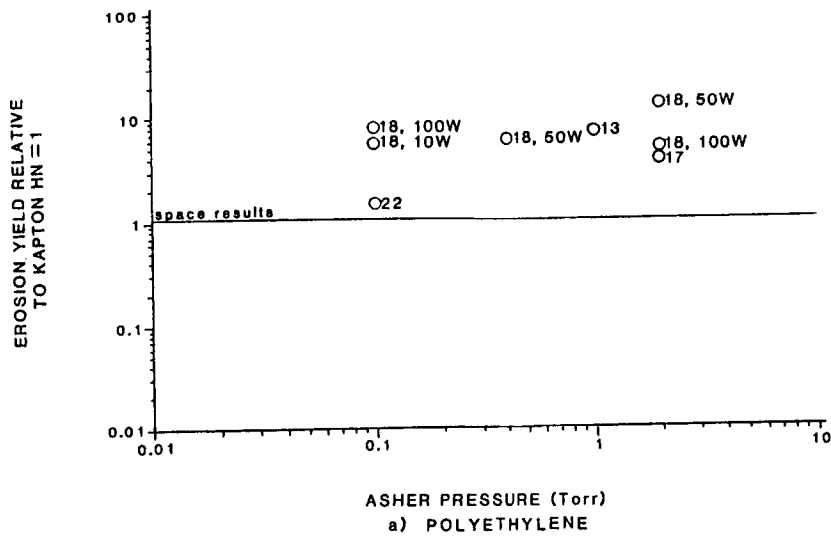
FIGURE 5. – EROSION YIELDS RELATIVE TO KAPTON AS A FUNCTION
OF FACILITY OPERATING PRESSURE

63
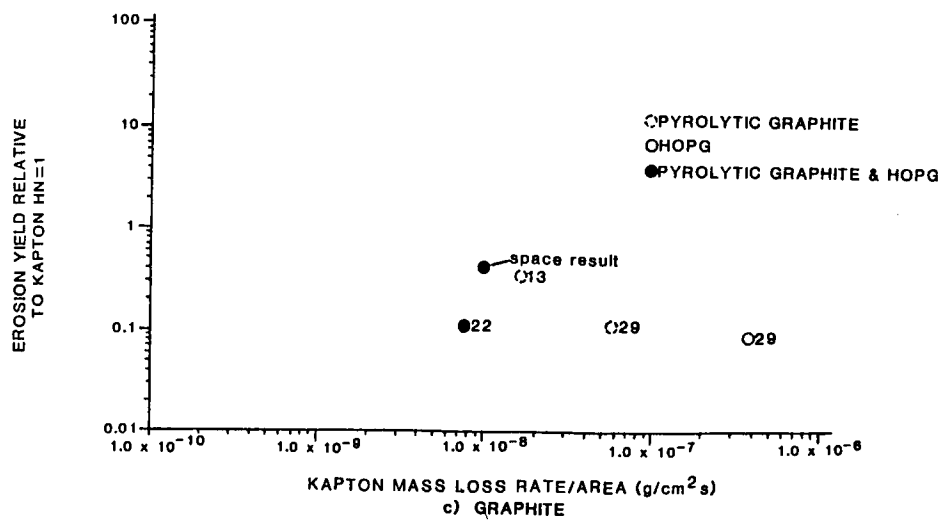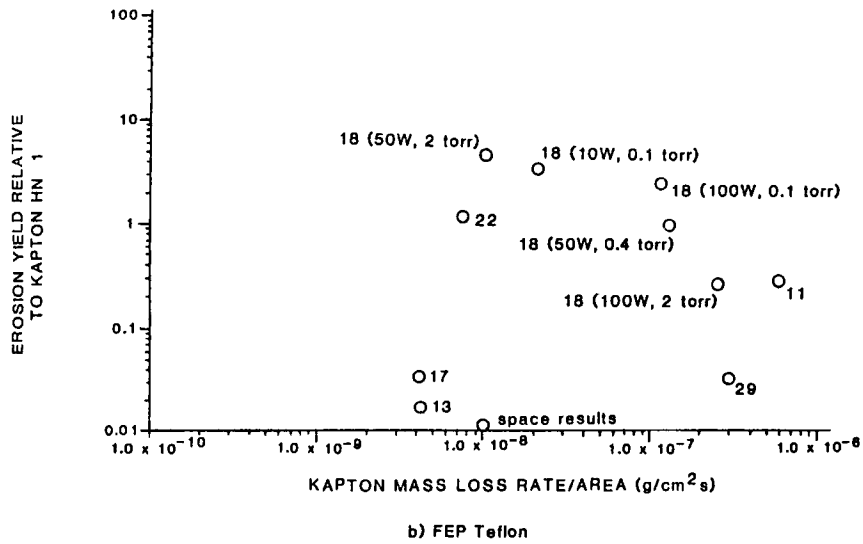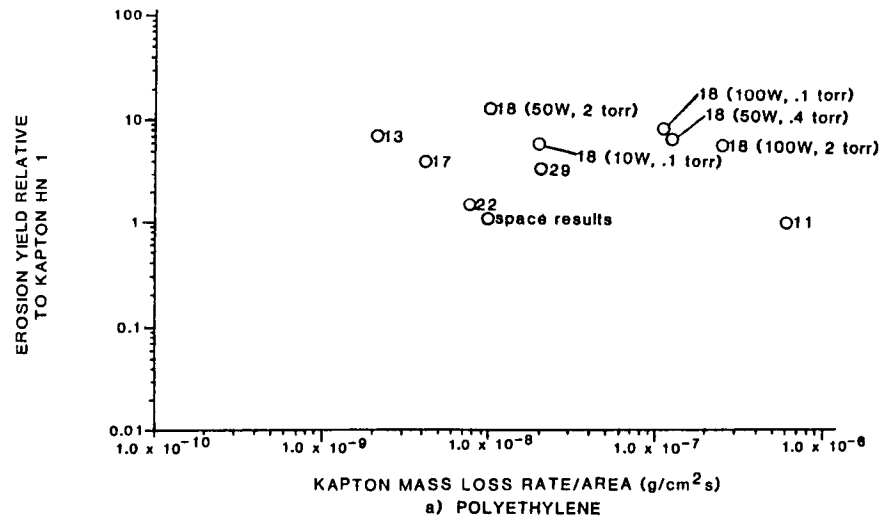
FIGURE 6 – EROSION YIELDS RELATIVE TO KAPTON VERSUS KAPTON HN
MASS LOSS RATE PER UNIT AREA

64
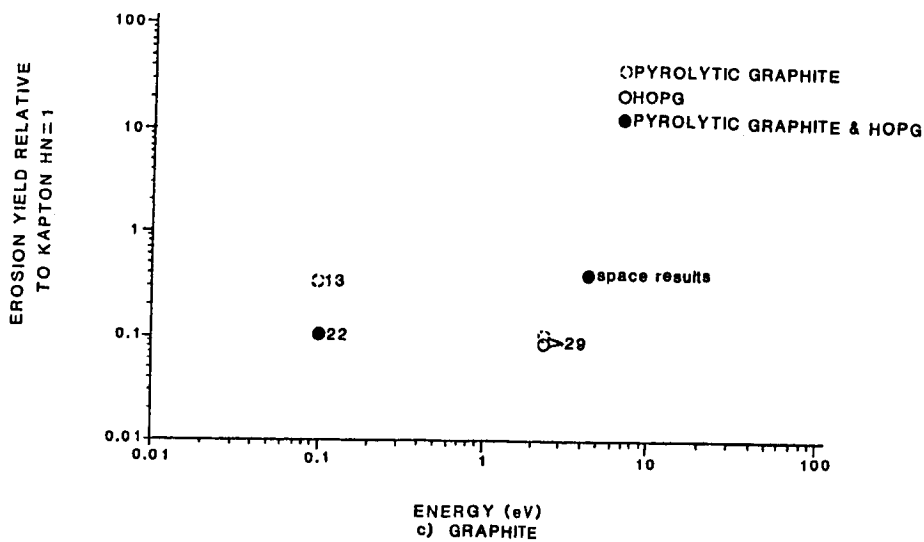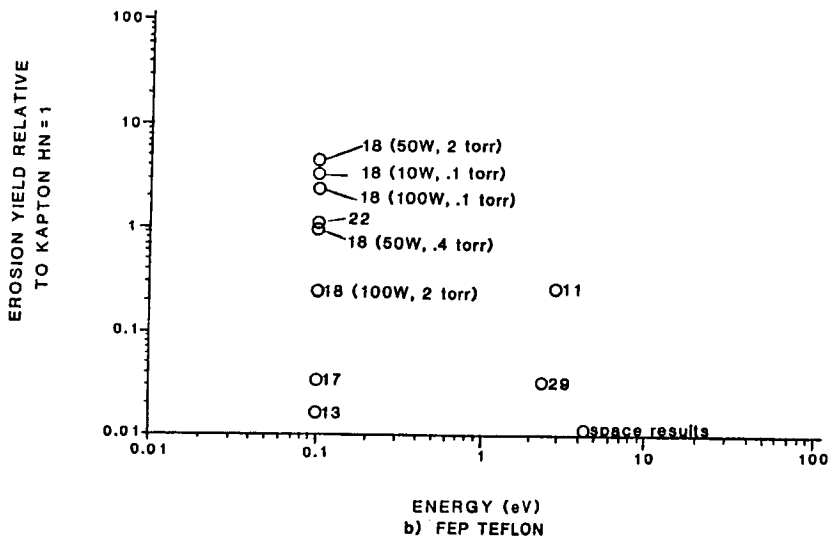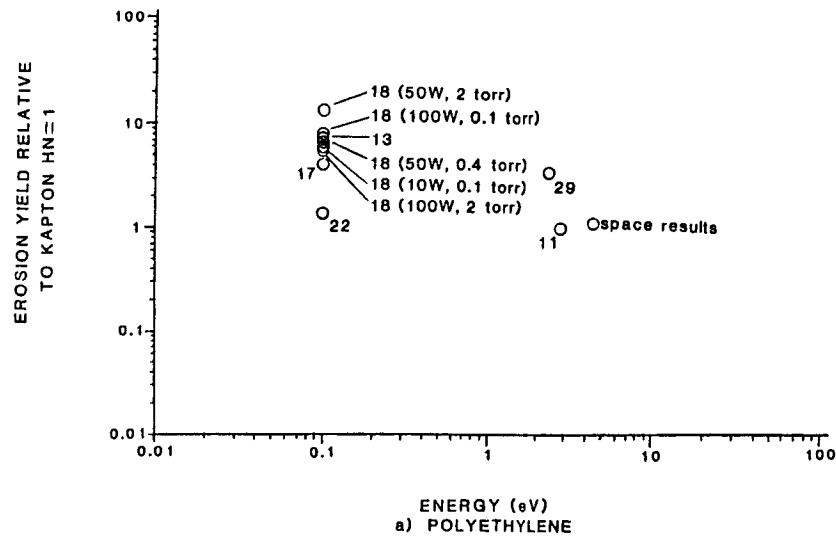
FIGURE 7. – EROSION YIELDS RELATIVE TO KAPTON AS A FUNCTION
OF ATOMIC OXYGEN ENERGY

65

# MATERIALS SELECTION FOR LONG LIFE IN LEO: A CRITICAL EVALUATION OF ATOMIC OXYGEN TESTING WITH THERMAL ATOM SYSTEMS

S. L. Koontz, J. Kuminecz, L. Leger, and P. Nordine
NASA/Johnson Space Center

## Abstract

The use of thermal atom test methods as a materials selection and screening technique for low-Earth orbit (LEO) spacecraft is critically evaluated in this paper. The chemistry and physics of thermal atom environments are compared to the LEO environment. The relative reactivities of a number of materials determined in thermal atom environments are compared to those observed in LEO and in high quality LEO simulations. Reaction efficiencies ($cm^3$ $atom^{-1}$) measured in a new type of thermal atom apparatus are one-hundredth to one-thousandth those observed in LEO, and many materials showing nearly identical reactivities in LEO show relative reactivities differing by as much as a factor of 8 in thermal atom systems. A simple phenomenological kinetic model for the reaction of oxygen atoms with organic materials can be used to explain the differences in reactivity in different environments. Certain specific thermal atom test environments can be used as reliable materials screening tools. Using thermal atom methods to predict material lifetime in LEO requires direct calibration of the method against LEO data or high quality simulation data for each material.

## Introduction

Materials degradation resulting from atomic oxygen attack is an important long life issue for spacecraft operating in the low Earth orbit (LEO) environment. The cost and limited availability of materials test time in flight or in high quality LEO environment simulators has generated considerable interest in the use of thermal energy (0.04 to 0.1 eV) oxygen atoms for materials testing. Thermal atom methods include oxygen plasma ashing, low pressure flowing discharges, and thermal energy beams. While most of these methods can deliver a useful flux of thermal oxygen atoms to the surface of a material test specimen, several fundamental issues need to be resolved before the results of thermal atom testing can be used to support materials selection and development or to estimate the functional life of spacecraft in the LEO environment.

In this paper a critical evaluation of the various thermal atom test methods is presented. The important differences between the thermal atom test environments and the LEO environment are reviewed as are the ways in which various environmental factors may influence materials reactivity measurements. Finally, materials reactivity measurements in several thermal atom environments are compared with measurements made in LEO or in the high quality LEO simulation at Los Alamos National Laboratory (LANL)[24]. The reactivities of organic materials and graphites are the primary focus of this paper. Only passing attention is given to the reactivities of metals and semiconductors. Many of the materials reactivity measurements were made in a new type of flowing discharge apparatus reported here for the first

time. The new apparatus is designed to permit a reasonably accurate estimate of the thermal atom flux at the surface of a material test specimen so that reaction efficiencies can be measured at thermal energies. Thermal atom reactivition efficiencies of several materials are reported here for the first time. The limitations of the reactivity and reaction efficiency measurements are discussed. The availability of direct measurements of materials reactivities in LEO, the LANL simulation facility, and three different thermal atom environments led naturally to the development of a phenomenological kinetic model for the reaction of oxygen atoms with organic surfaces over the range of energies 0.03 to 5 eV. While still highly speculative, we present the model here to stimulate discussion and further work in the atomic oxygen community. Space limitation prevents any discussion of atomic oxygen damage morphology. Morphology will be treated in detail in future publications.

## Background

Spacecraft operating at altitudes between 200 and 900 km are operating in LEO, where the residual atmosphere is composed predominantly of oxygen atoms with comparable concentrations of nitrogen molecules up to 400 km[1,2]. Spacecraft orbiting at these altitudes travel at velocities of 8 to 12 km/sec (depending on eccentricity), so that ambient oxygen atoms strike ram oriented spacecraft surfaces with translational energies of 5 to 8 eV. The atom flux depends on altitude, solar activity, orbital inclination, and time of day[1,2], with about $10^{15}$ atoms $cm^{-2}$ $sec^{-1}$ being a nominal value for the NASA Space Station. The effects of the oxygen atom ram flux on about 300 different materials have been investigated in three Space Shuttle flight experiments and one satellite recovery, and are summarized in Table I. Detailed treatments of the flight data are found in refrences 3 through 23. Impact on spacecraft design is discussed in refrences 25, 26, and 27. It has been well-established that oxidation reactions are the mechanistic basis for materials degradation by atomic oxygen in LEO[27]. No significant contribution from ablation or sputtering has been demonstrated at this writing.

In addition to oxygen atoms, surfaces in the LEO environment encounter low energy charged particles (ionospheric plasma), solar ultraviolet and vacuum ultraviolet (UV and VUV). In polar orbit, high energy charged particles will also be encountered[25]. Synergism between oxygen and other environmental factors is expected to influence the reaction efficiencies of materials in some circumstances but has not yet been investigated in a systematic way. Thermal atom test environments differ significantly from the LEO environment is several important respects. The translational energy of the atoms is about 0.04 eV, not 5.0 eV. In many thermal atom environments, molecular oxygen is more abundant than atomic oxygen and may influence measurements. The relative dose of UV and VUV radiation varies from one type of thermal atom system to another and is not generally well characterized. Finally, some thermal atom environments expose sample materials to a plasma environment much more severe than the ionospheric plasma in LEO and can also heat conductive samples by radio frequency induction. The thermal atom environments investigated in this work are compared, in a general way, with the LEO environment in Table II. The radio frequency (RF) plasma asher and the flowing afterglow are discussed at greater length in the next two sections.

67

## The RF Plasma Asher Environment

The RF plasma asher can be operated over a fairly wide range of pressures and RF powers, producing a wide range of environments. When operating with pure oxygen as the source gas, atomic oxygen yield can vary from 1 to 60 percent, depending on a number of operating variables. Similarly, charged particle density and temperature as well as ultraviolet (UV) flux and spectra can vary over fairly wide ranges[28-31]. Asher environments share one common factor, however. The sample material is always exposed directly to a plasma and an RF field, unless a faraday cage is used to enclose the sample material[32,33]. The RF field can heat conducting samples, or samples containing conducting components, by induction. Charged particle and UV bombardment of the sample can dramatically change the atomic oxygen reactivity, as shown in the results section below. Charged particle bombardment is a common technique for controlling morphology and reactivity in the fabrication of semiconductor devices[34-36].

The most striking differences between the LEO environment and the asher environment are the kinetic energy of the oxygen atoms, the very large flux of oxygen molecules and UV/VUV photons which also strike the test specimen surface. Atoms in LEO have a translational energy of 5 eV, while those in the asher are between 0.04 and 0.06 eV.

For a dissociation yield of 2 percent at a total pressure of 2 torr the oxygen molecule flux on any surface in the plasma is $1 \times 10^{21}$ molecules cm$^{-2}$ sec$^{-1}$, while the atom flux is only $4 \times 10^{19}$. By themselves, the oxygen molecules are inert, but they can react with sites created by oxygen atom attack in some materials, as indicated by the formation of organic peroxide radicals from alkyl radicals and oxygen in the gas phase[37] as well as the photochemical weathering of polymers[38]. Ozone, hydroxyl radical, and molecular oxygen in excited states are also potential reactants at the sample surface.

Ultraviolet radiation deserves special mention because low pressure discharges in oxygen are a popular means of generating the 130 nm (9.4 eV) resonance line of atomic oxygen. In LEO the flux of short wavelength (high energy) UV radiation is determined by the solar Lyman Alpha line at 121.6 nm (10.1 eV) with a typical flux of about $4 \times 10^{11}$ photons cm$^{-2}$ sec$^{-1}$ nm$^{-1}$ in LEO. In discharge lamps and plasma ashers, the flux at the oxygen line can be thousands of times higher, providing more opportunity for photochemistry with these high energy, bond-breaking photons[39,40].

## The Flowing Afterglow Environment

The flowing afterglow environment is much easier to define than the plasma asher environment. In the flowing afterglow method, a gas containing oxygen flows through a microwave or RF discharge region where oxygen atoms are produced[37,41]. The gas then flows out of the discharge region and cools to near room temperature before contacting the surface of the test material. The flowing afterglow has a long and venerable history as a device for studying the kinetics of oxygen atom reactions in the gas phase[37,41-43], but has seen only limited use in the study of surface reactions[44,49]. The total pressure of the gas is usually between 0.1 and 2 torr. Pure oxygen or

oxygen diluted in an inert gas such as argon or helium may be used[37,41]. The flowing afterglow environment consists of a gas at or near room temperature and containing ground state oxygen atoms and molecules. Low levels of metastable excited states of molecular and atomic oxygen have been observed in flowing afterglows in some circumstances[41]. The concentration of ions and electrons is negligible[37,41], and it is easy to configure the test specimen so that no electromagnetic radiation from the discharge zone reaches the sample. When using pure oxygen as the operating gas, low levels of water vapor (about 0.3 percent by volume) are added to boost oxygen atom yield.

If the concentration of oxygen atoms and the temperature in the gas near the sample surface can be measured or estimated, the atom flux and kinetic energy at the surface can be calculated from classical kinetic theory[50,51]. The surface flux is simply the atom concentration near the surface multiplied by one-fourth the gas kinetic speed ($F=[O]v/4$), and the kinetic energy distribution can be calculated directly from the Boltzman equation ($E=3kT/2$).

Atoms reaching the surface are lost as a result of reaction with the substrate or recombination to form molecular oxygen. The atom concentration near the surface depends on the relative rates of transport to, and atom loss at, the surface, as well as losses in the gas phase and on other surfaces in the system[52]. It is possible that some test system configurations produce transport limited surface reaction measurements instead of true surface reactivities. An analysis of the transport-reaction process is a vital part of test system design and an important aid in understanding test data.

Oxygen atoms are only one of several species striking the test specimen surface. Molecular oxygen, ozone, and hydroxyl radical are also potential reactants, as in the plasma asher environment. The major differences between the asher and the afterglow rest in the flux of excited species, charged particles, and UV photons at the sample surface, which is much smaller for the afterglow than the asher[28,41].

## Experimental

Reaction effeciencies with thermal atoms were measured in two different thermal atom systems. Plasma asher measurements were conducted in an LFE Corporation model LTA-302 low temperature plasma asher, operating at 13.56 MHz. Forward Rf powers ranging from 10 to 100 watts were used with working gas pressures ranging from 0.1 to 2 torr. The test matrix is given in the results section below. The working gas was Liquid Air Corporation analyzed (>99.5 percent pure) avaitor's breathing oxygen (MIL-0-27210 E), containing 12 ppm total hydrocarbon and less than 4 ppm water vapor. Except for highly oriented polycrystalline graphite (HOPG) and pyrolytic graphite, all test samples were 2.54 cm diameter disks of film material. Test specimens were exposed to the plasma environment in a pyrex glass sample holder which positioned the samples horizontally on the long axis of the plasma chambers (parallel to the axis of the field coil), as shown in figure 1. The samples rested on a pyrex glass plate. A pyrex cover plate having three 2.03 cm diameter holes (one for each sample position) covered the samples and exposed 3.24 $cm^2$ of the sample material. The cover plate

69

protected the edges of the sample from attack by the plasma environment. Other investigators have observed enhanced attack at the edges of organic film samples placed in oxygen plasmas[53,54]. Only the center and forward (i.e., torward the chamber door) sample positions were used in this study. No attempt was made to measure the atomic oxygen concentration in the asher for this study, but the molecular oxygen flux is almost certainly much larger than the atomic oxygen flux at any sample surface. Oxygen atom kinetic energy is estimated to be between 0.04 and 0.05 eV (Temperature is uncertain in the nonequilibrium environment of the asher).

The flowing afterglow apparatus is shown in figure 2. A Raytheon PGM-10 microwave power supply operating at 2450 MHz was used with an Evenson-type discharge cavity to generate a discharge in flowing oxygen gas at pressures between 0.2 and 2 torr. The forced air cooled Evenson cavity was placed near the center of a 20-cm long, 1-cm I.D. quartz tube. About 9 cm downstream from the discharge chamber, the inside diameter of the flow system increased to 4.0 cm. A valve for introduction of $NO_2$ titrant gas was placed 14 cm downstream from the discharge region, and the sidearm-sample-holder assembly was placed 53 cm downstream from the discharge region. A cold trap was maintained at -50°C between the flow system and a rotary vane vacuum pump. Flow system pressure was measured with an MKS baratron capacatence manometer. All glassware was given a final cleaning before use by soaking overnight, first in concentrated nitric acid and then in concentrated hydrochloric acid, with a final rinse in demineralized distilled water.

Avaitor's breathing oxygen from Liquid Air Corporation (>99.5 percent pure, MIL-O-27210 E), containing less than 14 ppm hydrocarbon and 0.5 ppm water vapor, was used as the working gas. The gas flow rate was measured with a calibrated MKS, Inc. mass flow meter. About 10 percent of the total gas flow was diverted through a humidification chamber operated at 1.4 atm and 24°C. As a result, the working gas in the afterglow contained about 0.3 percent water vapor, the value which gave a maximum yield of oxygen atoms as measured by both titration and catalytic probes. Oxygen concentrations of 3 to $4 \times 10^{15}$ atoms/cm³ were obtained at the titration point, with about $1 \times 10^{14}$ at the sample position. For a working pressure of 2.0 torr, the oxygen flow rate was 93.2 sccm, which corresponds to an average linear velocity of 58 cm/sec and a Renyolds number of 0.0036. In 2 torr of pure oxygen, the half life of atomic oxygen is 0.017 seconds, due almost entirely to recombination. The half life for ozone formation is 0.379 seconds[1,37]. Water vapor should be completely converted to hydroxyl radical near the discharge region, but hydroxyl is lost rapidly by surface reactions on pyrex glass flow systems, so that hydroxyl concentrations at the sample are believed to be negligable[37]. As was the case for the asher, the molecular oxygen flux is much greater than the atomic oxygen flux.

Afterglow oxygen atom concentrations were measured by chemiluminescent titration with $NO_2$[37,41] and with catalytic recombination probes prepared by coating copper-constant-thermocouples with molten silver[55,58]. The atom kinetic energy is estimated as E = 3kT/2 = 0.039 eV.

Except for the HOPG, all afterglow material samples were run as 1.90 cm diameter disks. When mounted at the sample position at the end of a side-arm in the flowing afterglow system, 1.59 cm² of the sample disk is exposed

to atomic oxygen. The remainder of the sample rests on the end of the side-arm tube and is protected from attack. The end of the side-arm tube does not form a vacuum seal with the sample film. A 1.90 cm diameter black anodized aluminum plug presses aginst the back side of the sample and contains a heating element and thermocouple which permit the sample to be heated to a known temperature. The assembly is held in place and a vacuum is maintained with a modified 1.90 cm Cajon tubing union as shown in figure 2.

Kapton HN, FEP teflon, polyethylene, Tedlar, and Mylar samples were all cut from sheets of 2 mil film. The Kapton, FEP teflon, polyethylene, pyrolytic graphite and HOPG were obtained from Bruce Banks at NASA's Lewis Research Center as part of the atomic oxygen effects test program (oxygen effects round-robin). The pyrolytic graphites were cut into a 1.90 cm diameter disks. Tedlar and Mylar film samples were obtained from E. I. duPont de Nemours and Co., Inc. All samples except the HOPG were cleaned by brief rinsing with optical grade solvent, a mixture of 1,1,1, trichloroethylene (75 percent) and ethanol (25 percent) from Analytical Research Laboratories, Monrovia, California. The same sample preparation procedure was used for JSC flight samples for STS-8 and for samples prepared at JSC for test in the LANL high energy beam system [59]. After air drying, the samples were stored in a dessicator for at least 48 hours before use. Clean surfaces of HOPG were prepared by applying adhesive tape to the basal plane of the crystal and peeling the top layer, leaving a fresh, clean surface. The HOPG was exposed directly to the afterglow environment at the end of a sidearm, with no attempt to protect the sides of the square sample from reaction. The HOPG samples were squares, about 1 cm on an edge and less than 0.3 cm thick.

## Results and Discussion

All the materials examined in the RF asher showed dramatic variation in reaction rates, with changes in RF power and total pressure. The samples in the rear and middle sample positions were weighed at various times during the exposure and the mass loss rate determined by a linear regression analysis of sample mass and time ($M(t) = M_0 - R*t$). The correlation coefficient (Pearson's r) was better than -0.99 for most data and never became greater than -0.98, indicating a good fit to a linear model. Plots of the mass loss data for some materials indicated a brief nonlinear induction period early in the test, but the effect on the data fit was small. A typical data plot is shown in figure 3. Table III shows the values of R/A (units of mg cm$^{-2}$ min$^{-1}$) and the standard deviation calculated by averaging the rates for both sample positions. Inspection of the data in Table III clearly shows that polyethylene has a much higher mass loss rate than Kapton for all combinations of RF power and total pressure used. Teflon also has a higher mass loss rate than Kapton under most conditions.

Trends in the asher data are more easily discerned if the data is normalized and presented as relative rates. In Table IV the rate is normalized to the Kapton rate for a given set of asher conditions; and in Table V the rates are normalized to the 2 torr, 100 watt condition for each material. Comparison of Tables IV and I shows that the 2 torr, 100 watt condition gives the best agreement with the flight results; but even so, the agreement is qualitative at best. Inspection of Table V shows that Kapton,

71

polyethylene, and single crystal graphite show similar relative changes in rate with conditions, but that FEP teflon does not, suggesting that FEP teflon is responding to different environmental factors than the other materials, or perhaps reacting by a different mechanism. The reactivity of FEP teflon is greatest at high RF power and low total pressure, suggesting that charged particle or photochemical effects dominate the reaction of fluorocarbons in the asher environment.

Reaction rates obtained in the flowing afterglow were substantially lower than those obtained in the asher. Reaction rates in the flowing afterglow were determined by both single time measurements ($R = (M_1 - M_2)/(t_1 - t_2)$) and by measurement of sample mass at several times, followed by linear regression analysis ($M(t) = M_0 - R*t$), as for the asher. Correlation coefficients better than -0.99 were obtained in most cases, and data plots show no evidence of nonlinearity. A typical data plot is shown in figure 4. Oxygen atom concentrations were determined by $NO_2$ titration during each run, and rates were corrected for changes in atom concentration. The average rates, relative rates, and reaction efficiencies are reported in Table VI.

The relative rates of polyethylene and single crystal graphite are nearly the same for the asher and the afterglow. Significantly, the relative rate for FEP teflon was much lower than that observed in the asher, supporting the idea that the teflon reaction in the asher depends on factors other than, or in addition to, atomic oxygen. Tedlar and Mylar also gave relative rates much higher than Kapton in the afterglow. Except for Teflon, these materials showed nearly the same reaction efficiency as Kapton in LEO and in the LANL beam[60].

Reducing the afterglow total pressure and oxygen atom concentration by a factor of 10 gave rates about one-tenth those observed at higher pressure and oxygen concentration. Similar results have been observed by at least one other group, using a plasma asher with an optional faraday cage[61]. With no faraday cage, plasma directly contacts the sample surface, and the relative rates observed are much the same as those reported here. When the samples are placed inside the faraday cage, the plasma cannot come into direct contact with the sample surface. Reactive species diffuse to the sample through openings in the faraday cage, so that the environment is more like that in the afterglow. When the samples are placed inside the faraday cage, the relative rates are comparable to those reported here for the afterglow.

The reaction efficiency of materials with oxygen atoms at thermal energies ($3kT/2 = 0.039$ eV) has been the subject of considerable uncertainty and speculation, though the bulk of the evidence available to date suggests that thermal atoms are much less reactive than hyperthermal atoms[62]. The data shown in Table VI indicate reaction efficiencies one-hundredth to one-thousandth those observed in flight (5 eV) or in the hyperthermal beam (3 eV) at LANL. The thermal atom reaction efficiencies reported here do agree in magnitude with those reported by other workers[62,63] using thermal energy beam systems. More work is needed to improve the precision and accuracy of these reaction efficiencies. Molecular oxygen is the most abundant species striking any surface in the asher or the afterglow, and molecular oxygen should react with organic radical sites produced by oxygen atoms[38]. The effects of molecular oxygen and other species, such as ozone and hydroxyl

radical, are being evaluated as part of an ongoing project at the Materials Branch, Johnson Space Center.

As shown above, the thermal atom test systems reported here produce materials reactivities very different from those observed in LEO or in high quality LEO simulations. Most important, while the relative reactivities of Kapton, polyethylene, Tedlar, and Mylar lie within a few percent of each other in LEO and in the LANL beam, they range over an order of magnitude in the thermal atom systems. If the reaction effeciencies of Kapton, Mylar, Tedlar, and polyethylene are plotted vs the atomic fraction of aliphatic hydrogen (fraction R-H) in the polymer repeat unit, we obtain the results shown in figure 5. The correlation coefficient for reaction efficiency and fraction R-H is 0.98, indicating a strong relationship between chemical structure and reactivity in the afterglow. Relationships between chemical structure and reactivity have also been reported for the asher environment in connection with photoresist stripping[64].

Many of the observations presented above can be rationalized with a simple phenomenological model describing the kinetics of mass loss when a hydrocarbon polymer is attacked by atomic oxygen. The essentials of the model are shown in figure 6. Mass loss occurs sequentially. First, hydrogen atoms are removed, and then more massive atoms, such as carbon. The key idea here is that the hydrogen abstraction rate ($k_1$) has a strong dependence on atom kinetic energy, and also varies substantially with the type and quantity of C-H bonds in the material. The rate constant for oxygen attack, with mass loss, on the hydrogen depleted surface ($k_2$) is the same for the materials studied. Fresh surface is exposed at a rate which depends on net mass loss through a proportionality constant $k_3$. Both reaction rates depend on atom kinetic energy and sample surface temperature, but the hydrogen abstraction rate is limiting at thermal energies, as first proposed by Gramm Arnold[62]. If the Arrhenius activation energies and pre-exponential factors for oxygen atom reaction with gas phase organic compounds can be used as a guide, then an activation energy of about 0.3 eV for hydrogen atom abstraction can be expected with pre-exponential factors which vary by as much as a factor of 10 for different hydrocarbons[42].

If most of the oxygen atom kinetic energy is available for overcoming activation barriers, then as kinetic energy increases from 0.04 eV to 5 eV, the activation barrier for hydrogen atom abstraction will be exceeded and $k_1$ will become very large. Equation 4 shows that when this happens the mass loss rate will be determined by $k_2$, and all hydrocarbon materials will have the same or similar mass loss rates as observed in LEO. Table I shows several organics, for example epoxy and polybenzimidazole, for which $k_2$ is different from that for the four materials considered here, perhaps due to effects of the massive heteroatoms. Polymers containing silicone groups form an inert surface oxide layer which prevents or slows further attack.

## Summary and Conclusions

The thermal atom test environments examined as a part of this work produce relative material reactivities and reaction effeciencies markedly different from those produced in LEO or in high quality simulations for several different materials. The LFE corporation LTA-302 plasma asher produces the best (i.e., most like the LEO rates) relative rates with 2 torr of oxygen

and 100 watts of forward power; but even better relative rates are produced when a faraday cage is used to isolate samples from the plasma environment[61]. In either environment, materials which have nearly the same relative rates in LEO vary by a factor of as much as 10, even when the faraday cage is used. These results are not suprising, given the radical differences between the LEO environment and the plasma environment in the asher.

The JSC flowing afterglow produced better relative rates than the LTA-302, and reaction efficiencies between one-hundredth and one-thousandth those observed in LEO or in the LANL beam. Mass loss rates were much lower in the afterglow, as presently configured, due mostly to lower atom flux at the sample surface. Work is in progress to increase the atom flux produced by the afterglow.

The thermal atom test methods examined to date can function as materials screening tools, but only if used cautiously. Accurate life-on-orbit data cannot be produced unless the thermal atom method is calibrated using LEO or high quality simulation data. Care must be taken to avoid environments where photochemical or charged particle processes can swamp or confuse oxygen effects data. The flowing afterglow, the asher-faraday cage combination, and the asher at high oxygen pressure seem the best candidates for development into reliable screening tests at this time. Even so, the environments are still very unlike the LEO environment, and many questions remain to be answered before a reliable screening test can be said to exist. The role of molecular oxygen, if any, and other potential reactants is not clear at this time. Most important, the nature of oxygen atom translational energy effects must be understood as it impacts the chemistry of a wide range of materials.

# References

1. Chamberlain, Joseph W.: Theory of Planetary Atmospheres. Academic Press, 1978.

2. Hedin, A. E.; Reber, C.A.; Newton, G.P.; Spencer, N.W.; Brinton, H.C.; Mazer, H.G.; and Pottes, W.E.: A Gobal Thermospheric Model Based on Mass Spectrometer and Incoherent Scatter Data MSIS 2 Composition. J. Geophysical Res., vol. 82, 1977, pp. 2148-2156.

3. Leger, L.J: Oxygen Atom Reaction With Shuttle Materials at Orbital Altitudes. Nasa TM-58246, May 1982.

4. Leger, L.J.; Visentine, J.T.; and Schliesing, J.A.: A Consideration of Atomic Oxygen Interaction with Space Station. AIAA Paper 85-0476, AIAA 23rd Aerospace Sciences Meeting, Reno, Nevada, January 14-17, 1985.

5. Leger, L.J.; et al.: STS Flight 5 LEO Effects Experiment - Background Description and Thin Film Results. AIAA Paper 83-2631, AIAA Shuttle Environment and Operations Meeting, Washington, DC, October-November 1983.

6. Whitaker, A.F.; et al.: LEO Oxygen Effects on Spacecraft Materials. AIAA Paper 83-2632, AIAA Shuttle Environment and Operations Meeting, Washington, DC, October-November 1983.

7. Park, J.J.; et al.: Effects of Atomic Oxygen on Paint and Optical Coatings. AIAA Paper 83-2634, AIAA Shuttle Environment and Operations Meeting, Washington, DC, October-November 1983.

8. Zinner, E.; et al: Erosion of Mylar and Protection by Thin Metal Films. AIAA Paper 83-2636, AIAA Shuttle Environment and Operations Meeting, Washington, DC, October-November 1983.

9. Liang, R.; and Gupta, A.: Mechanistic Studies of Kapton Degradation in Shuttle Environments. AIAA Paper 83-2656, AIAA Shuttle Environment and Operations Meeting, Washington, DC, October-November 1983.

10. Visentine, J.T.; et al: STS-8 Atomic Oxygen Effects Experiment. AIAA Paper 85-0415, AIAA 23rd Aerospace Sciences Meeting, Reno, Nevada, January 14-17, 1985.

11. Whitaker, A.F.: Orbital Atomic Oxygen Effects on Thermal Control and Optical Materials STS-8 Results. AIAA Paper 850416, AIAA 23rd Aerospace Sciences Meeting, Reno, Nevada, January 14-17, 1985.

12. Banks, B.A.; et al.: Ion Beam Sputter-Deposited Thin Film Coatings for Protection of Spacecraft Polymers in Low Earth Orbit. AIAA Paper 85-0420, AIAA 23rd Aerospace Sciences Meeting, Reno, Nevada, January 14-17, 1985.

13. Liang, R.H.; and Gupta, A.: Mechanistic Studies of Interaction of Materials With Energetic Oxygen Atoms in Low Earth Orbit. AIAA Paper 85-0422, AIAA 23rd Aerospace Sciences Meeting, Reno, Nevada, January 14-17, 1985.

14. Gull, T.R.; et al.: Effects of Optical Surfaces at Shuttle Altitudes. AIAA Paper 85-0418, AIAA 23rd Aerospace Sciences Meeting, Reno, Nevada, January 14-17, 1985.

15. Gregory, J.C.; and Peters, P.N.: Measurement of Reaction Rates and Activation Energies of 5 eV Oxygen Atoms With Graphite and Other Solid Surfaces. AIAA Paper 85-01417, AIAA 23rd Aerospace Sciences Meeting, Reno, Nevada, January 14-17, 1985.

16. Smith, K.: Evaluation of Oxygen Interaction with Materials (EOIM) - STS-8 Atomic Oxygen Effects. AIAA Paper 85-7021, AIAA Shuttle Environment and Operations II Conference, Houston, Texas, November 1985.

17. Whitaker, A.F.; et al.: Protective Coatings for Atomic Oxygen Susceptible Spacecraft Materials - STS41-G Result. AIAA Paper 85-7017, AIAA Shuttle Environment and Operations II Conference, Houston, Texas, November 1985.

18. Fromhold, A.T.; et al.: Reaction of Metals in Lower Earth Orbit During Space Shuttle Flight 41-G. AIAA Paper 85-7018, AIAA Shuttle Environment and Operations II Conference, Houston, Texas, November 1985.

19. Zimcik, D.G.; and Maag, C.R.: Results of Apparent Atomic Oxygen Reactions With Spacecraft Materials During Shuttle Flight STS41-G. AIAA Paper 85-7029, AIAA Shuttle Environment and Operations II Conference, Houston, Texas, November 1985.

20. Peters, P.N.; Gregory, J.C.; and Swann, J.T.: Effects on Optical Systems From Interactions With Oxygen Atoms in Low Earth Orbits. Applied Optics, vol. 25, no. 8, April 15, 1986.

21. Visentine, J.T.; and Leger, L.J.: Material Inertactions With the Low Earth Orbital Environment: Accurate Reaction Rate Measurements. AIAA Paper 85-7019, AIAA Shuttle Environment and Operations II Conference, Houston, Texas, November 1983.

22. Proceedings of the SMRM Degradation Study Workshop. The Satellite Servicing Project, Goddard Space Flight Center 408-SMRM-79-0001, May 9-10, 1985.

23. Visentine, J.T.; and Leger, L.J.: Atomic Oxygen Effects Experiments: Current Status and Future Directions, NASA TM, JSC, May 18, 1987.

24. Cross, J.B.; and Cremers, D.A: "High Kinetic Energy (1-10 eV) Laser Sustained Neutral Atom Beam Source." Nuc. Instr. Methods, B13, 658 (1986).

25. Durcanin, J.T.; Chalmers, D.R.; and Visentine, J.T.: The Definition of the Low Earth Orbital Environment and its Effect on Thermal Control Materials. AIAA Paper 87-1599, June 1987.

26. Leger, L; Visentine, J.; and Santos-Mason, G.: Selected Materials Issues Associated with Space Station. SAMPE Quarterly, vol. 18, no. 2, January 1987.

27. Brinza, D.E., ed.: Proceedings of the NASA Workshop on Atomic Oxygen Effects. JPL Publication 87-14, November 10-11, 1986.

28. Jacob, Adir: Plasma Processing - An Art or a Science? Solid State Technology, April 1983.

29. Jacob, Adir: Applications of Low Temperature RF Plasma Etching to Thin-Film Technology. Extended Abstracts, vol. 75, The Electrochemical Society, May 1975.

30. Jacob, Adir: The Versatile Technique of RF Plasma Etching. Solid State Technology, June 1977.

31. Corbin, G.A.; et al: Surface Fluorination of Polymers in a Glow Discharge Plasma; Photochemistry. Macromolecules, vol. 18, 1985, pp. 98-103.

32. Jacob, Adir: The Faraday Cage Patent. United States Patent 4,362,632, Dec. 7, 1982.

33. Photoresist Removal With and Without Equi-etch Chamber Insert. LFE Corporation, Bulletin 8216-TA1, August 1975.

34. Choe, D.HG.; Knapp C.; and Jacob A.: Production RIE -I. Selective Dielectric Etching. Solid State Technology, April 1984.

35. Leahy, Michael F.: Superfine IC geometries. IEEE Spectrum, February 10, 1985, pp. 36-43.

36. Choe, D.HG.; Knapp C.; and Jacob A.: Production RIE -II. Selective Aluminum Alloy Etching. Solid State Technology, March 1985, pp. 165-171.

37. Finlayson-Pitts, B.J.; and Pitts Jr., J.N.: Atmospheric Chemistry: Fundamentals and Experimental Techniques. John Wiley & Sons, 1986.

38. Hawkins, L.W., ed.: Polymer Stabilization. Wiley-Interscience, 1972.

39. Zaidel', A.N.; and Shreider, E.Ya: Vacuum Ultraviolet Spectroscopy. Ann Arbor-Humphrey Science Publishers, 1970.

40. Tanaka, I.; and Lossing, F.P.: Photoionization as a Source of Ions for Mass Spectrometry. The Journal of Chemical Physics, vol. 25, no. 5, November 1956, pp. 1031-1034.

41. Setser, D.W., ed.; Reactive Intermediates in the Gas Phase. Academic Press, 1979.

42. Kerr, J.A.; and Moss, J.S.: CRC Handbook of Bimolecular and Termolecular Gas Reactions. vol. I, CRC Press, Inc., 1981.

43. Herron, J.T.; and Huie, R.E.: Rate Constants for the Reactions of Atomic Oxygen ($O^3P$) With Organic Compounds in the Gas Phase. J. Phys. Chem. Ref. Data, vol. 2, no. 3, 1973.

44. Paraszczak, J.; Hatzakis, M.; Babich, E.; Shaw, J.; Arthur, E.: Plasma Etching of Polymers for Multilayer Lithography. Microcircuit Engineering, Academic Press, London, 1985.

45. De Jaegere, S.; Willems, M.; and Vinckler, C.: Interactions between Afterglow Products of Microwave-Induced Plasmas and Solids, J. Phys. Chem. 86, 3569-3577, 1982.

46. Dzioba, S.; Este, G.; and Naguib, H.M.: Decapsulation and Photoresist Stripping in Oxygen Microwave Plasma. J. Electrochem. Soc., Solid-State Science and Technology, vol. 129, no. 11, pps. 2537-2541, Nov. 1982.

47. Harteck, P.; and Reeves Jr., R.R: Formation and Reactions of the Excited $O_2(A^3\Sigma^+_u)$ Molecules, Disc. Faraday Soc. 37, 82, 1964.

48. Brennen, W.; and McIntyre, P.: Vibrational Relaxation and Electronic Mutation of Metastable Nitrogen Molecules Generated by Nitrogen Atom Recombination On Colbalt and Nickel. Chemical Physics Letters, vol. 90, no. 6, August 20, pp. 457-460 1982.

49. Chu, Ang-Ling; Reeves, R.R; and Halstead, J.A.: Surface-Catalyzed Formation of Electronically Excited Nitrogen Dioxide and Oxygen. J. Phys. Chem., vol. 90, no. 3, pp. 466-67, 1986.

50. Eggers Jr., D.F.; Gregory, N.W.; Halsey Jr., G.D.; and Rabinovitch, B.S.: Physical Chemistry. John Wiley and Sons, Inc., New York, London, Sydney, 1964.

51. Eyring, H., ed.: Physical Chemistry: An Advanced Treatise. Volume II, Statistical Mechanics, Academic Press, New York, London, 1967.

52. Krongelb, S.; and Strandberg, M.W.P.: Use of Paramagnetic-Resonance Techniques in the Study of Atomic Oxygen Recombinations. J. Chem. Physics, vol. 31, no. 5, pp. 1196-1210 November 1959.

53. Colony, J.A.; and Sanford, E.L.: Mechanisms of Polymer Degration Using an Oxygen Plasma Generator. NASA TM-100681, September 1987.

54. Demonet, C.M.; and Milnes, M.V.: Low Earth Orbit (LEO) Atomic Oxygen Effects Simulation with a Low Temperature Asher. NASA TR IRD 85-001, Rockwell International Space Transportation Systems Division, September 1985.

55. Linnett, J.W.; and Marsden, D.G.H.: Reactions of Oxygen Atoms. Proc. Roy. Soc, A234, 489, 504, 1956.

56. Greaves, J.C.; and Linnett, J.W.: Reactions of Oxygen Atoms. Trans. Faraday Soc., 54, 1323, 1958.

57. Greaves, J.C.; and Linnett, J.W.: Reactions of Oxygen Atoms. Trans. Faraday Soc., 55, 1338, 1959.

58. Marsden, D.G.H.; and Linnett, J.W.: Reactions of Oxygen Atoms. 5th Combustion Symposium, Reinhold, pp. 685, 1955.

59. Evaluation of Oxygen Interaction with Materials-III Experiment: Procedures for Assembly of Disk Sample Specimens Into Passive Sample Carrier. NASA JSC-22054, Materials Branch, Structures and Mechanics Division, LBJ Space Center, February 1986.

60. Cross, J.: Atomic Oxygen Exposure ($1.5 \times 10^{17}$ atoms/($cm^2$ sec) at 3eV in neon carrier gas). Samples Prepared and Analyzed at Johnson Space Center. Nuc. Instr. Methods, B13, 658 (1986).

61. Smith, L.A.; and Ian, E.: Unpublished data. Materials and Process Branch, Engineering Division, McDonnel Douglas Astronautics Company, Huntington Beach, California.

62. Arnold, G.S; Peplinski, D.R.; and Cascarano, F.M.: Translational Energy Dependence of the Reaction of Atomic Oxygen with Polyimide Films. J. Spacecraft, vol. 24, no. 5, pp. 454-458 Sept.-Oct. 1987.

63. Zimcik, D.G., Tennyson, R.C.; Kok, L.J.; and Maag, C.R.: The Effect of Low Earth orbit Space Environment on Polymeric Spacecraft Materials. Proceedings of the Third European Symposium on Spacecraft Materials in Space Environment, Noordwijk, The Netherlands, 1985.

64. Golub, M.A.; Lerner, N.R.; and Wydeven, T.: Reactions of Atomic Oxygen [O($^3$P)] with Polybutadienes and Related Polymers. JPL 87-14, see Ref. 27.
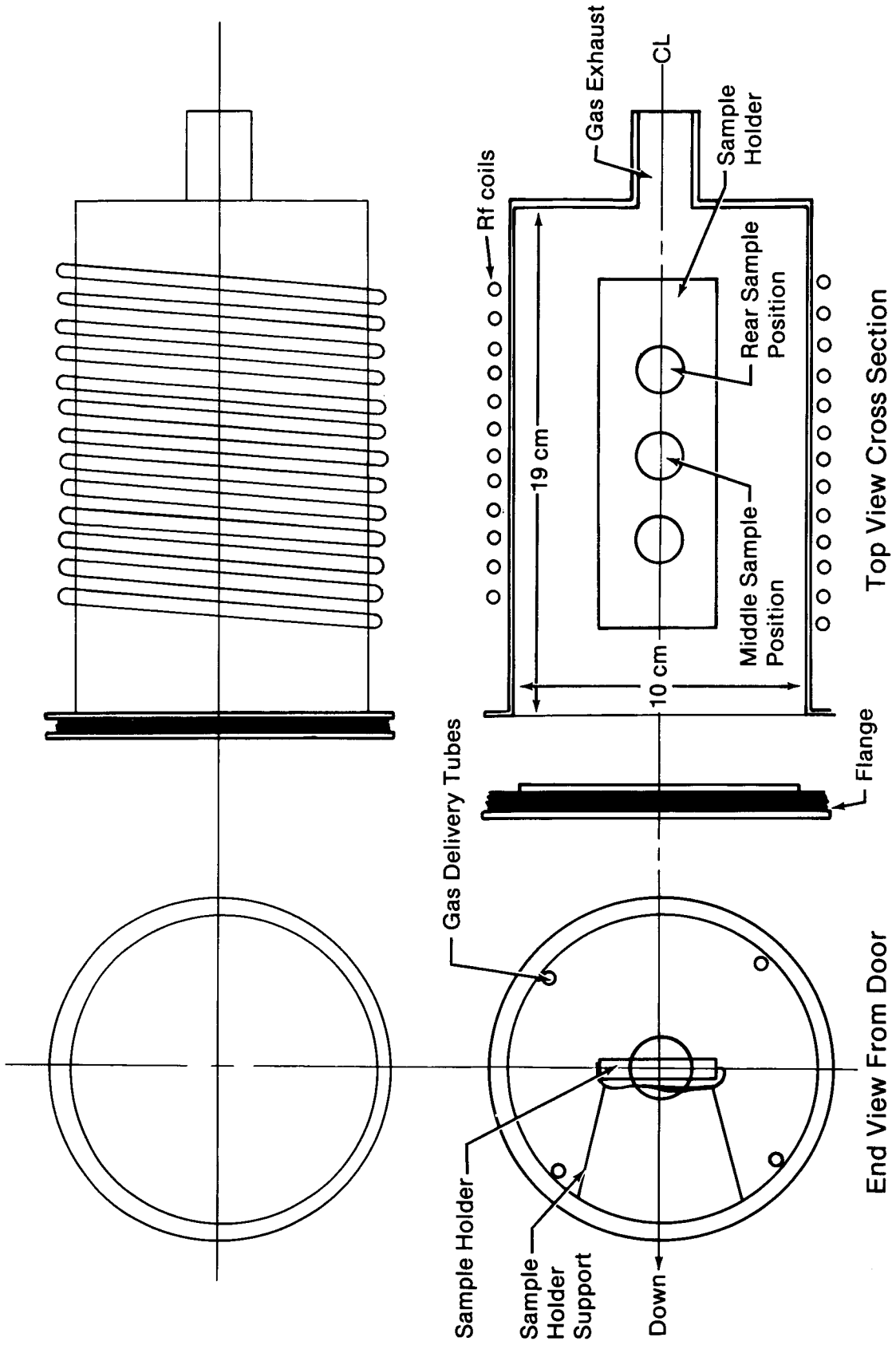
Figure 1.- The plasma asher apparatus configuration.
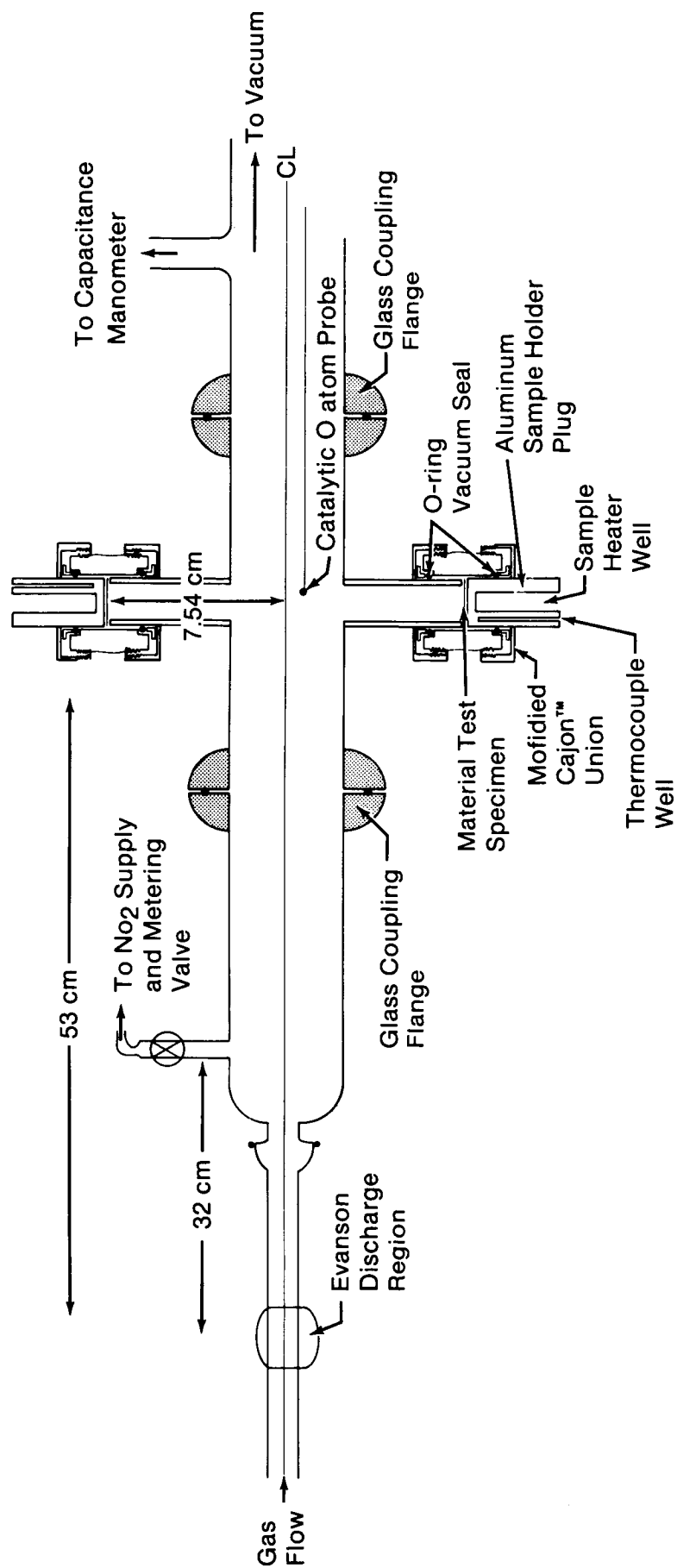
Figure 2.- The following afterglow apparatus configuration.
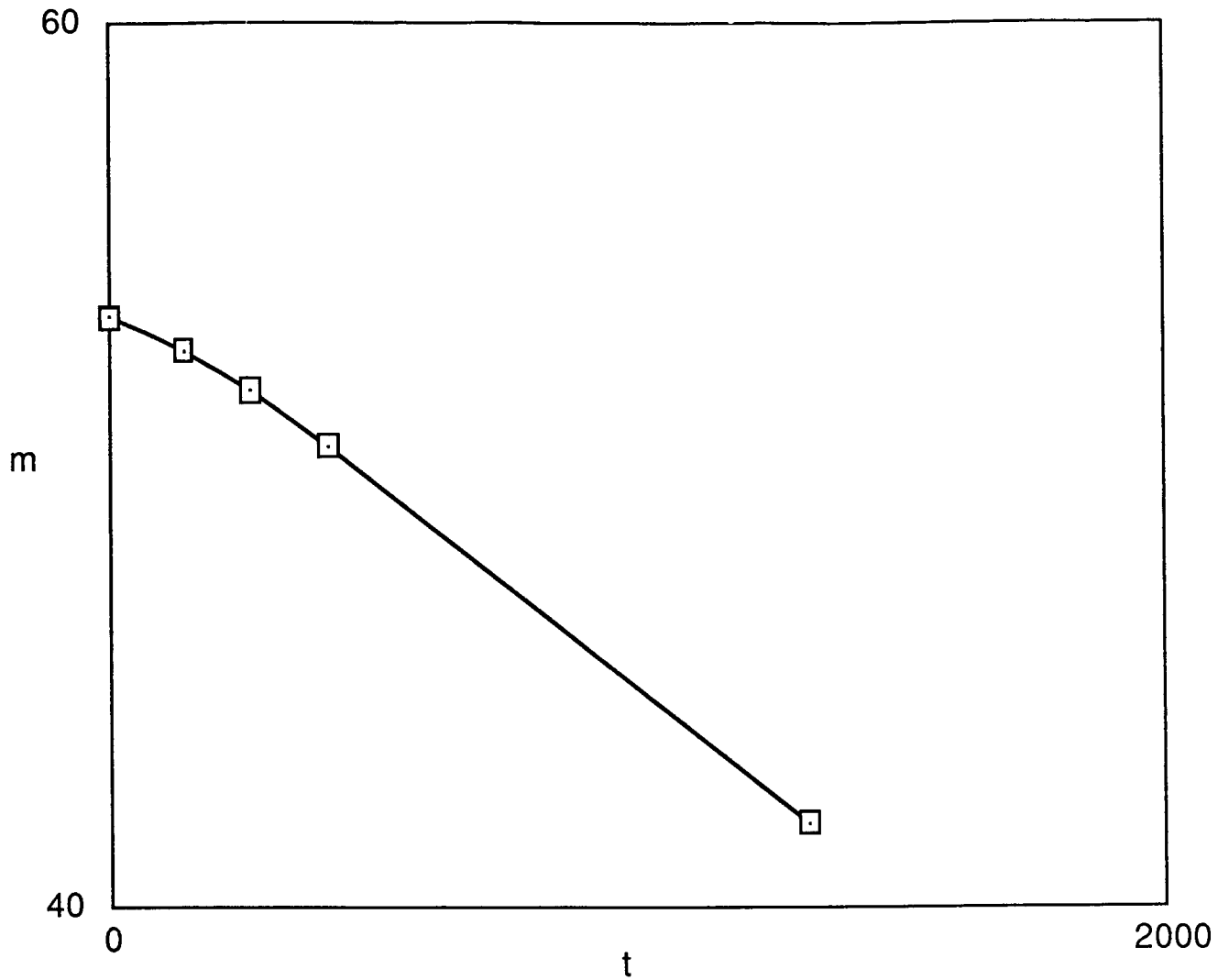
Figure 3.- Sample mass in milligrams vs exposure time for FEP teflon. Typical mass loss data drom exposure of materials to the plasma asher environment. The total pressure was 0.1 torr and the RF power was 10 watts. The small nonlinearity at early exposure times is not typical of all materials and conditions.

25

M

□ Kapton
◆ Polyethylene
■ Mylar
◇ Tedlar

5

0                                                    50

t

N802750M
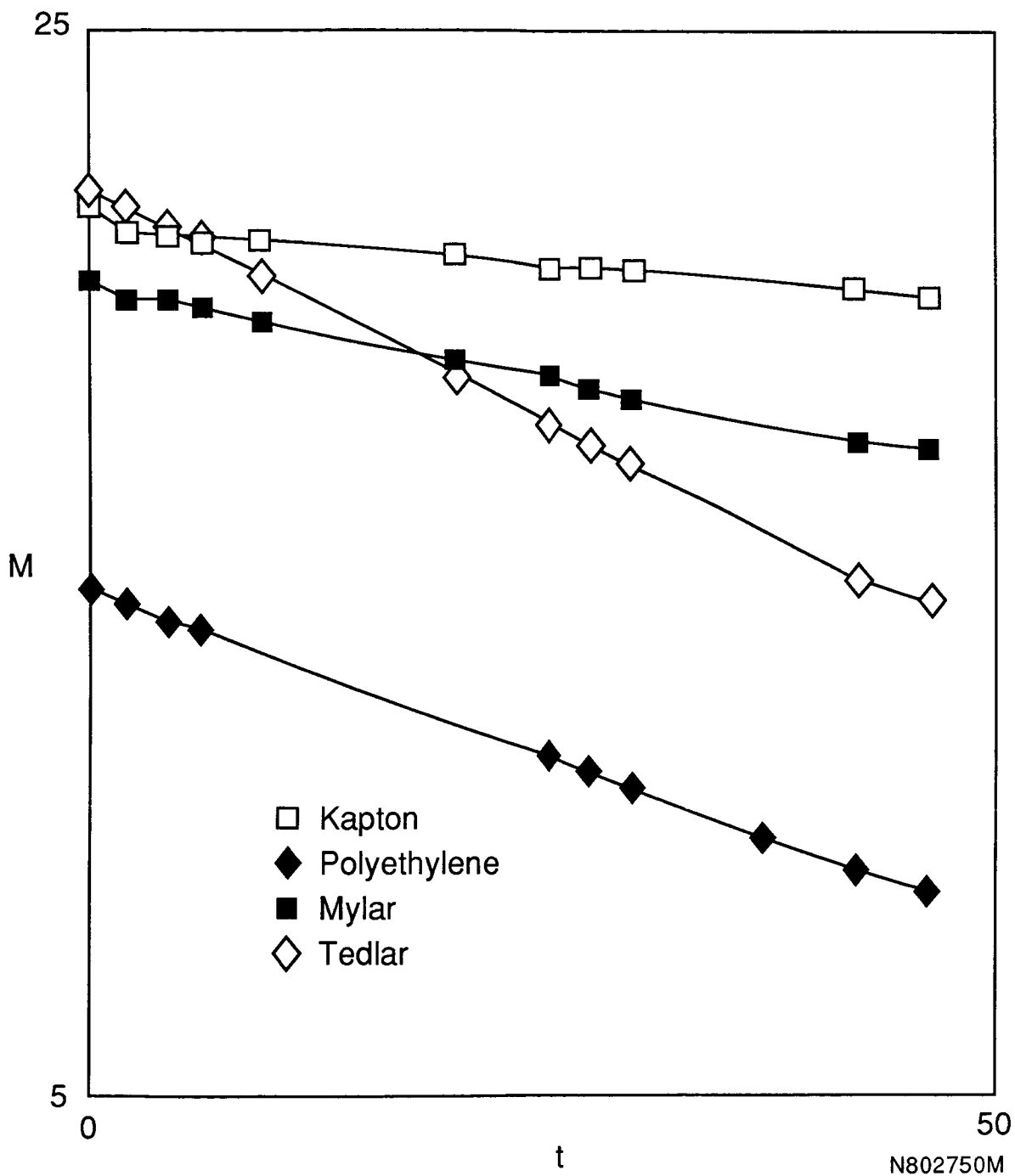
Figure 4.- Sample mass in milligrams vs exposure time hours.  Typical mass loss data for exposure of Kapton, Mylar, Tedlar, and polyethylene films to the flowing afterglow thermal atom environment.  The oxygen atom flux was $2.1 \times 10E^{18}$ atoms $cm^{-2}$ $sec^{-1}$, and the total pressure was 2 torr.

N802751M
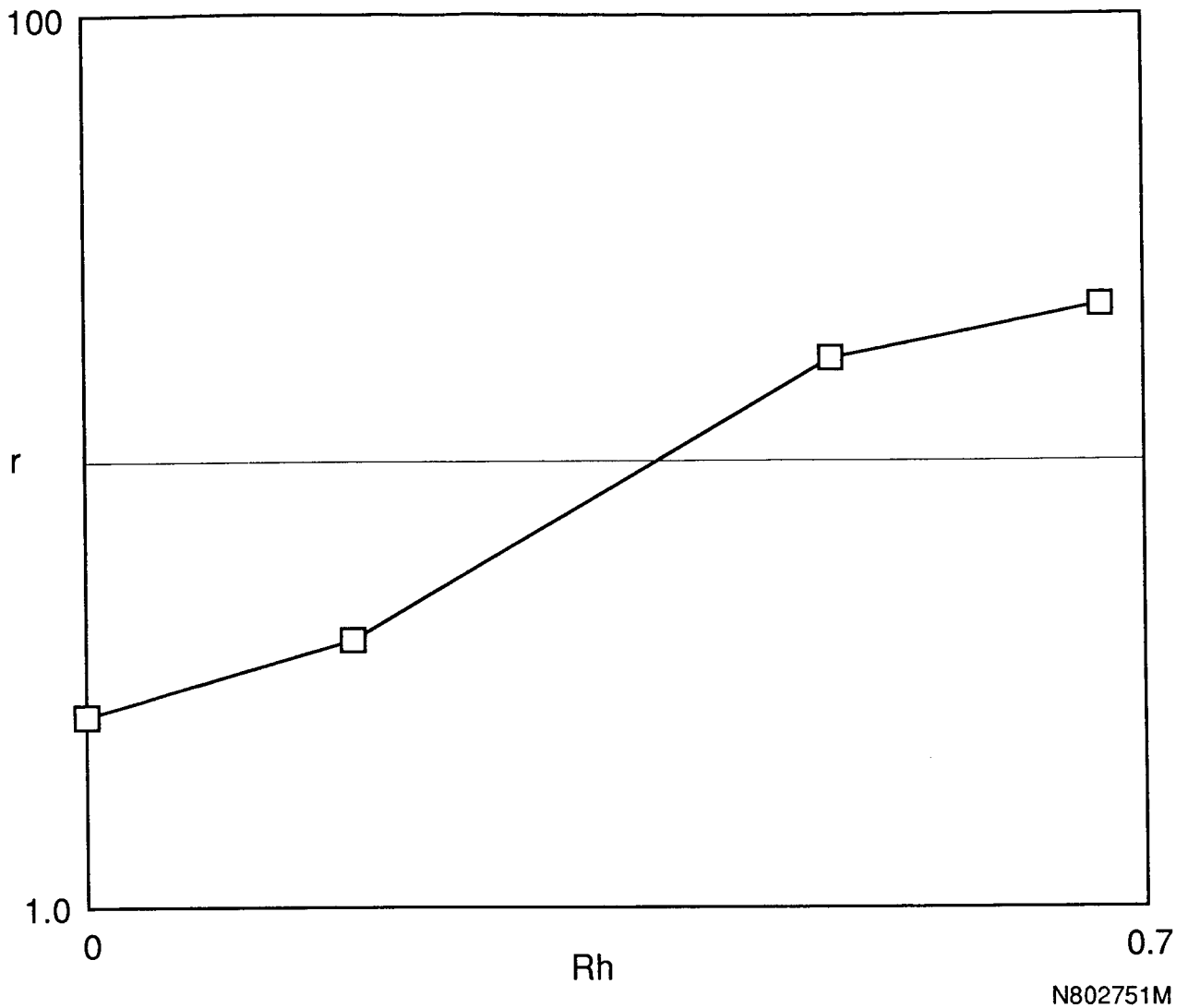
Figure 5.- Reaction effeciency, r is plotted against the aliphatic hydrogen fraction RH in the polymer repeat unit.
RH = # aliphatic hydrogens/total number of atoms.  A log plot is used only as a convenience for display of the wide data range.  The correlation coefficient for RH and r is 0.969.  The correlation coefficient for RH and log(r) is 0.967.

M = sample mass per square centimeter

[R-H] = surface concentration of reactive hydrogen, atoms $cm^{-2}$

[R- ] = surface concentration of dehydrogenated mass loss sites, molecules $cm^{-2}$

$\theta$ = fraction of surface in [R-] state, i.e. fractional dehydrogenation.

At steady state all surface concentrations are constant. The rate constants k1 and k2 contain the atomic oxygen flux implicitly; e.g., k1 = K1F, k2 = K2F where F is flux in atoms $cm^{-2}$ $min^{-1}$.

(1)        $d[R-H]/dt = -k_1(1-\theta) + k_3 dM/dt = 0$

(2)        $d[R- ]/dt = -k_2\theta + k_1(1-\theta) = 0$

The chemical reaction rates are related to the mass loss rate.

(3)        $dM/dt = -Ak_2\theta - Bk_1(1-\theta) = $ constant (see figures 3 and 4)

A and B are proportionality constants relating mass loss to particular chemical reaction rates.

Combining equations 1,2, and 3 we obtain

(4)        $dM/dt = \dfrac{1}{k_3/k_2 - 1/Bk_1(1 + Ak_3)}$

Figure 6.- The essentials of a simple phenomenological model describing the kinetics of mass loss when a hydrocarbon polymer is attacked by atomic oxygen.

85

## TABLE I.- MATERIALS REACTIVITY DATA IN LEO AND LANL BEAM

| Material | Rel. Rates* | Reaction Efficiency cm3/atom | |
|---|---|---|---|
| | | LEO (3-23) | LANL (24,60) |
| Kapton | 1 | $3.0 \times 10^{-24}$ | $2.7 \times 10^{-24}$ |
| Polyethylene | 0.9 | $3.7 \times 10^{-24}$ | $2.8 \times 10^{-24}$ |
| FEP Teflon | < 0.03 | $< 0.05 \times 10^{-24}$ | $7.7 \times 10^{-25}$ |
| Mylar | 1 | $3.4 \times 10^{-24}$ | |
| Tedlar | 1 | $3.2 \times 10^{-24}$ | |
| Graphite (various forms) | 0.7 | $0.9 - 1.7 \times 10^{-24}$ | $10^{-24}$ |
| Polybenzimidazole | 0.5 | $1.5 \times 10^{-24}$ | |
| Polysulfone | 0.8 | $2.4 \times 10^{-24}$ | |
| Siloxane-imide block copolymers (25%/75%) | 0.1 | $0.3 \times 10^{-24}$ | |
| Epoxy | 0.6 | $1.7 \times 10^{-24}$ | |
| FEP Teflon (Solar Max) | 0.6 | $1 \times 10^{-24}$ | |

*Mass loss rates in LEO normalized to Kapton rate.

## TABLE II.- COMPARISON OF ENVIRONMENTS

| Environment | O Atom flux, Energy | $O_2$ molecule flux, Energy | Electron density, Energy | VUV flux, wavelength |
|---|---|---|---|---|
| LEO | $10^{15}$ atoms cm$^{-2}$ sec$^4$ <br> 5 eV | $10^{13}$ <br> 10 eV | $10^5$-$10^6$ e cm-3 <br> 0.1 eV | ~$4 \times 10^{11}$ <br> 121.6mm |
| Plasma Asher | $10^{19}$-$10^{20}$ <br> 0.04-0.06 eV | $10^{21}$ <br> 0.04-0.06 eV | $10^9$-$10^{12}$ e cm-3 <br> 1 to 10 eV | $10^{12}$ to $10^{14}$ <br> 130mm |
| Flowing Afterglow | $10^{18}$-$10^{19}$ <br> 0.04 eV | $10^{21}$ <br> 0.04 eV | $<10^8$ e cm-3 <br> 0.04 eV | 0 |

TABLE III.- MATERIALS REACTIVITY DATA - PLASMA ASHER ENVIRONMENTS

| Pressure (torr) | RF (watts) | Kapton* | Polyethylene* | FEP Teflon* | HOPG Graphite* |
|---|---|---|---|---|---|
| 2 | 100 | 1.6 ± 0.3 | 5.3 ± 0.2 | 0.27 ± 0.005 | 0.59 ± 0.006 |
| 2 | 50 | 0.06 ± 0.01 | 0.5 ± 0.2 | 0.18 ± 0.04 | ------- |
| 0.4 | 50 | 0.80 ± 0.2 | 3.2 ± 0.5 | 0.49 ± 0.06 | ------- |
| 0.1 | 100 | 0.71 ± 0.2 | 3.6 ± 0.5 | 1.1 ± 0.09 | 0.24 ± 0.06 |
| 0.1 | 10 | 0.12 ± 0.01 | 0.45 ± 0.02 | 0.26 ± 0.02 | ------- |

*Mass loss rates in mg min$^{-1}$ cm$^{-2}$ x 100

TABLE IV.- MASS LOSS RATES RELATIVE TO KAPTON
(mass loss rate divided by Kapton rate)

| Pressure (torr) | RF (watts) | Kapton | Polyethylene | FEP Teflon | HOPG Graphite |
|---|---|---|---|---|---|
| 2 | 100 | 1.0 | 3.4 | 0.17 | 0.12 |
| 2 | 50 | 1.0 | 8.5 | 3.0 | ------- |
| 0.4 | 50 | 1.0 | 4.0 | 0.6 | ------- |
| 0.1 | 100 | 1.0 | 5.1 | 1.6 | 0.09 |
| 0.1 | 10 | 1.0 | 3.6 | 2.1 | ------- |

TABLE V.- MASS LOSS RATES RELATIVE TO 2 TORR, 100 WATTS CONDITION
(mass loss rate/2 torr, 100 watt rate)

| Pressure (torr) | RF (watts) | Kapton | Polyethylene | FEP Teflon | HOPG Graphite |
|---|---|---|---|---|---|
| 2 | 100 | 1.0 | 1.0 | 1.0 | 1.0 |
| 2 | 50 | 0.04 | 0.1 | 0.7 | ------- |
| 0.4 | 50 | 0.5 | 0.6 | 1.8 | ------- |
| 0.1 | 100 | 0.4 | 0.7 | 4.2 | 0.4 |
| 0.1 | 10 | 0.08 | 0.08 | 1.0 | ------- |

TABLE VI.- FLOWING AFTERGLOW MATERIALS REACTIVITY DATA

| Material | Rel. rate (mass loss) | Mass Loss Rate* (mg cm$^{-2}$ min$^{-1}$) | Reaction Efficiency* (cm$^3$ per atom) |
|---|---|---|---|
| Kapton | 1 | $(2.9 \pm 0.3) \times 10^{-4}$ | $2.6 \times 10^{-27}$ |
| Polyeth. | 4.1 | $(1.2 \pm 0.2) \times 10^{-3}$ | $2.2 \times 10^{-26}$ |
| FEP Teflon | 0.07 | $(2 \pm 5) \times 10^{-5}$ | $< 10^{-28}$ |
| Mylar | 2.4 | $(7.0 \pm 0.05) \times 10^{-4}$ | $4.1 \times 10^{-27}$ |
| Tedlar | 5.9 | $(1.7 \pm 0.24) \times 10^{-3}$ | $1.7 \times 10^{-26}$ |
| Graph. (HOPG) | 0.2 | $6 \times 10^{-5}$ | $2 \times 10^{-28}$ |
| Graph. (Pyro) | 0.07 | $2 \times 10^{-5}$ | $0.5 \times 10^{-28}$ |

* Average atom flux = $1 \times 10^{20}$ atoms cm$^{-2}$ min$^{-1}$

# ATOMIC OXYGEN STUDIES ON POLYMERS

W. D. Morison, R. C. Tennyson, J. B. French, T. Braithwaite
University of Toronto, Institute for Aerospace Studies

M. Moisan and J. Hubert
Université de Montréal

## ABSTRACT

The purpose of this research investigation was to study the effects of atomic oxygen on the erosion of polymer based materials. This report describes the development of an atomic oxygen 'neutral' beam facility using a 'SURFATRON' surface wave launcher that can produce beam energies between 2 and 3 eV at flux levels as high as $\sim 10^{17}$ atoms/$cm^2$-sec. Thin film dielectric materials were studied to determine recession rates and reaction efficiencies ($R_e$) as a function of incident beam energy and fluence. Accelerated testing was also demonstrated and the values of $R_e$ compared to available space flight data. In addition, SEM photomicrographs of the samples' surface morphology were compared to flight test specimens.

## INTRODUCTION

The space environment is characterized by the presence of charged particles, various atomic species (in low concentrations), "vacuum", micrometeoroids, radiation, temperature extremes and man-made debris. To some degree, all of these factors influence the design of satellites, depending upon the orbital altitude. Of particular concern is the presence of atomic oxygen, the concentration of which is shown in figure 1 (ref. 1) along with other atomic species and charged particles. The operation of many satellites, the Space Shuttle and the future U.S. Space Station, in low earth orbit (LEO), presents a major design problem since it is well established that atomic oxygen seriously erodes many of the commonly employed spacecraft materials (see ref. 2, for example). Although the concentration values shown in figure 1 may appear to be insignificant compared to the particle concentration at the earth's surface ($\sim 10^{19}$/$cm^3$), the actual flux of atoms impinging on an orbiting vehicle is quite high because of the satellite orbital velocity of $\sim 8$ km/sec (corresponding to an incident atomic oxygen energy of $\sim 5$ eV. Figure 2 (ref. 3) presents a plot of the incident flux as a function of altitude and solar activity. For reference purposes, the space shuttle altitude is indicated, corresponding to a flux of between $10^{14} \sim 10^{15}$ (atoms/$cm^2$-sec).

To qualify materials for spacecraft applications, it is necessary to assess

their sensitivity to atomic oxygen, as measured by their reaction efficiency ($R_e$) at orbital conditions. This is defined to be the volume of material lost per incident oxygen atom. Up to this point in time, limited flight test data at LEO conditions is available (see ref. 4). Consequently, it is imperative that ground-based systems be developed that can accurately simulate the neutral atomic oxygen environment in LEO. Such a system is described in this report together with comparative test data on mass loss rates, reaction efficiencies and surface morphology changes. Many of the materials tested in this simulator are compared to flight test data to ascertain the "validity" of the simulation. It will also be demonstrated that "accelerated testing" is possible, in that it yields erosion results consistent with flight data.

## UTIAS ATOMIC OXYGEN (AO) BEAM FACILITY

A schematic of the UTIAS AO facility configuration is presented in figure 3. This system is comprised of three major components (see photographs, fig. 4): a microwave induced plasma torch, a sampler-skimmer interface, and a vacuum chamber with the associated support electronics. The plasma torch is used to generate a stream of essentially neutral oxygen atoms seeded in a helium gas carrier. The sampler-skimmer system strips off a portion of the lighter carrier gas from the plasma and produces a diverging AO beam which is then directed into the connecting vacuum chamber. The chamber, in the form of a glass 'cross', maintains candidate AO bombardment samples at approximately $10^{-5}$ torr, to approximate low earth orbit spacecraft surface conditions.

## SURFACE WAVE LAUNCHER (SURFATRON)

There are various ways of producing plasmas with microwave (>300 MHz) power. The device used at UTIAS (fig. 5) is referred to as a 'SURFATRON' because it operates by propagating an electromagnetic surface wave along the plasma column. With such a device, a wave is excited at a given location along a cylindrical vessel containing the gas to be ionized. Providing the wave power flow is large enough, as this wave propagates, its energy is used to sustain the plasma column. It is called a surface wave because most of the power flows axially, very close to the surface of the dielectric vessel that contains the plasma column. This situation corresponds to the wave field decreasing radially, away from the plasma column, in an exponential-like fashion.

The surface wave is a natural propagation mode (an eigen-mode) along a plasma column. The efficient transformation of the microwave power into the plasma is a consequence of the use of this mode.

There are essentially two distinct elements in the SURFATRON surface wave launcher: the launching gap — a small interstice of circular symmetry through which the electric field leaks out toward the plasma — and an impedance matching system. In terms of an equivalent circuit, the gap can be represented by a capacitance and a resistance, and the impedance matching part is generally equivalent to two LC circuits (ref. 5). When properly designed and tuned, the two circuit components cancel out any imaginary component at the launcher input part and permit impedance matching of the launcher-plasma assembly and the transmission line. This ensures optimum power transfer from the generator (ref. 6).

## PLASMA CHARACTERISTICS

The microwave generated, atmospheric pressure helium plasma has been studied and characterized in terms of excitation temperature, gas temperature and electron density (ref. 7).

The SURFATRON is normally operated with a metered 98.5% helium/1.5% oxygen gas supply and is powered by a 200 Watt, 2450 MHz Microtron microwave power supply. The plasma is located in a 2 mm ID × 4 mm OD alumina (AL23) discharge tube. The power is set at 195 W and the total input flow rate is maintained at 3ℓ/min. Under these conditions, the excitation temperature is on the order of 2800 K, the degree of dissociation of $O_2$, as determined by mass spectrometer measurements, is approximately 64 percent, and the fraction of oxygen in the excited state is less than 1.2 percent (ref. 8).

## SAMPLER-SKIMMER SYSTEM

The helium/oxygen plasma is discharged at atmospheric pressure and allowed to expand supersonically toward the sampler-skimmer system. This system (fig. 6) consists of two nickel sampling/skimming orifice cones which are separated by an evacuated, water-cooled interface chamber. As the plasma discharge impinges upon the sampler cone, a portion of the central plasma core is drawn into the interface. Further, rapid expansion of the discharge takes place in the interface toward the skimmer core. A fraction of one percent of the flow through the sampler is stripped out by the skimmer cone and passed into the test chamber. The skimmer throughput is a largely mono-energetic, slightly divergent beam of helium, atomic oxygen and molecular oxygen, with a mean free path in excess of 1 metre. The interface pressure and the sampler-skimmer geometry govern the rate of molecular flow through the skimmer and consequently, the pressure in the test chamber and the atomic oxygen flux at the target.

Over a period of time, erosion of the sampler cone was observed, as manifested by an increase in interface pressure. An extensive series of measurements of the increase in orifice diameter ($D_{sa}$) were made as a function of system time. The results of these tests are given in figure 7. This data was necessary to permit accurate calculations of the atomic oxygen flux, as detailed in the Appendix.

## TORCH ALIGNMENT

Clearly, the key to conducting a successful experiment is the ability to produce repeatable results. Results from early operation of the facility suggested some difficulty associated with the alignment of the torch and the sampler-skimmer interface.

The optimum system alignment should maximize the amount of atomic oxygen in the beam. Since slight misalignment of the system leads to entrainment of room air into the chamber, an alternate approach is simply to minimize the amount of room air being entrained. Since room air is the system's only source of nitrogen, this is easily accomplished by tuning the mass spectrometer to the $N_2^+$ peak, and adjusting the SURFATRON's position until the peak height is minimized. The $N_2^+$ peak minimization method proved viable, as AO damage to samples became consistently better correlated. It was then realized that the total chamber pressure would also

be minimized along with the partial pressure of the nitrogen. This fact allowed a more precise alignment, as the Bayard-Alpert gauge is much "smoother" and easier to read than the mass spectrometer. When coupled to a digital voltmeter, the Bayard-Alpert gauge permitted the system to be aligned to a fine tolerance. Subsequent tests demonstrated that this alignment procedure reduced scatter to approximately 4% (ref. 9).

## VACUUM SYSTEM AND ELECTRONICS

The test chamber, a 15 cm diameter × 25 cm diameter 'Visiflow' glass cross (figs. 3, 4), incorporates fixtures to hold both control and test samples, Bayard-Alpert and Penning type gauges for pressure measurement, and an Aerovac AVA-1 mass spectrometer for beam analysis. An Edwards 250/200M 'Diffstak' pump extracts gas from the chamber at a rate of 2300 $\ell$/s to produce system pressures on the order of $10^{-5}$ torr.

A time-of-flight chopper system is currently being installed for beam energy surveys. These features allow complete monitoring of changes in beam properties such as atomic oxygen flux, energy, average molar mass, and degree of oxygen dissociation, as the system gas flow and geometry parameters are varied.

## CHARACTERISTICS OF THE ATOMIC OXYGEN BEAM

The enclosed Appendix contains a detailed gas flow analysis for the AO facility.

## BEAM ENERGY

From equation (18) (Appendix), it is clear that for a given molar mass of gas, measurements of the plasma temperature will define the peak oxygen atom energy. Since nozzle beam systems produce beams with relatively narrow velocity distributions (ref. 10), the peak energy will correspond closely to the average value.

Figure 8 shows plots of beam energy (E) versus molar mix ($M_{mix}$) for various plasma temperatures. As the constituents of the gaseous mixture ($He/O_2/Ar$) are varied, corrections to the plasma temperature must be made. The resulting "adjusted" experimental curve is shown in figure 8.

Because the beam is diverging slightly from the sampler-skimmer interface, intermolecular collisions in the test chamber are very infrequent. As a result, the energy distribution within the beam should remain undisturbed, except for a broadening associated with the beam divergence and the corresponding reduction in the atomic oxygen flux.

## ATOMIC OXYGEN FLUX

From the Appendix, the atomic oxygen flux at some distance $x_i$ is given by equation (13), i.e.,

92

$$\Phi_{AO} = \frac{3.45 \times 10^{18}}{(10.65 + x_i)^2} \quad (atoms/cm^2 \text{-} sec)$$

for $x_i > 7.86$ cm.

For the positions defined by $3.93 < x_i < 7.86$ cm, the significant beam blocking effect of the sample produces multiple atomic oxygen strikes and enhances the effective flux such that

$$\Phi_{AO} = \frac{1.695 \times 10^{27}}{(10.65 + x_i)^{8.86}} \quad 3.93 < x_i < 7.86 \text{ cm}$$

This phenomenon produces highly accelerated erosion rates for samples in this region. Figure 9 depicts the flux variation described by the above functions and shows the relative testing 'acceleration factor', based upon the ratio of the simulator flux to the nominal atomic oxygen flux in low earth orbit (250 km, $\approx 3 \times 10^{14}$ atoms/cm$^2$-s). Figure 9 clearly shows that acceleration factors, nominally in the range 3 to 275, are achievable with the present facility configuration.

BEAM EROSION PROFILE

The variation in flux across the beam diameter was assessed initially by profiling exposed samples using a Sloan Technology Corporation DEKTAK 3030 surface profile measuring system. This device uses a diamond tipped stylus to scan the surface of a sample in 2000 steps, with a vertical resolution of 20 μm. Figure 10 shows a plot from the DEKTAK. Because of the irregular surface profiles, it is difficult to obtain an accurate measurement of the volume of material eroded.

RECESSION RATE PROFILE

One parameter used to assess the erosion effects of atomic oxygen is the recession rate ($R_r$), which is a measure of the depth of material removed per unit time (cm/s). When a thin film is completely eroded, the recession rate is known exactly at the edge of the hole, and is given by,

$$R_r = h/t$$

where h = thickness of film (cm) and t = exposure time (s). If a series of identical films is exposed to the same beam for varying periods of time, a recession rate profile can be produced. The plot of $R_r$ versus hole radius should not only give the recession rate distribution, but should also depict the beam profile in terms of the cross-sectional variation in flux. Figure 11 shows recession rate versus hole radius for a $2.29 \times 10^{-3}$ cm (0.9 mil) Kapton®-H film. The profile has been extended out to $r = \sim 1.0$ cm although examination of the samples suggests that the maximum effective beam radius is approximately 0.575 cm. Note that, except for vertical scaling, the profile of figure 11 is consistent with the profilimeter results in figure 10.

# EXPERIMENTAL RESULTS

## SENSITIVITY TO BEAM ENERGY

A set of experiments was undertaken to determine if the reaction efficiency was dependent upon the incident AO beam energy. Because of the present upper limit on energy for the UTIAS AO simulator, it was necessary to demonstrate that material mass loss rates comparable to those obtained in space flight tests could be achieved.

From equation (18) (Appendix), it is shown that the beam energy can be controlled by changing the molar mass ($M_{mix}$) of the gas mixture and the plasma temperature. For the UTIAS system, the temperature change that occurs with varying $M_{mix}$ is given in figure 8. By varying the concentration of the gas mixture ($He/O_2/Ar$) it was possible to obtain a sensitivity curve of reaction efficiency as a function of beam energy for Kapton, as shown in figure 12. Note that reaction efficiency for Kapton can be calculated from equation (16) (Appendix) once the mass loss rate is determined. It is quite apparent that a threshold exists for Kapton reaction efficiency near 1.5 eV. For comparison purposes, the space flight value (ref. 2) of $3 \times 10^{-24}$ cm$^3$/atom is plotted at 5 eV. Similar results were also obtained for Mylar.

## SENSITIVITY TO BEAM FLUX

Tests were conducted on Kapton-H film using a 2.2 eV atomic oxygen beam for different flux levels. The mass loss versus exposure time curves are presented in figure 13. It can be seen that at the higher flux values ($> 10^{16}$ atoms/cm$^2$-sec) there is a transition region in which the material mass loss rate response changes. This is particularly evident for the curve at $10^{16}$ atoms/cm$^2$-sec. It was found that beyond this transition region, at flux levels $< 10^{16}$ atoms/cm$^2$-sec, the mass loss rates approached a constant. For Kapton-H film, $\Delta m / \Delta t \approx 0.075$ (mg/sec). Substituting this value into equation (16) (Appendix) yields a reaction efficiency for Kapton of $R_e \simeq 2.99 \times 10^{-24}$ (cm$^3$/atom).

SEM photomicrographs of the Kapton samples' surface morphology are presented in figure 14, for different exposure times, at a flux of $\Phi \approx 8.3 \times 10^{16}$ (atoms/cm$^2$-sec). It is quite apparent that the surface characteristics are changing with fluence. This is particularly evident when one compares photos (a) and (b) in the transition region discussed above.

## ACCELERATED TESTING

One of the major applications of ground-based simulators is the potential to do accelerated testing. Clearly, the validity of such a procedure rests on the assumption that for constant fluence tests (F = $\Phi$ × time), the same material reaction efficiency will be obtained. Experiments were conducted with Kapton-H film, at different flux levels, at exposure times beyond the transition range. Two test samples, (A) and (B), are compared (see figure 13) in the following table:

| Sample* | Beam Area ($cm^2$) | $\Phi$ (atoms/$cm^2$s) | t (s) | F (atoms/$cm^2$s) | $\Delta m/\Delta t$ (mg/s) | $R_e$ ($cm^3$/atom) |
|---------|--------------------|------------------------|-------|-------------------|----------------------------|---------------------|
| A | 1.995 | $8.3\times10^{16}$ | 2,700 | $2.24\times10^{20}$ | $.395\times10^{-3}$ | $3.06\times10^{-24}$ |
| B | 1.765 | $10^{16}$ | 21,600 | $2.16\times10^{20}$ | $.075\times10^{-3}$ | $2.99\times10^{-24}$ |

*$\rho$ = 1.42 (gm/$cm^3$)

It can be seen that the same value of $R_e$ is obtained, providing the tests are conducted at fluences beyond the transition range. Furthermore, comparing photomicrographs for samples (A) (figure 14(b)) and (B) (figure 15), shows a remarkable match in surface morphology. Thus it seems reasonable to assume that accelerated testing is valid for assessing material sensitivity to atomic oxygen.

MATERIAL REACTION EFFICIENCY

Using the procedures previously described, a series of tests were conducted on the materials listed in table 1. Comparisons with LEO flight data reported in reference 2 are also included. Note that the results have been "normalized" to Kapton as a reference material. To convert the data to $R_e$ values, assume $R_e$(Kapton) $\simeq 2.99\times10^{-24}$ (atoms/$cm^2$-sec). In general the results are in reasonable agreement with flight data. However, it should be noted that some uncertainty exists in the flight data because of errors in estimating the incident flux.

Figure 16 presents some SEM photomicrographs for several of the thin-film materials. These results provide a further basis for comparison with flight samples for given fluences.

CONCLUSIONS

An AO beam facililty has been developed based on a microwave powered SURFATRON device that can produce AO energies up to 2.2 eV, at flux levels as high as $8\times10^{16}$ (atoms/$cm^2$-sec). This system operates continuously and can yield target diameters up to 4.9 cm.

Reaction efficiencies ($R_e$) have been measured for a variety of materials and good correlation with LEO flight data has been obtained. It has been demonstrated that accelerated testing can be employed to yield the same value of $R_e$ for a given fluence. SEM photomicrographs exhibit "identical" surface morphology for the accelerated test comparisons. Other notable observations include an energy threshold that must be achieved to obtain values of $R_e$ consistent with flight tests, and that a start-up transition region exists at certain flux levels in which material mass loss rates differ from longer term exposure values.

# REFERENCES

1. Van der Waal, P. C.: Effect of Space Environment on Materials. Royal Netherlands Aircraft Factories Fokker, Rept. RV-22, 1968.

2. Leger, L.; Visentine, J.; and Santos-Mason, B.: Selected Materials Issues Associated with Space Station. Proc. 18th International SAMPE Technical Conference, Oct. 1986.

3. Peplinski, D. R.: Satellite Exposure to Atomic Oxygen in Low Earth Orbit. NASA CP 2340, 1984.

4. Leger, L.; Santos-Mason, B.; Visentine, J; and Kuminecz, J.: Review of LEO Flight Experiments. Proc. NASA Workshop on Atomic Oxygen. Nov. 1986, JPL Pub. No. 87-14, June 1987.

5. Moisan, M.; Zakrzewski, Z.; and Pantel, R.: The Theory and Characteristics of an Efficient Surface Wave Launcher (Surfatron) Producing Long Plasma Columns. J. Phys. D: Appl. Phys., Vol. 12, 1979.

6. Moisan, M.; Ferreira, C. M.; Hajlaoui, Y.; Henry, D.; Hubert, J.; Pantel, R.; Ricard, A.; and Zakrzewski, Z.: Properties and Applications of Surface Wave Produced Plasmas. Rev. Physique Appliquée, Vol. 17, 1982, pp. 707-727.

7. Besner, A.; Moisan, M.; and Hubert, J.: Fundamental Properties of Radiofrequency and Microwave Surface-Wave Induced Plasmas. J. Anal. Atom. Spectrosc., to be published Sept. 1988.

8. Lam, Calvin K.: Development of a Nozzle Beam Containing Atomic Oxygen. University of Toronto Institute for Aerospace Studies, UTIAS Tech. Note No. 153, July 1970.

9. Braithwaite, T. H.: Development of an Atomic Oxygen Beam Facility for Low Earth Orbit Simulation. M.A.Sc. Thesis, University of Toronto Institute for Aerospace Studies, 1988.

10. Knuth, Eldon L.; and Kuluva, Neil M.: Performance of an Arc-Heated Supersonic Molecular Beam and Its Application to Molecule-Molecule Collision Studies. Rec. Adv. in Aerothermochemistry, Vol. 1, NATO AGARD, Paris, 1967.

TABLE 1 - MATERIAL REACTION EFFICIENCY ($R_e$) COMPARISON WITH LEO FLIGHT DATA (REF. 2)

| Material | LEO Flight Data $R_e$ ($cm^3$/atom) | $R_e/(R_e)_{Kapton}$ | AO Simulator $R_e/(R_e)_{Kapton}$ |
|---|---|---|---|
| Kapton-H | $3 \times 10^{-24}$ | 1 | 1 |
| Polyethylene | 3.7 | 1.23 | 0.987 |
| Mylar | 3.4 | 1.13 | 1.360 |
| Tedlar | 3.2 | 1.07 | 1.260 |
| Pyrolytic Graphite | — | — | 0.318 |
| HOPG* | — | — | 0.478 |
| Carbon | 0.9~1.7 | 0.30~0.57 | — |
| Teflon FEP | <0.05 | <0.017 | 0.019 |

*Highly Oriented Pyrolized Graphite
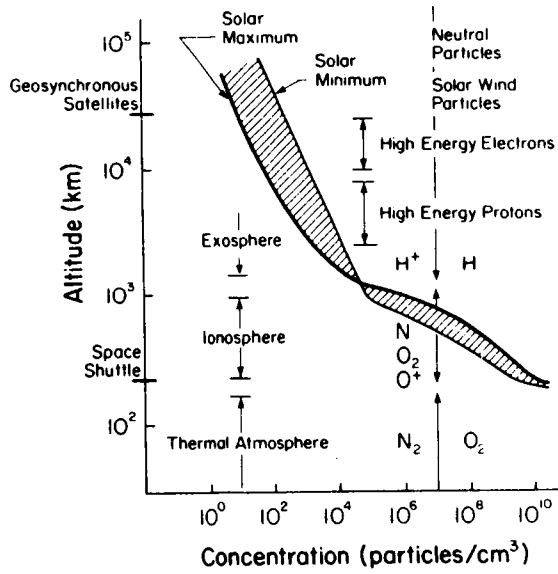
Fig. 1 (from Ref. 1)
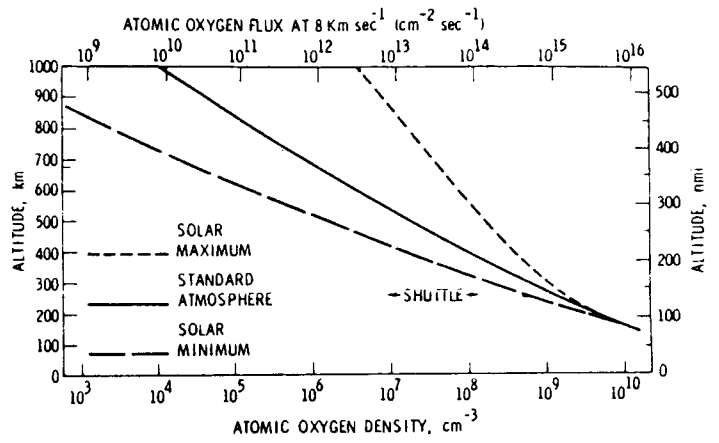


Fig 2 (from Ref 3)
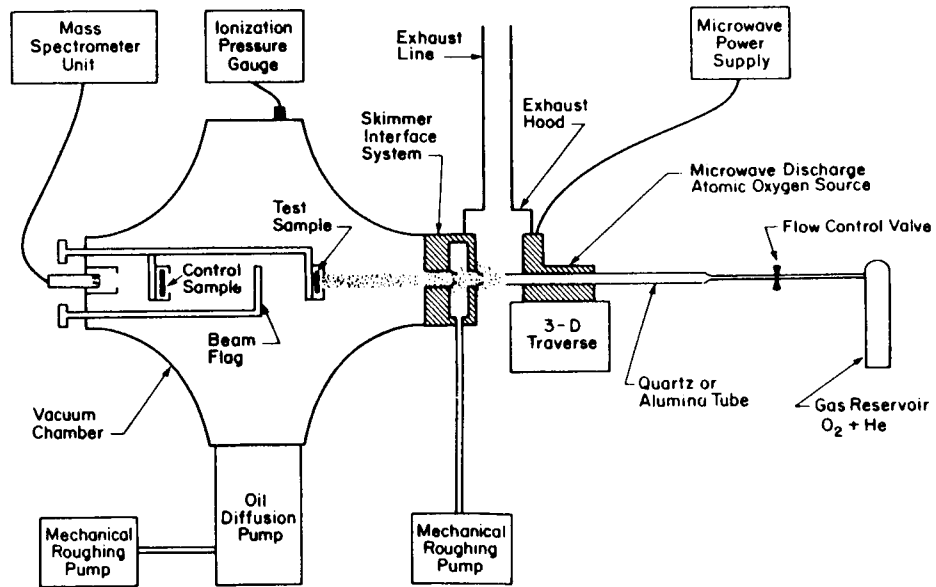


Fig. 3 Schematic of UTIAS Atomic Oxygen Beam Facility

Gas Mixture
Meter Control

Vacuum
Gauge
Output
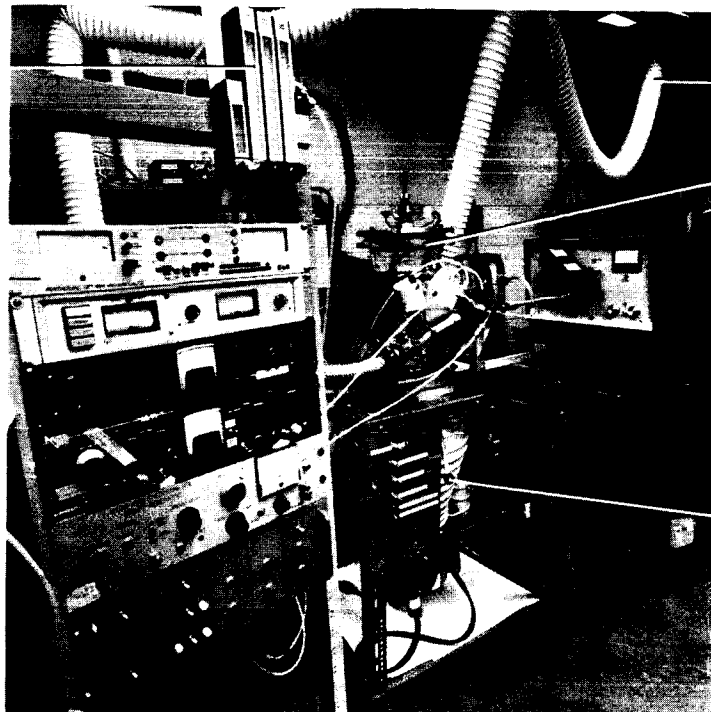
Ozone
-Ventilation Line

-Test Chamber

200 Watt
Microwave
Power Supply

2300 ℓ/sec
Vacuum Pump

Ionization Pressure
Gauge

Glass Cross
Vacuum Chamber

Pressure Gauge

Interface with
Orifice and
Skimmer

Roughing Pump Line
(30 ℓ/sec) for
Skimmer Interface

Cooling Air
for Surfatron
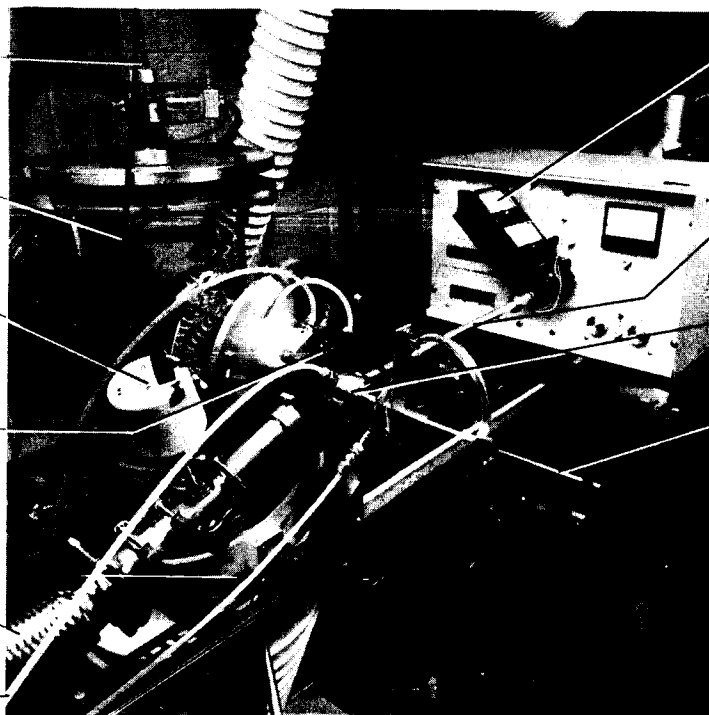
Reflected
Power Meter

Rigid 'Low Loss'
Power Line
to Source

Surfatron

3D Traverse for
Lining up Beam
with Inlet
Orifice

Fig. 4  The UTIAS Atomic Oxygen Beam Facility
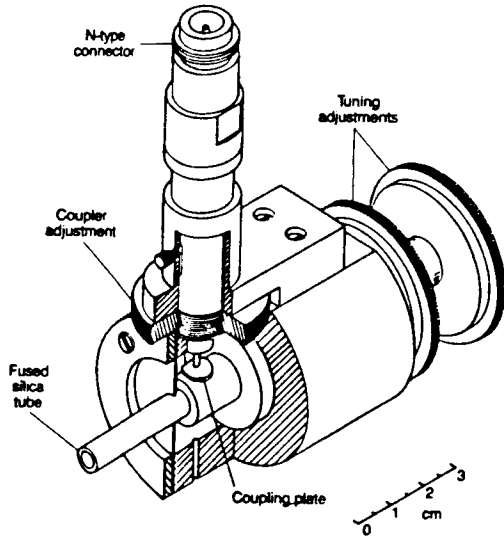
Fig. 5 Surfatron - a Microwave Surface Wave Launcher
(from Ref. 3)
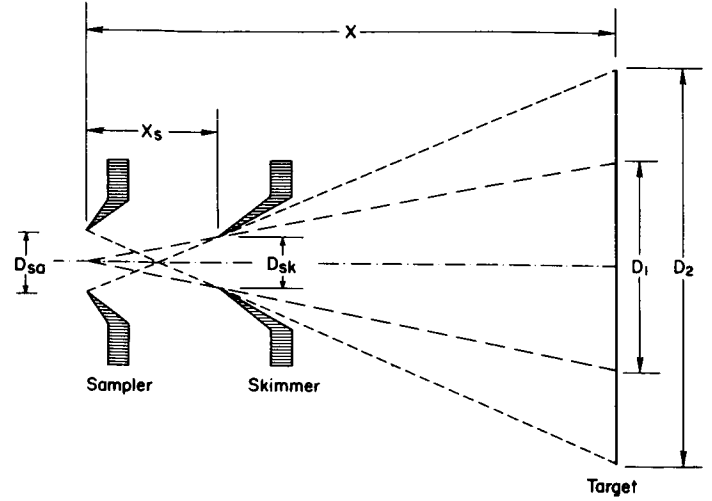


Fig. 6 Sampler Skimmer Geometry
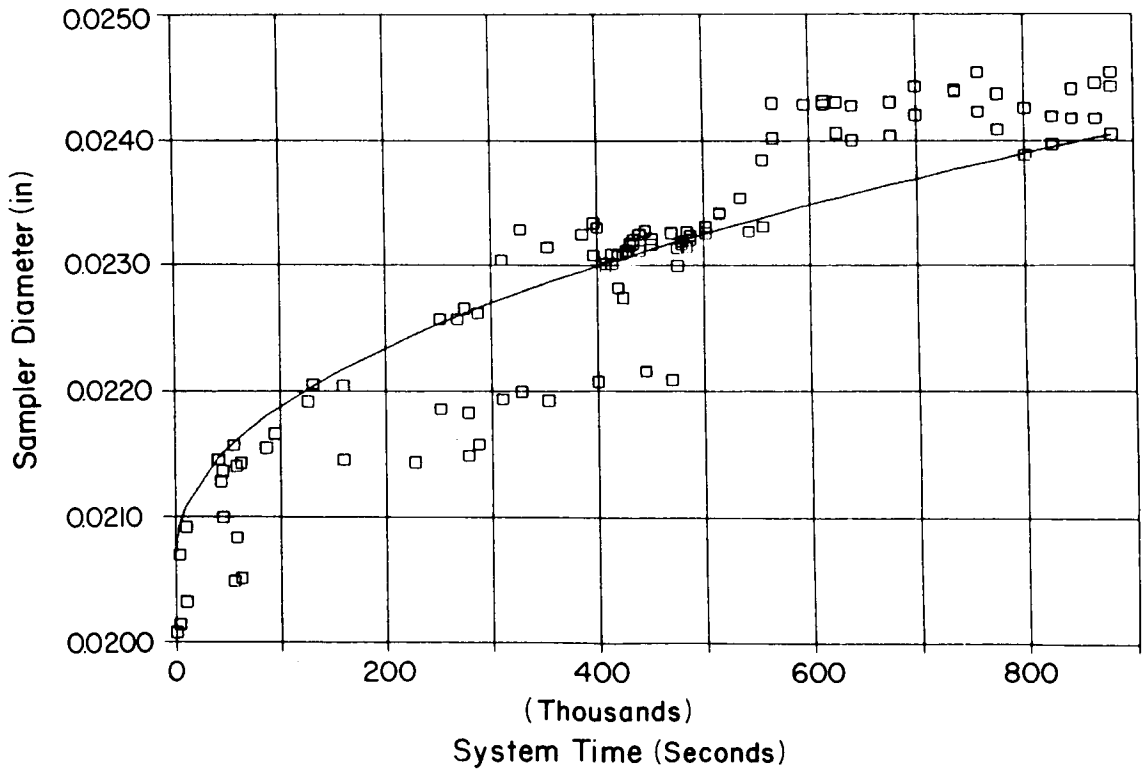


Fig. 7 ORIFICE DIAMETER vs SYSTEM TIME
Sampler #2 Initially .0207"
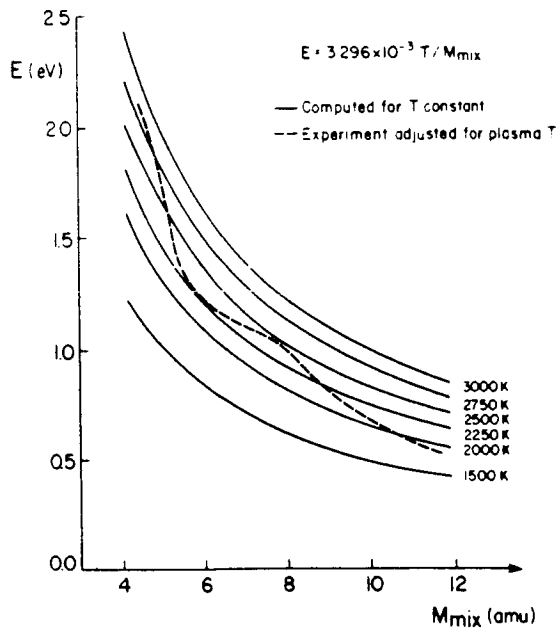
Fig. 8 Beam Energy as a Function of Gas Mixture

$$E = 3.296 \times 10^{-3}\ T/M_{mix}$$

— Computed for T constant
—— Experiment adjusted for plasma T

3000 K
2750 K
2500 K
2250 K
2000 K
1500 K



LEO : 250 km
$\Phi$ : $3 \times 10^{14}$/cm²-sec
E : 5 eV
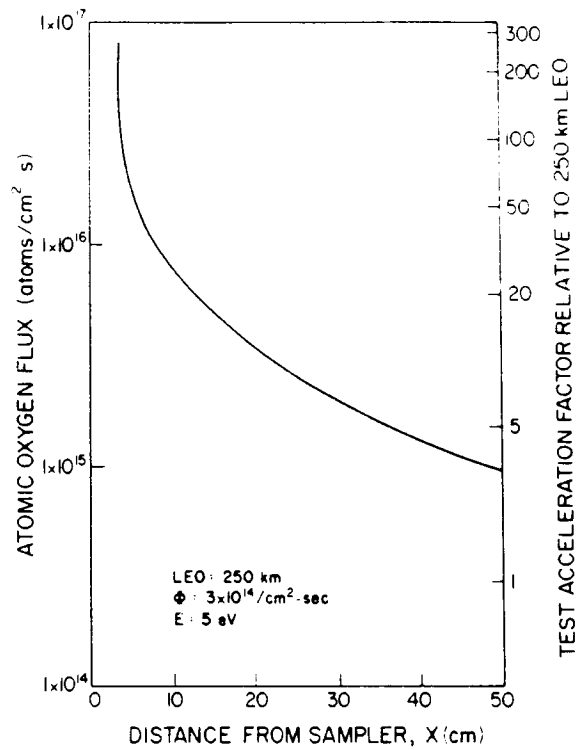
Fig. 9 Atomic Oxygen Flux and Accelaration Factor
vs Distance from Sampler Orifice



Vert : OA
Horiz : −7297 μm

Material : Kapton® .H (.0127cm)
Time : 3600 S
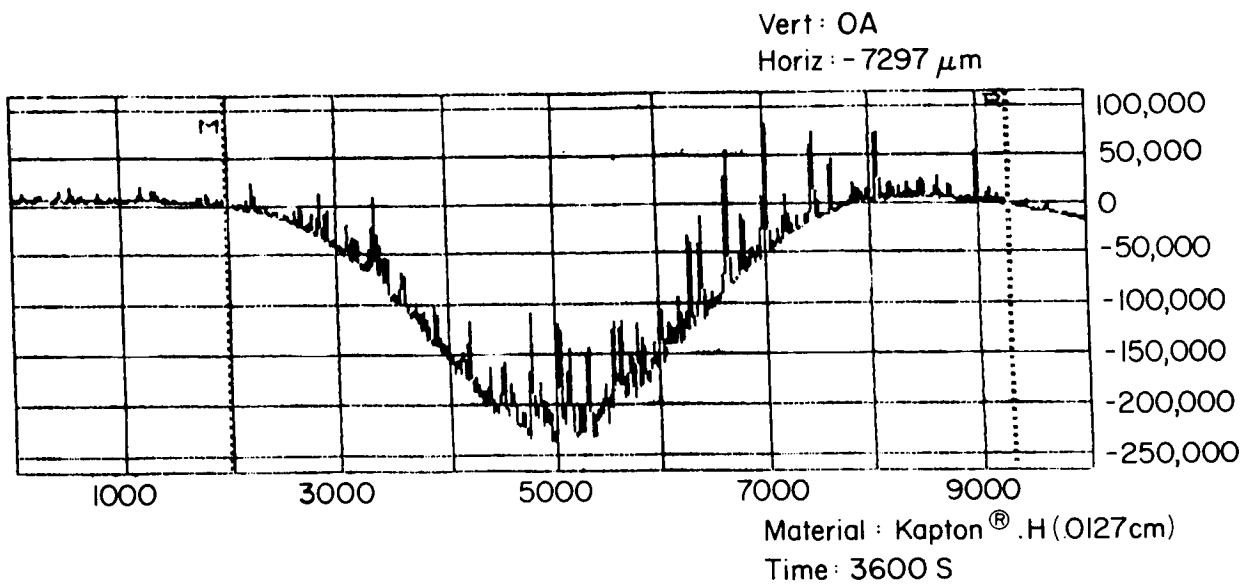
Fig. 10 AO beam profile using DEKTAK Profilimeter

101

## KAPTON at 3.93 cm
### Recession Rate vs Beam Radius
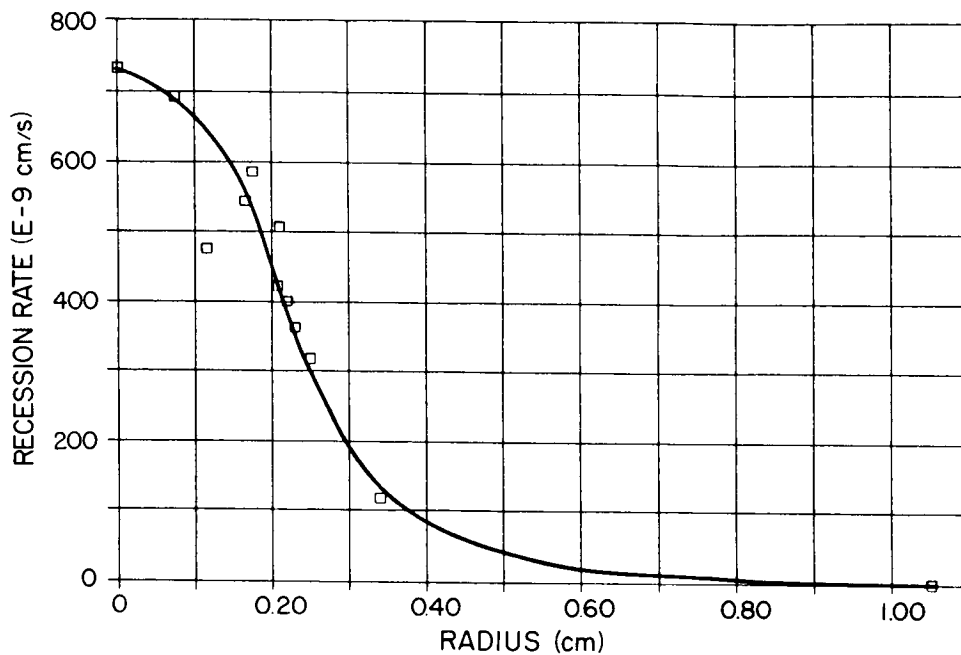


Fig. II  AO beam profile using hole radii

### KAPTON
#### Reaction Efficiency vs Energy
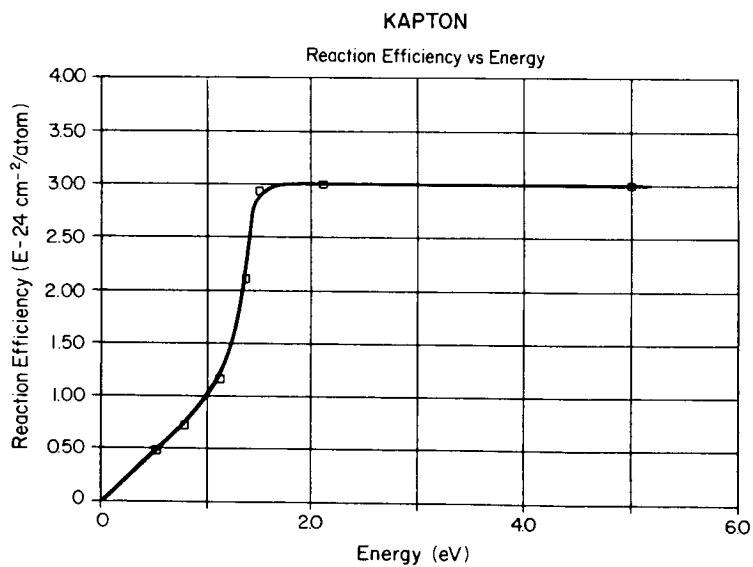


Fig. 12
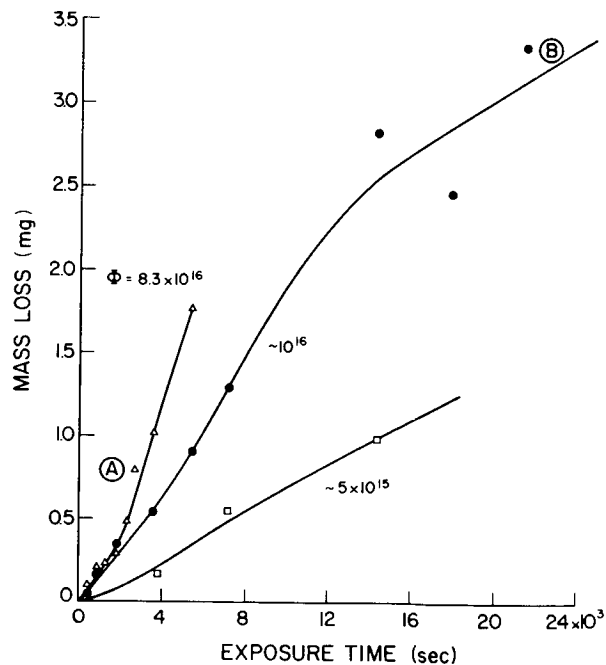


Fig. 13  Effect of Atomic Oxygen Flux on the Erosion Rate of KAPTON-H in UTIAS AO Beam Facility

102
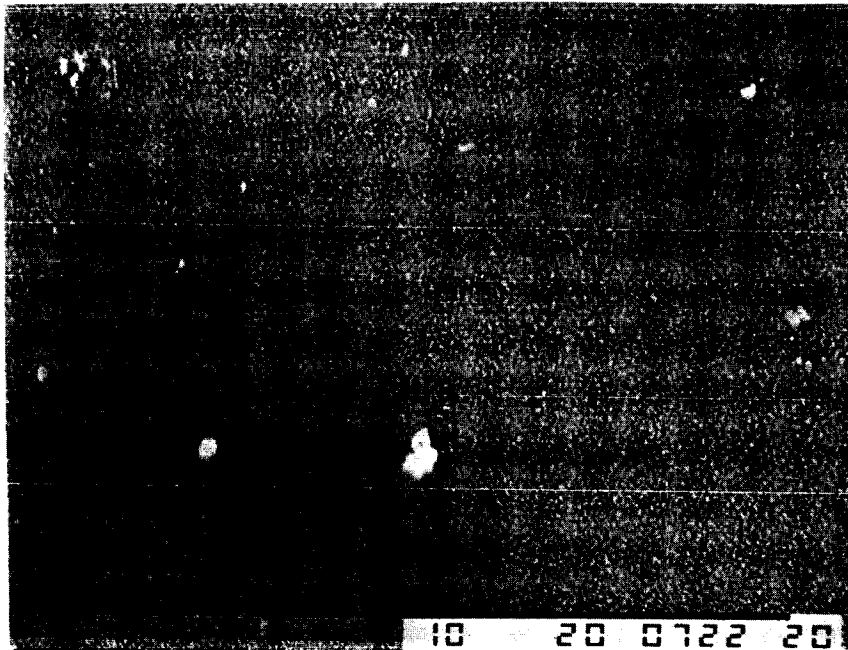
a) $t = 240$ s, $F \simeq 2 \times 10^{19}$ (atoms/cm²)
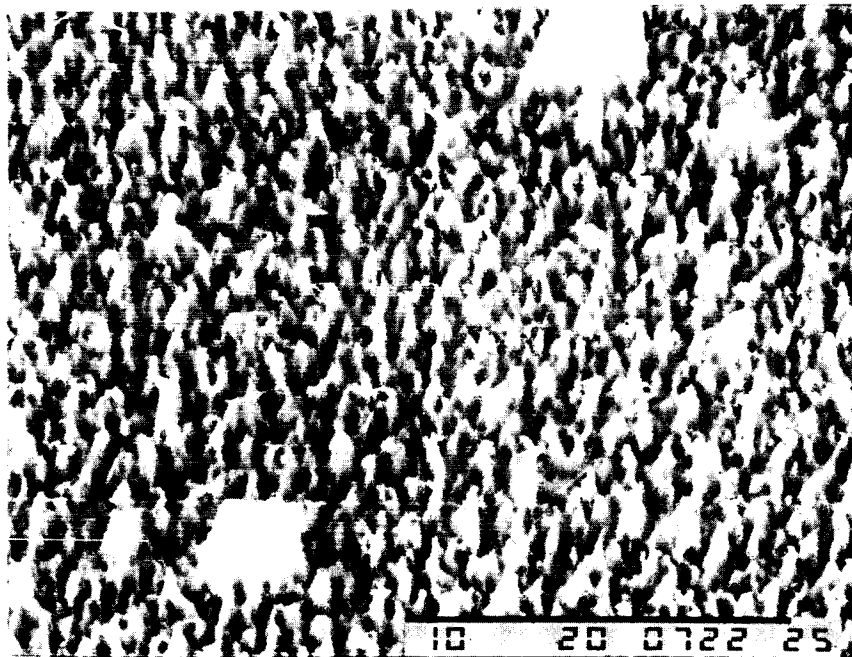


b) $t = 2700$ s, $F \simeq 2.24 \times 10^{20}$ (atoms/cm²)

Fig. 14  SEM Photomicrographs of Kapton® -H Film at 5000X,
7° tilt, $\Phi \simeq 8.3 \times 10^{16}$ (atoms/cm²-s)

103
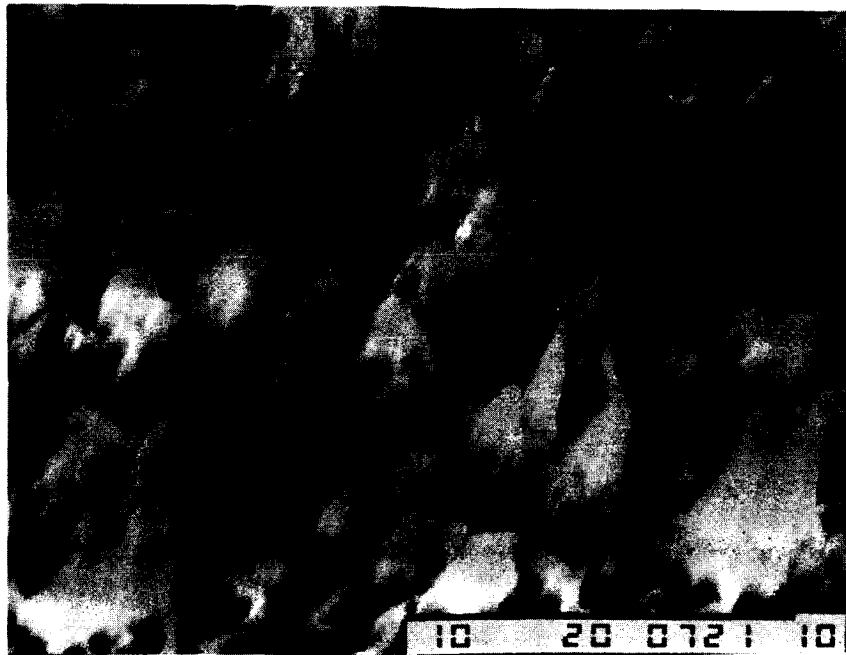
c) $t = 5400\,s,\ F \simeq 4.48 \times 10^{20}\,(atoms/cm^2)$



d) $\Phi \simeq 10^{16}\,(atoms/cm^2\text{-}s),\ t = 21,600\,s,$
$F \simeq 2.16 \times 10^{20}\,(atoms/cm^2)$

Fig. 15 SEM Photomicrographs of Kapton® -H Film at 5000X, 7° tilt

104
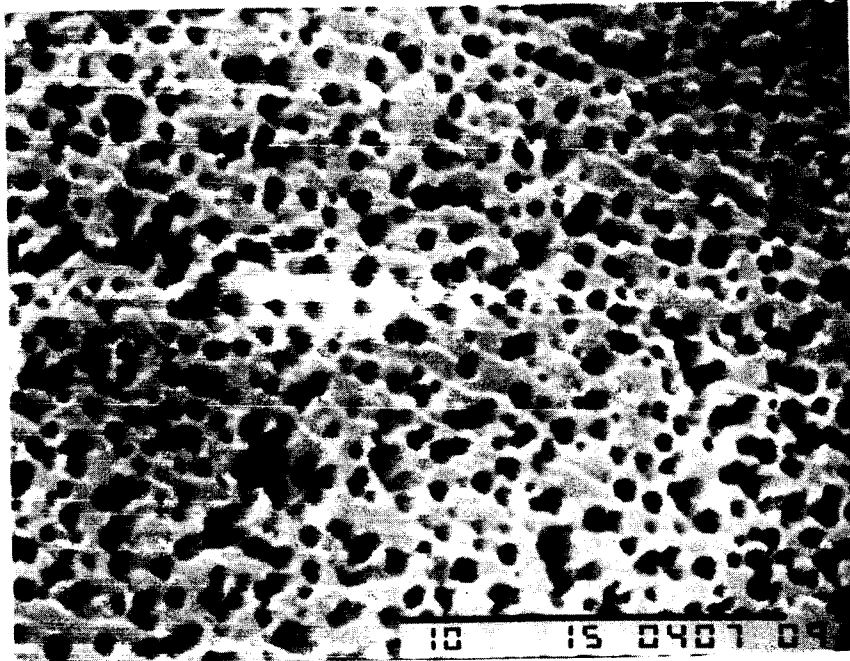
Polyethylene : $\Phi \simeq 5.6 \times 10^{15}$ (atoms /cm$^2$-s)

$F \simeq 3.4 \times 10^{20}$ (atoms /cm$^2$)
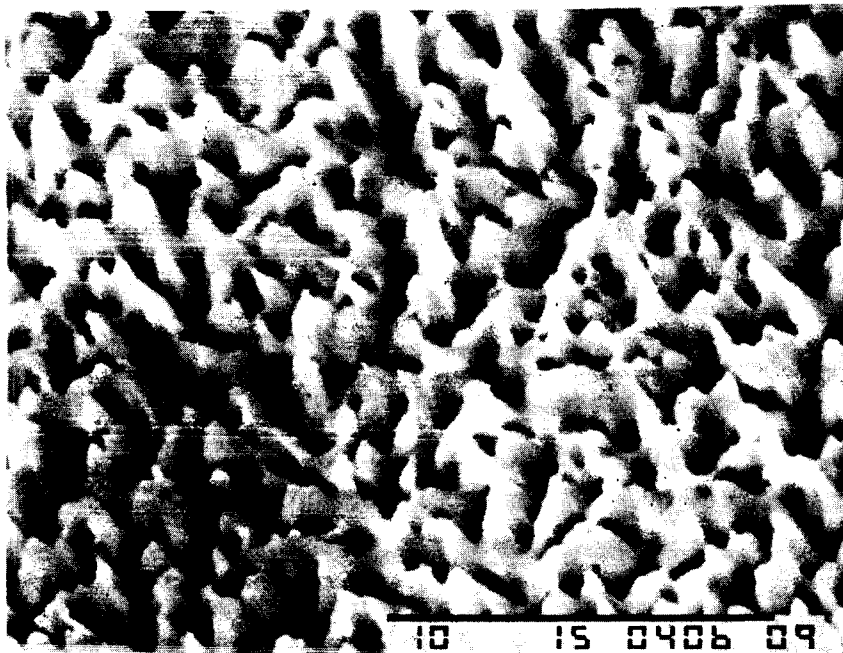


TEFLON FEP : $\Phi \simeq 3 \times 10^{16}$ (atoms /cm$^2$-s)

$F \simeq 1.4 \times 10^{21}$ (atoms /cm$^2$)

Fig. 16  SEM Photomicrographs at 5000X, 7° tilt

# APPENDIX - GAS FLOW ANALYSIS FOR AO BEAM FACILITY

It has been shown (refs. 8, 9) that the gas flow rate through the sampler orifice is described by

$$G_{sa} = n^{*}a^{*}A^{*} = \left(\frac{2}{\gamma+1}\right)^{\frac{1}{2}\left(\frac{\gamma+1}{\gamma-1}\right)} \cdot n_0 a_0 A_0 \quad \text{(molecules/sec)} \tag{1}$$

where $\gamma \simeq 1.62$, $n_0$ = molecular density at orifice (molecules/cm$^3$), $a_0$ = speed of sound (cm/s), and $A^0$ = orifice area (cm$^2$). Since

$$a_0 = 11.736 \times 10^3 \sqrt{T/M} \quad \text{(cm/s)} \tag{2}$$

where T = absolute gas temperature (K), M = average molar mass (amu), and

$$n_0 = n \frac{T_{ref}}{T} = \frac{7.339 \times 10^{21}}{T} \quad \text{(molecules/sec)} \tag{3}$$

where n = Lochschmidt number = $2.687 \times 10^{19}$ atoms/cm$^2$, and $T_{ref}$ = 273.16 K.

Also
$$A = \frac{\pi}{4} D_{sa}^2, \qquad D_{sa} = \text{orifice diameter}$$

so that
$$G_{sa} = 3.833 \times 10^{25} \frac{D_{sa}^3}{\sqrt{TM}} \tag{4}$$

If the flow into the chamber through the skimmer orifice is neglected, the pressure in the interface can be determined from

$$G_{sa} = 3.24 \times 10^{19} P_x S_x \quad \text{(atoms/sec)} \qquad \begin{array}{l} \text{where } P_x = \text{interface pressure (torr)} \\ \quad\quad\;\; S_x = \text{pump speed (}\ell\text{/sec)} \end{array} \tag{5}$$

For nozzle beam systems (refs. 8, 9), the flow through the skimmer orifice and into the test chamber is given by

$$G_{sk} = 0.631 \, G_s \Omega, \qquad \begin{array}{l} \text{where } \Omega = \text{solid angle subtended by skimmer orifice} \\ \quad\quad\;\; = A_{sk}/x_s^2 \end{array} \tag{6}$$

and $\quad A_{sk} = \dfrac{\pi D_{sk}^2}{4},$ $\quad$ $D_{sk}$ = skimmer orifice diameter = 0.04826 cm

$\qquad\qquad\qquad\qquad x_s$ = sampler skimmer spacing = 0.754 cm $\qquad\qquad$ (7)

so that $G_{sa}$ = 1.231×$10^{21}$ molecules/sec and $G_{sk}$ = 2.498×$10^{19}$ molecules/sec. The flow of oxygen atoms in the chamber is given by

$$G_{AO} = \left(\dfrac{2\alpha}{1+\alpha}\right)\beta \cdot G_{sk},$$

where $\alpha$ = degree of dissociation of $O_2$

$\beta$ = fraction of plasma-source $O_2$ in beam

The degree of dissociation is determined from mass spectrometer measurements of the beam. Analysis of the relative change in oxygen peak heights, originally presented by Lam (ref. 8), was modified to include a correction for room air entrained by the plasma. Mass spectrometer data are also used to quantify the change in gas stream composition that results from room air entrainment. The parameter $\beta$ expresses the amount of plasma-source oxygen in the beam relative to the total molecular flow through the skimmer orifice.

For the sampler-skimmer geometry defined above, and for a 0.985 He/0.015 $O_2$ plasma, the mass spectrometer data yields: $\alpha$ = 0.632 and $\beta$ = 0.0092 so that $G_{AO}$ = 1.78×$10^{16}$ (AO/sec). An average volumetric erosion rate can be determined from mass loss measurements on a sample, following exposure to the atomic oxygen beam, as

$$\dot{V} = \Delta m/t\rho \qquad (cm^3/s) \qquad\qquad (9)$$

where $\Delta m$ = mass loss (g), t = exposure time (s), and $\rho$ = specific gravity (g/cm$^3$). The reaction efficiency ($R_e$) for the material can then be determined from $G_{AO}$ and $\dot{V}$ as

$$R_e = \dfrac{\dot{V}}{G_{AO}} \qquad (cm^3/atom) \qquad\qquad (10)$$

Alternatively, the material reaction efficiency may be determined from $G_{AO}$ and a study of beam diameter as a function of distance from the sampler orifice:
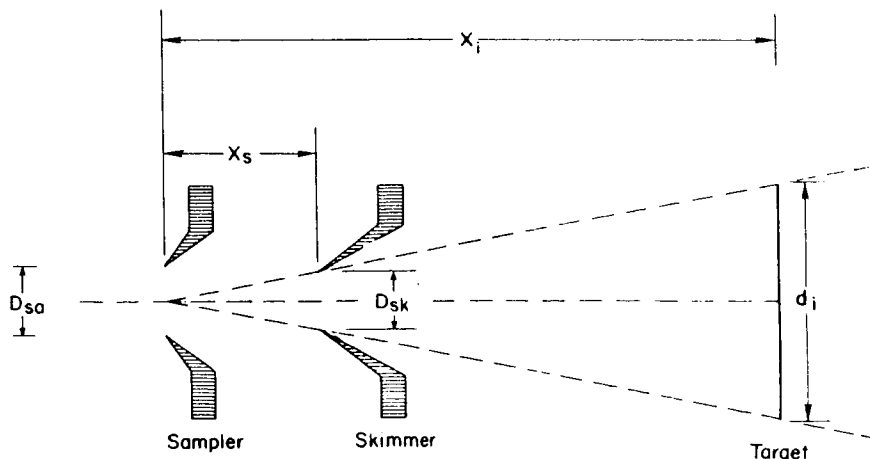
If $A_t$ = target area (beam area) = $\pi d_i^2/4$ at a distance $x_i$, it has been found that the system yields the following expression for target beam diameter

$$d_i = 0.081 \ (10.65 + x_i) \tag{11}$$

and so

$$A_t = 5.15 \times 10^{-3} \ (10.65 + x_i)^2 \ , \ x_i > 7.86 \ cm \tag{12}$$

Then the atomic oxygen flux at the target is

$$\Phi_{AO} = \frac{G_{AO}}{A_t} = \frac{3.45 \times 10^{18}}{(10.65 + x_i)^2} \ (atoms/cm^2\text{-}s) \ for \ x_i > 7.86 \ cm \tag{13}$$

The atomic oxygen fluence (F) is computed simply from the flux and the exposure time as

$$F = \Phi_{AO} \cdot t = \frac{3.45 \times 10^{18} t}{(10.65 + x_i)^2} \ (atoms/cm^2) \tag{14}$$

The material recession rate $(R_r)$ is determined from the volumetric erosion rate $\dot{V}$ by

$$R_r = \frac{\dot{V}}{A_t} = \frac{194.06 \ \dot{V}}{(10.65 + x_i)^2} \ (cm/s) \tag{15}$$

The material reaction efficiency can be computed in an equivalent fashion as

$$R_e = \frac{R_r}{\Phi_{AO}} = 5.62 \times 10^{-17} \ \frac{\Delta m}{\rho t} \tag{16}$$

The average energy of the oxygen atoms can be evaluated from

$$E = \frac{5}{2} kT \frac{M_{O_1}}{M_{mix}} \tag{17}$$

where k = Boltzmann constant $\equiv 8.24 \times 10^{-5}$ (eV/K), T = average plasma temperature (K), $M_{O_1}$ = oxygen atom molar mass = 16 amu, $M_{mix}$ = average molar mass of plasma input gas so that

108

$$E = 3.296 \times 10^{-3} \frac{T}{M_{mix}} \quad (eV) \tag{18}$$

The value of $M_{mix}$ is fixed by the input gas stream (and slightly altered by the influence of the dissociated oxygen), so that a valid measure of the plasma temperature yields the oxygen atom energy directly.

In practice, the expression shown below and in figure 14 is used to determine the plasma temperature:

$$TM_{mix} = 1.40 \times 10^{12} \frac{D_{sa}^4}{P_x^2 S_x^2} \tag{19}$$

# ATOMIC OXYGEN EFFECTS ON CANDIDATE COATINGS FOR LONG-TERM SPACECRAFT IN LOW EARTH ORBIT

E. H. Lan and C. A. Smith
McDonnell Douglas Astronautics Company

J. B. Cross
Los Alamos National Laboratory

## ABSTRACT

Candidate atomic oxygen protective coatings for long-term low Earth orbit (LEO) spacecraft have been evaluated using the Los Alamos National Laboratory O-atom exposure facility. The coatings studied include Teflon, $Al_2O_3$, $SiO_2$, and SWS-V-10, a silicone material. Preliminary results indicate that sputtered PTFE Teflon (0.1 $\mu$m) has a fluence lifetime of $10^{19}$ O-atoms/cm$^2$, and sputtered silicon dioxide (0.1 $\mu$m), aluminum oxide (0.1 $\mu$m), and SWS-V-10, a silicone, (4 $\mu$m) have fluence lifetimes of $10^{20}$ to $10^{21}$ O-atoms/cm$^2$. There are large variations in fluence lifetime data for these coatings. Further investigations are under way to determine the failure mechanisms.

## INTRODUCTION

The low Earth orbit (LEO) environment is known to react with many spacecraft materials, especially organic polymers.[1,2] Samples retrieved from Space Shuttle flights after being exposed to LEO had mass loss as well as surface morphology changes. The primary constituent of the LEO environment at Space Shuttle altitudes, atomic oxygen, is suspected to be the principal cause of the erosion of materials because of its high oxidative ability, flux ($10^{15}$ atoms/cm$^2$-sec) and collision energy (5 eV) for a spacecraft traveling at 8 km/sec.

Spacecraft for long duration missions such as the Space Station must utilize materials that can withstand the environment without undergoing significant changes in material properties. Reactive materials must be coated with a protective coating if they are to achieve longevity in LEO. A variety of protective coatings, such as ion-beam sputter-deposited thin films,[3] silicones and Teflon[4] have been proposed and developed for extended use in LEO. Some of these coatings have been tested on Space Shuttle flight experiments, but Space Shuttle flight data provide only limited information on the feasibility of long-term use of these materials in LEO. Space Shuttle flight experiments provide relatively small fluence exposures ($10^{20}$ O-atoms/cm$^2$) in comparison to the exposure a spacecraft such as Space Station will experience during 20-30 years in LEO ($10^{22} - 10^{23}$ O-atoms/cm$^2$).[1] It is, therefore, necessary to evaluate materials using ground-based simulation facilities which can perform accelerated testing at flux levels up to $10^{17}$ O-atoms/cm$^2$-sec.

## INSTRUMENTATION

The Los Alamos National Laboratory O-atom source[5,6] uses a CW plasma produced by focusing a high power $CO_2$ laser beam in a hydrodynamic expansion nozzle that has an oxygen/rare gas mixture flowing into it. The resulting temperature of the plasma is about 15,000° K. Using argon or neon as the rare gas, the percentage dissociation of molecular oxygen into atomic oxygen is about 85%. The facility is capable of producing atomic oxygen fluxes of up to $10^{17}$ O-atoms/$cm^2$-sec, energies of 1-5 eV, and total fluences of $10^{22}$ O-atoms/$cm^2$.[6]

## TECHNIQUE TO EVALUATE COATINGS

A technique to evaluate candidate coatings for atomic oxygen resistance has been developed, which uses silver oxidation as an atomic oxygen detector.[7] Silver oxidizes to silver oxide in the presence of atomic oxygen, and the electrical resistance of the oxide is dramatically higher than that of pure silver. Coatings of known thicknesses are deposited on top of a thin (250 Å) silver film and as atomic oxygen penetrates or diffuses through the coatings, the measured electrical resistance increases. The technique has been demonstrated to be highly sensitive to atomic oxygen and can also provide quantitative measurements of atomic oxygen flux.[6] A schematic of the sensor is shown in figure 1.

Samples are mounted on a sample manipulator and accurately placed perpendicular to the O-atom beam axis. Electronic instrumentation was arranged so that continuous in-situ resistance measurements can be obtained during atomic oxygen exposure. Figure 2 shows the resistance-measuring circuit for the actinometers. A constant current is supplied to the silver films and resistance data is obtained through voltage measurements. A high impedance voltage-to-frequency converter feeds a multichannel analyzer, which stores the voltage measurements as a function of exposure time. The data is then fed to a computer for data analysis.

## SAMPLE PREPARATION

The actinometers were coated with PTFE Teflon, $Al_2O_3$, $SiO_2$, and silicone SWS-V-10 materials. The PTFE Teflon was sputtered using a Teflon target at the NASA-Lewis Research Center. The thicknesses of the PTFE Teflon coatings were 800 Å and 1250 Å, as determined by performing profilometry on separate witness samples. The $Al_2O_3$ and $SiO_2$ coatings were sputtered using $Al_2O_3$ and $SiO_2$ targets at the MDAC-HB facility. The $Al_2O_3$ and $SiO_2$ coatings were 950 Å, as determined by performing ellipsometry on witness silicon wafer samples. We estimate the measured thicknesses of all the sputtered coatings to be within ±10%. The SWS-V-10 silicone coating was brushed on at NASA-Marshall Space Flight Center. The thickness of the brushed coating is estimated to be between 4 and 10 µm. For data analysis of these samples, we will assume that the coatings had a thickness of 4 µm.

## O-ATOM BEAM FLUX CALIBRATION

The time history of oxidation of 250 Å thick bare silver films when exposed to the O-atom beam can be used to calculate the oxidation rate in monolayers/second, which can then be converted to a beam flux in atoms/cm²-sec. The oxidation rate and beam flux were calculated using the assumptions that: 1) the sticking probability of O-atoms on bare polycrystalline silver is unity over the entire range of oxide formation, 2) the nearest neighbor distance (NND) in polycrystalline silver is 2.9 Å, the same as that for the silver face centered cubic structure, and 3) the $O_2$ molecules in the beam (about 15%) do not react with silver to form silver oxide. The flux is then calculated from:

$$\text{Oxidation rate (monolayers/sec)} = \frac{\text{Thickness of Ag film (Å)}}{\text{Time of oxidation (sec) x NND (Å/monolayer)}}$$

$$\text{Beam flux (atoms/cm}^2\text{-sec)} = \text{Oxidation rate x No. of Ag atoms/cm}^2\text{-monolayer,}$$

where No. of Ag atoms/cm²-monolayer = $1.2 \times 10^{15}$, as determined from the NND.

In these experiments, when bare 250 Å thick silver films were placed 15 cm from the nozzle, the estimated atomic oxygen flux was $1 \times 10^{17}$ atoms/cm²-sec. With the exception of Teflon, all of the coatings were exposed to an O-atom beam (using an $O_2$/Ar mixture) having a kinetic energy of 1.5 eV (Teflon 3 eV) and a flux of $1 \times 10^{17}$ atoms/cm²-sec (Teflon $6 \times 10^{16}$ atoms/cm²-sec).

## RESULTS

An example plot of the electrical resistance/conductance of silver under-lying a protective coating as a function of O-atom fluence is provided in figure 3. The shapes of the resistance/conductance vs. fluence graphs, however, do vary from coating to coating as well as from sample to sample of the same coating. Please see Table I for a summary of the results obtained for the coatings studied.

PTFE Teflon:

ESCA analysis of the sputtered PTFE Teflon coatings before exposure showed that their atomic concentration was 45% C and 55% F. Two PTFE Teflon-coated actinometers (800 Å and 1250 Å) were exposed to an O-atom beam (using an $O_2$/Ne mixture) having a 3 eV kinetic energy and $6 \times 10^{16}$ atoms/cm²-sec flux. Visual examination of the beam spot on the actinometers after O-atom exposure indicated that the Teflon was eroded away. Bulk Teflon has been tested in the LANL O-atom beam and profilometry measurements after exposure indicate there is erosion of Teflon through reaction with atomic oxygen. The PTFE Teflon tested at 3 eV kinetic energy gave a reaction efficiency of $0.22 \times 10^{-24}$ cm³/atom for the 800 Å sample and $0.82 \times 10^{-24}$ cm³/atom for the 1250 Å sample. Previous exposure of a 800 Å thick PTFE Teflon-coated actinometer to a flux of $9 \times 10^{15}$ atoms/cm²-sec at 1.5 eV kinetic energy (using an $O_2$/Ar mixture) gave a reaction efficiency of $0.13 \times 10^{-24}$ cm³/atom. The fluxes used in the Teflon exposures were reduced because of reduced gas flows in the nozzle.

112

$Al_2O_3$:

Auger analysis of the $Al_2O_3$ coating before exposure showed an atomic concentration of 33% Al, 65% O, and <2% C. SEM photographs of the coating up to a magnification of 20,000X did not reveal any obvious porosity. Two $Al_2O_3$-coated actinometers, both of 950 Å, were exposed to an O-atom beam (using an $O_2$/Ar mixture) having a 1.5 eV kinetic energy and $1.0 \times 10^{17}$ atoms/$cm^2$-sec flux. Complete oxidation of the underlying silver occurred after a fluence of $1.0 \times 10^{20}$ atoms/$cm^2$ for one sample, whereas complete oxidation of the underlying silver occurred after a fluence of $8.3 \times 10^{20}$ atoms/$cm^2$ for the other sample. Analyses of the $Al_2O_3$ coating after exposure are under way.

$SiO_2$:

Auger analysis of the $SiO_2$ coating before exposure showed an atomic concentration of 35% Si, 58% O, 5% N and 2% C. SEM photographs of the sputtered coating up to a magnification of 20,000X did not reveal any obvious porosity. Three $SiO_2$-coated (950 Å) actinometers were exposed under the same conditions as the $Al_2O_3$ samples. Complete oxidation of the underlying silver occurred after fluences of $1.2 \times 10^{20}$ atoms/$cm^2$, $7.3 \times 10^{20}$ atoms/$cm^2$, and $11.0 \times 10^{20}$ atoms/$cm^2$. Visual inspection of the $SiO_2$-coated actinometers after the test runs indicated that the coating was still intact, and erosion of the coating as observed in the exposed PTFE Teflon samples did not occur.

ESCA and Auger analyses were performed on the $SiO_2$ coated silver strip after O-atom exposure and only a small percentage of silver (about 2%) was present on the sample surface. Auger elemental depth profile of a $SiO_2$-coated actinometer after exposure to a $11.0 \times 10^{20}$ O-atom/$cm^2$ fluence is provided in figure 4. The profile confirms that the $SiO_2$ coating was not eroded away. There is a layer of $SiO_2$ on the surface, and silver does not appear until part of the coating is sputtered away. The profile does show, however, silver over a broad depth range, which may be due to the high surface roughness of the alumina substrate (>1 μm) and/or diffusion of silver into the coating.

SWS-V-10 Silicone:

The three SWS-V-10 silicone-coated actinometers (4 μm thickness) tested under the same conditions as the $Al_2O_3$ and $SiO_2$ samples showed complete oxidation of the underlying silver after fluences of $1.8 \times 10^{20}$ atoms/$cm^2$, $4.9 \times 10^{20}$ atoms/$cm^2$, and $6.0 \times 10^{20}$ atoms/$cm^2$. Visual inspection of the silicone samples after exposure indicated that the coating was also intact, although the underlying silver had oxidized. Further analysis of these samples will be performed by NASA/MSFC.

DISCUSSION

The oxygen atom source provides, in addition to atomic oxygen, a flux of visible and infrared photons. With the exception of the PTFE Teflon-coated samples, which did not experience a temperature rise during the course of the

113

test runs, all of the other samples, aluminum oxide, silicon dioxide, and SWS-V-10 silicone, did experience sample heating. A thermocouple placed on the side of the sample substrate, but not in the beam spot, indicated that the substrates reached temperatures of up to 100° C by the end of the exposures. Readings from another thermocouple that was placed directly in the beam spot indicated that the beam spot temperature was another 20° C higher. The rate of temperature rise was not controlled.

Measurements of the vacuum UV (VUV) intensities[6] produced by the plasma have been taken using a vacuum monochrometer with a CsTe solar blind and bialkali photomultiplier tubes. The 1.5-eV ($O_2$/Ar) beam produced VUV intensities about 3 times higher than that produced by solar radiation, while the 3-eV ($O_2$/Ne) beam produced VUV intensities about equal to solar VUV. The inorganic coatings ($SiO_2$ and $Al_2O_3$) are not likely to be affected by the VUV radiation, but organic coatings such as Teflon and silicones may degrade to the point where atomic oxygen has an enhanced reactivity with the photoproduct backbone of the polymer.

Auger analysis (figure 4) and visual inspection after exposure indicated that the $SiO_2$ coating was intact, although the underlying silver had oxidized. Diffusion of O-atoms into inorganic thin film coatings, therefore, may be a significant process that warrants additional attention. Since Auger analysis after exposure also revealed a broad distribution of silver in the thickness of the coated area, diffusion of silver into the coatings may have also occurred. Temperature effects could be significant in both of these processes.

The test results of the sputter-coated actinometers reveal a large scatter in the data (see table I), even though the coatings were coated during the same run and should be of the same thickness. Some of the parameters that would contribute to scatter in the data include temperature, coating continuity, coating impurities, and substrate surface roughness. Since the surface of the actinometers used in these experiments had roughness on the order of microns and the sputtered coatings were only about 0.1 μm in thickness, it is unknown whether continuous uniform coatings were protecting the actinometer surfaces. The quality of the coatings in terms of chemical composition and codeposited impurities is another factor to be considered in assessing their ability to protect reactive substrates. For future spacecraft parts, if thin film coatings are to be used, the ability to apply the coatings consistently on a large-scale basis and to certify the coating quality will be essential to ensure the substrate protection for the life of the spacecraft.

Of the coatings we tested to date (0.1 μm of sputtered Teflon, $Al_2O_3$, and $SiO_2$ and 4 μm of silicone), none of them have provided protection for the full atomic oxygen fluence of $10^{22}$ to $10^{23}$ atoms/$cm^2$ expected for long-term spacecraft such as Space Station. Our results indicate that the coatings of the above-specified thicknesses may provide protection for O-atom fluences of $10^{20}$ to $10^{21}$ atoms/$cm^2$. It is unclear at this point whether increasing the thickness of the coatings will proportionately increase the total O-atom fluence that these coatings can withstand. Future work will emphasize the fundamental mechanisms responsible for the interaction of these materials with O-atoms.

Of particular interest are thin film inorganic coatings and the relationship of diffusion-limited kinetics to the atomic oxygen kinetic energy.

## ACKNOWLEDGEMENTS

REFERENCES

1. Leger, L.; Visentine, J.; and Santos-Mason, B.: "Selected Materials Issues Associated with Space Station," 18th International SAMPE Technical Conference, October 1986.

2. Whitaker, A. F.; Little, S. A.; Harwell, R. J.; Griner, D. B.; DeHaye, R.F.; and Fromhold, A. T., Jr.: "Orbital Atomic Oxygen Effects on Thermal Control and Optical Materials," STS-8 Results, AIAA-85-0146, AIAA 23rd Aerospace Sciences Meeting, January 1985.

3. Banks, B. A.; Mirtich, M. J.; Rutledge, S. K.; Swec, D. M.; and Nahra, H. K.: "Ion Beam Sputtered Deposited Thin Film Polymer Coatings for Protection of Spacecraft in Low Earth Orbit", AIAA 23rd Aerospace Sciences Meeting, January 1985.

4. Leger, L. J.; Visentine, J. T.; and Schliesing, J. A.: "A Consideration of Atomic Oxygen Interactions with Space Station," AIAA-85-0476, AIAA 23rd Aerospace Sciences Meeting, January 1985.

5. Cross, J. B.; Spangler, L. H.; Hoffbauer, M. A.; and Archuleta, F. A.: "High Intensity 5 eV CW Laser Sustained O-Atom Exposure Facility for Material Degradation Studies," 18th International SAMPE Technical Conference, October 1986.

6. Cross, J. B.; and Blais, N. C.: "High Energy/Intensity Atomic Oxygen Beam Source for Low Earth Orbit Materials Degradation Studies," 16th International Symposium on Rarefied Gas Dynamics, July 1988.

7. Cross, J. B.; Lan, E. H.; and Smith, C. A.: "A Technique to Evaluate Coatings for Atomic Oxygen Resistance," 33rd International SAMPE Technical Conference, March 1988.

TABLE I. - SUMMARY OF COATINGS RESULTS

| Coating | Thickness | Fluence Lifetime (Atoms/cm$^2$) |
|---------|-----------|----------------------------------|
| PTFE Teflon | 800 Å | $6.0 \times 10^{19}$ (Reaction Efficiency of $0.13 \times 10^{-24}$ cm$^3$/atom) |
| | 800 Å | $3.5 \times 10^{19}$ (Reaction Efficiency of $0.22 \times 10^{-24}$ cm$^3$/atom) |
| | 1250 Å | $1.5 \times 10^{19}$ (Reaction Efficiency of $0.82 \times 10^{-24}$ cm$^3$/atom) |
| Al$_2$O$_3$ | 950 Å | $1.0 \times 10^{20}$ |
| | 950 Å | $8.3 \times 10^{20}$ |
| SiO$_2$ | 950 Å | $1.2 \times 10^{20}$ |
| | 950 Å | $7.3 \times 10^{20}$ |
| | 950 Å | $11.0 \times 10^{20}$ |
| SWS-V-10 | 4 μm | $1.8 \times 10^{20}$ |
| | 4 μm | $4.9 \times 10^{20}$ |
| | 4 μm | $6.0 \times 10^{20}$ |

Figure 1.    The O-atom actinometer pattern used in which
             constant current is supplied to each strip
             and voltage is then measured using the same
             contacts (see also figure 2).   The actinometers
             were parepared by first imprinting gold leads
             onto an alumina substrate.   Silver was then
             vacuum evaporated onto the substrate to a
             thickness of 250 A.
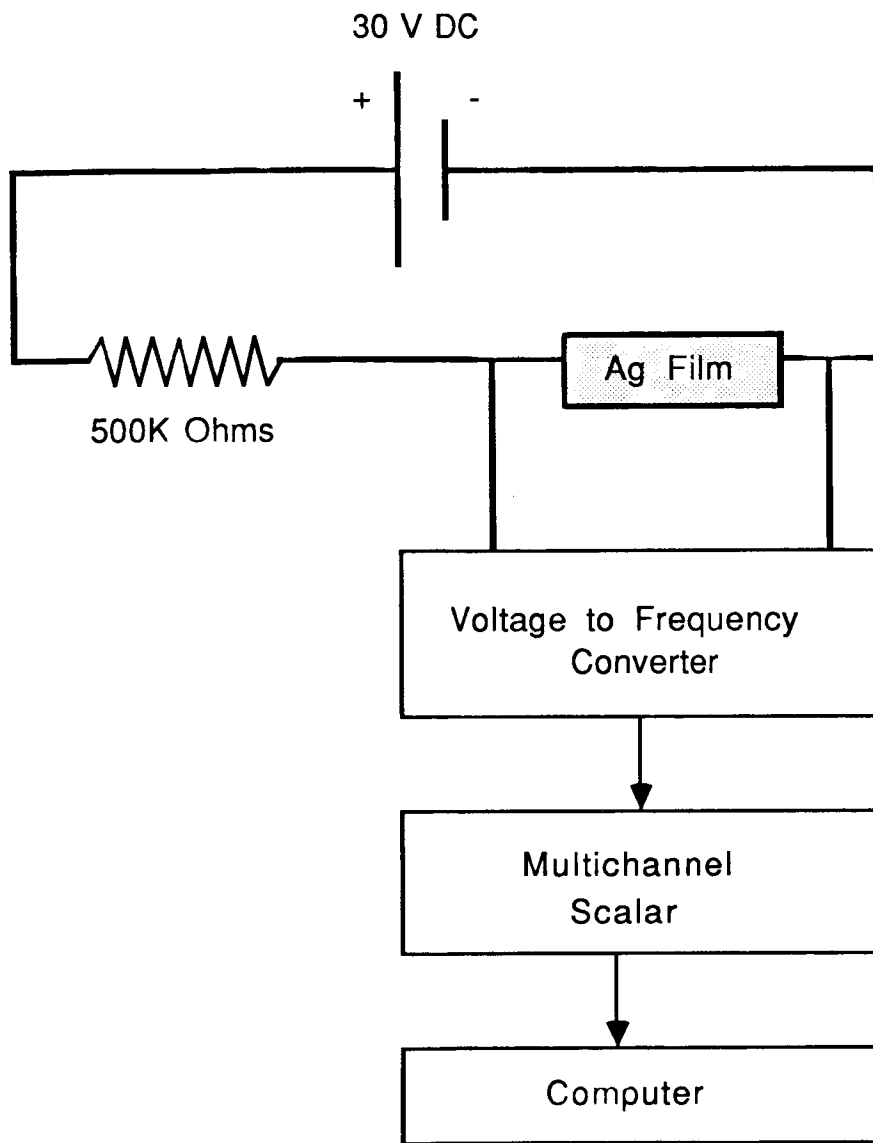
Figure 2.   Electrical Circuit for Actinometer Resistance Measurements.
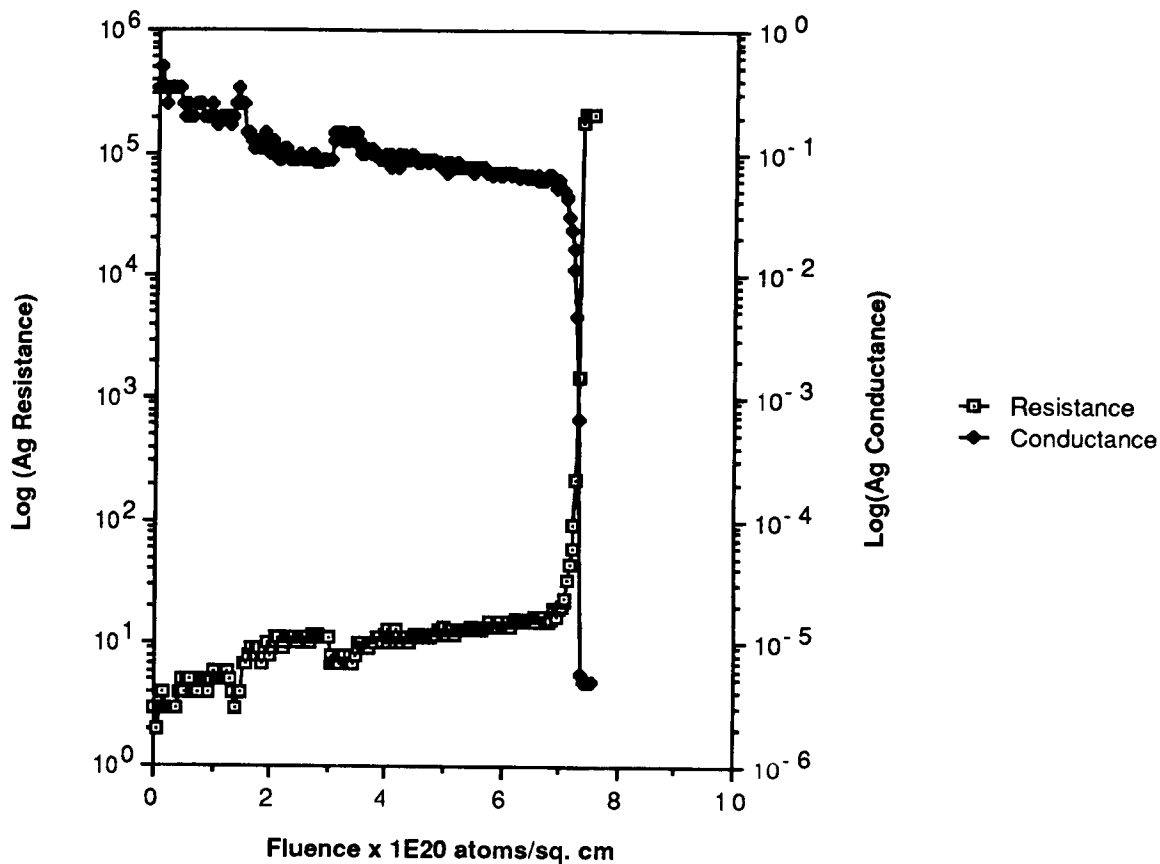
Figure 3. Plot of electrical resistance/conductance of silver underlying a protective coating (950 Å SiO$_2$) shows the variation of log(electrical resistance) and log(electrical conductance) as a function of O-atom fluence. The shapes of the silver electrical resistance/conductance vs. fluence graphs do vary from coating to coating and from sample to sample of the same coating.
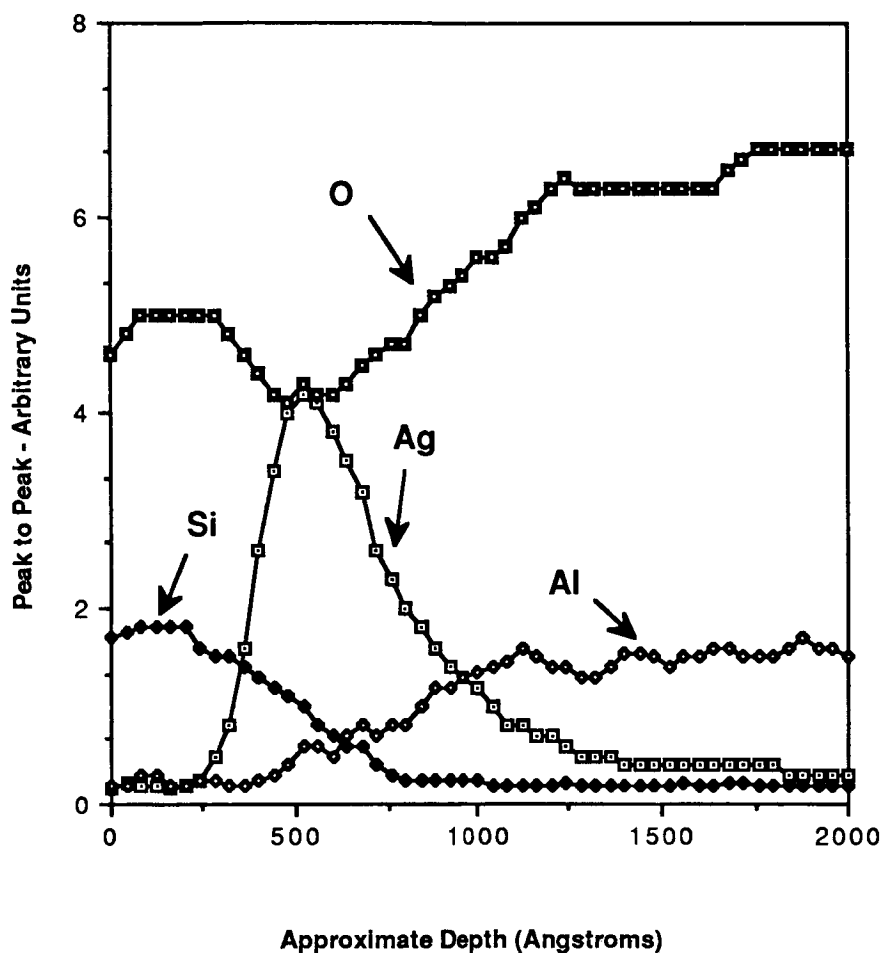
Figure 4. Auger elemental depth profile of Si, O, Ag, and Al in a $SiO_2$-coated silver actinometer after an O-atom exposure fluence of $11.0 \times 10^{20}$ atoms/$cm^2$ shows that the $SiO_2$ coating was not eroded away. The actinometer has an alumina substrate, which accounts for the presence of Al. The depth is only an approximation, because it is based on an estimated sputtering rate.

Session IV

# DYNAMIC TESTING

# PYRO SHOCK SIMULATION:
## EXPERIENCE WITH THE MIPS SIMULATOR

Thomas J. Dwyer and David S. Moul
GE Astro Space Division, Valley Forge, PA

## ABSTRACT

The MIPS (Mechanical Impulse Pyro Shock) Simulator at GE Astro Space Division is one version of a design which is in limited use throughout the Aerospace industry, and is typically used for component shock testing at levels up to 10,000 response g's. Modifications to the force input, table and component boundary conditions have allowed a range of test conditions to be achieved. Twelve different designs of components with weights up to 23 Kg (50 Lb) are in the process or have completed qualification level shock testing in the Dynamic Simulation Lab at GE Astro in Valley Forge, PA. This paper presents a summary of the experience gained through the use of this simulator, and presents examples of shock environments that can be readily simulated at the GE Astro MIPS facility.

## INTRODUCTION

The MIPS has been used successfully on numerous programs in the past three years at GE Astro. In general, all testing done to date has been successfully completed with all pre-test objectives satisfied. Achieving the desired Shock Response Spectrum (SRS) for 12 different component designs requires a dedicated and innovative test staff, as well as a thorough understanding of the MIPS facility.

The GE Astro MIPS test setup is illustrated by Figure 1. Components are mounted to a 122 cm x 183 cm x 1.3 cm (4' x 6' x 1/2") thick 7075-T6 aluminum plate, which rests on a 7.6 cm (3") thick foam pad. The shock is generated via the impact of a pneumatic actuator which is rigidly attached to a moveable bridge. The bridge is secured to the table frame at the desired position, which typically places the impact point within 15 cm (6") of the component. Instrumentation location varies depending on the test objectives, but the usual control point is less than 5.1 cm (2") from the component on a line between the impact point and the test specimen. A typical triaxial accelerometer response for the control point is shown in Figure 2, along with the time history of the shock pulse.

The data to date indicates that the MIPS test environment is relatively consistent from test to test. Because pyrotechnic shock results from an explosion and is a high frequency phenomena, the actual pyrotechnic shock environment tends to vary considerably from firing to firing. However, comparison of the SRS for all axes indicates that the MIPS results are relatively repeatable. Although there are some exceptions, the MIPS shock environment tends to have less than 10 percent variation from test to test, which is a considerable achievement for these types of environments.

The MIPS at GE Astro has been used to perform shock qualification testing on a wide variety of components. The majority have been flange mounted black boxes with weights up to 23 Kg (50 Lb) but the fabrication styles have ranged from laser welded housings to cast aluminum boxes. The housing fabrication method determines

the stiffness of the structure and affects the response of the MIPS table.  One de-
sign was constructed of several stacked modules and another included a free-standing
antenna.  Specific devices instrumented and monitored during test have included
printed wire boards (PWB's), gyroscopes, relays and passive dampers.  Modifying the
boundary conditions of the table determines the response of the table to the shock
input, thus allowing a wide range of components to be successfully tested.  Several
environments that have been simulated are illustrated by Figure 3, with Shock
Response Spectrum (SRS) levels of over 40,000 response g's obtained for specific
setups.


## DYNAMIC MODELS

The use of dynamic models is necessary to prevent damage to flight hardware
during setup of the MIPS table.  Fine tuning the table to achieve the proper shock
response spectrum can often require up to 80 shocks.  With different shock profiles
and various size boxes, each configuration becomes a unique technical challenge.
Since the control point is on the table, the dynamic models must be designed to
simulate the effect the box has upon the table.  Box weight and mounting style are
the most important factors affecting the response of the table to the shock input,
but the effect of cables must also be evaluated for each case.  The response of a
good dynamic model can be within 2 dB of the flight unit as shown in Figure 4.

The box weight can be simulated with separate masses distributed in such a
manner as to correspond to lumped masses within the component.  Such lumped masses
include power supplies and circuit boards.  Figure 4 shows the generic dynamic model
design developed at GE Astro for dual flange mounted components.  Aluminum blocks
are currently used for these masses, and the design has been standardized to allow
these blocks to be used in several different dynamic models.

The mounting style is the most critical factor that must be simulated.  For
flange mounted components, the effect can be duplicated via use of thin rails.  The
weights, which are sized to provide the proper mass distribution, are attached to
the rails at locations between the bolts holding the rails to the shock table.  The
rail should be of a similar material and thickness to the flange.  The effect of
structural gussets on the component flange may be neglected for shock response
simulation, since only the immediate flange will effectively respond to the .0005
second shock pulse.

The effect of cables depends on the quantity and type of the cables.  Properly
suspended, flexible cables need not be simulated.  Rigid and semi-rigid coaxial
cables have been found to have a low frequency effect and should always be simulated
with the dynamic model.  The cable attachment to the model should duplicate the
stiffness of the prime mounting configuration.


## CASE HISTORIES

For the successful use of the MIPS Simulator, the operator needs to develop an
understanding of the nature of the shock response, as well as an appreciation of the
effect that various boundary conditions have upon the table.  In general, these
modifications to the boundary conditions affect either the impact area or the table
supports.  The following guidelines have been developed at GE Astro and each
particular setup employs a combination of these variations to achieve the desired
SRS:

| Variation | Resultant |
|---|---|
| Paper (cardboard) under striker......Damps high frequencies |
| Steel plate under striker | Increases high frequencies |
| Clamp table edges to frame | Shifts resonance lower |
| Support table on wood blocks | Damps high frequencies |
| Jackstand under impact point | Reduces low frequencies |
| Component on transition plate | Attenuates all frequencies |
| Bags of lead shot on table | Damps high frequencies |
| Lower striker height | Evenly attenuates entire spectrum |
| Reduce ram pressure | Unevenly attenuates entire spectrum |

The striker has a rounded aluminum head, which can be replaced with various profiles to acquire the proper impact. Buffering the impact point with paper or cardboard limits the high frequency 'ringing' of the table, but, as seen in Figure 5, equivalent thicknesses of paper and cardboard affect the low frequency end of the SRS differently. Combinations of paper and cardboard are often used to achieve the desired damping. Steel, on the other hand, will increase the high frequency content of the spectrum.

The use of a jackstand beneath the impact point reduces the deflection of the MIPS plate. This deflection results in an increased low frequency component to the SRS. Varying amounts of back pressure upon the jackstand will preload the table and can be used to eliminate undesirable low frequency responses. The air pressure driving the ram also has an effect upon the low frequency response of the table as shown in Figure 5. Increased ram pressure deflects the table to a further extent, and will add a 'DC' effect. Ram pressure is adjusted in accordance with jackstand preloading to achieve the desired response.

Clamping the plate edges to the table will effectively shorten the table length and will shift the table resonance accordingly. Supporting the plate on wood (aluminum) blocks above the foam changes the boundary condition from free-free to simply supported. Variations to these and other boundary conditions have allowed the operators of the MIPS at GE Astro to meet every program specification.

Specific case studies typify some of the common problems and solutions for the operator of the MIPS table:

Components A & B are typical aerospace black boxes consisting of multiple mechanical and electrical components coupled with numerous printed wire boards (PWB's) supported within the rigid containers. Integration of passive viscoelastic damping treatments into the design of spacecraft component mounting structures (including PWB's) significantly improves spacecraft reliability. An additional benefit is increased damping in orbit which reduces response to onboard disturbances. Constrained Layer Damping Assemblies (CLDA's) are typically applied in strips running lengthwise across the board with a Viscoelastic Material (VEM) sandwiched between a stiff constraining layer and the board surface. The CLDA is placed to maximize the strain energy in the VEM, although this is not always possible due to PWB component mounting. All PWB's within Components A & B have CLDA's, as well as several other critical box surfaces. A typical PWB with CLDA is shown in Figure 6. A unique Component B feature is that boundary conditions were applied

to several of the PWB's by strips of flexible silicon rubber pads forming the interface between the container bottom and PWB surfaces on some boards.

During the vibration and shock testing, the boxes were internally instrumented for the purpose of determining the internal dynamic environment resulting from the shock application and the effectiveness of the passive damping treatment used to reduce the response of PWB's. The input to the components was characterized by triaxial locations less than 7.6 cm (3") from the component mounting flanges, and the internal and external component responses were measured with microminiature accelerometers. The PWB accelerometers were positioned near the center of the PWB's to measure the vibration normal to the board. The remaining accelerometers were located on the covers and structural bulkhead. A triaxial location was included at the upper corner of the component near the application of the shock to evaluate the amplification of the overall box structure. Additional detailed information is listed in Reference [1].

The general test geometry is illustrated in Figure 7. Two shock applications were applied for each condition illustrated in Figure 7, with functional tests both before and after the shock applications, and no anomalies were detected in any test.

The data summarized in Table 1 and Table 2 provides a definition of the environment within the components resulting from the MIPS simulation of the pyrotechnic environment. They indicate relatively high SRS levels for electronic parts mounted on the PWB's on the order of 1 – 2000 g's. The PWB's do provide a significant attenuation of the MIPS plate environment which ranged from 6000 – 13,000 g's, and the component structural environment (3000 – 7000 g's). This attenuation is expected in view of the relatively low resonant frequency of the PWB's. The PWB's having the lowest resonant frequency typically have the lowest SRS, while PWB's with the higher resonant frequencies had the higher SRS. Responses in these boxes are thought to be typical for similar application throughout the industry and can be scaled for other shock environments by analysts wanting to determine PWB response characteristics for their application.

**Component C** utilized a box design which consisted of a heavy, cast aluminum container. This design required the mounting bolts to have an excessive grip to pass through the thick flange. To compound the problem, the customer required the use of titanium mounting bolts during test. Since the modulus of titanium is lower than steel 1.1 x 10" PA versus 2.0 x 10" PA (16.5 x $10^6$ psi versus 29 x $10^6$ psi), the extra grip length and the bolt size (#8) were a concern. As feared, after a number of setup runs with a dynamic model, several bolts deformed and one bolt snapped at the mounting plane. The use of titanium bolts required a higher ram pressure to achieve a similar shock response as high strength steel bolts. It is believed that the titanium, with a lower elasticity, stiffened the table much more effectively with the component than the steel. The steel bolts would elongate slightly under the shock impulse and would tend to be more forgiving than titanium. The test was successfully completed when the mounting holes were enlarged to accommodate #10 bolts, which were also titanium.

**Component D** testing was the first attempt to use a transition plate for the MIPS table. Currently, each component is mounted directly to the MIPS plate, which requires an ever increasing amount of holes. Concentrated hole patterns in the plate affect the boundary conditions of the plate, which in turn add a new unknown to the setup. A transition plate for each component would have mounted to a common bolt pattern in the table, thus maintaining the integrity of the setup. The transition plate for Component D was designed to fit an existing hole pattern which

surrounded the component mounting pattern.  A 1.3 cm (0.5") thick aluminum plate was used for the adapter.  This method was successful,  but the setup was difficult due to the effect of this secondary plate.  While the MIPS table design was driven by the need to have the plate 'ring' near the crossover point, this secondary plate had its own resonance which made shaping the shock response difficult.  For this reason, it was decided to continue with the original method of mounting directly to the large MIPS plate.

Component E was a small passively damped device which required testing in three orthogonal axes.  Normally, the MIPS requirement is for the shock to be solely in the plane of the component mounting surface.  This test was accomplished by mounting the device in a metal cube, which could be rotated to achieve the three planes.  The cube was fabricated from solid steel to provide maximum transmissibility of the shock impulse.  The device was not only instrumented with teardrop accelerometers, but also contained mirror cube mounts for collimator readings.  Although this method would not be feasible for large components, it has proven to be an alternative for small components requiring three axis shock.

Component F was unique in that it sustained catastrophic internal damage and mounting feet deformation during prior pyro shock testing at another facility. That facility (Figure 8) is quite different than the MIPS facility, thus affecting the path taken by the shock wave from the impact point to the unit.  In addition, in the previous test, the flight unit itself was used during system setup with some 67 hits made during the calibration resulting in probable unit over testing.  To resolve the question of whether the component failures resulted from being over tested/over exposed or whether the design was susceptible to normal axis shock, another unit was tested at the GE Astro MIPS facility.

The shock spectrum illustration in Figure 9 was applied to the component. The axis definition and instrumentation details for this test are given in Table 3. The control accelerometer was located within 5.1 cm (2") of the mounting foot, and a second reference triaxial accelerometer location was approximately 17.8 cm (7") laterally from the central control as indicated in the figure.  All response accelerometers on the component were bonded to tape which was secured to the (flight) unit.

The test sequence consisted of applying three consistent shocks with a dummy in place of the flight unit for calibration, and then a single shock to the flight unit.  The procedure was repeated when the unit was rotated 90 degrees.  The normal axis input, as measured by station 1 norm, is shown in Table 3 for the XZ test and the YZ test.  The three lines in the vicinity of the solid response curve represent the desired levels with +3/-6 dB limits indicated.  It is clear that in no band did the response exceed either the +3 or -6 dB limit.

Results of the pyro shock test are summarized in Table 3 with peak time history values tabulated.  The unit was exposed to an approximate SRS peak input of 5000 g's in both tests and, upon examination of the test data presented in Table 3, it is clear that the component responses were grossly different between the two test methods.  For an approximate normal axis input of 3300 g's, responses at the top of the component for the MIPS test were on the order of 2500 g's, whereas responses with the other Impact Facility illustrated by Figure 8  were some 12,000 g's.  It is obvious that the unit as tested on the MIPS assembly experienced grossly lower response levels than experienced on the other test apparatus.  The primary difference is due to the path the energy takes before reaching the component and a 200 Hz component response that was magnified by a system resonance with the Impact Facility in the same frequency band.  It was

concluded that the MIPS setup is a better representation of the actual environment that the unit will experience in flight and imposes far less structural risk due to the test assembly than the Impact Facility.


CONCLUSION

The MIPS facility provides a unique capability for repeatable shock testing of large components. The manipulation of the boundary conditions allows a wide range of test specifications to be met. Peak levels of 40,000 response g's have been reached with the bare table. The MIPS pyro shock simulator at GE Astro has been used to successfully qualify a variety of components for flight use. Achieving the desired Shock Response Spectrum for different size boxes is a matter of skill and experience, but will always remain an art. This paper presents a few of the 'tricks of the trade' necessary to succeed in using the MIPS. The information presented herein was gathered through the testing of twelve different components. Each component required, on the average, approximately 80 setup shocks on a dynamic model to achieve the proper shock spectrum. As the database grows with each new component, and as communication between MIPS users increases, the setup time and cost can be dramatically reduced.


REFERENCES

[1]  T. J. Dwyer:  Design and Dynamic Testing of an Instrumented Spacecraft Component, 58th Shock & Vib Symposium, NASA Conference Publication 2488 Volume II.

TABLE 1:    ACCELEROMETER LOCATIONS AND RESPONSES FOR COMPONENT A

| Location | Station | XY Axis – Peak SRS (g) | | ZY Axis – Peak SRS (g) | |
|---|---|---|---|---|---|
| | | Hit 1 | Hit 2 | Hit 1 | Hit 2 |
| Input – Norm | 1X | 12,930 | 12,623 | 1,706 | 1,808 |
| Input – Long | 1Y | 6,083 | 6,131 | 6,314 | 6,280 |
| Input – Lat | 1Z | 1,694 | 1,902 | 10,629 | 10,560 |
| Box Corner | 2X | 3,406 | 3,362 | 4,728 | 4,623 |
| Box Corner | 2Y | 5,921 | 5,761 | 5,522 | 5,524 |
| Box Corner | 2Z | 4,341 | 4,179 | 3,147 | 3,289 |
| PWB – 5 | 3 | 873 | 928 | 393 | 458 |
| PWB – 6 | 4 | 3,771 | -- | -- | 557 |
| PWB – 7 | 5 | -- | -- | 763 | 650 |
| PWB – 8 | 6 | 1,086 | 1,280 | 1,207 | 1,371 |
| PWB – 9 | 7 | 1,514 | 1,654 | 938 | 1,043 |
| PWB – 10 | 8 | 980 | 1,248 | 1,771 | 1,867 |
| PWB – 11 | 9 | -- | -- | -- | -- |
| PWB – 12 | 10 | 1,174 | 856 | 1,918 | 2,007 |
| PWB – 13 | 11 | 427 | 650 | 532 | 1,096 |

TABLE 2:    ACCELEROMETER LOCATIONS AND RESPONSES FOR COMPONENT B

| Location | Station | XY Axis – Peak SRS (g) | | ZY Axis – Peak SRS (g) | |
|---|---|---|---|---|---|
| | | Hit 1 | Hit 2 | Hit 1 | Hit 2 |
| Input – Norm | 1X | 4,000 | 4,000 | 4,000 | 4,000 |
| Input – Long | 1Y | 4,000 | 4,000 | 3,600 | 3,600 |
| Input – Lat | 1Z | 850 | 900 | 650 | 750 |
| Box Corner | 2X | 2,100 | 2,250 | 2,250 | 2,250 |
| Box Corner | 2Y | 1,000 | 900 | 900 | 900 |
| Box Corner | 2Z | -- | 1,950 | 1,700 | 1,650 |
| PWB – 4 | 4X | 550 | 550 | 500 | 550 |
| PWB – 4 | 4Y | 1,100 | 1,200 | 550 | 800 |
| PWB – 4 | 4Z | 350 | 300 | 1,000 | 1,050 |
| PWB – 5 | 5X | 275 | 300 | 125 | 130 |
| PWB – 6 | 6X | 450 | 375 | 170 | 180 |
| PWB – 7 | 7X | 450 | 450 | 150 | 135 |
| PWB – 8 | 8X | 375 | 360 | 95 | 165 |
| PWB – 9 | 9X | 260 | 270 | 150 | 110 |
| PWB – 10 | 10X | 450 | 500 | 14 | 18 |
| PWB – 11 | 11Y | 250 | 260 | 500 | 650 |

131

TABLE 3: ACCELEROMETER LOCATIONS AND RESPONSES FOR COMPONENT F

| Location | Station | XZ Axis – Peak SRS (g) | | ZY Axis – Peak SRS (g) | |
|---|---|---|---|---|---|
| | | MIPS | Other | MIPS | Other |
| Control - Lat | 1X | 800 | -- | 3,400 | -- |
| Control - Long | 1Y | 4,900 | -- | 800 | -- |
| Control - Norm | 1Z | 3,400 | 3,363 | 3,200 | 3,363 |
| Box Corner | 2Z | 1,900 | -- | 1,700 | -- |
| Box Near Impact | 3X | 500 | -- | 1,100 | -- |
| Top Near Impact | 4Z | 3,400 | 5,443 | 2,900 | 5,443 |
| Top Center | 5Z | 3,300 | 11,954 | 2,500 | 11,954 |
| Top Away Impact | 6Z | 2,900 | 5,443 | 2,300 | 5,443 |
| Box Far End | 7Y | 1,800 | -- | 850 | -- |
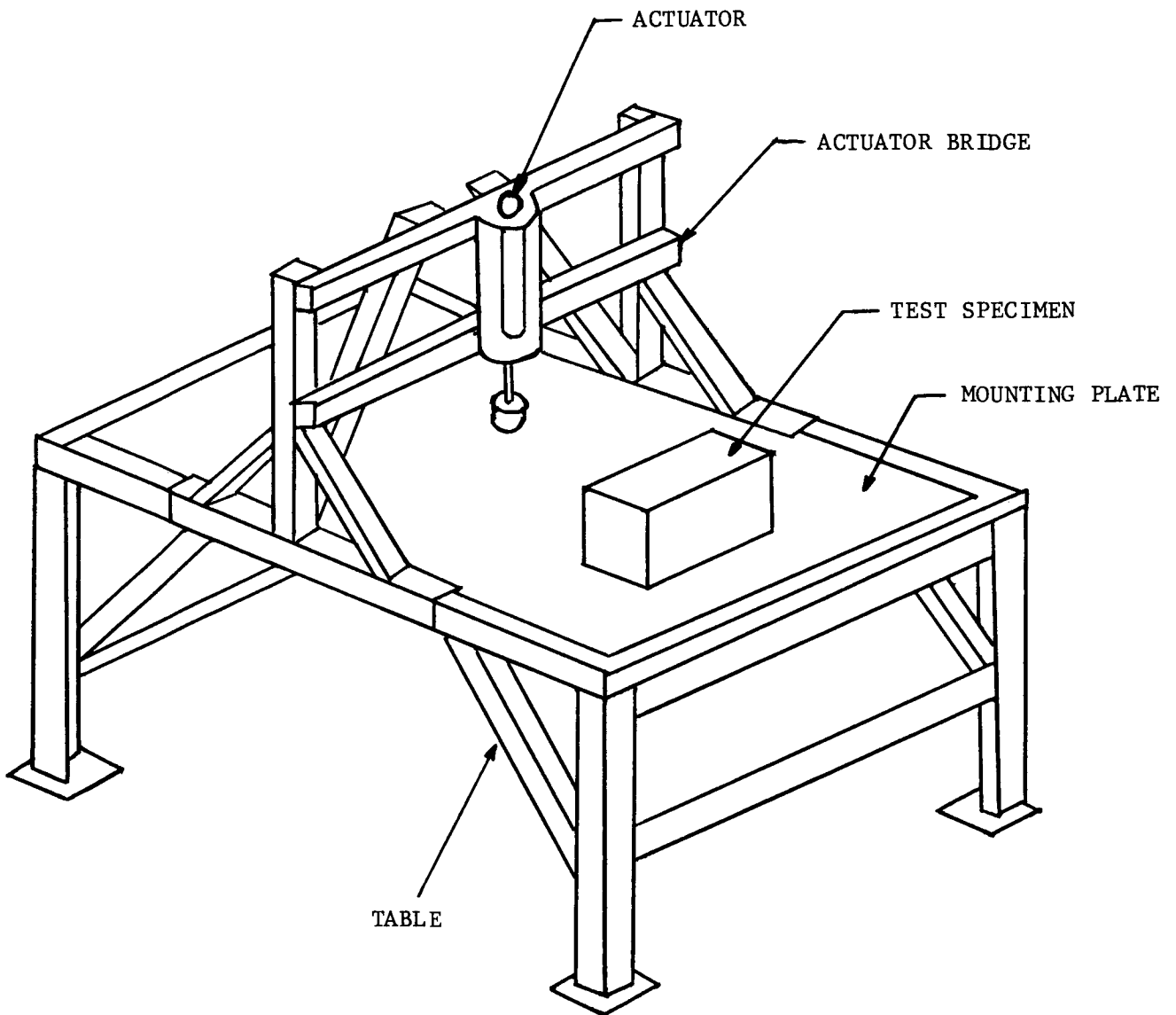


FIGURE 1: GENERAL CONFIGURATION OF MIPS SIMULATOR

Time History of Shock Pulse
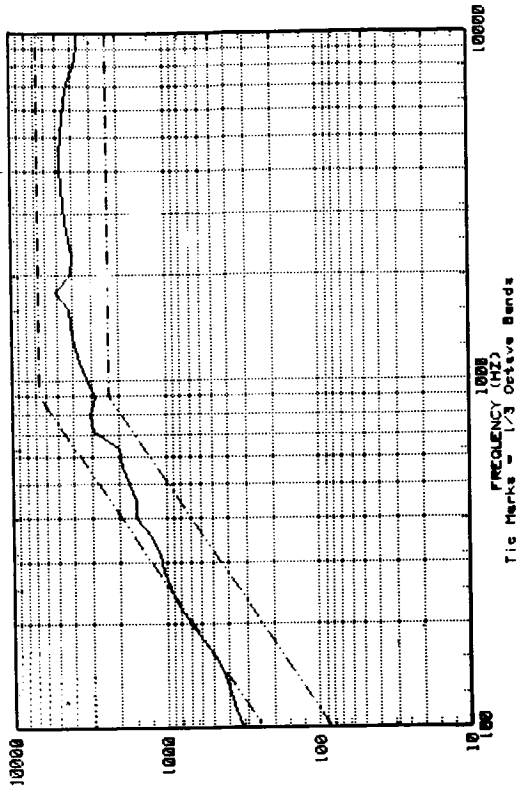
Normal Axis Response
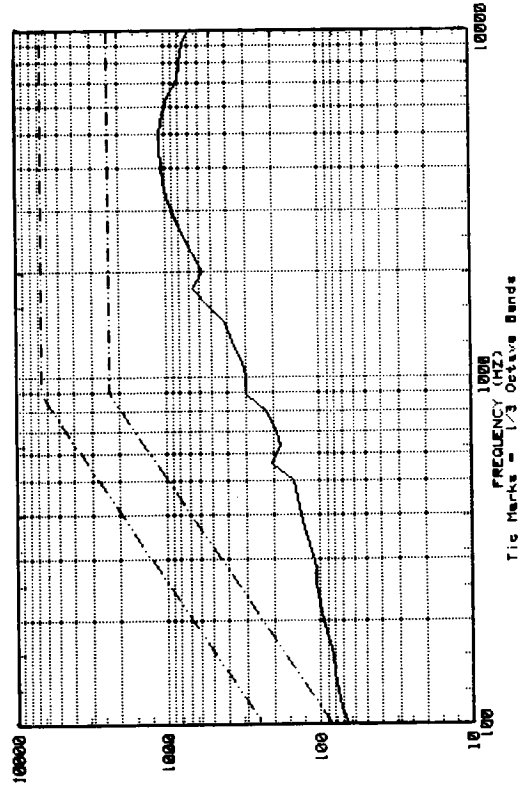
Lateral Axis Response
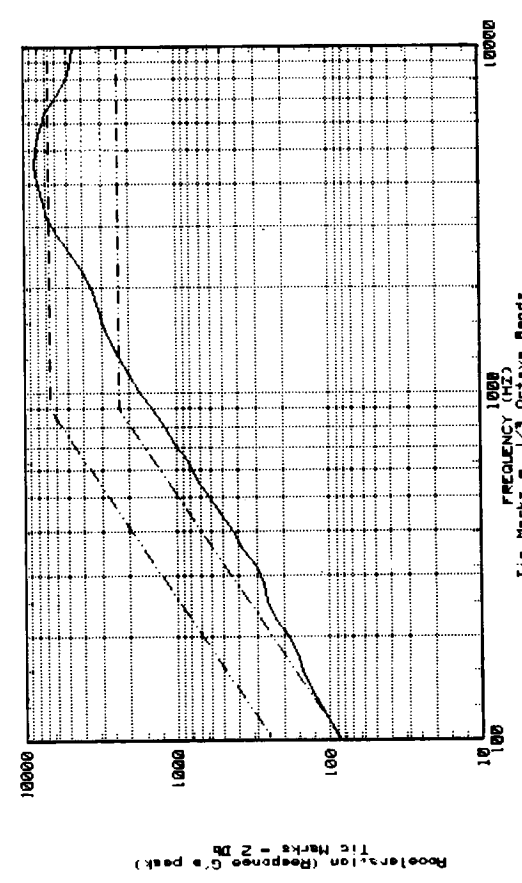
Longitudinal Axis Response

FIGURE 2:   TYPICAL TRIAXIAL RESPONSE OF CONTROL POINT

133
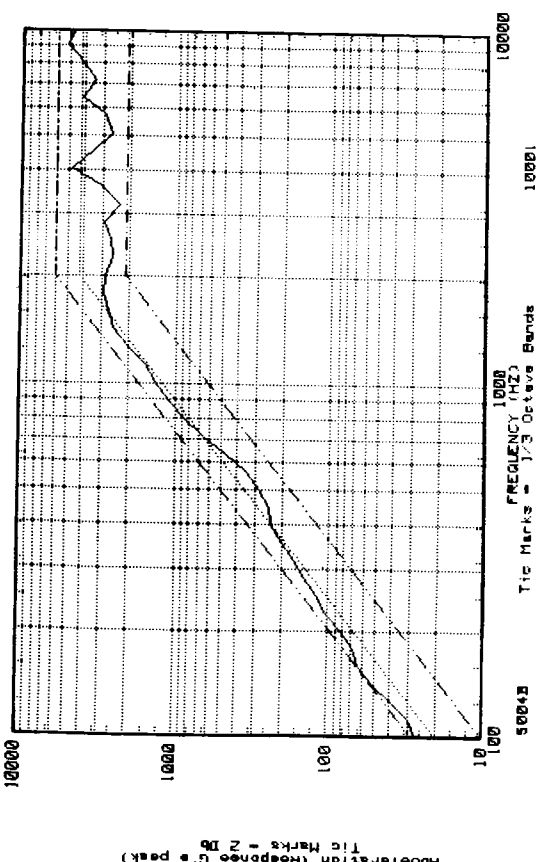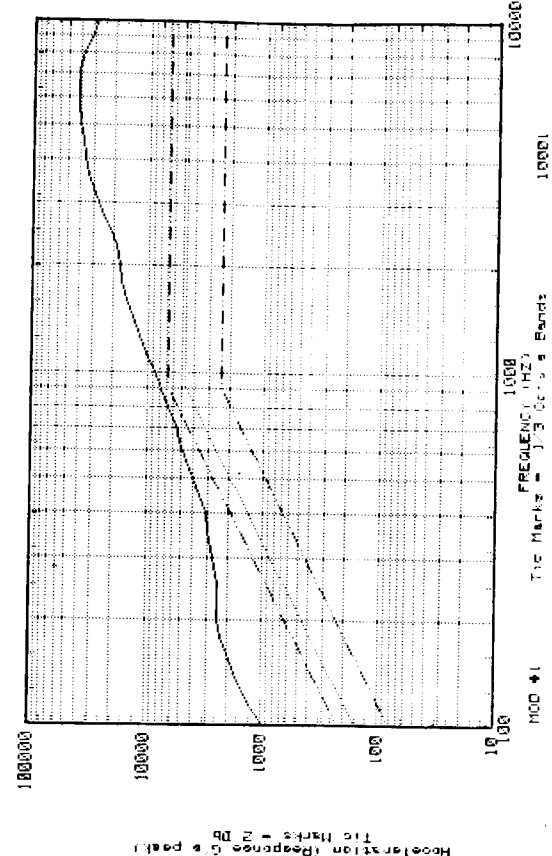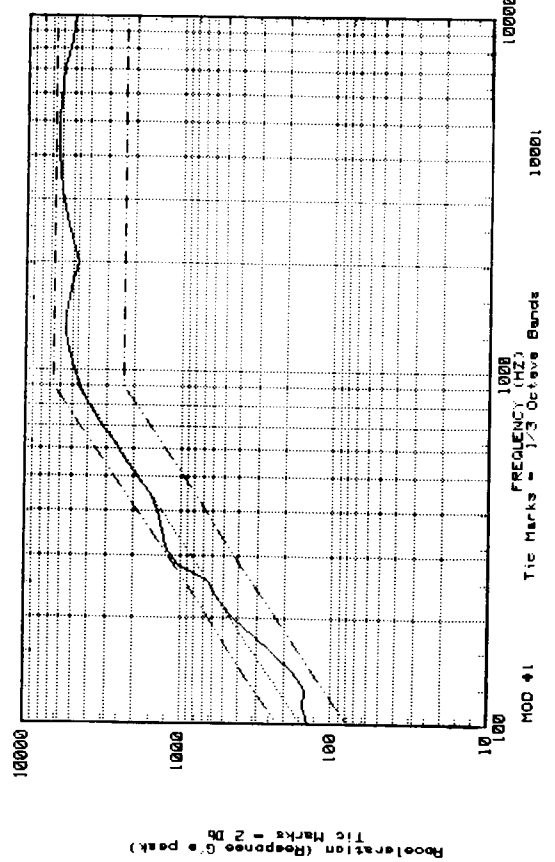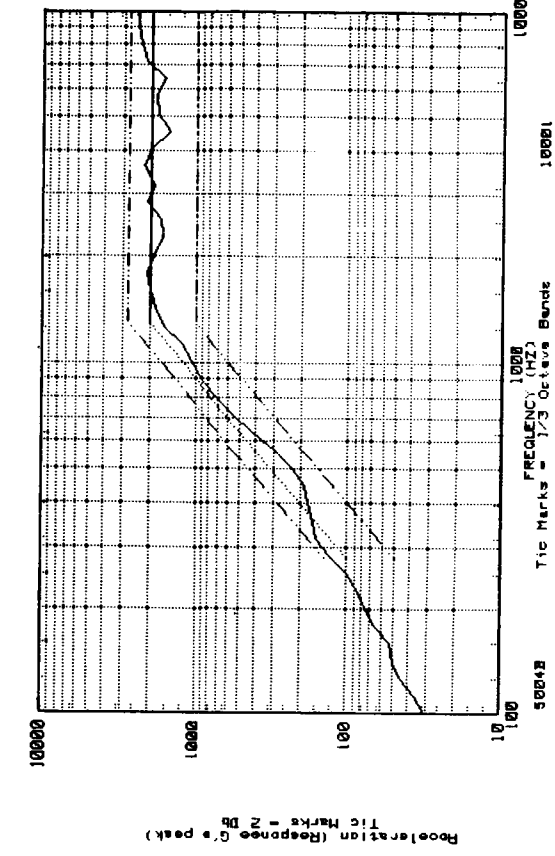
FIGURE 3:    FOUR TYPICAL MIPS SHOCK RESPONSE SPECTRA

134
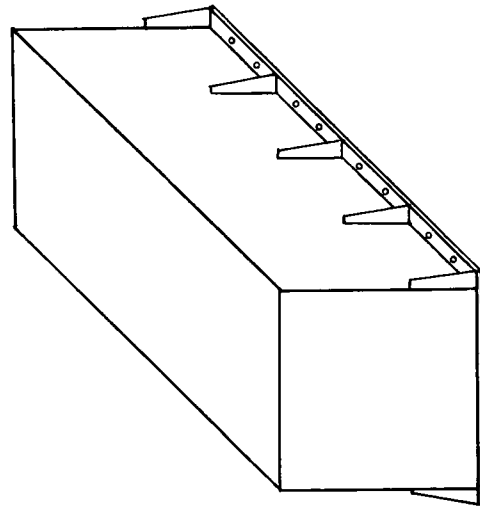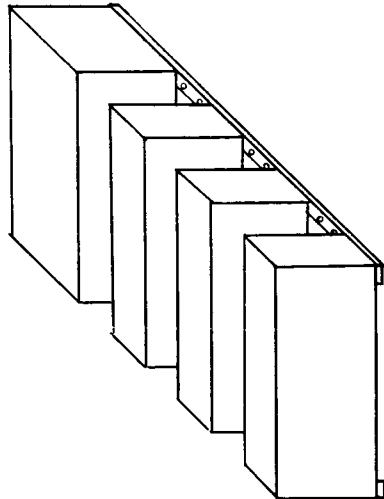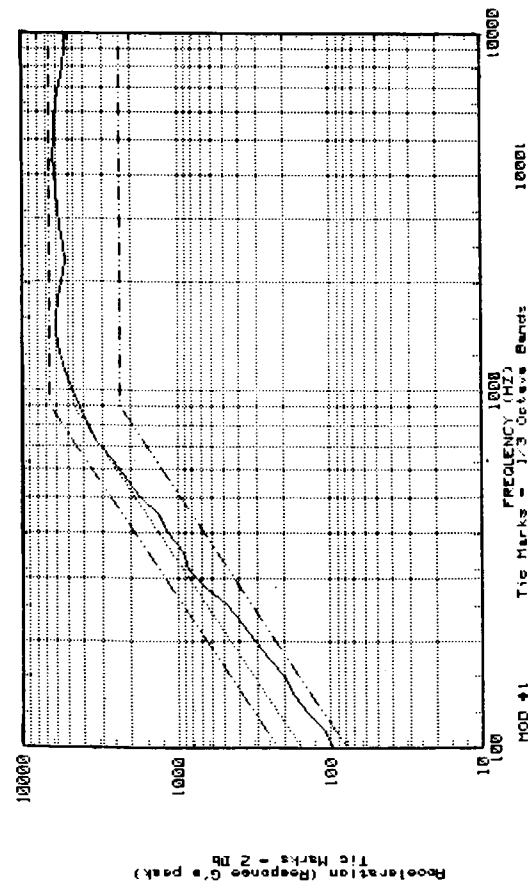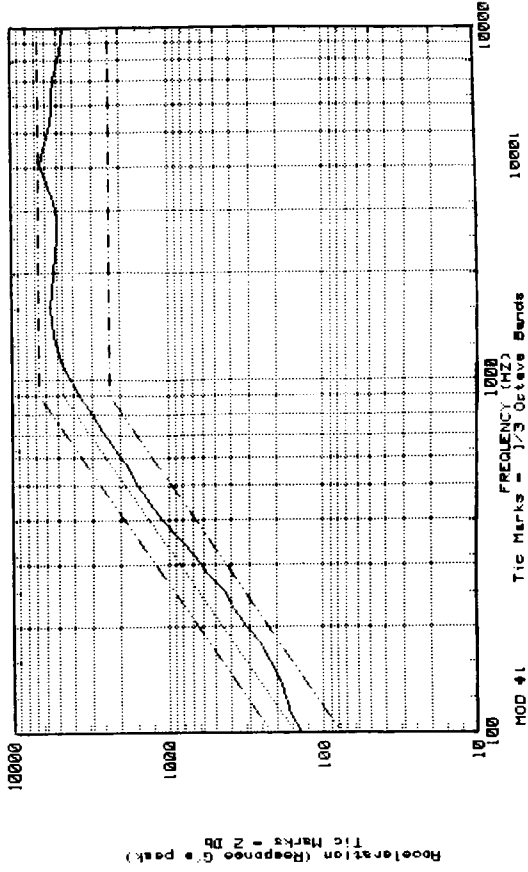
FIGURE 4: COMPARISON OF FLIGHT DESIGN AND TYPICAL DYNAMIC MODEL

135
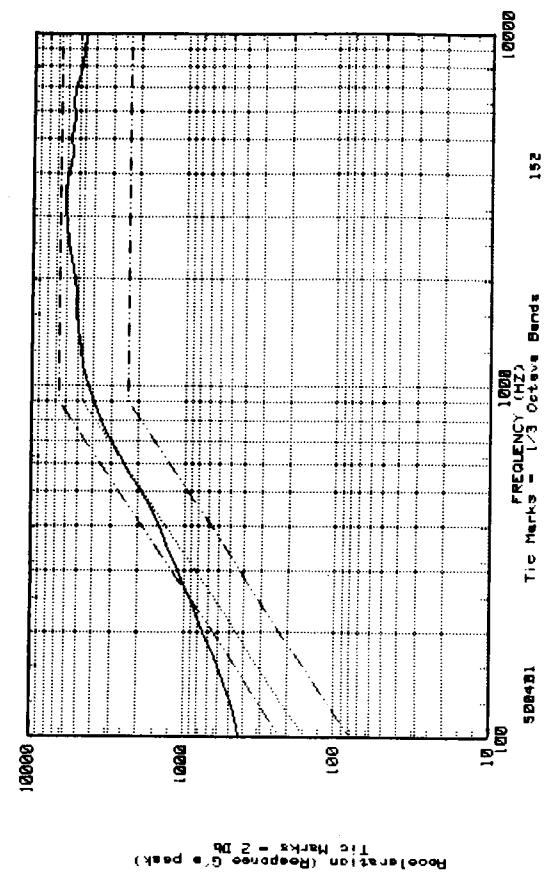
250 PSI Ram Pressure
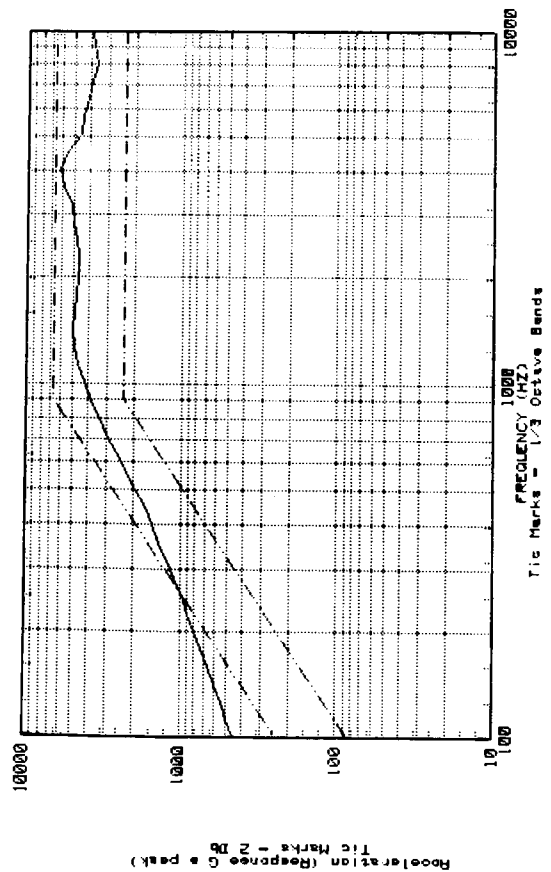
Six Pieces of Paper Beneath Ram

200 PSI Ram Pressure

Cardboard Beneath Ram

FIGURE 5:    SRS COMPARISONS OF FORCE INPUT VARIATIONS

136
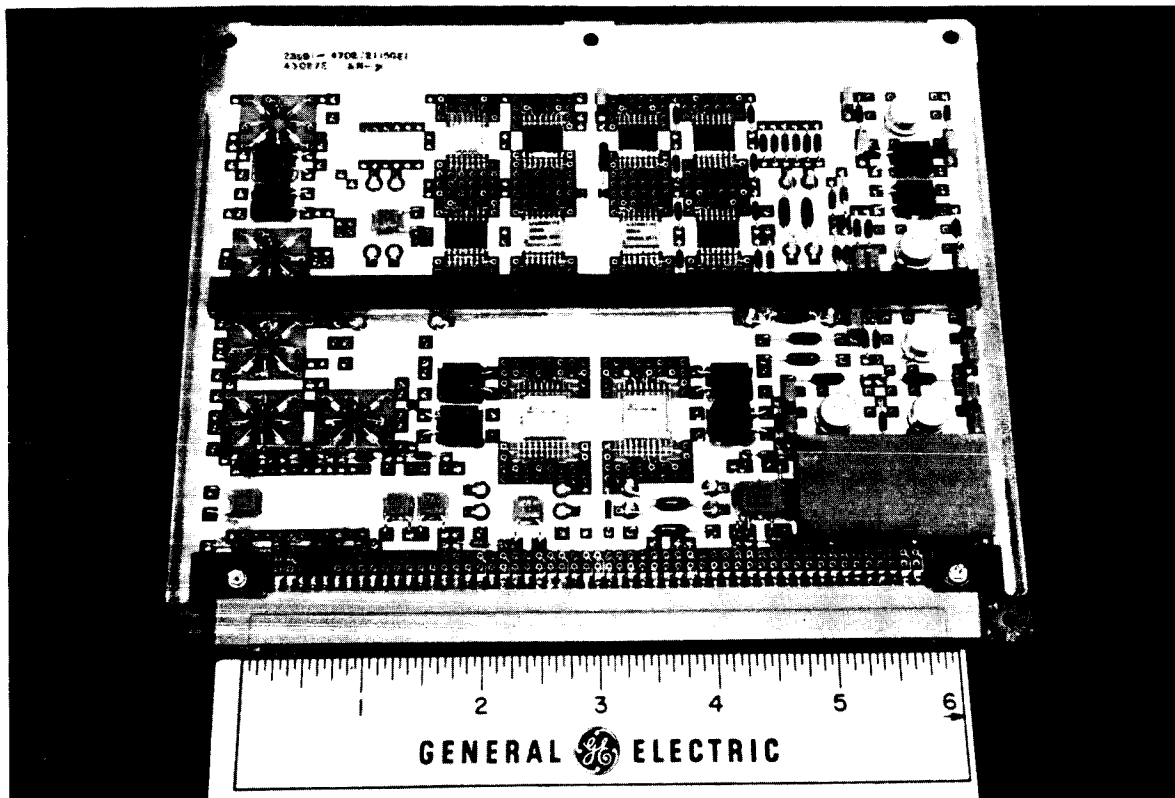
FIGURE 6:    TYPICAL PLACEMENT OF CLDA UPON A PWB
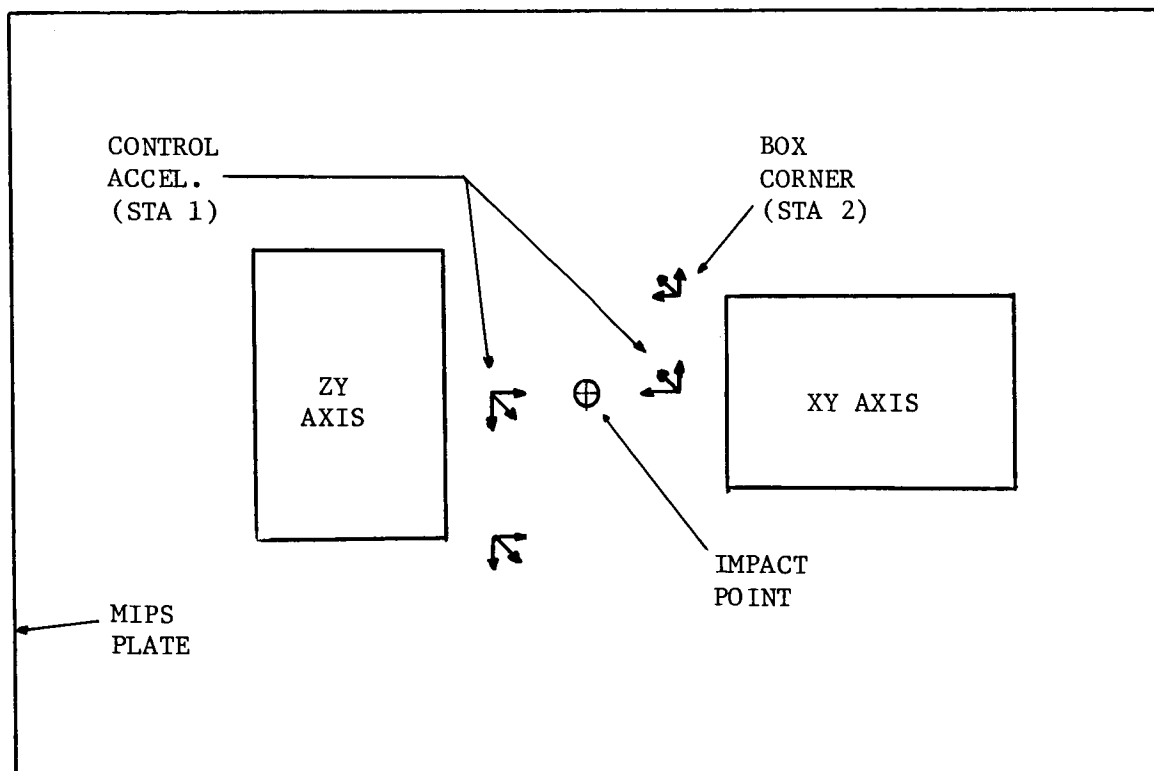


FIGURE 7:    TYPICAL TEST GEOMETRY OF BLACK BOX

137

IMPACT BLOCK

UPPER CONTROL
ACCELEROMETER

LENGTH - 243.8 CM (96")

WIDTH - 25.4 CM (10")     BEAM (ALUMINUM)

THICKNESS - 2.5 CM (1")

COMPONENT F

LOWER CONTROL
ACCELEROMETER

TAPE BUFFERS
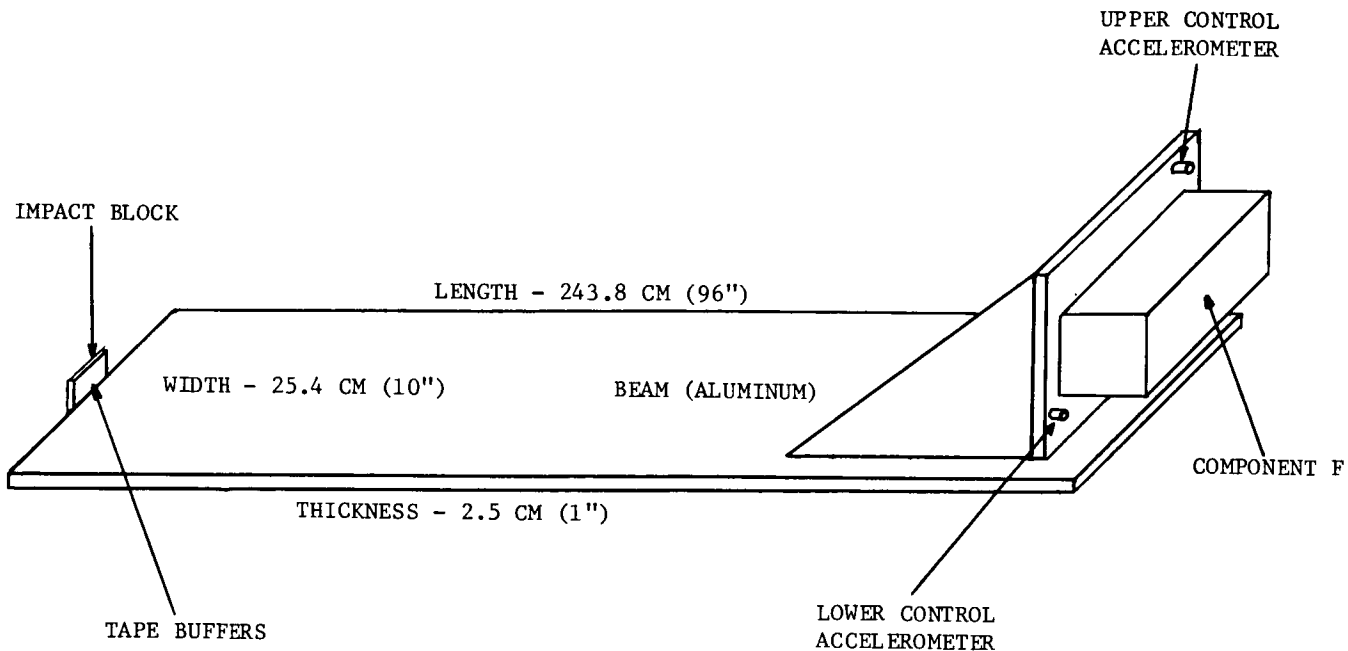
FIGURE 8:     NON-EQUIVALENT IMPACT SHOCK FACILITY
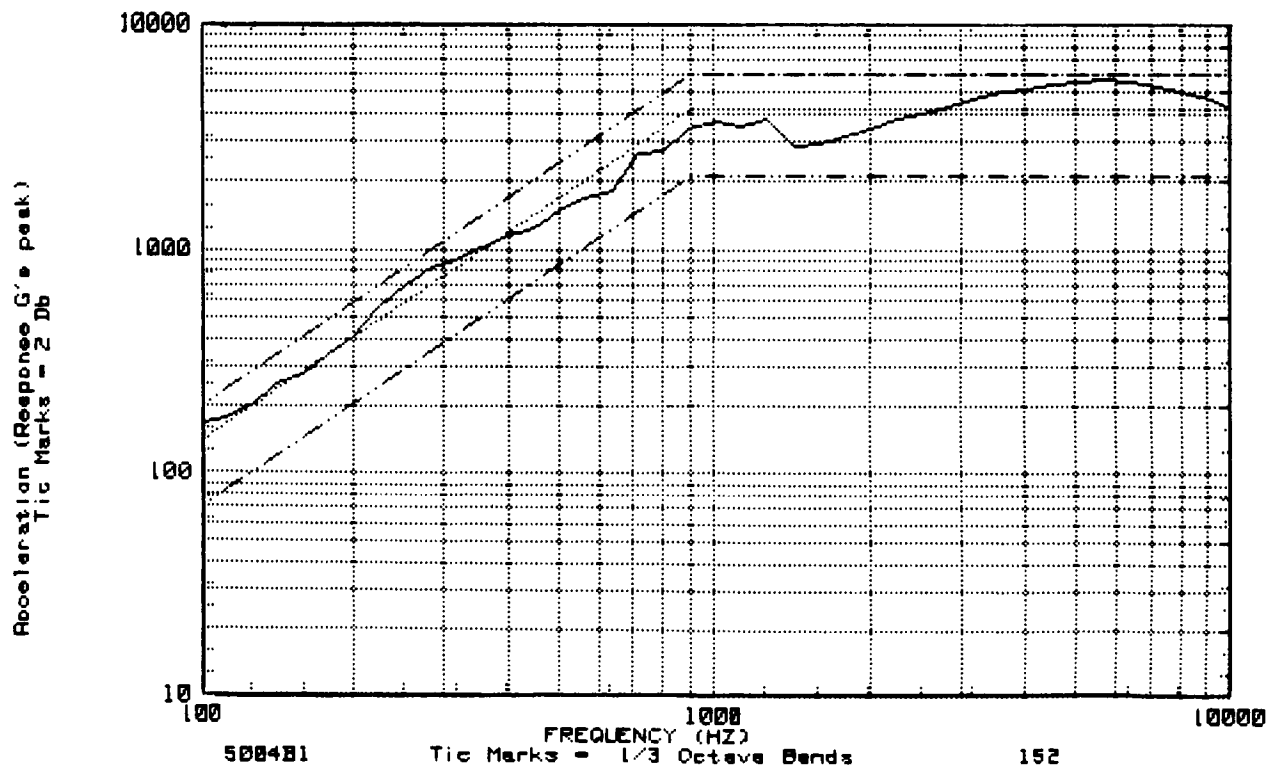


FIGURE 9:     COMPONENT F SHOCK SPECTRUM

138

# MULTIPLE INPUT/OUTPUT RANDOM VIBRATION CONTROL SYSTEM

James F. Unruh
Southwest Research Institute

## ABSTRACT

A multi-input/output random vibration control algorithm was developed based on system identification concepts derived from random vibration spectral analysis theory. The unique features of the algorithm are: 1) the number of input excitors and the number of output control responses need not be identical, 2) the system inverse response matrix is obtained directly from the input/output spectral matrix, and 3) the system inverse response matrix is updated every control loop cycle to accommodate system amplitude nonlinearities. A laboratory demonstration case of two inputs with three outputs is presented to demonstrate the system capabilities.

## INTRODUCTION

All products are subjected to vibration during their lives, either as a result of the manufacturing process, transportation or in-service environments. The capability of the product to withstand this vibration environment and to provide the desired reliability becomes a major design factor in high-technology applications where designs are constrained by severe environments, limited space envelopes, weight constraints and cost. These designs are often beyond the state-of-the-art in analysis procedures, and one is forced to simulate the product's environment to determine its reliability. To accurately estimate in-service reliability, it then becomes necessary to develop a simulation program which accurately reproduces field environments.

In the most general sense, a field vibration environment will consist of motion with six degrees of freedom. Presently available experimental hardware and control systems are limited in their capability to simulate this environment. Most tests are performed using uniaxial random excitation and repeating the excitation along three mutually perpendicular axes. The primary concern is that the mean-time-between-failure (MTBF) rates determined from uniaxial tests do not represent in-service MTBF rates. One problem is determining the duration of testing along each axis of a uniaxial test and the respective test level adjustments to account for physical coupling actually experienced in the field. Because of these uncertainties, the MTBF obtained from uniaxial test can only be considered an estimate of the in-service MTBF. For aerospace product development where product weight can have considerable influence on overall system performance, the need for reliable design evaluation is critical. A secondary consideration is the cost of three test setups to complete the simulation cycle in a uniaxial test.

To satisfy these shortcomings, it will be necessary to develop test facilities that simulate the field environments using multi-axis excitation. In the words of MIL-STD-810 (Ref. 1), the latest revision of the military's environmental test procedures, the test should be 'tailored' to measured field vibration. This will require multi-axis vibration systems with control of each axis and their interaction.

The objectives of the present study were to develop a multiple-input/output random vibration control algorithm based on system identification concepts derived from random vibration spectral analysis theory and to evaluate the usefulness of the algorithm via a laboratory-based demonstration.

A number of researchers have described in various detail the historical development of multi-axis/actuator control systems [Refs. 2-4]. Fisher at Lawrence Livermore Laboratory was one of the first to integrate a control theory and the required hardware to demonstrate system capabilities and limitations to perform multi-shaker vibration simulation [5]. The digital control system utilized a cross-coupling compensation matrix for signal control in the dc to 500 Hz frequency range. The major limitations of the system was the orthogonal axis excitation and the restriction that the number of response points must equal the number of excitation points.

Several multi-axis shaker systems are in present use; however, a number of them employ independent actuator control without cross-axis compensation. One exception is the facilities at Sandia National Laboratory [6-8] which has two-shaker random vibration control system with software capable of controlling up to four shakers. The control algorithm is based on determination of the inverse system frequency response matrix, which requires that the number of inputs and outputs must be identical. No capability exists for updating the system transfer function matrix directly during the control process, however, an incremental correction matrix is used to improve control.

There are several desired characteristics of a random vibration control algorithm that are believed to be important in simulating field vibration environments, they are: 1) Provide true stationary random excitation with near Gaussian amplitude distribution and signal crest factor (peak to r.m.s.) control; 2) Full control of cross-coupling between all output responses; 3) Number of input signals and number of output responses need not necessarily be the same; 4) Maintain loop equalization time to within a small fraction of total test time (say, less than 10%); and 5) Provide sufficient dynamic range and frequency bandwidth to meet simulation tolerances. Only when multi-axis testing becomes a reality can the degree of importance of each of these characteristics be determined.

In the sections to follow, a random vibration control algorithm is described that removes many of the limitations of existing algorithms, the software/hardware implementation of the algorithm is described, and an example of test results using the system are given to point out its capabilities and limitations. Several additional examples are given in Ref. 9.

## CONTROL ALGORITHM FORMULATION

The development of the random vibration control algorithm views the simulation problem as one of system identification. The approach uses the spectral analysis techniques discussed in Ref. 10. For the purposes of discussion, consider the two-input/three-output simulation problem shown in Fig. 1. Physically, the "system" represents the dynamic response between voltage signals input into the vibration exciters, denoted as $x_1(t)$ and $x_2(t)$, and the response accelerations of an item attached to the exciters, denoted as $y_1(t)$, $y_2(t)$ and $y_3(t)$. The finite period (T) Fourier transform of the kth sample record is denoted as $X_i^k(f,T)$, $i = 1, 2$; and $Y_j^k(f,T)$, $j = 1, 2, 3$, respectively. The signal Fourier transforms are used to construct one-sided input/output cross-spectral densities as

$$G_{xy}^{ij}(f) = \lim_{T \to \infty} \frac{2}{T} E \left[ X_i^k(f,T)^* \cdot Y_j^k(f,T) \right] \tag{1}$$

with input auto-spectra,

$$G_{xx}^{ij}(f) = \lim_{T \to \infty} \frac{2}{T} E \left[ X_i^k(f,T)^* \cdot X_j^k(f,T) \right] \tag{2}$$

The output auto-spectra $G_{yy}^{ij}(f)$ is constructed in a similar way. The operator E is the mathematical expectation, and when averaged over N sample records of length T, the one-sided spectral density functions take the general form

$$G_{xy}^{ij}(f) = \frac{2}{NT} \sum_{k=1}^{N} E \left[ X_i^k(f,T)^* \cdot Y_j^k(f,T) \right] \tag{3}$$

where the * denotes the complex conjugate operator. The signals are assumed to be stationary random and, therefore, a finite number of samples, N, may be used to estimate the desired cross- and auto-spectra.

The system frequency response function, $[H_{yx}(f)]$, is defined by

$$\{Y(f)\} = [H_{yx}(f)]\{X(f)\} \tag{4}$$

where the brackets { } denote the vector of response or input Fourier spectra. The inverse frequency response function, $[I_{xy}(f)]$, is defined as

$$\{X(f)\} = [I_{xy}(f)]\{Y(f)\} \tag{5}$$

where the two system matrices are generally considered to be the inverse of each other. Such a concept is only valid when the number of input channels equals the number of output channels, which is not the general case considered in present development. To estimate $[I_{xy}(f)]$, we use the concept of mathematical expectation applied to Eq. 5 after post multiplying by the conjugate transpose of $\{Y(f)\}$, which, after some algebra, results in

$$[I_{xy}(f)] = [G_{xy}^*(f)][G_{yy}^*(f)]^{-1}. \tag{6}$$

Thus, the system inverse response matrix is the product of the system input/output cross-spectral matrix and the inverse of the system output spectral matrix. It is important to note that when the system outputs are fully correlated, the output spectral matrix is rank deficient and the usual inverse is not defined. When this occurs one could drop control of one of the responses, combine two responses in an average or least squares way or define a pseudo inverse. The present algorithm employs a pseudo inverse as described by Greville [11]. The pseudo inverse routine produces the true inverse for rank sufficient matrices while producing unique inverses for rank deficient matrices. Due to extraneous noise at the output of most physical systems the pseudo inverse is often not necessary.

The relationship between the input auto-spectra and output auto-spectra is derived in a similar way as

$$[G_{xx}(f)] = [I_{xy}^*(f)][G_{yy}(f)][I_{xy}(f)]^T. \tag{7}$$

141

Given a required output auto-spectra $[R_{yy}(f)]$, which is generally an envelope of multiple field measurements, the required input auto-spectra is defined by Eq. (7) as

$$[G_{xx}(f)] = [I_{xy}^*(f)][R_{yy}(f)][I_{xy}(f)]^T. \qquad (8)$$

The control problem becomes that of defining $\{X(f)\}$ such that the $[G_{xx}(f)]$ of Eq. (8) is realized. If the input signals were statistically independent random signals, there would be no output cross-coupling control other than that fixed by the physical exciters and test item arrangement. Thus, it becomes necessary to introduce cross-coupling control. This is accomplished by considering a coupling matrix $[A(f)]$ such that

$$\{X(f)\} = [A(f)]\{S(f)\}, \qquad (9)$$

where the $[A(f)]$ matrix is lower triangular (upper triangular elements are all zero) and the input $\{S(f)\}$ vectors are mutually independent white noise sources (unit r.m.s. amplitude with random phase). Upon post multiplication of Eq. (9) by the conjugate transpose of $\{X(f)\}$, and taking the mathematical expectation, there results an expression for the coupling elements in $[A(f)]$,

$$[A(f)][G_{ss}(f)][A^*(f)]^T = [G_{xx}(f)]. \qquad (10)$$

Since the input $\{S(f)\}$ vectors are mutually independent white noise, their spectral matrix $[G_{ss}(f)]$ is a unit diagonal matrix. A solution for the coupling elements in $[A]$ is given on page 262 of Ref. 10.

A flow chart is given in Fig. 2 which summarizes the major tasks of the control algorithm. To insure test item safety during control signal shaping, an incremental buildup to the full level drive has been introduced as denoted by the constant a and increment $\Delta$ a. As can be seen in Fig. 2, system amplitude nonlinearities are compensated via iteration by updating the system inverse response matrix $[I_{xy}(f)]$ every control loop. Maximum control is often achieved within two to three loop cycles as will be discussed in the results section.

Overall spectral error $E_{yy}$ is generated for each output by computing the mean and standard deviation of the difference in logarithmic levels between the desired level $R_{yy}$ and the measured level $G_{yy}$ across the frequency spectrum. The maximum high and low values are also monitored. If control appears to be adequate, with less than a 2 to 3 dB mean variation, or improvement does not seem to be occurring, then individual spectrum plots are made to visually inspect the overall spectral matching achieved. The mean and standard deviation error estimates are useful for reducing the time consuming graphics data display during loop build up to the final drive level. Final judgment on acceptable drive levels are always made based on graphical inspection of the data.

## SOFTWARE/HARDWARE IMPLEMENTATION

The hardware configuration used to implement the control algorithm was configured from two main stand alone processors. The drive signal generation and overall loop control is carried out via a 32-bit virtual memory laboratory computer. The laboratory computer generates the drive signals via a digital-to-

analog (DTA) interface and supplies control signals to a multi-channel fast Fourier transform (FFT) analyzer. The multi-channel FFT analyzer is capable of digitizing, Fourier transforming, and sample averaging up to 8 channels of data while maintaining time correlation. The input drive signals are sampled simultaneously with the output response signals so as to maintain correlation of all input and output signals. The various sample-averaged cross-spectral densities required by the control algorithm are transferred from the FFT analyzer to the laboratory computer via direct memory access (DMA). The transfer of one channel pair of auto- and cross-complex spectra (400 line) requires approximately 50 milliseconds. A two-input/four-output system requires transfer of 14 channel pairs of information, thus requiring approximately 0.7 seconds. The spectra transfer generally requires far less time than the sample averaging time required for a confident data sample when considering random error.

## Drive Signal Generation

As previously stated, the approach taken to generate the required input drive signals is to consider the shaker inputs to be a combination of statistically independent random, stationary Gaussian signals $\{S_i\}$, i=1,2,3 ...M. In which case, the required drive signals $\{X_j\}$, j=1,2,3 ...N can be related to the ideal signals $\{S\}$ via a lower triangular coupling matrix [A]. The initial drive signals are generated first in terms of their spectral content; namely, unit amplitudes exist from the lowest frequency, $f_L$, to the highest frequency, $f_H$, of interest for output control. Using a uniformly distributed random number generator, the phase of each spectral component is generated with random variation from component to component. To be consistent with the FFT analyzer, a maximum of 400 spectral lines exist between zero frequency and the analyzer cutoff frequency. The analyzer cutoff frequencies, $f_C$, are predefined and selected such that $f_H \leq f_C$. As such, the Fourier spectrum of the drive signals initially consist of unit amplitude random phase components in the analysis range $f_L$ to $f_H$. Finite length time histories of the initial signals are then obtained via the inverse Fourier transform of each independent signal.

In order to capture a number of independent random sample averages of the system response, sequences of the time histories must be continuously generated. If the same time series for a particular channel is repeatedly generated, the output wave form becomes pseudo-random and not acceptable for environmental simulation. To form acceptable drive signals, sequences of the same signal were randomly delayed by approximately 25 percent of the signal period and summed for output. It was found that if the signal time delay were fixed and not randomized, the resulting signals showed marked periodic components with unacceptable coherence between "independent" drive signals, as is shown in Fig. 3. However, when introducing the randomized time delays, acceptable signals such as shown in Fig. 4 resulted. It was found that the random phase relationship between the original independent drive signals $\{S\}$ could only be maintained when introducing the coupling matrix in the following partitioned form (as for a two-input system):

$$[\frac{X_{11}}{X_{21}} | \frac{0}{X_{22}}] = [\frac{A_{11}}{A_{21}} | \frac{0}{A_{22}}] \; [\frac{S_1}{0} | \frac{0}{S_2}] \qquad (11)$$

Time histories are generated for the $X_{11}$, $X_{21}$ and $X_{22}$ signals individually where $X_{11}$ and $X_{21}$ maintain identical random phase shifts and random time lags as specified by the original generation of $S_1$, and $X_{22}$ that of $S_2$. The desired time history drive signals corresponding to the specified coupling (the A matrix) are then

and
$$x_1(t) = x_{11}(t)$$
$$x_2(t) = x_{21}(t) + x_{22}(t). \tag{12}$$

Additional important characteristics of the drive signals are that they be stationary and that the signal crest factor can be controlled. Stationarity is measured by the variation in signal mean and r.m.s. level as time progresses. For the present algorithm, the zero mean and r.m.s. variation are less than 1 percent. Control over peak-to-r.m.s. level is accomplished by introducing signal peak folding. All data points exceeding the desired peak value are folded back into the signal, not clipped at the peak value. Thus, signal peaks when folded become local valleys which tend to raise the signal r.m.s. level. Crest factor control in the range from 2.0 to 4.5 is readily accomplished.

**Output Spectra Specification**

In order to accommodate various levels of output control specification which presently exist for equipment under qualification and provide a means to evaluate the importance of all elements in a specification, the following specifications for the $R_{yy}$ spectral matrix were developed.

1) Full $R_{yy}$ Specification: where auto-spectra are specified by spectrum frequency and magnitude break point pairs and cross-spectra are specified by spectrum frequency, magnitude, and phase break point values.

2) Auto-Spectra and Coherence Specification: where auto-spectra are specified by spectrum frequency and magnitude break point pairs and cross-spectra are specified by frequency and coherence break point pairs. Herein, the cross-spectra magnitudes are generated from the definition of spectral coherence,

$$\gamma_{ij}^2 = \frac{|G_{ij}|^2}{G_{ii}G_{jj}} \tag{13}$$

and the phase of $R_{yy}$ is taken as that of the measured $G_{yy}$.

3) Auto-Spectra Only: where auto-spectra are specified by frequency and magnitude break point pairs. The cross-spectra magnitude and phase are generated from the measured $G_{yy}$ in proportion to the magnitude of the specified $R_{yy}$ via:

$$R_{ij} = \frac{(R_{ii} \cdot R_{jj})^{\frac{1}{2}}}{(G_{ii} \cdot G_{jj})^{\frac{1}{2}}} \cdot G_{ij} \tag{14}$$

For existing test specifications such as MIL-STD-810C/D, only the output auto-spectra may be known. If field measurements were made without specification of cross-spectra, one may be much better off to accept the cross-axis coupling of the

144

test setup rather than attempting to invoke a physically unrealizable specification for which control would be impossible or which may drastically alter the service life of the test item.

## TYPICAL RESULTS

Several types of exciters, exciter arrangements, and test item configurations were used to evaluate the proposed control algorithm and its limitations as reported in Ref. 9. The algorithm evaluation process will, of course, continue as the system is employed for equipment qualification purposes, and the author is confident that much is to be learned as opportunities arise for its use. The following example illustrates the general capabilities of the control algorithm.

### Multi-Resonant Beam

In order to study the control of sharp structural resonances a small cantilever beam was driven using two small voice coil shakers. Three accelerometers were used to record the beam response. The two-input/three-output system is schematically shown in Fig. 5.

The cantilever beam exhibited damping of less than 0.3% critical, which is uncharacteristic of built-up structures in which damping levels of 2 to 5% are more representative. Thus, the low damped beam provides a harsh test of the control algorithm to control resonances. The initial drive signals to the exciters are shown in Fig. 6 as being independent random signals in the frequency range from 5 to 250 Hz. The initial beam response to the drive signals and the desired output magnitude specifications are shown in Fig. 7. Due to the sharp resonances in the beam, exhibiting distinct phase between outputs, only the cross-axis coherence was specified since the excitors were of marginal power and, thus, not likely powerful enough to change system phasing. The coherence between output channels 1 and 2 was set at 0.50, as was that between channels 2 and 3. The coherence between channels 1 and 3 was set to 0.20. Control after three loop iterations resulted in the output spectra shown in Fig. 8. As can be seen, the primary beam resonance was well-controlled, as was the second beam resonance at outputs 2 and 3. Since output 1 was at an anti-node of the second beam resonance, sensitivity to the second mode was high at that location as is shown in Fig. 8a. The second beam resonance occurs around 90 Hz and with a critical damping ratio of 0.003, its half-power point bandwidth would be approximately 0.54 Hz. Thus, with a control bandwith of 0.625 Hz (250 Hz/400 lines), reasonably good control of the mode was realized. Control of the cross-spectra was reasonably good, however, not as good as the auto-spectra shown in Fig. 8.

### Aircraft External Store Vibration Simulation

The aircraft external store used to evaluate a two-input/four-output control configuration is shown in Fig. 9. The external store is a dummy test item with an overall length of 193.3 cm (76.12 inches). Major bulkheads are at Missile Stations (MS) 30.38, 55.06 and 66.125. The bulkheads provide for exciter attachment and free-free missile suspension via elastic bungy cords (2 Hz vertical). The test item is fitted with add-on damping material to raise modal damping values to 0.02 minimum. A dynamic modal analysis of the test item in the frequency range from 10 to 500 Hz revealed an abundance of normal mode resonances as shown in Table 1. It was felt that this multi-modal structure would provide a good evaluation of the proposed control algorithm.

145

Input excitation to the test item was provided by two electrodynamic modal shakers attached at MS 30.38 and MS 66.125. The shakers were aligned normal to the missile longitudinal axis and 45 degrees to the vertical (see Fig. 9). The acceleration response control points are located at MS 55.06 and MS 30.38 with one vertical and one horizontal transducer at each location. Response channels 1 and 4 are the horizontal responses and channels 2 and 3 the vertical responses. Field data were not available for the test item and, therefore, the control specification was a flat response in the frequency range from 20 to 500 Hz on each output with magnitude $10^{-4}$ $g^2$/Hz. The bandwidth of resolution was set at 1.25 Hz which should provide marginal resolution to control a 2% damped 100 Hz mode (half power point bandwidth of 4.0 Hz).

The output response specification for channels 1 and 3, along with the recorded responses after the initial broadband excitation and after three control loop cycles, are shown in Fig. 10. As can be seen by the data given in Fig. 10a, channel 1 response was initially dominated by the fuselage first and second horizontal modes; nevertheless, the control algorithm performed reasonably well. Similar trends were seen in the other responses as well as is shown in Fig. 10b for the channel 3 response. Close examination of the hay-stack response in the area of 460 Hz in channel 3 response shows the incompatibility of the control specification relative to the location of the excitors and response accelerometers. In this case, it was impossible to drive response 4 (not shown) in the horizontal direction to the desired level while maintaining vertical response to within limits in the frequency region of the third fuselage vertical bending mode at 462.5 Hz. For the most part, the control algorithm performed well, except at these incompatible areas. It is expected that measured field data would not reflect these incompatibilities if the exciters were placed at the store-to-aircraft attachment points and field data were recorded at the specified output locations.

Throughout the evaluations discussed above, 20 sample averages were used to obtain the results shown. In many cases, 5-10 averages would have been adequate during signal development. A higher number of averages, on the order of 200, are appropriate for random data analyses of the final drive signals to establish statistical confidence [10]. Control loop time is highly dependent on the frequency range of interest and the graphical display of results. Twenty sample averages at a maximum frequency of 62.5 Hz requires 128 seconds; while for an analysis out to 2000 Hz, the sample average time is only 4 seconds. Thus, in the former case, 10 seconds for control analysis time is insignificant while in the latter case it is measurable. In either case, the time to record graphical data to a hardcopy device is significant. Such intermediate output records can, of course, be avoided after developing confidence in the algorithm.

## CONCLUSIONS AND RECOMMENDATIONS

Based on the limited experience gained with the control algorithm thus far, the following conclusions and observations are made:

1) It appears that the control algorithm, as implemented, will allow different numbers of input and output channels. This feature can be useful in various practical test situations, including assurance of uniform excitation for a test item.

2) The algorithm updates the system inverse response matrix every control loop cycle which accommodates system amplitude nonlinearities and allows compensation for system degradation during life time simulation.

146

3) Full control of cross-coupling between all output responses can be invoked with the present algorithm. However, it appears that the extent to which control is achieved is highly dependent on the physical arrangement of the exciters.

4) Analysis bandwidth is an important parameter in controlling test item resonances. The 400-line analysis used in the present system appears to be marginal, with 800 to 1000-line analysis being preferred.

5) The dynamic range of the present system is set by the FFT analyzer, that being the 12-bit analog-to-digital converters. It is recommended that 16-bit resolution be used to insure sufficient dynamic range especially for random signal control where crest factors of 3 to 4.5 are required.

## SYMBOLS

Values are given in both SI and U.S. Customary Units. The measurements and calculations were made in U.S. Customary Units.

| | |
|---|---|
| $f_L, f_C, f_H$ | low, center, and high frequency, Hz |
| $t$ | time, sec. |
| $X_i$ | input voltages of the $i^{th}$ channel, volts |
| $Y_j$ | output accelerations of the $j^{th}$ channel, g |
| $A(t)$ | lower triangular coupling matrix |
| $E$ | mathematical expectation operator |
| $E_{yy}$ | Overall output spectral error, $g^2/Hz$ |
| $G_{xy}^{ij}(f)$ | one-sided input/output cross-spectral density, volt-g/Hz |
| $G_{xx}^{ij}(f)$ | one-sided input auto-spectral density, $volts^2/Hz$ |
| $G_{yy}^{ij}(f)$ | one-sided output auto-spectral density, $g^2/Hz$ |
| $H_{yx}(f)$ | system frequency response function, g/volt |
| $I_{xy}(f)$ | system inverse frequency response function, volt/g |
| $N$ | number of sample records |
| $S(t)$ | independent random white noise sources, volt |
| $T$ | finite period of time, sec. |
| $X_i^k(f,T)$ | $k^{th}$ sample record of finite period Fournier Transform of $X_i(t)$, g-sec |
| $Y_j^k(f,T)$ | $k^{th}$ sample record of finite period Fournier Transform of $Y_j(t)$, g-sec |
| $\gamma_{ij}$ | spectral coherence (Eq. 13) |
| $\star$ | complex conjugate operator |

## REFERENCES

1. MIL-STD-810D, "Environmental Test Methods and Engineering Guidelines", July 19, 1983.

2.  Everett, W. D., and Helfrich, T. M. "Triaxial Vibration System," 55th Shock and Vibration Bulletin, Part 2, June 1985, pp. 1-15.

3.  Fisher, K. K., "Theoretical and Practical Aspects of Multiple-Actuator Shaker Control," 43rd Shock and Vibration Bulletin, Part 3, June 1973, pp. 153-174.

4.  Smith, S., Stroud, R. C., Hamma, G. A., and Johnson, L#ntrol System for Testing a Single Test Item with Multiple Inputs," SAE Paper 821482, 1982.

5.  Fisher, D. K., and Posehn, M. R., "Digital Control for a Multiple-Actuator Shaker," 47th Shock and Vibration Bulletin, Part 3, September 1977, pp. 77-96.

6.  Tebbs, J. D., and Hunter, N. F., Jr., "Digital Control of Random Vibration Tests Using a Sigma V Computer," Proceedings, Institute of Environmental Sciences, 1974, pp. 36-43.

7.  Smallwood, D. O., "A Random Vibration Control System for Testing a Single Test Item with Multiple Inputs," SAE Paper 821482, 1982.

8.  Smallwood, D. O., "Random Vibration Testing of a Single Test Item with a Multiple Input Control System," Proceedings, Institute of Environmental Sciences, 1982, pp. 42-49.

9.  Unruh, J. F., "Multiple Input/Output Random Vibration Control System," Southwest Research Institute Internal Research Report No. 06-9465, April 1988.

10. Bendat, J. S., and Piersol, A. G., Engineering Applications of Correlation and Spectral Analysis, John Wiley & Sons, 1980.

11. Greville, T. N. E., "Some Applications of the Pseudo-Inverse of a Matrix," SIAM Review, II, pp. 15-32, 1960.

## Table 1. External Store Natural Frequencies

| Mode No. | Frequency (Hz) | Mode Description | |
|----------|----------------|------------------|---|
| 1  | 15.0  | 1st | Symmetric Wing Vertical Bending |
| 2  | 52.5  |     | Symmetric Wing Torsion |
| 3  | 57.5  |     | Coupled Tail/Wing Horizontal |
| 4  | 97.5  | 1st | Fuselage Vertical Bending |
| 5  | 102.5 | 1st | Fuselage Vertical Bending |
| 6  | 107.5 | 1st | Fuselage Horizontal Bending |
| 7  | 120.0 | 2nd | Symmetric Wing Vertical Bending |
| 8  | 202.5 | 2nd | Fuselage Horizontal Bending |
| 9  | 227.5 | 2nd | Fuselage Vertical Beding |
| 10 | 390.0 |     | Wing Panel Mode |
| 11 | 410.0 |     | Wing Panel Mode |
| 12 | 435.0 | 2nd | Fuselage Horizontal Bending |
| 13 | 462.5 | 3rd | Fuselage Vertical Bending + 2nd Wing |

$Y_1$ $Y_2$ $Y_3$ **Responses**

**System**

$X_1$ $X_2$ **Input Voltages**
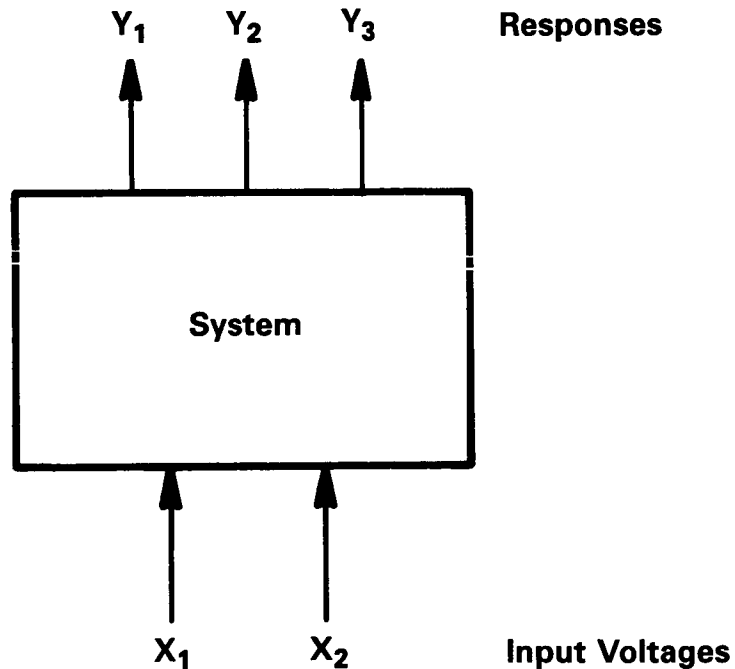
Figure 1. Two-Input/Three-Output System
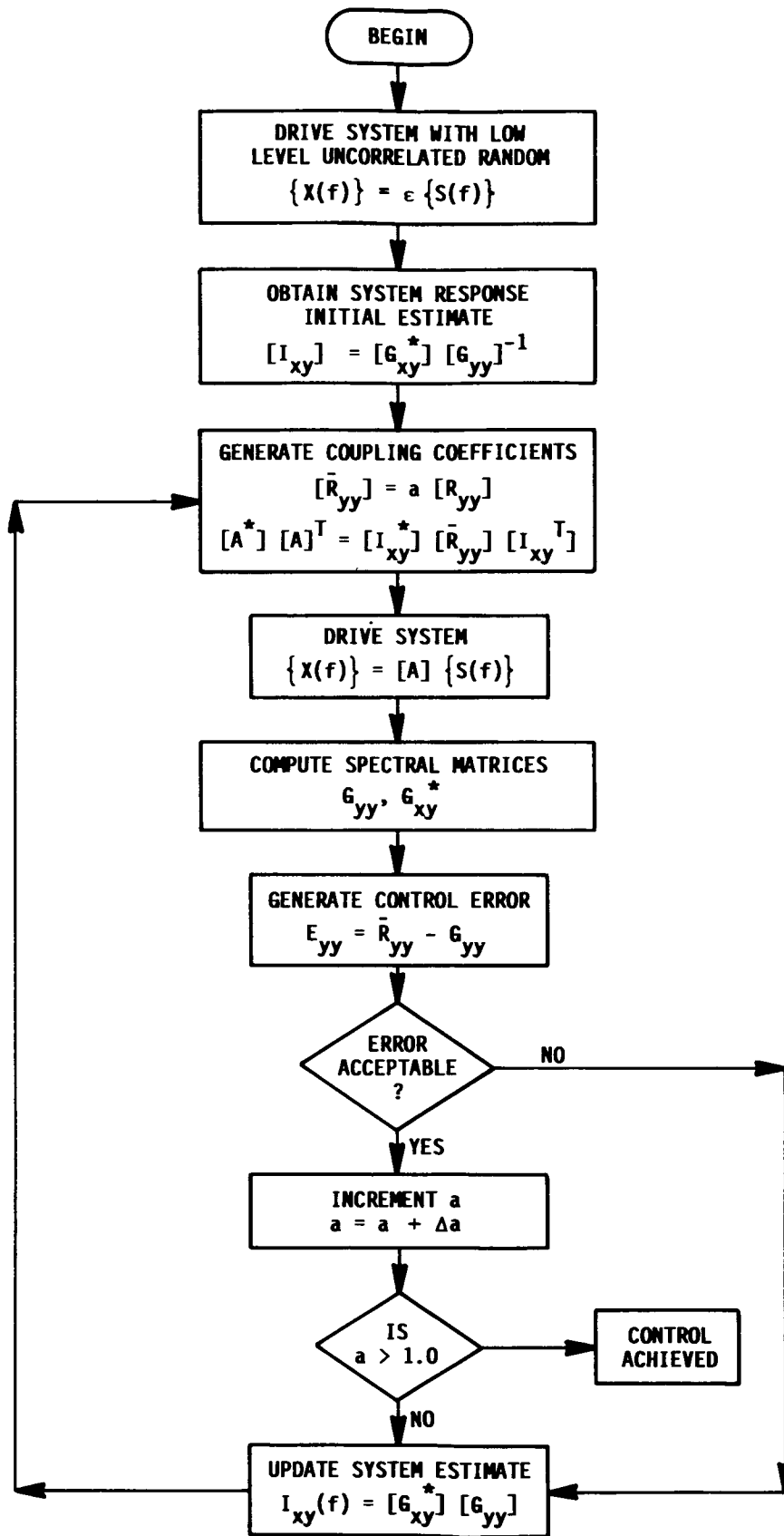
Figure 2. Control Algorithm Flow Chart

150
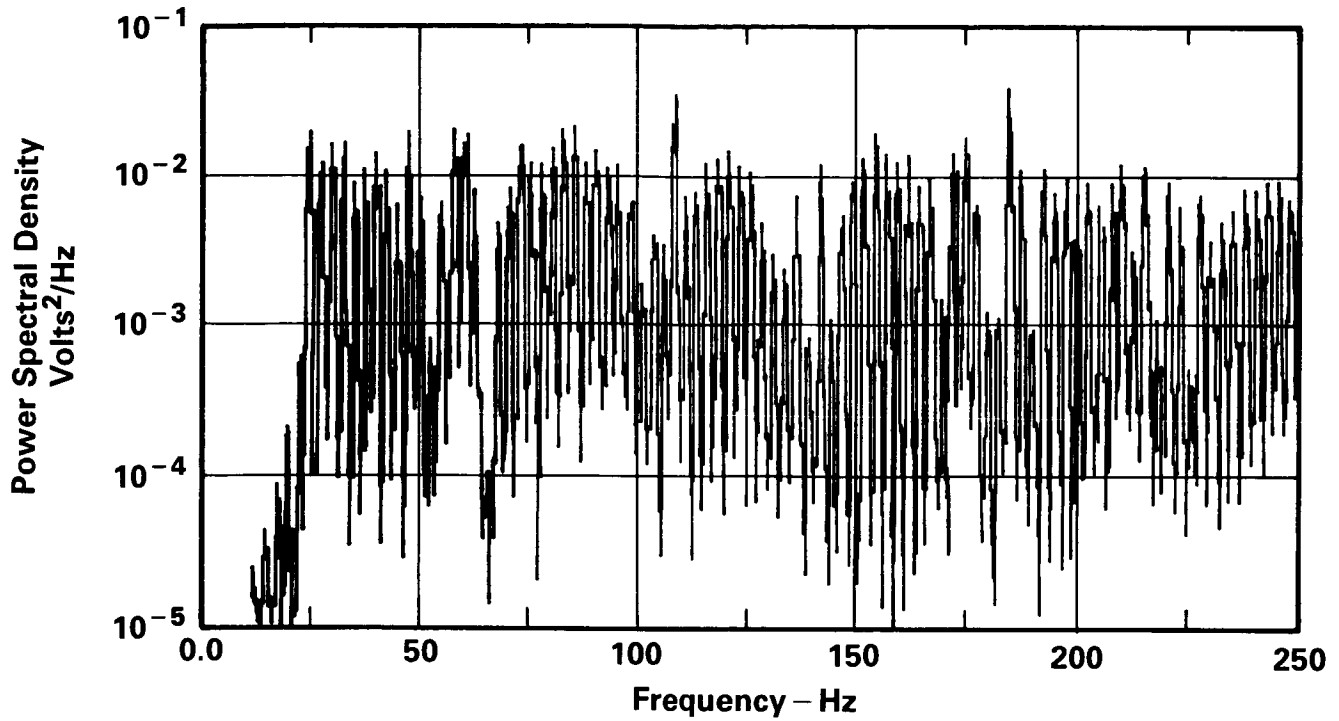
a) Auto Spectra Channel 2
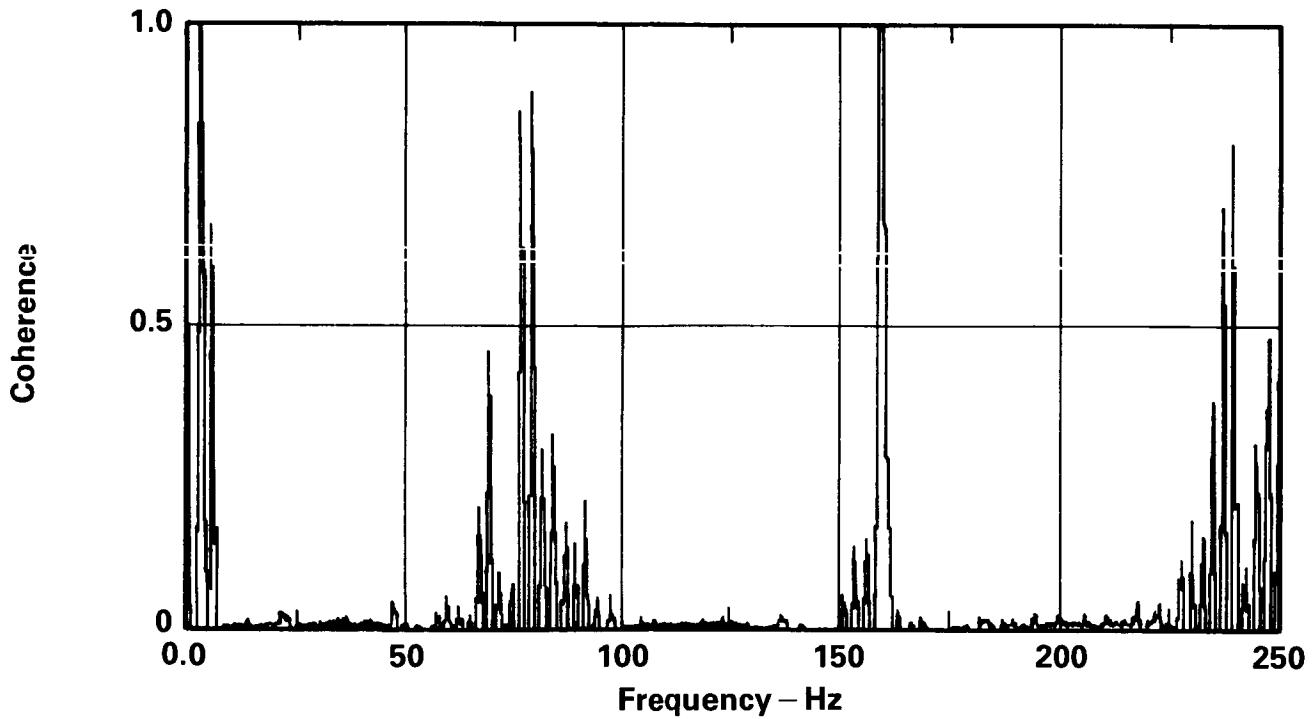


b) Coherence Between Channels 1 and 2

Figure 3.   Typical Spectral Averaged Drive Signals, Fixed Time Delay
During Time Sequence Generation

151
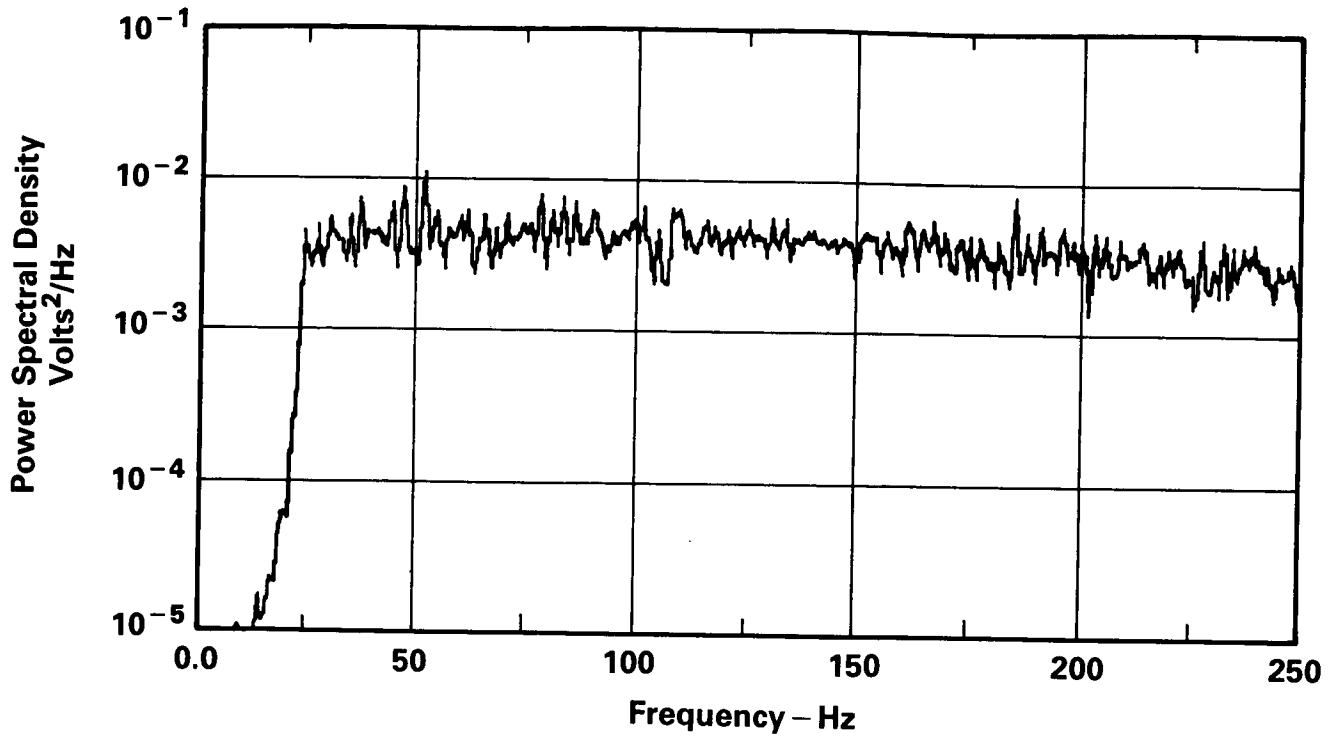
a) Auto Spectra Channel 2
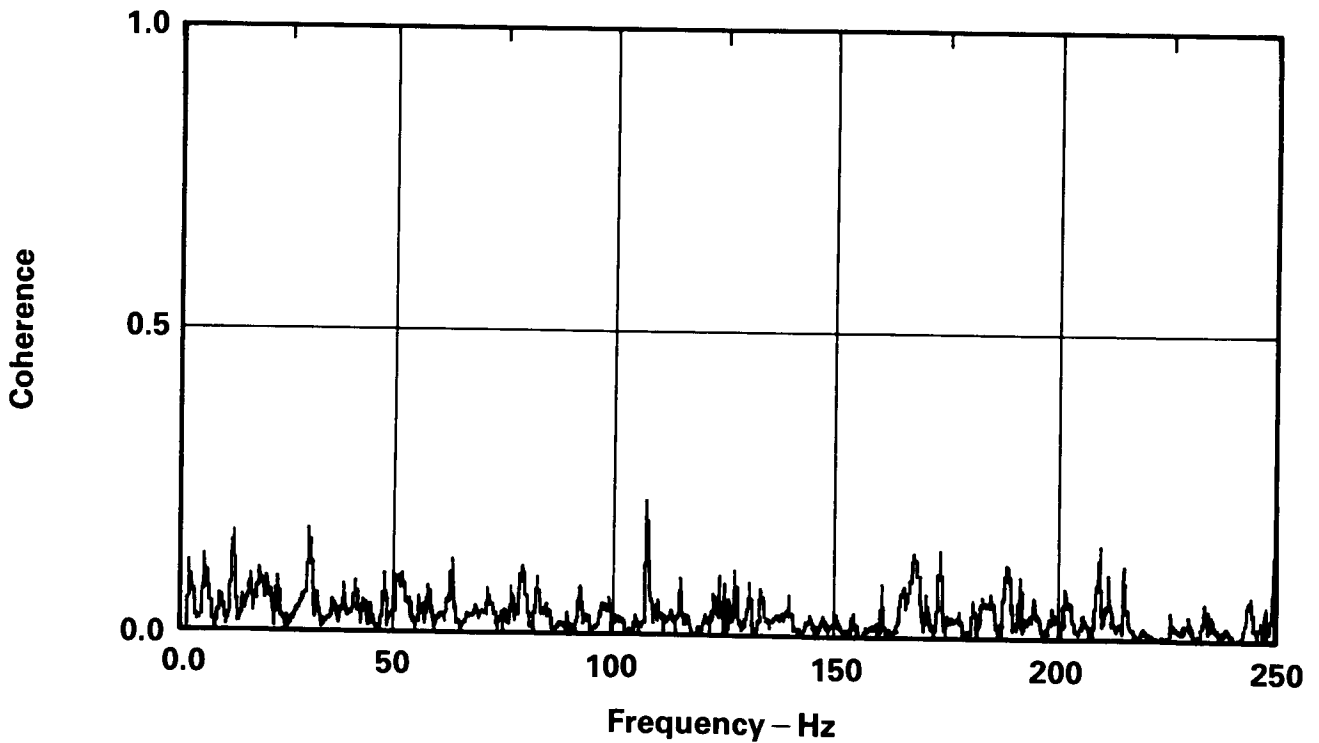
b) Coherence Between Channels 1 and 2

Figure 4.  Typical Spectral Averaged Drive Signals, Random Time Delay
During Time Sequence Generation
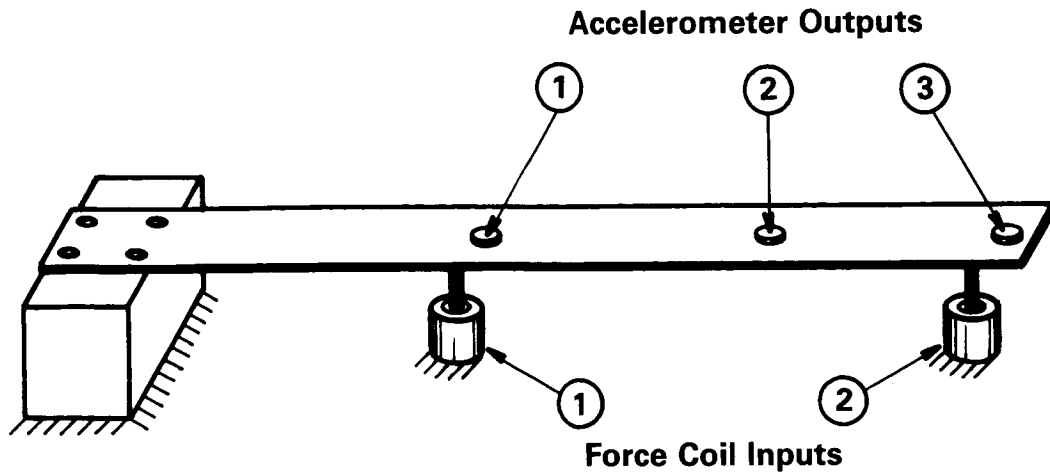
Figure 5. Schematic of the Two-Input/Three-Output System



a) PSD – Channel 1 or Channel 2



b) Coherence Channel 2 to Channel 1
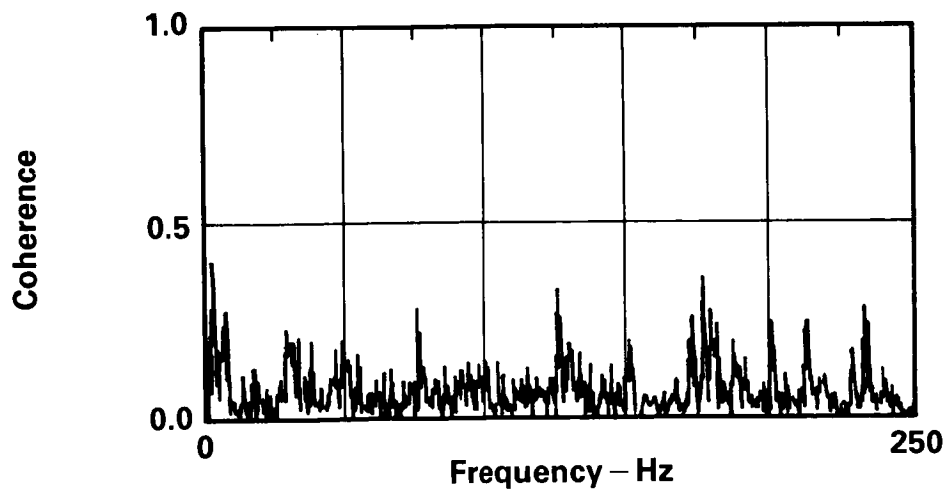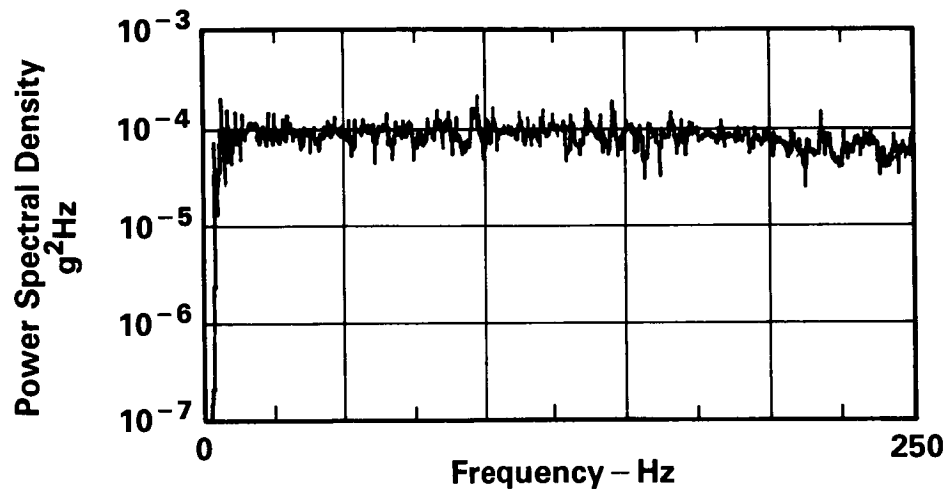
Figure 6. Initial Drive Signals

153
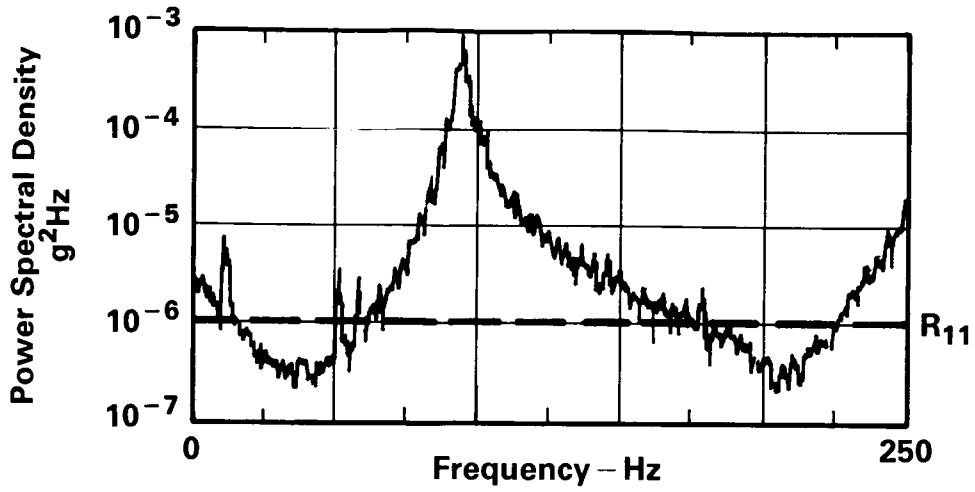
a) Output PSD Channel 1
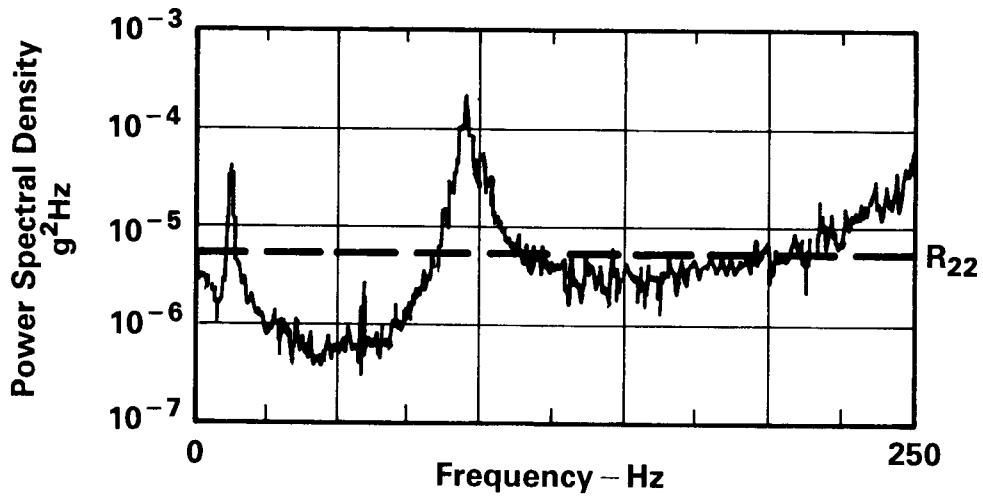
b) Output PSD Channel 2

c) Output PSD Channel 3

Figure 7. Initial Beam Response

154

Figure 8. Beam Response After Three Iterations

155

OUTPUT #4
HORIZONTAL

OUTPUT #3
VERTICAL

OUTPUT #2
VERTICAL

OUTPUT #1
HORIZONTAL

INPUT #1

INPUT #2
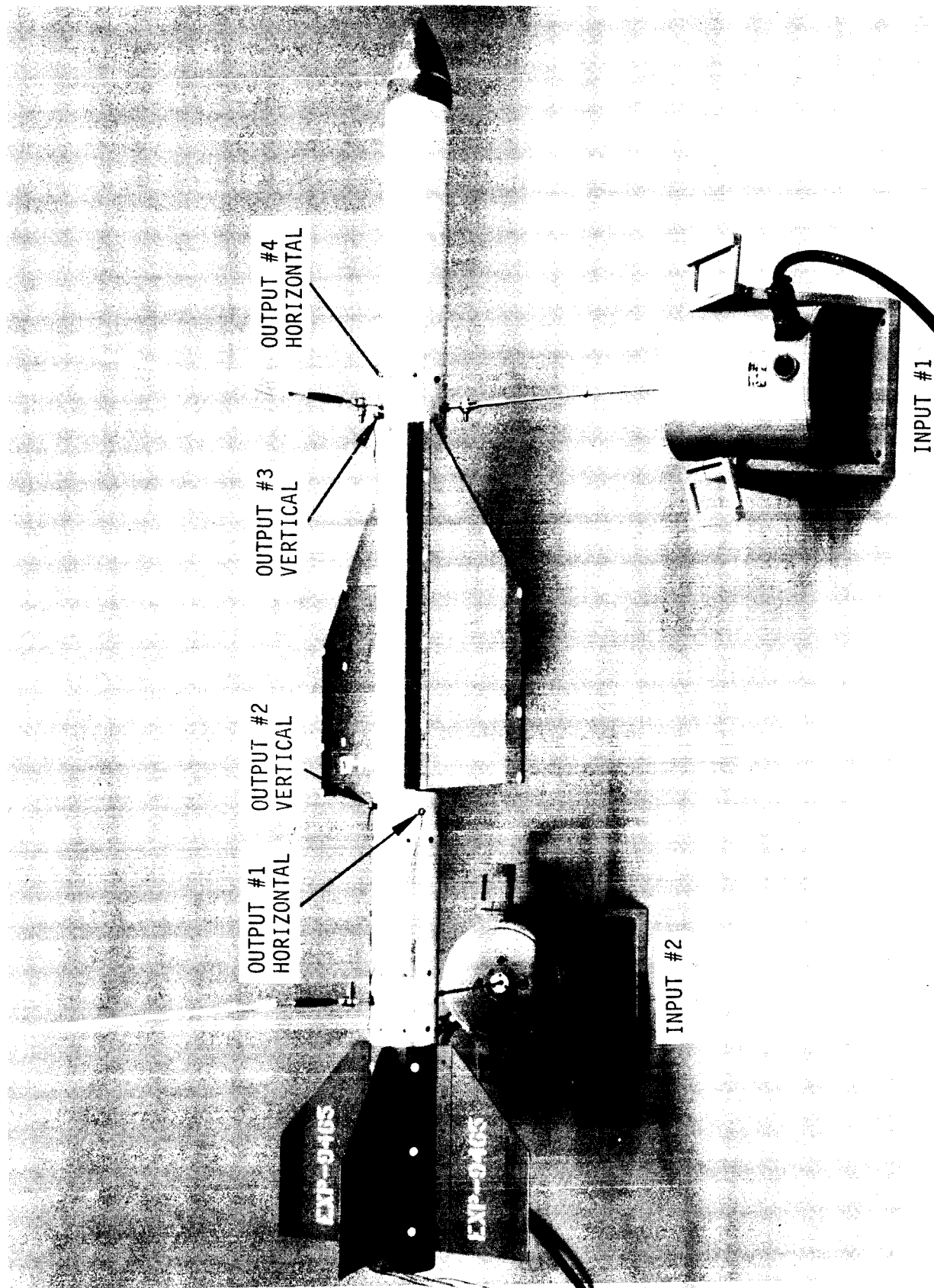
Figure 9.  Aircraft External Store Test Configuration
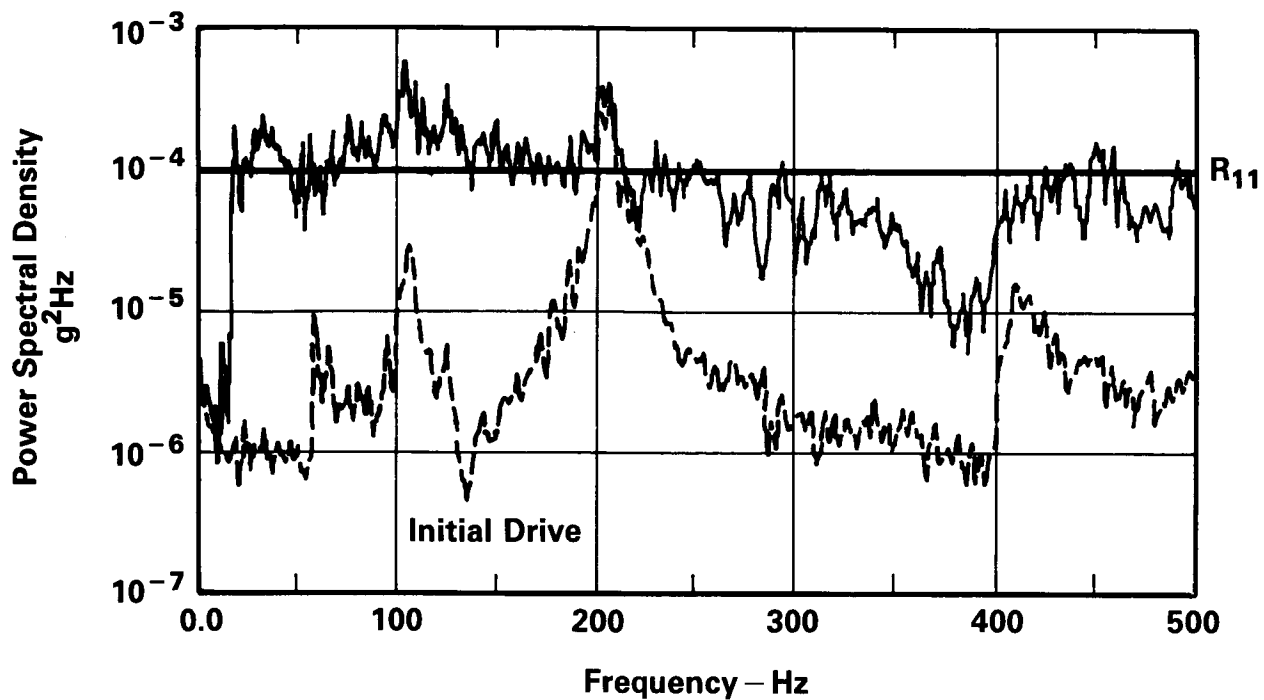
a) Output PSD Channel 1
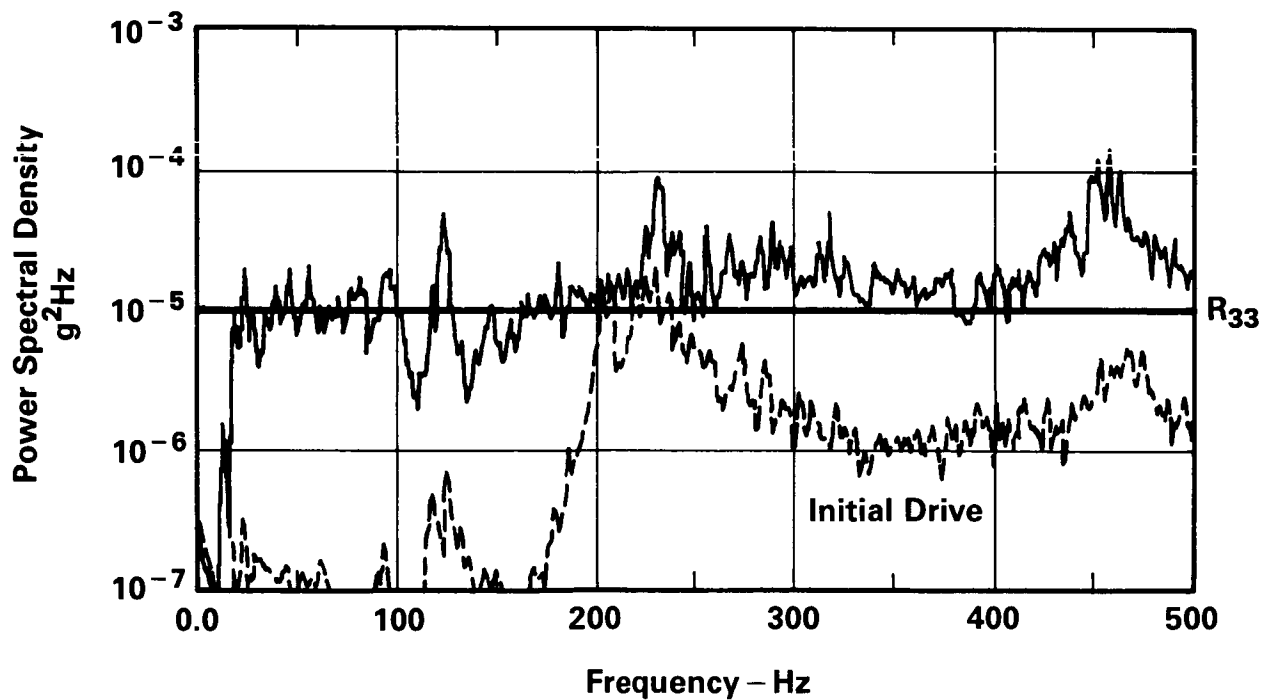


b) Output PSD Channel 2

Figure 10.  External Store Response

# THE FLIGHT ROBOTICS LABORATORY

Patrick A. Tobbe, Marlin J. Williamson, and John R. Glaese
Control Dynamics Company

## ABSTRACT

The Flight Robotics Laboratory of the Marshall Space Flight Center is described in detail. This facility, containing an eight degree of freedom manipulator, precision air bearing floor, teleoperated motion base, reconfigurable operator's console, and VAX 11/750 computer system, provides simulation capability to study human/system interactions of remote systems. This paper describes the facility hardware, software, and subsequent integration of these components into a real time man-in-the-loop simulation for the evaluation of spacecraft contact proximity and dynamics.

## INTRODUCTION

The Flight Robotics Laboratory of the Marshall Space Flight Center provides sophisticated simulation capability in the study of human/system interactions of remote systems. The facility consists of a four thousand square foot precision air bearing floor, a teleoperated motion base, a dynamic overhead target simulator (DOTS), a remote operator's reconfigurable station, various simulation mock-ups, and a VAX 11/750 computer system for real time operation.

The motion base is an air bearing vehicle, with limited capability in six degrees of freedom, which may serve as a controllable chaser craft or as a target vehicle. This vehicle contains six pressurized air tanks for pneumatic power of its thirty-two thrusters. This provides a means of remote operation and control.

The dynamic overhead target simulator (DOTS) is an eight degree of freedom (DOF), heavy duty electric manipulator capable of traversing over the entire air bearing floor. The system is composed of a precision overhead X-Y crane to which a six degree of freedom robot arm is mounted. The VAX 11/750 computer is used in real time to convert tip position and orientation commands into crane position and arm joint velocity commands. These commands are generated through inverse kinematic relationships and digital control laws housed on the computer. An elaborate real time safety algorithm is also driven by the computer to perform collision avoidance, end effector force/torque limiting, joint position and rate limiting, and communications checks.

The remote operator's workstation consists of hand controllers, two monitors, and a large screen display.

The tip commands for the manipulator are generated by a position model on the computer. This position model is simply a set of equations which model the hardware

---

that the facility is configured to simulate. For example, in order to perform studies of contact dynamics between two orbiting spacecraft, a position model consisting of the equations of motion for the two craft acted on by thruster, gravitational, and contact forces is used.

However, this facility is not limited to contact dynamics studies. With the correct position models, the facility may be used to simulate space station construction tasks in zero gravity or for the testing and training of personnel flying remotely piloted vehicles. These studies also investigate such human factor concerns as light and camera positions on the vehicle, control system sensitivity, and transmission time delays. Since the manipulator control law is implemented on the computer, it is a simple matter to use the facility as a testbed for new robotic control algorithms.

In the fall of 1988, the facility will be configured to perform real time, man-in-the-loop docking studies of the orbital maneuvering vehicle (OMV) with a moving target. This test series will make use of the manipulator, VAX 11/750, and the remote operator's work station. A FORTRAN 77 simulation consisting of the real time position model and arm controller, as well as dynamic models of the arm, actuators, and sensors, will be used to predict the results of the tests. These hardware models have been generated and incorporated into the simulation. The model parameters will be updated as the facility hardware becomes available for testing.

The purpose of this paper is to describe the hardware and software which will be used in these docking studies. It will explain the integration of these components and efforts taken to validate the facility.

## FACILITY CONFIGURATION

Currently, the facility is being configured to perform real time, man-in-the-loop docking studies of the OMV with a moving target using the three point docking mechanism. The active half of this mechanism is simply a set of three electromechanical jaws mounted on the verticies of an equilateral triangle. The passive half of this mechanism is a set of three bars or "towel racks", similarly mounted, which the jaws will grapple. The active half will be mounted to the arm while the passive half will be fixed at some location in the facility.

Shown in Figure 1 is a block diagram of the facility configuration. A pilot at the remote operator's workstation views a screen generated by a camera located on the end of the arm. The position and orientation of the camera with respect to the docking mechanism would be such that it duplicates the flight hardware configuration. The pilot then issues of commands for the OMV control system through a set of joysticks at the workstation. The output of the joysticks is fed into the computer for use in the position model.

The position model for the OMV docking studies consists of a computer simulation of two rigid vehicles, the target and chaser, in a circular orbit. The vehicles are modeled in the simulation using Hill's and Newton-Euler equations (ref. 1). The target is acted on by gravity and vehicle contact forces and torques. The chaser is acted on by gravity, vehicle contact, and control system thruster forces and torques.
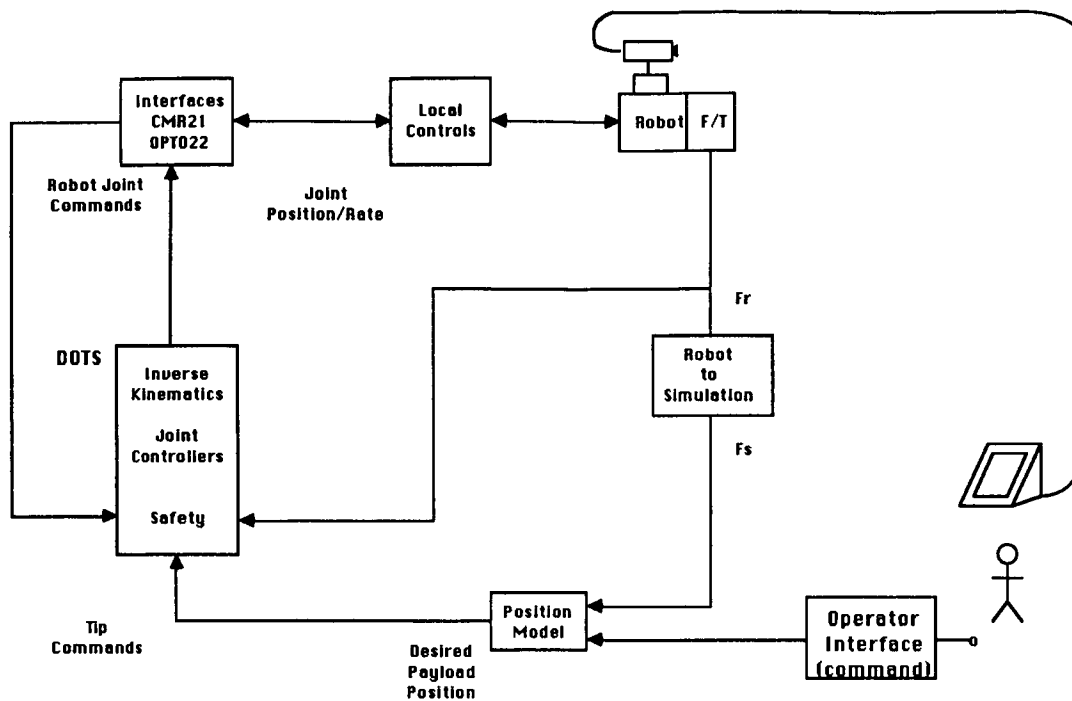
Figure 1   Facility Configuration

A force/torque sensor on the end of the arm senses contact, gravity, and small inertial forces and torques due to the motion of the arm,  The output of the sensor is filtered to generate vehicle contact forces and moments for use in the equations of motion.   The position model then produces the relative position and orientation of the chaser docking mechanism with respect to the target docking mechanism. Manipulator tip position and orientation commands are formulated such that the relative position and orientation of the docking mechanisms of the facility will match those produced by the position model.

The manipulator tip commands are now used by the inverse kinematics routine to produce commanded joint positions.   The commanded joint positions, along with joint encoder feedback, are used by the digital control algorithms to calculate joint rate commands for the local rate servo systems mounted on the arm.

The safety algorithm also uses commanded joint and tip positions for real time collision avoidance.   Safety envelopes are defined about the arm and various mock-ups on the floor.   These zones are described by equations and never allowed to intersect.   Safety also uses the output of the force/torque sensor to limit the reaction of the end effector.   Encoder and tachometer feedback are used to limit joint position and rate.

The local controllers on the arm initiate the desired motion to mimic the relative motion of the orbiting spacecraft.

160

## FACILITY HARDWARE DESCRIPTION

The DOTS is presented in Figure 2. It is a 6-DOF arm suspended from an industrial X-Y overhead crane. The crane's bridge spans the width and travels the length of the air bearing floor. The crane's trolley travels along the span of the bridge (covering the width of the air bearing floor). These two joints are controlled with localized position control systems. These control systems are composed of PID controllers and electronic distance meters (EDM). The design of the PID controllers is automated via the set-up software associated with the position control systems. Each of the position control systems for the crane also have a rate loop closed about the joint with DC pulse-width-modulated servo drives and DC motors. These servo loops are also found on the remaining arm joints.

The control algorithm implementation in the real time software regulates the rate commands for the 6-DOF arm. This arm is composed of five rotational and one translational degrees of freedom. Starting at the base of the arm attached to the crane, the waist rotation joint allows continuous rotation about an axis perpendicular to the floor via a slip ring. Using the rated speed of the motor selected to drive this joint and its gear ratio, the continuous joint speed is 1.3 rpm.
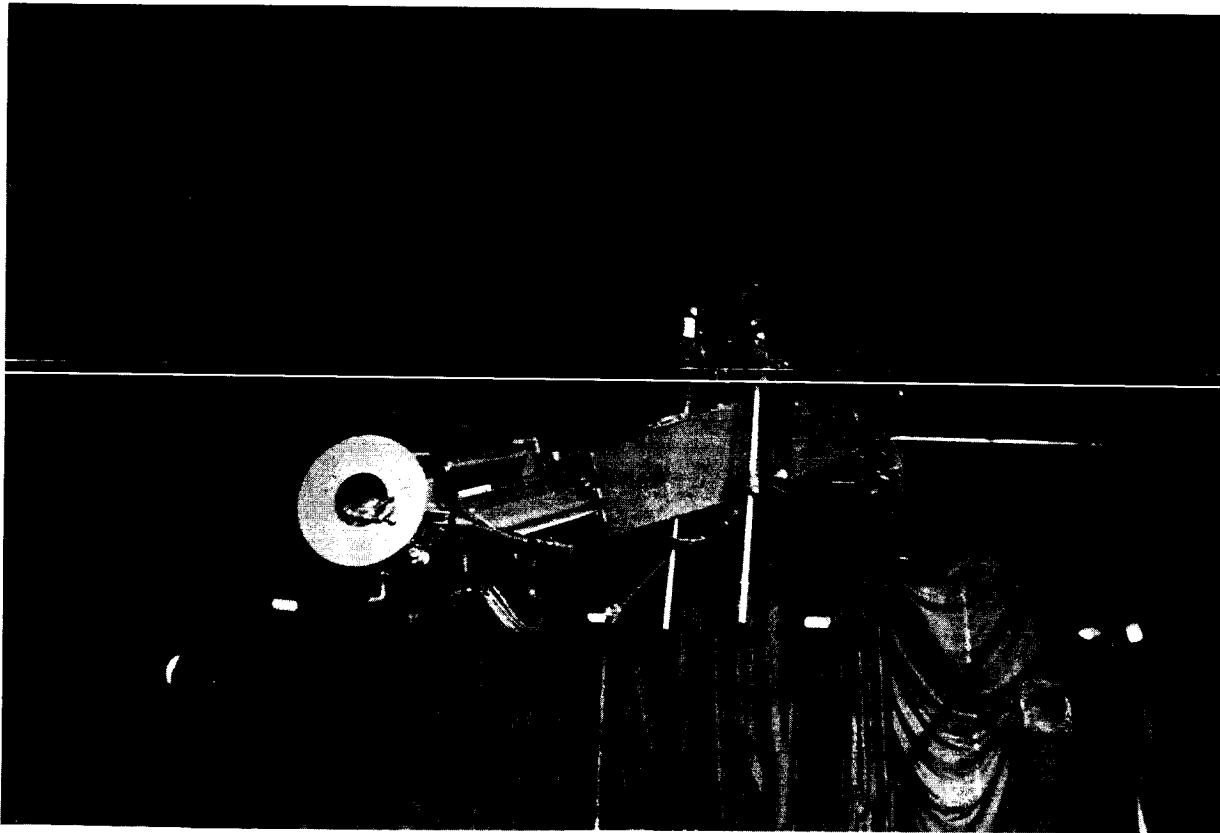


Figure 2   Dynamic Overhead Target Simulator (DOTS)

The next joint encountered is the shoulder pitch. This joint has a ± 50° range with respect to an axis parallel to the floor. A maximum continuous speed of 7.7 rpm is achieved. Two linear actuators (worm gear and motor) are used to drive this joint. A counter weight system offsets the loads seen by these actuators.

Farther up the arm, the lone translational joint is encountered. Its maximum continuous speed is 13.2 cm/sec (5.2 in/sec) with a range of 2.62 m (10 ft.).

The wrist assembly at the end of the arm is composed of three degrees of freedom; wrist yaw, pitch, and roll. The wrist yaw and pitch are linearly actuated with wrist pitch having two actuators (similar to the shoulder pitch). These joints are also limited to ± 50° travel and a maximum continuous rate of 0.2 rpm. The wrist roll has no limit in range due to a slip ring. Maximum continuous speed is 10 rpm for this joint.

Each joint is instrumented with 12-bit encoders and tachometers. The encoders record relative joint position. These values are read by the main computer system through the programmable serial communications device. Here, the values are transformed into a physical measurement of the joint positions.

The tachometers located at the motors (1:1 motor to tachometer shaft ratio) are integral parts of the servo loop systems. To get a reading of joint speed, the tachometer voltages are filtered (to reduce noise) and scaled (to match A/D input). Once filtered, digital measures are taken by a 12-bit A/D device. The main computer system reads these values via the programmable serial communication device. The integer values read are converted to real values and scaled to reform the tachometer voltages. The voltages are related to shaft speed by the voltage constants. Shaft speeds are transformed through kinematic relationships to a measured joint speed.

The programmable serial communication device used to read the tachometer and encoder settings is also used to send the rate commands to a D/A, which in turn generates voltage reference signals for each rate loop on the arm. It also writes the position commands to the position control systems for the overhead crane.

The payload capability of the arm is 454 kilograms (1000 pounds) with a center if gravity offset of 46 centimeters (18 inches) from the wrist roll axis.

The force/torque sensor mounted at the end of the arm has a capability of 44,482 newtons (10,000 pounds) and 6779 newton-meters (60,000 inch-pounds). The accuracy is one quarter percent of full scale.

## FACILITY REAL TIME SOFTWARE DESCRIPTION

All of the real time software to be used in this test series will be housed on the VAX 11/750. An executive routine coordinates the input/output operations between the computer and the crane/arm sensors and actuators, force/torque sensor, and operator's console. This routine also calls the inverse kinematics, joint controller, safety, and position model modules. It generates output for a test conductor's terminal screen in the form of commanded and sensed tip/joint positions and error messages. It is being modified to generate additional output to a currently undefined device. The real time simulation cycle time goal is 33 milliseconds. The position model has been described in the Facility Configuration section.

162
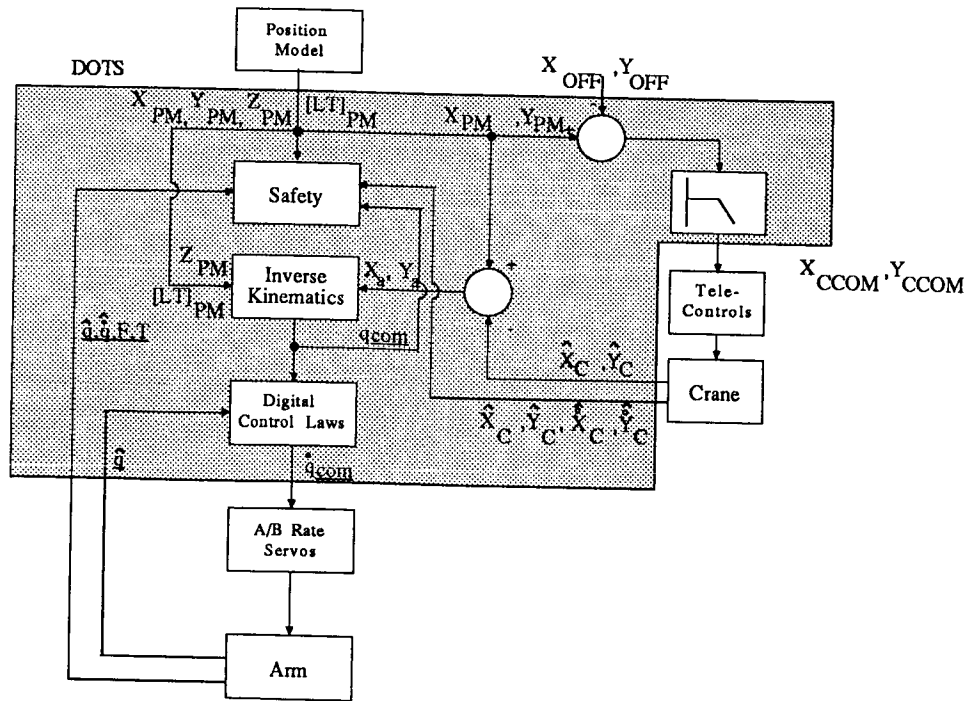
Figure 3  DOTS Controller

## DOTS Controller

The DOTS controller, highlighted in gray in Figure 3, is simply the collection of the inverse kinematics, joint controller, and safety routines. An implicit assumption made in this algorithm concerns the bandwidths of the crane and the arm joints. It is assumed that the bandwidths of the arm joints are significantly higher than those of the overhead crane. The crane is commanded to move within an offset distance of the position model output. The arm tip is then commanded to move a distance equal to the difference between the commanded position model output and the current crane position. In this way, as the crane slowly approaches its commanded position, the arm joints will "backoff" to keep the tip at the desired location. This will effectively match the bandwidth of the system to that of the arm within a limited range of motion. This algorithm will also tend to drive the arm to a "home" configuration which avoids joint singularities.

As seen in Figure 3, the output of the position model are the tip coordinates $X_{pm}$, $Y_{pm}$, and $Z_{pm}$ in a lab coordinate frame and the transformation matrix $[LT]_{pm}$ describing the orientation of the arm tip with respect to the lab frame. $X_{pm}$ and $Y_{pm}$ coincide with the overhead crane degrees of freedom. Offsets in X and Y are subtracted from these commands to keep the arm extension in the "home" position at the middle of its travel. The resulting commands are compensated by a second order filter with a 1 Hertz break frequency. The filtered commands, $X_{ccom}$ and $Y_{ccom}$ are then passed to the localized position control systems which drive the overhead crane. The sensed crane positions and rates, $\hat{X}_c, \hat{Y}_c, \hat{\dot{X}}_c$, and $\hat{\dot{Y}}_c$ are fed back to the computer.

163

The arm X and Y tip position commands, $X_a$ and $Y_a$, are calculated by subtracting the sensed crane positions from the outputs of the position model, $Xpm$ and $Ypm$. The inverse kinematics generates a set of six arm joint position commands, $qcom$. The digital control law produces a set of joint rate commands, $\dot{q}com$, based on the differences of the commanded joint positions, $qcom$, and sensed joint positions, $\hat{q}$.

The safety module uses the sensed arm joint position and rates, $\hat{q}$ and $\hat{\dot{q}}$ and the overhead crane sensed positions and rates, $\hat{X}_c, \hat{Y}_c, \hat{\dot{X}}_c, \hat{\dot{Y}}_c$, and the output of the force/torque sensor, F and T, to perform collision avoidance, joint position and rate limiting, and arm tip reaction force and moment limiting.

## Inverse Kinematics

As previously stated, the inverse kinematics routine generates a set of six arm joint positions to produce a desired tip position and orientation. Since this is real time software, it was very desirable to find a closed form solution and avoid any numerical solution techniques. Care must also be taken to generate a set of equations with a unique solution in order to eliminate 180 degree joint rotations for small changes in the commanded tip position and orientation.

Using the Denavit-Hartenberg notation, seven coordinate frames were located from the base of the arm to the point on the tip to be controlled (ref. 2). This notation places the degree of freedom between the i'th and the i'th+1 coordinate frames along the z axis of the i'th frame. The position vector of the origin of the i'th+1 frame with respect to the i'th frame is along a coordinate axis of the i'th frame. The transformation matrix between the i'th and i'th+1 frames was easily derived for the seven frames. The product of these six matrices is then equal to the transformation matrix of the position model.

The vector from the base of the arm to the tip of the end effector is written as the sum of the vectors between the seven coordinate frames. This vector, when expressed in frame 1 coordinates, is equal to the commanded tip position, Xa, Ya, and Zpm of Figure 3.

The transformation matrix between the frame at the base of the arm and the frame at the tip of the arm, as well as the position vector locating the arm tip with respect to the base of the arm, have now been described as a set of equations in terms of joint degrees of freedom. These equations were then manipulated into a set of equations which produced joint positions as a function of the output of the position model and known arm dimensions.

## Joint Controllers

The control algorithm for the DOTS is implemented on the main computer system via several series of digital filters. State variable techniques are used to implement each filter. Each joint (degree-of-freedom) is controlled separately. That is, each joint has its own series of digital filters. Currently, the filters are designed to an uncoupled plant. Each joint is isolated and linearized at nominal operating points prior to designing filters for that joint.

The digital control filters are composed of a first order filter series (first order polynomials over first order polynomials) and a series of second order filters (first

order over second order polynomials). The series are implemented so that the output of the i'th filter is the input to the i'th+1 filter and so on. The filters are serially connected with the last first order filter output being the input to the first second order filter. The input to the filter series (first, first order filter) for the overhead crane are the position commands generated by the inverse kinematic module. The output of these two filter series will be the position command to be sent to the local PID controllers for each crane axes. The other filter series will have position error (commanded minus measured position) as inputs. These filters are designed so that the output will be the desired joint rate in terms of a voltage to be applied to the servo controllers.

The user specifies the coefficients of each filter in the associated series as well as the number of first and second order filters in that series. The gain specified for the series is the product of the individual filter gains in the series and the design gain. This implementation also allows for only first order filters in the design or only second order filters in the design or just a gain to represent the design. With the current designs, the overhead crane axes were limited to a 1 Hertz bandwidth and the arm joints have bandwidths on the order of 3 Hertz.

## Safety

The safety software performs collision avoidance, force/torque limiting, joint position and rate limiting, and reasonableness checks on the integrity the sensor output. A failure in any of these tests will cause the simulation to stop and generate an error message on the test conductor's terminal.

To prevent undesirable collisions between the arm, simulation mock-ups, and the facility walls, floor, and ceiling, safety zones are defined in terms of planes, spheres, and shapes called cylindroids. A cylindroid is a cylinder with hemispherical ends. The facility walls, floor and ceiling are defined by planes. The arm is protected by a set of spheres and cylindroids which envelope it. A sphere is defined by locating its center and specifying a radius. A cylindroid is defined by locating the centers of the hemispheres and specifying a radius. The simulation mock-ups, which are held stationary, are also protected by user defined spheres and cylindroids. The collision avoidance problem then reduces to finding the minimum distance between the center of sphere and a plane, the centers of two spheres, the center of a sphere and the axis of a cylindroid, the axis of a cylindroid and a plane, and the axes of two cylindroids. These distances are then compared to the radii of the spheres or cylindroids to determine if the zones overlap. The locations of the spheres and cylindroids protecting the arm must be calculated in real time using encoder feedback and geometrical relationships which describe key points on the arm. Obviously, the zones must be large enough to allow for the system time delay and joint braking distances. The collision avoidance routine works on commanded positions to minimize the size of the zones. In order to allow contact necessary for docking studies, user defined zones may be turned off with respect to the sphere protecting the payload of the arm.

Force/torque and joint position/rate limiting is easily accomplished using appropriate sensor feedback. The integrity of the encoders and tachometers is tested in the following way. The encoder readings for consecutive cycles are numerically differentiated to produce an average joint rate. The tachometer readings of motor shaft rates, also for consecutive cycles, are averaged and transformed to joint rates.

If the difference of the calculations is larger than a specified band, the simulation is stopped.

There is also a limit on the magnitude of the error between commanded and sensed joint positions.

## VALIDATION EFFORTS

A series of test are in progress to validate the facility. These tests begin with the check out of the communications software between the main computer system, the programmable serial communications device, sensors, and remote operator's console.

The motor and servo drives and controllers will be tuned to generate desirable responses. Rate step responses for each joint will be obtained to measure the motor and tachometer voltage constants, sensor parameters, joint friction, and mass properties.

The information obtained in the hardware characterization tests will be used in a numerical computer simulation of the facility. The simulation will be exercised to predict open loop responses and tune up the digital control filters.

Closed loop position step responses will be measured and compared to similar numerical simulation results to verify the joint controllers. At the same time the safety code will be exercised.
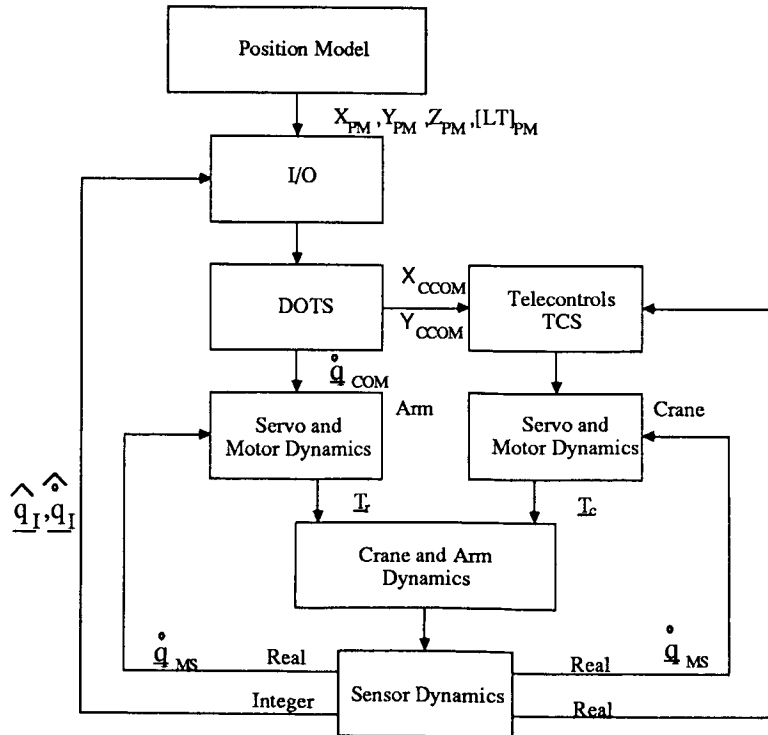


Figure 4  RF$^3$ Simulation

Upon successful completion of the joint controller and safety tests, simple springs will be used as docking mechanisms to validate the position model in end to end tests.

The numerical simulation of the facility is shown in Figure 4. It consists of the real time position model and DOTS controller software coupled with mathematical models of the manipulator, sensors, and actuators. The local PID controllers for the overhead crane are modeled as digital PID controllers (ref. 3) and generate voltage outputs for the servo drives. The commanded arm joint rates, $\dot{q}_{com}$, are converted to voltages and processed through a model of a 12 bit D/A for the servo systems. The motors are modeled as typical DC armature controlled motors neglecting second order effects (hysteresis) (ref. 4). Using voltage outputs from the servos, the motor models generate torques, $T_r$ and $T_c$, which are used by the dynamic model of the manipulator. The equations describing the manipulator were derived from a Lagrangian formulation assuming a connection of rigid bodies. These equations are not limited by small angle approximations. The manipulator dynamics module produces a set of joint positions and motor shafts rates for input to the sensor dynamics module. The sensor dynamics module generates output based on models of the encoders and tachometers with the 12 bit A/D quantization effects. The integer values of the joint positions and motor shaft rates are then converted to real numbers in the input/output routine preceding the DOTS controller.

Currently, this simulation is being updated to include a contact dynamics model of the docking mechanism and quantization effects of the force/torque sensor.

## CONCLUSIONS

The Flight Robotics Laboratory is currently undergoing validation testing. It will provide real time, man-in-the-loop simulation capability for the study of human/system interactions. The facility can be used for contact dynamics studies, remotely piloted vehicle tests, lighting and camera placement evaluations, and simulation of space station construction tasks.

Future test programs include the verification of an automatic rendezvous and docking system and capture systems for tumbling satellites.

Late next year, the air bearing floor will be expanded. The motion base will be integrated for use with the manipulator and VAX 11/750 computer system.

## REFERENCES

1. Kaplan, Marshall, Modern Spacecraft Dynamics and Control, John Wiley and Sons, New York, New York, 1976

2. Asada, Haruhiko; Slotine, Jean-Jaques, Robot Analysis and Control, Wiley-Interscience, New York, New York, 1986

3. Kuo, Benjamin, Digital Control Systems, Holt, Rhinehart, and Winston, New York, New York, 1980

4. Dorf, Richard, Modern Control Systems, Addison-Wesley, Reading, Massachusetts, 1981

# SPACE STATION DOCKING MECHANISM DYNAMIC TESTING

Thomas G. Howsman* and John R. Glaese**
Control Dynamics Company

## Abstract

A prototype docking mechanism for the Space Station has been designed and fabricated for NASA. This docking mechanism is actively controlled and uses a set of electromechanical actuators for alignment and load attentuation. Although the mechanism has been extensively modeled analytically, a series of dynamic tests will be performed for validation. These dynamic tests will be performed at the NASA Marshall Space Flight Center's 6-DOF Motion Simulator. The proposed tests call for basic functionality verification as well as complete hardware-in-the-loop docking dynamics simulations.

## Introduction

Over the past 25 years, the American space program has used only two basic classes of docking mechanism. Namely, the "probe-drogue" type, and the "clear pass-through" type. The probe-drogue concept was utilized on the Gemini, Apollo and Skylab projects. The pass-through concept was successfully used on the Apollo-Soyuz Test Project (ASTP) and is the type of docking mechanism being considered for Orbiter to Space Station docking.

The Space Station docking mechanism, shown in Figure 1, is the first fully actively controlled docking mechanism to be used by the United States. The active mechanism uses a set of eight electromechanical actuators to perform such tasks as capture, load attenuation, and alignment/retraction. In the typical docking scenario, two sets of latches are used. A set of "quick-acting capture latches" are used to quickly secure the two halves of the mechanism together after the initial contact. After all relative motion between the Orbiter and the Space Station has been dissipated, a set of 16 "structural latches" mechanically lock the two mechanism halves together.

The size of the docking port, as well as the performance capabilities of the mechanism have been modified over the past two or three years. The prototype geometry used by McDonnell Douglas, who designed the system for NASA, is shown in Figure 2. This geometry reflects the requirements of the docking mechanism as of 1985.

-----------------------------------

\* Staff Engineer, Member AIAA
\** Senior Staff Engineer, Member AIAA

Analytical contact dynamics models of the docking mechanism were incorporated into several multibody simulations so that the effectiveness of various control schemes could be measured. A "good" docking mechanism can be defined as one which has a large capture envelope, minimizes the contact and attenuation loads, and can complete the docking sequence time initial contact to structural latch quickly. The analytical contact dynamics tools developed for the docking mechanism were essentially the only means of judging the performance of various controllers proposed for the mechanism.

As a means of validating the docking mechanism, a set of dynamic tests will be performed on the prototype mechanism. These tests will take place at NASA's Marshall Space Flight Center's 6-DOF Motion Simulator. It is expected that these tests will verify much of the analytical work previously mentioned, and at a minimum the tests should provide insights to certain modeling deficiencies which are unobtainable elsewhere.


## Analytical Studies

Before evaluation of various candidate controllers of the docking mechanism could begin, two basic tasks had to be completed. The first was the establishment of a capture envelope, i.e. misalignments, inside of which the mechanism must successfully dock. The second task was the analytical formulation of the forces and moments generated by contact of the two mechanism halves, i.e. a contact dynamics model.

The capture boundaries shown in Table 1 have been generated primarily by man-in-the-loop proximity operation simulations located at JSC. (Ref. 1) The values listed in Table 1 essentially reflect the accuracy to which the pilot can control the Orbiter during a rendezvous with the Space Station.

Before developing the contact model for the docking mechanism, a review of previous work was made. Bodley applied Hamilton's principle to the probe-drogue contact problem. (Ref. 2) However, the significantly more complex geometry of the current docking mechanism (as compared to probe-drogue) make the use of Hamilton's principle rather unattractive. TRW developed a general contact model around 1970 (Ref. 3) which attacked the problem by modeling the geometry of one body as a set of nodes which may contact a surface on another body. Since either half of the "pass-through" docking mechanism has a great deal of surface area which may contact the other half, a very large number of points would be required for a high fidelity contact model. Thus, it was decided to formulate a contact model specifically for the mechanism under consideration, rather than modify a previous model.

The basic approach to formulating the contact model was to consider each type contact that could occur with the mechanism separately. (Ref. 4) The three basic types of contact that can occur with the "pass-through" type docking mechanism are: 1. docking ring to docking ring, 2. docking ring to guide, and 3. guide to guide. Instead of using a set of Lagrange multipliers to enforce geometric constraints, a "soft-constraint" (Ref. 5) method was employed. The soft-constraint method, which is analogous to penalty methods used in finite element analyses, places a reacting force at the point of contact whose magnitude is proportional to the penetration distance.

This is similar to the action of the Lagrange multipliers; however, with the soft-constraint method there are no Lagrange multipliers to be calculated.

Once the contact model was formulated, coded, and checked-out it was placed in a multibody simulation for use in parametric studies of control law parameters. A detailed discussion of the control law development is beyond the scope of this paper, however, the results of the study are germane. It was found that if the 8 electromechanical actuators were controlled in such a way that they effectively represented a 10 lb/ft axial spring, capture is assured if the minimum closing velocity is kept above 0.05 ft/sec and the misalignment is within the envelope specified in Table 1. A small amount of viscous damping (rate compensation) was given to each individual actuator through its own analog control loop to enhance the capture performance, e.g reduce the amount of "chattering" the mechanism undergoes during the capture phase.

## Dynamic Test Strategy

While the analysis of the docking mechanism has been indispensable as an aid to the design of the mechanism and its controllers, only a dynamic test can verify the functionality of the system. Of course, if the test results agree with the analytical predictions then the models can be used with confidence as predictive tools in other studies. A series of five tests are planned for the mechanism at MSFC. The first four tests are basically the system checkout tests, while the final test actually puts the mechanism through a number of complete docking sequences.

The first test to be run at MSFC is a latch test. The purpose of this test is to insure the quick-acting capture latches are functional. The second test is a control system function test wherein the docking ring on the active mechanism half is commanded to various positions from the control computer. The third test to be performed is the capture mode response test. For this test, the active mechanism will be placed into the capture mode from the control computer. The effective spring provided by the 8 electromechanical actuation should be 10 lb/ft in this model. The value will be verified. Test four is a mate and latch test, the purpose of which is to verify that the mechanism is stable after the capture latches have been thrown. If a stability problem is detected a frequency response test will be performed to identify the problem.

The final test is actually a series of full contact dynamic tests using the MSFC 6-DOF motion simulator. A total of 64 cases will be run, each of which have different misalignments between the mechanism halves at contact. The 64 cases have been selected such that they explore the envelope represented by Table 1. The 6-DOF simulator has the capacity of representing the dynamics of the orbiting bodies in near proximity. This capability will be discussed in detail in the next section.

## Test Facility Description

The dynamic testing to be performed with the prototype Space Station docking mechanism will be performed at the Marshall Space Flight Center's 6-DOF Motion Simulation Facility. The basic layout of this facility is illustrated in Figure 3. The active half of the docking mechanism will be mounted to the 6-DOF table, and the rigid half will be attached to the force/torque sensor which is mounted to the ceiling.

The 6-DOF facility basically works in the following way. The software residing in the VAX contains a dynamic representation of the orbiting vehicles. The software is aware of the contact forces acting on the two vehicles at all times, and is therefore able to compute what the relative position and orientation of the vehicles should be. This relative position data is converted to actuator lengths and sent to the 6-DOF table which attains the correct position by moving the 6 hydraulic actuators in concert. The forces and moments generated by contact between the two bodies are measured by the force/torque sensor from which the rigid half of the docking mechanism is suspended. The output of the force/torque sensor is continuously fed into the VAX, thus closing the loop between interacting contact forces and relative motion between the two vehicles.

The 6-DOF software requires the mass properties of the two vehicles, which will be those of the Space Station and the Orbiter for the tests being discussed. The initial conditions that the 6-DOF requires will be generated for each of the 64 dynamic test cases discussed in the previous section.

The analog signals generated by the 6-DOF system, such as force/torque sensor output and actuator lengths, can be made available to a bank of strip-chart recorders. All data processed by the VAX, e.g. relative positions and orientations, can be output to a standard plotting package for review after a test is complete.


Conclusion

A "pass-through" type of docking mechanism has been designed for use during Orbiter to Space Station docking operations. The half of the mechanism that is carried on the Shuttle is actively controlled, using a set of 8 electromechanical actuators to provide the necessary alignment and load attenuation capabilities.

Although the mechanism has been the subject of a great deal of analytical modeling, a dynamic test of the mechanism is needed to verify its capabilities. These dynamic tests will be performed at the MSFC's 6-DOF Motion Simulation Facility. This real-time simulation facility has the capability of simulating the dynamics of a pair of orbiting vehicles which are undergoing contact

# References

1. Buchanan, D. B. : "Berthing Mechanism Characteristics and Requirements," NASA Contract NAS8-36417 IDRL1, July 15, 1985.

2. C. Bodley, W. Holland, and G. Morosow: "A Method for Digital Computation of Spacecraft Response in the Docking Maneuver." Proceedings, ASME/AIAA 10th Structures, Structural Dynamics and Materials Conference, New Orleans, Louisiana, April 1969. p 66.

3. Flanders, H. : Documentation for Program Contac, TRW Houston, Oct. 1970.

4. Glaese, J. R.; Howsman, T. G. : "Space Station Docking Study, Final Report," McDonnell Douglas Subcontract No. 85726039, Jan. 1986.

5. Glaese J. R. : "The Mathematical Model Development for the MSFC Skylab Man-In-The-Loop Docking Simulator," NASA TMX-78312, Nov. 1973.

## TABLE 1



DOCKING CONTACT ALIGNMENT EXTREMES

| | | |
|---|---|---|
| Closing Velocity, m/s (f/s) | 0.06 | (0.20) |
| Lateral Velocity, m/s (f/s) | +/- 0.02 | (0.06) |
| Angular Velocity, deg/s | | |
| -- Roll | +/- 0.05 | |
| -- Lateral | +/- 0.15 | |
| Lateral Misalignment, m (in) | +/- 0.11 | (4.5) |
| Angular Misalignment, deg | | |
| -- Roll | +/- 3.0 | |
| -- Lateral | +/- 4.5 | |
| Relative CG Velocity, m/s (f/s) | | |
| -- Closing | 0.06 | (0.21) |
| -- Lateral | +/- 0.02 | (0.07) |
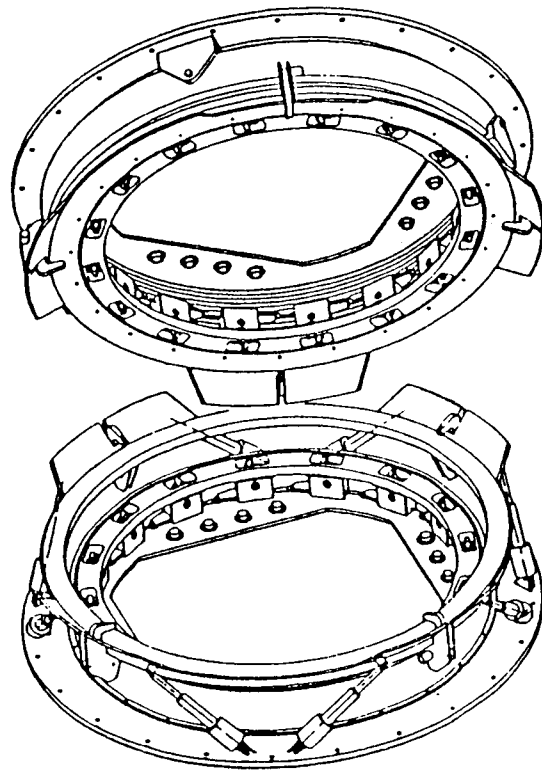
RIGID HALF MECHANISM
ATTACHED TO SPACE STATION

ACTIVE HALF MECHANISM
ATTACHED TO ORBITER

FIGURE 1. Proposed Space Station Docking Mechanism.



5.50 in

R40.00 in

22.50°

45.00°
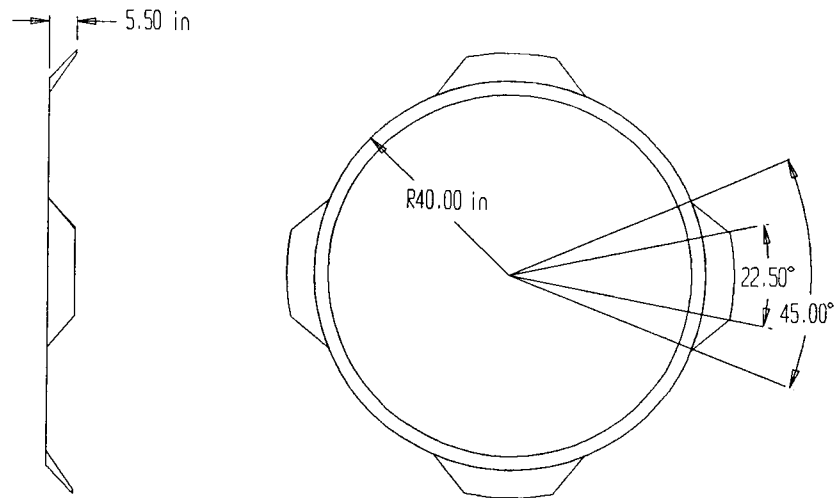
FIGURE 2. Geometry of Docking Mechanism.
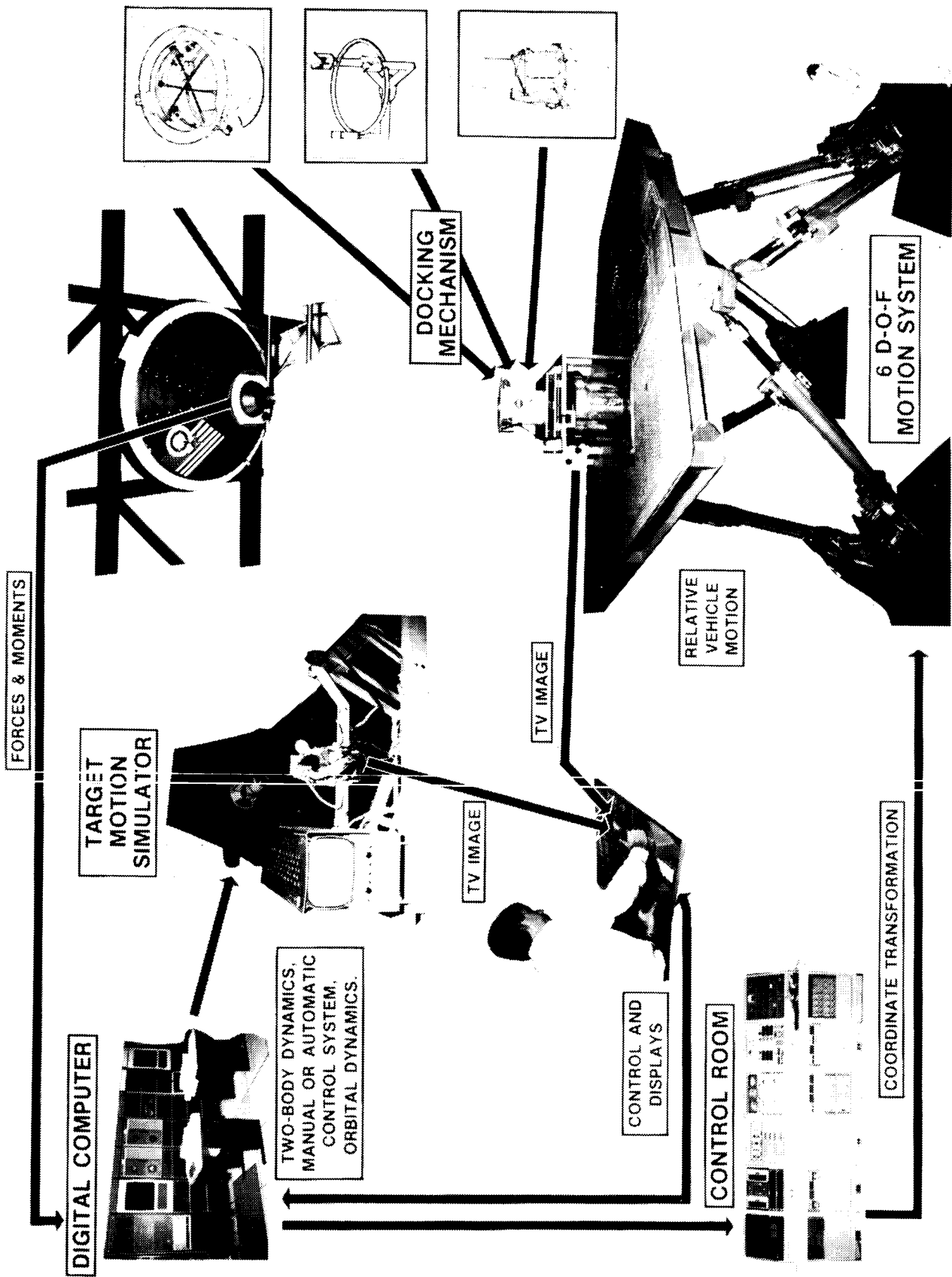
Figure 3. MSFC 6-DOF Motion Simulation Facility

Session V

# SPACE SIMULATION I

# SPACE SIMULATORS FOR LASER OPTICS

Frank H. Gardner
Tenney Engineering, Inc.

I am going to describe different approaches that are being utilized in the testing of laser optical systems. One of the most crucial areas in the testing phase is the stability of the laser optics that is mounted inside the space simulator.

In each case the individual user has his own ideas as to how to approach setting up the space simulating facility and how it should be utilized.

In all of the cases we are going to discuss, you will notice that the customers all utilize different high vacuum pumping systems and different temperature simulation thermal systems, as well as different ways that they mount the laser optical system to provide what they feel is the best possible stability.

## FIRST SLIDE

This shows a comparatively large space simulation facility that is 6' in diameter x 6' deep. The reason for the large size of this facility is the fact that this particular customer is mounting a Newport table inside the space simulator with the legs going through the bottom of the chamber via special vibration isolation connections.

The vacuum system for this chamber utilizes a turbomolecular pump with a valved system, as well as roughing pump of the mechanical type with a molecular sieve absorber and a main foreline valve. This enables the customer to obtain high vacuums in the $10^{-7}$ torr range, and as a safety when they do their actual testing, they shut the pump off and close the valve to the roughing pump and the turbomolecular pump. This eliminates any possible vibration transmition to the chamber. All vacuum piping contains vibration isolation bellows as a safety.

The chamber is furnished with a multitude of windows all around the chamber for easy viewing by the customer, and all of the windows are provided with special covers. An inside shroud is designed for operation with a flooded nitrogen system, providing only the extreme low temperature that can be obtained utilizing liquid nitrogen.

From the customer's liquid nitrogen storage tank a nitrogen pump provides the liquid to the shroud connection, which has liquid nitrogen control valves tied into a liquid nitrogen temperature controller. It is a once-through system discharging, through insulated piping, out of building.

This is an extremely costly system, not only because of the large chamber required to hold the Newport table, but also because of the high cost of the special

179

bellows assembly need for the penetration of the Newport table leg assembly. The large chamber requires a bigger pumping system and a large cryogenic shroud assembly, adding to the cost. The advantage is the laser system is mounted directly to the Newport table, providing for direct vibration isolation.

SECOND SLIDE

This shows a smaller thermal vacuum system, again with windows and covers, but with a mounting fixture such that the chamber and its mounting fixture sit directly on a Newport table. Thus the isolation is provided not only for the test item, but for the chamber itself. The chamber in this case only has to be sized for the laser test item.

The chamber vacuum system in this case is a cryopumping system with a main valve and a mechanical roughing pump with its valve. Again, as in the previous condition, when the customer is ready to do his testing, the pumps are shut down and the valves are closed. For the 10 to 15 minute testing required, this short time period without the vacuum system operating has almost no effect on the vacuum level.

A shroud is provided inside the chamber that is both cooled and heated with a mechanical refrigeration system. This refrigeration system is of the cascade type, cooling a secondary brine which also has a heater in the circuit for the heating of the brine. A special brine circulating pump is provided in a closed loop condition for circulation of the conditioned brine through the shroud. This provides the chamber with a thermal conditioning system giving a temperature range of from -73°C to +125°C. The refrigeration system is also provided with valves in the line, so that it too may be shut down during actual testing to help eliminate any external vibration.

The chamber and the Newport table with the control panel are all mounted inside a clean room facility, whereas all of the machinery, the roughing pump, and the cryopump compressor are mounted on an external framework outside the clean room facility.

With a brine thermal system, temperature control of ±.5°C is able to be maintained. A temperature microprocessor programmer, with built-in control functions and logic for operation of the refrigeration/brine thermal system, enables accurate stabilization control on the shroud, as well as very accurate ramp rates and cycling all automatically controlled. To further automate the operation, the vacuum system contains a Granville Phillips microprocessor ionization gauge with a digital Convectron gauge, allowing for automatic programming of the vacuum system from roughing to high vacuum, automatic opening and closing of vacuum valves, as well as shut-down of the roughing system when the cryopump is in full operation.

THIRD SLIDE

This shows a small thermal space simulator, again with windows and cover plates, except that this chamber sits directly on the Newport table. It utilizes a cryopump with a main valve, as well as a mechanical forepump with a valve. The

refrigeration system is all mechanical and is actually the same refrigeration system package that was utilized for the chamber shown in Slide 2.

This customer utilizes one or the other of his two chambers, but never both chambers at the same time. This is being done because of two different laser systems that are being tested independently, each of a different configuration, and the space chamber system is required to be shipped with the laser system.

The chamber again is mounted inside the clean room, with all machinery external of the clean room area, and during actual testing, the vacuum system and the thermal system are shut down, and the main valves are closed off to the chamber.

This thermal space simulator also incorporates a thermal microprocessor programmer, as well as a vacuum microprocessor, for complete automation of both thermal ramping and cycling and vacuum automation of operation.


FOURTH SLIDE


This shows a space simulator, again with windows and cover plates, that is mounted on an isolated foundation, not a table. This unit also utilizes a cryopump with a main valve, a mechanical roughing system with a valve, both of which are shut down and provided with quick disconnects that are utilized during the actual testing.

The thermal system is a conditioned recirculated gaseous nitrogen system. It consists of a high pressure blower, electric heaters, and liquid nitrogen injection valves. A hermetic enclosure encapsulates not only the blower and heaters, but also the blower motor, eliminating all seals with their inherent problems. The enclosure and piping are pressurized with gaseous nitrogen and recirculated via the blower. The gaseous nitrogen is cooled via the injection of liquid nitrogen and heated via the electric heaters in the enclosure. This provides a thermal system with a temperature range of -300°F to +300°F (-185°C to +150°C). Since we are recirculating a gas, not a liquid, we must provide large diameter interconnecting piping and shroud tubes, to minimize pressure drop. Control is provided via the injection of liquid nitrogen and the energizing of the electric heaters. Shut-off valves and quick disconnects are provided.

All of the machinery is mounted remote of the chamber in a completely separate area, and this customer not only shuts off the valves to the chamber, but utilizes the quick disconnects to remove the lines to the chamber, so that no vibration can be transmitted from the external equipment to the chamber while tests are being accomplished.

A remote control console contains all instrumentation for the space chamber facility. Microprocessor digital-type instrumentation for both the thermal system and for the vacuum system are provided, as well as recording capabilities for both temperature and vacuum. An umbilical cord connects the instrumentation to the chamber proper.

181

## CONCLUDING REMARKS

Regardless of the size or configuration of the space chamber, the basic shell of the chamber is manufactured of type 304 stainless steel that is heliarc welded, with the inside of the shell polished to a number 4 finish. All of the shrouds are manufactured of deoxidized copper sheet that has tubes welded to the exterior, and designed with the proper circuiting and headering for the heat transfer medium that is to be circulated. The outside of the shroud is then polished, with the inside treated and provided with a black finish having an emissivity of .9 or better. Copper is utilized for the shroud because of its high thermal conductivity and its ease of manufacture.

All completed units are thoroughly pre-tested for vacuum and thermal conditions with the space chamber empty of a test item and without the isolation system.

In all of the above cases the chamber is under a deep vacuum of a minimum of $10^{-6}$ torr or better, and all of the testing is accomplished within a 10 - 15 minute period. In all of the cases the 15-minute period is short enough so that there is no appreciable deterioration of either vacuum or thermal conditions while tests are being accomplished and with all of the machinery shut down or disconnected from the chambers.

Each customer feels very strongly that he has completely isolated any vibration being transmitted to his test item.

All of the above units are currently in operation successfully from the customer's point of view, and the ultimate determination of which type of approach for the design of the facility must be made by the customer, not by the manufacturer.
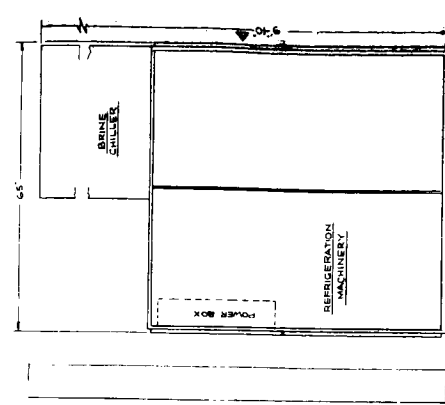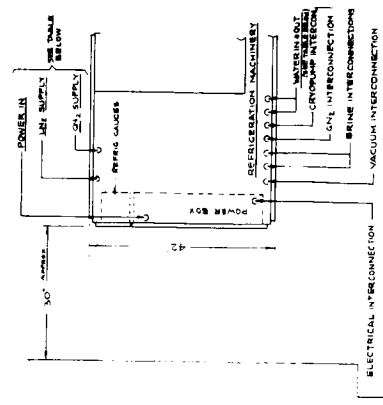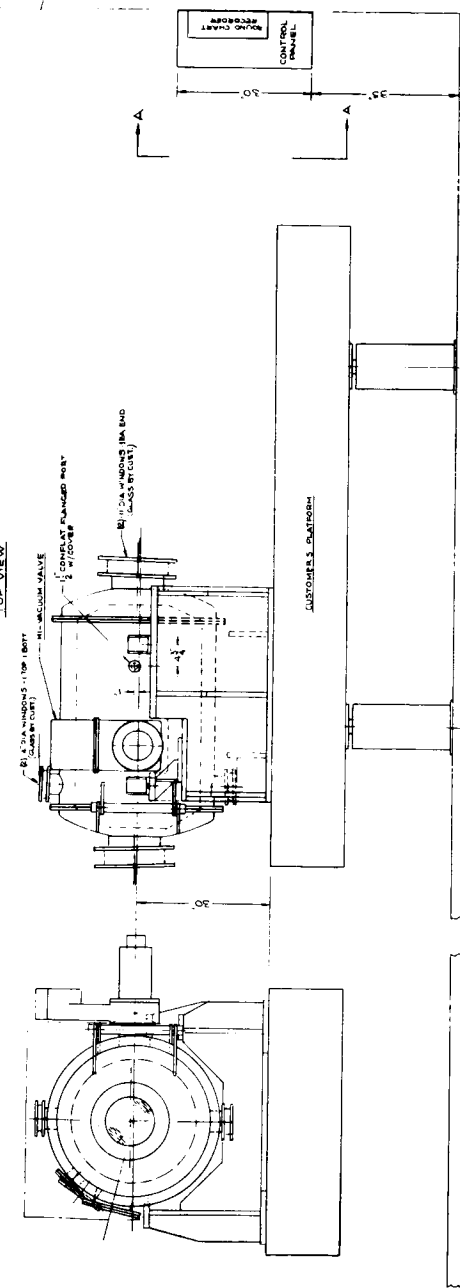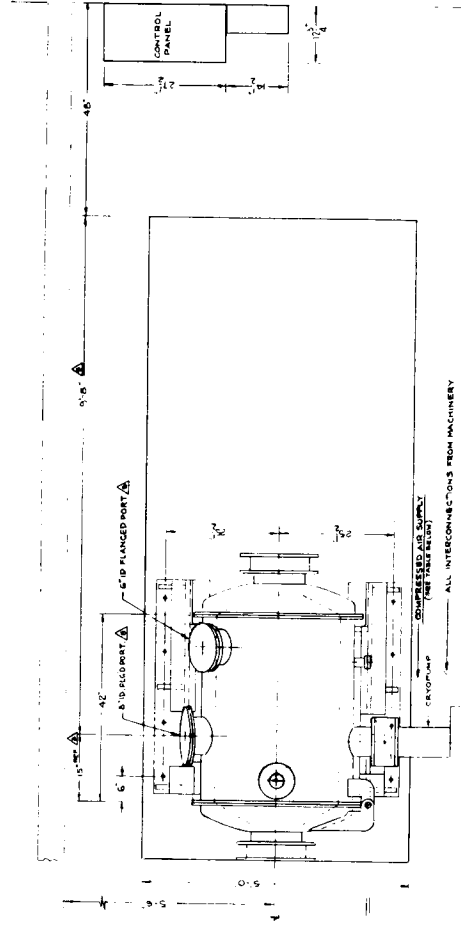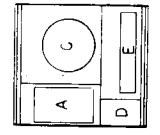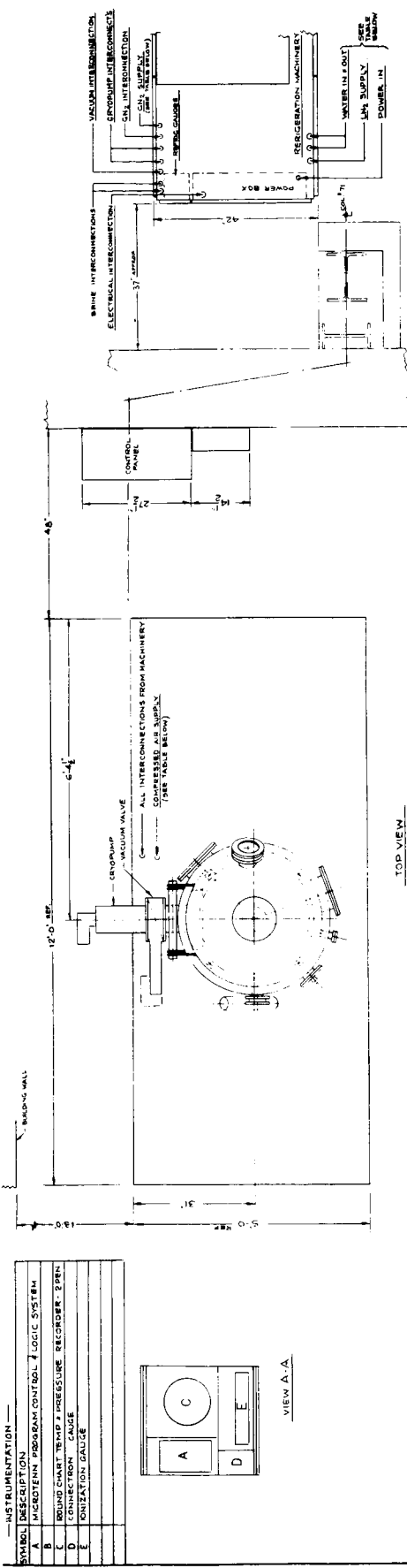
# DEVELOPMENT OF A TWO AXIS MOTION SIMULATION SYSTEM
# FOR THERMAL/VACUUM SATELLITE TESTING

David Henderson, Bert Popovich, Louis DeMore, and Joe Elm
Contraves Goerz Corporation

## ABSTRACT

A two-axis motion simulation system for thermal/vacuum testing of large satellites, in a space simulation chamber, has been developed. Satellites as large as 3000 kilograms with a 4-meter diameter and a 5-meter length can be tested. This motion simulator (MS) incorporates several unique features which result in a less complicated design with improved performance when compared to previous satellite motion simulators. The structure is welded aluminum and, with the exception of the slip ring, completely vented to the simulated space environment. The use of aluminum and large diameter direct drive motors produces structural resonances greater than 7 Hz and allows a passive cooling system to be used. A vented structure, which greatly simplifies the design and manufacturing tasks, is possible because AC servo motors and position transducers are used which have no corona or brush wear problems. The slip ring module is hermetically sealed and maintained at atmospheric pressure to eliminate corona from its exposed rings and brushes. Other components including the thermocouple multiplexing system, bearing lubrication, motors, and transducers are fully compatible with the high vacuum environment. Finally, the control system can produce motion with arc-second precision via local or remote computer interfaces. This cost effective solution fully meets the thermal/vacuum test requirements for axis stiffness and alignment, solar source shadowing, system reliability, position and rate accuracy, outgassing, corona, temperature stability, and data transmission.

## INTRODUCTION

A two-axis motion simulation system has been designed and manufactured by Contraves Goerz Corporation (CGC) for testing satellites in a large thermal/vacuum space simulation chamber. This development has been completed under contract to the Indian Space Research Organization for use at their Satellite Center in Bangalore, India and will be operational in 1989. Figure 1 is an artist's concept of the motion simulator mounted inside the space simulation chamber.

## THERMAL/VACUUM TEST REQUIREMENTS

### Space Simulation Chamber

As shown in Figure 1, the space simulation chamber consists of a vertical cylinder with an intersecting horizontal auxiliary chamber which can achieve vacuum levels for testing of $5 \times 10^{-5}$ millibar. The internal $LN_2$ shroud diameter of the vertical cylindrical chamber, is 8 meters and the MS rotates within this swing diameter. These shrouds, and shrouds mounted on the MS arms, are painted black and cooled to 100 degrees K to maintain a uniform cold space background. Finally, the solar simulation beam enters through the horizontal auxiliary chamber and illuminates the satellite which is being supported by the MS.

### Satellite and Motion Simulator

The satellite, attached to the spin axis shaft, is shown in Figure 1 as a horizontal cylinder 4 meters in diameter and 5 meters in length, with a specified weight of 3000 kg. The satellite geometric center is aligned with the chamber centerline and

the centerline of the solar simulation beam. In addition to the orientation shown, the satellite can also be supported with its cylinder axis perpendicular to the MS spin axis, which requires the swing clearance to be 3.2 meters from the top of the tilt axis. In both orientations the MS is capable of rotating the satellite about the spin and tilt axes to accurately simulate orbital motions with a minimum of interference to the solar simulation. Connectors for more than 1000 instrumentation channels are mounted on the spin axis shaft, providing signal transmission capabilities as summarized in Table 1.
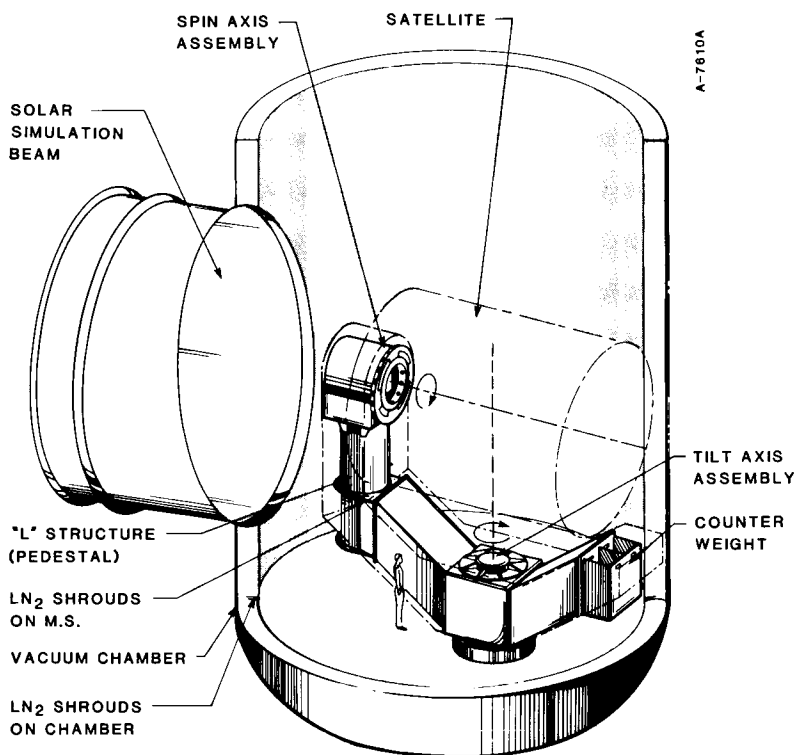


Figure 1. Artist's Concept of Motion Simulator

TABLE 1. SATELLITE SIGNAL TRANSMISSION REQUIREMENTS

Pressurized Slip Ring Assembly

| | |
|---|---|
| DC Lines | 350 |
| Direct Thermocouple Channels | 50 |
| Co-ax Slip Ring Channels (up to 400 Mz) | 15 |
| RF Rotary Joint Channels (Up to 8 GHz) | 2 |

Thermocouple Multiplexing System

| | |
|---|---|
| Number of Channels | 640 |
| Accuracy | ±1 degree C |

## MOTION SIMULATOR DESIGN PHILOSOPHY

To develop this two-axis motion simulator CGC integrated its experience in producing inertial guidance test equipment and range tracking instruments with requirements for thermal/vacuum testing of a large satellite. Typically, inertial guidance test

equipment and range tracking instruments require high stiffness structures, precision bearings, precise axes alignments, direct drive motors, and arc second resolution rotary transducers. In addition, the control system must produce a wide variety of high accuracy motion scenarios, including Earth rates and independent axis operation, through manual or remote computer control. Finally, the payload mechanical and electrical interfaces are critical and must provide stable mounting flanges, clear line of sight, and signal-power transmission via slip rings.

This MS for thermal/vacuum satellite testing requires all of these capabilities and combines them with the need to operate in a space simulation chamber while supporting a satellite the size of a truck. For this project, CGC's previous experience with "off-the-shelf" brushless AC motors, resolvers, and Inductosyns* and their supporting control electronics meshed very well with high vacuum operation. Thus, the general approach was to vent as much of the MS as possible to the high vacuum and avoid the complexities and cost of pressurizing and sealing the MS's internal volume. As a result, the principal design challenges of this project were supporting this large payload, while minimizing the solar source shadowing, and achieving compatibility with, and reliability in the high vacuum and thermal extremes of the space chamber.

## MOTION SIMULATOR DESCRIPTION SUMMARY

The MS assembly is shown in Figure 1 with its major components labeled. The overall simulator weight, less the satellite, is 30,000 pounds and the lowest structural resonance is 7 Hz. The spin axis is supported on top of the "L" shaped MS structure with its rotating axis horizontal and intersecting the chamber center. Attached to the structure, opposite the spin axis, is a counterweight which minimizes the overturning moment that the tilt axis and mounting stand must support. The tilt axis supporting the satellite, spin axis, and "L" structure also intersects the chamber center. Table 2 is a performance specification summary of the tilt and spin axes.

TABLE 2.  PERFORMANCE SPECIFICATION SUMMARY

|  | Spin Axis |  | Tilt Axis |
|---|---|---|---|
| Rotational Limit | Continuous |  | ±180 degrees |
| Position Resolution |  | 0.0001 degrees |  |
| Position Accuracy |  | ±0.003 degrees |  |
| Rate Resolution |  | 0.0001 degrees/second |  |
| Rate Accuracy |  | 0.0005 percent of setpoint |  |
| Rate Drift |  | Essentially Zero |  |
| Maximum Rate | ±10 RPM |  | ±1.0 RPM |

## Spin Axis

A cross-sectional drawing of the spin axis is shown in Figure 2. This axis is capable of continuous rotation up to ±10 RPM by using a 500-line slip ring assembly which transmits electrical signals from the rotating shaft to the stationary housing. The slip ring assembly is maintained in a atmospherically pressurized and sealed module. The dynamic seal is a ferrofluidic unit and the electrical feedthroughs are molded epoxy in stainless steel fittings. With the exception of this slip ring module, the entire MS is completely vented to the space chamber environment. Rotating inside the spin axis shaft is one-half of the thermocouple multiplexing system.

---

*Trademark of Farrand Inc., Valhallen, New York.

The spin axis supports the large cantilevered satellite using an aluminum structure and wire race cross roller bearings lubricated with a fluoroether grease. A direct drive AC servo motor drives the axis, and a separate modular readout package provides rate and position feedback for the servo control and motor drive systems. The readout package contains an Inductosyn*, two resolvers, and a DC tachometer. All of these components, except the tachometer, are brushless non-contacting transducers. During times when the axis must be stationary, a pin and bushing stow lock is provided. Finally passive cooling and active heating are used to maintain safe operating temperatures.

An additional feature of the spin axis is that it can be operated as a stand alone unit. A complete set of in-line connectors is provided at the mounting flange. Thus, this assembly can be mounted on a separate support stand in the chamber to provide single axis test simulations.

## Tilt Axis

A cross sectional drawing of the tilt axis is shown in Figure 3. It has a limited rotational freedom of ±180 degrees and can rotate at a maximum speed of 1.0 RPM. A simple twist cable passes all electrical signals from the rotor to stator and a cushioned stop prevents excessive over travel and damage to the flexible cable. This axis is essentially the same design as the spin axis assembly except the rotors and stators are reversed. That is, the same bearings and grease, motor, readout package, stow lock , and temperature control system are used but the housing rotates and the shaft is stationary. This approach simplified the design process and enhances commonality for training, spares, and maintenance. Figures 4, 5 and 6 show the spin axis and tilt axis assemblies in various stages of manufacture.

## Control Console

The servo control console is located in the system control room. In addition to providing independent control for each axis of the motion simulator, it also contains the safety interlock status chassis, temperature control system chassis, and the receiver chassis for the thermocouple multiplexer (MUX).

Closed loop feedback control is achieved by using the position and rate information from the readout transducers to generate torque commands to the motor drive console. Positions can be commanded with a resolution of 0.0001 degrees and angular rates with a resolution of 0.0001 degrees per second using manual keyboard entries or an RS-232 computer interface. A separate digital display for each axis provides, at the operator's choice, real-time position or rate information. Safety interlocks including engaged stow locks, overtravel, and power amplifier faults are displayed on the interlock chassis. The computers, which control the entire thermal/vacuum test process, can command the MS and determine the status of all safety interlocks.

## Motor Drive System

A motor drive console is located in a separate room away from the sensitive instrumentation, and has its own isolated power supply. This isolation prevents interference from the high-power pulse-width-modulated (PWM) signals, which drive the AC servo motors.

The motor drive console receives torque commands from the servo controller and powers the AC servo motors using a PWM high current, high voltage signal. Position

---

*Trademark of Farrand Inc., Valhallen, New York.
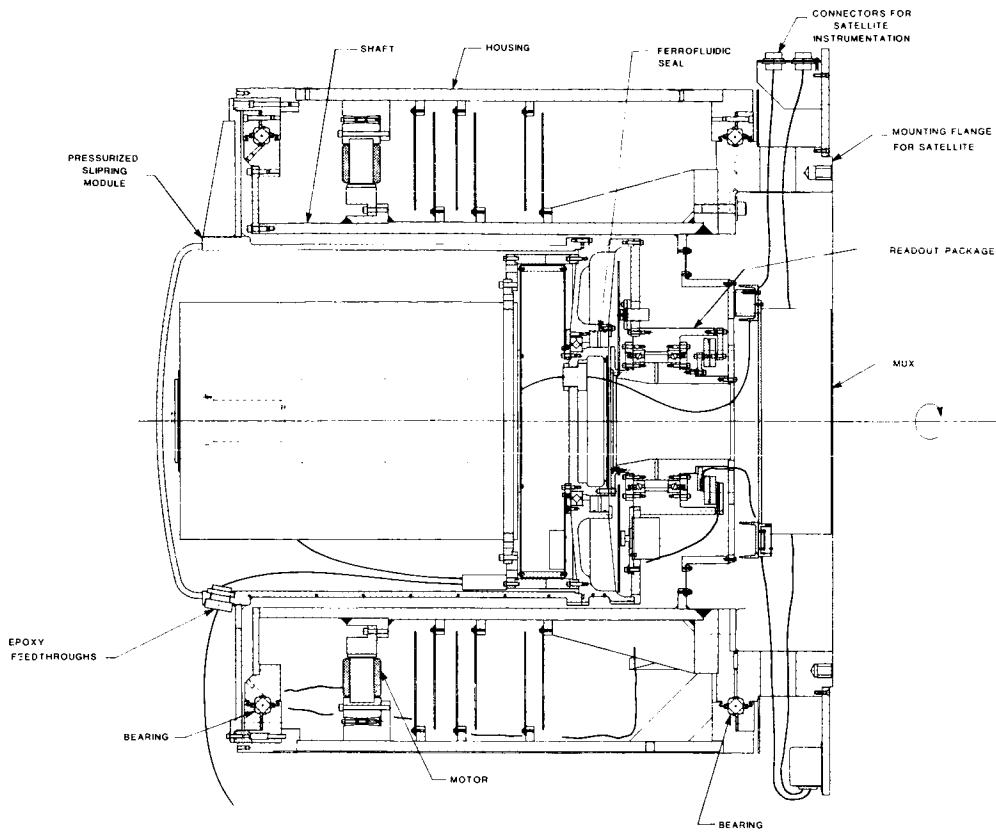
Figure 2. Spin Axis Assembly
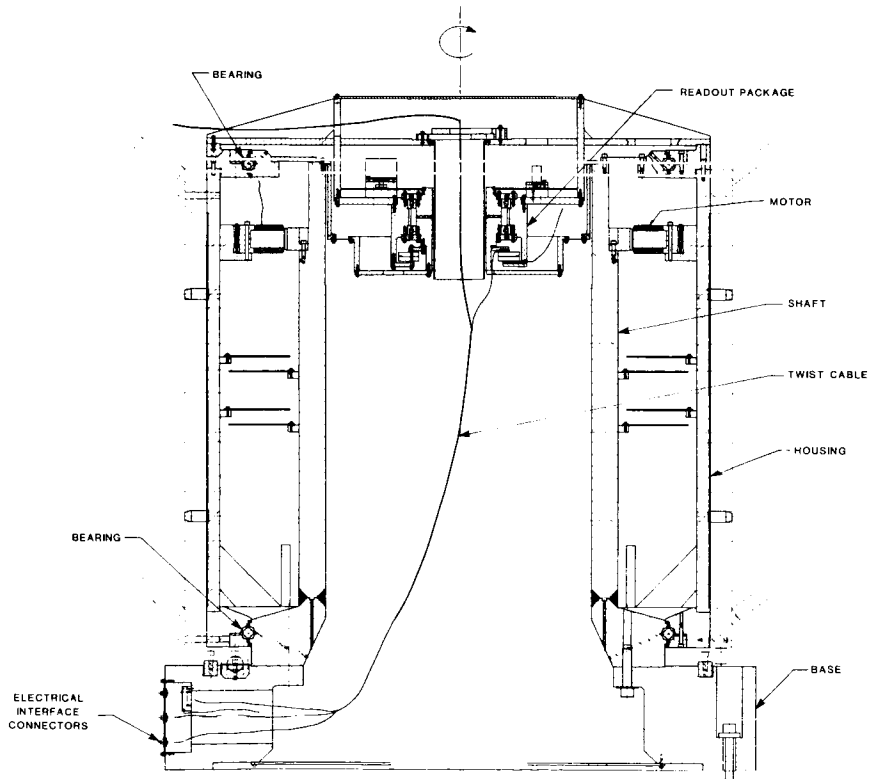


Figure 3. Tilt Axis Assembly
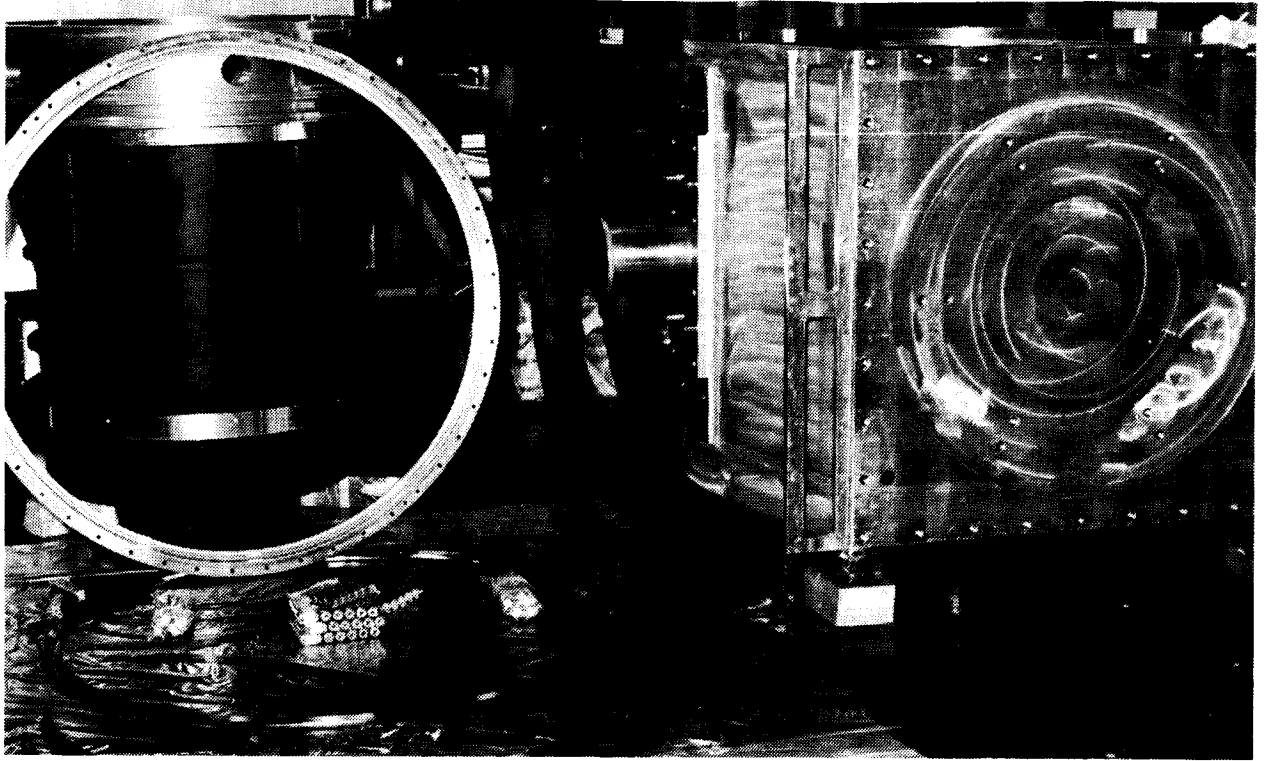
Figure 4. Spin Axis Shaft, Housing, and Bearing Components
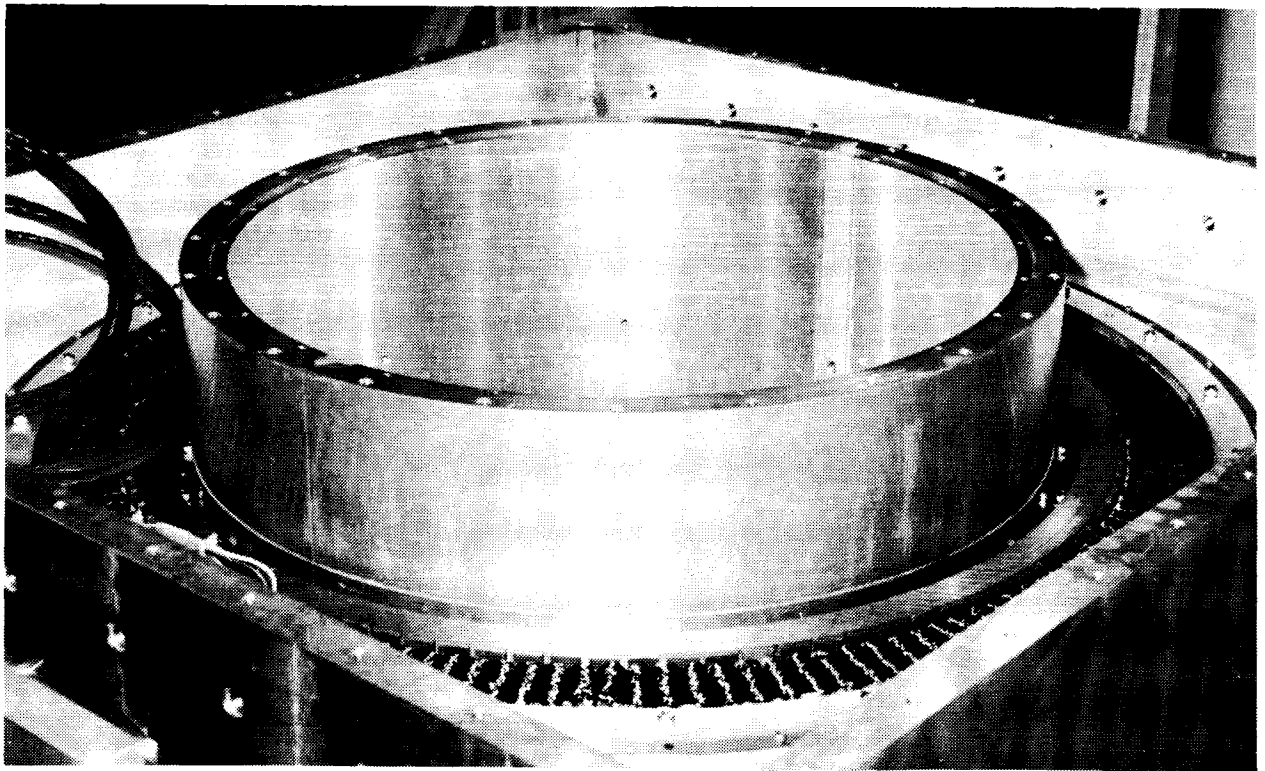


Figure 5. Tilt Axis Assembly with AC Brushless Motor Uncovered
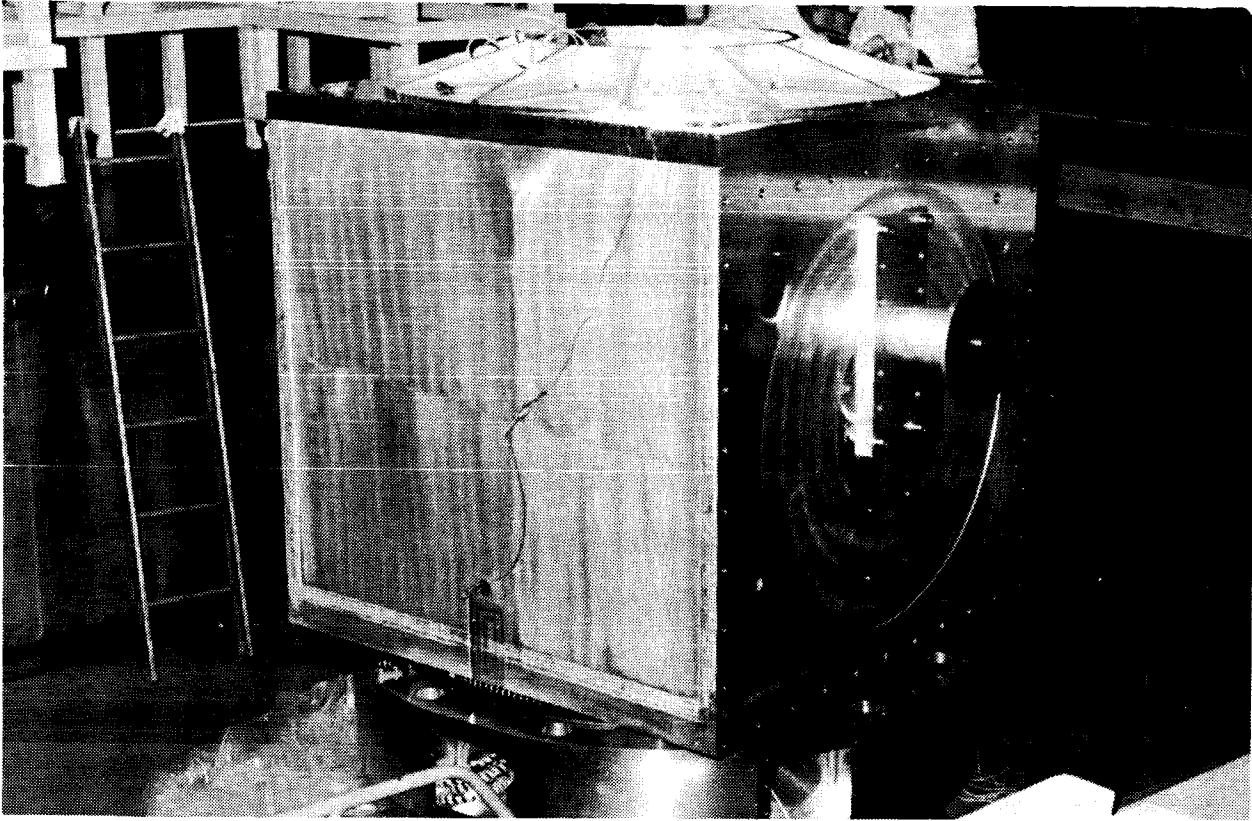
Figure 6. Completed Tilt Axis Assembly

information is received from the resolver on each axis to electronically commutate the motor.

## IMPORTANT DESIGN CONSIDERATIONS

### Structural Stiffness vs. Solar Source Shadowing

An important compromise inherent in developing the motion simulator was the structural stiffness versus the solar source shadowing. A large structure is the most effective way to support the payload, but this interferes with the solar simulation beam. This interference, or shadowing, can be minimized only by reducing the structure's cross-sectional area, which results in lower stiffness.A smaller and more compliant structure has lower resonances, which may be excited by fluid flow in the shrouds or vibrations in the mounting platform. In addition, low simulator structural resonances may couple the satellite structural resonances and make it more difficult to compensate the axes control systems resulting in a low gain/low bandwidth servo loop. Finding an acceptable compromise to this problem is further complicated by the asymmetry of the "L" shaped configuration and the cantilevered satellite mass.

It should be noted that a major contributor to solar source shadowing is the spin axis assembly. However, its diameter is determined by the space requirements for the satellite instrumentation (slip ring, MUX and connectors). Thus, the diameter of the spin axis shaft and housing was fixed prior to completing the FEM analysis.

A compromise solution was developed with ANSYS* 4.2B, a finite element modeling

*Trademark of Swanson Analysis Systems.

193

(FEM) software package. The design goal was a MS with its lowest resonance at 7 Hz and a minimum cross sectional area shadowing the solar beam. As a secondary goal, the overall weight was to be as low as possible.

The final FEM meets these requirements. This half symmetric model is constructed of shell and beam elements (structural walls, fasteners, etc.), spring elements (bearings), and point mass elements (payload and non-structural components). The satellite is modeled at the intersection of axes as a 3000 kg mass and its corresponding inertia. Finally, two important assumptions for this analysis are that the satellite and mounting stand have very high stiffness.

Figure 7 is an ANSYS plot of the lowest predicted mode shape and frequency, and clearly shows the "up and down" vibration of the satellite and its associated 7.44 Hz frequency. To achieve this result several decisions were made. The bearings are a cross roller wire race configuration with a 48-inch pitch diameter. This type of bearing has excellent stiffness using modest preload and low friction. In addition, cross roller bearings are self-preloading which, in conjunction with the split races, makes them less sensitive to temperature changes. Aluminum is the structural material, not stainless steel, because it allows thicker walls to be used while achieving the equivalent mass and sectional stiffness properties. This characteristic allows aluminum to avoid the buckling problems of stainless steel
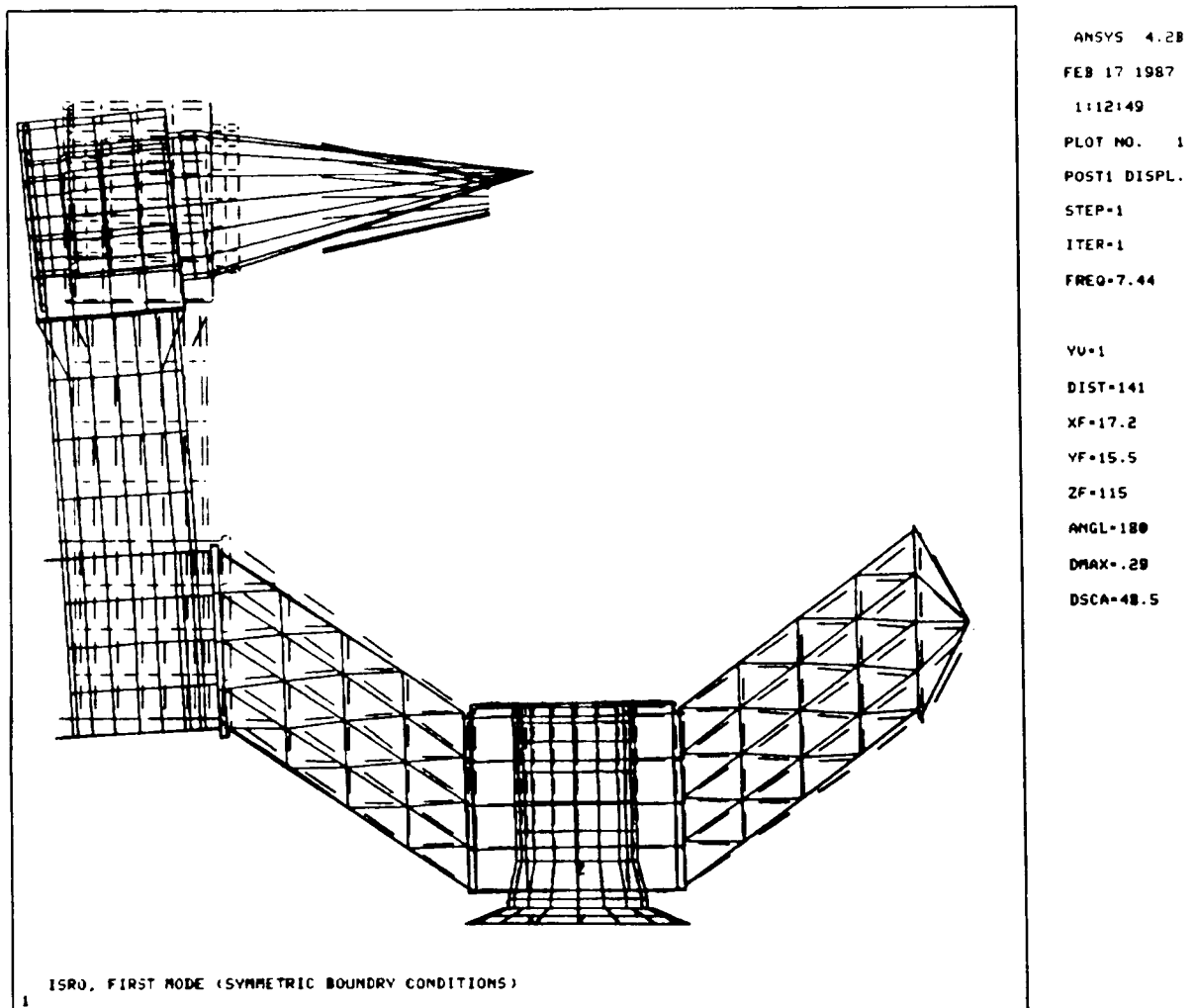


Figure 7. First Made Symmetric Boundary Conditions

with fewer stiffeners. In addition, aluminum's high thermal conduction and capacity fit well with a passive cooling scheme, which is discussed in a later section. The upward sloped arms are configured to minimize the unsupported length of the vertical pedestal while meeting the satellite clearance requirements. Finally, the diameter of the pedestal, which shadows the solar beam, is the minimum size that meets the 7 Hz requirement. Figure 8 shows the pedestal and support arms ready for assembly. Figure 9 shows the support arm assembled on tilt axis.
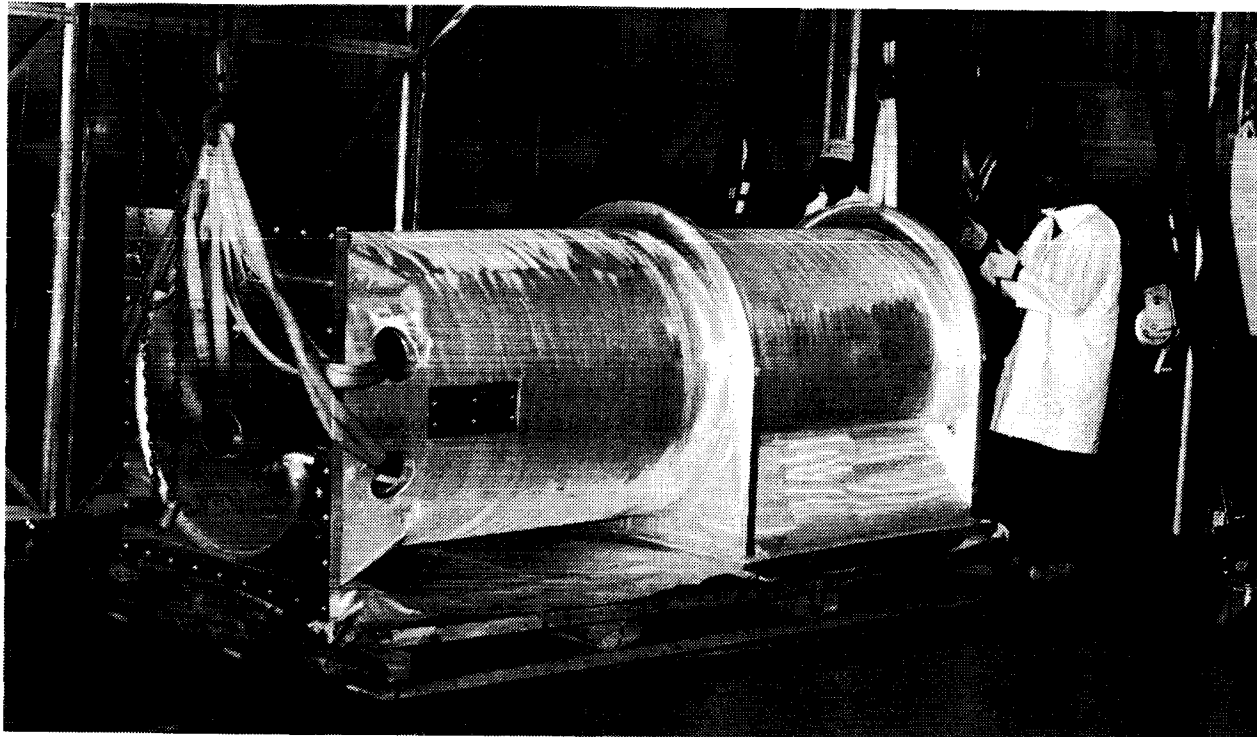


Figure 8. Pedestal Ready for Assembly

## Satellite Data Transmission

The two-axis motion simulator provides for the transmission of all of the satellite signals necessary for thermal/vacuum testing. The specifications for these satellite signals are summarized in Table 3.

TABLE 3. SATELLITE DATA TRANSMISSION SPECIFICATIONS

| Category | Quantity | Specifications |
|---|---|---|
| Single-Shielded Lines | 250 | 100 V at 100 mA |
| Direct Thermocouple Channels | 50 | Copper-Constantan |
| 10 Amp Power Channels | 10 | 100V at 10A |
| 5 Amp Power Channels | 35 | 100V at 5A |
| Co-axial Channels | 15 | DC to 400 MHz |
| RF Rotary Joint Channels | 2 | DC to 8 GHz and 2 to 8 GHz |
| Multiplexed Thermocouple Channels | 640 | Copper-Constantan |

Satellite signals connect to the MS via a set of vacuum-qualified connectors located at the spin axis shaft. Over 50 connectors are mounted radially on the outside of the shaft. The signals are passed through the continuous rotation spin axis via a

pressurized slip ring assembly. Vacuum feedthroughs are used to interface to the pressurized vessel containing the slip ring. An additional set of connectors is provided at the mounting flange of the spin axis enabling the spin axis to be operated as a stand alone assembly. The satellite signals pass through the limited rotation tilt axis by way of a flexible twist cable. Another set of connectors is mounted at the base of the MS. These connectors are identical to the connectors located at the spin axis mounting flange enabling the same external cables to be used whether testing is performed with the two-axis MS or spin axis by itself.
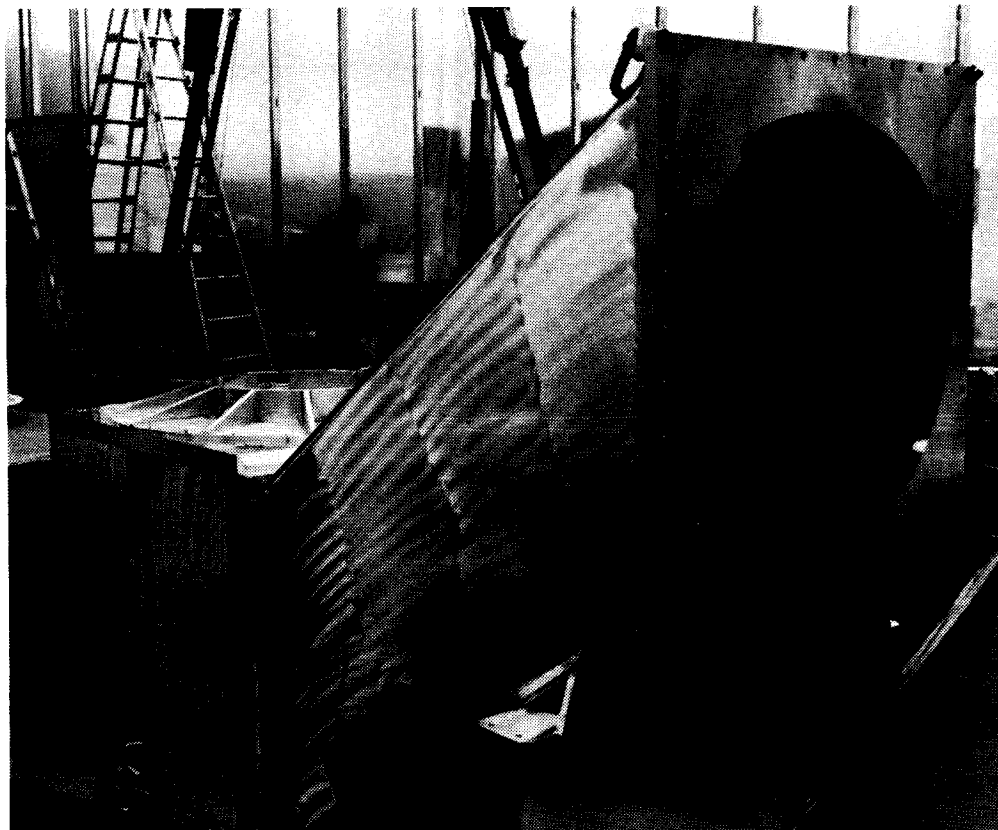


Figure 9. Support Arm Assembled on Tilt Axis

The key components of the satellite data transmission system are the slip ring and thermocouple multiplexer. Both are manufactured to CGC's specifications by outside vendors. This slip ring is shown in Figure 10 and has over 500 lines. This large number of lines requires a dual concentric drum configuration to fit within the spin axis shaft. Silver-teflon* brushes and silver rings are fully compatible with both pressurized and vacuum operation. This feature allows slip ring operation, at low voltages, if the module seal fails. Finally, a two channel high frequency rotary joint is nested inside the slip ring.

The thermocouple multiplexing system (MUX) transmits 640 channels of temperature information using only a few slip ring circuits. The analog thermocouple signals are converted and combined into a digital signal inside the spin axis shaft. This digital information is transmitted, using the slip ring, to a receiver in the console and is available through an RS-232 computer interface. This method eliminates measurement errors introduced by the thermo-electric junctions of the connectors, rings, brushes, and solder joints.

---

*Trademark of Dupont

196
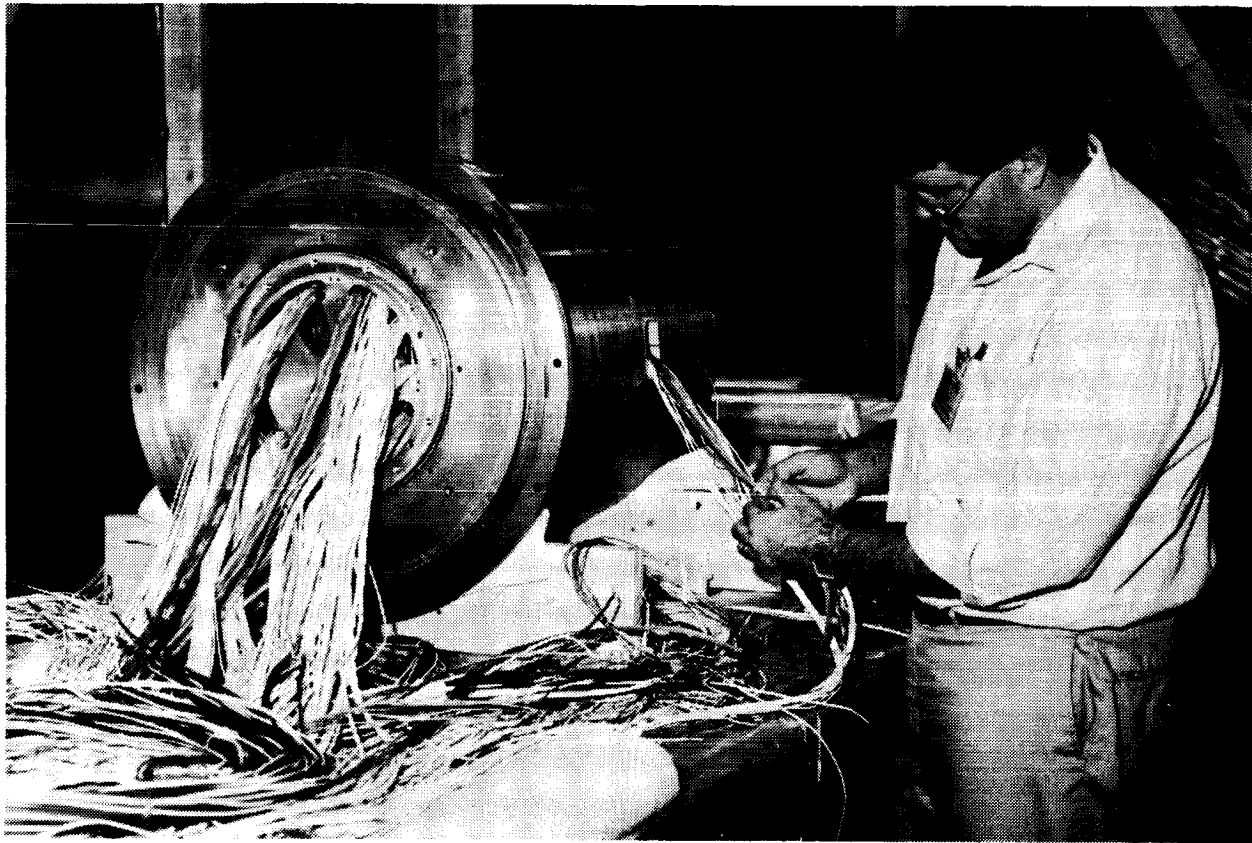
Figure 10.  Picture of Slip Ring Assembly

## Outgassing and Leak Rates

Low outgassing and low leak rates are important requirements for successful thermal/vacuum testing. Excessive amounts of outgassing and leakage will prevent the chamber from reaching its required pressure of $5 \times 10^{-5}$ millibar. In addition, the escaped material contaminates the satellite, optics, and chamber. No quantitative specification is given for total MS outgassing because of the inherent measurement difficulties. To limit outgassing, an alternative contamination control plan, devised in consultation with the vacuum system engineer, is used. Rather than specifying the total outgassing rate, it is controlled by specifying the MS design configuration, materials selected, and the manufacturing processes used. In contrast, the slip ring leak rate can be measured directly and is limited to less than $5 \times 10^{-5}$, millibar liter/second.

Outgassing

These steps are taken to limit outgassing:

● All welds, bolted joints, and interfaces are vented to avoid virtual leaks. This is achieved by proper placement and interruption of weld beads, tapping holes through, and using vented screws.

● Castings are not used to avoid the porosity and corresponding virtual leakage which results when the chamber pressure is cycled.

● Where possible, all surface finishes meet 63 RMS which limits absorption and facilitates cleaning.

197

- The primary structure is MIG welded aluminum. Stainless steel is used for some small components. Carbon steel is not used.

- All organic materials used in the MS are evaluated using SP-R-0022A[3] criteria for thermal vacuum stability (TVS). Generally all materials have less than 1.0% total weight loss (TWL) and 0.1% volatile condensable material (VCM).

- The bearing grease is a prefluorinated polyether compound with molybdenum disulfide which exceeds SP-R-0022A TVS criteria.

- A vacuum backout is used to clean and precondition the motors, resolvers, tachometers, and MUX prior to assembly.

- The MS components are completely cleaned, prior to assembly, using soap, water, and alcohol. Assembly is completed in a controlled access clean area.

## Leakage

The only source of leakage from the MS is the pressurized slip ring assembly. This module is maintained at room ambient pressure, irrespective of the chamber pressure, by a vent line to the atmosphere. The dynamic seal, between the rotating and stationary components, is a permanent magnet ferrofluidic seal which provides extremely low leakage combined with high reliability, and zero maintenance. The electrical feedthroughs are molded epoxy and all static seals are either viton "O" rings or copper gaskets. The final assembly is leak tested to verify hermeticity.

## TEMPERATURE CONTROL

Temperature control is a critical requirement for the MS reliability. The safe operating temperature range is 280 to 310 degrees K. Many variables in thermal/vacuum simulation make this temperature range difficult to maintain. The MS produces heat in its motors and bearings. The solar simulation beam shines on the spin axis and pedestal. Small heat fluxes can also occur, via conduction, at the satellite mounting flange and the base support stand. Finally the $LN_2$ shrouds attached to the chamber walls and mounted to the MS can vary in temperature from 100 degrees K to ambient, causing wide variations in radiant heat transfer.

The traditional solution to this thermal control problem is to place heat exchangers on the MS and pump a thermal exchange fluid through a closed loop at an externally controlled temperature. This method, while effective, has the disadvantage of potential leaks and high operating and maintenance costs.

To avoid these problems, a thermal control system using passive cooling and active reheat was developed. This "semi-passive" system uses conduction links to the $LN_2$ shrouds, mounted on the MS, to remove heat at a constant rate of approximately 1500 watts. Electric heaters, RTDs, and electronic controllers provide four zones of active reheat control.

A semi-passive thermal control system is possible because of several important MS features. A multilayer insulation blanket, wrapped around the MS exterior, isolates it from $LN_2$ shroud's and solar beam's radiative thermal loads. The thick walled aluminum structure effectively distributes the cooling and heating loads to minimize temperature gradients. The large thermal mass of the aluminum also ensures that, even when the shrouds provide no cooling, the maximum temperature rise is only one degree K per day. In addition, the interior surfaces of the shafts and housings are coated with a high emissivity paint to increase the thermal radiation coupling between the

rotating and stationary components. This paint combined with the conduction of the bearings minimizes temperature gradients between the rotors and the stators.

The efficiency of the bearings and motors is a critical factor in the success of a semi-passive thermal control system. The bearings generate heat in direct proportion to their friction and the expected value for each axis is less than 500 ft-lbs. Just as important, however, is the ability of the round wire races to flex in their housings. This characteristic ensures that even under high loads, which may cause eccentricities, the bearing friction remains unchanged. Finally, the high efficiency AC servo motors produce only 90 watts of power at their maximum expected duty cycle. Unlike traditional motors with brushes, the heat load is produced in the stationary windings and is easily dissipated into the large diameter housings.

## Corona Protection

Since the MS is almost entirely vented to the vacuum environment and since operational scenarios were identified that could drive the environment into a regime where corona might occur; the elimination of corona within the MS was a critical design requirement. The slip ring assembly; which contains the highest risks for arc over, is the only electrical element that is completely sealed. All other electrical elements such as motors, axis rate and position sensors, and connectors are designed to operate within the vacuum environment without arc discharge. The final configuration is a robust, simple design without the need for costly, large rotating seals.

Arc-over is most likely to occur at intermediate pressure (typically between 100 torr and $10^{-3}$ torr) where the air can become ionized and then be able to pass a high current. The breakdown voltage is directly proportional to the gas pressure and the distance between the electrodes. "Typical" Paschen curves of this phenomena are shown in Figure 11. The curve is a plot of breakdown voltage versus the product of electrode distance and gas pressure. The "work function" parameter; which is a measure of electrical resistance, demonstrates the dependence of the curve on



Figure 11.

199
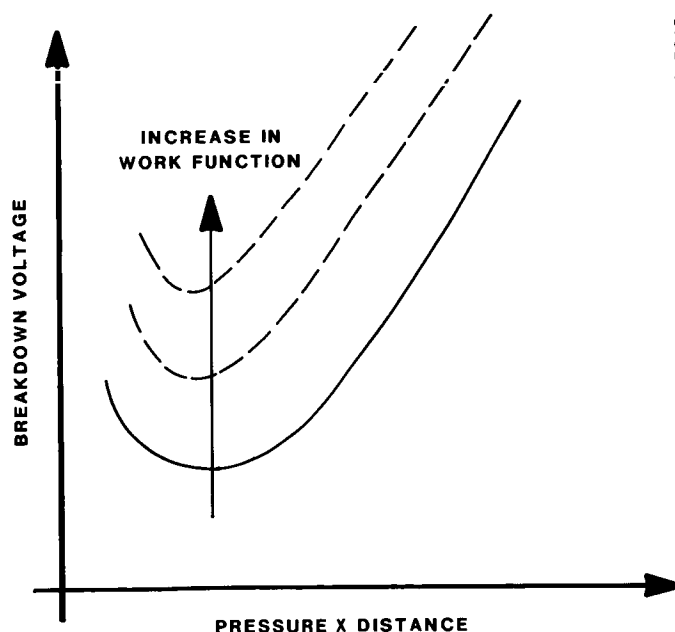
electrode material and the type of gas used in the system. As an example, the minimum breakdown voltage for silver electrodes in pure helium is approximately 200 volts. Various techniques and designs have been employed throughout the design of the motion simulator to reduce the probability of corona onset.

To the extent possible, the operating voltage of all electrical systems has been set below 200 volts. The thermal control system, axes sensors, and data multiplexer operator well below 200 volts. Only the spin and tilt axes motors operate above this voltage; the motors will intermittently reach a voltage of 300 volts (RMS). The motors are AC synchronous (brushless) motors with permanent magnet fields. This motor design eliminates the need for brushes and commutator which are common to DC motors, or motor slip rings that are common to AC motors with separately excited fields. By eliminating brushes, commutators, and motor slip rings, the most likely sources for arc discharge have been eliminated. The remaining elements in the system that have potential for arc-over are the motor wiring, cables, connectors, and terminations. Techniques have been described in the literature (1), (2) that have been used to eliminate corona; the electrical design of the MS follows these techniques, e.g.,

- Cables and connector with large differences of potential are kept segregated.

- All cables and motor external wires are Teflon insulated.

- Grounded shields are used over the insulation of high voltage cables.

- Exposed conductors at the interface of connection receptacles and plugs are eliminated.

- Connections are vented to eliminate trapped gas.

Corona onset is best described as a statistical phenomena. To prevent the occurrence of corona, the most likely conditions for its existence must be eliminated. Every attempt has been made to accomplish that in the design of the MS.


**Precision Motion Control**

The motion control techniques utilized on the MS were originally developed for the inertial guidance test industry. The instrumentation is configured in the CGC Modular Precision Angular Control System (MPACS) and provides a closed-loop, multi-mode servo system for each axis.

Each axis incorporates "direct drive" concepts to maximize motion performance. Each axis is driven by a direct-coupled AC servo motor and incorporates a DC tachometer velocity transducer, resolver position transducer, and direct-coupled Inductosyn position transducer. Through the use of the shaft-mounted Inductosyn and motor, non-linearities and low frequency resonances associated with other drive systems (e.g., gear drives, belt drives, chain drives, hydraulic drives, etc.) are eliminated. This permits the configuration of high gain, high bandwidth servos to provide accurate motion control.

The Inductosyn position transducer (Figure 12) is utilized in the primary modes of position and velocity control. This device is actually a high-accuracy 360-speed resolver used to measure axis position. The stator of the Inductosyn contains two windings which are mechanically arranged so that the inductive coupling between the SIN winding and the rotor varies sinusoidally over one degree of rotor travel. The coupling for the COS winding varies as the cosine over one degree of rotor travel. These two windings are excited by precision current sources within the MPACS .

STATOR (INPUT)

ROTOR (OUTPUT)

$I_p \cos (2\pi ft)$    $I_p \sin (2\pi ft)$

$\sin (360\,\theta)$    $\cos (360\,\theta)$

MAGNETIC
FIELD
COUPLING

$\dfrac{360}{N}$  $V_o = \sin (\omega t + N\theta)$
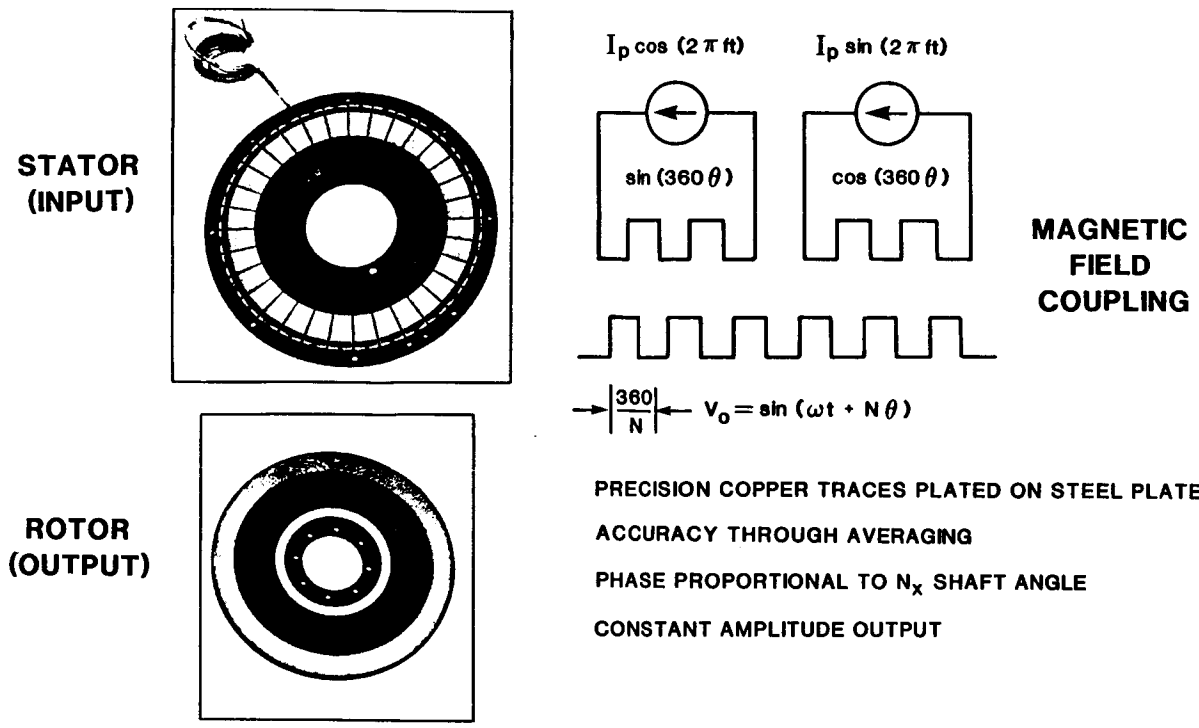
PRECISION COPPER TRACES PLATED ON STEEL PLATES

ACCURACY THROUGH AVERAGING

PHASE PROPORTIONAL TO $N_x$ SHAFT ANGLE

CONSTANT AMPLITUDE OUTPUT

Figure 12.  Inductosyn Position Transducer

The amplitudes and phases of these signals are accurately controlled by amplitude and phase servos within the MPACS. The output of the Inductosyn rotor is a constant amplitude sinusoid of frequency "f", whose phase varies through 360 degrees with respect to the sin reference signal for each mechanical degree of axis motion. The resolver mounted on the axis is utilized in the same manner to provide another phase-modulated feedback signal which varies through 360 degrees of phase for each complete ventilation of the axis.

The MPACS instrumentation system receives the feedback signals from the resolver and Inductosyn and converts them to a digital format for use by the encoding and control systems.

**Control System**

Position Mode (See Figure 13)

The MPACS controls axis motion primarily through the use of a position servo. In the Position control mode, the Inductosyn and resolver feedback signals are utilized to drive the axis to a commanded position input. Analog "low resolution error" (LRE) and "medium resolution error" (MRE) position error signals are generated from the resolver feedback signals. These signals represent the difference between commanded and actual axis positions. An analog "high resolution error" (HRE) signal is generated from the Inductosyn feedback. The Position control mode uses a dual-mode servo control mechanism. A "coarse" position loop responding to the resolver generated MRE signal moves the axis to the vicinity of the terminal position. In this mode, the MRE signal acts as a velocity command to an inner velocity loop using tachometer feedback. A clamping circuit is included to limit this velocity command to a preset value. In this manner, the slew rate between positions may be controlled. When the axis approaches the terminal position, control is transferred from the "coarse" loop to the "fine" position loop utilizing the Inductosyn generated HRE signal. "Bumpless" transfer is accomplished by monitoring the MRE, HRE, and HRE rate.

201

Transfer to the "fine" loop occurs only when:

● the MRE indicates a position error of less than 0.2 degrees.

● the HRE indicates a position error of less than 0.02 degrees

● The rate of change of the HRE is less than 3 deg/sec

Satisfaction of these tests transfers control to the Type III "fine" position servo. The tachometer velocity loop utilized in the "coarse" loop is eliminated in the "fine" loop. This allows increased stiffness and small signal bandwidth. With this type of control, MS positioning accuracies of 10 arc seconds and repeatabilities of 1 arc second are readily achievable.
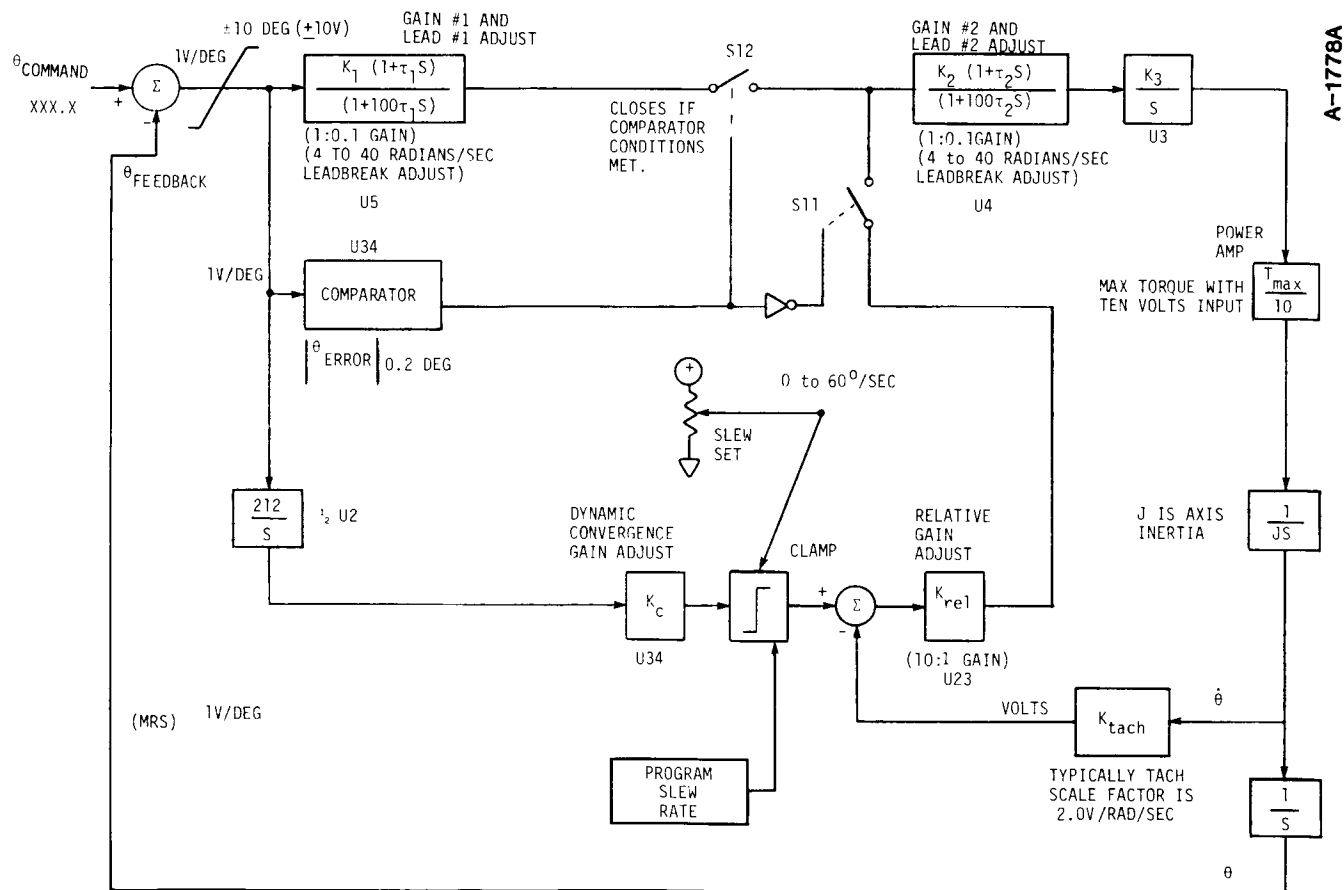


Figure 13. Position Mode Diagram

Precision Rate Mode (See Figure 14)

Axis velocity control is obtained in the Precision Rate mode. This mode is also implemented using the Type III fine position servo detailed in the Position mode description. This implementation provides the generation of highly accurate velocities, and eliminates the "ripple" error inherent in tachometer based velocity loops. In this mode, precision velocities are produced by incrementing the position command at a rate based upon the commanded velocity. The position command is incremented in steps of 0.0001 degrees; hence, an axis velocity of 1 deg/sec requires

202

10,000 increments per second. Since the position loop is a Type III servo, it is capable of responding to this command with no following error.

The direct-coupled nature of the axis components permits the configuration of high gain, high bandwidth servos. This, in turn, provides the ability to reject disturbance torques due to friction, load imbalance, motor cogging, etc. The result is precision rate performance accurate and stable to 0.0005%. Furthermore, the rate generator producing the position increment pulses is crystal controlled. By synchronizing this crystal oscillator with the timing crystal of the satellite data acquisition system, it is possible to obtain satellite parameter measurements which are fully correlated with axis position.

## Encoding System

The digitized, phase-encoded signals from the resolver and the Inductosyn on each axis are utilized by axis encoders within the MPACS to provide real-time axis position readouts. Each encoder contains separate circuits to encode the "coarse" position from the resolver and the "fine" position from the Inductosyn. These outputs are correlated to provide a 7-digit position readout available for visual display or computer interface.

Each encoding circuit is structured as a phase-locked loop. A high-speed digital ring counter is driven by a 0-24 MHz voltage controlled oscillator (VCO). This counter is



Figure 14. Precision Rate Mode

203

used to generate a square wave over a complete counter cycle. This square wave is phase-detected, and compared with the square wave signal derived from the phase-encoded Inductosyn feedback.The resulting error signal is compensated and fed as an input to the VCO. The result is a digital ring counter which cycles synchronously with the Inductosyn feedback. The value in this counter at the zero crossing of the sin reference to the Inductosyn is loaded into a second counter. Hence, this value represents the phase shift between the sin reference and the inductosyn feedback which is linearly related to the axis position. The second counter is also clocked by the VCO output; therefore, it tracks axis motion and provides a digital measurement of axis position.

An equivalent circuit processes the resolver feedback in the same manner. The two digital values are combined to form a 7-digit position measurement.

This system is capable of encoding axis positions accurate to 1 arc second, with a resolution of 0.36 arc seconds (0.0001 deg). The use of a Type II servo in the phase-locked loop permits zero tracking error for static positions and constant velocities.

Motor Drive System (Figure 15)

The MS utilizes AC servo motors for axis actuation. These 3-phase permanent magnet motors are driven in a "vector control" mode by high-power pulse width modulation (PWM) amplifiers. These amplifiers operate by measuring the axis position
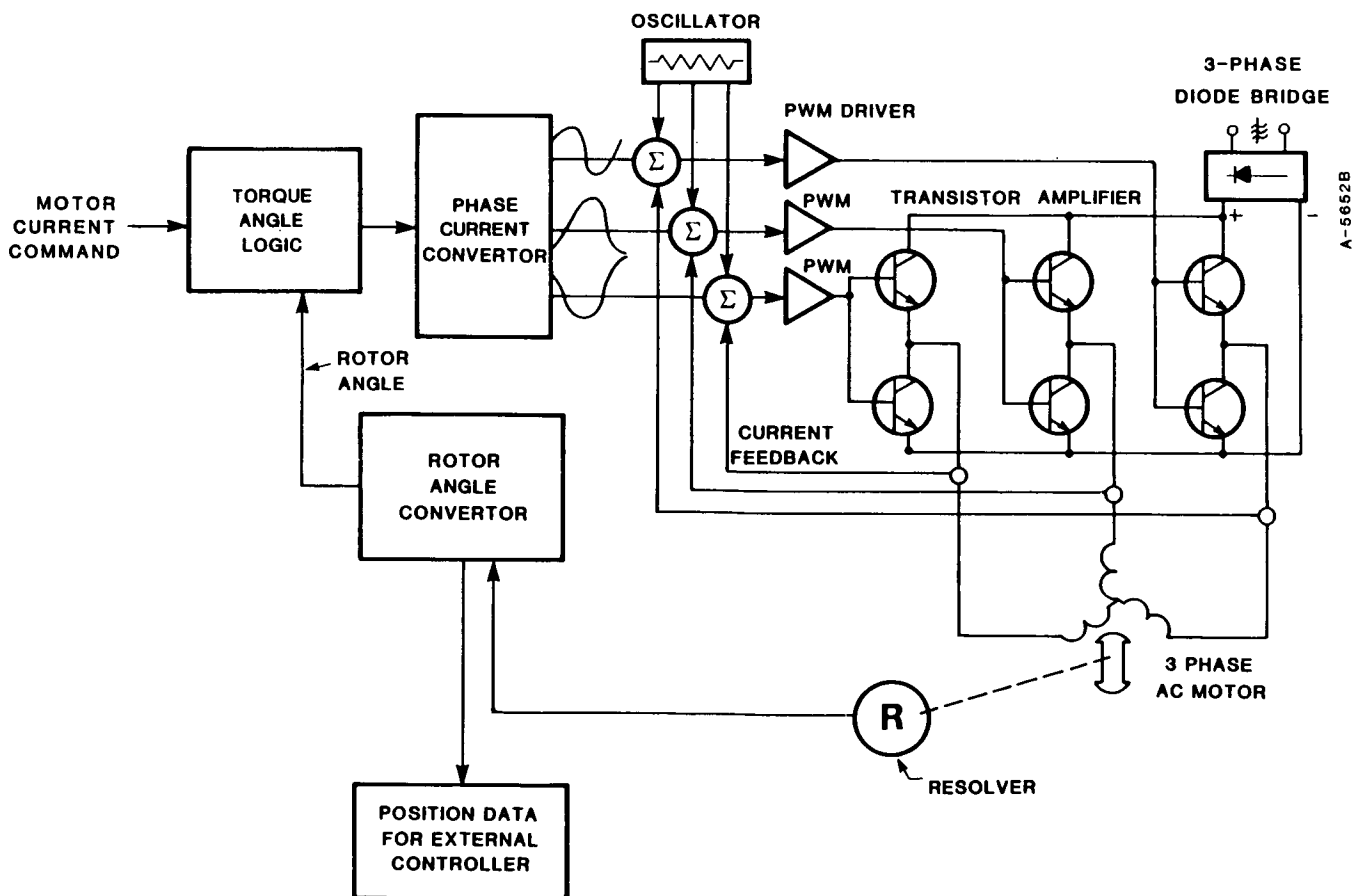


Figure 15. Brushless AC Servo Drive Block Diagram

204

using a resolver. From this measurement, the drive computes the coordinates of the three-phase sinusoidal motor currents required to produce optimum torque. The magnitude of these currents is then adjusted as a function of the torque command magnitude and direction. This process is repeated continuously within the drive. The result is low torque-ripple brushless motor drive system which responds to torque commands from the servo electronics.

## SUMMARY

This two axis motion simulator fully meets all requirements for thermal/vacuum simulation. Large satellites can be tested with minimal solar source shadowing and sufficient structural stiffness to achieve resonances greater than 7 Hz. The motors and transducers are directly coupled devices which eliminates the inherent instabilities of gear drive mechanism. Over 1000 channels are available for satellite data transmission via slip rings and thermocouple multiplexing system. Corona risk is eliminated by using brushless motors, special connectors, and pressurizing the slip ring assembly. Except for the slip ring, the balance of the motion simulator is completely vented. This greatly simplifies the design and manufacturing process and the risk of leakage. Leakage from the slip ring is eliminated using ferrofluidic seals and epoxy feedthroughs. All components exposed to the vacuum meet SP-R-0022A requirements for thermal vacuum stability to limit outgassing. Temperature control is achieved using passive cooling and active reheating which eliminates the need for expensive and unreliable fluid heat exchangers. Precision motion control with arc-second resolution and zero drift is achieved using Inductosyns, MPACS controller, and a pulse width modulated three phase motor amplifier. Motion commands, are accepted manually or using remote computer control. The end result is a two-axis satellite motion simulation system which provides an extremely accurate, flexible, reliable, and cost effective solution for thermal/vacuum space simulation testing.

## ACKNOWLEDGEMENTS

## BIBLIOGRAPHY

1.  V.C. Robinson, A.M. Mocek, Corona: Simple Technique used to Eliminate In Connection and Cable Assemblies", IEEE (77 Ch. 1 203-9 NAECON), N.Y., N.Y., 1977, pp. 850-856.

2.  Dunbar, W.G., Corona Evaluation of Spacecraft Wires and Connection", Wire and Cable Symposium, 18th International, Atlantic City, NJ Dec. 3-5, 1969.

3.  SP-R-0022A, General Specification Vacuum Stability Requirements of Polymeric Material for Spacecraft Application, Johnson Space Center, 1974.

# LIGO VACUUM SYSTEM STUDY

Jeffrey C. Livas
Massachusetts Institute of Technology

Boude C. Moore
California Institute of Technology

## ABSTRACT

A laser interferometer gravitational wave observatory (LIGO) is being developed with sensitivities which will have a high probability of detecting gravitational waves from astrophysical sources. Detectors are also planned by others in Europe and eventually in space. A major component of the proposed LIGO is a total of 16 km of 1.2 m (48 inch) diameter tube at a pressure of less than $10^{-8}$ torr. It will be of 304L stainless steel procured directly from the steel mills with the initial hydrogen content specially reduced. (Target is 1 ppm by weight.) Projections of the outgassing rates of hydrogen and of water vapor as a function of time will be given and the uncertainties discussed. Based on these, a preliminary analysis of the vacuum system will be presented.

## INTRODUCTION

The development of laser interferometric gravitational wave detectors is proceeding at the prototype level in several countries: France, Germany, Italy, Japan, United Kingdom, and the United States. Plans to build a full scale detector in each of the countries are being considered; the result would be an international network of detectors capable of doing useful astronomy with gravitational waves. The network would open a new window on the universe complementing the existing windows in the optical, infrared, radio, and X-ray bands and add to our understanding of the cosmos as did the opening of the radio window in the 1930's and the X-ray window in the 1960's. A particularly interesting possibility would be the direct observation of black holes.[1] Descriptions of the physics of gravitational wave detection and recent prototype developments have been described elsewhere.[1,2]

In the United States, a collaboration of Caltech and MIT scientists, funded by the National Science Foundation (NSF), is planning the construction of two separate full-scale detectors under a single management (the LIGO project). At least four spatially separated detectors are required to unambiguously determine the location of a source; the two in the U.S. will provide a solid foundation on which to build the international network. Two detectors are also needed for a cross-correlation analysis to eliminate false signals caused

by environmental noise at each separate detector. Since many of the theoretically predicted sources of gravitational waves emit at frequencies below 10 Hz where ground motion and gravity gradient noise reduce the sensitivity of earth-based detectors, there are plans to construct space-based detectors.[3]

The objective of this study is to ensure that the technical requirements for the vacuum system are met with minimum cost. A similar study has been published for the detector planned in the United Kingdom.[4] A classical approach to reduce costs of pumping systems is to bake and thereby reduce the gas load. For the LIGO project, the cost and time for baking the system are significant. It is therefore useful to determine if the requirements for the vacuum can be met without baking. A brief description of a proposed detector is presented together with the vacuum requirements. The outgassing characteristics of stainless steel will be shown for hydrogen and for water vapor. Based on these, a conceptual design of the vacuum system will be presented.

## FACILITY DESCRIPTION

The LIGO Project proposal is for a single observatory consisting of two detectors, separated by a continental baseline. Each LIGO detector consists of two lengths of vacuum pipe connected to form the two arms of a right angle. (This geometry takes advantage of the polarization of the gravity wave and reduces the demands on the frequency stability of the laser.) Laser beams travel back and forth between mirrors in each arm. Each arm will be four kilometers in length and 1.2 meters (48 inches) in diameter. Components of the laser interferometer will be contained in chambers located at the junction of the arms, at their midpoints, and at their ends, as illustrated in Fig. 1. Thus the same beam tube design can be applied to the four identical 2 kilometer sections between chambers. A sketch of a 2 kilometer section and its vacuum system is shown in Fig. 2.

The laser interferometer measures changes in the distance between the two masses in each arm and then compares the changes in the two arms.[1] To indicate the level of difficulty of the measurement, these changes are expected to be on the order of .004 of the diameter of a proton for the LIGO detectors. Vibration from vacuum pumps or equipment could obviously interfere with this measurement.

The arms must be evacuated so that scattering of the laser beam by the residual gas molecules is reduced. However the acceptable levels of pressure (which increase with arm length) can be achieved with existing technology. If all the gas were hydrogen, then a pressure of $1.3 \times 10^{-6}$ Pa ($1 \times 10^{-8}$ torr) would be acceptable. Similarly, if all the gas were water vapor, $1.2 \times 10^{-7}$ Pa ($9 \times 10^{-10}$ torr) would be acceptable. An important feature of these requirements is that they need not be met immediately on facility completion. The laser interferometers are in a state of development, and are not expected to reach the planned sensitivity for some time. Initial operations may be conducted at somewhat higher pressures without limiting the observations.

Considered as a vacuum system, the LIGO is unusually large. Each of the eight 2 kilometer beam tubes (four at each site) has a volume of $2.3 \times 10^6$ liters, and a surface area of $7.7 \times 10^7$ cm$^2$. Because of its large size, the cost of baking the system, as is often done to reduce the gas load, would be very high. Again because of its size, the option of using vacuum melted steel to reduce outgassing would be prohibitive.

Gate valves are provided at each end of the 2 kilometer sections so that the vacuum chambers can be brought up to atmosphere for access to the laser interferometer equipment, while the beam tubes remain under vacuum. It is planned that these tubes will not be exposed to the atmosphere after the initial pumpdown and leak testing.

## STAINLESS STEEL OUTGASSING – HYDROGEN

The most difficult gas to remove in a stainless steel vacuum system is the hydrogen. In fact, it has only been reduced, not eliminated, in efforts to date. Messer and Treitz[5] report an outgassing rate of $10^{-14}$ Pa L/s·cm$^2$ ($10^{-17}$ torr·L/s·cm$^2$) or 300 molecules/s·cm$^2$, after high temperature (875K) bake in a vacuum oven. Such low levels are not economically feasible on a large chamber, but a rate of $1.3 \times 10^{-10}$ Pa L/s · cm$^2$ ($10^{-12}$ torr · L/s · cm$^2$) is often achieved.[6]

Typically, 99% or more of the residual gas in a baked system is hydrogen.[6] The source of this gas is atomic hydrogen dissolved in the bulk material during the manufacturing processes. This diffuses out to the surface, combines into molecular hydrogen and is released into the gas phase. The diffusion is greatly accelerated at high temperatures. A quantitative description of this process has been given by Calder and Lewin.[6]

$$Q = 4\,C_o\,\frac{D}{d}\left[\sum_{n=o}^{\infty} e^{-\left(\frac{\pi(2n+1)}{d}\right)^2 Dt}\right] + \frac{K}{d}\,P_H{}^{1/2} \qquad (1)$$

where:

$Q$ = outgassing rate, torr liters/cm$^2$ second

$C_o$ = initial gas concentration in the metal, standard torr liters/cm$^3$, uniformly distributed

$D$ = diffusion coefficient, cm$^2$/second

$d$ = wall thickness, cm

$t$ = time, seconds

K = permeability constant ($= 1.2 \times 10^{-16}$ torr$^{1/2}$ L/cm · s at room temperature)

$P_H$ = partial pressure of atmospheric hydrogen[4] ($= 5.3 \times 10^{-2}$ Pa ($4 \times 10^{-4}$ torr))

To use this formula, it is necessary to know the values of $C_o$ and D. Values for $C_o$ given in the literature vary from 1.1 to 4.5 parts per million (ppm) by weight.[6,7] A half dozen random samples recently tested were found to have concentrations between 1.5 and 3.7 ppm. These appear to be small differences but they cause a very large change in the degassing time of unbaked systems, as will be shown below.

The other value required is the diffusion coefficient, D. The value used in the calculations below is $5 \times 10^{-14}$ cm$^2$/second at 27C. This value was extrapolated[6] from measurements by Eshbach, et al[8] taken on 304 stainless steel at much higher temperatures. The value is uncertain, due to the large extrapolation, and also due to changes which have been observed in iron over this temperature range. Alpha iron[9] has shown much lower rates at room temperature than would be extrapolated from high temperatures. Thus if there is an error in the diffusion coefficient it may be in the direction of less outgassing.

The outgassing rate at 27C according to Equation (1), as a function of *time since manufacture,* is shown in Fig. 3 for levels of initial hydrogen concentration of 0.5, 1, 2, and 4 ppm by weight. The wall thickness is assumed to be .4 cm (.155 inch) thick (a value suitable for the LIGO application). The outgassing rate will decline from the time of manufacture rather than time under vacuum, since the internal concentration is so much higher than the equilibrium due to ambient hydrogen. Initially, the outgassing rate declines as $1/\sqrt{t}$, and the concentration at the center of the chamber wall is unchanged. After sufficient time, about 30,000 years, this center concentration begins to fall, and then the outgassing rates fall exponentially. Finally they reach a constant level due to permeation of atmospheric hydrogen through the wall, There may be additional permeation as a result of the water vapor in the air.

The important part of the curves in Fig. 3, for this problem, is expanded in Fig. 4. The time to reach any specified rate varies as the square of the initial concentration. The 8:1 range of concentrations plotted becomes a 64:1 range in the time required to reach a given rate.

This estimate of the rate of hydrogen outgassing as a function of time and of initial concentration will be used below in the conceptual design of the LIGO vacuum system. It will also be a guide for the future procurement of steel for the facilities.


## STAINLESS STEEL OUTGASSING – WATER VAPOR

Water vapor is relatively simple to remove from a vacuum system. After bakeout, it is frequently reported to be unobservable. For practical purposes, it can often be ignored as a residual gas in a baked system.

However, in an unbaked system most of the initial outgassing is water vapor.[7] The initial rate is observed to decrease as $1/t$ and its magnitude will vary with the surface cleaning procedures used. We found no data for degassing times greater than 100 hours[7,10] for unbaked systems. Dayton's[7] review gives a rate of $1.9 \times 10^{-5}$ Pa L/s $\cdot$ cm$^2$ (1.4 $\times$

$10^{-7}$ torr$\cdot$L/s$\cdot$cm$^2$) after one hour. The outgassing rate can be expressed as:

$$Q = Q_1 \times (t_1/t) \qquad (2)$$

where:

$Q$ = outgassing rate

$Q_1$ = outgassing rate at time $t_1$ (= Dayton's value at 1 hour)

$t$ = time

As $t$ becomes large the outgassing rate is expected to become less than given by this expession,[7] else the quantity outgassed would exceed the quantities observed. Further evidence for this view is provided by outgassing experiments at higher temperatures, to be discussed below.

The simplest model of gas sorption on a surface is that of an average sojourn time which is a function of the heat of adsorption.[11] The surface coverage is then:

$$S = Q\,\tau \qquad (3)$$

where:

$S$ = quantity of gas adsorbed per cm$^2$ of surface

$Q$ = quantity of gas adsorbed or desorbed per cm$^2$ per sec.

$\tau$ = average sojourn time on surface, in seconds

Frenkel's equation (1924) for the variation of sojourn time with temperature[11] is:

$$\tau = \tau_o\,e^{\,H/RT} \qquad (4)$$

where:

$\tau$ = sojourn time on surface, as defined above

$\tau_o$ = time of oscillation of adsorbed molecules, normal to surface, assumed = $10^{-13}$ seconds[11]

$H$ = heat of adsorption, cal/mole

$R$ = gas constant = 1.9872 cal/mole K

$T$ = temperature, Kelvin

The heat of adsorption, $H$, has been given as 22 to 25 kcal/mole for water on metals.[12] In a recent desorption experiment[13] a 304 stainless steel cylinder was heated at a rate of 0.2 degrees Kelvin per second. Two desorption peaks were reported, one at 22 and the other at 25 kcal/mole. The corresponding temperatures were 55C and 93C.

This measurement of outgassing rates at higher temperatures can be used to estimate the rate at room temperature. If a surface holding a quantity $S_o$, of adsorbed gas is allowed to desorb, starting at time $t = O$, then from equations (3) and (4) it follows that the outgassing rate would be:[12]

$$Q = \frac{S_o}{\tau} e^{-\frac{t}{\tau}} \tag{5}$$

where:

Q, t, and $\tau$ are as defined above,

$S_o$ = quantity of gas adsorbed on the surface at the time $t = 0$

The plot in Fig. 5 shows the exponential decay for four values of the heat of desorption, $H$: 22, 23, 24, and 25 kcal/mole. These have been normalized to Dayton's[7] estimate of the outgassing rate after one hour under vacuum. The extrapolated $1/t$ function has also been shown. It is clear that the average sojourn model does not explain the initial $1/t$ outgassing observed.

In an attempt to resolve this discrepancy, Dayton[7] suggested that the $1/t$ function could be a result of the water being desorbed from the surface with a spectrum of energies rather than any single value, reflecting the complexity of a real surface. To illustrate this approach, the outgassing rates of the four groups of molecules, with the heats of desorption shown above, were added in a weighted fashion at each point in time. The details of the weighting are given in the Appendix. The result is shown in Fig. 5, and it is seen to follow the $1/t$ function for a few hundred hours and then decay exponentially. The subsequent large gap between these two functions demonstrates the uncertainty of the outgassing rate for times greater than 1000 hours.

To summarize this water outgassing discussion, no observations of unbaked systems have been found in the literature for times greater than 100 hours. A rough estimate can be made based on outgassing at higher temperatures, but the accuracy of this estimate is open to question at this time.

## CONCEPTUAL VACUUM SYSTEM DESIGN

A conceptual design of the vacuum system for a 2 kilometer beam tube is shown in Fig. 2, and its performance over time is given in Fig. 6. Ion pumps are used for low vibration. (Other pumps will be used to reduce the pressure from atmosphere but they will be turned off during laser interferometer operation.) Seven pumps are spaced at 250 meter intervals. Their operational pumping speed is assumed to be 2000 L/s for hydrogen,

and 1000 L/s for water vapor. The ends of the tube are assumed to be open to the vacuum chambers, where additional pumps and gas load result in the same pressures as in the tube.

The ratio of the peak pressure (halfway between the pumps), to the minimum pressure (at the pumps) is 1.08 for hydrogen, and 1.11 for water vapor.[14] The average pressure is the important parameter for beam scattering, so this is shown in Fig. 6. The average is 1.05 of the minimum pressure for hydrogen, and 1.074 for water vapor.

The hydrogen is plotted for an initial concentration of 1 ppm of this gas within the walls of the vacuum system. The time required to reach the design pressure for hydrogen is 8 months from the time of manufacture, here assumed to be 1000 hours before pumpdown.

The water vapor plots are limits. It can be seen that a completely unbaked system may be quite feasible, but in the absence of direct experimental data this is not certain. Experiments to provide this information are underway.


## SUMMARY

The vacuum levels required for the LIGO are well within the state of the art. However, the unusually large size of the vacuum vessels dictates that every effort be made to minimize the system's initial and operating costs. The 2 kilometer beam tubes will be permanently under vacuum. They may not need to achieve the vacuum design goals immediately. These conditions suggest that the possibility of an unbaked system be examined.

For the most difficult task, reducing the hydrogen partial pressure, the unbaked system is feasible; the required pressure can be achieved in an acceptable time. The partial pressure of water vapor, on the other hand, can only be estimated within limits until more outgassing data is obtained. Experiments to provide this information are now underway.


## APPENDIX

Four groups of molecules adsorbed on a surface have been defined with heats of adsorption of 22, 23, 24, and 25 kcal/mole. The magnitude of each group has been adjusted so it fits Dayton's outgassing rate at one hour. These groups have been plotted on Fig. 5.

These four groups are now weighted and combined as follows:

$$D(t) = A_{22}(t) + A_{23}(t)/B + A_{24}(t)/B^2 + A_{25}(t)/B^3$$

$$Q(t) = K \ D(t)$$

$$K = \frac{Q_1}{D_1}$$

where:

$A_{22}(t)$ = outgassing rate of 22 kcal/mole water at time t. $A_{23}(t)$ thru $A_{25}(t)$, similar

$Q(t)$ = outgassing rate at time $t$. $Q_1$ = rate at 1 hour

$D(t)$ = weighted sum of outgassing rates

$D_1 = D(t)$ at 1 hour

$B$ = constant. $B = 3$ is plotted

This sum is shown in Fig. 5.

# REFERENCES

1. Jeffries, A. D.; Saulson, P. R.; Spero, R. E.; and Zucker, M. E.: *Gravitational Wave Observatories.* Scientific American, **255**, no. 8, June 1987, pp. 50–58.

2. Thorne, K. S.: *Gravitational Radiation.* In 300 Years of Gravitation, ed. Hawking and Israel, Cambridge University Press, 1988.

3. a) *Space Science in the 21st Century.* Task Group on Fundamental Physics & Chemistry, National Academy Press, Washington D.C., 1988, pp. 38–44.

   b) Faller, J. E.; Bender, P. L.; Chan, Y. M.; Hall, J. L.; Hills, D.; Hough, J., *Laser Gravitation Wave Experiment in Space.* Proceedings 10th International Conference on General Relativity & Gravitation, p. 960, ed. Bertotti, de Felice, Pascolini, 1983.

4. Bennett, J. R. J.: *The Vacuum System for a British Long Baseline Gravitational Wave Detector.* JVST, **A5**, 1987, pp. 2363–6.

5. Messer, G.; and Treitz, N.: *Sensitive Mass-Selective Outgassing Rate Measurements on Baked Stainless Steel and Copper Samples.* Proc. 7th Intern. Vac. Congr. & 3rd Intern. Conf. Solid Surfaces (Vienna), ed. Dobrozemssky, et al, pp. 223–6, 1977.

6. Calder, R.; and Lewin, G.: *Reduction of Stainless-Steel Outgassing in Ultra-High Vacuum.* Brit. J. Appl. Phys., **18**, 1967, pp. 1459–1472.

7. Dayton, B. B.: *Outgassing Rate of Contaminated Metal Surfaces.* 1961 Transactions of the Eighth National Vacuum Symposium (American Vacuum Society) and Second International Congress, ed. Preuss, Vol. 1, pp. 42–57, Pergamon Press, 1962.

8. Eschbach, H. L.; Gross, F.; and Schulien, S.: *Permeability Measurements with Gaseous Hydrogen for Various Steels.* Vacuum, **11**, 1963, pp. 543–7.

9. Johnson, E. W.; and Hill, M. L.: *The Diffusivity of Hydrogen in Alpha Iron.* Transaction of the Metallurgical Society of AIME, **218**, 1960, pp. 1104–12.

10. Elsey, R. J.: *Outgassing of Vacuum Materials -1 and -11.* Vacuum, **25**, 1975, pp. 299–306 and 347–61.

11. deBoer, J. H.: *The Dynamical Character of Adsorption.* Oxford University Press, 1953.

12. Santeler, D. J.; Holkeboer, D. H.; Jones, D. W.; and Pagano, F.: *Vacuum Technology and Space Simulation.* NASA SP-105, 1966.

13. Pang, S. J.; Gao, W.; and Yang, Y.: *Thermal Desorption Measurements for Aluminum Alloy 6063 and Stainless Steel 304.* JVST, **A5**, 1987, pp. 2516–2519.

14. Welch, K.: *Pressure Profile in a Long Outgassing Tube.* Vacuum, **23**, 1973, pp. 271–276.
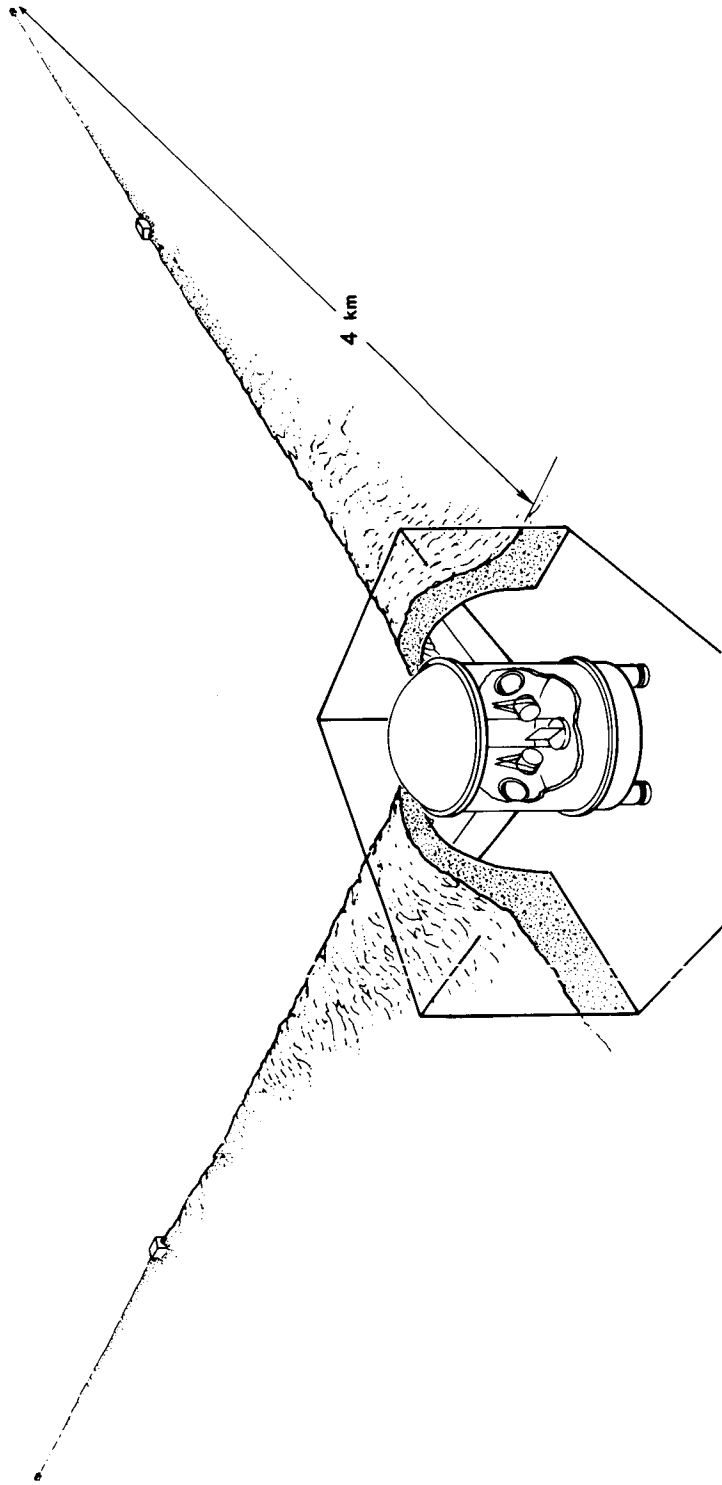
Fig. 1 Artist's conception of a LIGO detector installed at one of the two sites.

4 km
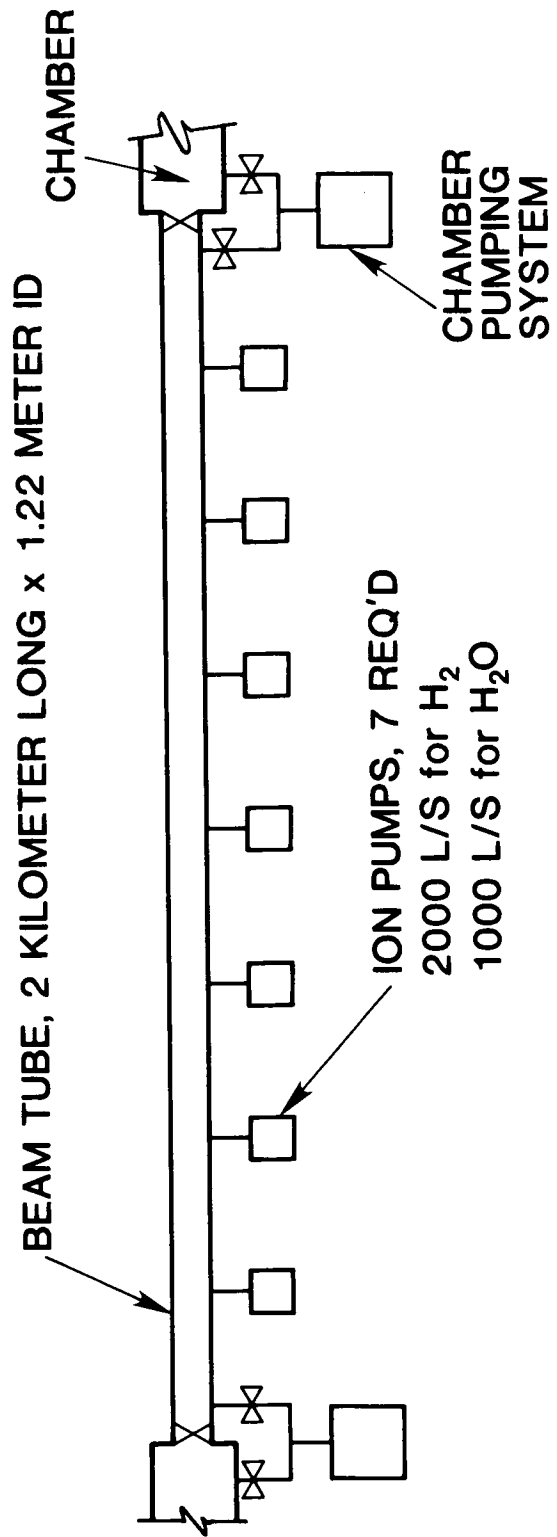
Fig. 2 Concept of LIGO 2 kilometer beam tube, with ion pumps at 250 m intervals.
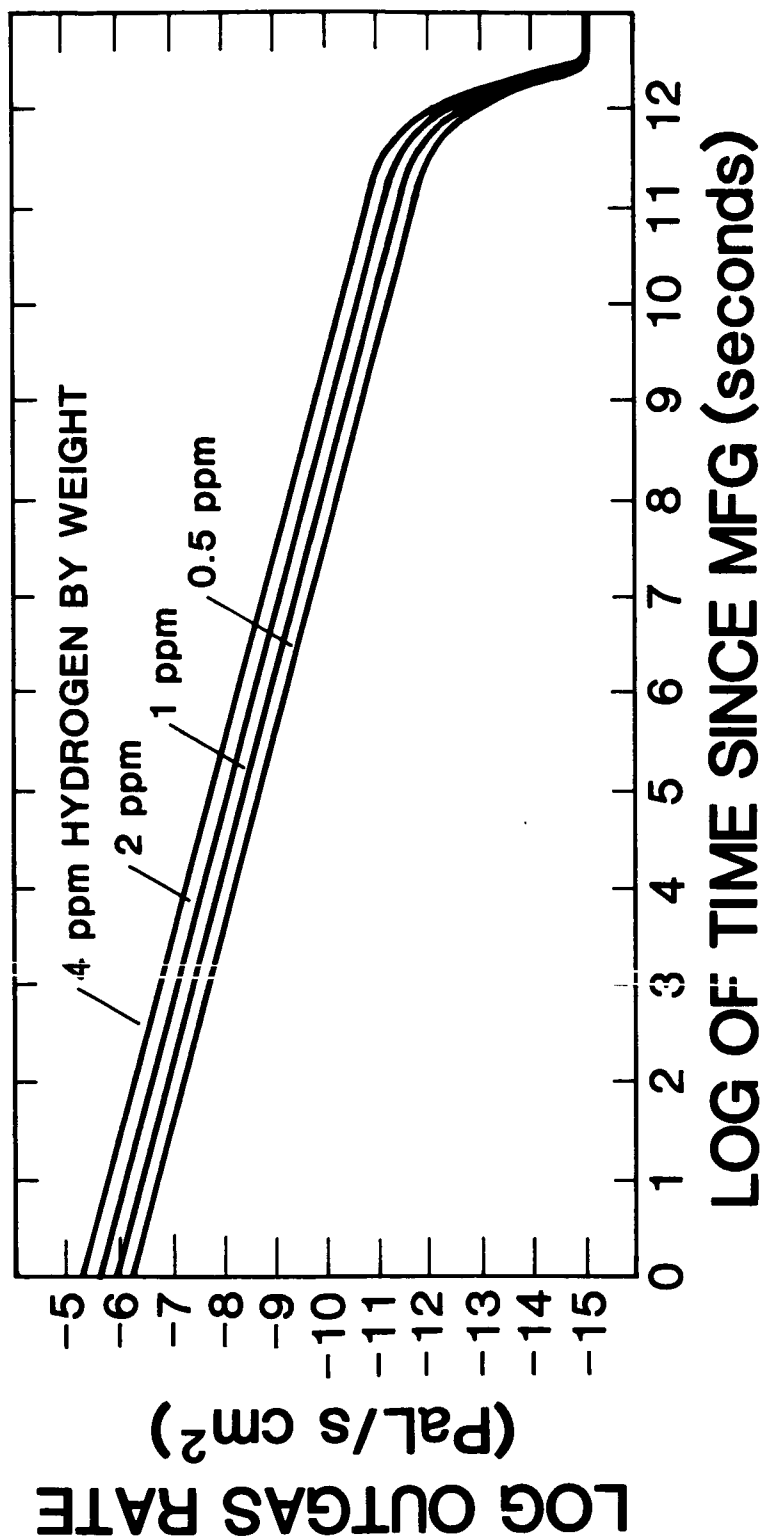
Fig. 3 Hydrogen outgassing rate from 304 stainless steel vs. time since manufacture for initial concentrations of 0.5, 1, 2, and 4 ppm by weight.
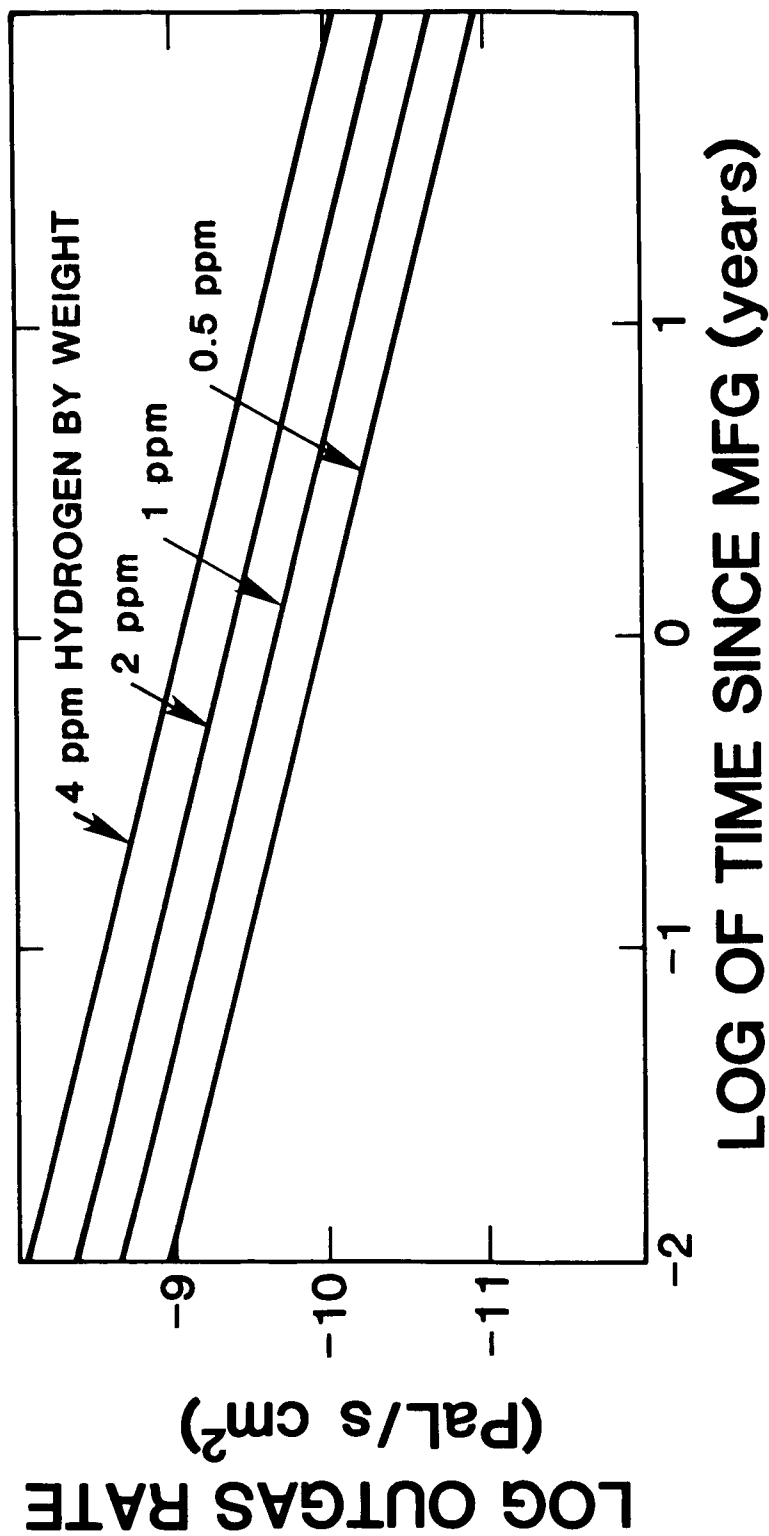
Fig. 4 Same as Fig. 3, with expanded time scale.
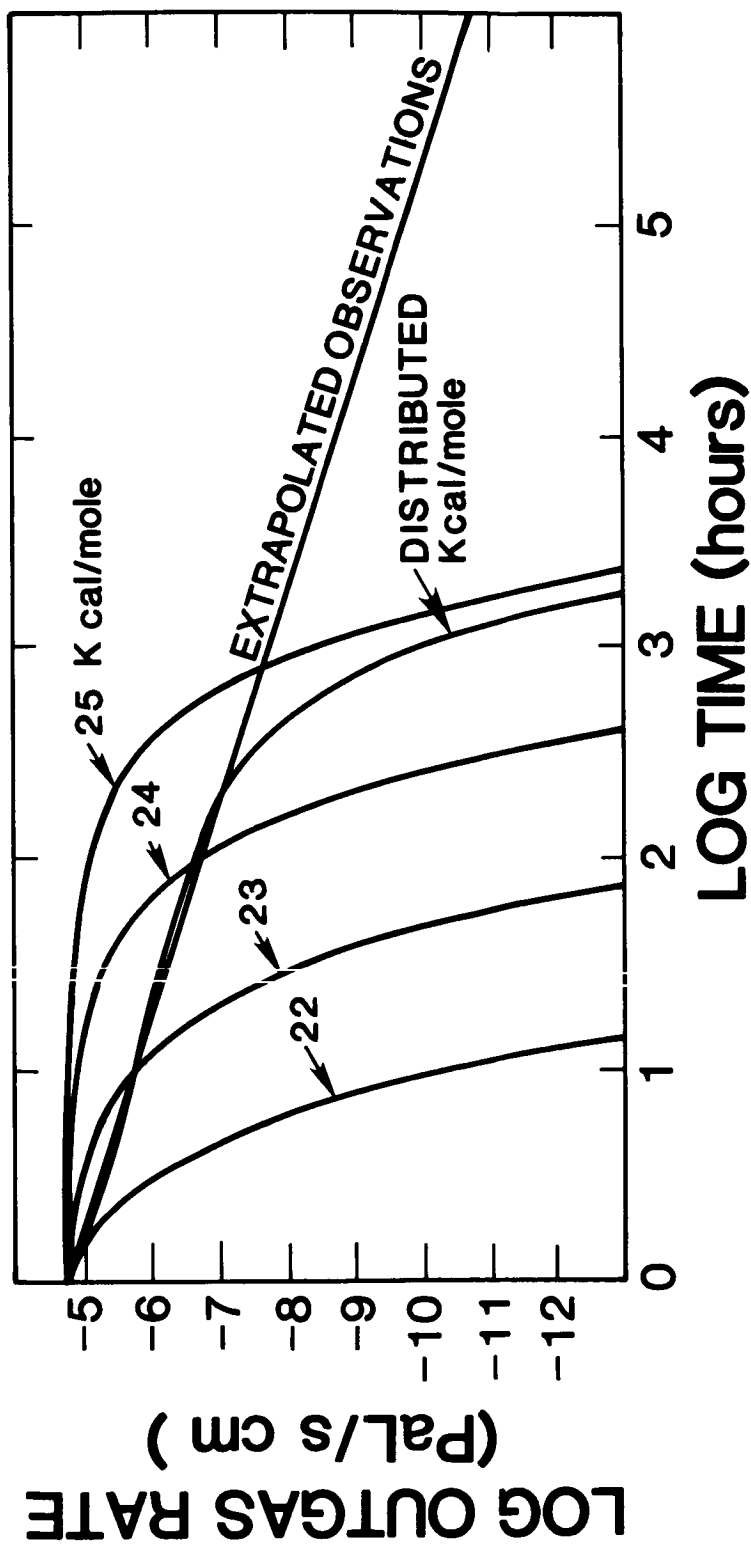
Fig. 5 Water vapor outgassing rate for 304 stainless steel vs. time under vacuum with in-
dicated heats of adsorption, using the "average sojourn time" model. These are fit
to Dayton's[7] upper limit. A distributed heat of adsorption model, combining the
outgassing from several fractions held to the surface with different energies, is also
shown.
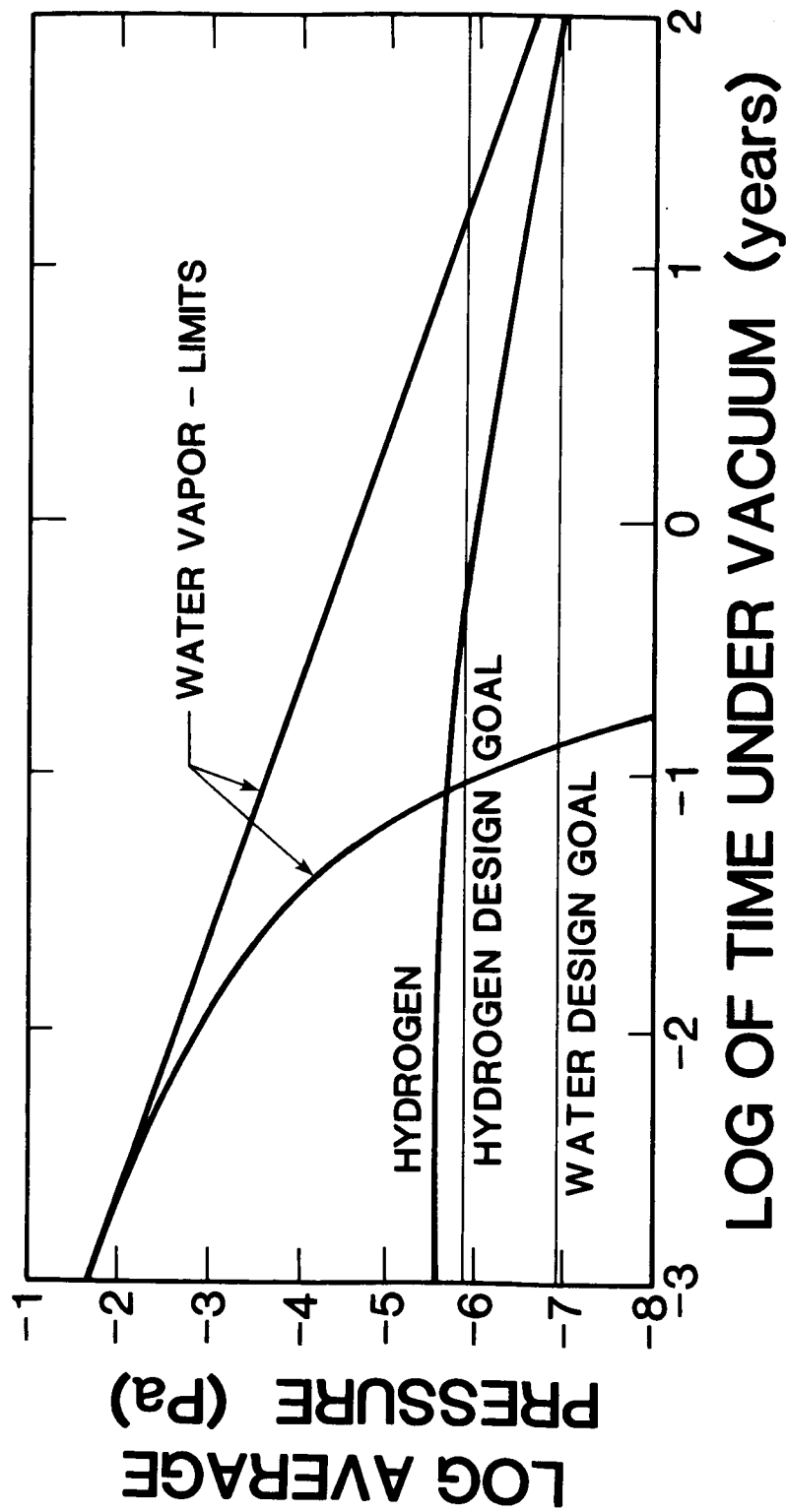
Fig. 6 Average pressure vs. time for hydrogen and water vapor in 2 km beam tube. Hydrogen time between manufacture and vacuum pumpdown = 1000 hours. Initial concentration of hydrogen = 1 ppm by weight. Design Goals for single gas species.

# THE TWO AXIS MOTION SIMULATOR FOR THE
# LARGE SPACE SIMULATOR AT E.S.T.E.C.

Kurt A. Beckel and Joop Hutchison
European Space Research and Technology Center (ESTEC)

## ABSTRACT

The Large Space Simulator at ESTEC has recently been equipped with a Motion Simulator capable to handle test articles of 5 tons mass and having a volume of 7m in diameter and a length of 7m. The Motion Simulator has a modular set-up, it consists of a Spinbox as basic unit on which the test article is mounted and which allows continuous rotation (spin). This Spinbox can be used in two operational configurations:

o    Spin axis vertical to 30° inclination when mounted on a Gimbalstand;
o    Spin axis horizontal when mounted on a Turntable - Yoke combination.

The Turntable provides rotation within ± 90°. This configuration allows to bring a test article in all possible relative positions vis-à-vis the sun vector (which is horizontal in this case).

The Spinbox allows fast rotation between 1 - 6 rpm or slow rotation between 1 - 24 rot./day as well as positioning within ± 0.4° accuracy. The Spinbox is provided with a slipring having considerable transmission capacity, totally some 480 direct channels ranging from low level DC (thermocouples) till UHF and power channels with an overall rating of 310 Amps in total. Additional multiplexing of thermocouple lines is possible.

The Motion Simulator in both configurations is shrouded so that no warm spots are visible from the test volume. It is specially designed for quick installation and removal. Provision is made for a later implementation of a Levelling System allowing precise levelling when tested satellites are carrying heat pipes.

## INTRODUCTION

In order to give the new Large Space Simulator at ESTEC the full operational capabilities it was necessary to install an appropriately large Motion Simulator. This facility should be capable to accept test articles in size and mass corresponding to the possibilities of the Space Simulator. In addition it should provide the highest possible flexibility, it should allow simple installation and removal and stay within minimum costs.

In early 1985 prestudies began and the technical requirements were defined. A modular concept was chosen. The basic unit is the Spinbox on which the test article is mounted via a test adaptor. It allows continuous rotation at normal spinning speed as well as at very low speed for the simulation of geostationary orbits. The Spinbox is provided with a Slipring having considerable transmission capabilities for electrical signals and power. Altough the Spinbox is designed to operate in any position in respect to the gravity vector, two basic configurations have been chosen as follows:

o    Spin axis vertical to 30° inclination when mounted on a Gimbalstand (Figures 1 and 5);
o    Spin axis horizontal when mounted on a Turntable - Yoke combination (Figures 2 and 6).

In the latter configuration the Turntable can be positioned within ± 90° thus allowing to bring the test article on the Spinbox in any relative position vis-à-vis the sun radiation. Both configurations are built up on the existing seismic structure inside the vacuum chamber. A shroud subsystem exists for both configurations shading the test article from unwanted thermal radiation.

The facility performance requirements are summarized in Tables I and II. Contracts for design and manufacture of the 4 main subsystems namely the Spinbox, the Turntable, the Gimbalstand and the Slipring were placed in late 1985/early 1986; the procurement of the other items, the integration at ESTEC, the system engineering and management has been provided by the ESTEC engineering services.

The installation of the Motion Simulator was completed in December 1987, the acceptance test followed in January 1988, the acceptance review took place in February 1988. Immediately after that, a flight unit of an ESA Astronomy satellite (Hipparcos) was installed on the Motion Simulator and the first operational test using this equipment was successfully completed one month later.


## DESCRIPTION OF THE DIFFERENT ITEMS OF THE MOTION SIMULATOR


### SPINBOX

A schematic cross-section of the Spinbox is given in Figure 3. The hollow shaft provides room for the installation of the Slipring including the necessary clearance for the cooling air around the Slipring. The bore in the shaft has a diameter of 328 mm. Since the interior of the Spinbox is at ambient pressure, a rotary seal consisting of 3 individual graphite embeded teflon lip-seals is installed.

The first interseal volume after the ambient is backed up by a vacuum line, the pump of which is installed under the vacuum chamber. Also the second interseal volume is connected to a vacuum line which, however, is only pumped in emergency cases. The shaft is guided by means of a cross-roller bearing which came out in a preceeding detailed study as best compromise between deformation requirements and volume constraints. The bearing is inside the air compartment of the Spinbox and has the necessary gearing on its inner ring.

It is driven via a pinion on the cyclodrive by two servo motors, one for fast and one for slow motion. A clutch separates the slow motor from the cyclodrive when the fast motor is in operation. A break prevents rotation of the shaft when the motors are stopped.

All the potentional high energy dissipating units: motors, cyclodrive, bearing and seal are connected to a water cooling system. In addition, cooling air circulates in a controlled way inside the Spinbox. This air flow backed up by the electrical heaters also keeps the Spinbox at a sufficient temperature level in cold test phases to avoid condensation. A dome on the spacecraft side of the Spinbox is provided with the necessary vacuum feedthroughs for the signal and power lines. It is noticable that the dome on the spacecraft side as well as the backcover of the Spinbox are easily interchangeable. This was already necessary during the first operational test with the Motion Simulator as will be explained in the paragraph of the Slipring.

A final remark shall be made on the rotary seal. Because initial doubts were existing regarding the reliability and lifetime of friction based seals, a study was performed about the feasibility to install a magnetic seal. Altough the magnetic seal has an ideal performance, high reliability and practically unlimited lifetime it was refrained from the utilisation of this type of seal because the pressure difference acting on the seal in combination with its diameter (600 mm) required a gap clearance between shaft and housing at the seal so small that it was not practical for manufacturing and could not be safely maintained with a loaded Spinbox.

## YOKE

For the configuration with horizontal spin axis the Yoke is interfacing to the Spinbox on the top side and to the Turntable on the bottom side (see Fig. 2). The Yoke is a box type structure of high torsion and bending stiffness. The box interior is vented to the vacuum. A heater system keeps the Yoke at a certain minimum temperature. On both sides of the Yoke runs a tube of 210 mm diameter. These tubes are connected to the air compartment of the Spinbox on one side and to a central air compartment in the lower part of the Yoke which in turn mates to the interior of the Turntable on the other side. One tube contains all Slipring lines, the other contains all Spinbox housekeeping lines. The two tubes also serve as outflow for the Spinbox cooling air.

## TURNTABLE AND ROTARY CABLE GUIDING DEVICE

A schematic view of the Turntable and the rotary cable guiding device is shown in Figure 4. The Turntable is built up of a massive tubular support structure. Its inside is at atmospheric pressure. The lay-out of the drive is similar to that of the Spinbox. For reasons of keeping sparepart costs down the following elements are identical to those of the Spinbox: main bearing, fast and slow motor and cyclodrive. The rotary seal is also of the same build-up as on the Spinbox only the seal diameter is considerably larger (1390 mm). Also in this case the main bearing is in the air compartment.

Its inner rotating ring is fixed to a circular plate which interfaces to the Yoke. In its centre this plate has a large circular hole allowing the two cablebundles coming from the Spinbox through the tubes of the Yoke to pass. The Turntable rests on a massive baseplate which is fixed to the seismic structure. The same baseplate is also required for the Gimbalstand and therefore normally stays in the chamber. It is connected via a tube of 570 mm diameter to the bottom flange of the chamber. The interior of this tube again is at ambient pressure. Inside this tube is another centric rotating tube placed which is resting on a system of rollers supported by the baseplate. It is driven via an upper mating tube fixed to the rotating part of the Turntable.

The interspace between the outer and the inner tube carries the (stationary) housekeeping lines of the Turntable, the inner tube carries the 2 cable bundles coming from the Spinbox. The inner (rotating) tube protrudes through the chamber bottom flange into the room under the chamber. There it mates to the rotary cable guiding device located under the vacuum chamber.

This rotary cable guiding device is necessary to assure an orderly bending of the 2 cable bundles coming from the Spinbox when the Turntable is rotated. It consists of two large chains supporting the two cable bundles. The chains are guided in a controlled manner throughout the full operational range of the Turntable.

## GIMBALSTAND

The Gimbalstand consists of a massive framework supporting the Spinbox. The inclination of the Spinbox is provided by a drive unit mounted on one side of the Gimbalstand. The drive unit is a sealed compartment at ambient pressure. It houses the servo-controlled drive motor acting via a wormgear onto the Gimbalstand inclination axis.

In the case of the Gimbalstand configuration the two cable bundles coming from the Spinbox are routed via 2 x 2 vacuum tight flexible umbilicals ending on their lower end to a dome located under the Gimbalstand and mating to the baseplate. By this means a direct air connection of the Spinbox and the facility exterior is provided as has been realised in the Yoke configuration.

The Gimbalstand also serves as a maintenance stand for the Spinbox outside the chamber. In this mode 360° rotation is possible. In order to avoid an override over the 30° position when located in the chamber (which would destroy the umbilicals and LN$_2$ lines) special safety devices have been installed. Below the Gimbalstand a room of 360 mm is left free allowing the later implementation of a levelling system for accuracte levelling when tested satellites are carrying heat pipes.

## SLIPRING

In the baseline configuration the Slipring has an overall length of 1080 mm and a diameter of 302 mm. It consists of totally 54 discs carrying up to 12 rings on both sides. A controlled air stream flows over the outside of the Slipring maintaining a controlled temperature environment and carrying away excessive heat. An inside bore of 75 mm diameter provides room for other rotary feedhroughs e.g. waveguides.

During the first operational test a special rotary feedhrough for two venting lines leading to the satellite under test had to be installed. In all these special cases the baseline length of the Slipring will be exceeded. It was therefore necessary to foresee a possibility to extend the Spinbox on the satellite side as well as on the opposite side providing the necessary additional room. It is foreseen to equip the Slipring in the future with a digital multiplexing device for thermocouple signals.

## SHROUD SYSTEM AND MOTION SIMULATOR THERMAL CONTROL

In order to minimise heat exchange with the environment all parts of the Motion Simulator located inside the vacuum chamber are covered by easily removable and remountable multilayer insulations. To prevent excessive cooling down in cold test phases, electrical heater foils are installed at critical locations. Spinbox and Turntable have in addition their own internal water and air temperature control systems which are microprocessor controlled from the control console.

All parts of the Motion Simulator inside the chamber are covered with flat shrouds. In the configuration Gimbalstand, the Spinbox shroud not only shields the Spinbox but also serves as protection of the test article from thermal radiation of the Gimbalstand and the unprotected areas of the seismic structure.

The Yoke carries two shrouds: one on its inclined middle part and a horizontal shroud on its lower part. In order to allow the Turntable rotation, the in and outgoing $LN_2$ lines to the Yoke shrouds are passing via a spiral type up and offwinding device which is attached to the under side of the Yoke lower shroud. All shrouds are connected in serie in order to assure uninterrupted $LN_2$ flow.

## DATA, POWER AND HOUSEKEEPING TRANSMISSION LINES

The lines coming from the test article enter the rotating part of the Spinbox via vacuum feedthroughs located on the dome. In both configurations they pass from there on entirely in ambient environment to the outside of the vacuum chamber. The housekeeping lines stay entirely in ambient environment on their way to the facility exterior. This constitutes a considerable costsaving factor taking into account the prices for vacuum feedthroughs and vacuum suitable cabling. Furthermore, a great number of additional leak sources are eliminated. Connectors for the Slipring lines and the Spinbox housekeeping lines are located at the Spinbox and below the chamber before entering the rotary cable guiding device.

## CONTROL CONSOLE

A Control Console located in the control room allows to control and monitor all active and passive parts of the Motion Simulator. For operation under ambient conditions of the Spinbox, Turntable or Gimbalstand in the storage / maintenance area and inside the chamber a local panel is provided which can be connected at test floor level and storage floor level. When this local panel is connected it is impossible to operate the Motion Simulator from the Control Console in the control room.

## HANDLING AND STORAGE HARDWARE

Due to the complexity of the system and the requirement of quick installation and removal a substantial amount of special hardware had to be provided.

## TABLE I.- MOTION SIMULATOR PERFORMANCE DATA

### GENERAL CHARACTERISTICS

| | | |
|---|---|---|
| o | Test volume | : 7000 mm diameter |
| o | Max. test specimen mass | : 5000 kg |
| o | Max. Moment of Inertia $I_x = I_y = I_z$ | : 8000 kg.m$^2$ |
| o | Max. unbalance | : 200 kg.m |
| o | Max. overall leakrate | : $1,5 . 10^{-2}$ mbarl/sec |

### SPINBOX

o **FAST MOTION**

Continuous rotation (both directions)

| | | |
|---|---|---|
| - | Velocity | : 1 - 6 rpm |
| - | Velocity accuracy | : ± 3% of selected speed |
| - | Max. acceleration/deceleration | : ± 1,0 rad/sec$^2$ |

o **SLOW MOTION**

Continuous rotation (both directions)

| | | |
|---|---|---|
| - | Velocity | : 1 - 24 rot/day |
| - | Position accuracy | : ± 0,4° |

o **POSITION MODE**

Rotation in both directions

| | | |
|---|---|---|
| - | Speed | : 30° - 60°/min |
| - | Position accuracy | : ± 0,4° |

### TURNTABLE

POSITION CONTROL ONLY

| | | |
|---|---|---|
| - | Rotation angle | : ± 90° |
| - | Position accuracy | : ± 0,4° |
| - | Positioning velocity | : max. 60°/min |
| - | maximum angular acceleration/ deceleration | : ± 1.0 rad/sec$^2$ |

TABLE II.- MOTION SIMULATOR PERFORMANCE DATA (cont'd)

## GIMBALSTAND

o   Rotation angle                          :   Vertical to 30° inclination
o   Position accuracy                       :   ± 0,1°
o   Position velocity                       :   1 - 60°/min
o   Max. angular acceleration/deceleration  :   ± 1,0 rad/sec$^2$

## SLIPRING CHANNEL OVERVIEW

|  | TYPE | NO. OF CHANNELS | NO. OF SEPARATE SHIELDS | NO. OF GROUNDINGS |
|---|---|---|---|---|
| BASELINE: | Low level | 216 | 12 | |
| | 1 Amp/100V D.C. | 144 | 8 | 4 |
| | 5 Amp/100V D.C. | 33 | 3 | |
| | 100 KHz | 60 | 60 | |
| | 10 MHz | 20 | 20 | |
| | VHF | 8 | | |
| | UHF wide band * | 2 | | |
| OPTION : | Waveguide | 2 | | |
| | UHF narrow band | 2 | | |
| | TOTALS | 485 | 103 | 4 |

* Replaced by UHF narrow band for option.

228

SATELLITE

GIMBAL STAND

SEISMIC STRUCTURE

ROTARY CABLE GUIDING DEVICE

SUN

SPINBOX SHROUD

SPINBOX

UMBILICALS

FIG. ' - MOTION SIMULATOR VERTICAL CONFIGURATION

229
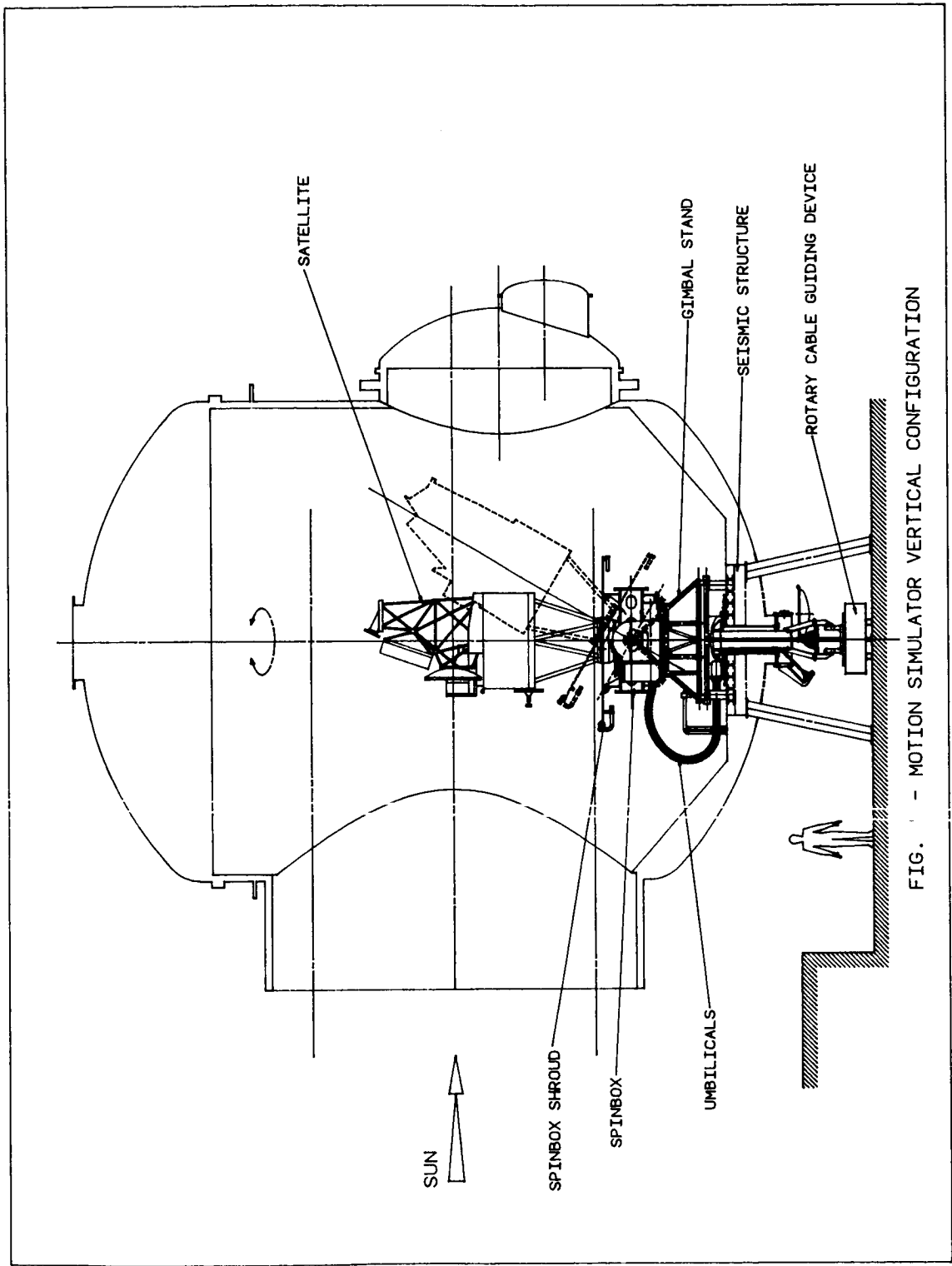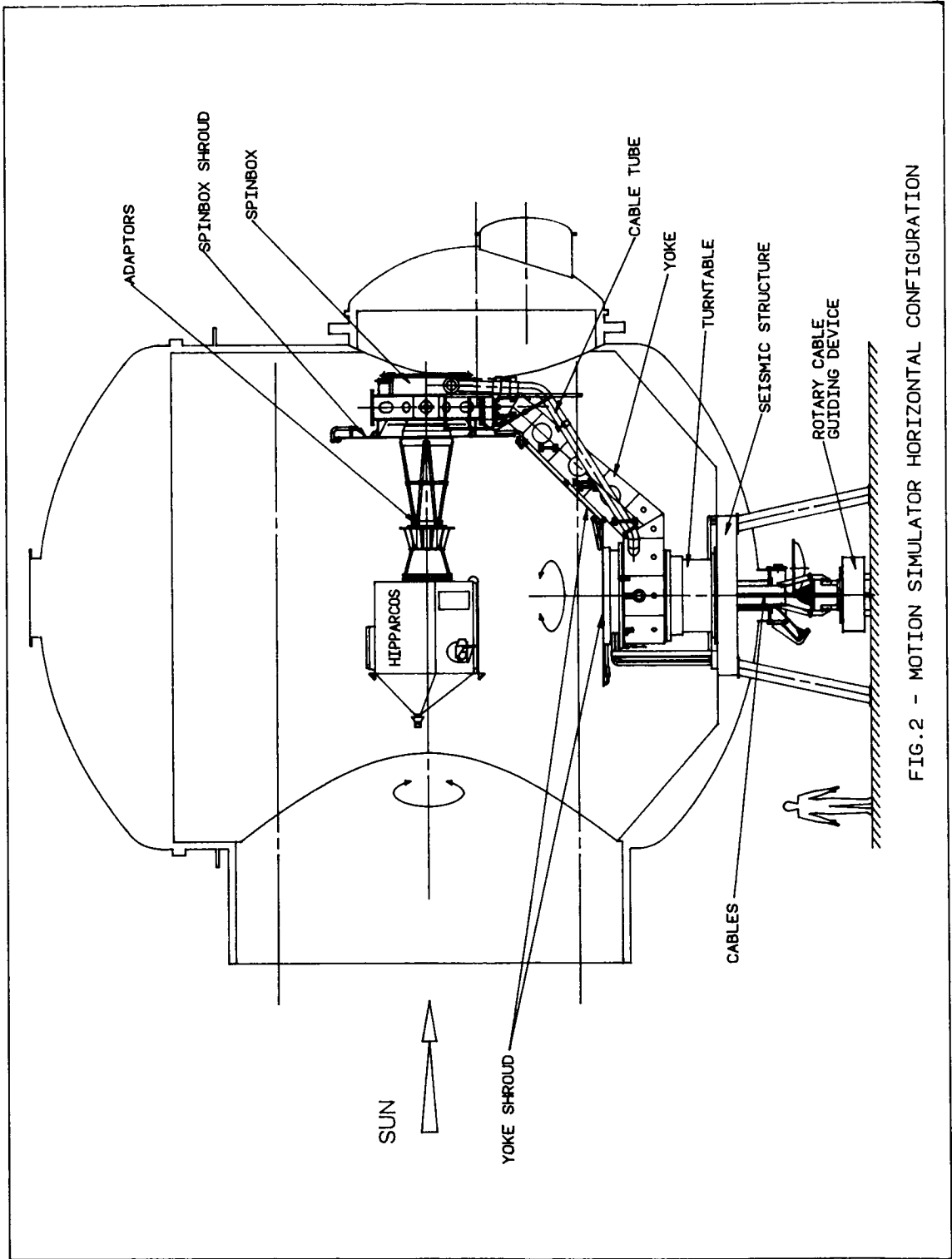
FIG.2 - MOTION SIMULATOR HORIZONTAL CONFIGURATION

ADAPTORS

SPINBOX SHROUD

SPINBOX

CABLE TUBE

YOKE

TURNTABLE

SEISMIC STRUCTURE

ROTARY CABLE GUIDING DEVICE

HIPPARCOS

CABLES

YOKE SHROUD

SUN

7m TESTSPHERE

PINION

CYCLO DRIVE

BACK COVER

SEALS

TEST SPECIMEN
INTERFACE

VACUUM
FEEDTHROUGHS

SLIPRING

CROSS-ROLLER BEARING

CABLE TUBE

MOTOR

SHROUD SPINBOX

YOKE INTERFACE
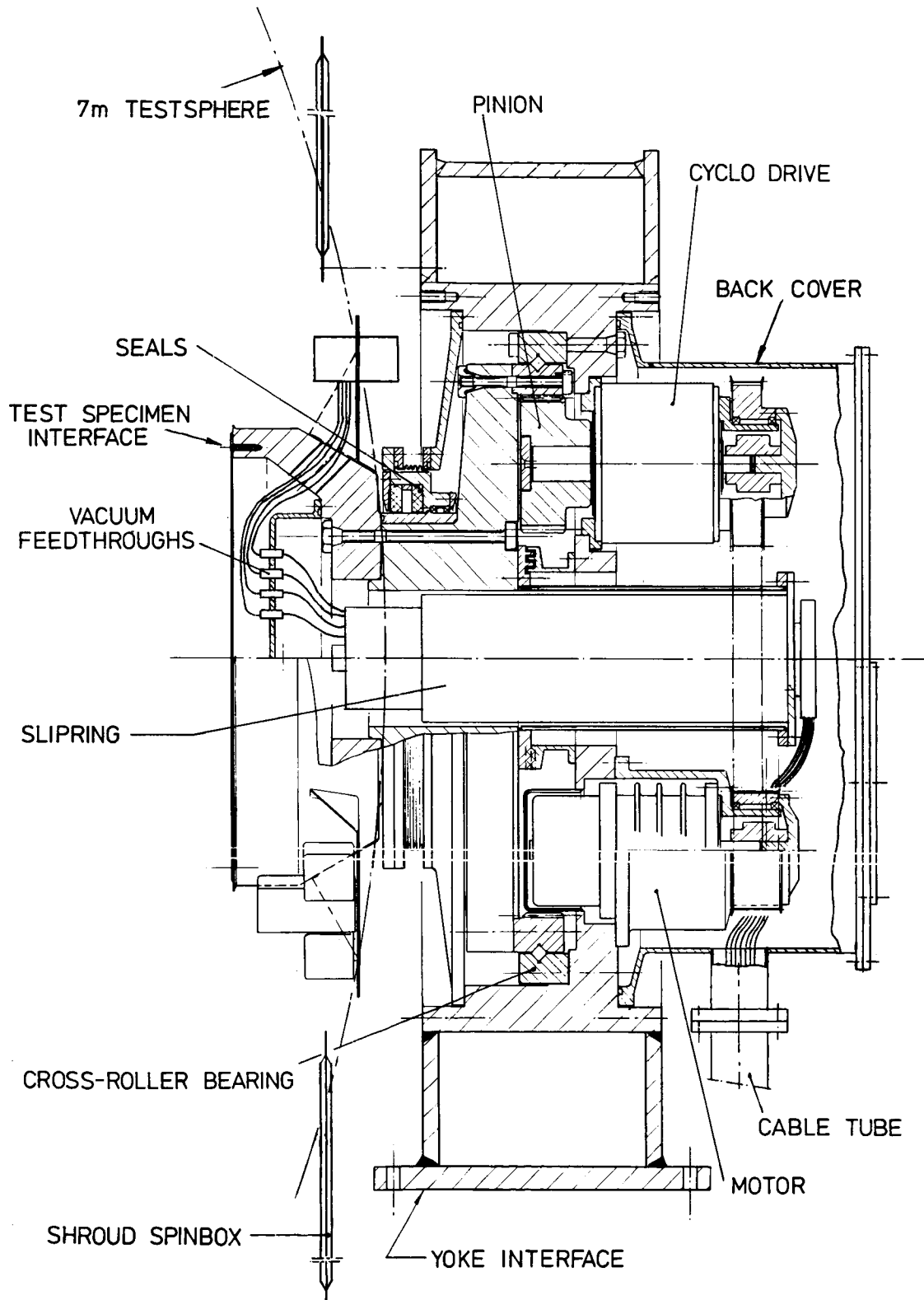
FIG. 3 SPINBOX SCHEMATIC OVERVIEW

YOKE

TURNTABLE (CROSS SECTION)

DRIVE MOTOR

CABLES

PLUGPLATE

ROTARY CABLE GUIDING DEVICE

SEALS

CROSS-ROLLER BEARING
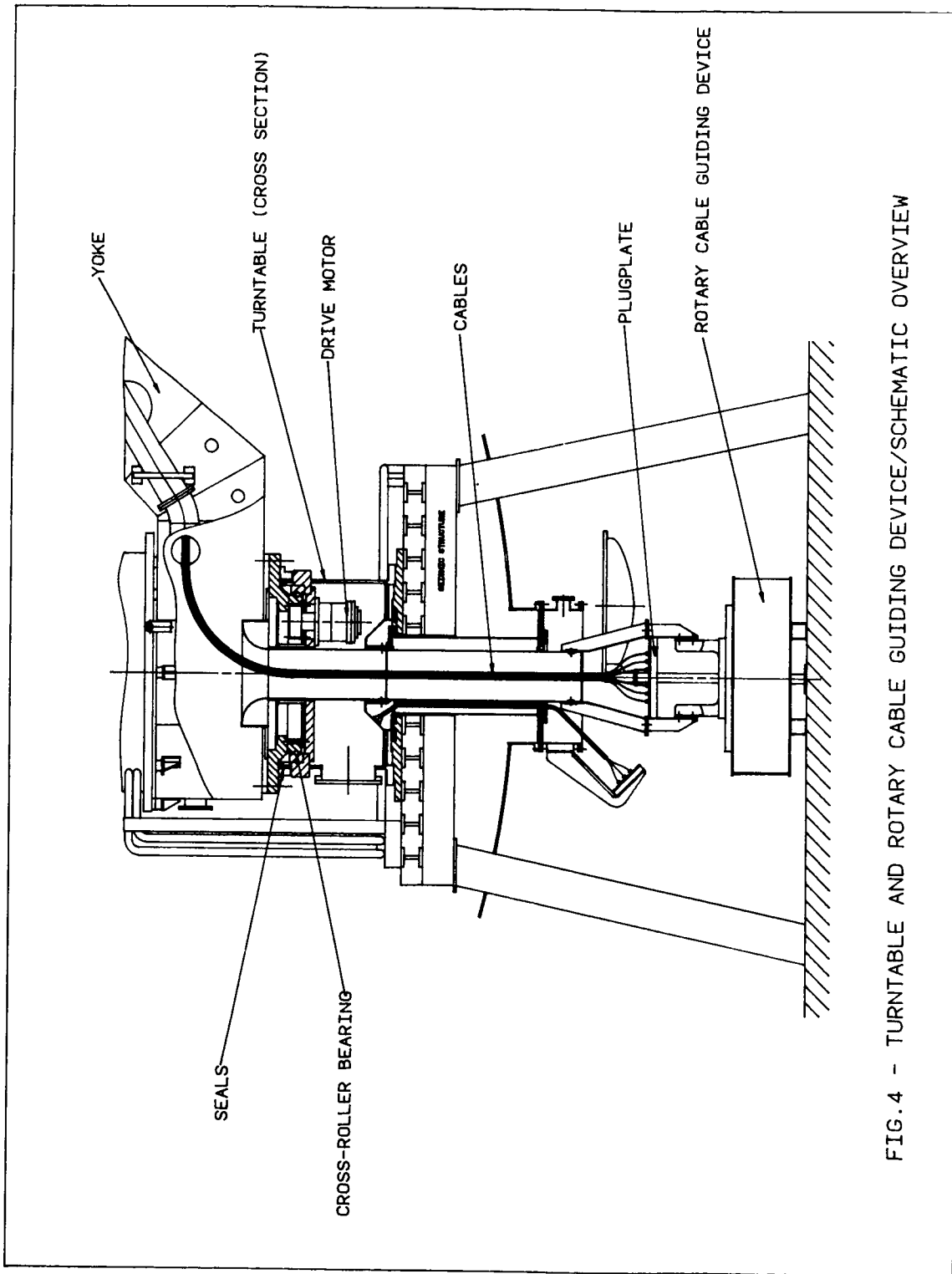
FIG.4 - TURNTABLE AND ROTARY CABLE GUIDING DEVICE/SCHEMATIC OVERVIEW

FIG. 5 – MOTION SIMULATOR IN VERTICAL SPIN AXIS CONFIGURATION DURING
ACCEPTANCE TEST. SPIN AXIS 30° TILTED.
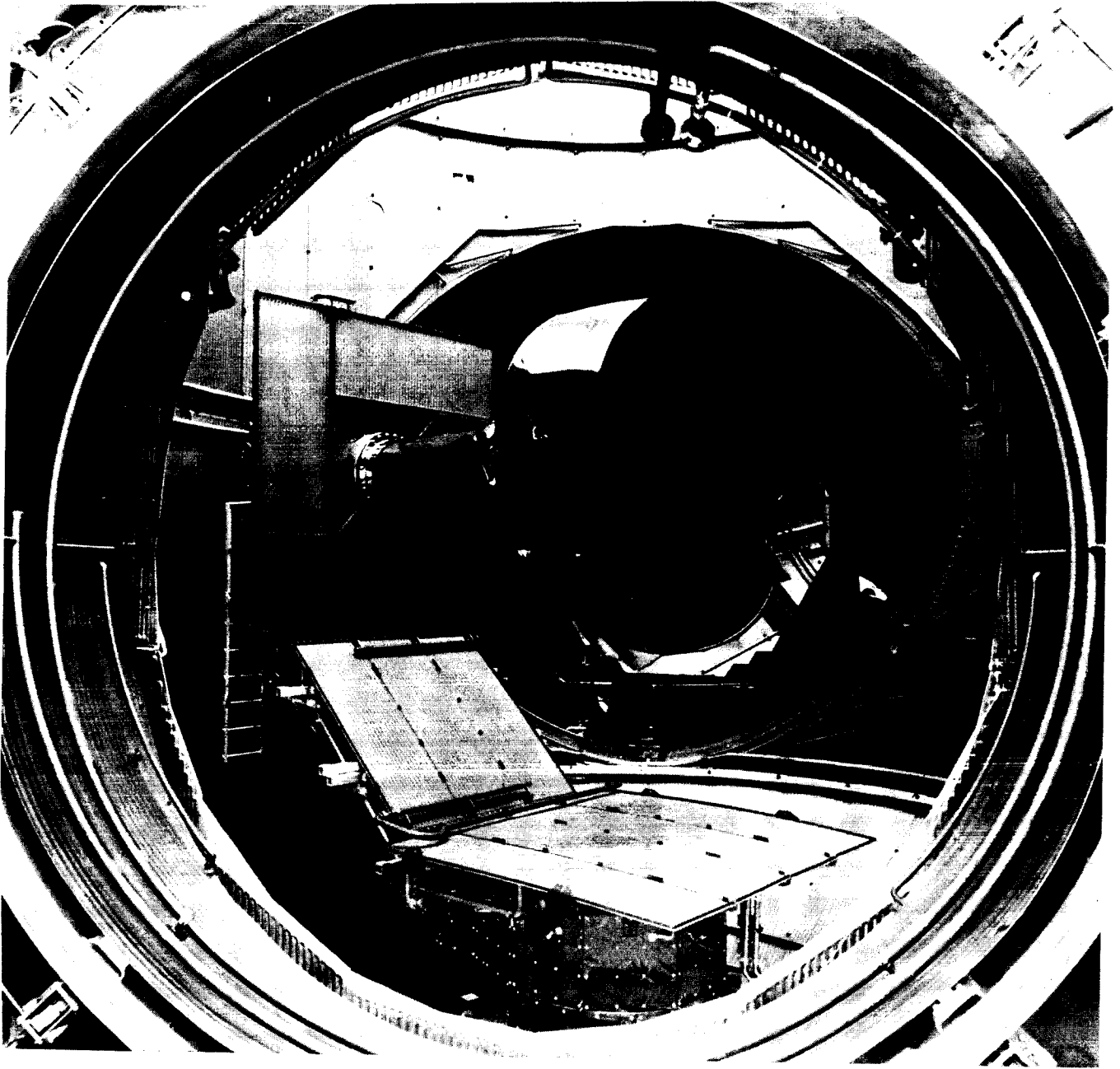
FIG. 6 – MOTION SIMULATOR IN HORIZONTAL CONFIGURATION
DURING ACCEPTANCE TEST.

# INDIAN LSSC FACILITY

A. S. Brar
High Vacuum Equipment Corp.

V. S. Prasada Rao
Bharat Heavy Plate & Vessels Ltd

R. D. Gambhir and M. Chandramouli
ISRO Satellite Center

## ABSTRACT

The Indian Space Agency has undertaken a major project to acquire in-house capability for thermal and vacuum testing of large satellites. This large Space Simulation Chamber (LSSC) facility will be located in Bangalore and scheduled to be operational in 1989. The facility is capable of providing 4 meter diameter Solar Simulation with provision to expand to 4.5 meter diameter at a later date. With such provisions as controlled variations of shroud temperatures, and availability of infrared equipment as alternate sources of thermal radiation, this facility will be amongst the finest anywhere. This paper presents the design concept and major aspects of the LSSC which is currently under construction.

## INTRODUCTION

A Large Space Simulation Chamber (LSSC) with 4-meter solar beam expandable to 4.5 meters is being erected at ISRO Satellite Center, Bangalore, India with projected completion in late 1989. This facility, upon completion, will be used for the purpose of solar simulation tests, thermal-vacuum tests, infrared mode thermal balance tests, and vacuum temperature tests on satellites. Besides these, the chamber may be used as vacuum temperature envelope for deployment tests of panels/antenna, Thermal cycling of solar panels, optical tests, and dynamic balancing of various space craft hardware.

## SYSTEM DESCRIPTION

The baseline configuration of the LSSC consists of two-part 304 SS chamber; the 9-meter diameter vertical main chamber and 7-meter diameter horizontal auxiliary chamber. The horizontal chamber is juxtaposed onto vertical chamber which will accept the test satellite mounted on a vibration isolation support platform via a motion simulator. The auxiliary chamber houses the collimating mirror, and the spout with chamber window provides interface with the lamphouse. The lamphouse houses lamp modules, transfer optics and the douser in a protected environment. The vacuum chamber is lined with shrouds through which nitrogen is circulated to attain temperature in the range of 100K to 373K. The entire facility is operated from a centrally located control console. There are six normal modes of the LSSC operation, and are described as follows:

Vacuum Mode:
This is for the purpose of dynamic balancing and other mechanical tests wherein the chamber shrouds remain at ambient, and the pressure is selectable at 1 mbar and $10^{-5}$ mbar. The main chamber shrouds are designed to be removable in order to gain larger working envelope in this mode.

Vacuum and Cryogenic Mode:
This mode is for the purpose of thermal tests in the infrared mode or eclipse situation wherein the chamber pressure is held less than $10^{-5}$ mbar, and the shrouds are held at 100K by means of recirculating subcooled $LN_2$.

Solar Simulation Mode:
In this mode the solar simulator is 'ON' under high vacuum conditions

with shroud temperature 100 K similar to the Vacuum and Cryogenic Mode.

## Vacuum-Temperature/Thermal Vacuum Mode:

This mode is for thermal vacuum testing and bakeout wherein the shrouds can be maintained at any programmed temperature for any interval of time in the range of 173 K to 373 K under high vacuum conditions of less than $10^{-5}$ mbar. The Constant density $GN_2$ dense gas circulation system is provided to attain the desired temperatures.

## Solar Simulation Calibration Mode:

This mode is for intensity distribution of the solar beam wherein the solar simulator is turned on under ambient temperature and pressure in the chamber.

## Mirror Degas Mode:

In this mode, the collimating mirror housed inside the auxiliary chamber is heated/cooled from ambient to 393 K and back to ambient by means of $GN_2$ dense gas circulation system at the rate of 5K/hr. with the chamber shrouds lagging behind the mirror temperature.

## DESIGN DESCRIPTION

The following provides some of the salient design features of various components/subsystems of the LSSC.

## Chamber:

The design of the chamber is in accordance with ASME Sec. VIII/BS 5500. The 9-meter main chamber accommodates the test payload. The 7-meter auxiliary chamber housing the collimating mirror and the spout for solar beam entry is juxtaposed onto the main chamber. The 4-meter cutout for the main entry and provision for top loading of the test payload onto the motion simulator platform by means of an overhead crane are also provided in the main chamber. The chamber shell is made of 304L stainless steel, and all external stiffeners are A-36 steel, with inner surface polished to reduce contamination and minimize

heat in-leak. Provisions of illumination inside the chamber are made, operable under vacuum conditions to facilitate mechanical tests as well as CCTV monitoring operations.

## Shrouds:

The shrouds are made of 304L stainless steel, single-embossed platecoil design. They are selected for ease of weldability and very low outgassing characteristics. Their outer flatside is electropolished to reduce emissivity thereby reducing heat in-leak from chamber walls, and the inner embossed side is glass-beaded and painted with flat black paint Sikkens 463-6-5. The shrouds are designed for maximum operating pressure of 100 psi, and can handle 100 KW internal load in conjunction with the $LN_2$ subcoolers. The shrouds are divided into 42 active flow controlled zones for temperature control of main and auxiliary chamber shrouds.

## $LN_2$ & $GN_2$ System:

The $LN_2$ system is designed for heat dissipation of 100 KW inside the main chamber, with localized flux of $2KW/M^2$. The $LN_2$ is circulated in sub-cooled condition by means of independent centrifugal pump systems for the main and auxiliary chamber shrouds.

The $GN_2$ system utilizes centrifugal blowers, maintaining constant density over entire working temperature by means of the active pressure control. The system is designed for 15KW heat load in the main chamber with localized heat flux of 1.4 $KW/M^2$. It is also capable of programmed warmup or cooldown of the shrouds in the temperature range of 100 K to 373 K at the rate of 1K/min.

## Vacuum System:

A helium cold gas cryopanel, located in the 4-meter port of the main chamber, is used as the primary high vacuum pump with free $N_2$ pumping speed in excess of 250,000 1/sec. The helium cold gas refrigerator/liquifier is

capable of supplying 92 watts/39 liters of $LH_e$ per hours from a single RS-compressor with $LN_2$ precooling. Two 48" cryopumps, each with nominal pumping speed for $N_2$ of 55,000 1/sec. with chamber shrouds at ambient are also provided. In addition, two 2200 1/sec. turbomolecular pumps, are installed to handle light gases, and to form a part of the pressure reduction system for use in conjunction with the RGAs. The main roughing system comprising a pair of identical skids, are equipped with roots-type blower cascades backed with the sliding vane mechanical pumps. These roughing systems can pump down the chamber from ambient to 1 mbar in under $1\frac{1}{2}$ hours.

## Solar Simulator:

The solar simulator consists of lamp modules, transfer optics and douser, all housed in a protected environment inside the lamphouse, and the main chamber window located in the spout along with the collimating mirror located inside the auxiliary chamber.

There are eleven 20-KW Xenon lamp modules for use with 4-meter beam size, which may be increased to fourteen 20-KW Xenon lamps to expand the beam to 4.5 meters. In either configuration the intensity range of 0.65 $KW/M^2$ to 1.7 $KW/M^2$ is provided with intensity uniformity of ± 4% in the reference plane at the center of the main chamber.

The collimating mirror is fabricated as a mosaic of 55 hexagonal mirrors positioned onto the mirror support structure supported inside the auxiliary chamber on a kinematic mount. The mirrors are made of an aluminum alloy, diamond turned and subsequently aluminized and anti-reflection overcoated for protection. The mirrors and the support structure are held at ambient temperature except during the mirror degas mode.

Lamp modules, transfer optics and lamphouse panels are cooled by close-loop D.I. Water System exchanging heat with the facilities refrigerated water

supply.

## Motion Simulator:

The motion simulator, fabricated from aluminum alloy, is designed to be installed on top of vibration isolation platform inside the main chamber. It is a two axis mount, providing tilt capability of ± 180° and adjustable spin rate from 0 to 10 rpm with drift less than 0.05 rpm as accumulated over any 24-hour period. The simulator is designed to handle payloads up to 3,000 kg with static unbalance-up to 100 N.M. and physical size of 4-meter diameter x 4.5 meter long.

The motion simulator is equipped with shrouds to provide the same temperature as the surrounding main chamber shrouds, while its main structure is maintained at near ambient temperature for satisfactory operation of critical mechanical components, such as bearings, etc. The MLI blankets are utilized to thermally isolate the support structure from the motion simulator shrouds to affect the required design criteria.

## Data Acquisition & Instrumentation Control System:

The LSSC test facility is a complex system consisting of the chamber vacuum system, shrouds and nitrogen circulation system, solar simulator and motion simulator along with auxiliary facilities, like $LN_2$ storage, etc. Each system has some parameters which require monitoring, processing and controlling in order to achieve the designed function. In addition, the space craft flight model, and subsystems within it require subjecting them to various tests within the chamber. In view of these requirements a computer based instrumentation control and data acquisition system has been implemented.

The overall system architecture includes the utilization of a 32-bit microprocessor as the primary host, and another such machine as the back up

237

host. The test satellite data acquisition is handled by four 16-bit monitor RTUs to provide capability for 1024 TC, 256 V, 256 I, 64 RTD, and 32 Strain data monitoring. Also forming a part of motion simulator is a 600 TC channel multiplexer located on the spin axis of the motion simulator. Four 16-bit Control RTU are employed to handle 128 infrared heaters, each handling 64 TC, 32 I and 32 V. The ninth 16-bit RTU is used to handle signals from thermal, vacuum, and auxiliary facilities systems.

The individual PLCs controlling thermal, vacuum and auxiliary facilities are connected directly with the host via the data highway. The PID loop controllers for shroud and mirror temperatures communicate with the host via RS-232C links, and with their dedicated processor through RS-422 links. The PLCs/microprocessors for the solar and motion simulators are also linked directly with the host.

Two operator terminals and four user terminals together with various numbers of dot matrix printers, line printers, video hard copiers, winchester, cartridge, mag tape and floppy drives constitute the peripheral equipment.

The PLCs along with the control and instrumentation and mimic panels are located in free standing control console which also provides the alarm and status of the total LSSC facility.

SUMMARY

The salient design concepts of the Indian LSSC, expected for completion in late 1989, will rank it amongst the best test facilities anywhere. It is equipped with solar, motion and infrared simulation capable of testing satellites up to 4 meters in size.

Session VI

# SPACE SIMULATION II

# THERMAL/STRUCTURAL DESIGN VERIFICATION STRATEGIES
## FOR LARGE SPACE STRUCTURES

David Benton
The Analytic Sciences Corporation

## INTRODUCTION

As space missions become increasingly ambitious, requirements for larger
and more precise structures have collided with demands for greater cost
effectiveness and more routine operations. This has led to a search for
alternate methods of verifying that key design/performance requirements
have been met. This search has resulted in increasing reliance on
analysis with less experimental verification. If this is to be done
without a large increase in technical risk, it is necessary to integrate
testing and analysis, looking at them as alternate means of reaching the
same end, each with its own peculiar advantages and disadvantages.

The substitution of analysis for test has been enthusiastically pursued
in the area of large space structures due to the difficulty of accurately
simulating the flight environment of the very large structures under
consideration. This applies to two principal areas:  thermoelastic
behavior and dynamic performance. This paper examines methods of
verifying thermal and thermoelastic performance. The options available
for ground thermal testing are summarized, and corresponding analytical
methods are enumerated. Finally, alternate paths which combine test and
analysis to arrive at a verified thermal/structural design are traced.
Options for reducing test requirements by testing smaller assemblies

and/or testing in simplified environments are outlined. A generic large deployable structure is examined in light of these considerations.

## GROUND THERMAL TESTING OPTIONS

Common thermal testing options are listed in Table I. Thermal test environments are selected with one of three goals in mind. One goal is to simulate the operational environment as closely as possible. Alternatively, the goal can be to impose appropriate environmental conditions which facilitate correlation of analytical models against test results. Both of these serve to verify the thermal design of the system under test. A third goal is to demonstrate the ability of a design ("qualification testing") or a particular item ("acceptance testing") to withstand expected temperature extremes. This last goal is often combined with an attempt to verify the thermal/structural design. Thermal/structural design of space structures must control the thermoelastic behavior of the structure. The design parameters include conductive heat paths, radiative exchange properties, active heater control, and structural design parameters. Generally, structural parameters are driven by nonthermal design requirements. The flight thermal environment includes direct solar radiation, planetary reflected solar radiation ("albedo"), planetary emitted IR radiation, and on-board heat loads.

Thermal testing goals are determined by the thermal/structural design verification approach. With one approach, the design is verified if the test article does not respond with unacceptable temperatures or distortions. Ideally, this approach requires very little analysis. However, the results are valid only insofar as the test environment is an accurate simulation of the flight environment and the test article conforms to the flight hardware. The alternate approach does not require an accurate simulation of the flight environment or precise duplication of the flight hardware configuration. In this approach an analytical model of the test article in the test environment is correlated against

actual test results. The resulting "test-validated model" is then modified to reflect the operational environment. This modified analytical model is then used to generate predictions of flight performance. In this case, the test environment is generally defined to bound "worst case" conditions of maximum temperature, minimum temperature, and/or temperature gradients predicted for flight. This relatively simple test environment is typically much easier to create on the ground than is a full simulation of the flight environment.

The test environment consists of heat sources and sinks. These can be convective, conductive, or radiative. A convective source or sink is simply temperature-controlled gas (dry air, $N_2$, etc.) in a (non-vacuum) thermal chamber. They cannot usually be used to generate large gradients. Conductive sources and sinks include temperature-controlled fluid loops, heaters contacting the test article, test article internal dissipation, and any supporting fixtures attached to the test article. Usually conductive heat leaks are minimized by test fixture design. Radiative sinks and sources are important in a vacuum environment since there is no convective heat transfer. Radiative sinks include shrouds which view but do not contact the test article. The shrouds themselves are temperature controlled by heaters and/or fluid loops. Shrouds become sources by definition whenever their temperature exceeds the temperature of the test article. Other radiative sources are IR lamps and solar simulation lamps. When shrouds alone are used, the flight environment is reduced to an "equivalent sink temperature" for the shroud. When IR lamps are available, or heaters can be attached directly to the exterior of the test article, an "equivalent sink heat rate" flux is used. In both cases accounting for solar radiation requires accurate knowledge for the test article's thermo-optical properties. Solar simulation lamps are used to directly simulate solar fluxes. These are commonly employed for geometrically complex test items where considerable doubt exists as to the solar flux levels resulting from reflections and shadowing between different parts of the test article. Internal electrical dissipation can be simulated by heaters if the actual electronics are not in place.

243

Costs increase rapidly with greater fidelity of the text environment to the actual flight environment. Nonvacuum thermal tests are the least expensive, but are incapable of creating realistic gradients because of high convective heat transfer rates. Thermal vacuum tests cannot simulate the spectral and reflecting/shadowing characteristics of the radiative flight environment without solar simulation lamps which greatly increase cost. At any given level of test fidelity, increasing the test article's size results in increased cost.

Data collected during thermal tests includes temperature, strain, displacement, heat fluxes and power usage, and test article function/ performance data. Function/performance data requirements are specific to each test article and can include both electrical and mechanical function data. Radiative heat flux is measured with radiometers. With heaters or electronic equipment, current flow is measured to determine heat rates. Temperatures are measured with thermocouples or thermistors. Strain gauges are used to measure local thermoelastic strain. Thermoelastic deformations are measured by mechanical or optical means. Depending upon the resolution required, photogrametry or interferometric optical methods can be used. In some cases large-scale thermoelastic deformations can be inferred from local strain measurements.

COMBINING TEST WITH ANALYSIS

Both thermal tests and analytical models can be considered in terms of input and output, as illustrated in Figure 1. Ideally, the relationship between input and output is the same for test and analysis. If this is true for the range of inputs seen during flight, analysis and test are interchangeable for use in predicting flight performance. In reality, there can be a significant discrepancy between analytical and empirical (test) performance. Analysis is generally less expensive and time consuming. Test is usually more representative of actual flight performance. Thus, the trade-off is between lower cost (analysis) and lower risk (test), keeping in mind that perfect tests are as impossible as perfect analyses.

244

Thermal analysis of a space structure actually involves a number of interrelated analyses, listed in Table II. A typical analysis flow is shown in Figure 2. Listed in Table III are types of thermal tests which have inputs and outputs corresponding to various analyses. If analysis alone is used for thermal/structural design performance verification, thermal testing is required only to qualify the structure and its components to the appropriate temperature and vacuum conditions.

It is often useful to test large structures as subassemblies, using analysis to extrapolate the performance of the total system. This is especially attractive if the heat flows between subassemblies are small or well defined. Some structures are periodic assemblies of identical subassemblies, allowing a single subassembly test to be readily extrapolated to the entire structure.

## DESIGN VERIFICATION OF A LARGE DEPLOYABLE TRUSS BEAM

A deployable truss beam which is representative of future large space structures provides an instructive example.

GENERIC DEPLOYABLE TRUSS BEAM

A number of deployable truss beam structures have been described in References 1 and 2. These structures consist of a series of collapsible bays. Generally, these beams have a slenderness ratio (deployed length/ deployed diameter) between 30 and 50 and an extension ratio (deployed length/stowed length) of about 20. The are deployed by a mechanism which extends each bay in turn and latches the joints. Reversing the process retracts the beam. For the purposes of this example, a 100 meter beam can be postulated, as shown in Figure 3. This structure could be used to deploy an experiment package from the Space Station. The beam and deployment mechanism can be easily designed to deploy a single bay vertically in a one gravity environment.

The thermal design must accommodate the requirements of the experiment on the truss beam tip. Thermal control of the truss beam structure is achieved passively with coatings. The deployment mechanism uses heaters plus insulation and coatings. This thermal/structural design is driven by three requirements. The first requirement is to survive the thermal environment without unacceptable degradation. The second is to reliably deploy and retract the truss beam in the flight thermal environment. Finally, thermal distortions must be minimized to avoid compromising the experimental data.

THERMAL/STRUCTURAL DESIGN VERIFICATION APPROACH

Verification of the thermal/structural design requires a combination of analysis and test due to the size of the deployed structure. The verification approach is summarized in Figure 4. Flight temperature predictions can be made from analytical models for both stowed and deployed configurations. A structural model can then be used to predict component stress levels due to thermal loads, as well as structural distortions. These analyses rely upon testing of individual elements (such as tubes and joints) and material samples for properties data. Key structural assemblies are proofloaded to levels incorporating the thermal loads. A single bay is cycled to the predicted extremes of temperature and stress. Because of the periodic nature of the beam structure, the behavior of a single bay is representative of the entire beam. Combined with thermal qualification testing of the materials and mechanisms, this test verifies that the structure will not degrade unacceptably in the flight thermal environment.

Verification of the deployment kinematics under flight thermal conditions involves the effects of both local and global thermal distortions. To evaluate local thermal effects, representative joints and mechanism devices are cycled through their full range of motion at predicted temperature extremes plus margin. This verifies performance of truss beam joints and the deployment devices. To verify deployment and

retraction under global thermal loads, the entire assembly undergoes a thermal-vacuum deployment and retraction test as shown in Figure 5. This adds confidence to the analytically predicted performance of the beam and the deployment mechanism. Although this test is relatively expensive, failure of the beam to deploy would be a costly failure. In addition, the heat exchange within a complex collection of devices such as the deployment mechanism is difficult to predict accurately. Because of the periodic nature of the beam structure, deployment of a single bay is sufficient to verify the kinematics. The beam is deployed in worst-case hot and cold environments, then the worst side-to-side gradient is imposed by adjusting shroud temperatures on opposite sides of the beam. These worst-case temperatures are those predicted by analysis.

Thermoelastic distortion predictions for the deployed beam cannot be directly verified by ground test because of vacuum chamber size limitations and gravity effects. Reliance is placed upon analysis plus measurements of the coefficient of thermal expansion of individual structural elements. Additionally, predicted temperature extremes and thermoelastic stress levels are used to cycle individual structural elements to determine the change in the thermoelastic properties of the elements after exposure to flight environment.

CONCLUSIONS

Requirements for space structures of increasing size, complexity, and precision have engendered a search for thermal design verification methods that do not impose unreasonable costs, that fit within the capabilities of existing facilities, and that still adequately reduce technical risk. This requires a combination of analytical and testing methods. This results in two approaches. The first is to limit thermal testing to subelements of the total system or to test the system only in a compact configuration (i.e., not fully deployed). The second approach is to use a simplified environment to correlate analytical models with

test results. These models can then be used to predict flight perfor-
mance. In practice, a combination of these approaches is needed to
verify the thermal/structural design of future very large space systems.

REFERENCES

1.  Mikulas, Martin M. Jr. and Harold G. Bush:  "Advances in Structural
Concepts" Large Space Antenna Systems Technology, 30 Nov - 3 Dec 1982,
NASA CP-2269

2.  Rhodes, Marvin D:  "New Concepts in Deployable Beam Structures",
Large Antenna Systems Technology, 4-6 Dec 1984, NASA CP-2368

**TABLE I - TERMINOLOGY AND INPUT/OUTPUT DATA
FOR TYPICAL THERMAL TESTS**

| Type of Test | Input Variables | Output Data |
|---|---|---|
| THERMAL (THERMAL CYCLE) - Test article immersed in a temperature-controlled dry gas bath | Test article bulk temperature(s) | Functional and survival data |
| THERMAL VACUUM - Test article in a vacuum environment with spatially uniform heat sources and sinks | Temperature(s) of the sink and/or test article | Functional and survival data |
| THERMAL BALANCE - Test article in a vacuum environment with spatially and temporally non-uniform heat sources and sinks | External heat fluxes ("Q -test") or sink temperatures ("T-test") | Test article temperature(s), especially gradients |
| SOLAR THERMAL VACUUM - Test article in a vacuum environment with spatially and temporally non-uniform heat sources including simulated solar flux and heat sinks | External sink temperatures and solar fluxes | Test article temperature(s) and incident fluxes |

**TABLE II - ANALYTICAL THERMAL MODELS**

**OF SPACE STRUCTURES**

| Type of Model | Input Data | Output Data | Typical General Purpose Program |
|---|---|---|---|
| Radiation Exchange | • Geometry<br>•Surface properties | •Internal radiation exchange factors | TRASYS |
| Heat Rate | •Exterior geometry<br>•Exterior surface properties<br>•External environment<br>•Radiation exchange factors | •Nodal heat fluxes and boundary conditions (BCs) | TRASYS |
| Thermal Balance | •Internodal conductances<br>•Nodal heat fluxes and BCs<br>•Radiative exchange factors<br>•Internal heat sources<br>• Nodal heat capacities | •Steady-state nodal temperatures<br>•Transient nodal temperatures | SINDA MITAS |
| Thermoelastic | •Structural BCs<br>•Element temperatures<br>•Element pre-loads<br>•Element stiffness<br>•Element coefficient of | •Displacements<br>•Rotations | NASTRAN |

TABLE III - CORRESPONDENCE BETWEEN TEST AND ANALYSIS

| Type of Test | Input Data | Output Data | Corresponding Analytical Model(s) |
|---|---|---|---|
| Thermal - Vacuum (Uniform heat sinks and sources) | External (uniform) sink temperature or test article temperature | Functional and survival data | Thermal balance (with simplified heat fluxes and BCs) + radiation exchange |
| Thermal Balance (Non-uniform heat sinks and sources) | External (non-uniform) sink temperatures and BCs | Test article temperatures (transient and/or steady-state | Thermal balance + radiation exchange |
| Solar Thermal-Vacuum | External sink temperatures and solar fluxes | Test article temperature (transient and/or steady-state) | Thermal balance + radiation exchange + heat rate |

If temperature-induced distortions are measured, then the thermoelastic analytical model is included among the corresponding analytical models
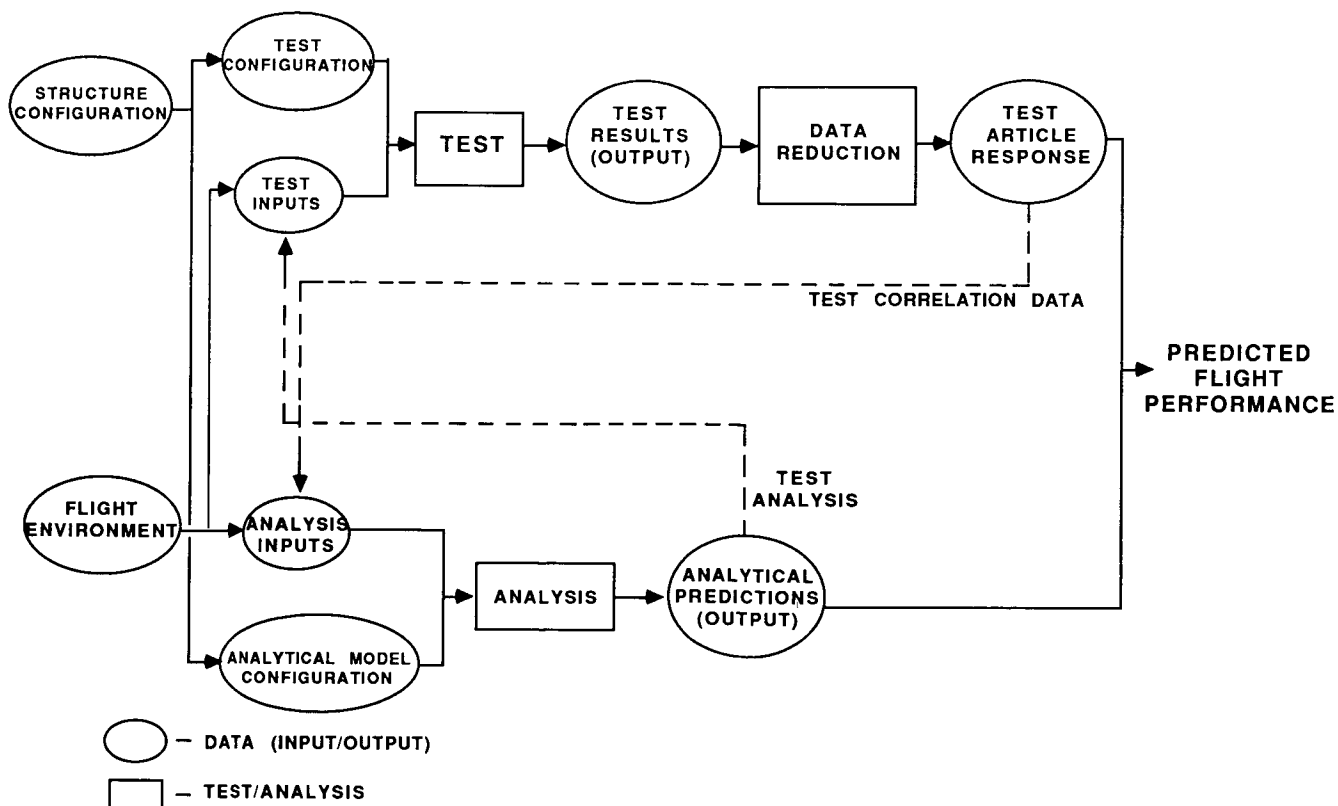


FIGURE 1. INPUT/OUTPUT RELATIONSHIP BETWEEN ANALYSIS AND TEST

# INPUTS

SURFACE GEOMETRY
SURFACE PROPERTIES

# ANALYTICAL MODELS

RADIATION EXCHANGE
MODEL

# OUTPUTS

RADIATION EXCHANGE
FACTORS

EXTERNAL ENVIRONMENT

HEAT RATE
MODEL

RADIANT (EXTERNAL) FLUXES

INTERNAL GEOMETRY
THERMOPHYSICAL PROPERTIES

THERMAL BALANCE
MODEL

TEMPERATURES
HEAT FLUXES

MECHANICAL PROPERTIES

THERMOELASTIC
MODEL

STRESS/STRAINS

SYSTEM CHARACTERISTICS

SYSTEM
PERFORMANCE
MODEL

SYSTEM PERFORMANCE

FIGURE 2. THERMAL ANALYSIS INPUTS, OUTPUTS, AND MODELS

SINGLE (DEPLOYED)
BAY

5 m

2.5 m

GRAPHITE/EPOXY
TUBE WITH
THERMAL COATING

LATCHING
JOINT HINGE
WITH THERMAL
COATING

BEAM DIAMETER
2.5 m

EXPERIMENT
PACKAGE

TOTAL
DEPLOYED
LENGTH
100M

BAY LENGTH
5m

STOWED LENGTH
5M

SUPPORT
STRUCTURE

STOWED CONFIGURATION

SUPPORT
STRUCTURE

DEPLOYED CONFIGURATION
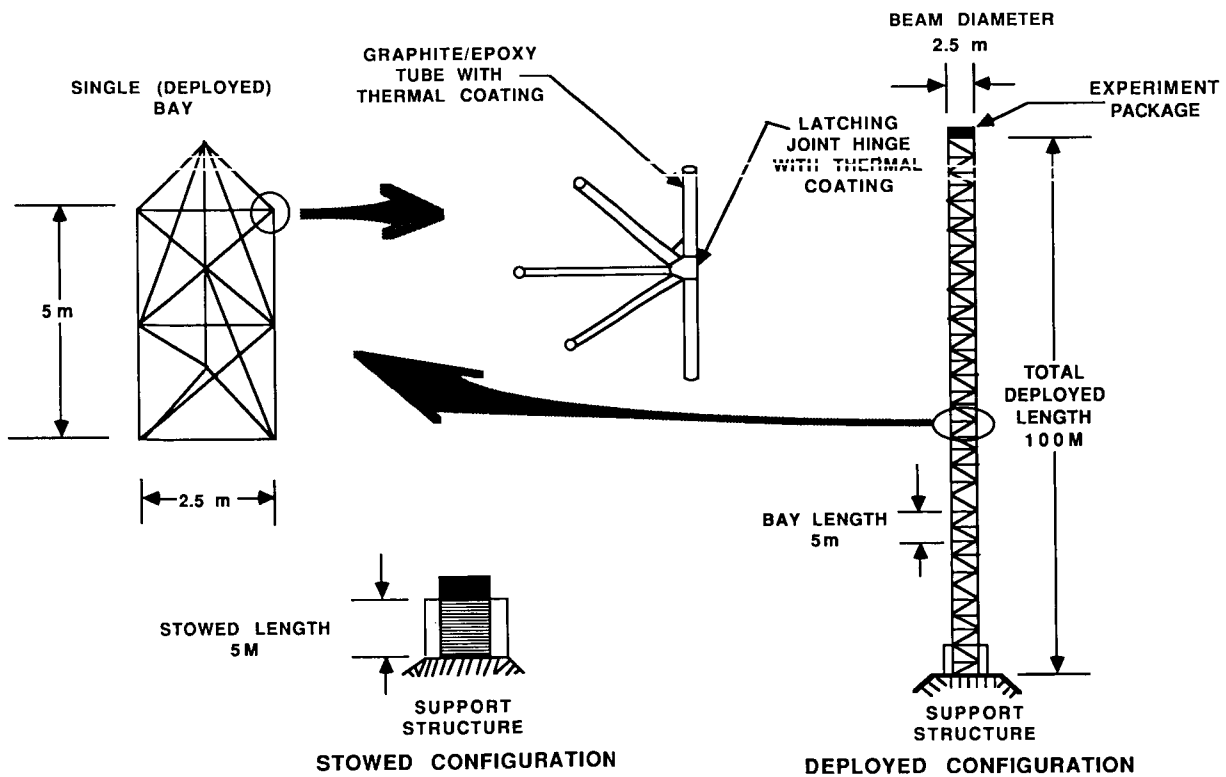
FIGURE 3. GENERIC DEPLOYABLE/RETRACTIBLE TRUSS BEAM

251
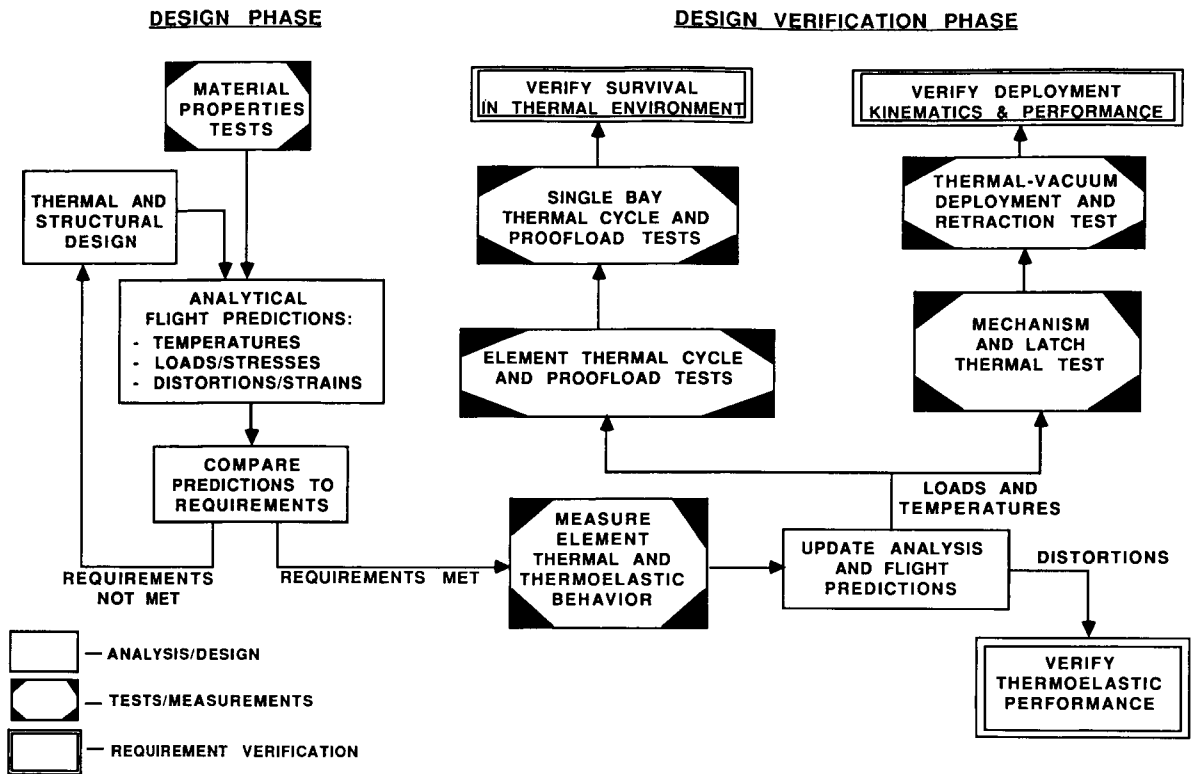
FIGURE 4. DESIGN VERIFICATION STRATEGY FOR GENERIC DEPLOYABLE TRUSS BEAM
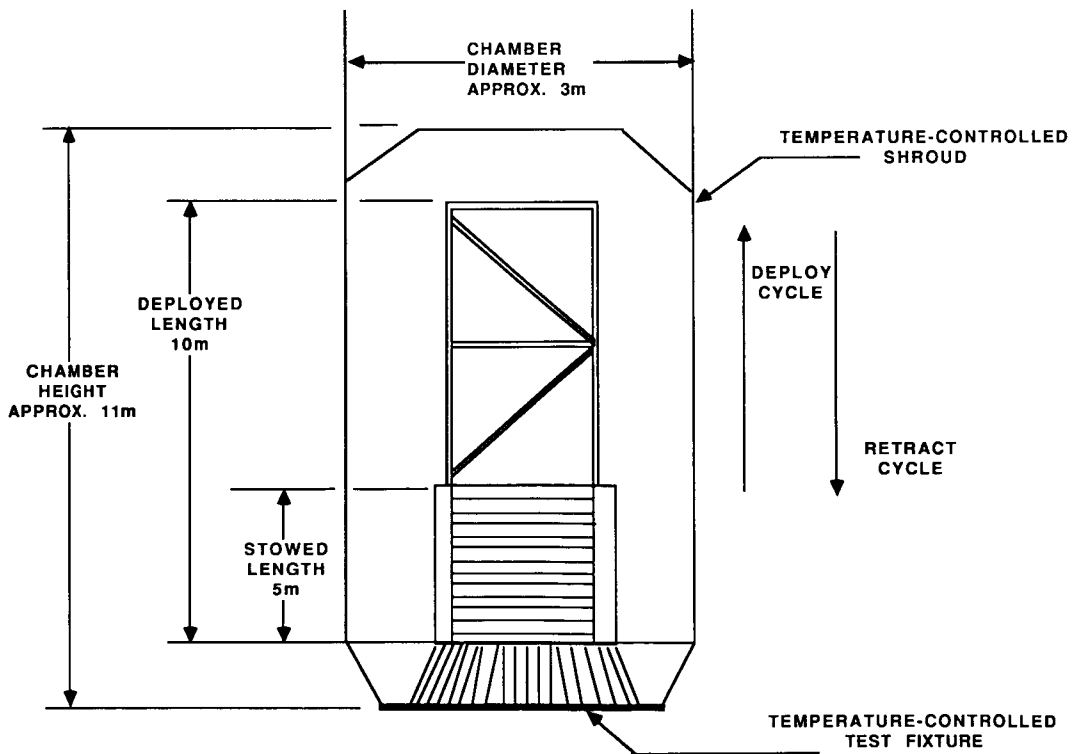
FIGURE 5. DEPLOYMENT/REFRACTION TEST CONFIGURATION IN VACUUM CHAMBER

# IRIS THERMAL BALANCE TEST WITHIN ESTEC LSS

Piero Messidoro and Marino Ballesio
AERITALIA SAIpa Space Systems Group

J. P. Vessaz
ESA/ESTEC

## ABSTRACT

The IRIS thermal balance test has been successfully performed in the ESTEC Large Space Simulator to qualify the thermal design and to validate the thermal mathematical model. Characteristics of the test were the complexity of the set-up required to simulate the Shuttle cargo bay and allowing IRIS mechanism actioning and operation for the first time in the new LSS facility. Details of the test are presented, and test results for IRIS and the LSS facility are described.

## INTRODUCTION

IRIS (Italian Research Interim Stage) is the first European launcher to complement the NASA Space Shuttle System with an expendable, spinning solid upper stage, capable of placing satellites into orbits with energy requirements beyond the Shuttle basic capabilities. The system consists of the Airborne Support Equipment (ASE) and the IRIS Spinning Stage (ISS).

The IRIS system is being developed by an Italian industrial team led by the AERITALIA Space Systems Group. The program is being financed by the Italian government through CNR/PSN (National Research Council/National Space Plan) and is now approaching the end of phase C/D.

The IRIS system verification philosophy is based on a three-model approach. One of the models is the Structural/Thermal Model (STM) which was subjected to the structural and thermal test campaign (thermal balance, modal survey, acoustic, spin and deployment, and static tests).

In order to qualify the thermal design and to validate the thermal mathematical models, the system has been tested in two configurations:

- ASE/ISS mode, simulating the IRIS system within the Orbiter cargo bay,

- ISS only mode, simulating the ISS system during the coasting phase after deployment from the Orbiter.

The ASE/ISS mode thermal balance test was performed at the beginning of 1987 in the Large Space Simulator (LSS) at ESTEC-Holland, and was the first test in this new facility.

To facilitate installation of the test article and its operations, and to provide representative Shuttle cargo bay interfaces, a multipurpose IRIS Test Support Hardware (ITSH) was developed by ESTEC and bolted directly to the "seismic structure" of the LSS.

This paper summarizes the characteristics of the IRIS thermal balance test in the LSS. It provides a description of the test article, set-up and facility; a report of the test sequence and events; and a presentation of the test results from both the IRIS and LSS facility point of view.

# IRIS SYSTEM

## CONFIGURATION

IRIS (ref. 1) is a system to launch satellites, with a maximum mass of 900 kg, from the Space Shuttle (fig.1). It takes the form of an upper stage of the family comprising Boeing IUS, McDonnell Douglas PAM D and PAM A and it covers the lower mass range suitable for scientific satellites and small communications/broadcasting satellites.

The IRIS system consists of two main modules:

- an Airborne Support Equipment (ASE) that is mounted in the Space Shuttle cargo bay. It supports the deployable stage and the payload during ground operations, as well as during launch and ascent up to the on-orbit separation. The ASE is a reusable module with all subsystems needed to fulfil the mission requirements;
- an IRIS Spinning Stage (ISS) that is the deployable and expendable part carrying the payload to be launched. The ISS is spin stabilized and has a solid rocket motor to provide the necessary impulse for payload insertion into transfer orbit.

The reusable ASE consists of a cradle in the form of a truss structure for mounting the deployable stage and its payload inside the Shuttle cargo bay. The cradle takes up 1/8 of the cargo bay length, measures 4.5 m wide, 4.5 m high and 2.1 m deep. It supports the deployable stage through the spin table (at the base of the solid rocket motor) and two restraints attached to the deployable stage payload attach fitting (PAF). The spin table can provide rates between 45 and 100 rpm to the ISS/satellite assembly.

On the cradle are mounted all the avionics which interface with both the Orbiter and the ISS, controlling IRIS functions and monitoring the health status of both IRIS and the satellite. A power supply controls and distributes power to all ASE subsystems, to the ISS and payload until deployment. The on-board computer is responsible for the operating sequence with delivery of commands to the various subsystems.

The cradle also supports the sunshield, which is environmental protection consisting of multilayer insulation of Betacloth and aluminized Kapton sheets. The sunshield has a fixed part as well as movable "clamshell" type segments that are opened to allow the ISS deployment. The movable segments are driven by an aeronautical type wiring mechanism with redundant motors and electronic control units.

The thermal environment is controlled using a full insulation approach. In fact, the cradle is also enveloped by multilayer insulation. This means that IRIS is completely insulated with respect to space. The internal environment is thermostatically controlled using ambient heaters attached to the cradle. This solution also provides suitable environmental protection to the ISS module and to the payload.

The ISS consists of a high performance solid rocket motor using a Kevlar case. The case, on one side, interfaces with the spin table and, on the other side, interfaces with the PAF, which is a truncated cone adaptor supporting a honeycomb platform on which are placed all the electronics necessary to fulfil mission requirements of the 45 minute coasting phase. Batteries and power control units control and distribute power to all ISS subsystems; the nutation control subsystem controls the coning of the composite, after deployment; and the electrical sequencing units command and control the preprogrammed mission sequence until final payload separation.

## TEST PROGRAM

As described in ref. 2, the verification of the IRIS system is based on several methods such as: test, analysis, similarity, inspection and review of design.

In particular, the test program is the most important part of the overall verification activities oriented to demonstrating that the IRIS design fulfils the performance requirements (qualification) and that the flight hardware/software is identical to the qualified one, free of workmanship defects and is ready to be flown (acceptance).

The models required to carry out the IRIS test program respectively at equipment, subsystem/module and system levels are outlined in fig. 2 with an indication of the relevant test activities.

In particular, the system structural/thermal qualification is performed on a dedicated model (STM) by means of the following tests:
- thermal balance (completed in April 1987)
- modal survey (completed in October 1987)
- acoustic (completed in January 1988)
- spin & deployment (completed in July 1988)
- static (to be completed in December 1988).

The STM is thermally representative of the IRIS system in its operational configuration, including flight standard structural and thermal parts and thermally representative dummies of the electronic equipment, the solid rocket motor and the payload.

# THERMAL BALANCE TEST DESCRIPTION

## TEST PHILOSOPHY

The purpose of the IRIS thermal balance test was to qualify the thermal design and to validate the mathematical model.

From a thermal design point of view it was necessary to verify the adequacy of the concept of full insulation (MLI all around IRIS) together with the multilayer insulation composition (verify number of internal aluminized layers). In addition, the behaviour of the ambient heaters had to be checked. The heat transfer from these heaters to the surroundings is via thermal radiation, whereas normally the heater foils are attached directly to the surfaces to be heated.

From a mathematical model point of view it was necessary to verify the model approach of the cradle truss structure, ambient heater representation and the MLI conductivity value.

To achieve these objectives, the most relevant flight phases were identified (see ref. 3). These were the pre-deployment quiescent phase with the flight heaters thermostatically controlled (400 W and 800 W), the worst hot and cold deployment phases with the opening of the sunshield; and a final recovery phase.

In addition to these phases (all transient) two steady state test phases had to be identified in order to:

correlate more easily some aspects of the thermal mathematical model (radiative and linear conductors, geometrical description, etc.),

identify well defined starting points for the transients.

As a general criteria it was attempted to be as close as possible to the flight temperature levels.

The above considerations led to the test sequence shown in fig. 3.

## TEST FACILITY AND SET-UP

### a) Test Facility

The test was performed in the Large Space Simulator (LSS) of the European Space Research and Technology Center (ESTEC) located at Noordwijk, the Netherlands. The commissioning of this facility took place in 1986 and it was officially inaugurated on January 14, 1987 at which time the IRIS-STM test preparation was underway at ESTEC. The LSS is undoubtedly the foremost installation of its kind in Europe (see ref. 4). This installation is composed of the following main parts:

- **LSS Chamber**

The chamber, with an overall volume of 2150 m$^3$, consists of two parts:
- the "main chamber", a vertical cylinder 10 m diameter and 15 m heigh,
- the "auxiliary chamber" with a horizontal cone/cylinder 11.5 m diameter and about max. 15 m long.

The two vessels are interfaced by a nozzle 8 m in diameter. The configuration is illustrated in figure 4.

### ●Shrouds

The inner surface of the main chamber and the nozzle are completely lined with shrouds. The surfaces facing the specimen are painted black and the remaining surfaces are polished. The auxiliary chamber is equipped with baffle (disc) shrouds. Liquid nitrogen is circulated in all shrouds. The achieved temperature during the test was 85 K with a temperature distribution of about 5 degrees celsius.

### ●Vacuum System

The full, high-vacuum pumping system was used during the test. It is composed of:

- 2 multivane pumps
- 3 root pumps
- 4 turbo molecular pumps
- 1 L He cryopump for $N_2$
- 2 cryopanels

The achieved vacuum was $7 \times 10^{-5}$ Pa with the following profile:

100 Pa (1 mbar) in 2 hours 30 minutes; 3 Pa in 6 hours; 7 x 10-3 Pa in 12 hours; $10^{-4}$ Pa in 18 hours.

### ●Sun Simulator

The lamp house of the sun simulator is equipped with 19 Xenon lamps of 20 kW each. Its transfer optic is put in a nitrogen environment to avoid ozone production and corrosion. A quartz window 1.08 m in diameter and 82 mm thick provides the interface between the vacuum chamber and the lamp house. The light beam coming from the lamp house is projected onto a collimation mirror 7.2 m in diameter that is suspended at the rear of the auxiliary chamber, and from there illuminates the test volume with a 6 m diameter parallel beam in the reference plane.

The sun simulator was used at two levels of sun intensity:

- $400 \ W/m^2$ achieved with 4 lamps,
- $1420 \ W/m^2$ achieved with 13 lamps.

The measured intensity distribution inside the test volume during the pre-test was within 7%.

The test volume is defined by a cylinder 6 m in diameter and 5 m long centered with respect to the axis of the main chamber.

### ●Data Handling Facility

The Data Handling Facility consists of two independent systems:

- the thermal data handling system dedicated to handling data from the test subject during thermal testing,
- the facility data handling system dedicated to data handling for thermal test facility control.

The thermal data handling system can provide data acquisition, reduction and presentation of a maximum of 1032 analog sensors and 128 digital sensors. The safety of the test article is assured by the generation of messages and alarm signals when sensors or derived values exceed pre-defined limits. Warning messages and signals are also issued on the basis of extrapolated values.

The reliability of the data handling system is assured by:

- a dual computer system where each computer checks the other
- a dual sensor measurement system
- high redundancy on peripheral equipment
- continuous monitoring of tasks under software control.

Data presentations, on color graphic monitors, terminals and printers, are available in the customer areas and, if needed, anywhere inside or outside ESTEC through the public telephone network (the latter was not used during this test).

By monitoring detailed facility parameters, the facility data handling system provides, both the test operation team and the customer, with fast up-to-data and accurate information on the performance of the facility.

Data are acquired directly from temperature, pressure, flow, solar intensity sensors etc. as well as through digital communication links with the LSS subsystems.

Early warning capabilities, integrated into the system to detect and analyse deviations from the nominal conditions at the earliest moment, ensure a safe and reliable operation of the facility at all times.

Spacecraft sensor information can also be included in the early warning capability. Performance data and warnings are presented in the facility control and data handling areas only.

During the test, 676 sensors were used as follows:
- 473 thermocouples installed on IRIS itself
- 34 thermocouples installed on the ITSH
- 31 voltage measurement channels from calibrated resistances to measure current of flight heaters and guard heaters
- 131 virtual sensors
- 25 power supplies for the infra-red lamps on the ITSH.


## b) Test Set-Up

The test article was placed on a dedicated structure called IRIS Test Support Hardware (ITSH) (see ref. 6). This structure allows the test article to be centered within the LSS test volume with the sunshield facing the collimation mirror.

The test set-up also included an additional set of 6 shrouds connected to the liquid nitrogen system of the facility; a Space Shuttle cargo bay simulator; and a gravity compensation system for the opening and closing of the sunshield segments. All these complementary elements were fixed to the ITSH structure. The test set-up is illustrated by the photographs in figures 5, 6 and 7.

### • IRIS Test Support Hardware (ITSH)

A special multipurpose structure has been designed to allow thermal tests on large items in the LSS with a representative Space Shuttle interface. ITSH was developed primarily to allow two different IRIS test configurations: in a horizontal position for the thermal balance test described here, and in a vertical position for a thermal vacuum test of the IRIS flight model.

Because of its modular concept, this structure is particularly flexible in use and allows easy adaptations for various test configurations and project specific requirements. The ITSH is illustrated in figure 8.

### • IRIS-STM Thermal Balance Test Configuration

In this configuration the ITSH permits the mechanical coupling with split bearings among the five IRIS trunnions (two main fittings, two stabilizer fittings and one keel fitting) onto the stable platform of the LSS chamber, and makes it possible to center the test article in its horizontal position within the solar beam.

The Space Shuttle cargo bay was simulated by means of a cargo bay simulator equivalent in size and thermal properties.

To allow opening/closing of the sunhield, a Gravity Compensation Unit (GCU) is also provided.

### • Cargo Bay Simulator

The cargo bay simulator is used to simulate the solar trapping phenomena that occur between the cargo bay walls and the cradle walls.

The cargo bay simulator consists of a light structure holding multilayer insulation of seven layers of Double-sided Aluminized Mylar (DAM) separated by polyester netting material. The insulation is covered on both sides by Single Aluminized Kapton (SAK) and, on the inside facing the test article, by Nomex polyester.

### •Additional Shroud System

Suitable cryogenic shrouds cooled by LN2 are installed under the sunshield plane to avoid the radiative heat exchange between the ITSH base structure and the test article.

### •Sunshield Gravity Compensation Unit

The Sunshield Gravity Compensation Unit (GCU) unloads the hinges of the sunshield segments during the test actuations by supporting them in the center of gravity. The GCU allows the automatic adjustment of the compensation weight and of its position with respect to the supporting rails.

### •Scaffoldings

To the basic test structure one can easily attach scaffoldings, working platforms as well as access bridges and telescopic stairs to reach the test article during installation and preparation activities in the test facility. All these elements are designed to be installed and removed quickly by two people.

**•Thermal Control**

For temperature control of the ITSH, 28 infrared lamps (500 W) were fixed to the legs and the base frame of the structure and 7 foil heaters were attached where infrared lamps could not be mounted. Eight additional infrared lamps were installed on the LSS stable platform. During the test the ITSH temperature was maintained at about - 50 degrees celsius. The power used was only 1 kW during the test and about 8 kW during the recovery phase.

**• Other ITSH uses**

The ITSH is also designed to be used for the IRIS flight model thermal vacuum test. This requires some modifications of the split bearings support legs and additional shroud elements. However, due to the modular concept of the ITSH, it is easily achieved at a minimum of cost.

In the mean time ITSH has also been used for the European Retrievable Carrier (EURECA) thermal balance test with minor adaptations to the basic ITSH elements.

The test set-up was completed by means of photovoltaic cell sensors to automatically control and measure the solar flux; a power supply and control unit to feed the IRIS dummy boxes; a sunshield special test equipment to remotely actuate and control the mechanism; and an observation camera system to control the actuation of the sunshield from outside the chamber.

## TEST PREDICTIONS

The thermal mathematical model (see fig. 9) used for the test predictions was basically the one already used in the analysis campaign for the thermal control design definition.

Changes were made to take into account the IRIS test configuration and the test boundary conditions.

The following items of the STM in the thermal configuration were not flight standard:

- the electronics, except for a few exceptions, were thermal dummies
- the motor was empty
- the bolt cutters were inert
- a dummy payload simulating the mass (900 kg) of a nominal payload was included.

The thermal vacuum chamber and the test fixture configuration were considered in the thermal mathematical model. The main implementations are the following:

- The introduction of a cargo bay simulator. This represented a compromise between the worst hot and cold conditions for IRIS in the Space Shuttle cargo bay. The front and the bulkheads were semi-circular; so it was possible to experience worst cold conditions in the cargo bay (high radiative link with space). The simulation of worst hot conditions was permitted by maintaining reduced gaps between the test article and the cylindrical part of the cargo bay simulator. This configuration allowed sun trapping to be simulated.
- The large collimation mirror was considered in the pre-test thermal mathematical model for two reasons: the large dimensions (viewfactor between mirrors and test article around 0.05); and the temperature during the test that was maintained at + 20 C for contamination reasons. It was represented in the thermal mathematical model by a disc (7.1 m in diameter) having the thermo-optical properties of the mirror.
- The chamber was modelled as a sphere of radius 18 m centered on the IRIS axes. It was considered a boundary with the following properties: absorptivity and emissivity equal to 1, temperature of 100 K. The true absorptivity and emissivity of the shroud is 0.9. However, due the large size of the chamber with respect to the ASE, multiple reflections can be ignored.
- The trunnions were made adiabatic by the application of guard heaters on the test fixture side of the attachment interface. All linear conductors between ASE and the cargo bay have therefore been deleted.

In order to perform the test successfully and safely, a set of pre-test temperature and power level predictions were required. All the test phases were analysed except the pump down/cool down and warm up (ref. 5).

The thermal analysis predictions for the two steady states allowed the determination of the ambient heater power level to reach the correct mean temperature range inside the IRIS: 100 W for phase 2 and 60 W for phase 5.

The analyses for the two slow transients gave the duration of the two test phases: 25 hours for phase 3, and 23 hours for phase 6.

The analyses for the two deployment phases allowed the evaluation of the thermal behaviour of the operative electronics, particularly the flight-standard ones. To better appreciate the temperature trends the deployment phases were longer than planned in flight.

The analysis for the recovery phase gave an indication of the length of phase required.

It has been found that the general level of temperatures within the ASE is very sensitive to variations in the parameters: solar intensity, flight heater power and MLI conductance. A sensitivity analysis was therefore performed in order to assist in the adjustment, during the test, of the power levels to meet the test objectives. Under the same conditions a double or a half thermal conductance of the MLI gave a variation in temperature of $\pm 10°$ C.

## TEST EXECUTION

The test required an intense test preparation and pre-test period of about three months.

Before the proper test execution could start, the following pre-test activities were performed:

- sun simulator calibration two weeks before test article arrival
- calibration (e.g. thermocouples, sun simulator cells)
- pre-test of the ITSH to verify the leak tightness of the specific shrouds, to monitor the cool down of the structure and to check the effectiveness of the heaters; to perform the leak test during video filming and window observation; to check the proper operation of the LSS in the test configuration. This pre-test revealed defects in painting of the ITSH specific shrouds. Repainting was done and the shroud panels successfully retested in time.

The test itself was carried out during February, 1987. The test started on the morning of February 20 and terminated at night on February 27 following the phases as specified in the applicable procedure (ref. 7). The only exception was the deletion of phase 8: "earth facing recovery" because during the previous preparatory phase, with sunshield closing, a failure occurred and the movement stopped at 1/4 of the run.

The failure was due to the unexpected change in the size of a bearing of the GCU system wheel when exposed to the sun flux. In fact, the sunshield closed as soon as the temperature decreased.

Apart from this failure, the test was considered satisfactorily executed from both points of view: LSS performance and IRIS behaviour, as extensively described within ref. 8 and 9.

During the execution of the test, standard mass-spectrometric measurements were performed to monitor the quality of the LSS vacuum. Seven sensors were placed inside the facility during the test to control organic contaminant (hydrocarbon equivalent and ester equivalent). The measured values were less than $1.3 \times 10^{-7}$ gcm$^{-2}$.

## TEST RESULTS

The test results confirmed a high level of confidence in the ASE/ISS thermal design.

Generally the temperatures of the test were in accordance with the predicted ones.

In the two steady states the internal environment of IRIS was as predicted (temperature level around $15°$ - $18°$ C). These results mean that the design of the thermal blankets and the concept of full insulation are acceptable and allow adequate control.

The results from the two slow transients showed that the duration of the 2 phases are 25.5 hours for phase 3, and 21 hours for phase 6. The differences from the prediction are very small: 2% more and 8% less in time respectively. This result confirms the design of the MLI. Moreover, it shows that the ambient heaters work properly and that the thermostat set points are adequate. The location of these thermostats (on the ISS annular plate) is acceptable.

The considerations that arise from the evaluation of the results of the two deployment phases are in accordance with the above statements.

During the hot deployment phase, when the sunshield was open, some items reached relatively high temperature values. They are: the cylindrical structure that connects the SRM and the spin table; the springs; and the clamp band of the separation subsystem. The temperature was around 40° C. This problem led to the reconsideration of the requirements for these items. The temperature excursion, however, was considered acceptable, because the test conditions of this phase were conservative.

As already explained, it was not possible to have information on the recovery time from the hot excursion, owing to the sunshield failure during the closure phase.

Taking into account all of the above considerations, the thermal design of IRIS is considered qualified (see ref. 8).

Suitable test correlations have been performed to compare the test results with the post-test predictions which were updated by introducing actual test boundary conditions (shroud temperatures, heat dissipation, measured thermo-optical properties, power on/off times, etc.). The correlation criteria (delta temperature predicted/measured less than 1.5° C, standard deviation less than 3° C) were reached for all IRIS internal nodes requiring only a few mathematical model modifications. An example of the statistical histogram for phase 2 is shown in fig. 10. Details of the correlations are contained in ref. 10.

## CONCLUSIONS

The execution of the Thermal Balance Test allowed the achievement of the stated goals. The thermal design of IRIS has been qualified. The thermal mathematical model has been updated and validated, and is now ready to be used for IRIS payloads.

The cargo bay simulator allowed the creation of the in-cargo bay boundary conditions. This approach gave suitable results, together with the overall test concept.

This first operational test with the LSS was carried out without problems. The facility performed well and good results were obtained, in particular, concerning the stability and uniformity of the solar intensity in the test volume. The facility showed a very good efficiency which resulted in low operational costs.

Interesting facility information was collected for later improvements.

## REFERENCES

1 E. VALLERANI, F. VARESIO and L. BUSSOLINO "IRIS - A New Italian Upper Stage System"
   IAF-83-25 (Paper IAF Budapest 1983)
2 M. BALLESIO, M. MODENA
   "IRIS Assembly, Integration and Verification Plan"
   IS-PL-AI-008 (AERITALIA Doc.)
3 R. PAVANELLO "IRIS Thermal Balance Test Specification"
   IS-SP-AI-022 (AERITALIA Doc.)
4 P. W. BRINKMANN "Main Characteristics of the LSS at ESA/ESTEC", NASA CP-2340
   (Proceedings 13th Space Simul. Conference, Orlando 1985)
5 IRIS ASE/ISS Thermal Balance Pre-Test Predictions
   IS-RP-AI-121 (AERITALIA Doc.)
6 R. STOLK "Technical Specification for the ITSH for the Thermal Tests in the LSS at ESTEC" D4-4120-001/C
   (ESA/ESTEC Doc.)

7 G. NOARO "IRIS STM Thermal Balance Test Procedure"
   IS-PR-AI-038 (AERITALIA Doc.)

8 R. PAVANELLO "IRIS Thermal Balance Engineering Test Report"
   IS-RP-AI-124 (AERITALIA Doc.)

9 Y. COSTANTIN "IRIS STM Thermal Balance Facility Test Report"
   YTO/RAP/LSS/349/1.0/YC (ESA/ESTEC Doc.)

10 M. BOVERI "IRIS ASE/ISS Test Correlation Report"
   IS-RP-AI-132 /AERITALIA Doc.)
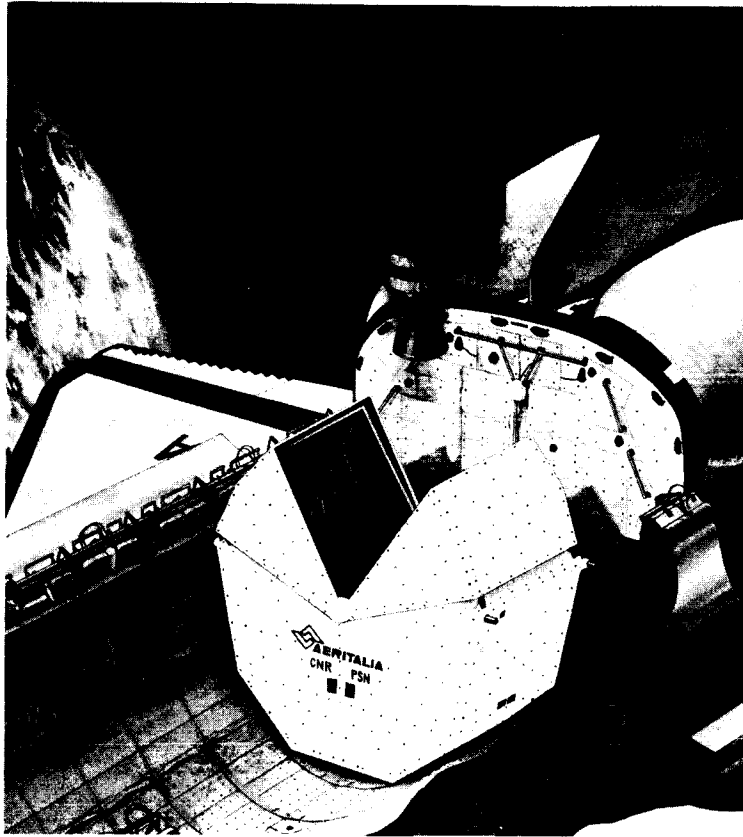
Fig. 1 - IRIS in the Space Shuttle
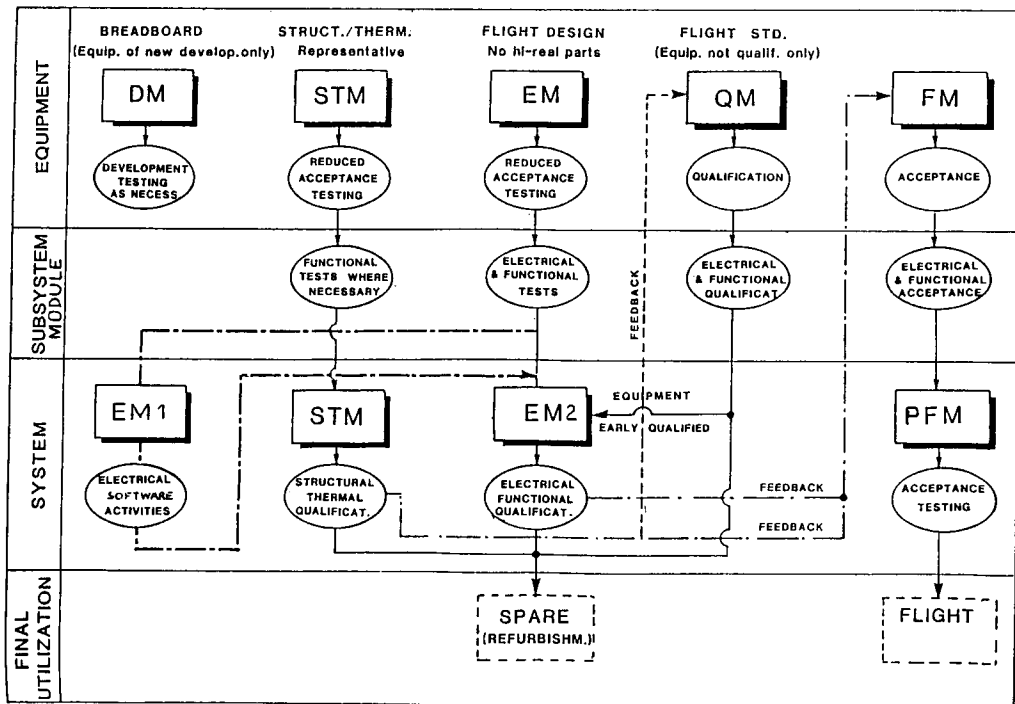


Fig. 2 - Model Philosophy

| PHASE NUMBER | 1 | 2 | 3 | 4 (1st part) | 4 (2nd part) | 5 | 6 | 7 (1st part) | 7 (2nd part) | 8 |
|---|---|---|---|---|---|---|---|---|---|---|
| PHASE DESCRIPTION | pump down cool down | earth facing steady state | earth facing cycling | cold active phase | cold active phase | earth facing steady state | earth facing cycling | hot active phase | hot active phase | earth facing recovery |
| SPACECRAFT ATTITUDE | | ↓FLUX | ↓FLUX | | | ↓FLUX | ↓FLUX | ↓FLUX | ↓FLUX | ↓FLUX |
| FLUX INTENSITY | zero | $400\ W/m^2$ | $400\ W/m^2$ | zero | zero | $400\ W/m^2$ | $400\ W/m^2$ | $1420\ W/m^2$ | $1420\ W/m^2$ | $400\ W/m^2$ |
| CHAMBER PRESSURE | from ambient to $< 10^{-3}$ Pa | $< 10^{-3}$ Pa | $< 10^{-3}$ Pa | $< 10^{-3}$ Pa | $< 10^{-3}$ Pa | $< 10^{-3}$ Pa | $< 10^{-3}$ Pa | $< 10^{-3}$ Pa | $< 10^{-3}$ Pa | $< 10^{-3}$ Pa |
| SHROUD TEMPERATURE | from ambient to 100 K | 100 K | 100 K | 100 K | 100 K | 100 K | 100 K | 100 K | 100 K | 100 K |

Fig. 3 – Test Sequence
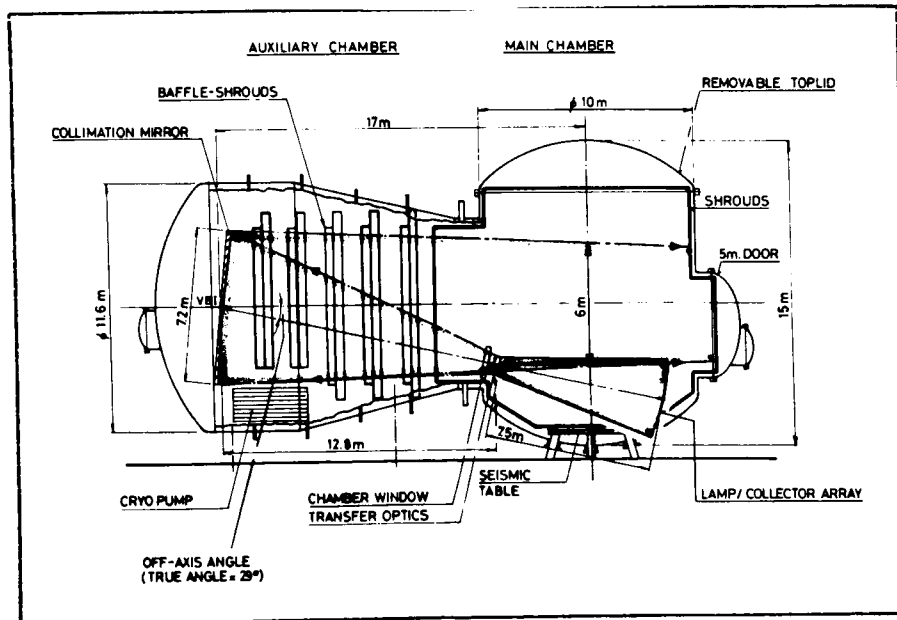


Fig. 4 – Lay-out of the Large Space Simulator (LSS)
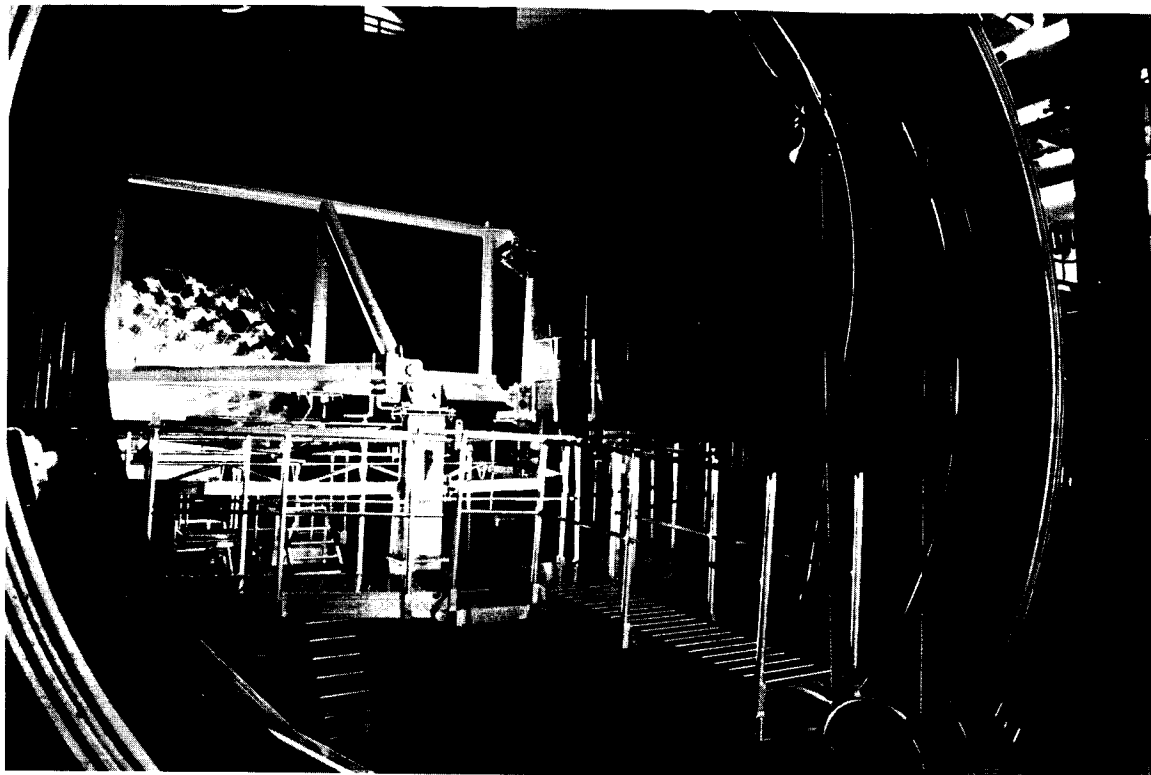
Fig. 5 – ITSH with dummy load frame inside the LSS
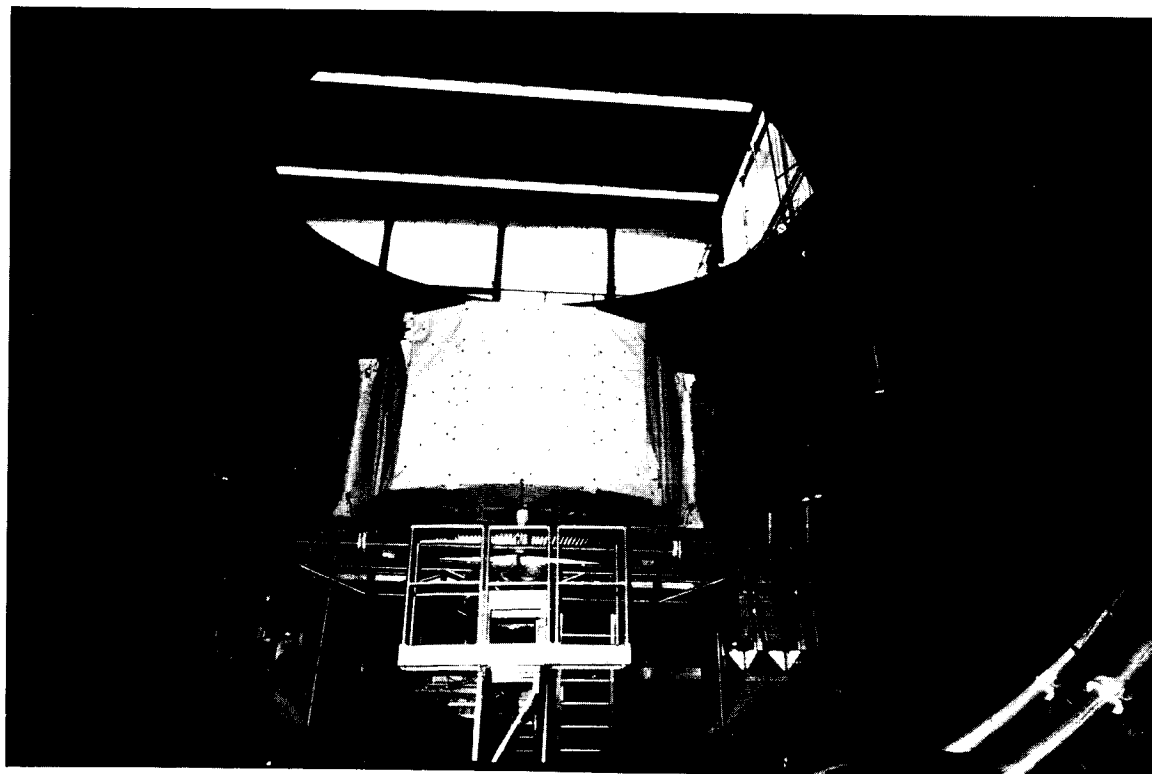


Fig. 6 – Test set-up front view
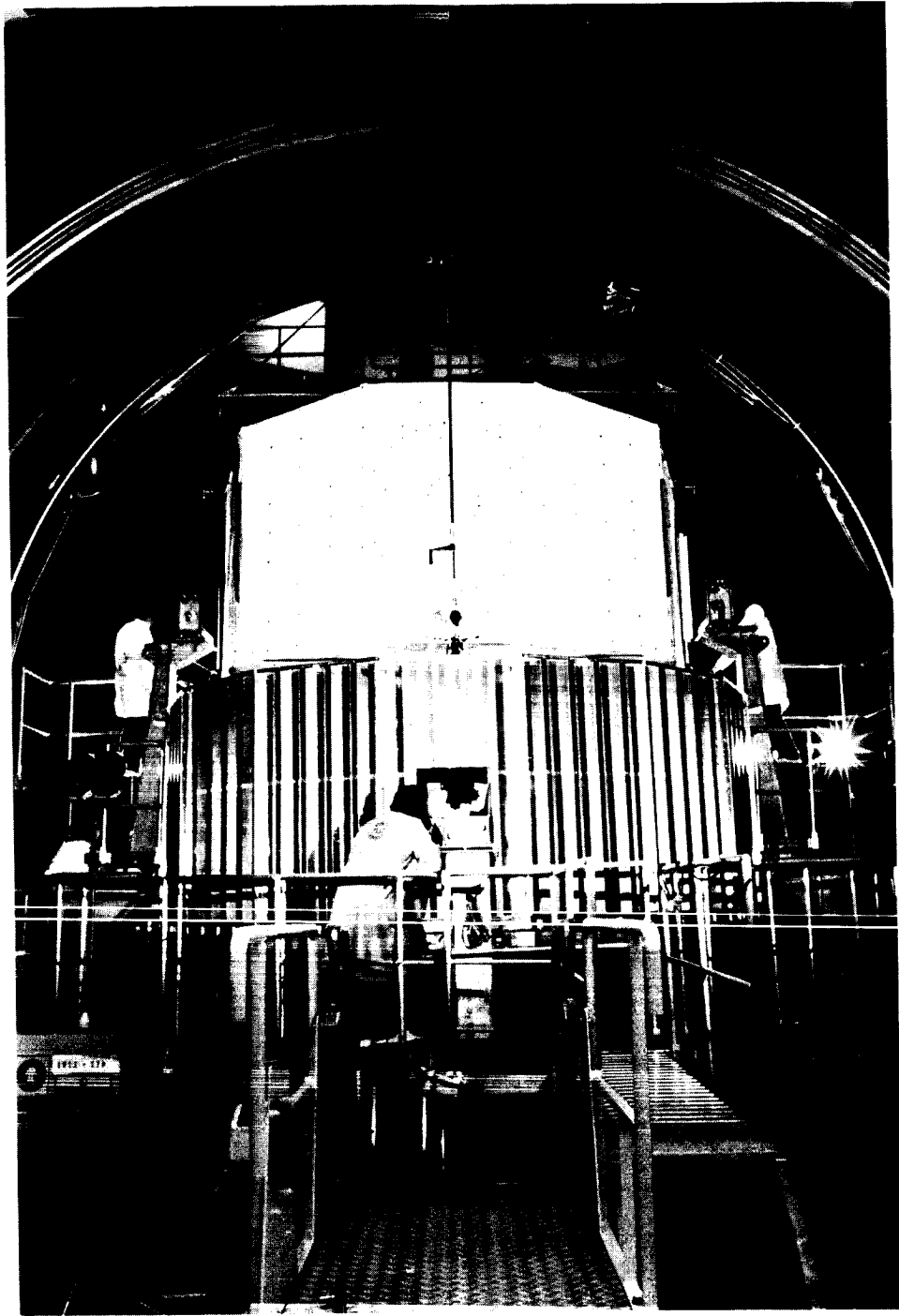
Fig. 7 – Test article installation in the LSS
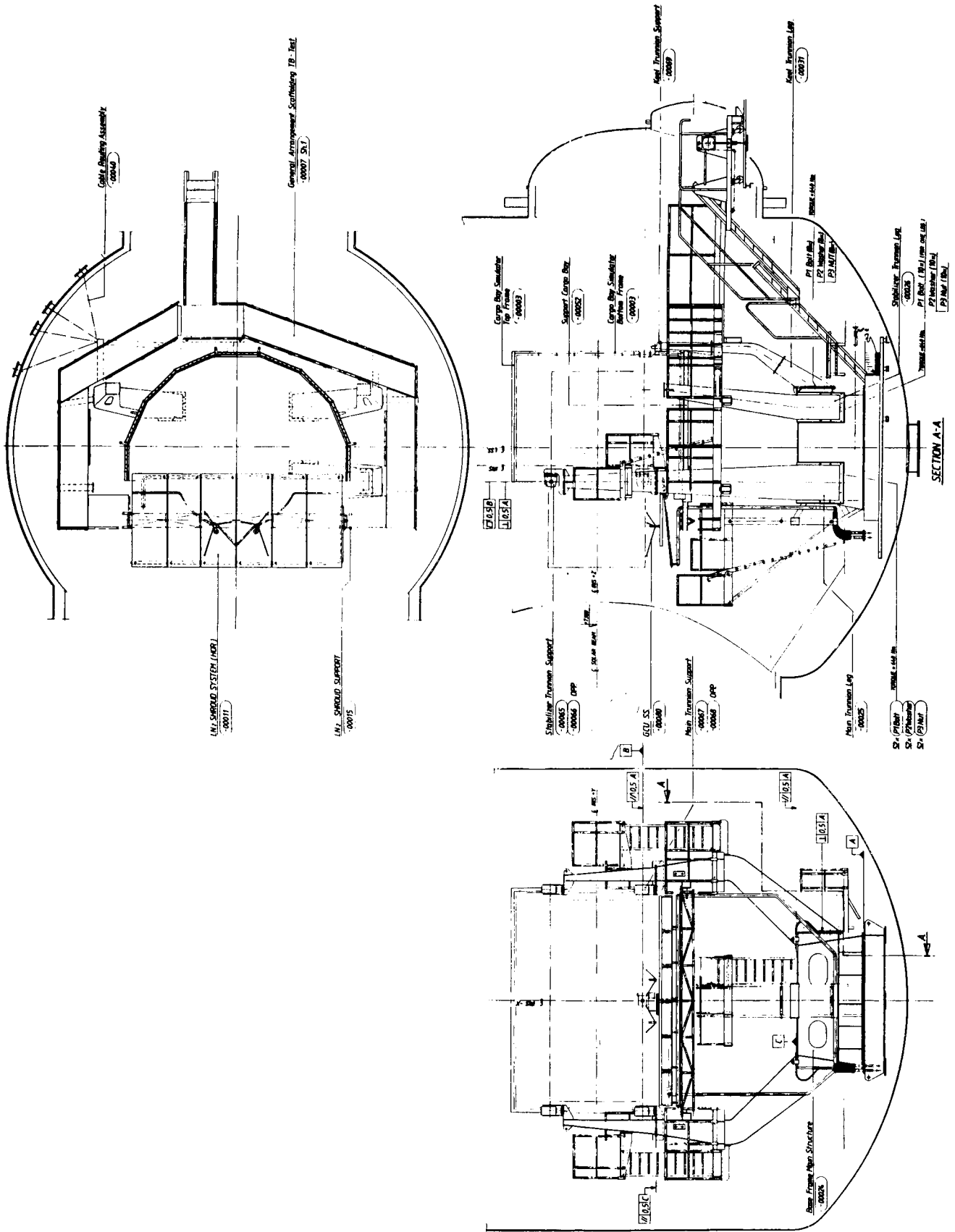
Fig. 8 – ITSH Thermal Balance Test Arrangement
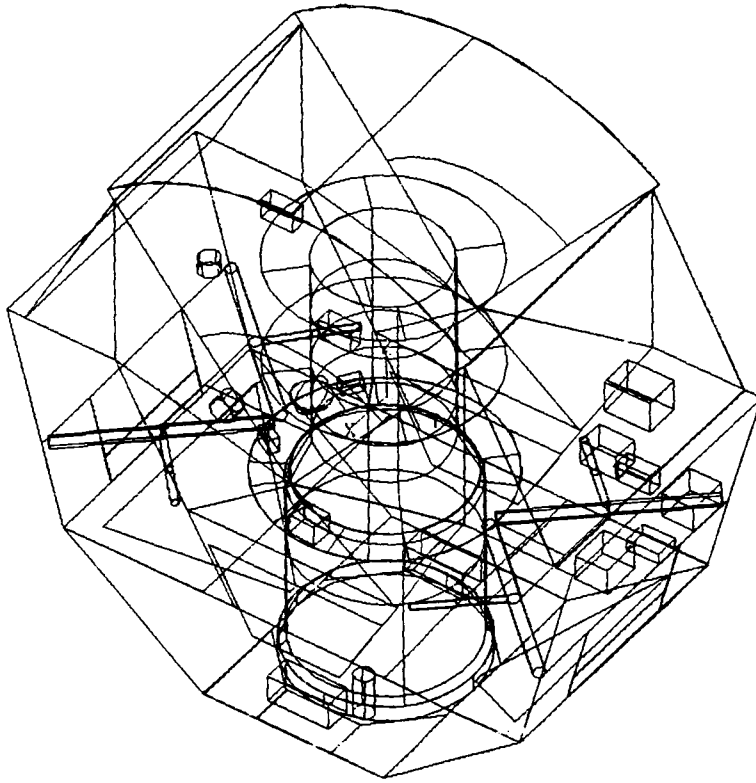
Fig. 9 – IRIS Thermal Mathematical Model
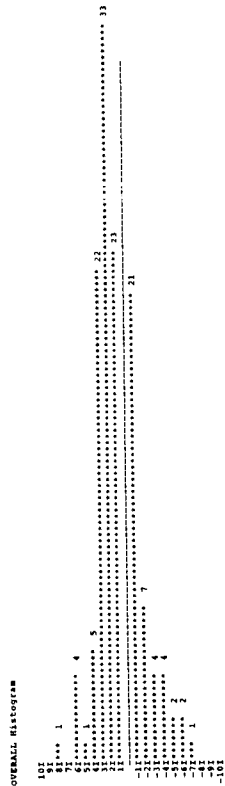


Fig. 10 – IRIS Phase 2 Histogram as elaborated by a statistical program

267

# THE INSTRUMENT TEST DEWAR:
## TESTING SATELLITE INSTRUMENTS AT 1.5 K

Laura J. Milam
NASA/Goddard Space Flight Center

## ABSTRACT

The Instrument Test Dewar (ITD) is a cryogenic facility designed and built to test Cosmic Background Explorer (COBE) Satellite instruments at 1.5 K. The facility provides a high vacuum and thermal environment with payload thermal, electrical and optical interfaces. There are two concentric vacuum spaces which are not hermetically sealed. The instrument vacuum space is 81.28 cm x 243.84 cm and is cooled by an LHe shroud. The guard vacuum space surrounds an LN2 shroud. There are two separate cryosorption pumping systems and a mechanical LHe pumping system. Two data acquisition systems provide payload and housekeeping data. There have been various problems with the facility, and changes and improvements have been made to assure optimum test conditions. COBE instrument testing has been completed on structural, thermal model hardware and the protoflight units.

## INTRODUCTION

The Cosmic Background Explorer (COBE) is an in-house project at the Goddard Space Flight Center. The purpose of the satellite is to study the Big Bang Theory of how the universe was formed. Two of the three COBE instruments are cryogenically cooled. The Far Infrared Absolute Spectrophotometer (FIRAS) is a liquid helium cooled interferometer and the Diffuse Infrared Background Experiment (DIRBE) is a liquid helium cooled filter photometer. Both instruments are housed together in the Cryogenic Optical Assembly (COA) which is cryogenically cooled in the inside of a flight liquid helium dewar. COBE project requirements for development of instruments dictated the need for a test facility capable of testing at 1.5 K, but there was no test facility with this capability.

The Instrument Test Dewar was built specifically to simulate the COBE flight dewar and to provide a 1.5 K vacuum environment for the COBE instruments (see figure 1). The facility was developed by the Goddard Cryogenics Technology Section and was built by Janis of Massachusetts. The facility was turned over to the Simulation Test Section to complete COBE instrument testing. The facility is housed in a Class 10,000 clean room where strict contamination conditioning and monitoring is maintained. The COBE instruments can be tested together as the Cryogenic Optical Assembly (COA) or can be tested individually. Six tests were completed at various stages of hardware development including a thermal structural unit, thermal unit and a protoflight unit.

## SYSTEMS DESCRIPTION

### GENERAL

An external shell surrounds two concentric vacuum spaces inside of which is a liquid nitrogen (LN2) reservoir and a liquid helium (LHe) reservoir. The ITD is 3.35 m (11 feet) high by 1.52 m (5 feet) diameter. The instrument test space is 81.28 cm (32 inches) by 243.84 cm (96 inches) high (see figure 2). The dewar weighs 4,500 pounds without cryogens and approximately 5,270 pounds with cryogens.

### VACUUM

#### High Vacuum System

The Instrument Vacuum Space (IVS) and the Guard Vacuum Space (GVS) are two concentric vacuum spaces but are not hermetically sealed. Each space has its own roughing pump and cryosorption pump. The cryosorption pumps are good to a static pressure of less than 1 x 10E-4 torr. When the cryogens are added and the dewar is cold, a pressure of less than 1 x 10E-7 torr is achieved.

#### LHe Pumping System

A mechanical pumping system is used to lower the pressure above the 4.2 K LHe to lower the temperature to approximately 1.5 K. The mechanical pumping system consists of a Roots blower in tandem with a rotary vane pump. The LHe bath temperature can be adjusted slightly by throttling valves.

### CRYOGENIC

#### Liquid Nitrogen

The liquid nitrogen reservoir (surrounded by the guard vacuum space) holds 277 liters of liquid nitrogen. The reservoir is initially filled with LN2 from the house supply and thereafter can be topped off either manually or automatically from 160 liter LN2 dewars.

#### Liquid Helium

The LHe reservoir surrounds the instrument vacuum space. The reservoir is filled to its 475 liter capacity from 500 liter LHe dewars. The reservoir is always backfilled with GHe to atmospheric pressure before LHe is transferred. The LHe is transferred through a flexible vacuum jacketed (V-J) line which connects the 500 liter supply dewar dip tube to the ITD internal fill line.

## THERMAL INTERFACE

The mechanical interface which also serves as the main thermal interface in the ITD is the Instrument Interface Flange (IIF). The IIF is bolted onto the bottom flange of the LHe reservoir, and the COA is bolted to the IIF during testing. There are also several attachment points at the top of the LHe reservoir for copper thermal straps which are connected to the payload.

## ELECTRICAL INTERFACE

The electrical interface at the IIF consists of five 196-pin blindmate connectors wired to nineteen 61-pin external connectors. At the top of the instrument vacuum space there are six 196-pin blindmate connectors wired to twelve 61-pin external connectors, which provide for additional instrumentation and housekeeping instrumentation.

## OPTICAL INTERFACE

On the IIF there is a blindmate assembly wired to a 12-pin external optical fiber connector. The ITD has ports which were originally aligned with the COBE instrument axes at the top of the dewar. These ports can be blanked off or special optical quartz windows (for laser alignment) may be installed.

## DATA ACQUISITION AND CONTROL

The facility is operated from a central control console which houses the controls and gauges for the high vacuum system, LHe pumping systems and the cryogen level monitors.

There are two separate identical data acquisition systems for test monitoring. The systems work independently; one system is dedicated to the payload and one to internal ITD housekeeping. Each system can read up to 140 channels of 4-lead resistance measurements, 2-lead voltage measurements or a combination of both. The systems are configured to read 4-lead Germanium Resistance Thermometers (GRT) or Platinum Resistance Thermometers (PRT) and either 4 or 2 lead strain gauges. Ten channels of data may be plotted on the CRT screen. The test data is stored on hard disk, floppy disk and magnetic tape. During testing hard copies of data can be obtained in real time. The wait period between scans can be pre-set and varied during the test. Plots of data can be obtained after the end of the test. The ITD has 18 GRTs and 4 PRTs for housekeeping purposes. The PRTs are accurate from 300 K to 60 K and the GRTs are accurate from 80 K to 1.2 K. There are four cryogenic accelerometers installed on the IIF which can be monitored if requested. The dewar internal cabling consists of Teflon coated manganin wire and stainless steel coax cable.

## TEST DESCRIPTION

The ITD GVS and IVS are roughed down to 100 micron before opening the main valves to the cryosorption pumps which pump the system down to a static pressure of 1 x 10E-4 torr (figure 3). At this time the LN2 shroud can be filled. It typically takes 2 hours to fill the LN2 shroud to 100 percent. The LN2 shroud is allowed to cool the ITD before starting the flow of LHe. After LHe flow has begun, it takes approximately 72 hours to fill the LHe reservoir to 100 percent. A typical cooldown curve from 300 K - 4.2 K is shown in figure 4. It takes six to eight 500 liter LHe dewars to initially fill the reservoir. The helium is pumped on by the mechanical pumping system to obtain the superfluid helium. Superfluid temperatures can be obtained in 24 hours and can be maintained at an average of 72-90 hours depending on power being dissipated from the payload. A typical cooldown from 4.2 K - 1.5 K is shown in figure 5. The LHe reservoir can be backfilled with GHe to atmosphere, refilled and pumped back down to superfluid conditions as many times as required for the test. The warm-up of the facility is highly dependent on the payload. It is desirable to begin warm-up when the LHe is pumped out for the last time, however, it is possible to force any remaining LHe out of the reservoir. The LN2 is drained out of the LN2 shroud. After all internal temperatures are above 45 K the facility can be backfilled with GN2 to 1 torr. The only internal heat source is the payload itself. If the payload can be turned on it helps to expedite the warm-up. The facility has been warmed to ambient temperature in 4 days.

## DISCUSSION

The facility has been used for instrument testing for the past 4 years. After each test, improvements and changes for project needs were made to the systems. There was one continuing problem with the facility which was solved this year and that was with iceplugs forming in the ITDs internal LHe fill line. The ice plugs would form during the changing of the 500 liter dewars and always just after some liquid had started to accumulate inside the reservoir. It was suspected that when the V-J line was disconnected from the supply dewar, some air was cryopumped into the line and would cause a plug inside the internal fill tube. The plugs were not dangerous but caused delays in the test and were tedious to break. The problem was solved by having a valve added to the flexible V-J fill line which connects the 500 liter supply dewar to the internal fill preventing any air leakage and since the line was modified no ice plugs have formed. The internal ITD cabling consisting of #28 and #36 teflon coated manganin wire and Type S1 stainless steel coax cable was replaced in the facility. This was necessary because during two different tests the project had poor resistance readings, shorts and open circuits which was determined to be attributed to the dewar cabling. All of the testing in this state-of-the-art facility was completed successfully. Approximately 6000 test hours were logged over a 4.5 year period.

**SUMMARY**

The Instrument Test Dewar is highly unique facility. It is the only known facility of its kind which can test a full size spacecraft instruments at superfluid liquid helium conditions. The facility was built to simulate the COBE spacecraft flight dewar, but now that the facility is no longer needed for testing COBE instruments it will be maintained and modified as necessary for future cryogenic satellite instrument testing.

REFERENCES

1. "Engineering Services Division Facilities and Capabilities Handbook", Engineering Services Division, NASA-Goddard Space Flight Center, January 1987.

2. "Facility 223 Operating Procedure", NSi Procedure Number 21-01-102-4, Revised February 1988, SSOS Mission, Northrop Services, Inc., NASA/Goddard Space Flight Center.

3. "Plan/Procedure for the Cryogenic Thermal Testing of the DIRBE and FIRAS PFU's in the ITD Facility", COBE-PP-750-1200-01, October 1987.
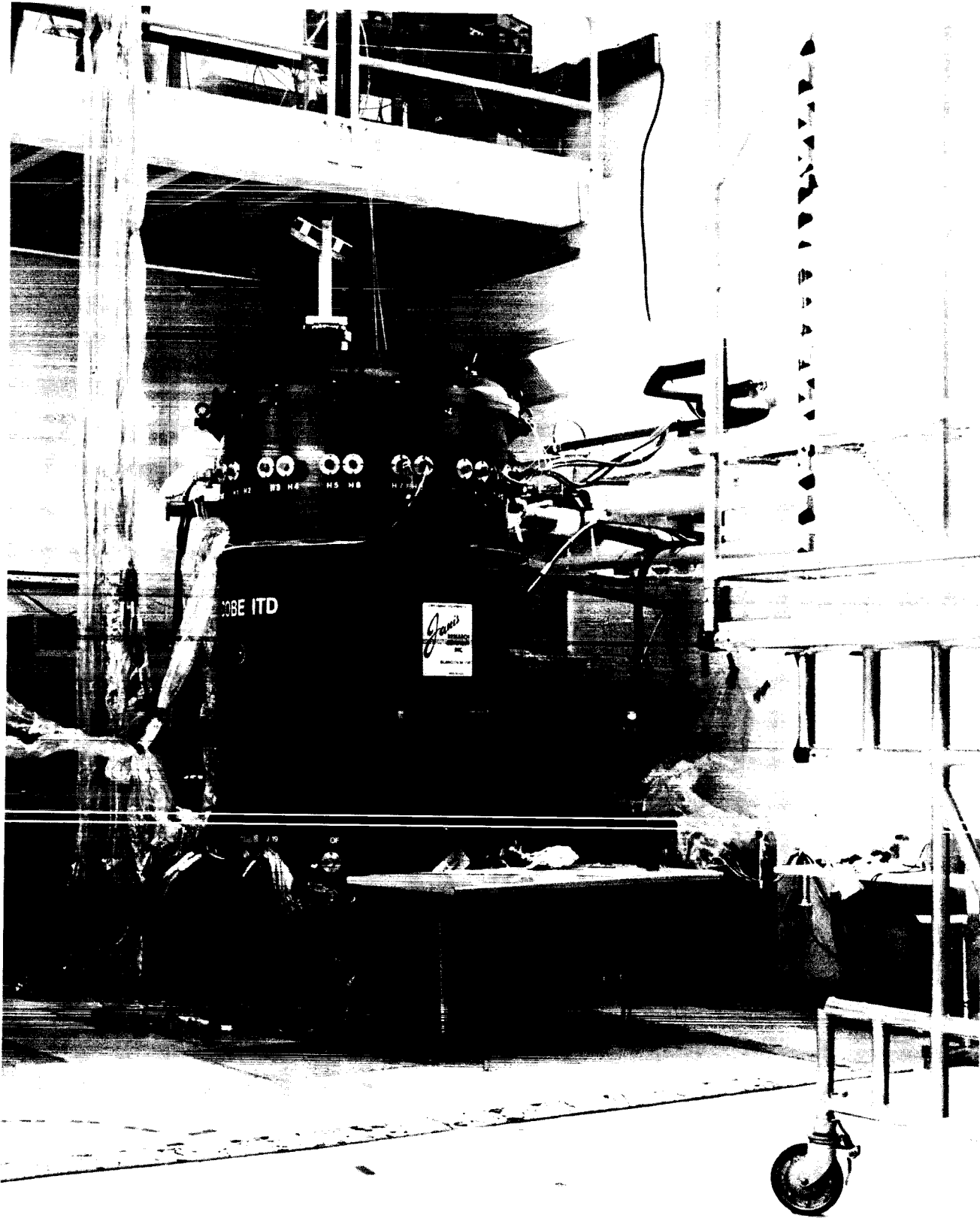
Figure 1.  Instrument Test Dewar

273
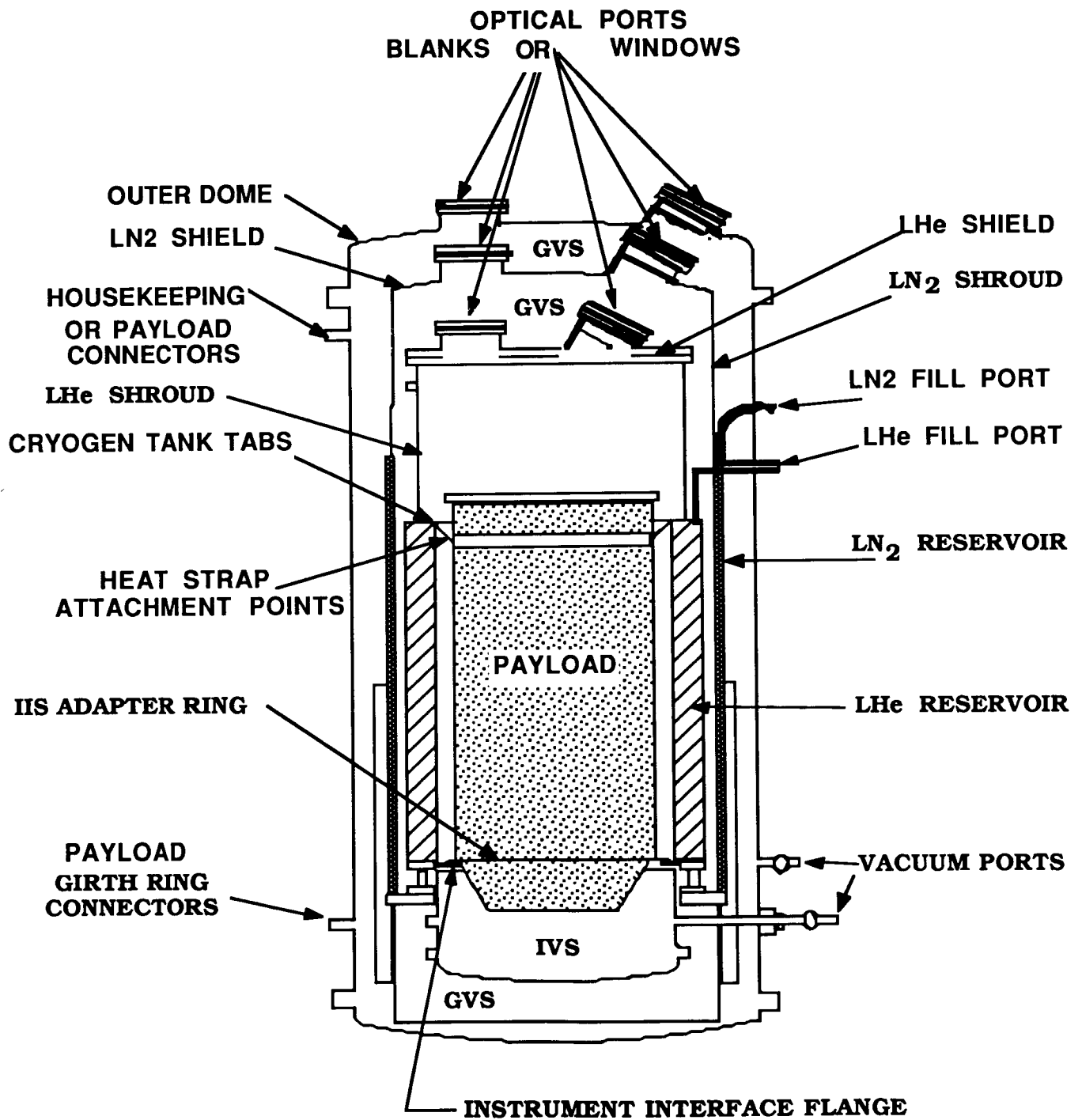
Figure 2. Cutaway View of the ITD

274
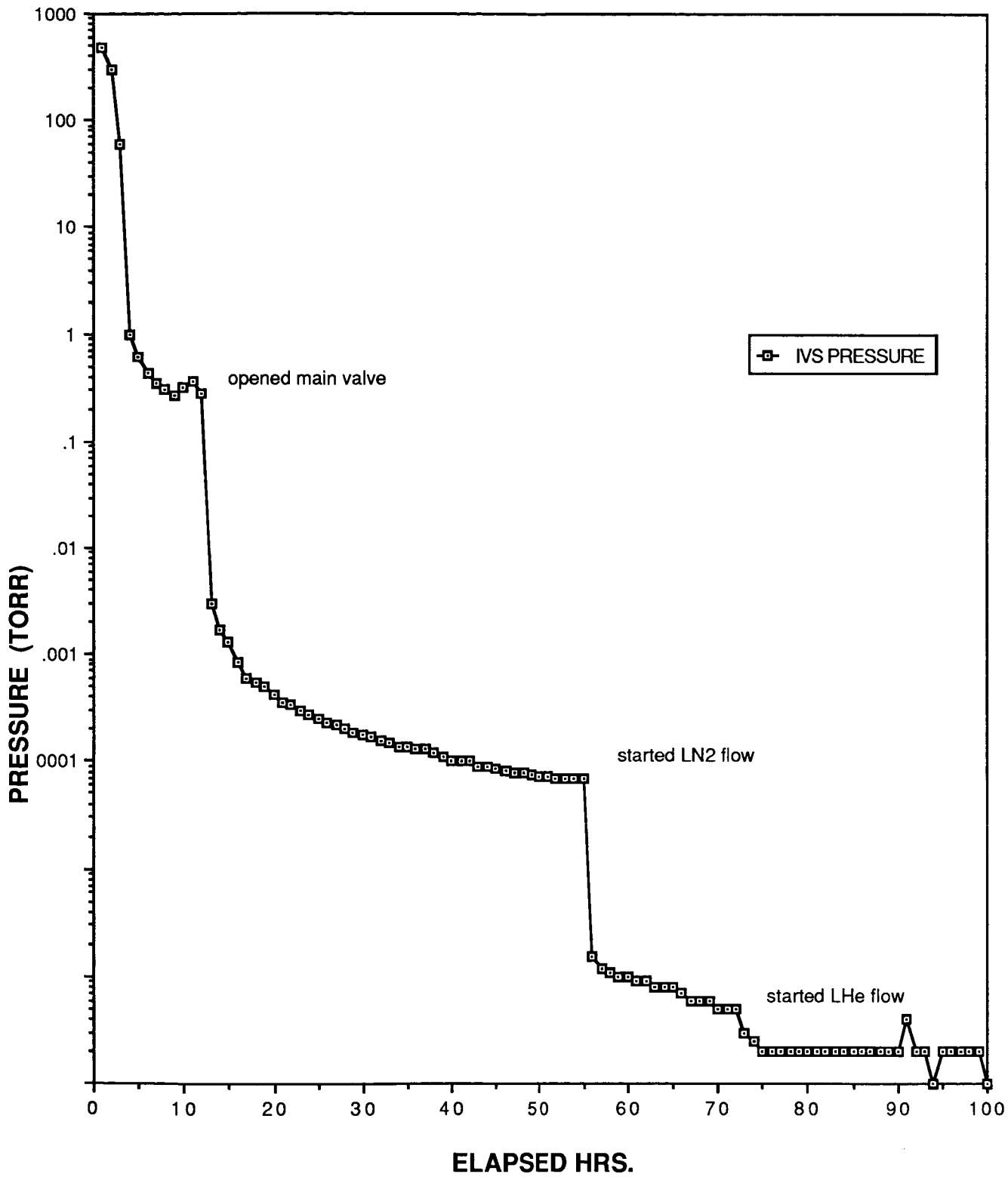
Figure 3. Typical ITD Pumpdown
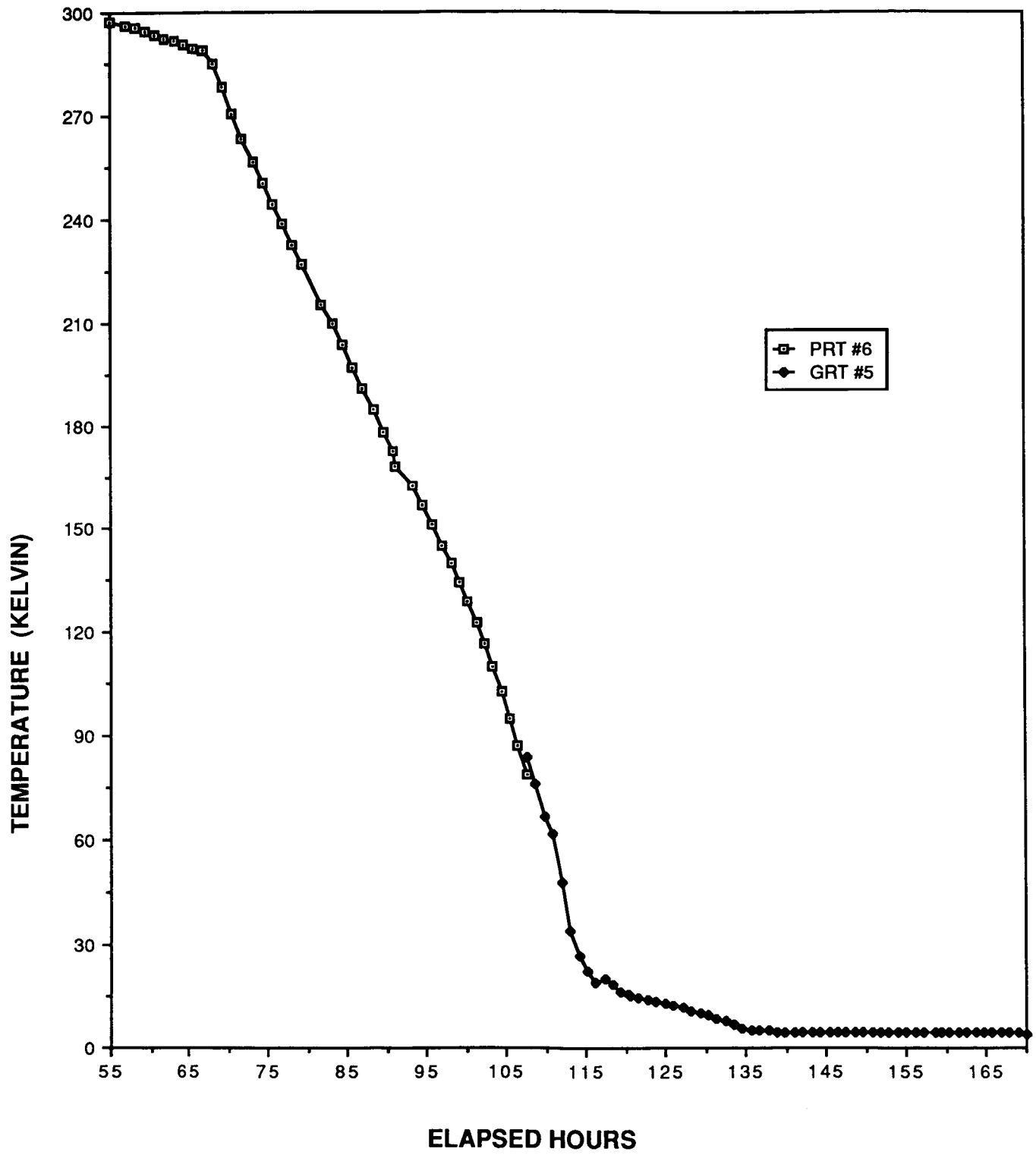
Figure 4. Typical Cooldown Curve 300 K – 4.2 K
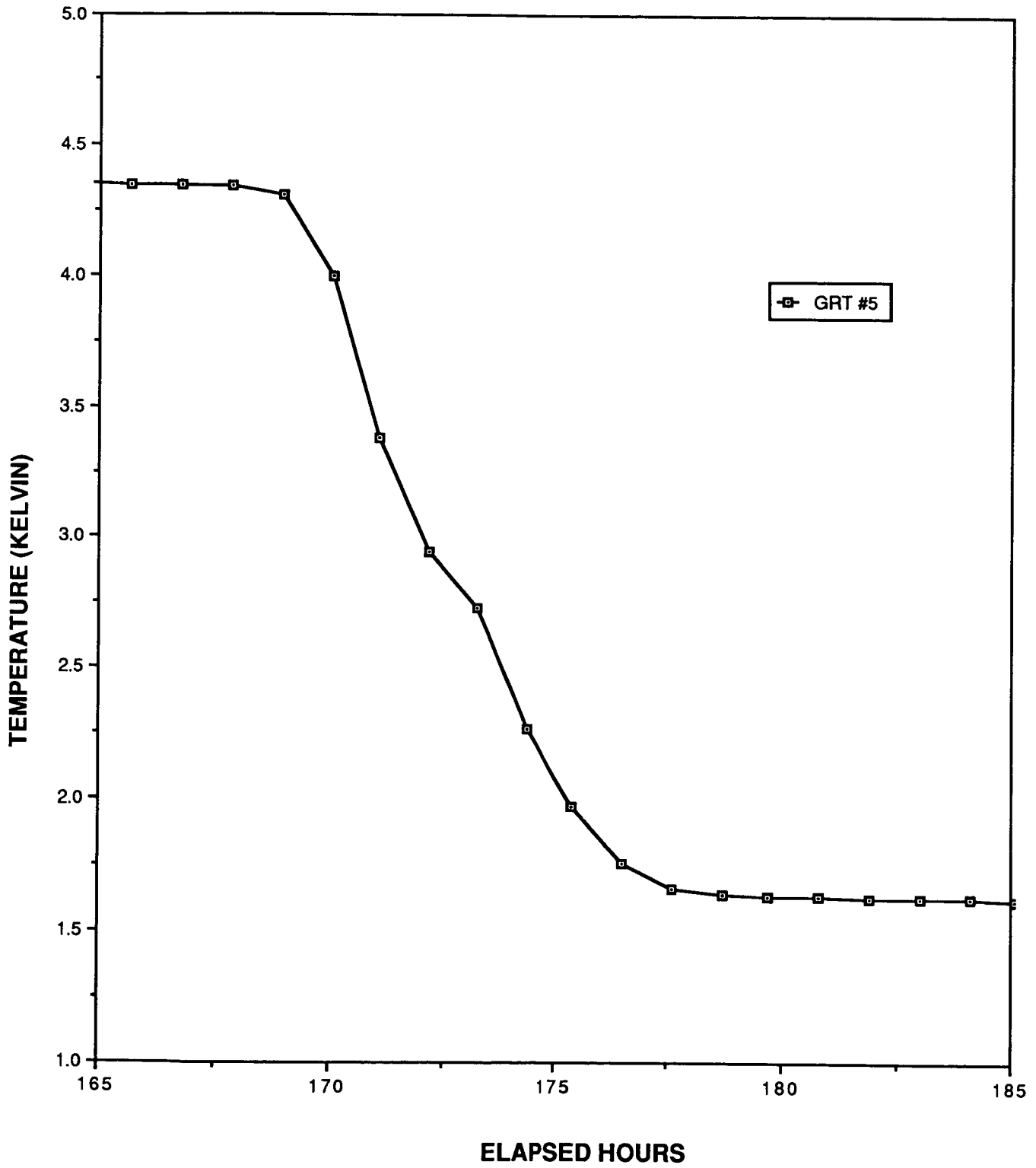
Figure 5. Typical Cooldown 4.2K-1.5K

# SOLAR SIMULATION WITH A RECTANGULAR BEAM

O. G. Feil and H. U. Frey
IABG, Munich, West Germany

## ABSTRACT

An existing space simulation test facility was modified by enlarging the solar simulator. Because of restrictions imposed by existing equipment, the shape of the solar beam was altered from a circular to a rectangular cross section in order to adapt the test facility to test objects of increased size. This modification is described together with the results of prelimimary measurements.

## INTRODUCTION

Since the beginning of satellite production in West Germany, approximately 25 years ago, IABG has been involved in the testing of space hardware. In 1983 a new, relatively large space simulation test facility became operational[1], a schematic diagram of which is shown in fig. 1; fig. 2 shows a photograph of the open chamber. The main characteristics of the facility are:

Test Volume Dimensions

- Between Lid and Shutter:                     7.5 m
- Between Lid and Mirror:                       12.0 m
- Diameter:                           approx. 6.2 m

Solar Beam
- Diameter:                                     3.6 m
- Intensity max.:                               1.4 solar constants
- Parallel Beam with Collimation Angle:        $\pm 2^{\circ}$

Shroud

- Temperature Range:                                        <100 K to 400 K


Vacuum

- Pressure:                                                 $<10^{-5}$ mbar
- Oil free high vacuum pumps


Motion Simulator:
Two axes of rotation:
- Attitude axis:                                           $\pm 200^{\circ}$
- Spin axis continuous rotation up to 10 rev. per minute


Max. Dimensions of Test Specimen
- Height:                                                  approx. 5.0 m
- Diameter:                                                approx. 4.0 m
- Mass:                                                    approx. 2000 - 2500 kg


The facility has been used extensively for testing satellites and
subsystems of national and international programmes. It has also been
used for special deformation measurements by means of laser holography
which were reported during the 13th Space Simulation Conference in
1984[2].


MODIFICATION OF SOLAR SIMULATOR

With the increase of launcher capacities and a corresponding
increase in satellite sizes we began to study the possibilities of
enlarging the usable test volume of our facility. Since the dimensions
of the chamber itself and of the shroud could not be altered, we focused
our attention on the solar beam, which also represented the main
limitation.

The solar simulator consists essentially of (see fig. 1)

- the lamp housing with up to 7 lamps of 25 kw each
- the integrator, an array of lenses
- the window as interface between the vacuum inside and the atmospheric pressure outside the chamber
- the collimation mirror inside the chamber, consisting of hexagonal segments

This arrangement, the lay-out of which was developed at IABG, yields a very good intensity distribution across the solar beam ($\pm 3$ %) with a collimation angle of $\pm 2^o$. The efficiency is better than 12 %. These values were obtained by means of extensive analysis and optimisation using mathematical models. For example, the collector mirrors were designed for a light source of finite length with a given intensity distribution.

Each of the integrator lenses distributes the light over the total beam area; therefore, switching or exchanging of lamps has hardly any effect on the intensity distribution in the target area.

A further advantage of this solar simulator design is its modular concept, which allows easy exchange of lamps, power supplies, etc.

Due to restraints imposed by the building and the chamber, it was not possible to simply increase the number of lamps and, correspondingly, the size of the collimation mirror in order to enlarge the solar beam. Instead, the following modifications were made after a number of calculations aimed at an optimised solution:

o The integrator was replaced by a new one containing rectangular instead of circular lenses.
o The collimation mirror was enlarged by a number of hexagonal segments.

These measures yielded a solar beam with a cross section of 3.05 m by 4.5 m, suitable for larger spacecraft than the 3.6 m dia beam, which covers square shaped spacecraft cross sections of up to 2.5 m side length.

The essential parameters of the two solar beams are listed in fig. 3. It can be seen that an increase of illuminated area of approximately 35 % is gained compared to a "loss" of maximum intensity of 7 %. This reduction was considered acceptable since 1.36 SC leaves a comfortable margin above the standard 1 SC. The gain is mainly achieved by the improved packing factor of the rectangular integrator (27 %), a geometrical effect as shown in fig 4. The area covered by the support structure of the lenses, which does not transmit any light, is larger for the circular lenses than for the rectangular ones.

Fig. 5 shows photographs of the new integrator which was designed and manufactured by C. Zeiss at Oberkochen, West Germany.

Preliminary measurements of the rectangular solar beam show that the intensity distribution is better than $\pm 3$ % with the exception of the edges and very few points in the middle (Fig. 6). It should be noted that some mirror segments at the corners of the collimation mirror had not yet been installed at the time of these measurements; also the upper left corner of the beam is obstructed by the support structure of a radiometer.

These measurments were performed with an intensity of 0.83 kw/m$^2$; with full power of the 7 X 25 kw lamps a value of 1.8 kw/m$^2$ = 1.36 SC will be obtained.

## CONCLUSION

By a relatively simple modification and with relatively low cost, the usable test volume of IABG's space simulation test facility was considerably enlarged (e.g. for ARIANE 3 spacecraft) and the range of potential customers increased. A further advantage is that changeover between the two solar beams can be achieved easily by exchanging the integrator only; no other modifications are required.

## REFERENCES

1) H. E. Nuss und J. Reimann: The new space simulation and thermal vacuum facility WSA/TVA. Proc. of the International Symposium on Environmental and Thermal Systems for Space Vehicles, 1983, ESA SP-200

2) H. U. Frey: Distortion Measurement of Antennas under Space Simulation Conditions, 13th Space Simulation Conference, 1984, NASA Conference Publication 2340.

Fig. 1:  Space Simulation Test Facility

| | |
|---|---|
| ① = | vessel |
| ② = | shroud |
| ③ = | collimator |
| ④ = | window |
| ⑤ = | integrator |
| ⑥ = | lamps |
| ⑦ = | motion simulator |
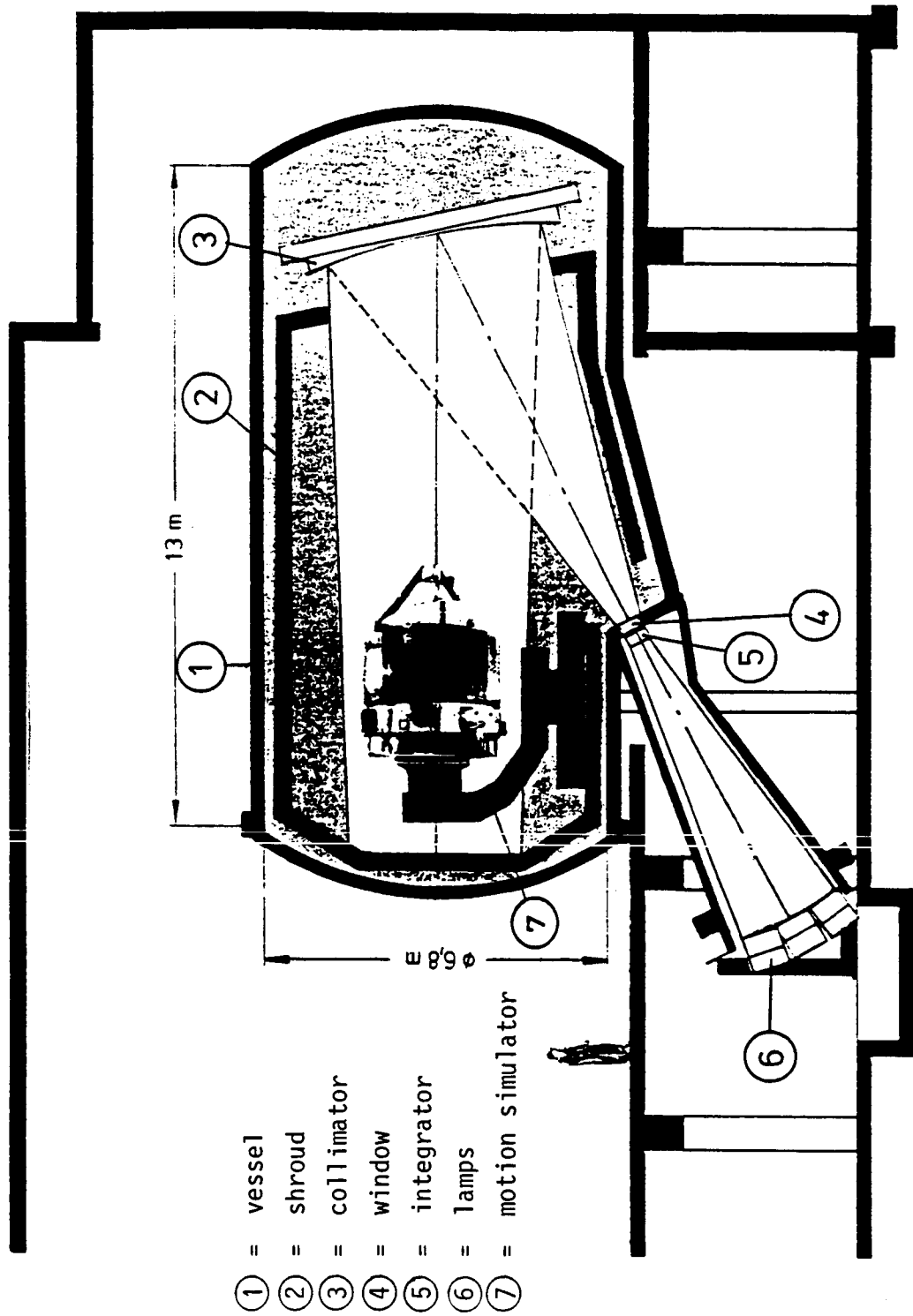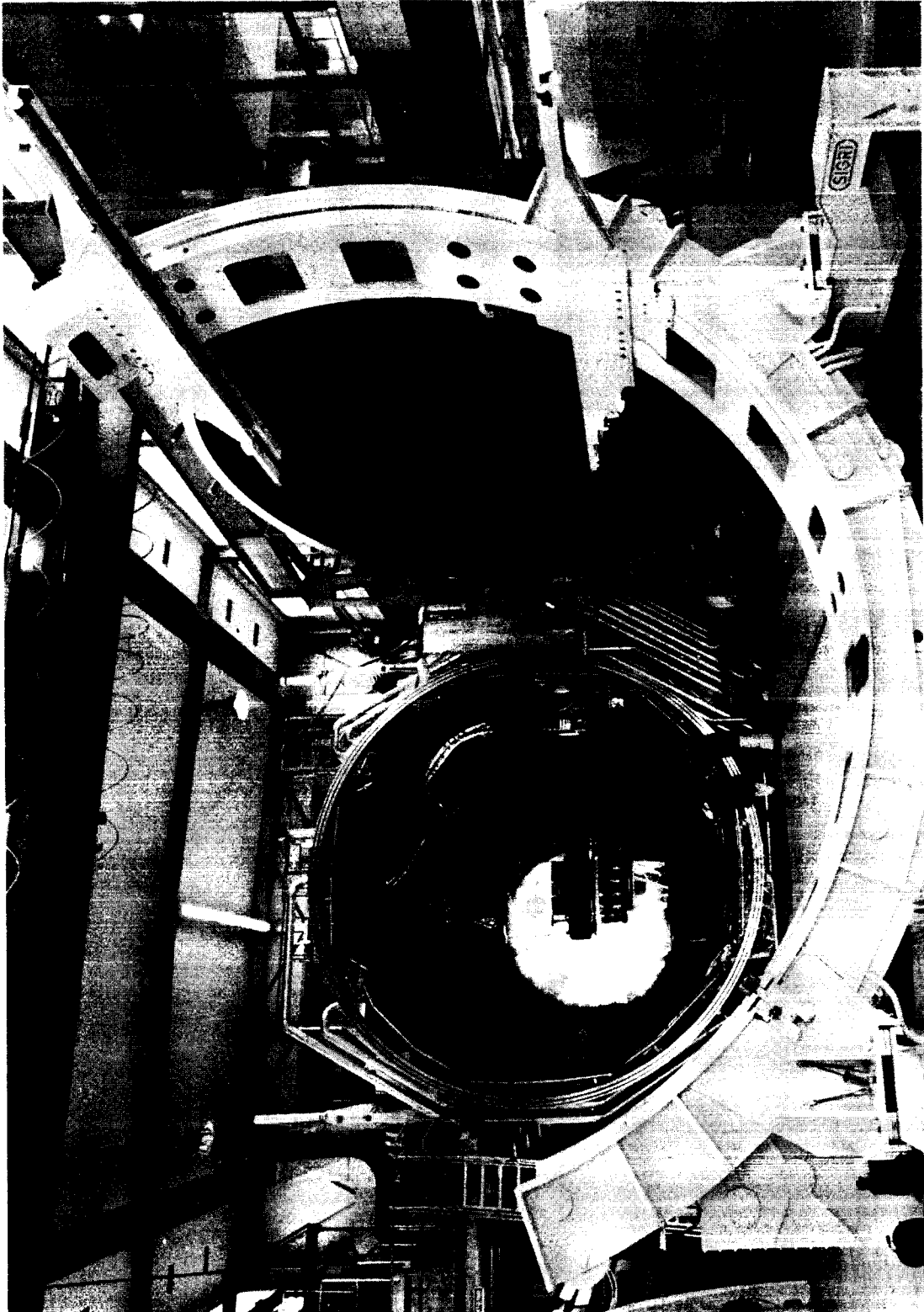
Fig. 2: View of the Space Simulation Test Facility

| BEAM DIMENSIONS | DIA 3.6 M | 3.05 M X 4.5 M |
|---|---|---|
| IRRADIATED AREA | 10.2 $M^2$ | 13.7 $M^2$ |
| NUMBER OF COLLIMATOR SEGMENTS | 61 | 84 |
| DIMENSIONS OF COLLIMATOR | 4.2 M MIN.<br>5.0 M MAX. | 4.2 M X 5.5 M |
| INTEGRATOR<br>- PACKING FACTOR | 2 x 31 CIRCULAR LENSES<br>0.71 | 2 x 65 RECTANGULAR LENSES<br>0.9 |
| MAXIMUM SOLAR INTENSITY<br>IN TEST PLANE | 1.44 SC | 1.36 SC |

Fig. 3: Parameters of Solar Beams

Circular Lenses

Rectangular Lenses
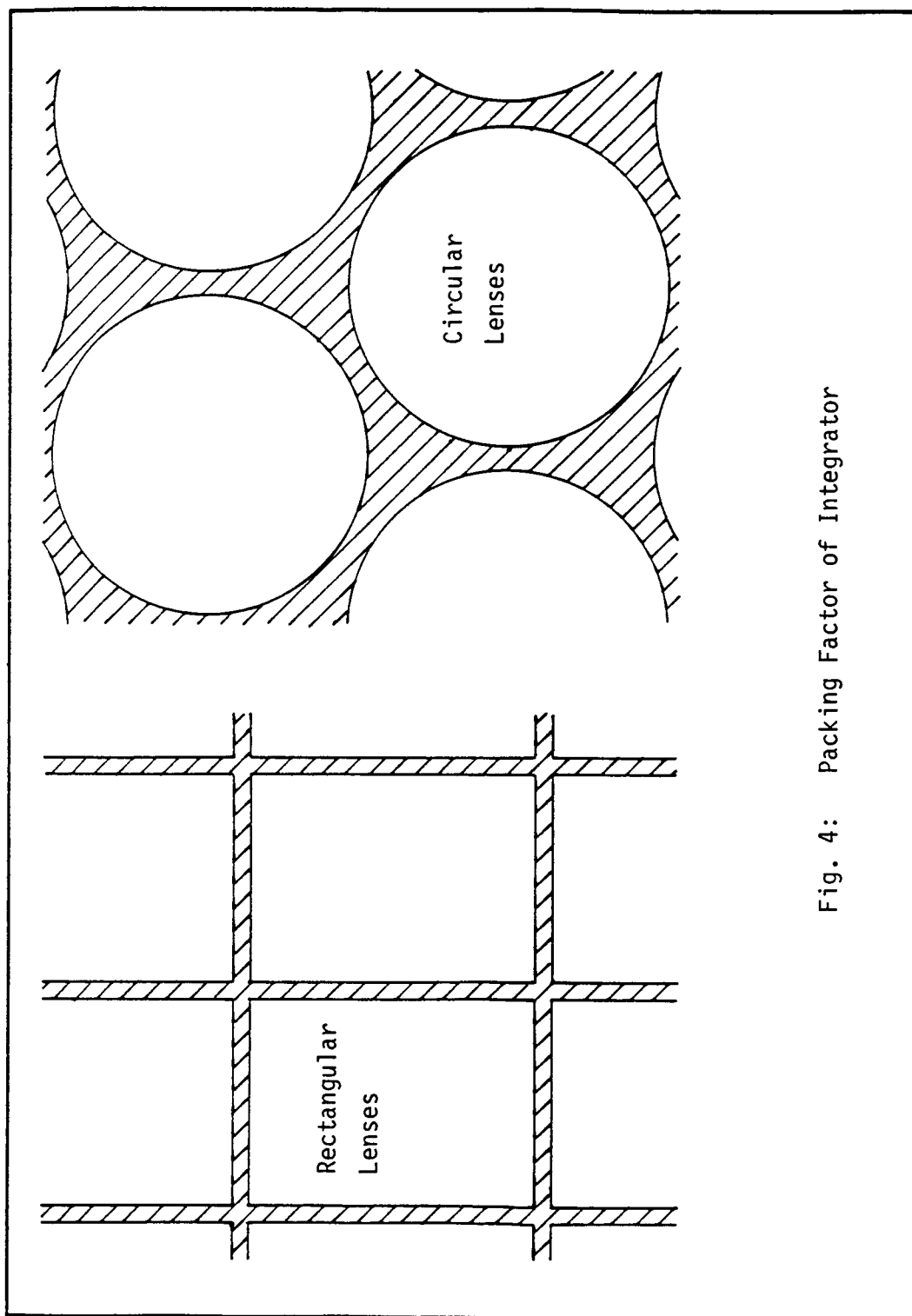
Fig. 4: Packing Factor of Integrator
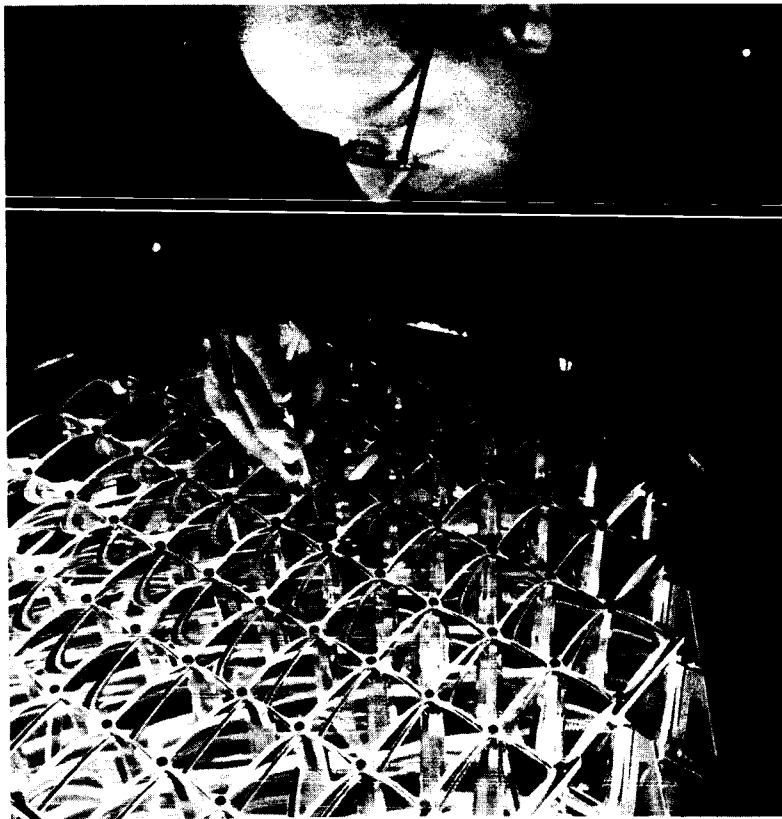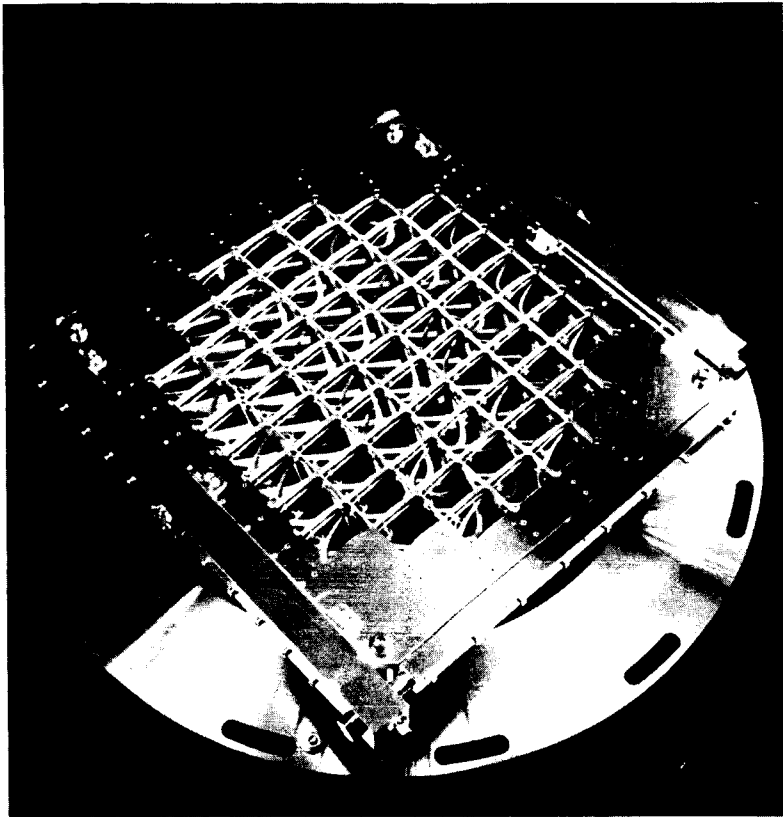
Fig. 5:   Rectangular Integrator

287
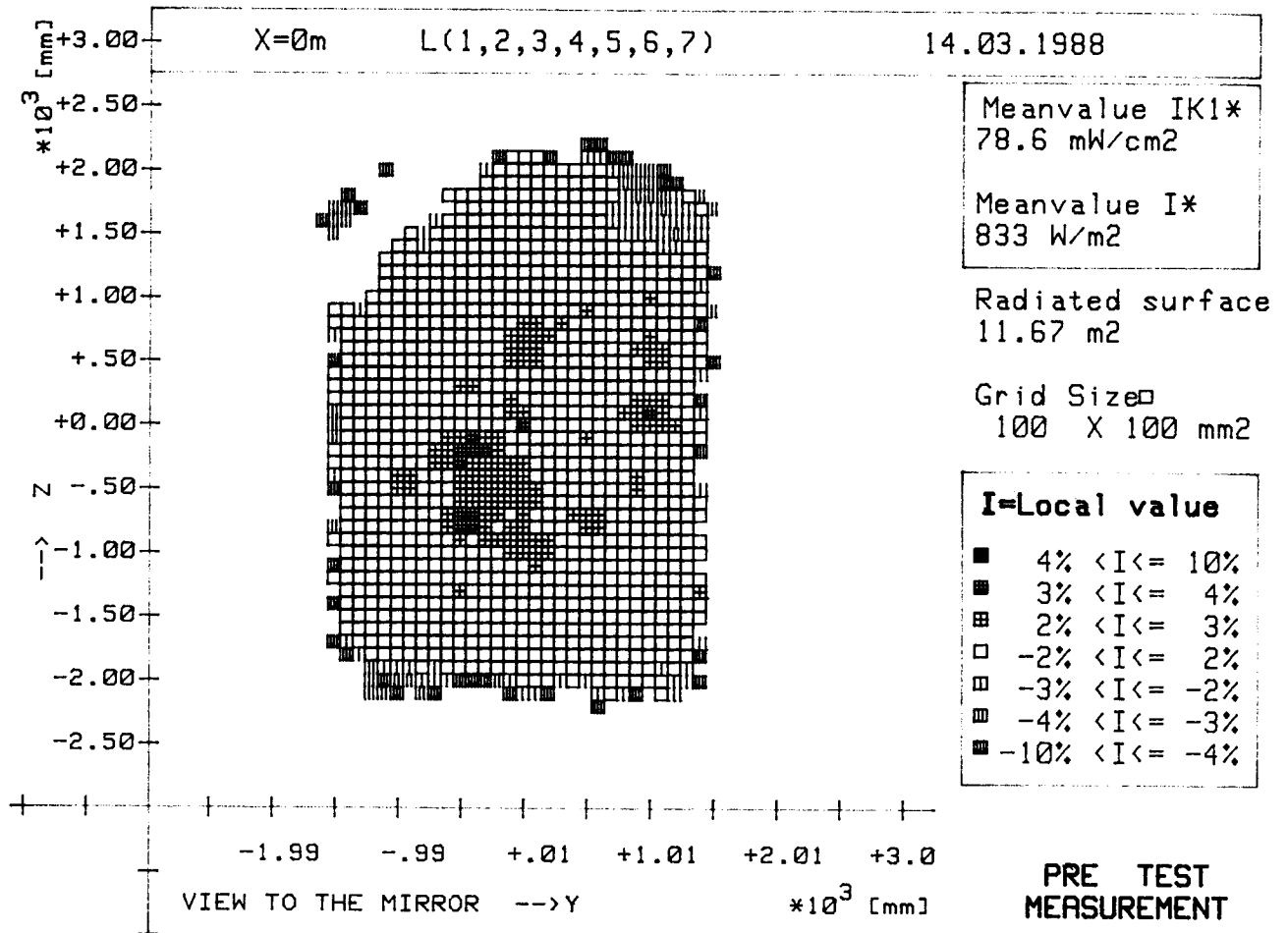
Fig. 6: Intensity Distribution - Rectangular Beam

# CONTROL OF THE INDUCED MICROGRAVITY ENVIRONMENT OF
# THE MAN TENDED FREE FLYER (MTFF)

Juergen Schlund
MBB/ERNO, Bremen, West Germany

## ABSTRACT

The MTFF one element of the European COLUMBUS program is an unmanned free-flying platform. It will mainly be utilized for long-duration science investigations and automatic processing, both requiring long periods of nearly zero-g conditions. At spacecraft/payload interface the sum of disturbances shall not exceed spectral 10E-6 g below 0.1 Hz and 10E-4 g above 100 Hz.

Based on past experience main sources of induced disturbances are expected to come from turbulent flow of air and fluid loops, imbalances of gyroscopes and reaction wheels.

The excitations are amplified by local and global structural resonances including low frequency modes of spacecraft flexible appendages and fuel sloshing and result in harmful accelerations of the sensitive payload. At the present stage worst case assessments basing on analyses and test results indicate that great effort and expense are necessary to meet the strong microgravity requirement.

With ongoing project realization especially during design and development phases microgravity control activities will become utmost significant for the realization of a minimized residual acceleration environment. They include design optimization and its verification by simulation and test, structural transmissibility measurements with the structural and the integrated engineering model, the creation of a qualified disturbance superposition model for the prediction of payload responses and in last consequence the implementation of passive and active anti-vibration mounts.

In future the performance of Microgravity Environment Compatibility (MEC) Tests on system, element and subsystem level will get high priority. Their results will constitute the basis for reliable predictions of the expected induced microgravity environment during the on-orbit operational phases.

## INTRODUCTION

The term microgravity is used to describe the physical environment in an orbiting spacecraft (S/C). The most obvious feature of this environment is extremely low gravity which is not obtainable on earth for long periods.

The MTFF is an unmanned free flying laboratory for the automatic performance of processes and experiments in the field of solidification physics, physical chemistry, liquid physics, biology and biotechnology

under low gravity conditions during a period of 180 days.

The present MTFF design assumes that about ten experiment dedicated double racks or twenty single racks can be accommodated and that the equivalent of ten further double racks is available for subsystem and experiment stowage. The orbital laboratory and main system data are shown on Figure 1.

The MTFF consists of a two segment Pressurized Module (PM2) providing the pressurized laboratory environment for research and application and its own Resource Module (RM) providing basic resources and services such as electrical power, heat rejection, guidance and navigation, attitude stabilization and control, communication and data transmission, orbital transfer and rendezvouz and docking capabilities. Exploded views of PM2 and RM elements are given with Figures 2 and 3.

The MTFF will be serviced by astronauts at intervalls of 180 days. It has been designed for a lifetime of 30 years.

Two main kinds of disturbance sources contributing to the low g environment at the spacecraft/payload interface have to be distinguished :

o The natural environment acts on the surface and center of gravity of the MTFF, results in position independant accelerations inside the MTFF and exhibits slow time variations along the spacecraft orbit. Natural disturbances sources are :

- drag forces due to ambient ionospheric medium, especially aerodynamic drag

- solar radiation pressure

- earth gravity gradient

- momentum transfer from micrometeorid fluxes

- self-gravitational field due to S/C internal mass distribution

o Induced disturbances are generated by on-board equipment and subsystems. Examples are given with :

- reaction wheels and gyroscopes of GNC subsystem (S/S)

- fans, pumps, centrifuges, air and fluid loops of ECLS- and TCS-S/S

- residual torque of GNC attitude control in combination with the excitation of low frequency dynamics of the S/C flexible appendages (solarr arrays, antenna and fuel sloshing).

For response predictions at P/L-S/C interfaces the disturbance force excitation functions have been multiplied with an empirically found vibration transfer function which has been derived from measurements with typical S/C lightweight structures.

In this paper main considerations are given to induced disturbances occuring during MTFF operational phases. From technical view it deals with disturbance source identification, vibration transmission, response predictions and their verification. Programatic aspects are covered by requirement definitions and the presentation of the project microgravity control plan.


## MICROGRAVITY REQUIREMENT DEFINITION

At the present stage the MTFF system microgravity requirement is defined as follows :

o The quasi-static steady state acceleration of the MTFF in its operational orbit shall be not greater than 10E-6 g.

o Distubances created by and within the MTFF, by its equipment, when added to the quasi-static level above shall not cause accelerations at the payload interface greater than :

> 10E-6 g below 1 Hz
> 10E-4 g above 100 Hz
> log-linear interpolation between 1Hz and 100 Hz

Payload interface acceleration must be understood as sum of natural and induced disturbances. Payload disturbance contributions are not included.

The requirement breakdown and microgravity budget allocation on element (PM2, RM) and subsystem level has been performed with respect to SPACELAB experience, equipment and subsystem similarity assessments and study results. The allocated microgravity budgets are given with Table 1.

The requirements define the resultant limit amplitude of the three translatory acceleration components at the microgravity payload/spacecraft interfaces. Below 0.1 Hz the system requirement breakdown has been performed linear, above 0.1 Hz on power basis (root-sum-square).

The definitions given above must be considered as preliminary, future corrections can be expected. Presently it is under discussion to compare equipment, subsystem and element disturbances against rms-values of third octave bands at their center frequency.

With ongoing design and development activities the results of equipment and assembly development tests may show the necessity of a microgravity budget reallocation mainly to be performed on equipment and subsystem level.


## IDENTIFICATION OF DISTURBANCE SOURCES

PM2 and RM equipment and subsystems are expected to be main contributors to the induced microgravity environment on board the MTFF. They are mounted in the PM2 subfloor area and in RM Orbit Replacable Units (ORU's). A detailed list of vibration and noise generating equipment and

their location is given with Tables 2, 3 and 4. The Tables must be seen in connection with Table 5 qualifying the excitation characteristics.

The drives of solar arrays and antenna pointing mechanism will be locked and thrusters not be activated during the MTFF operational phases.

The residual torques resulting from natural environment disturbance torque compensation in combination with low frequency S/C dynamics must be considered as contribution from RM GNC subsystem.

Earth ambient conditions within the PM2 element will be provided by the ECLS only during man tended servicing phases. It can be expected that the related equipment will not operate on full level condition during the MTFF operational phases.

Characteristics and original causes of structure-borne vibration mechanism are presented by Table 5. This kind of vibration will be transmitted directly via the structure from disturbance source location to the sensitive payload.

Additionally the coupling of structure-borne vibrations with air-borne sound must be be considered. Surfaces of cold plates, heat exchangers, ducts and S/S assembly housings radiate air-borne sound into subfloor, rack and cabin volume received by rack-, drawer surfaces and P/L casings. It is transformed into structure borne-vibrations and must be added to the structurally transmitted vibrations. Refined vibro-acoustic analyses to be performed in future will give reliable data on their parts of contribution.

## STRUCTURAL TRANSMISSIBILITY FUNCTION

The allocated microgravity budgets refer to S/C-P/L interfaces. The vibration transfer function allows the prediction of payload responses due to force excitation at source location. It is defined in terms of g's per Newton [g/N] and represents the reciproke value of the effective mass participating at vibrations. Rotational rigid body responses have to be considered at the utmost radius of possible P/L location on board the MTFF.

The structural dynamic vibration characteristics of typical S/C lightweight structures have been determined by measurements with SPACELAB paletts and SPAS-01 satellite under variation of excitation/receiver location and local mass loading. Although both S/C's are different in their structural design similar vibration transmission characteristics have been found. A detailed description is given by Reference [1].

The envelope of these measurements under assumption of worst case constraints is presented by Figure 4. It is expected that this function gives a well description of structural transmission behaviour of typical S/C lightweight structures. Consequently the function has been used for first response predictions during early project phases.

Vibration amplification at eigenfrequencies of S/C flexible appendages (solar array, antennas) and of fuel sloshing are not covered by the transfer function. These effects will be controlled together with the natural environmental disturbance torques by the GNC S/S momentum

management.

Future control activities must include verification and adaption to real MTFF transmissibility by numerical analyses and in the higher frequency range by measurements taken from Engineering and Structural Models . At source location the S/C mechanical impedances have to be determined for the coupling of equipment and assembly test results with the measured system vibration transfer characteristics.


## RESPONSE PREDICTION AT S/C - P/L INTERFACE

Acceleration responses to identified potential disturbing equipment have been assessed by determination of the force excitation functions and its multiplication with the spacecraft vibration transfer function. Assumptions and equipment characteristics being used for analyses are given in the following.

For four reaction wheels (RW's) static and dynamic imbalances and rotor axial bearing force have been superposed under consideration of :

| | | |
|---|---|---|
| rotating mass of RW | : | $m = 20$ kg |
| heigh of RW | : | $h = 0.2$ m |
| diameter of RW | : | $d = 0.5$ m |
| max. rotational speed | : | $n = 4000$ rpm |
| balance quality grade | : | $Q = 6.3$ mm/sec (rms) |
| axial bearing forces base on measurements results. | | |

The results of Freon and water fluid loop vibrations are derived from measurements. The test set-up consisted of :

1 pump package, 1 interloop heat exchanger, 1 standard coldplate, 1 throttle line and diverse flexible and hard lines with bends.

| loop medium | : | Freon | Water |
|---|---|---|---|
| flow rate | : | 1400 kg/h | 235 kg/h |
| total pressure drop | : | 1.73 bar | 0.95 bar |
| pump type | : | SL Freon 21 pump, 2-stage, centrifugal | REUSSER, 1-stage, centrifugal |
| no. of impeller blades | : | 12 | 6 |
| no. of diffuser blades | : | 9 | – |
| power | : | 300 W | 34 W |
| loop fundamental freq. | : | 180 Hz | 130 Hz |

Following data have been used for high data rate recorder (HDRR) disturbance force assessment :

| | | |
|---|---|---|
| tape diameter | : | $d = 0.38$ m |
| rotating mass | : | $m = 5$ kg |
| fast rewind speed | : | $u = 6$ m/sec |
| acceleration time | : | $t = 1$ sec |
| shape of excitation | : | rectangular force pulse |
| analysis bandwith of frequency transformation : 0.5 Hz | | |

293

The stiction-friction effects at structural bearings by sudden stress compensation due to thermal extension/contraction have been assessed with :

mean strain : 50 * 10E-6
modulus of elasticity : 70 * 10E3 N/mm2
cross section area : 940 mm2
shock duration : t = 1 sec
shape of excitation : rectangular force pulse
analysis bandwith of frequency transformation : 0.5 Hz

It is assumed that stick-slip will act as inner force/moment on the S/C and thus not induce any acceleration of the rigid body. A detailed description of this phenomena is given with Reference [2].

Gyroscope forcing functions base on the superposition of following forces and torques measurements :

force parallel to spin axis
force orthogonal to spin axis
torque around axis orthogonal to spin axis
wheel frequency : 400 Hz

Cabin and avionic fan induced accelerations at payload racks base on measurements performed in the SPACELAB Engineering Model.

Responses to acoustic excitation are derived from SPACELAB analysis and test data due to its similarity to the COLUMBUS pressurized module design.

The computed acceleration response amplitudes to excitations from equipment as listed above are presented graphically in terms of g's by Figure 5.

The responses to RW and gyroscope vibrations are given by the envelopes over all possible operating steady states. The equipment itself have been assumed to behave as rigid bodies. Structural resonances have not been considered.

The assessed disturbance level due to shock excitation shall only give an impression about the order of magnitude since the real values are strongly depending on time duration and shape of excitation pulse.

Many disturbances may occur at the same time. But their superposition will become very complex due to different types of excitation and the time dependant variation of their magnitudes and directions.

The checkered area on Figure 5 shows expected response level reduction by design modifications like for example the implementation of active or passive anti-vibration-mounts or refined manufacturing tolerances as the improvement of balance quality grades of rotors.

VERIFICATION BY ANALYSIS AND TEST

Based on the allocated budgets, verification of the induced microgravity environment has to be performed on system, element and subsystem level by analysis or test, and where appropriate in a combination of both. An overview on methods for the verification of induced and natural microgravity disturbances is given in the following.

ANALYSIS OF INDUCED DISTURBANCES

The evaluation of induced disturbances by similarity assessments shall be used if calculations by means of simplified mathematical models during design definition and early development phase are impossible due to lack of detailed data. The article should be similar or identical in design, manufacturing process, quality and set-up (as integrated system) to another article that has been previously certified to equivalent or more stringent criteria.

Similarity assessments should also substitute most thorough analyses if it can be expected that time and cost effort are unproportionally high related to the accuracy of the expected results.

The analyses of equipment and subsystem disturbances have to show the influence on S/C rigid body motions and by application of the S/C transfer function on payload responses in the higher frequency range.

Realistic safety margins have to be considered by the analyses in order to facilitate the implementation of subsequent test results.

The analytical treatment of low frequency structural dynamics should be covered by the GNC mathematical model and its numerical simulation.

ANALYSIS OF NATURAL DISTURBANCES

The verification of the MTFF natural microgravity environment shall be performed by analysis and computer simulation, because tests can not applied to drag, gravity gradient and S/C low frequency dynamics investigations.

MEASUREMENTS OF INDUCED DISTURBANCES

Where other verification methods do not provide reasonable assurance that the candidate design or procedure is adequate to meet the microgravity requirement tests and measurements taken from operational equipment and the integrated system will form a basis for verification of the higher frequency microgravity environment.

Development tests shall be performed to verify the design approach, indicate critical areas where design improvement is required, assure compliance with design requirements, confirm analytical methods or generate essential design data.

In general, subsystems are tested on assembly and equipment level. It will be nearly impossible to mock-up completely integrated subsystems. The test article will be attached to a reference structure with a dynamically free-free and low frequency suspension. Test outputs are equipment

interface forces and mechanical impedances to be combined analytically with the corresponding local S/C impedance and transfer function in order to derive its contribution to the induced microgravity requirement.

Development tests on element and system level with the Engineering and Structural Model shall determine structural vibration transmission characteristics, the dependency of structure borne vibrations from acoustic excitation and local S/C impedances for correlation with equipment test data.

Final PM2 and RM element verification is planned to be performed on system level in order to have realistic boundary conditions for each element.

Final system verification of the higher frequency contribution is provided by measurements taken of the fully equipped flight unit. Subsystems shall operate according to timeline.

It must be noted that ground tests will always be influenced by earth gravity and athmospheric pressure. Therefore on orbit verification may be foreseen for the support of payload performance evaluation during and after flight.

MICROGRAVITY QUALIFICATION APPROACH

Basis of the overall microgravity approach of induced disturbances are equipment and assembly development- and final verification tests. At the beginning of the design phase much effort should be spent to equipment and assembly development test preparation and performance. At early time necessary design modifications and microgravity budget reallocations could be recognized and implemented into overall approach.

The superposition of equipment and assembly test results will yield expected S/S disturbances. The superposition of S/S analyses results in expected element disturbances. Thus the quality of S/S, element and system analyses directly depends on the quality of equipment and assembly tests.

In parallel spacecraft vibration transfer characteristics have to be determined by early measurements with element Engineering and Structural Models.

PROJECT CONTROL PLAN

An overall control flow diagram given with Figure 6 shows the allocation of tasks and responsibilities to MTFF project contractors on system, element, subsystem and equipment level. The contractors shown on the Figure are representative for the remaining contractors. The project can be subdivided into one system responsible, two element contractors (PM2, RM), seven PM2-S/S contractors, nine RM-S/S contractors and one common subsystem contractor. Main tasks to be performed on each project level are :

o  requirement definition and breakdown into subordinated requirement

o  performance of disturbance analyses and tests

o  proposals for and decisions about budget reallocation and
   design modifications

o  preparation and performance of development and final
   verification tests

o  report about analyses and test results to customer

o  review of subcontractor tasks, review of analyses and tests
   and superposition of results to be delivered by subcontractors


## SUMMARY AND CONCLUSIONS

Induced disturbance sources have been identified on board the MTFF and are shown with Table 2, 3 and 4. Vibration responses at sensitive payload/spacecraft interfaces have been predicted by the application of an empirically found spacecraft dynamic transfer function which is given with Figure 4. Vibrations from fluid loops (Freon, water) and of reaction wheels are assessed to be main contributors to the induced microgravity environment. The expected payload acceleration response amplitudes presented by Figure 5 are more than hundred times higher than the admissible values given by the MTFF system requirement, not considering the structural stiction-friction effects which could be avoided by appropriate design in any case. Real responses will be significantly lower because the derivation of excitation and transmission functions base on worst case assumptions.

The results indicate that future activities must spent much effort mainly on equipment design improvements and the implementation of vibration reduction means along the disturbance transmission path.

The activities must be accompanied by early equipment and assembly development tests and transmissibility measurements with the integrated spacecraft engineering and structural models in order to improve the accuracy of payload response predictions.

**Table 1 : System, Element and Subsystem Allocated Microgravity Budgets (Payload Contributions not included)**

| ACCELERATION LIMIT LEVEL AT S/C-P/L I/F [g] | Frequency Range : f < 0.1 Hz | f > 0.1 Hz f < 1 Hz | f > 1 Hz f < 100 Hz | f > 100 Hz f < 200 Hz |
|---|---|---|---|---|
| **System Requirement :** | | | | |
| MTFF Overall Disturbances | 10E-6 | 10E-6 | f  10E-6 | 10E-4 |
| MTFF Natural Disturbances | 8  10E-7 | 7  10E-7 | 0 | 0 |
| **Element Requirement :** | | | | |
| PM2 Induced Disturbances | 10E-7 | 5  10E-7 | f  7 10E-7 | 7  10E-5 |
| RM Induced Disturbances | 10E-7 | 5  10E-7 | f  7 10E-7 | 7  10E-5 |
| **Subsystem Requirement :** | | | | |
| PM2-ECLS | 4  10E-7 | 3.2  10E-7 | f 4.5 10E-7 | 4.5  10E-5 |
| PM2-TCS | 4  10E-7 | 3.2  10E-7 | f 4.5 10E-7 | 4.5  10E-5 |
| PM2-DMS | 10E-7 | 1.6  10E-6 | f 2.2 10E-7 | 2.2  10E-5 |
| PM2-resid. S/S | 10E-7 | 1.6  10E-6 | f 2.2 10E-7 | 2.2  10E-5 |
| RM-GNC | TBD | TBD | TBD | TBD |
| RM-TCS | 4  10E-7 | 3.2  10E-7 | f 4.5 10E-7 | 4.5  10E-5 |
| RM-resid. S/S | TBD | TBD | TBD | TBD |
| vertical Requ. breakdown | linear | quadratic | | |

**Table 2 : PM2 Induced Microgravity Disturbances Sources**

| SUBSYSTEM | EQUIPMENT | LOCATION | CHARACTERISTICS (see Table 5) |
|---|---|---|---|
| ECLSS-Cabin Air Loop | fan assembly | subfloor (SF) | 1, 2, 3, 9, 13 |
| | condensing heat exchanger (CHX) | SF | 5, 7, 9, 10 |
| | outlet diffusers | cabin (C) | 9 |
| | ducts, bends | SF, C | 9 |
| | valves, restrictors | SF | 8, 9 |
| | CHX bypass valve actuator motor | SF | 1, 2, 3 |
| ECLSS-Humidity Control | cond. separat. (centrifuge) | SF | 1, 2, 3, 12 |
| ECLSS-CO2-Control | CO2 control assembly | SF | 1, 2, 3, 9 |
| ECLSS-Avionic and Experim. Air Cooling | fan assembly | SF | 1, 2, 3, 9, 13 |
| | heat exchanger | SF | 5, 7, 9, 10 |
| | rack inlet diffuser | rack (R) | 9 |
| | ducts, bends | overhead (O) | 9 |
| | shut-off-valves | R | 8, 9 |
| ECLSS-Atmosph. Pressure Control | control-, relief-, exp. vent. valves | SF, C | 8, 9 |
| ECLSS-Fire Detect. and Suppress. | smoke detectors | SF, R | 9 |

## Table 3 : PM2 Induced Microgravity Disturbances Sources

| SUBSYSTEM | EQUIPMENT | LOCATION | CHARACTERISTICS (see Table 5) |
|---|---|---|---|
| TCS water loop | pump assembly | SF | 1, 2, 3, 5, 11 |
| | valves | SF | 5, 7, 8, 10 |
| | cold plates | R | 5, 7, 10 |
| | tubing (flex/ hard line) | SF, C, R | 5, 7, 10 |
| STRUCTURE | bearings (joints, guides) bearing elements | module PM2-RM I/F | 4, 14 |
| EPS | DC/DC converter | SF | 1 |
| | relays | R | 8, 12 |
| | AC/DC inverter | R | 1 |
| DMS | mass memory (winch. drives) | R | 1, 2, 3, 8, 12 |
| | optical disk | R | 1, 2, 3, 8, 12 |
| | high data rate recorder | R | 1, 2, 3, 12 |
| COMMS | video tape recorder | C | 1, 2, 3, 12 |
| | video cameras | 3 internal 2 external | 1, 2, 3, 12 |

Table 4 : RM Induced Microgravity Disturbances Sources

| SUBSYSTEM | EQUIPMENT | LOCATION | CHARACTERISTICS (see Table 5) |
|---|---|---|---|
| TCS–freon loop | pump assembly | ORU | 1, 2, 3, 5, 11 |
| | interloop heat exchanger | main body MB | 5, 7, 10 |
| | valves | ORU, MB | 5, 7, 10 |
| | tubing (hard/flex lines) | ORU, MB | 5, 7, 10 |
| | ORU heat exchanger | ORU | 5, 7, 10 |
| TCS–radiator system | heat pipes | 2 fixed on RM | |
| | heat exchanger | 8 mounted on PM2 | 5, 7, 9, 10 |
| | flexible tubes | | |
| PROP | biprop. tank | prop. ORU | 6 |
| | thruster | MB | 8 |
| EPS | relays | ORU | 8, 12 |
| | DC/DC converter | | 1 |
| COMMS | antenna pointing mechanism | MB | 2, 3, 4 |
| SOLAR ARRAY | solar array drive | MB | 2, 3, 4 |
| STRUCTURE | bearings (joints, guides) bearing elements | RM, ORU | 4, 14 |
| GNC | reaction wheels | ORU | 1, 2, 3, 4 |
| | gyroscopes | ORU | 1, 2, 3, 4 |

## Table 5 : Original Causes of Induced Disturbances

| NO. | KIND OF EXCITATION | CAUSE | CHARACTERISTICS |
|---|---|---|---|
| 1 | magnetic | excentric variable field in rotor circumferential direct. | spectrum of discrete frequencies |
| 2 | mechanical | dynamic/static imbalances of rotors | discrete frequencies |
| 3 | mechanical | bearing friction | broadband noise |
| 4 | mechanical | stiction-friction | impact |
| 5 | fluid stream | vortex shedding, cavitation | broadband noise |
| 6 | fluid motion | fluid sloshing | discrete frequencies |
| 7 | mechanical borne sound | structure borne sound transmission | broadband noise |
| 8 | mechanical | switch on/off events | impact noise |
| 9 | aerodynamics | vortex shedding, turbulent flow | broadband noise |
| 10 | mechanical | resonance vibrations excited by fluid stream | nearly pure tone |
| 11 | fluid stream | pressure fluctuations within pump medium | single tones |
| 12 | mechanical | inertia forces/moments of accelerated/ delayed masses | impact |
| 13 | aerodynamics | periodically alternating forces | single tones |
| 14 | thermal | struct. stress compensation | impact |

302

System Data :

| | | |
|---|---|---|
| total mass | 18000 | kg |
| lenght | 11 | m |
| diameter | 4.1 | m |
| total el. power | 10 | kW |
| payload el. power | 5 | kW |
| data rate | 20 | MBPS |
| operational orbit | 430–490 | km |

DSR-ANTENNA

RESOURCE MODULE (RM)

PRESSURIZED MODULE (PM2)

SOLAR ARRAY

PM2-RM ADAPTER
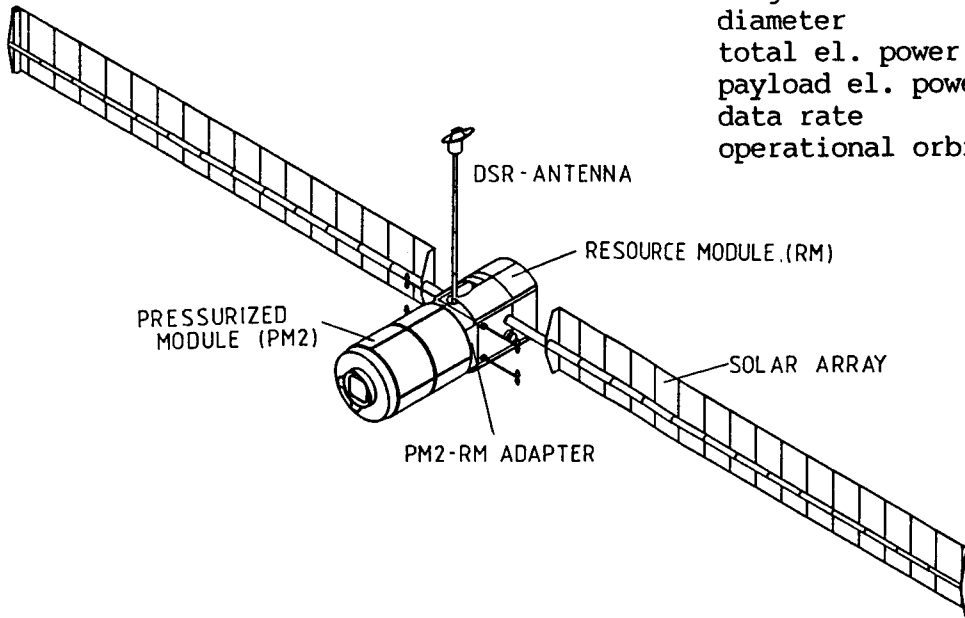
Figure 1 : MTFF Orbital Laboratory

DMS-S/S    TCS-RADIATORS

PM2-ELEMENT

PM2-RM ADAPTER

STRUCTURE

DATA TRANSMISSION

PAYLOAD RACKS

PAYLOAD

ECLS-S/S

ELECTR. POWER SUPPLY
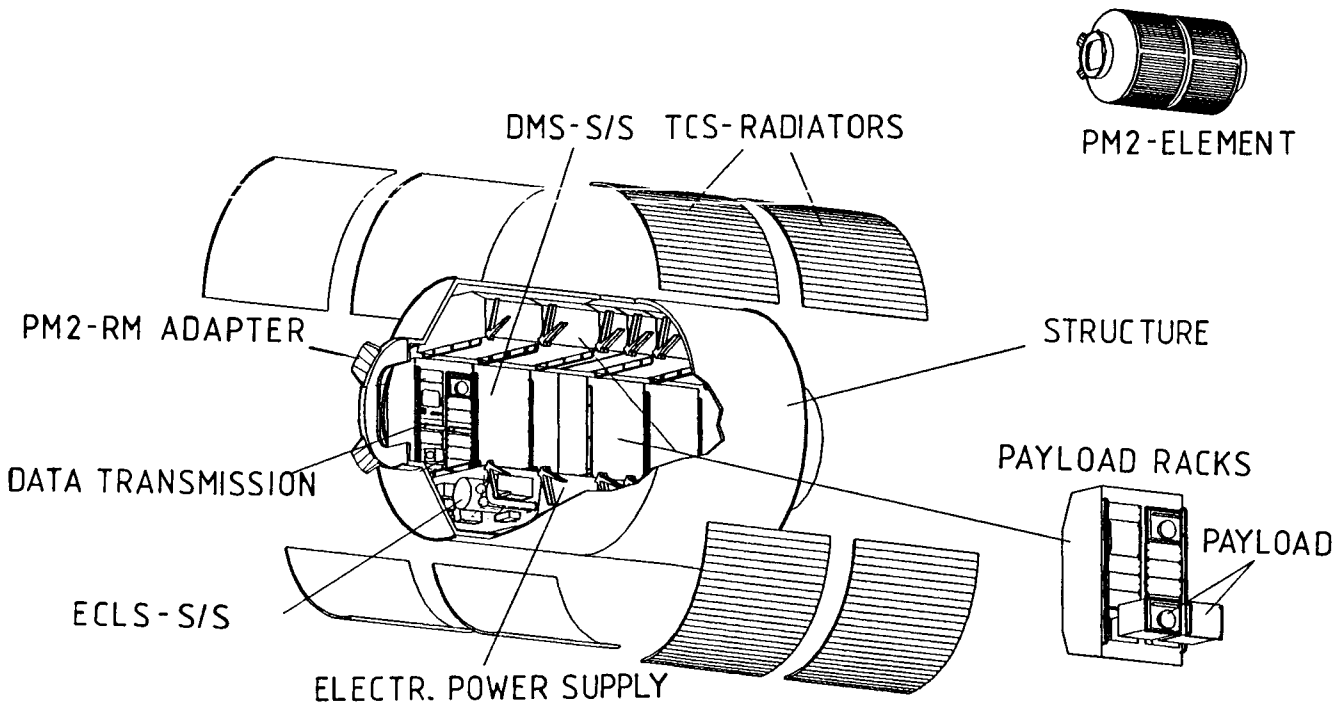
Figure 2 : Pressurized Module (PM2-Element) Exploded View

303
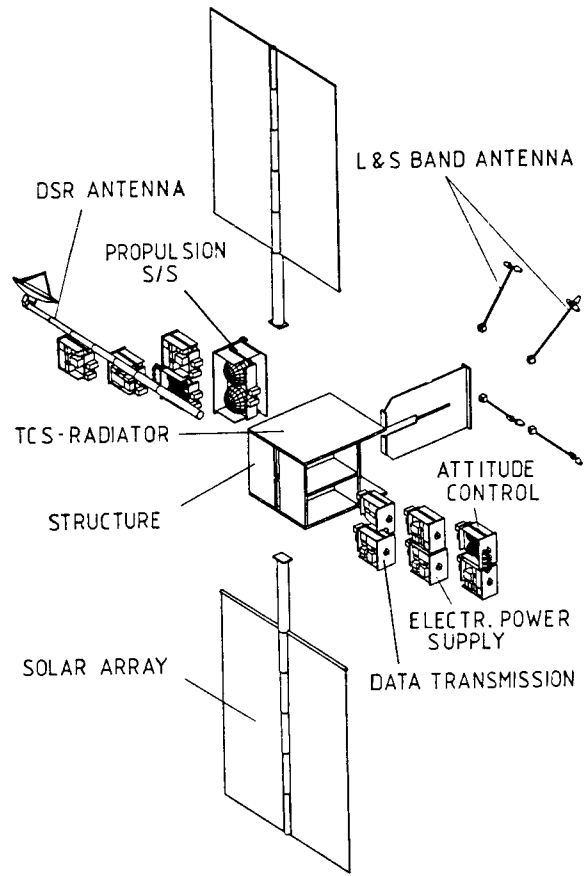
Figure 3 : Resource Module (RM-Element) Exploded View
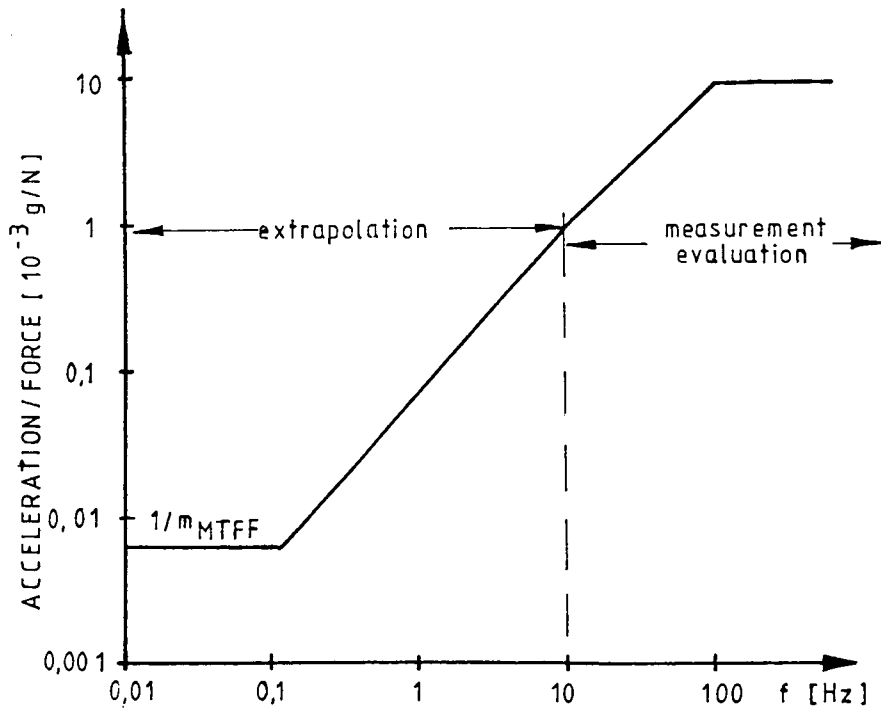


Figure 4 : MTFF Acceleration to Force Transfer Function
(Independent of Excitation Location and Direction)
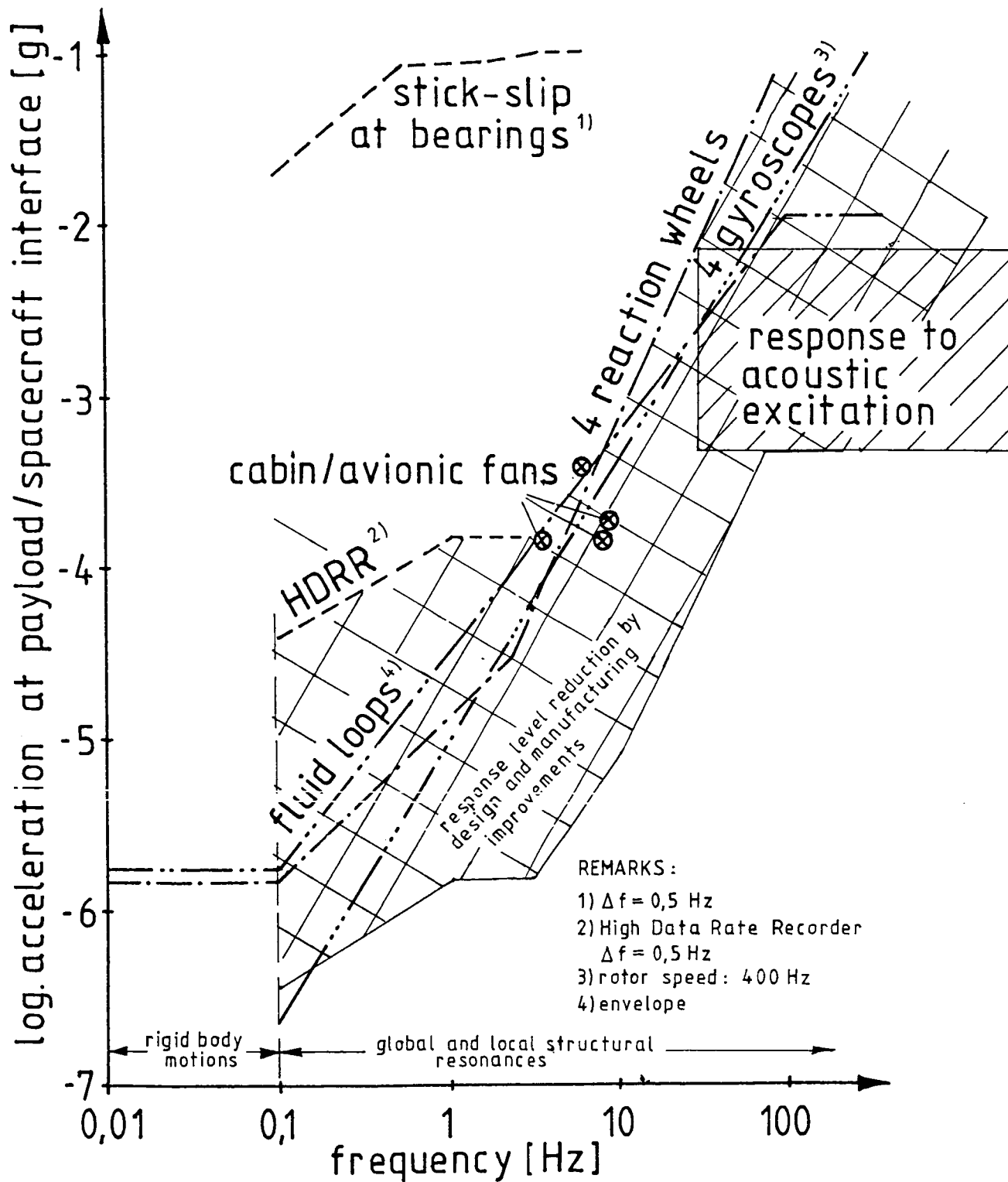
Figure 5 : Predicted Acceleration Response Spectra at Spacecraft/Microgravity
Payload Interfaces
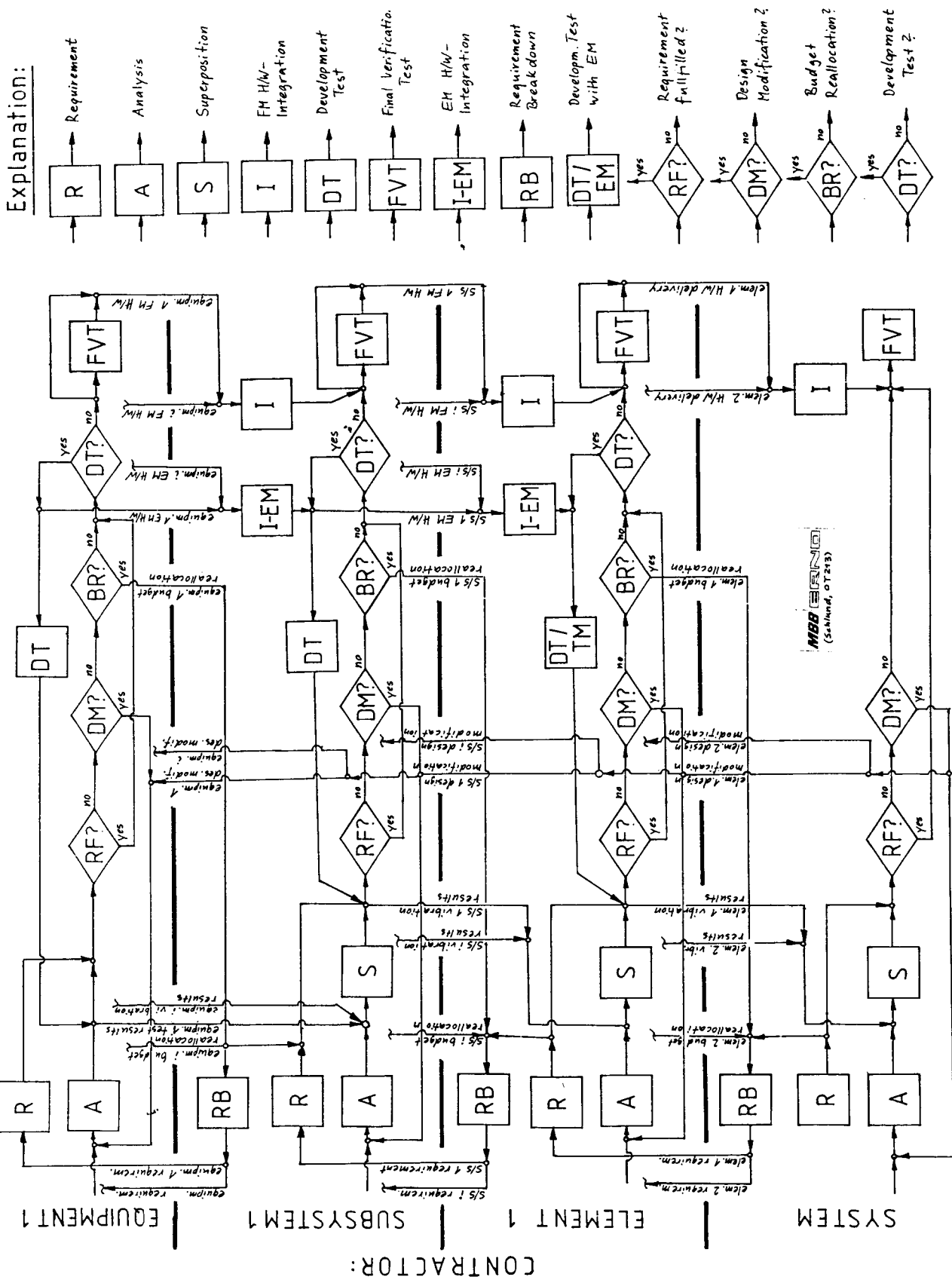
Figure 6 : Microgravity Control Flow Diagram

## SYMBOLS AND ABBREVIATIONS

COMMS    Communication S/S

DMS    Data Management Subsystem

ECLS    Environmental Control and Life Support S/S
EM    Engineering Model
EPS    Electrical Power Distribution S/S

GNC    Guidance, Navigation and Control

HDRR    High Data Rate Recorder

I/F    Interface

MTFF    Man Tended Free Flyer

ORU    Orbit Replacable Unit

P/L    Payload
PM2    Pressurized Module, 2 Segments

RM    Resource Module

S/C    Spacecraft
S/S    Subsystem
STM    Structural Model

TBD    To Be Determined
TCS    Thermal Control S/S

## REFERENCES

[1] Eilers, D.: Mikrogravitaets-Bedingungen orbitaler Plattformen, DGLR-Jahrestagung 1983, October 1983

[2] Space Shuttle STS-9 Final Flight Evaluation Report, Volume II, MSFC-RPT-1038, April 30, 1984

Session VII

# LAUNCHER FACILITIES

# SIMULATION OF THE EFFECTS OF THE ORBITAL DEBRIS ENVIRONMENT ON SPACECRAFT

Michael D. Bjorkman
Boeing Aerospace Company

## ABSTRACT

The past 30 years of spaceflight has resulted in the accumulation of man-made debris in earth orbit from both the operation and the deliberate destruction of spacecraft. Over the years as the flux of particles in earth orbit increased, the probability of impact with a sizable orbital debris particle went from being of negligible concern in the early 70's to the designers of Skylab to being of greater concern than meteoroid impact to the designers of the NASA/International Space Station in the present.

Directly testing for the effects of orbital debris impact on spacecraft exceeds the capability of current ground-based launchers. Closing velocities between spacecraft and orbital debris particles range from 0 to 16 km/s and are distributed so that there is a 50% probability of impact with particles traveling faster than 11 km/s. Laboratory techniques for launching projectiles, the most common being the two-stage light gas gun, are limited to less than 8 km/s, well below the median orbital debris particle velocity.

A remedy for the lack of a technique for testing the effects of orbital debris impacts has been sought along two paths at Boeing and elsewhere. Firstly, through the development of new launcher techniques capable of impact velocities between 8 and 16 km/s and secondly through the development of similitude techniques for modeling 8 to 16 km/s impacts using the present capabilities of projectile launchers.

Pioneering work by Hawke and Fowler in 1980 with electromagnetic rail guns indicated that it might be possible to accelerate projectiles into the 8 to 16 km/s range using a rather simple device. In the intervening years work has been performed at Boeing and a number of other laboratories around the world to bring this technique to fruition. However, it was shown early in the effort that the rail gun as originally conceived was incapable of launching projectiles to velocities larger than those of two-stage light gas guns. Results from our research which reveal some of the processes which limit the performance of rail guns will be discussed along with potential remedies.

Other work at Boeing has focused on developing techniques for performing model experiments at impact velocities less than 8 km/s which are similar to prototype experiments at impact velocities greater than 8 km/s. Through a combination of testing and numerical simulation it has proven possible to develop scaling laws for the motions resulting from perforation of thin plates and the resulting final hole diameters. These scaling laws will be discussed along with their limitations.

# A STEAM INERTING SYSTEM FOR HYDROGEN DISPOSAL
# FOR THE VANDENBERG SHUTTLE

Stuart B. Belknap
The Aerospace Corporation

## ABSTRACT

The Space Shuttle main engines (SSMEs) lead gaseous hydrogen (GH$_2$), run fuel rich, and lag GH$_2$ at shutdown during an SSME abort or flight readiness firing (FRF). At the Kennedy Space Center (KSC), the SSME plumes exhaust into an open trench that is vented and consequently considered safe. At Vandenberg Space Launch Complex Six (SLC-6), the plumes exhaust into a closed duct. There is a concern that the confined hydrogen could ignite, produce an accelerated deflagration or detonation, and damage the launch vehicle.

This paper surveys the two-year feasibility and development test program completed in December 1987 to solve this problem and to design a hydrogen disposal system (HDS) for SLC-6. It was necessary that the solution lend itself to evaluation and verification by subscale testing because of the cost and risk of full-scale experiments with the shuttle or associated flight hardware.

In December 1986, after screening concepts that attempt to burn excess GH$_2$ and open-duct designs that vent GH$_2$, the Air Force selected a novel steam inerting design for development. This concept superheats available sound suppression water to flash to steam at the duct entrance. Testing, analysis, and design during 1987 showed that the steam inerting system (SIS) solves the problem and meets other flight-critical system requirements. The SIS design is complete and available for installation at SLC-6 to support shuttle or derivative vehicles. Without the SIS, the Vandenberg Air Force Base (VAFB) facility might be unusable by hydrogen-fueled space launch systems.

## INTRODUCTION

This paper concerns a postulated threat to the Space Shuttle vehicle (SSV) from unburned hydrogen at SLC-6 at VAFB (figure 1). The SSMEs lead GH$_2$, run fuel rich, and lag GH$_2$ at shutdown during an SSME abort or FRF. At KSC, the SSME plumes exhaust through the mobile launch platform (MLP) into an open trench that is vented and consequently considered safe. At VAFB, the SSME plumes exhaust through the launch mount (LM) into a closed duct (figure 2).

In November 1984, the National Aeronautics and Space Administration (NASA) raised the concern that unburned confined hydrogen might ignite, producing an accelerated deflagration or detonation, and damage the launch vehicle. In September 1985, the Air Force formed a team to develop a solution, make necessary facility modifications, and verify effectiveness in time to support a May 1986 FRF and subsequent shuttle launch at Vandenberg. Program participants are listed in figure 3. This paper surveys the
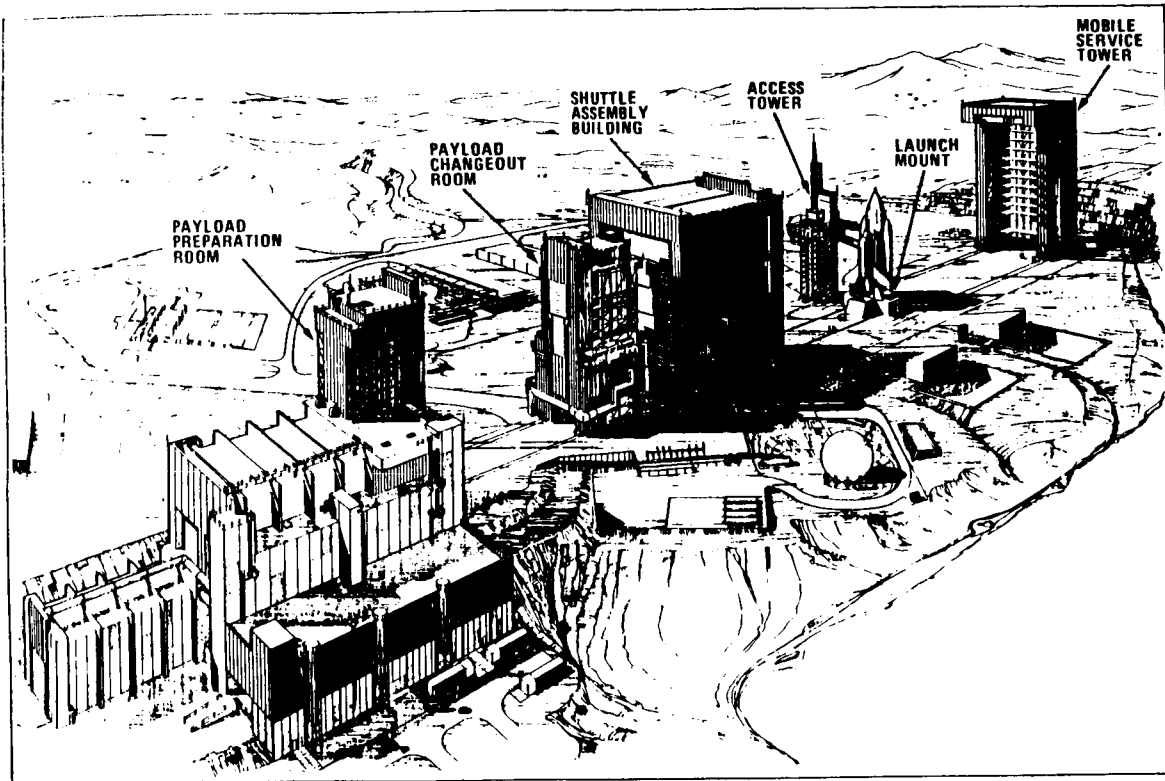
Fig. 1   Space Launch Complex Six at Vandenberg



CHARACTERISTICS
LENGTH 300 ft
VOLUME 727,000 ft$^3$
SOUND SUPPRESSION
WATER FLOW 125,000 GPM

ZONE A
(130 ft)

ZONE B
(115 ft)

ZONE C

ZONE D

ZONE E

EXTEND
ZONE E WALL

10 ft    36 ft

ZONE A
ZONE B       30 ft
(115 ft)   ZONE C

ZONE D

36 ft
ZONE E

90 ft

GROUND LEVEL
EL 100 ft
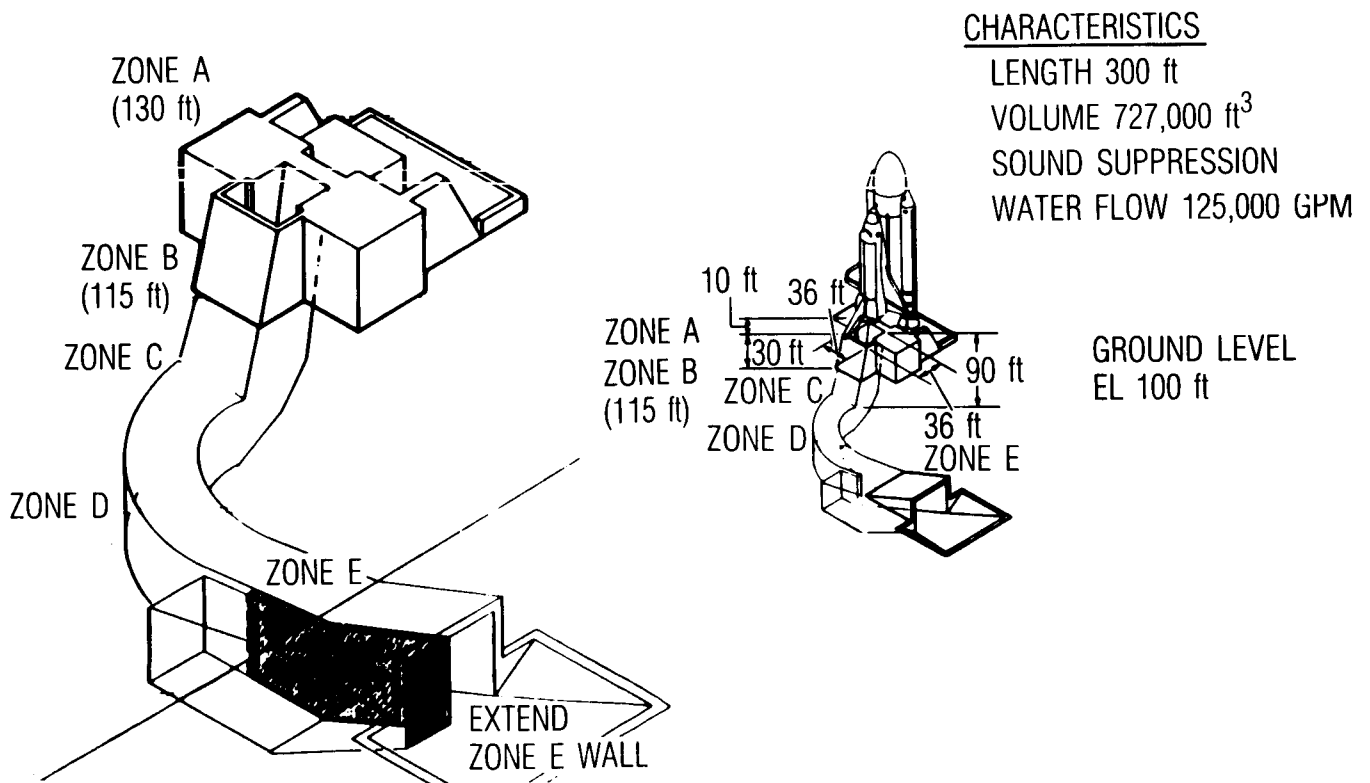
Fig. 2   SSME Duct at Vandenberg

| Organization | Scope of Work |
|---|---|
| United States Air Force | Program Management |
| Aerospace Corporation | Program and Technical Support<br>1/20 Scale Cold Testing<br>Instrumentation Development |
| Martin Marietta Corporation | |
|    Vandenberg | Integrating Contractor for HDS<br>Concept Selection |
|    Denver | Technical Support and 1/7<br>Scale Testing |
| Shuttle Processing Contractor | Integrating Contractor for SIS<br>Development Program |
| Astron Engineering | Steam Inerting Concept<br>Technical Support, 1/100 Scale Testing<br>Nozzle and Header Design |
| Wyle Labs | 1/20 Scale Hot Testing<br>Nozzle and Header Testing |
| S. Levy Corporation | Technical Support<br>Scaling |
| Lockheed Missiles and Space Company | |
|    Sunnyvale and Palo Alto | Technical Support<br>Instrumentation Development |
|    Santa Cruz | 6.4% Transient Testing |
|    Huntsville | MSFC Support |
| Eagle Engineering | Technical Support |
| Cermak Peterka Peterson | Wind Effects Testing<br>Technical Support |
| Grumman | Instrumentation |
| Sverdrup Corporation | Architecture and Engineering |
| Perkin Elmer | Instrumentation Development |
| Jaycor | Computational Fluid Dynamics |
| NASA | |
|    JSC | Program Management Support |
|    KSC | Technical Support |
|    MSFC | 6.4% Scale Induced Environment Testing |
|    Ames | Computer Support |
| Rockwell | |
|    Downey and Vendenberg | Technical and Testing Support |
|    Huntsville | MSFC Testing |

Fig. 3   HDS/SIS Program

314
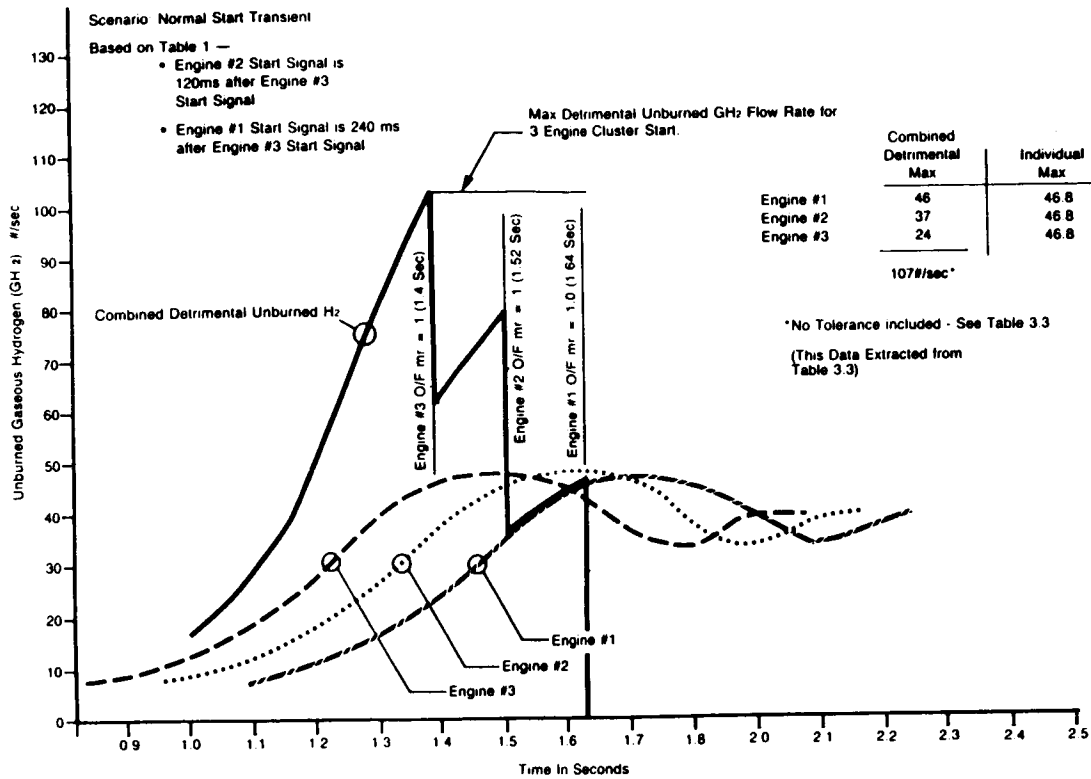
## Fig. 4(a). SSME Ignition Transient

Scenario: Normal Start Transient

Based on Table 1 —
- Engine #2 Start Signal is 120ms after Engine #3 Start Signal
- Engine #1 Start Signal is 240 ms after Engine #3 Start Signal

Max Detrimental Unburned GH₂ Flow Rate for 3 Engine Cluster Start.

Combined Detrimental Unburned H₂

Engine #3 O/F mr = 1 (1.4 Sec)
Engine #2 O/F mr = 1 (1.52 Sec)
Engine #1 O/F mr = 1.0 (1.64 Sec)

|  | Combined Detrimental Max | Individual Max |
|---|---|---|
| Engine #1 | 46 | 46.8 |
| Engine #2 | 37 | 46.8 |
| Engine #3 | 24 | 46.8 |
|  | 107#/sec* | |

*No Tolerance included - See Table 3.3

(This Data Extracted from Table 3.3)

Engine #1
Engine #2
Engine #3

Unburned Gaseous Hydrogen (GH 2) #/sec

Time In Seconds

## Fig. 4(b). FRF Abort Shutdown

Scenario: Three engines at RPL
Engine Shutdown Sequence - No. 1, No. 2, No. 3

|  | Combined Detrimental Max | Individual Max |
|---|---|---|
| Engine #1 | 64 | 75.4 |
| Engine #2 | 51 | 75.4 |
| Engine #3 | 24 | 75.4 |
|  | 139#/sec | |
| 3 Sigma Data Tolerance | 20#/sec | |
| Design Total | 159#/sec | |

(This Data Extracted from Table 3.4)

Shutdown Signal for Engine #1

Engine #1 O/F mr = 1

Engine #2 O/F mr = 1

Engine #3 O/F mr = 1

139 #/sec Max Detrimental Unburned GH₂ Flow Rate

Combined Detrimental Unburned GH₂

Engine #1 Profile
Engine #2 Profile
Engine #3 Profile

Unburned Gaseous Hydrogen (GH2) - #/sec

Time In Seconds

315

two-year feasibility and development program completed in December 1987 to solve this problem and to design an HDS for SLC-6.

## BACKGROUND

During SSME operation, combustion occurs in the chamber when the oxidizer-to-fuel ratio equals or exceeds (approximately) 1, $O/F = 1$ (the stoichiometric ratio is $O/F = 8$). Unburned hydrogen refers to the quantity of $GH_2$ not burned in the engine. Figure 4(a) shows unburned hydrogen time histories from a normal three-engine start to rated power level (RPL). Figure 4(b) shows an FRF shutdown from RPL. The HDS program considered these threat scenarios and other shutdown cases, including an abort during the start transient and a clustered abort that produce a high maximum rate of unburned hydrogen of 190 lb/sec (refs. 1 and 2).

The ground rule in the HDS system specification (ref. 2) is that hydrogen is detrimental only when expelled from a nonburning SSME ($O/F < 1$) predicated on the assumption that $GH_2$ from a burning engine is pyrophoric with air. This position suggests the partial summation of unburned hydrogen flows in figures 4a and 4b. A more conservative assumption is that all unburned hydrogen may be detrimental, suggesting a complete summation over the time histories. In either case, for scenarios considered, the maximum threat is an unburned hydrogen flow on the order of 160 to 200 lb/sec.

NASA supplied an estimate of 1.32 psid (as an indicator) of the maximum steady overpressure allowable at the orbiter base heat shield. This overpressure is produced by the detonation of as little as 1.0 lb of hydrogen at free space distances corresponding to locations in the Vandenberg duct.

Successful hydrogen disposal requires some combination of benign burning, inerting, or venting of excess $GH_2$. At KSC, radial outward firing initiators (ROFIs) mounted near the SSME nozzles provide an ignition source for unburned hydrogen during the SSME start transient. A ROFI is, in effect, a small rocket motor filled with zirconium pellets. These pellents flood the area between the SSME nozzles and the duct entrance with small (550-micron), extremely hot zirconium sparklers. During an FRF or abort shutdown at KSC, it is assumed that the SSME plumes are adequately vented as they exhaust through the MLP into an open trench and excess hydrogen continues to burn.

Between September 1985 and December 1986, the HDS team reviewed several HDS concepts for VAFB: (1) high-energy burnoff igniters (HBOIs) to burn excess hydrogen with zirconium igniters in the duct; (2) jet mixing to force burn the $GH_2$ at the duct entrance; (3) open duct designs to emulate the MLP at KSC; and (4) inerting, initially using carbon dioxide, but later using steam.

During 1986, it became evident that attempts to burn all excess hydrogen, whether by igniters in the duct or by forced air at the entrance, are dangerous and impossible to verify without prohibitively expensive full-scale tests. The Space Shuttle 51-L accident on 28 January 1986

316
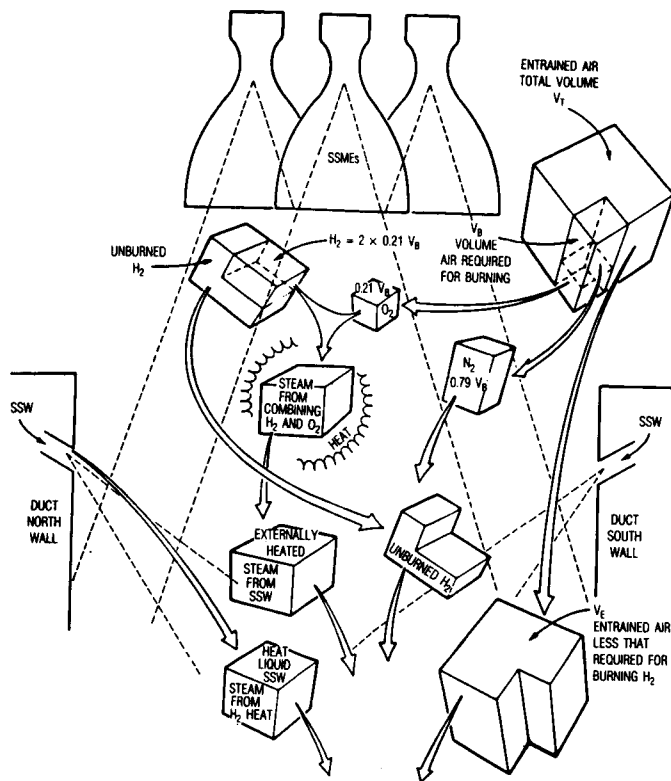
Fig. 5  Steam Sources in the Duct
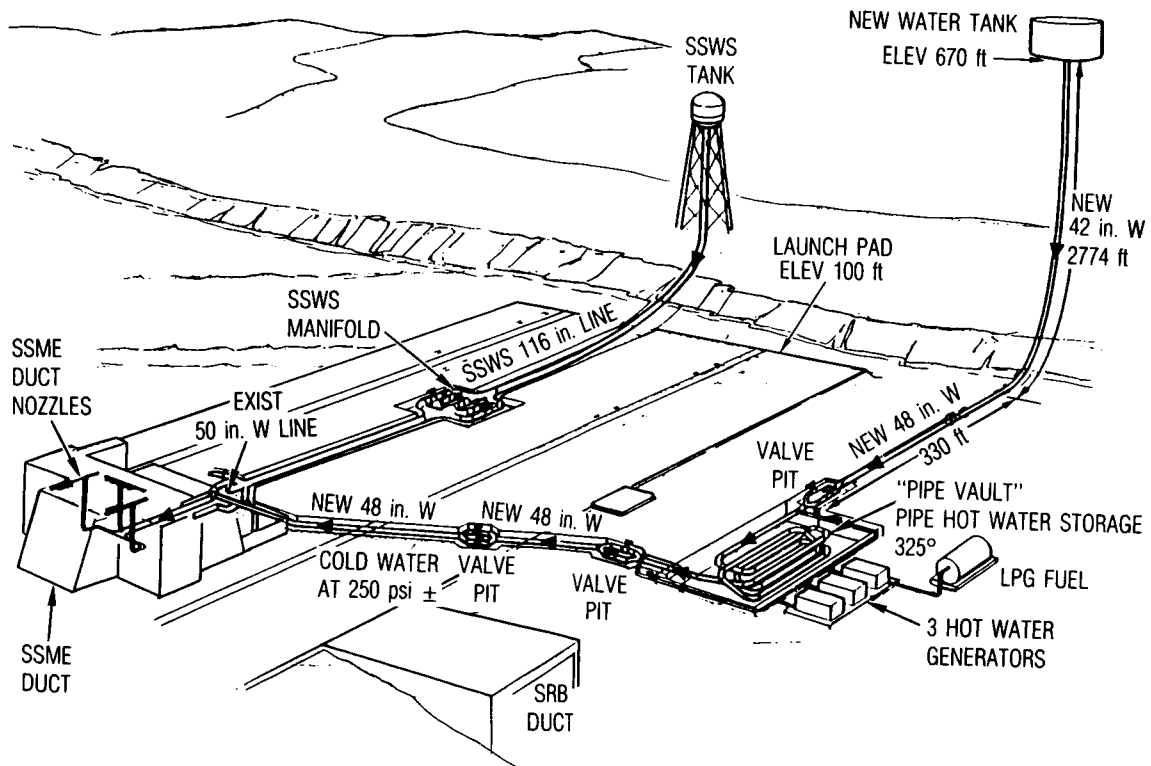


Fig. 6  Steam Inerting System/HDS Concept

317

suspended the imperative for a May 1986 FRF and subsequent launch at VAFB, and also intensified flight safety concerns.

Open-duct options have the advantage of resembling configurations that NASA considers safe. However, such an implementation at Vandenberg requires massive facility modifications. The open geometry also has a disadvantage with respect to analysis and evaluation by subscale testing. With the open boundary condition, controlling effects are very difficult to analyze and scale.

With inerting, the idea is to guarantee that, if combustion stops within the duct (because of a natural or induced condition), the mixture remains inert until safely vented past the duct exit. This sort of inert state should be relatively safe. Also, inert flow within a confined duct should be controlled by linear momentum and lend itself to simple geometric scaling.

After the Concept Selection Review in December 1986, the Air Force baselined the SIS for design and development for use at SLC-6 (ref. 1).

STEAM INERTING

The sound suppression water system (SSWS) at SLC-6 provides fire suppression, deluge, and sound suppression flow. The system introduces 122,000 gpm water flow at the SSME duct entrance for acoustic suppression. The steam inerting system superheats this water such that a prescribed fraction flashes to steam and inerts the duct. This approach guarantees thorough mixing of the inertant with the SSWS flow and avoids the need for a large steam generating plant. The SIS augments inerting processes caused by the SSME.

As shown in figure 5, entrained air of some total volume provides oxygen to oxidize unburned hydrogen from the SSME. A fraction of this air (containing 21 percent oxygen) combines stoichiometrically with part of the unburned $GH_2$ to yield steam. The remaining 79 percent is excess nitrogen, which also serves as an inertant in the duct. The exothermic combustion of the hydrogen releases large quantities of heat, causing a fraction of the SSWS flow to vaporize. This is in addition to the quantity of steam developed at the SSWS nozzles as a consequence of the flashing superheated SSWS flow. Therefore, constituents in the duct include possible residual unburned hydrogen, residual air, excess nitrogen, and steam from three sources. The SIS augments the SSME inerting process to guarantee that the duct remains benign past any station at which combustion stops.

Design Concept

The SIS does not use the as-built SSWS system for SSME flow; rather, it provides a new and separate source of superheated, pressurized water at 122,000 gpm. This design concept is illustrated in figure 6.

The design goal is 55 percent steam by volume in the duct to assure an inert condition for any hydrogen-to-air ratio (refer to requirements
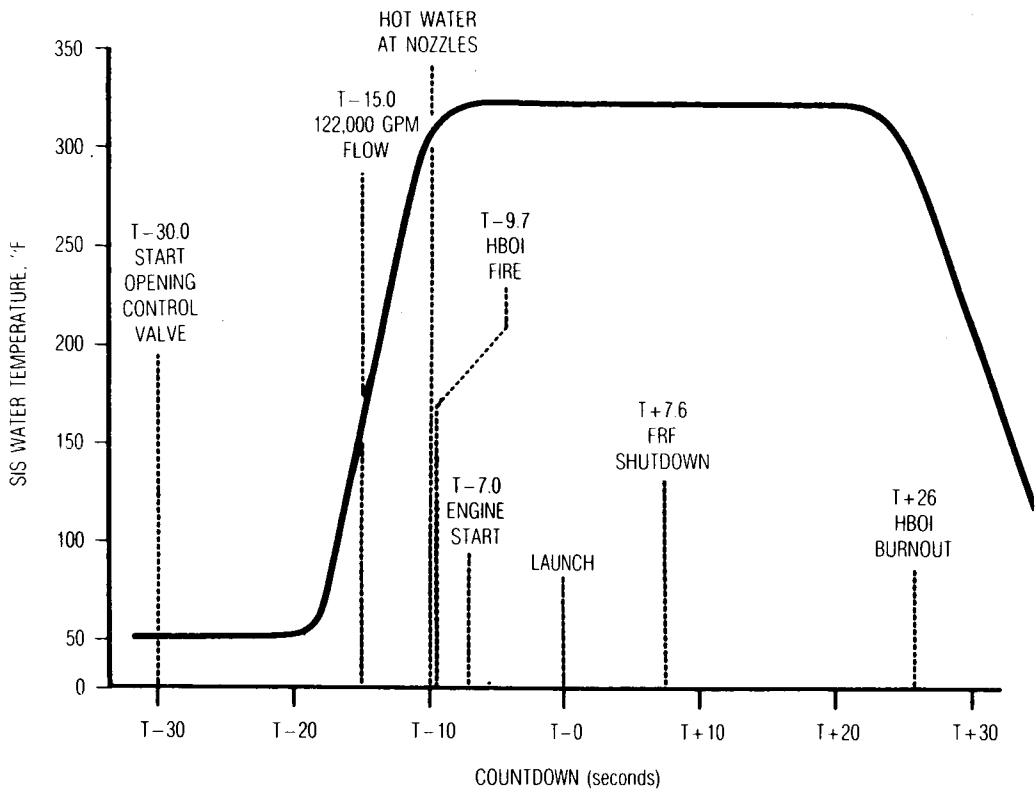
Fig. 7   SIS Operational Time Line
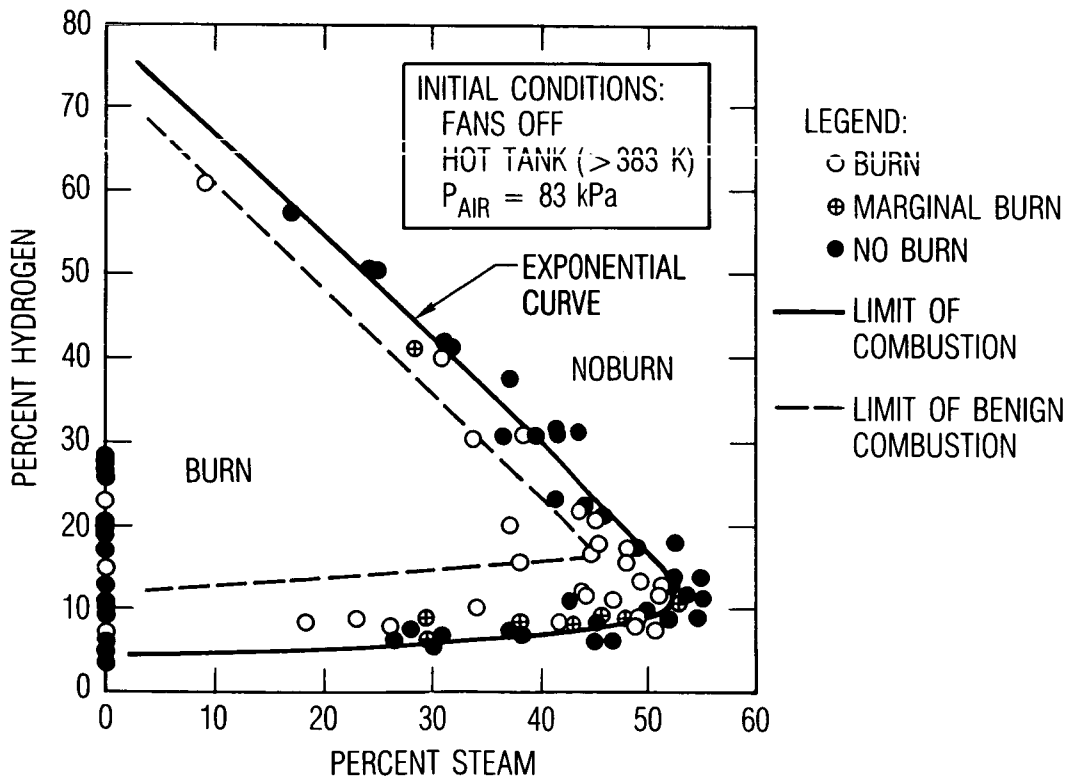


Fig. 8   Flammability Diagram

319

below). Analyses and tests show that this requires a header temperature of 310°F at 145 psig. There is a requirement that the SSWS not splash above the duct entrance level; in particular, it should not introduce water droplets into the SSME exit bells and past the throat prior to SSME fully developed thrust. Therefore, the SIS leads cold water to establish aspiration before the onset of steam. The SIS flow scenario is illustrated in figure 7.

The SIS design includes the use of long-burning HBOIs to augment the SSMEs as ignition sources above the duct entrance. KSC experience and White Sands Test Facility (WSTF) testing (ref. 3) indicate that zirconium sparklers are a safe and effective way to accomplish this objective.

## Requirements

The SIS must inert the duct, vent unburned hydrogen safely at the exit, and not induce the following environments, which may be detrimental to the vehicle or to the facility: splash, overpressure, acoustic, or thermal.

Experiments at Sandia National Laboratories define flammability and detonation limits for hydrogen, steam, and air mixtures. Tests show that flammability limits are independent of scale; however, deflagration to detonation depends on scale. Factors promoting flame acceleration include increased size, obstacles, turns and bends, and turbulence. The requirement, therefore, is that the SIS prohibit combustion of unburned hydrogen in the duct (past the critical surface at the entrance at which combustion from the SSMEs or HBOIs stops). This allows the extrapolation of subscale test results to full scale and avoids the threat of accelerated deflagration in an environment which is, in fact, large in size and turbulent.

A flammability diagram applied to SIS testing is shown in figure 8. The figure includes combustion limits (ref. 4) and benign combustion limits (ref. 5). Then, the (derived) requirement is that the SIS maintain a state in the duct at all locations at all times corresponding to benign points in the figure. A most conservative goal is to achieve 55 percent steam with the SIS alone, because this assures a safe duct for any ratio of hydrogen to air. Failing this, a reasonable objective (with the SSME plume present and ignited at the duct entrance) is to stay beyond the limit of combustion, with additional distance to this limit as margin.

The steam inerting concept has the advantage of providing an easy way to measure system effectiveness. Experiments and analysis show that beyond the duct entrance, past a control surface at which burning has stopped, the duct is in thermal equilibrium. Liquid and gas phases are close to the same temperature such that temperature measurements yield the local concentration of steam.

## FEASIBILITY AND DEVELOPMENT PROGRAM

Each test site provides a scaled flow of superheated water, the scaled hydrogen plume, and instrumentation. Feasibility and development tests flow

320
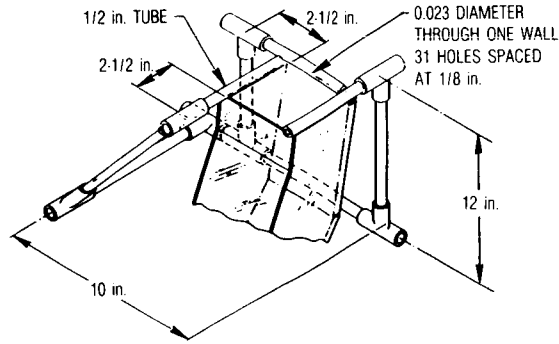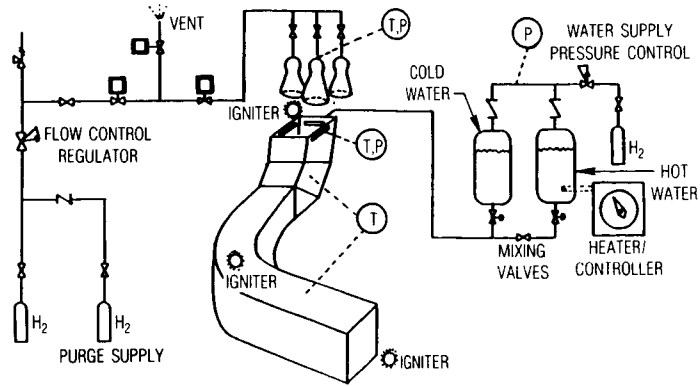
**Fig. 9  Astron 1/100 Scale Test Facility**
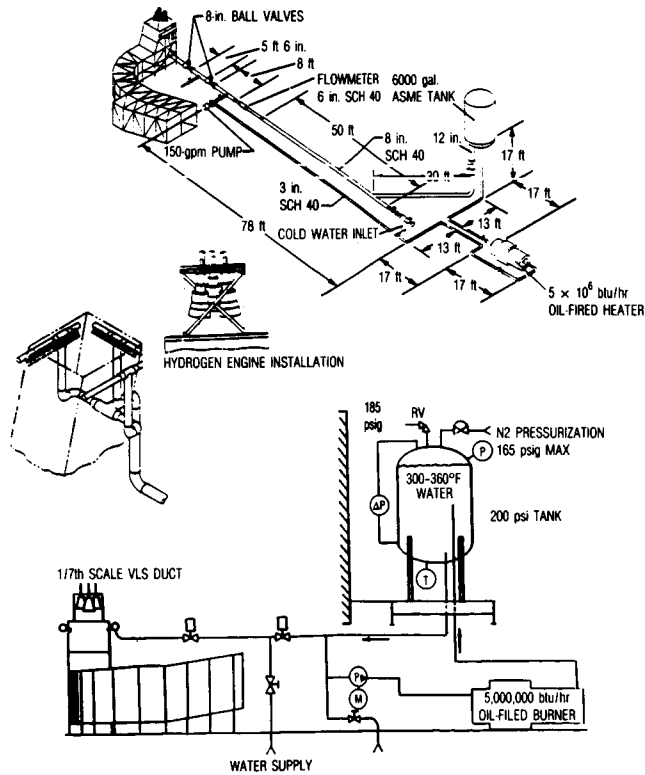


**Fig. 10  MMC/EPL 1/7 Scale Test Facility**

321

the steam header alone to trade splash back against inerting performance. This supports preliminary design of the hot water header and flashing steam nozzles. Subsequent tests use cold gas (helium) to simulate the SSME plume. Then, hot fire tests, with burning hydrogen at the duct entrance, evaluate induced effects and inerting performance. Finally, tests use spark igniters within the duct, and at the duct exit, to verify inert, as opposed to flammable, flow conditions.

The hot fire tests at each site inject a scaled, steady flow of unburned hydrogen into the model SSME duct. The flow corresponds to a maximum (design point) rate of unburned hydrogen entering the duct during a transient SSME startup, FRF, or SSME abort (figure 4). Igniting the $GH_2$ at the SSME nozzles emulates the function of mainstage or HBOI ignition above the duct entrance.

## Astron Tests

The test configuration at Astron includes a 1/100 scale duct with viewports, three scaled SSME exit nozzles (with an igniter), a hot water supply system, and a header with tiny holes to simulate SSME steam nozzles, as shown in figure 9 (ref. 6). The water system has the capability to ramp temperature and pressure up and down or maintain constant operating conditions for a relatively long time. Typical temperature time histories, above 180° but below 212°F, suggest an inert condition in excess of 55 percent steam at points in the duct.

Astron experiments with the steam header alone show that splash above the duct entrance is very sensitive to header and nozzle design. The eventual choice is a header on the east SSME wall depressed 40 deg from the horizontal with 19 nozzles, no header on the west wall, and identical headers on the north and south walls depressed 52 deg with 18 nozzles each.

## Aerospace Laboratories

The Aerospace Aerophysics Laboratory conducted cold flow tests with a 1/20 scale plexiglass model to evaluate flow and mixing effects in the VAFB SSME duct. Hydrogen flow was simulated by a helium jet emanating from a 1/20 scale aluminum SSME nozzle. Instrumentation included pitot pressure and composition sampling probes and hot wire anemometry for air flow velocities. Wool tufts and Schlieren photography supported visualization of streamlines. Aerospace also used a wet duct in which water and carbon dioxide flows operated with and without the helium jet flow.

## Wyle Tests

The test configuration at Wyle resembles that at Astron but at 1/20 geometric scale with correspondingly large holes in the hot water manifolds (ref. 6). Instrumentation includes gas sampling and improved flow velocity measurements. Selected Wyle tests used a bell jar hood arrangement over the duct entrance for accurate measurement of induced aspiration.

## Martin/Denver EPL Tests

As shown in figure 10, the test facility at the Engineering Propulsion Laboratory (EPL) at Martin/Denver employs a 1/7 scale steel model of the VAFB SSME duct (ref. 7). The EPL hot water manifold is a high-fidelity analog of the Vandenberg configuration at 1/7 geometric scale. The EPL manifold uses 1/7 scale steam nozzles rather than simple holes in pipe as used at Astron and Wyle. Instrumentation rakes in the duct, with locations common to Astron and Wyle, include thermocouples, pitot probes, and gas sample ports connected to collection bottles. Instrumentation at EPL included a concept developed by the Aerospace Labs: a memory tube that produces continuous gas samples at a specific point as a function of time.

The development tests at EPL established requirements for the SIS full-scale headers and nozzles. The optimum nozzle is a converging-diverging (CD) type with a full scale 16:1 exit-to-throat ratio (6:1 at 1/7 scale). The CD nozzles increase air entrainment (relieve splash) without compromising performance (inert state in the duct). Phase III tests included use of fans to evaluate wind effects on entrance splash and an air ejector to simulate effects of transient air entrainment.

## Cermak Peterka Peterson (CPP) Wind Tunnel Tests

Wind effects testing was a major part of the SIS development work. This includes wind tunnel tests at CPP at 1/100 scale and fan tests at MMC/EPL at 1/7 scale. The subsonic wind tunnel at CPP simulates the planetary boundary layer for specific terrain, including wind magnitude, direction, and turbulent intensity (ref. 8).

Phase 1 tests modeled the VAFB terrain at 1:1200 scale. This provided boundary layer characteristics for the subsequent 1:100-scale Phase 2 experiments, which included the working model SIS from Astron testing (figure 11). In Phase 3, CPP used an indicator gas to study SIS venting effects at the duct exit.

## Marshall Space Flight Center (MSFC) Testing

NASA developed the 6.4 percent shuttle test facility at MSFC to evaluate the following SSME launch-induced effects: ignition overpressure, vibro acoustic, and thermal. Following open-duct HDS testing at MSFC, the SIS development program evaluated induced environments at Marshall (ref. 9).

## Lockheed Santa Cruz Testing

Lockheed's Santa Cruz Test Facility (SCTF) conducted experiments using a 6.4 percent scale model of the SSME exhaust duct, steam inerting system, and SSV. The orbiter model includes three model SSMEs that faithfully simulate transient as well as steady-state operation of the full-scale engines, including sequential start and shutdown (refs. 10 and 11).

The test program had five tasks. Tasks I through IV developed the model SSME start/shutdown transients, provided SIS steady performance data for

DEFINITIONS:                    MODEL M/PROTOTYPE P

                                SPEED        TIME       DISTANCE

GENERAL                         $u_M/u_P$      $t_M/t_P$     $d_M/d_P$
FREE STREAM REFERENCE           $u_{RM}/u_{RP}$
TOWER 301 REFERENCE             $u_{TM}/u_{TP}$
LOCAL POINT                     $u_{LM}/u_{LP}$

SCALING RELATIONS:              $(V_M/V_P)(t_M/t_P)(d_P/d_M) = $ CONSTANT

                                $(u_{RM}/u_{RP}) = (u_{TM}/u_{TP}) = (u_{LM}/u_{LP})$
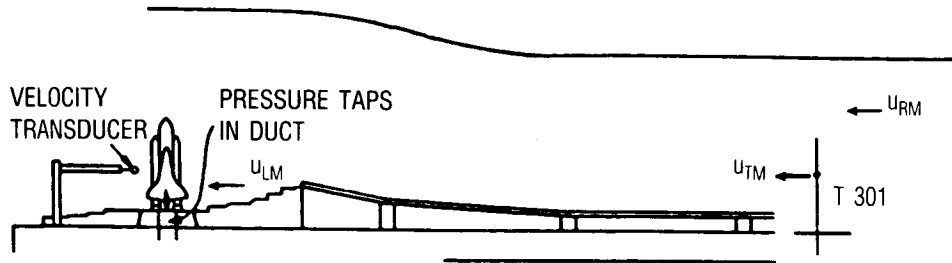


STATISTICS

DEFINITIONS:

DENSITY DISTRIBUTION OF SPEEDS                    $f_U(u)$
DENSITY DISTRIBUTION OF PEAKS IN TIME T           $f_{UP}(u)$
MEAN SPEED                                        $m_U$
RMS SPEED                                         $s_U$
TIME INTERVAL                                     T
NUMBER OF UPWARD CROSSINGS PER TIME               N

MODE OF PEAK SPEEDS                               $m_{UP}^0$

STATISTICAL RELATIONS:   TURBULENT INTENSITY = $s_U/m_U$

$m_{UP}^0/m_U = 1 + (s_U/m_U)[-2 \ln (1/NT)]^{1/2}$
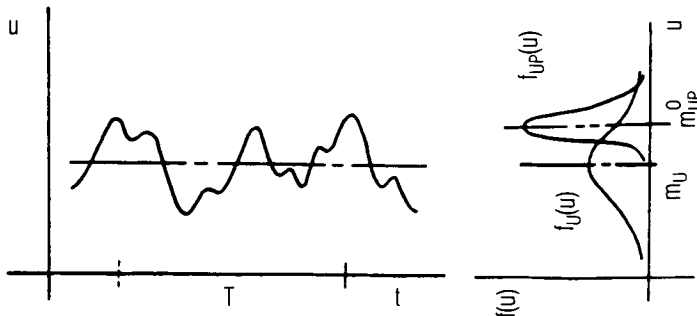


Fig. 11   Wind Tunnel Scaling and Statistics

correlation with other sites, studied transient effects on performance, and evaluated induced effects. Task V provided data to resolve issues. Task V tests included an improved SSME start simulation, improved thermocouples to deduce steam concentration, and a test with the SIS using cold water only.

## RESOLUTION OF ISSUES

The Test and Analysis Program addressed concerns with SIS performance and function.* By December 1987, in the judgement of the program's Technical Advisory Committee (TAC), all concerns were answered with no outstanding issues (ref. 12). Discussion follows.

### Induced Environment

This issue refers to environments induced on the facility and vehicle by the SIS; specifically pressure, acoustic, thermal, and splash.

The SIS must exert no unacceptable back pressure (induce no significant reverse flow) on the SSME during transient or steady operation. The 6.4 percent model SSME engines developed at SCTF provide an excellent emulation of the full-scale article. The model chamber pressure rise rate is tailored to 29,000 psi/sec, equivalent to the SSME rise rate of 1900 psi/sec, such that transient and steady overpressure results apply to full scale. Tests show that levels are acceptable according to Rocketdyne experience.

Results from the 6.4 percent facility at MSFC show that the SIS does not significantly increase steady-state acoustic levels on the facility or on the vehicle (ref. 9). Rockwell concluded that, from an acoustics standpoint, there are no known limitations on the use of the SIS modification at VAFB.

The SSWS, with or without the SIS, must not splash above the duct entrance for all wind conditions. Specifically, it must not introduce water into the SSME bell and past the throat prior to fully developed thrust. Wind tunnel tests with the Astron 1/100 scale SIS at CPP established worst-case winds (ref. 8). Phase 1 tests at 1:1200 scale provided boundary layer characteristics for the Vandenberg terrain for the subsequent Phase 2 (high-fidelity) 1:100-scale experiments.

Conditions in the tunnel are nearly independent of Reynolds' number, and other similarity requirements are met; therefore, speed ratios in the tunnel are equivalent to corresponding ratios at full scale for a particular wind azimuth. Figure 11 illustrates the relation between model and prototype ratios. The launch commit criteria for Vandenberg specifies peak wind speed. This, therefore, provides the criteria for wind tunnel testing. The CPP tunnel is set according to mean speed; consequently, a peak gust to mean ratio is required to set test conditions (figure 11). This ratio was measured during the 1:1200-scale test and also calculated from theory.

---

* Aerospace White Papers (18 February 1987) and Lockheed Responses to White Papers (24 March 1987).

| 15 SEPT 1987 | | MMC/EPL | MSFC STEAM ONLY | | SCTF STEAM ONLY | | | |
|---|---|---|---|---|---|---|---|---|
| | | | | | ORIGINAL H2O SYSTEM | | MODIFIED H2O SYSTEM | |
| TEST NUMBER | | #3 | P216-071 | P216-071 | 24683 | 24673 | 25104 | 25104 |
| TEST DATE | | APRIL 1987 | 30 JULY 1987 | 30 JULY 1987 | 9 JULY 1987 | 9 JULY 1987 | 14 SEPT 1987 | 14 SEPT 1987 |
| TIME SLICE, SECONDS | | AVERAGE | 7.5 TO 7.8 | 9.8 TO 10.1 | 7.5 to 7.8 | 9.8 TO 10.1 | 6.0 TO 6.3 | 7.6 TO 7.9 |
| AVG. HEADER PRES, PSIA | | 149 | 142 | 142 | APROX 160 | APROX 158 | APROX 155 | APROX 158 |
| AVG. HEADER TEMP, DEG F | | 300 | 302 | 302 | APROX 295 | APROX 305 | APROX 294 | APROX 303 |
| ID | LOCATION | TEMP / % STM | TEMP / % STM | TEMP / % STM | TEMP / % STM | TEMP / % STM | TEMP / % STM | TEMP / % STM |
| TD 7 | EAST TOP ZONE D EXIT | 172.60 / 54.83 | 180.94 / 53.08 | 183.18 / 53.76 | 168.83 / 43.30 | 167.93 / 42.41 | 177.38 / 52.61 | 177.98 / 53.33 |
| TD 8 | EAST BOT/MID ZONE D EXIT | 174.20 / 56.86 | 184.63 / 57.55 | 184.58 / 57.49 | 163.10 / 37.87 | 161.35 / 36.32 | 172.27 / 46.87 | 174.63 / 49.46 |
| TD 9 | EAST BOTTOM ZONE D EXIT | NA | 184.34 / 57.19 | 179.74 / 51.68 | 163.08 / 37.85 | 161.80 / 36.72 | 172.43 / 47.04 | 174.18 / 48.96 |
| TD 4 | CENTER TOP/MID ZONE D EXIT | 173.50 / 55.97 | 182.91 / 55.43 | 183.46 / 56.10 | 168.20 / 42.68 | 164.60 / 39.23 | 171.87 / 46.44 | 172.47 / 47.09 |
| TD 5 | CENTER BOT/MID ZONE D EXIT | 173.90 / 56.48 | 183.64 / 56.32 | 182.31 / 54.70 | 159.20 / 34.50 | 156.98 / 32.69 | 173.07 / 47.73 | 173.13 / 47.80 |
| TD 6 | CENTER BOT ZONE D EXIT | 172.00 / 54.08 | 183.35 / 55.96 | 180.36 / 52.63 | 166.05 / 40.59 | 165.25 / 39.84 | 171.98 / 46.56 | 174.06 / 48.82 |
| TD 1 | WEST TOP ZONE D EXIT | 165.40 / 46.42 | 182.83 / 55.33 | 183.64 / 56.32 | 169.43 / 43.91 | 172.70 / 47.33 | 172.18 / 46.77 | 173.19 / 47.87 |
| TD 2 | WEST BOT/MID ZONE D EXIT | 169.10 / 50.60 | 183.63 / 56.31 | 182.94 / 55.46 | 166.60 / 41.12 | 164.40 / 39.05 | 168.48 / 42.96 | 173.80 / 48.53 |
| TD 3 | WEST BOTTOM ZONE D EXIT | 168.30 / 49.67 | 182.18 / 54.55 | 180.68 / 52.77 | 163.73 / 38.43 | 164.20 / 38.87 | 170.18 / 44.68 | 171.93 / 46.51 |
| ZONE D EXIT AVERAGE | | 53.11 | 55.75 | 54.77 | 40.03 | 39.16 | 46.85 | 48.71 |
| TD 3 PRIME | WEST BOTTOM ZONE D EXIT | 168.30 / 49.67 | NA | NA | 177.15 / 52.34 | 183.68 / 60.74 | 156.31 / 32.17 | 168.98 / 43.46 |
| TD 4 PRIME | CENTER TOP/MID ZONE D EXIT | 173.50 / 55.97 | NA | NA | 161.50 / 36.46 | 166.88 / 41.38 | 160.85 / 35.89 | 170.28 / 44.78 |
| TD 9 PRIME | EAST BOTTOM ZONE D EXIT | NA | NA | NA | 165.68 / 40.24 | 168.80 / 43.28 | 149.10 / 26.92 | 167.30 / 41.80 |
| ZD EXIT AVG PRIME | | 52.82 | NA | NA | 43.01 | 48.47 | 31.66 | 43.35 |

Fig. 12    Steam Concentrations from SCTF Compared to MMC/EPL and MSFC

| Parameter | Aston | Wyle | Santa Cruz | Martin |
|---|---|---|---|---|
| Scale | 1/100 | 1/20 | 1/16 | 1/7 |
| Phase | II | II | II | II |
| Test Number | 1371 | 2A | 68 | 45 |
| Header Temperature, °F (Sea Level) | 310 | 307 | 300 | 307 |
| N/S Header Dip Angle | 53/37 | 53/37 | 60/40 | 60/40 |
| Nozzle Spacing | NonVLS | NonVLS | VLS | VLS |
| Nozzle Configuration | HIP* | HIP* | 6:1 C/D | 6:1 C/D |
| Method of Measuring | Bell Jar | Bell Jar | Anemometers | Thermocouples |
| Full-Scale Air Entrainment, lb/s | 2380 | 2036 | 2227 | 2150 |
| HIP = Hole in Pipe | | | | |

Fig. 13   Air Entrainment Rates

326

Worst-case wind directions at CPP are 180 deg azimuth for maximum pressure differential and 135 deg for worst observed aerosol. The puff of aerosol comes off the west wall, rises a quarter of the way to the SSME nozzles, and curves back into the center of the duct. Effects in the duct are such that the splash boundary should be the same at all scales; however, the magnitude of the splash does not geometrically scale and is probably much worse at small sizes. The next step, therefore, is to exercise these worst-case winds at the higher-fidelity MMC/EPL test facility.

Tests at EPL used large fans to induce flows representative of CPP worst-case winds. There was some splash back during the water start transient at EPL, although none as high as the SSME exit plane. A definitive test of splash effects on the engine employed a properly scaled helium purge of 3.5 ft/sec through the SSME. For worst-case winds, the purge velocity is not reversed; therefore, no steam passes the throat. And droplet trajectory analysis indicates that no large drops would reach the SSME exit plane at full scale (ref. 7).

## Burning at the Duct Entrance

The specific issue here is whether or not detrimental excess hydrogen, ignited by the SSMEs or HBOIs above the duct entrance, continues to burn in a robust and global fashion down to some (defined as) critical surface within the duct.

Analysis and study by Aerospace* concludes that single-point ignition above the duct results in a fully burning (turbulent combustion) flame for SSME conditions. Maximum flame lift-off is less than eight inches (flames are inside the nozzle). Blow-off does not occur. These conclusions agree with test observations.

## Inerting in Duct

It is convenient to define a critical surface at the duct entrance at which combustion stops because of a deficiency of hydrogen or air (or because of an excess of inertants from the combustion process or the SIS flashing sprays). There may also be a critical surface at (or beyond) the duct exit past which the inert mixture becomes weakly flammable. The criterion for an inert duct is that points between these surfaces correspond to benign states in the flammability diagram (figure 8).

As part of an early evaluation of SIS feasibility, Aerospace performed a control volume analysis, injecting steam plus burning hydrogen into a duct.* This study shows that the SIS should inert the duct and that the process is self-compensating: increased hydrogen or air flow increases combustion and returns the duct to an inert state. All subsequent testing confirms these conclusions.

---

* Aerospace White Papers (18 Feburary 1987) and Lockheed Responses to White Papers (24 March 1987).
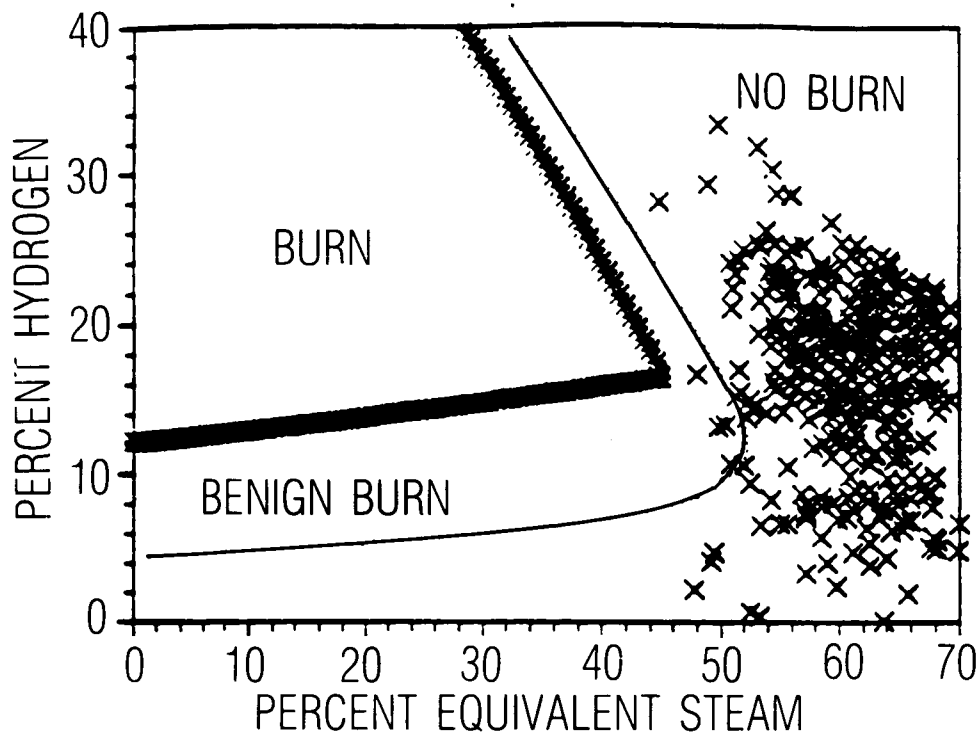
Fig. 14(a)   Hydrogen vs Steam Concentrations for All EPL Tests
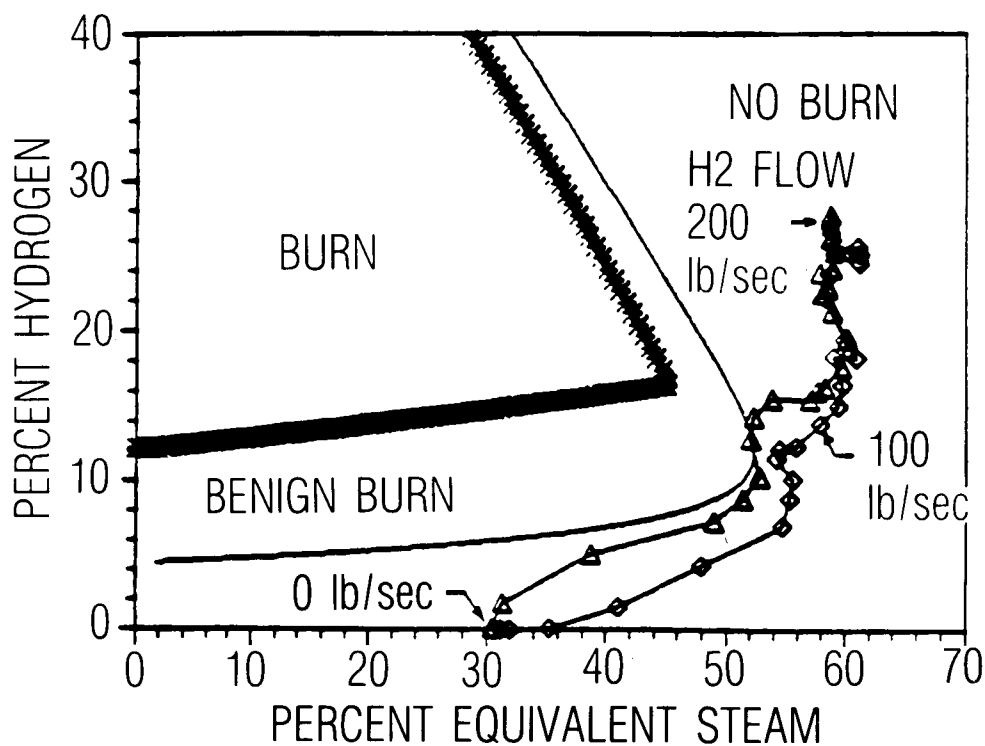


Fig. 14(b)   Hydrogen vs Steam Concentrations During EPL Startup Transients

328

For tests with the steam header alone, figure 12 compares steam concentrations from the SCTF 6.4 percent test with data from MMC/EPL at 1/7 scale and MSFC and 6.4 percent (refs. 7, 9, and 11). Results compare well, although the SCTF values are systematically a few percent lower.

Figure 13 presents full-scale equivalent entrainment rates from steam-only tests for the four different scales and indicates excellent agreement. The MMC/EPL calculation of air entrainment is predicted on the volume fraction of steam indicated by duct thermocouples. Calculations from Wyle use a bell jar. The SCTF tests use hot wire anemometers to calculate entrainment. Agreement among these different sites and methods supports two key conclusions about conditions in the duct: geometric scaling applies, and the assumption of local thermal equilibrium is valid.

For hydrogen experiments, the state in the duct is more complex. In the neighborhood of a burning hydrogen plume, temperatures are very high -- well in excess of the boiling point of water, 212°F. During SSME mainstage, such a condition may extend well into the duct. During the ignition or shutdown transient, this condition exists near the entrance (above the critical surface at which combustion stops). The SIS must inert the duct past this surface. Tests verify this condition in that steam fractions (from temperature data) compared to hydrogen concentrations (from samples) correspond to benign points in the flammability diagram of figure 8. At a specific location, of course, the thermocouple must be robust enough to survive the plume and fast enough to track the inerting process.

The MMC/EPL tests provide additional data pertaining to steam concentrations in the duct. These include experiments to study system margin using an air ejector to augment air entrainment by factors up to 2.5 times the steady state design point level. Figure 14(a) shows that all measurement locations for all EPL tests are safe on the flammability diagram (figure 8). Figure 14(b) illustrates trajectories on the diagram during the startup transient for two EPL tests (ref. 7). The trajectories begin and remain safe. This constitutes a dynamic verification of the (statically derived) flammability boundary.

Test and analysis work at MMC/EPL answered several special performance issues: time required to fill the duct with steam, steam concentration in the region of air between the three SSME plumes, and the effects of condensation at the duct walls (ref. 7).

Scaling

The S. Levy Corporation provided scaling analysis during the SIS program. Theory and experiment, as reviewed above, show that, within the duct, inerting performance scales geometrically as required. Parameters affecting buoyancy at the duct entrance and exit are Froude scaled. Momentum scaling is used to match the 1/100 header flow to simulated winds. As noted, water sprays, droplets, and agglomerations do not scale. However, associated testing is very conservative, because effects are much more severe at small size than at large size.
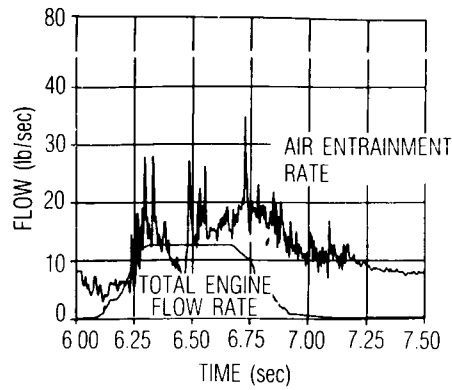
Fig. 15  Air Entrainment for SCTF 6.4% FRF Test
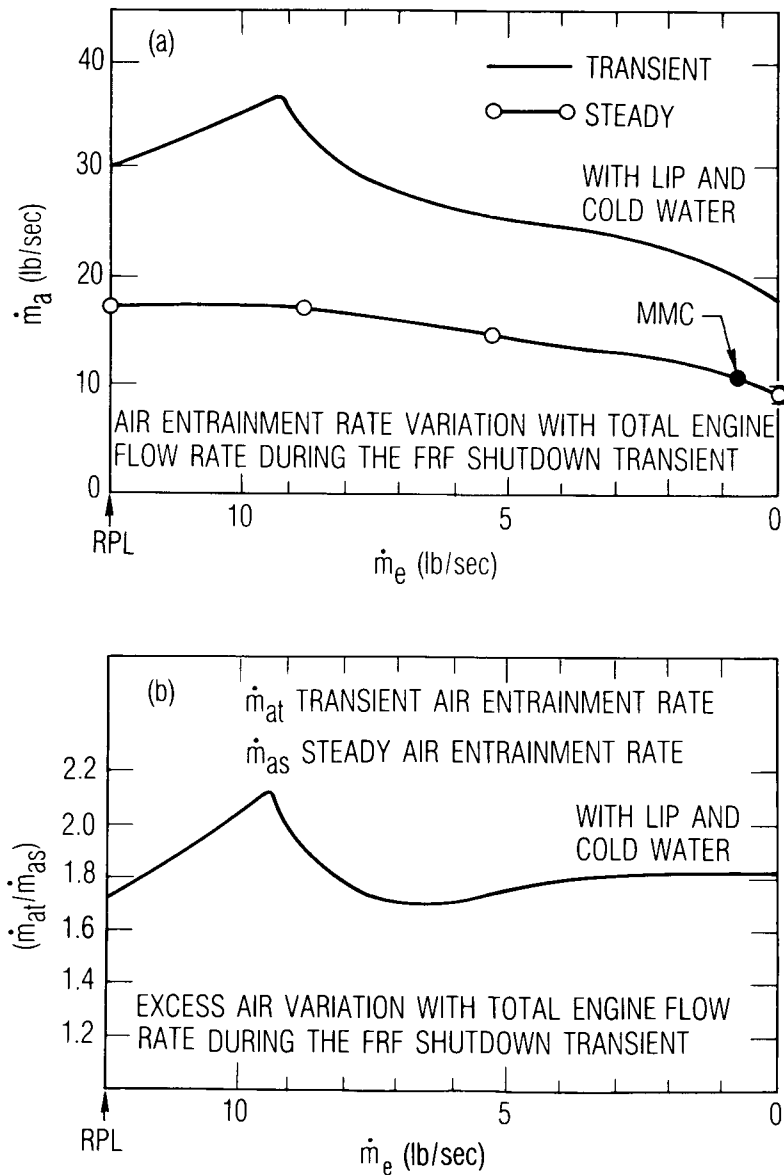


Fig. 16  Transient Compared to Steady Air Entrainment During FRF Shutdown
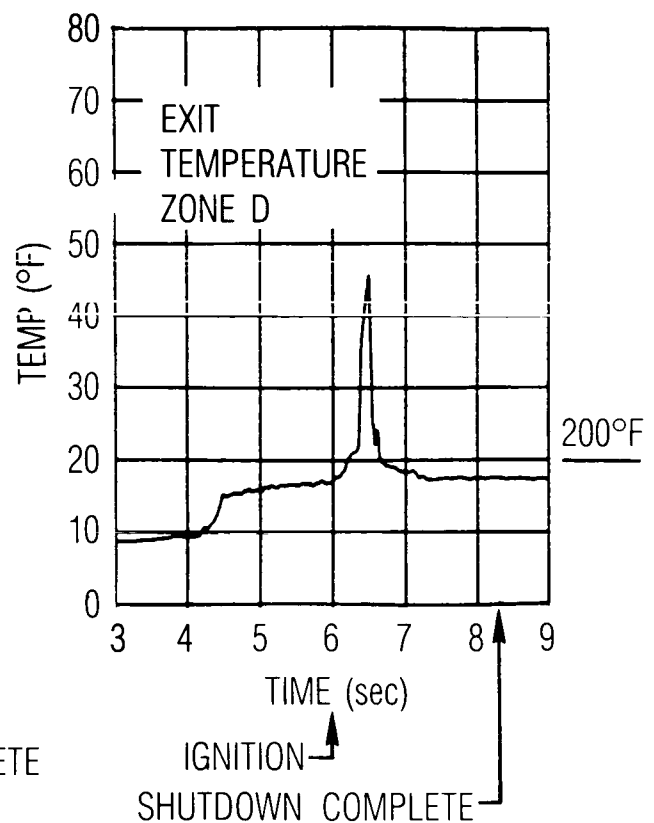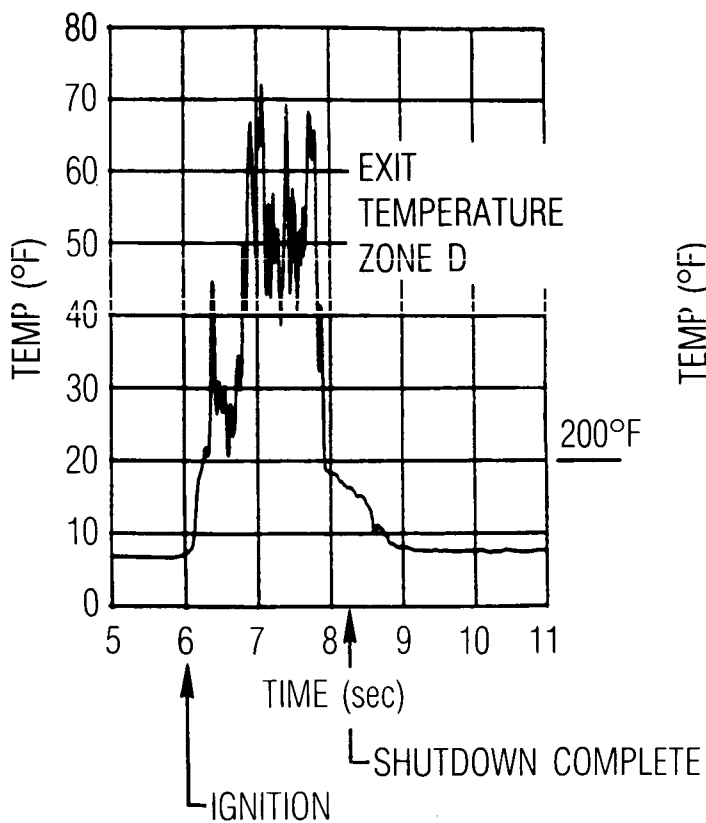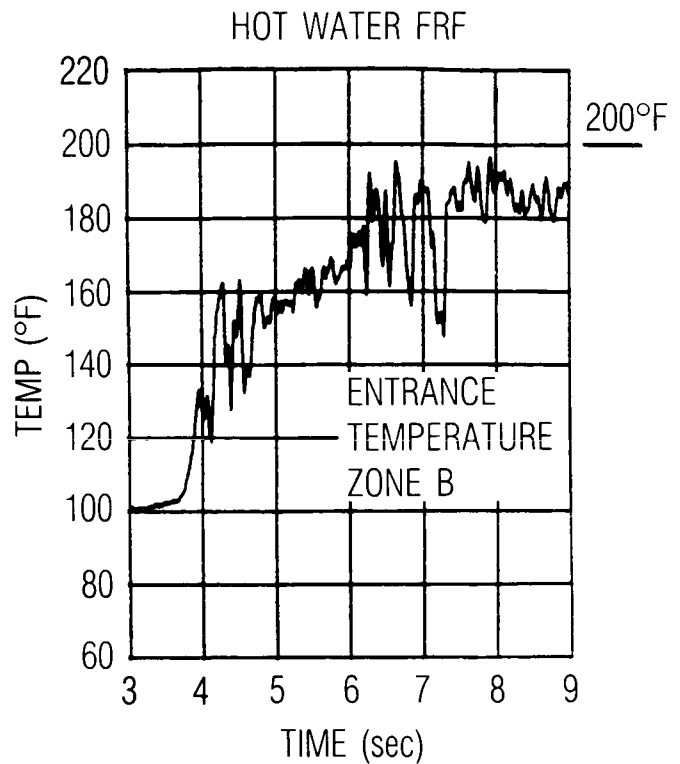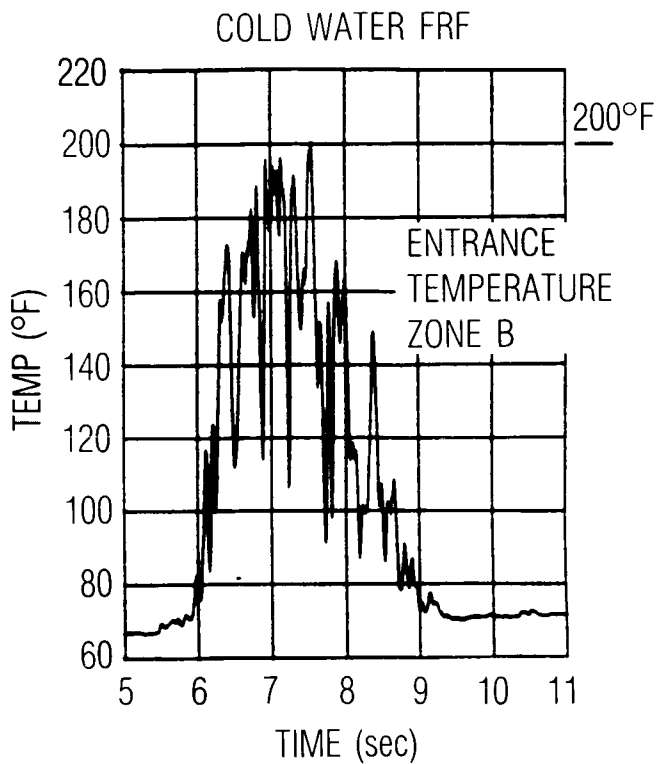
Fig. 17  Temperature in Duct During FRF With and Without Heated Water

This credibility of performance scaling is most important. It is this feature of steam inerting that supports acceptance of the SIS without a prohibitively expensive, full-scale SSME test prior to FRF.

## Transient Effects

The 6.4 percent tests at SCTF satisfy a postulated need for data with SSME engines, including a transient hot fire phase. There was a question concerning whether or not steady tests at the maximum rate of unburned hydrogen (design point threat) are an adequate representation of the corresponding transient condition. The concern is that dynamic lag might significantly increase aspiration in the transient shutdown case.

The SCTF tests simulated FRF and clustered abort shutdown scenarios. Figure 15 illustrates air entrainment and total engine flow rate for a 6.4 percent FRF with SIS superheated water. For comparison, SCTF tests included an FRF run with ambient SIS water. The ratio of air entrained to engine flow rate at SSME rated power level (RPL) is approximately 2.40 for cold water as opposed to 1.35 for the baseline hot water SIS. That is, the cold water case aspirates 78 percent more air than the hot water system.

The final tests at SCTF used a small lip on the SSME duct to reduce subscale splash. These experiments included increased test duration at RPL and steady operation at 72 percent and 43 percent RPL toward the end of a run to diagnose transient aspiration effects. The (final) cold water test happened to have the longest run duration; therefore, is best for this diagnosis. Figure 16 compares transient to steady aspiration for values of total engine flow rate for the cold water test. The lower sketch shows the ratio, which has a maximum value of 2.10. With a correction for hot water, this ratio is 2.10/1.78 = 1.18. Therefore, the maximum increased air entrainment because of transient lag ranged from 18 percent for hot to 110 percent for cold SSWS water.* As explained above, MMC/EPL testing shows that the SIS meets requirements and is safe for as much as 150 percent extra air (ref. 7).

Comparison of SCTF hot and cold water tests contributes insight into the steam inerting process. Figure 17 compares temperatures for the hot and cold tests at the floor of the duct entrance (zone B) and at the center of the duct exit (zone D).

With the hot water SIS, the entrance temperature near the wall advances to 180 and then to 190°F, continuing after mainstage shutdown -- indicating a continuing inert condition. The SSME plume evidently does not reach the lower wall of the duct. The exit condition is 180°F (inert) and jumps briefly to 450°F at SSME start. This suggests that the plume initially projects burning or superheated gas well into the duct. But, very quickly, the added steam from combustion inerts the entire duct. Conditions remain inert after combustion stops. This supports the key SIS operational requirement.

---

* Gogineni, P. R.: Transient Flow Effects. Lockheed Interoffice Corresponsdence (20 Oct. 1987).
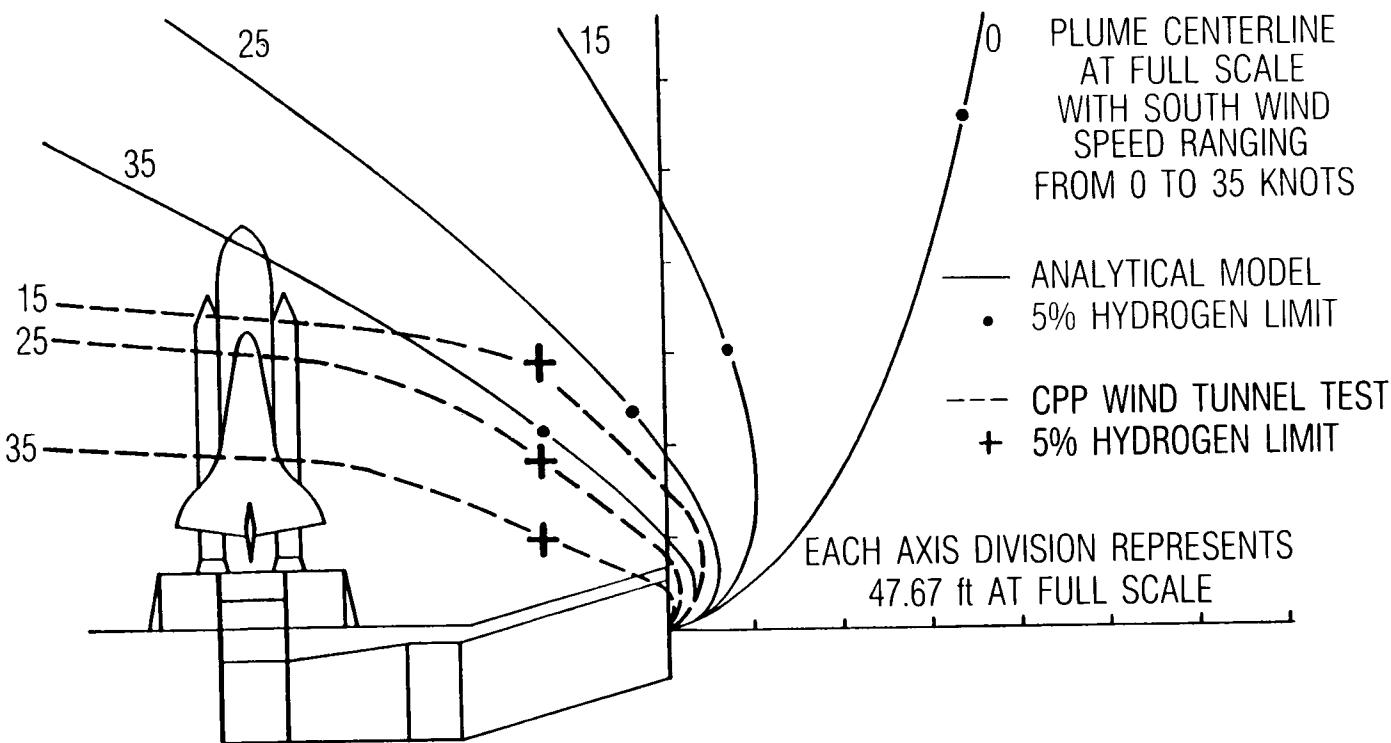
Fig. 18   Exit Plume Concentrations Test Results

PLUME CENTERLINE
AT FULL SCALE
WITH SOUTH WIND
SPEED RANGING
FROM 0 TO 35 KNOTS

——— ANALYTICAL MODEL
•  5% HYDROGEN LIMIT

--- CPP WIND TUNNEL TEST
+  5% HYDROGEN LIMIT

EACH AXIS DIVISION REPRESENTS
47.67 ft AT FULL SCALE

FLAMMABILITY DIAGRAM
FULL SCALE WITH NO SOUTH WIND
(phase change included)

----- MIXTURES ALONG PLUME AXIS
▲ EXIT PLANE
• END OF FLAMMABLE PLUME
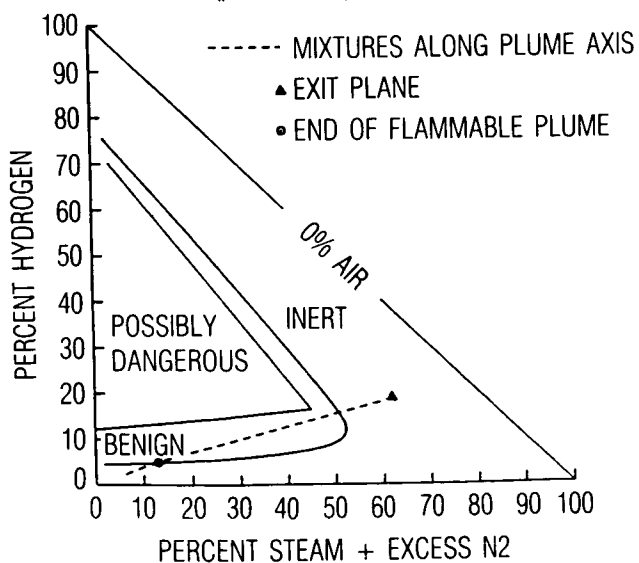
FLAMMABILITY DIAGRAM
FULL SCALE WITH 35-KNOT SOUTH WIND
(phase change included)

----- MIXTURES ALONG PLUME AXIS
▲ EXIT PLANE
• END OF FLAMMABLE PLUME

PERCENT HYDROGEN

0% AIR
INERT
POSSIBLY DANGEROUS
BENIGN

PERCENT STEAM + EXCESS N2
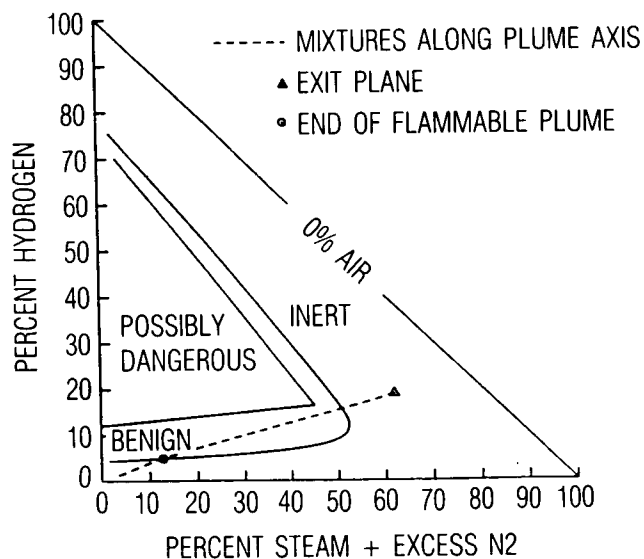
Fig. 19   Exit Plume Concentrations on Flammability Diagram

333

With cold water, the SSME plume quickly raises the temperature at the entrance floor to 190°F and at the exit to 550°F. For approximately 0.5 sec, just before mainstage shutdown, the cold test entrance temperature is well below 180°F. The exit temperature gradually ramps down from 180°F to ambient during this interval.

Therefore, with the hot water SIS, the duct remains inert and safe throughout the FRF. Without the SIS (with cold water), these data do not prove that the duct remains inert. Very possibly, in the cold water experiment, sufficient hydrogen has burned between the entrance and points in question such that the duct is safe. But detailed sampling over repeated runs would be required to show this, and arguments would be statistical. The SIS (with hot water) makes the duct safe with generous margin.

## Purging and Venting Duct

Toward the end of the operational scenario in figure 7, the SIS must provide sufficient momentum to purge the SSME duct of hydrogen. Planetary wind tunnel tests at CPP established worst-case winds at the duct exit (ref. 8). EPL performed corresponding worst-case tests with fans at 1/7 scale (ref. 7). These experiments show that the ratio of duct exit flow to peak wind momentum is 1.33 -- indicating outflow. This verifies that wind will not enter the duct or reverse the exhaust flow.

Two requirements apply to the exhaust plume during SIS operation. There must be no possibility of a deflagration at or beyond the duct exit, and the plume must not be flammable near the shuttle vehicle for worst-case winds.

Figure 18 includes results of an Aerospace analysis of interaction of the exhaust plume with ambient air and south winds.* Corresponding state trajectories for no wind and 35 knots are shown in figure 19. The calculation includes condensation and evaporation in the plume. The trajectories remain in the benign region of the flammability diagram. Therefore, free space detonation is not possible.

The calculation in figure 18 indicates that the exit plume is not flammable (below 5 percent) near the vehicle for all wind conditions. On the same figure, data from the CPP Phase 3 tests, with an indicator gas, verify this result (ref. 8). The experimental trajectories are more depressed and differ somewhat from theory -- probably because the analysis is quasi-one-dimensional. However, in no case is there a flammable condition near the shuttle vehicle.

---

* Moody, D.: Effects of Wind and Scale on Plume. Aerospace Interoffice Correspondence (11 Feb. 1987).

REFERENCES

1. Breit, T. and G. Elliott: Hydrogen Disposal Investigation for the Space
   Shuttle Launch Complex at VAFB. Proceedings IES, 1986.

2. Breit, T: Hydrogen Disposal System Specification. DOD STS Ground
   Systems, Martin Marietta Corporation, VCR-86-0506, 1 Aug. 1986.

3. Williams, R., et al.: VLS Shuttle Support Hydrogen Igniter/Water Spray
   Test Program. Test Report TR-531-002, NASA/WSTF, 25 Nov. 1987.

4. Marshall, B. W.: Flammability Limits and Combustion Characteristics of
   Hydrogen. Sandia National Laboratories, SAND 84-0383, Dec. 1986.

5. Sherman, M. P. and S. E. Slezak: Hydrogen-Air-Stream Combustion Regimes
   in Large Volumes. Proceedings 25th Space Conference, Cocoa Beach,
   26-29 Apr. 1988.

6. Torok, R. C. and T. Derbidge: Steam Inerting Feasibility and Development
   Studies. Astron Research and Engineering, Final Report 7099-300,
   July 1987.

7. Schmitt, D.: 1/7 Scale VLS Duct Steam Inerting System. Phase III
   Tests, Final Report, Vol 1 and 2, MCR-87-536, No. 084859, Sept. 1987.

8. Wind Tunnel Testing of the Impact of Surface Winds and Terrain on the
   VAFB Steam Inerting System. Cermak Peterka Petersen Inc, CCP Project
   87-0394, Aug. 1987.

9. Miller, J.: MSFC 6.4% Model Steam Inerting System Test Results.
   SPC Report LSO-600670-6560, 15 Oct. 1987.

10. Mathias, R. G.: Test Report, Santa Cruz Test Facility, Space Shuttle
    Vandenberg Closed Exhaust Duct, MS-42, LSOC TM81-11/372, LMSC,
    28 Aug. 1987.

11. Orciuch, C.: Test Report Supplement, Santa Cruz Test Facility, Space
    Shuttle, Vandenberg SSME Closed Exhaust Duct. SPC Report
    LSO-600669-65-60, 6 Nov. 1987.

12. Tatum, R.: Hydrogen Disposal System Final Report, Steam Inerting System
    Summary. Vol I to III, LSO-600672-6560, 18 Dec. 1987.

# TEST STAND DESIGN AND ANALYSIS FOR
# TITAN 34D STATIC FIRING[1]

Shayan Pazargadi
Wyle Laboratories

## ABSTRACT

The Test Stand 1C at the Air Force Astronautics Laboratory (AFAL), Edwards AFB, CA, was originally designed for F-1 liquid propellant engines. The stand was modified to handle a 5½-segment Solid Rocket Motor (SRM) Titan 34D vertical static firing test. The new configuration is the only nozzle-down test stand of long SRM's in the United States, which had to withstand 6.2MN (1.4M pounds) thrust load, and 2444 KN (550 Kips) rocket weight, as well as seismic and wind loads. The 3230 cm (106 feet) high stand was made of stainless steel truss system supported by a massive reinforced concrete foundation. The vertical and lateral thrust loads were mainly resisted by a four-legged pylon structure attached to the test stand and foundation. A superstructure was designed to house the rocket and provide working platforms for stacking operations. Several finite element models of the combined test stand-pylon-rocket were developed on ANSYS, NASTRAN and IMAGES-3D softwares. The models were analyzed for a variety of static, dynamic and transient loads to ensure the structural integrity of the test stand. This paper discusses the main design drivers and analysis effort utilized in the modification of the test stand.

## INTRODUCTION

The Test Stand 1C located at the Air Force Astronautics Laboratory (AFAL) at Edwards Air Force Base (EAFB) was one of the three nearby identical stands which were

---

[1]Prepared under contract to the United Technologies Corporation, Chemical Systems Division, UTC-CSD Contract Number 268024.

designed, built and used to test liquid F-1 engines during the 1960's and was used for the last time in the early 1970's. The Titan 34D mishap in 1984 brought about a new Recovery Program that proposed the modified version of the existing test stand for static firing test of the Titan 34D Solid Rocket Motor (SRM) in the vertical nozzle-down configuration.

The main objectives of the program were as follows:

1.    Perform a nozzle-down static firing test of a full scale 5½-segment solid rocket motor to evaluate the motor segment joints, to evaluate the accept/reject criteria established from the non-destructive tests on the candidate insulation material and to inspect and evaluate fleet motors. Criteria to meet primarily this objective were:

o   normal test conditions and motor performance

o   adequate measurements of motor performance

o   reasonable ablation rates calculated from insulation measurements

The motor would be conditioned cold (4.4°C or +40°F mean bulk) and test fired without thrust vector control or axial thrust measurement. A water quench system would be used to extinguish post test residual insulation burning and reduce soak-out temperatures.

2.    Perform nozzle-down short burn and inert gas pressurization test of 2-segment fullscale motor configurations to evaluate the dynamics and the integrity of the joints at joint temperature and motor case pressurization rates

## ORIGINAL DESIGN

The Test Stand 1C was originally designed for liquid rocket engines and was configured for the Rocketdyne F-1 engines with 305 cm (120 in.) diameter and 406 cm (160 in.) long and a thrust force of 6.67 MN (1.5 Mlb) on liquid oxygen/RP-1 fuel. The engine was supported on a four-legged pylon which could support vertical upward loads of up to 35.56 MN (8 Mlb) and horizontal loads of 4.44 MN (1 Mlb).

## NEW REQUIREMENTS

The test stand had to modified to configure to the 305 cm

(120 in.) diameter, 1859 cm (61 feet) long Titan 34D SRM
dimensions, 2444 KN (550 kips) weight and 6.2 MN (1.4 Mlb)
thrust load for 2 minutes burntime with a nozzle canting of 6°
outward. A superstructure was required to be built on the
existing stand to protect the rocket from wind loads, provide
fixed and removable platforms for stacking operations, and to
provide a lateral restraining structure at the forward end of
the motor. The configuration was set up primarily for static
firing test without any thrust vector control or axial thrust
measurement. The load vectors that are imposed on the motor at
launch and under planned test setup for the two conditions of
the pre-firing static and the post-lift-off burn are shown in
Figures 1 and 2. The test setup did not exactly reproduce the
external loads on the motor because the test stand supported and
restrained the motor uniformly at the aft stub skirt. This
arrangement was acceptable based on the following reasons:

- o  There were no requirements for thrust vector control or
     axial thrust measurement

- o  The aft stub skirt was able to react the total thrust
     with an adequate margin of safety

- o  Lateral thrust loads resulting from the 6° nozzle cant
     could be reacted through the aft stub skirt interface
     tooling

- o  Motor case and joint loads induced by motor
     pressurization during firing were considerably in excess
     of those resulting from externally applied loads, so it
     was not necessary to simulate external loading
     conditions.

The other loading criteria were as follows:

- o  wind load of 31.3 m/sec (70 mph)

- o  seismic load of 0.5 g (Zone 4) in the two horizontal
     axes acting simultaneously

- o  flight restraint lateral loads of 1280 KN (288 kips) in
     front-to-back and 364 KN (82 kips) in side-to-side
     directions applied to the superstructure at the forward
     end of the motor

- o  platforms in the superstructure had to carry a load of
     12 persons per level

## NEW DESIGN

The following modifications were made to the original stand (Fig.3) to adapt to the new requirements of Titan 34D static firing tests on the modified stand (Fig.4):

o   removal of the following

    five tone jib crane and liquid oxygen tanks from the top platforms above the tanks
    Two 36 WF beams from the top of the existing stand
    plumbing between the tanks
    Firex piping
    engine mount and thrust measuring H-beam
    tank support columns

o   Superstructure of K-type A36 steel frame added to the existing stand. The superstructure was to provide wind protection to the motor, fixed and removable platform for stacking operations and lateral restraint at the forward ring attachment at the 1463 cm (48 feet)  level above the existing stand.

o   A forward ring (Fig.5) at the forward end of the motor that provided axial restraint through the anti-flight restraint cables and lateral restraint through snubber connection to the superstructure in both horizontal directions.

o   Pylon adaptor made of A36 steel and aft skirt fixture made of 4130 steel both designed to 44.4 MN (10 Mlb) vertical thrust load to provide interface between the pylon and the rocket aft end (Fig.6). The pylon adapter was designed to connect the existing rectangular pylon opening with the 305 cm (10 feet) diameter thrust cylinder. The aft skirt fixture was designed to provide the interface between the pylon adapter fixture and the motor aft stub skirt.

o   The pylon was attached to the test stand to provide better dynamic stability of the motor-pylon assembly. This improvement will be discussed later in the paper in more detail.

o   A working platform was added at 244 cm (8 feet) below the top of the existing stand to support a 6800 Kg (15000 lb) x-ray machine. The 5½ segment setup and configuration of the platforms are shown in Figure 7.

339

## ANALYSIS OF NEW DESIGN

Finite element analyses of the modified test stand were performed to ensure the structural integrity of the new design concept. Preliminary finite element analysis of the existing stand had been performed by IMAGES-3D structural code (Fig. 8). Trusses T-4 and T-5 (also shown in Fig. 4) are the main load carrying members of the existing stand to support the superstructure weight of 411 KN (92.5 Kips). The structure would reach its yield condition at a vertical load of 711 KN (160 Kips). Two of 12 WF members were found inadequate and were replaced by 24 WF 76 beams members. ANSYS and NASTRAN codes were used to model the test stand, the pylon and the motor. Three stand-pylon configurations were analyzed to obtain the most effective design concept:

I.      Unattached: the pylon-motor assembly was completely detached from the stand

II.     Partially attached: the pylon-motor assembly was attached at its forward ring elevation to the superstructure via snubbers

III.    Completely attached: the pylon-motor assembly was attached to the superstructure by snubbers at the forward end and the pylon was attached to the stand at the pylon top level by steel plates.

## DYNAMIC ANALYSIS

Dynamic analysis of the unattached configuration indicated fundamental frequencies of 1.16 Hz for the pylon-motor assembly and 3.89 Hz for the test stand. Concerns were made at the dynamic characteristic of the pylon motor assembly at such low frequencies (Fig. 9). The fundamental frequency increased to 2.51 Hz for configuration II and to 2.79 Hz for configuration III with the latter one being adopted as an improved design over the unattached or partially attached concepts. Natural frequencies of the completely attached configuration are shown in Table 1.

## WIND LOAD ANALYSIS

The finite element model of the completely attached configuration was analyzed for wind load of 70 mph. The worst combination of wind loading on a rectangular cross section was

considered as being 1693 N/m$^2$ (36 psf) on the front face, 1317 N/m$^2$ (28 psf) on the back face in the direction of the wind and 1317 N/m$^2$ (28 psf) sideway pressures acting outward. Analyses were performed separately for the major and minor axes of the stand. Results of the stress analysis are shown in Table 2. Factor of safety of order of 6 against the yield was reported for the wind loading.

SEISMIC ANALYSIS

The combined model was analyzed for simultaneous application of 0.5 g seismic acceleration acting in the two horizontal axes of the stand. The lowest factor of safety of 1.47 against the yield was identified for a localized beam on the top of the existing stand which was considered insignificant due to large structural redundancies already built into the stand.

THRUST LOAD ANALYSIS

The SRM thrust profile was enveloped to a ramp function reaching its peak of 6.2 MN (1.4 Mlb) at 0.30 seconds and staying flat up to 120 seconds at burnout.

Transient behavior of the stand was studied for the first few seconds after the start of firing. A maximum overshoot of 25% was observed in the displacement responses at 0.3 second, when the thrust force reached its peak, but it quickly damped out to its stationary value after one second from the start of firing. Transient responses of displacements and forces at the top and bottom of the motor are shown in Figure 11. A stress factor of safety of better than 3 was obtained under different stages of the thrust load.

REACTION ANALYSIS

Reactions at the base of the stand and pylon were analyzed for two conditions during the firing and at the end of burnout (Tables 3 and 4). It can be seen that most of the thrust load is carried by the pylon structure.

The pylon is mounted to concrete with forty steel anchors - ten anchors per leg. Each anchor is 5.72 cm (2.25 inches) in diameter and 1158 cm (38 feet) long. The anchors are made of 4340 quenched and tempered steel with an ultimate strength of 677 MN/m$^2$ (100 ksi) and yield strength of 542 MN/m$^2$ (80 ksi).

Detailed analysis of anchor/concrete interface has been performed taking into account anchor/concrete relative stiffness

and specified anchor bolt preload of 889 KN (200 kips). The results of the analysis limit maximum postulated thrust force to 35.56 MN (8 Mlb) which was consistent with the original design for liquid F-1 engine tests. The maximum required postulated thrust force of 44.44 MN (10 Mlb) did not exceed the ultimate strength of the anchor.

## CONCLUSIONS

The main design drivers in the modification of the F-1 liquid propellant engine Test Stand 1C to accommodate for the Titan 34D solid rocket booster nozzle-down static firing test were:

o vertical thrust load and lateral thrust load (caused by 6° nozzle cant) of the SRM are an order of magnitude larger than liquid engines and they have to be resisted primarily by the pylon structure.

o due to a much heavier and taller SRM with respect to liquid engines, resonance frequencies of the motor-pylon assembly will become a critical factor in the stability of the assembly under dynamic environments such as earthquake, wind and transient thrust loads. For this reason, the motor-pylon assembly had to be tied-in to the test stand at the pylon level and the motor forward end had to be attached to the superstructure. This tied-in configuration increased the fundamental frequency of the assembly by a factor of 2.4.

o no thrust vector control or axial thrust measurement was required for this Titan 34D static firing test. The anti-flight forward end restraint cables and snubbers and the uniform restraint pylon system at the aft end considered to be acceptable in lieu of the actual restraint system of the SRM to the core vehicle.

342

## TABLE 1. - GLOBAL NATURAL FREQUENCIES (Hz)

| | ANSYS | NASTRAN | MODE DIRECTION |
|---|---|---|---|
| **UNATTACHED PYLON-STAND (CASE I)** | | | |
| Pylon | 1.16 | 1.18 | 1x(*) |
| | 1.25 | 1.31 | 1z |
| Stand | 3.89 | 4.29 | 1z |
| | 5.42 | 6.38 | 1x |
| **PARTIALLY ATTACHED (CASE II)** | | | |
| | 2.51 | 2.74 | 1z |
| | 2.70 | 2.98 | 1x |
| | 5.12 | 5.26 | Combined |
| | 7.11 | 7.35 | 2z |
| | 7.31 | 7.49 | 2x |
| **COMPLETELY ATTACHED (CASE III)** | | | |
| | 2.79 | 3.0 | 1x |
| | 2.84 | 3.0 | 1z |
| | 7.09 | 7.36 | 2z |
| | 7.44 | 7.69 | 2x |

(*) x, y, z correspond to side-to-side, vertical and road-to-flame directions respectively.

343

TABLE 2. - STRESS AND DISPLACEMENT SUMMARY

| Loading/Condition | Maximum Stress MN/m² (ksi) | | Factor of Safety (Against Yield) | Displacement cm (inches) | |
|---|---|---|---|---|---|
| Dead Load (DL) | 22.35 | (3.3) | 10.91 | .28 | (.11y) (2) |
| Front wind and DL | 39.97 | (5.9) | 6.10 | .08 | (.03z) |
| Side wind and DL | 35.22 | (5.2) | 6.92 | .05 | (.02x) |
| Seismic (combined x & z) and DL | 165.96 | (24.5) | 1.47 | 2.29 | (.9 x and z) |
| Thrust and DL (Case II) | 29.81 | (4.4) | 8.18 | .15 | (.06y) |
| Thrust and DL (Case III) | 63 | (9.3) | 3.87 | .05 | (.02y) |
| Thrust (end of burnout) and DL (Case III) | 75.87 | (11.2) | 3.21 | .28 | (.11y) |
| Ultimate load(1) at top and DL | 216.77 | (32) | 1.13 | 3.38 | (1.33z) |

(1) 1280 KN (288 kips) in z- and 364 KN (82 kips) in x-directions applied at strut elevation.

(2) x, y, z correspond to side-to-side, vertical and road-to-flame directions respectively.

## TABLE 3. - REACTION FORCES OF THE RESTRAINT SYSTEM DURING THE STATIC FIRING TEST

| Item | Fx | | Fy | | Fz | | Mx | | My | | Mz | |
|---|---|---|---|---|---|---|---|---|---|---|---|---|
| Stand Base Reactions | 44 | (10) | 329 | (74) | -49 | (-11) | -497 | (-44) | 226 | (20) | 858 | (76) |
| | 44 | (-10) | 329 | (74) | -53 | (-12) | -576 | (-51) | -226 | (-20) | -835 | (-74) |
| | 62 | (14) | 271 | (61) | 4 | (1) | -2213 | (-196) | 293 | (26) | 847 | (75) |
| | -62 | (-14) | 267 | (60) | 9 | (2) | -2303 | (-204) | -305 | (-27) | -926 | (-82) |
| Stand Subtotal | 0 | (0) | 1196 | (269) | -89 | (-20) | -5589 | (-495) | -12 | (-1) | -56 | (-5) |
| Pylon Base Reactions | -169 | (-38) | -124 | (-28) | 36 | (8) | 2371 | (210) | 5159 | (457) | 13953 | (1236) |
| | 169 | (38) | -124 | (-28) | 36 | (8) | 2303 | (204) | -5159 | (-457) | -13885 | (-1230) |
| | 573 | (129) | -676 | (-152) | -302 | (-68) | -10792 | (-956) | -1897 | (-168) | -14867 | (-1317) |
| | -573 | (-129) | -676 | (-152) | -302 | (-68) | -10770 | (-954) | 1818 | (161) | 15082 | (1336) |
| Pylon Subtotal | 0 | (0) | -1600 | (-360) | -533 | (-120) | -16888 | (-1496) | -79 | (-7) | 283 | (25) |
| TOTAL | 0 | (0) | -404 | (-91) | -622 | (-140) | -22476 | (-991) | -90 | (-8) | 226 | (20) |

Notes:

(1) Force units are in KN, Kips in parentheses. Moments units are in KN-cm, Kips-in. in parentheses.

(2) (+) sign is in direction of positive global coordinates.

(3) Maximum force at top strut is 3316 N (746 lbs).

(4) Forces at the pylon to the stand connection are distributed as follows:

| | Fy | | Fz | |
|---|---|---|---|---|
| To the pylon | 2631 | (592) | 542 | (122) |
| To the stand | 1013 | (228) | 80 | (18) |
| TOTAL | 3644 | (820) | 622 | (140) |

(5) Rocket weight is 2444 KN (550 Kips).

(6) Force Checkout in vertical direction:

| | Fy | |
|---|---|---|
| Rocket and pylon weight | -3604 | (-811) |
| Stand Weight | -2213 | (-498) |
| Thrust Load | 6222 | (+1400) |
| Reaction at pylon | -1600 | (-360) |
| Reaction at stand | 1195 | (+269) |
| TOTAL | 0 | (0) |

345

TABLE 4. - REACTION FORCES OF THE RESTRAINT SYSTEM AT THE END OF FIRING

| Item | Fx | Fy | Fz | Mx | My | Mz |
|---|---|---|---|---|---|---|
| Stand Base Reactions | 13 (3) | 271 (61) | -49 (-11) | -542 (-48) | 214 (19) | 982 (87) |
|  | -13 (-3) | 271 (61) | -52 (-12) | -610 (-54) | -214 (-19) | -948 (-84) |
|  | 31 (7) | 213 (48) | 4 (1) | -2156 (-191) | 305 (27) | 971 (86) |
|  | -31 (-7) | 209 (47) | 9 (2) | -2235 (-198) | -305 (-27) | -1027 (-91) |
| Stand Subtotal | 0 (0) | 964 (217) | -88 (-20) | -5543 (-491) | 0 (-0) | -22 (-2) |
| Pylon Base Reactions | -529 (-119) | 622 (-140) | 209 (47) | 1558 (138) | 5069 (449) | 11966 (1060) |
|  | 529 (119) | -622 (-140) | 209 (47) | 1479 (131) | -5035 (-446) | -11763 (-1042) |
|  | 933 (210) | -1173 (-264) | -476 (-107) | -9968 (-883) | -2021 (-179) | -12745 (-1129) |
|  | -933 (-210) | -1173 (-264) | -476 (-107) | -9968 (-883) | 1919 (170) | 13095 (1160) |
| Pylon Subtotal | 0 (0) | -3590 (-808) | -534 (-120) | -16899 (-1497) | -68 (-6) | 553 (49) |
| TOTAL | 0 (0) | -2626 (-591) | -622 (-140) | -22442 (-1988) | -68 (-6) | 531 (47) |

Notes:

(1) Force units are in KN, Kips in parentheses. Moment units are in KN-cm, Kips-in. in parentheses.

(2) (+) sign is in direction of positive global coordinates.

(3) Maximum force at top strut is 3467 N (780 lbs).

(4) Forces at the pylon to the stand connection are distributed as follows:

|  | Fy | Fz |
|---|---|---|
| To the pylon | 4622 (1040) | 542 (122) |
| To the stand | 1244 (280) | 80 (18) |
| TOTAL | 5866 (1320) | 622 (140) |

(5) Rocket weight at the end of firing is 222 KN (50 Kips).

(6) Force Checkout in vertical direction:

|  | Fy |
|---|---|
| Rocket and pylon weight | -1382 (-311) |
| Stand Weight | -2213 (-498) |
| Thrust Load | 6222 (+1400) |
| Reaction at pylon | -3591 (-808) |
| Reaction at stand | 964 (217) |
| TOTAL | 0 (0) |

346
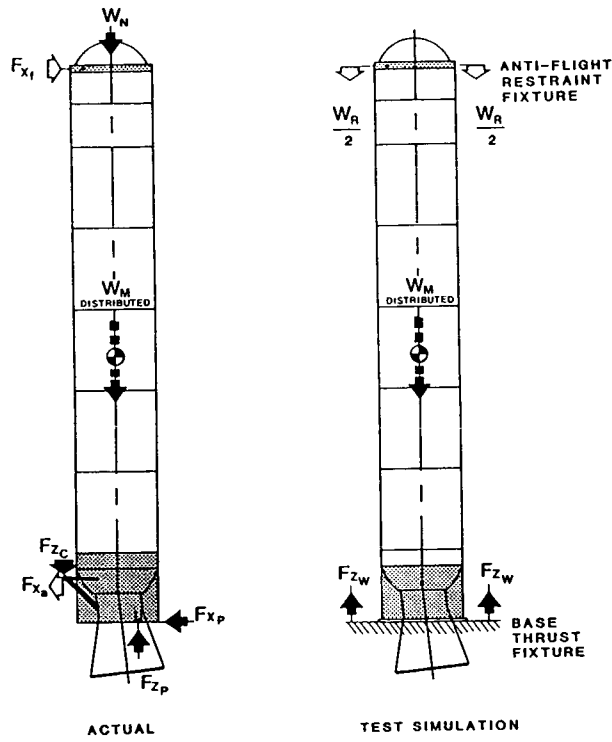
FIGURE 1. COMPARISON OF THE LOAD RESTRAINT SYSTEM BETWEEN ACTUAL AND TEST SIMULATION - PREFIRE
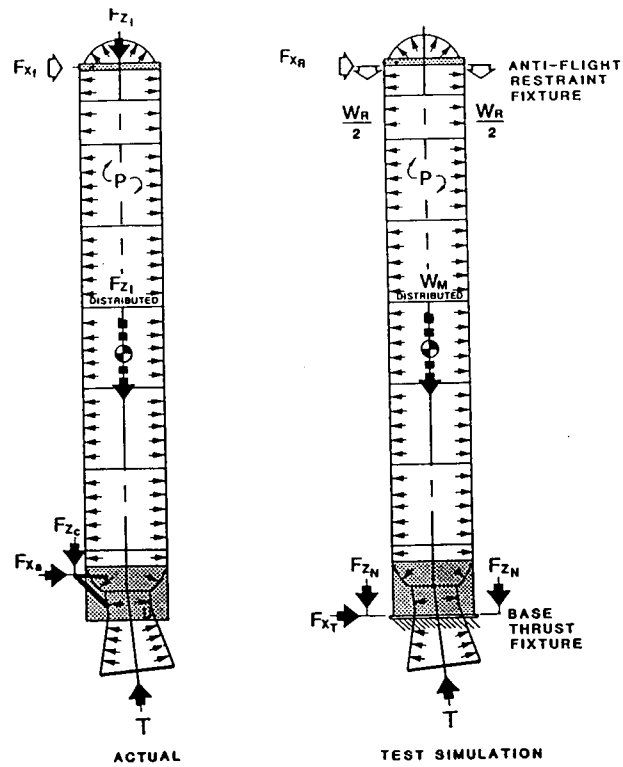


FIGURE 2. COMPARISON OF THE LOAD RESTRAINT SYSTEM BETWEEN ACTUAL AND TEST SIMULATION - POST LIFTOFF

347
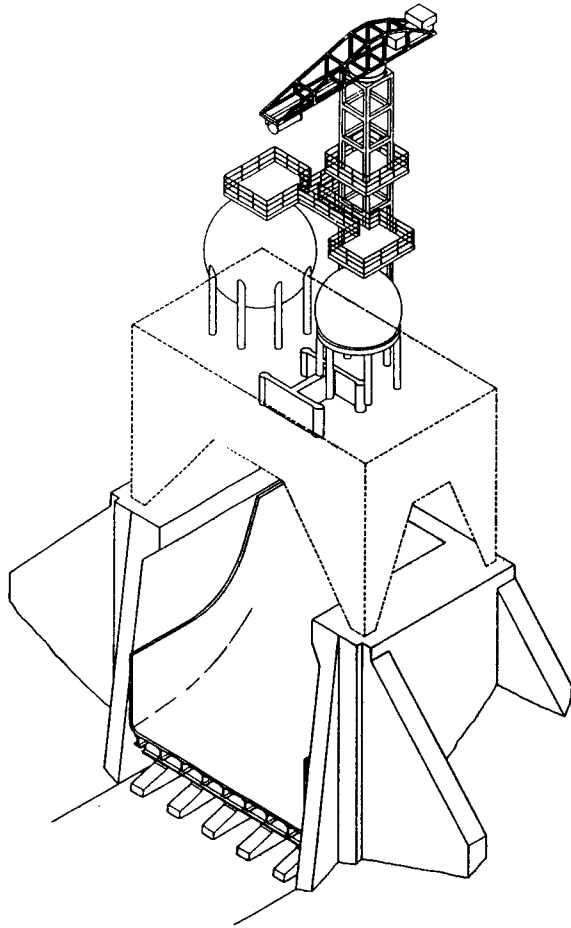
FIGURE 3. ORIGINAL TEST STAND
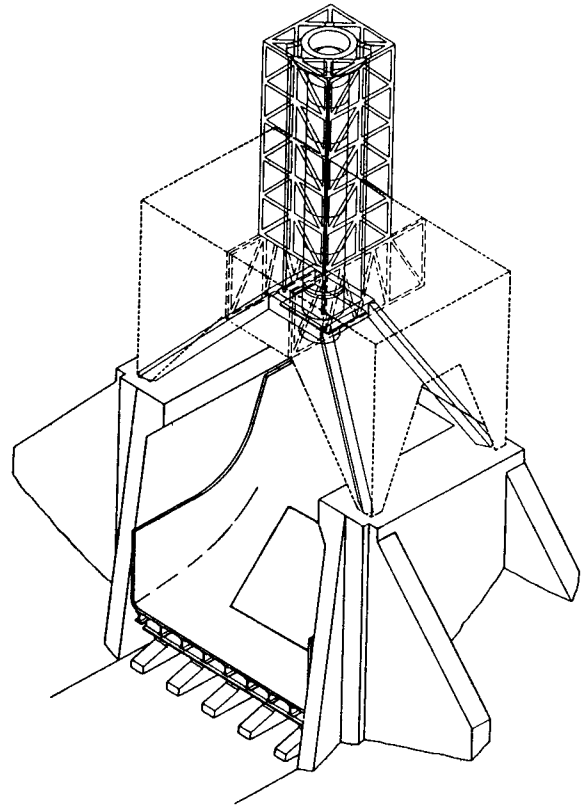


FIGURE 4. MODIFIED TEST STAND
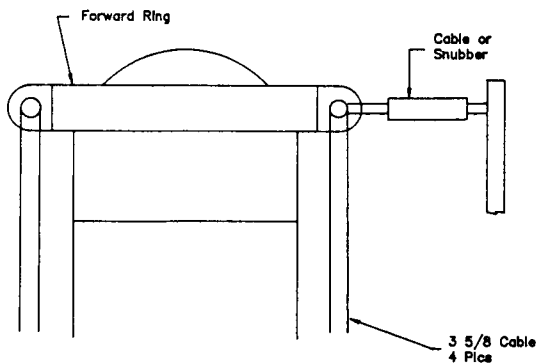


FIGURE 5. FORWARD END RESTRAINT SYSTEM
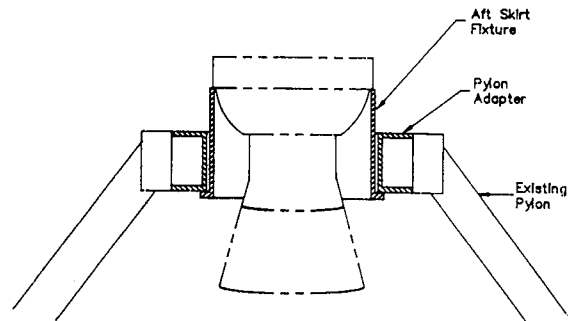


FIGURE 6. AFT END RESTRAINT SYSTEM

348
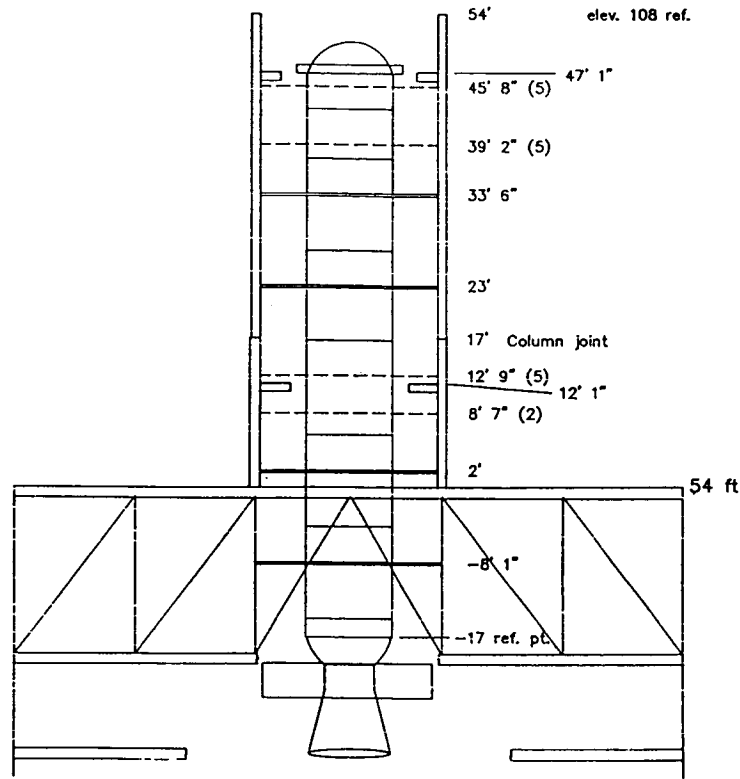
**FIGURE 7. 5-1/2 MOTOR SEGMENT SETUP**
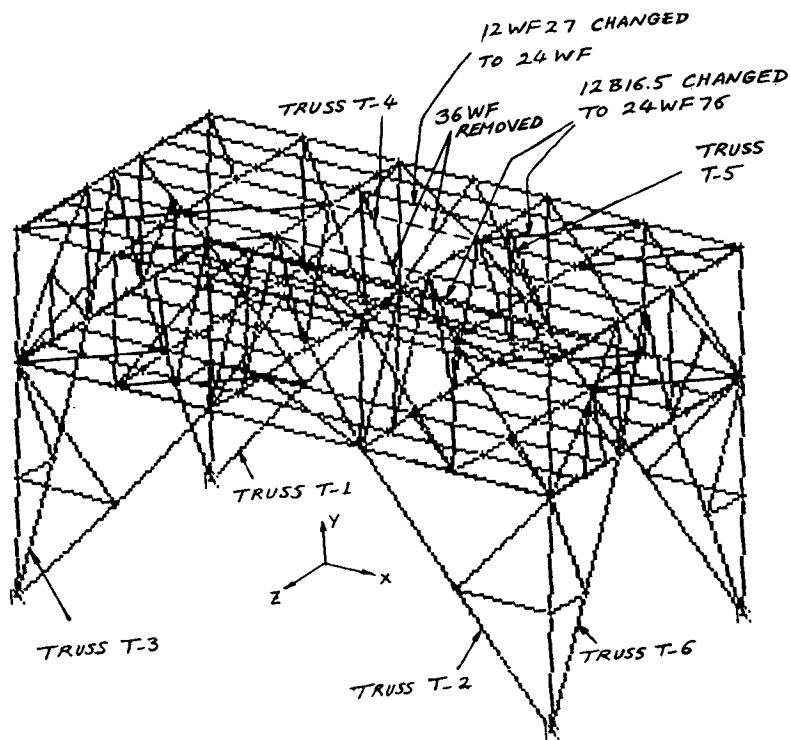


**FIGURE 8. FINITE ELEMENT MODEL OF THE EXISTING STAND**

349
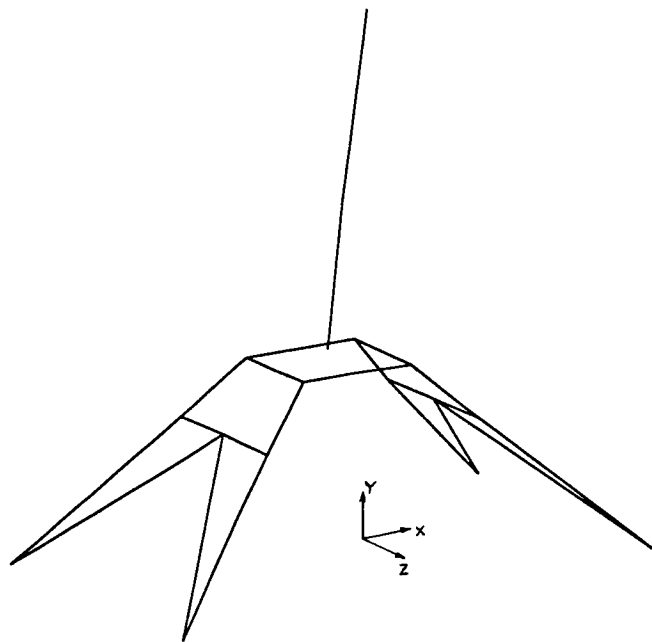
(A)　MODE 1 - 1.16 Hz
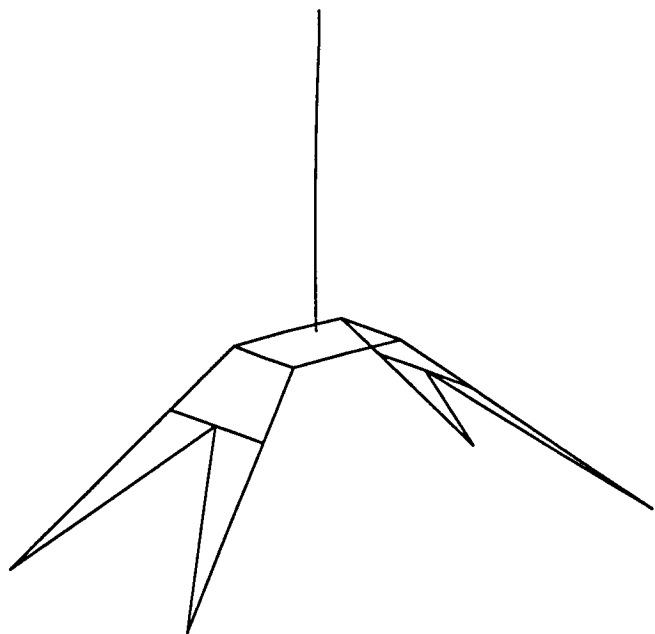
(B)　MODE 2 - 1.25 Hz
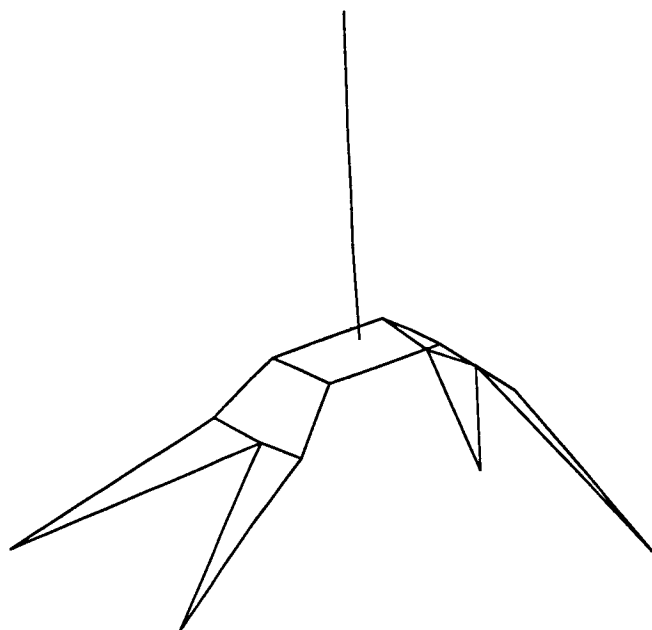
(C)　MODE 3 - 5.99 Hz
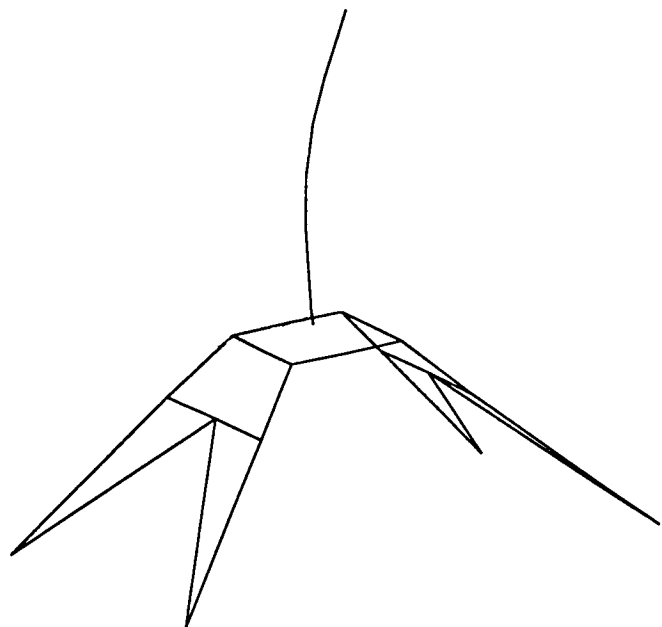
(D)　MODE 4 - 7.47 Hz

FIGURE 9. NATURAL FREQUENCIES OF THE PYLON-MOTOR ASSEMBLY
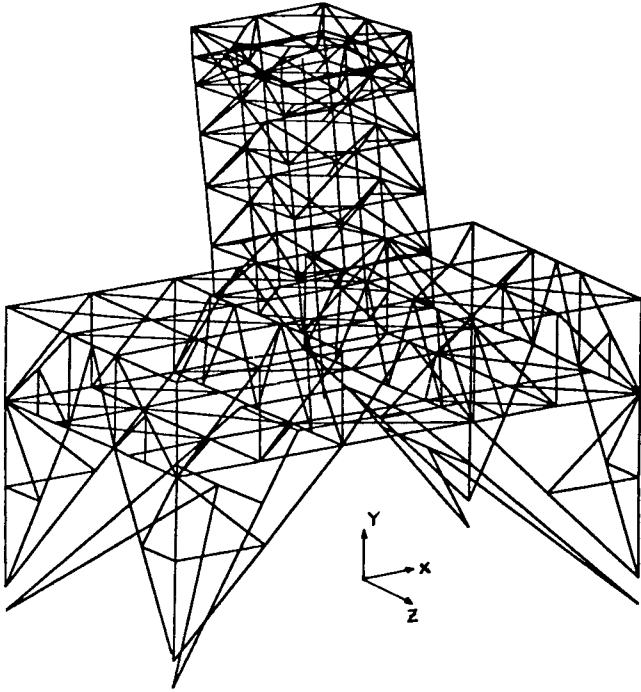
(A) MODE 1 - 2.79 Hz
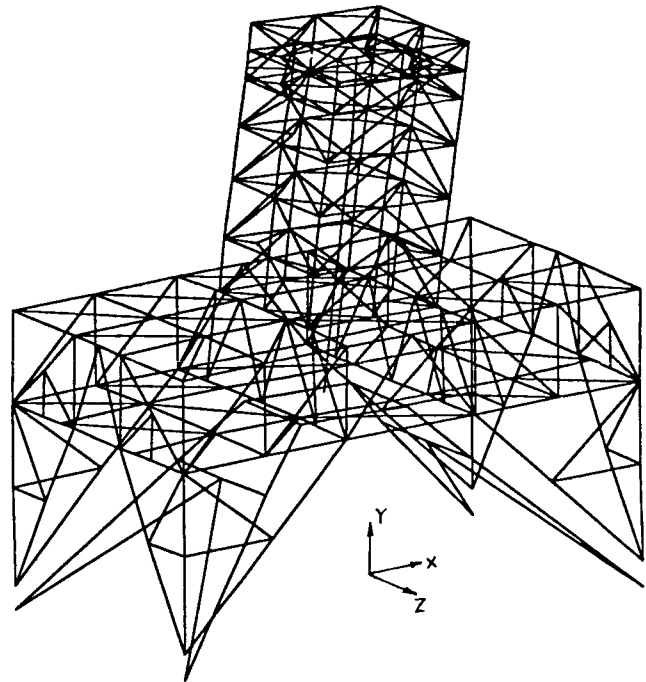
(B) MODE 2 - 2.84 Hz
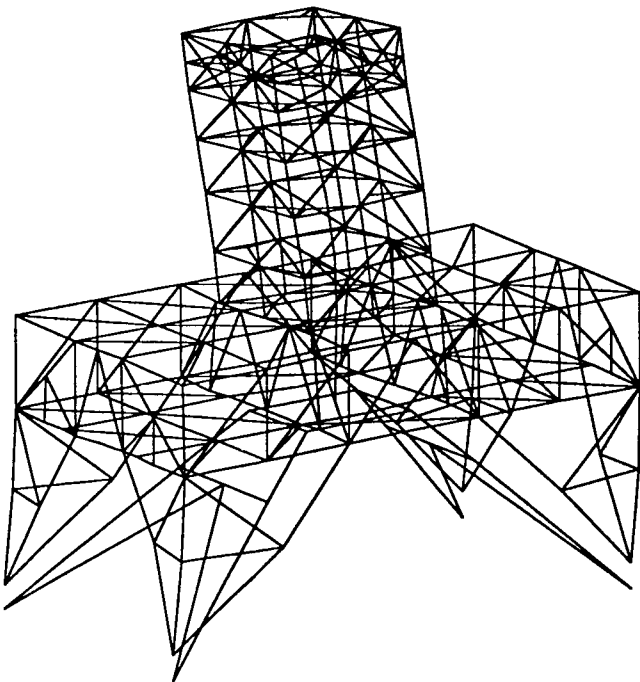
(C) MODE 3 - 7.09 Hz
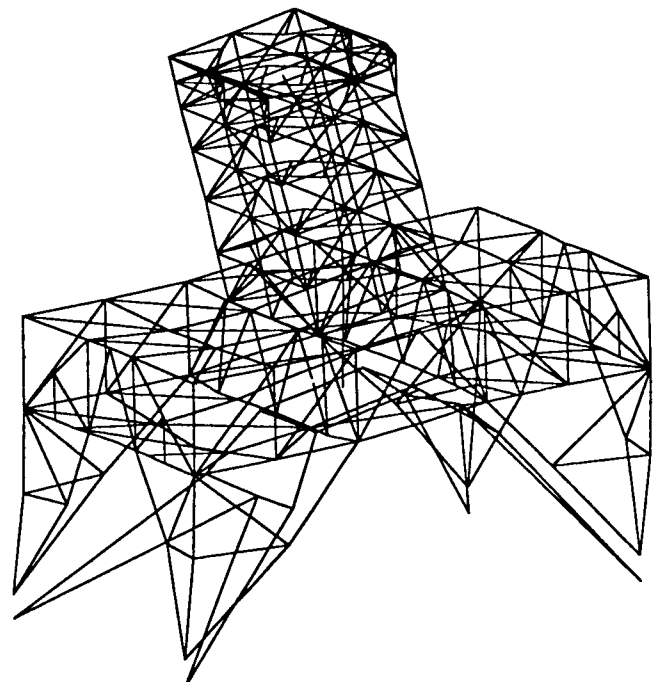
(D) MODE 4 - 7.44 Hz

FIGURE 10. NATURAL FREQUENCIES OF THE COMPLETELY ATTACHED
STAND-PYLON-MOTOR ASSEMBLY

351
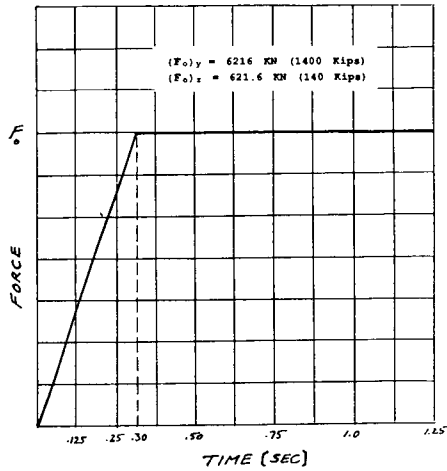
(A)     IDEALIZED THRUST LOAD
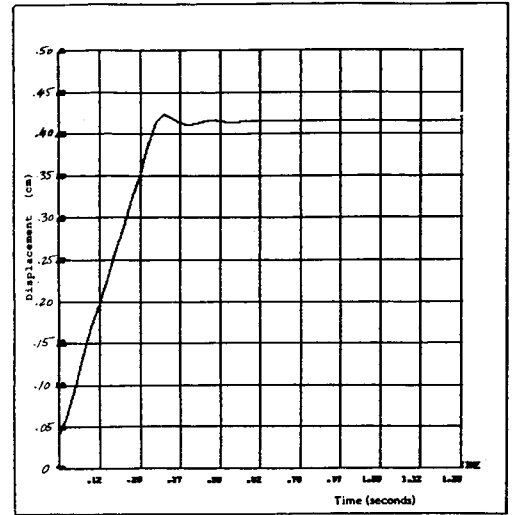
(B)     VERTICAL DISPLACEMENT AT THE BASE OF THE MOTOR
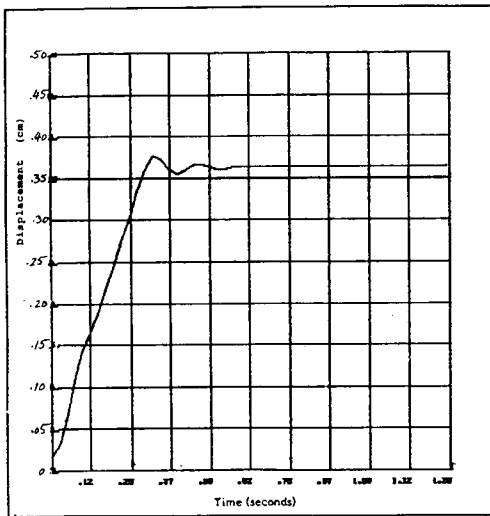
(C)     VERTICAL DISPLACEMENT AT THE TOP OF THE MOTOR
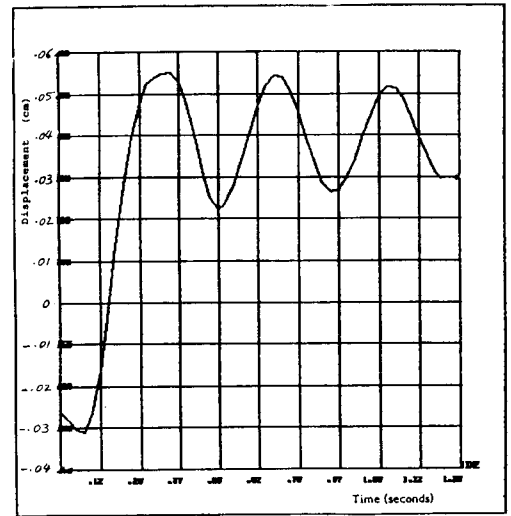
(D)     LATERAL DISPLACEMENT (Z) AT THE TOP OF THE MOTOR
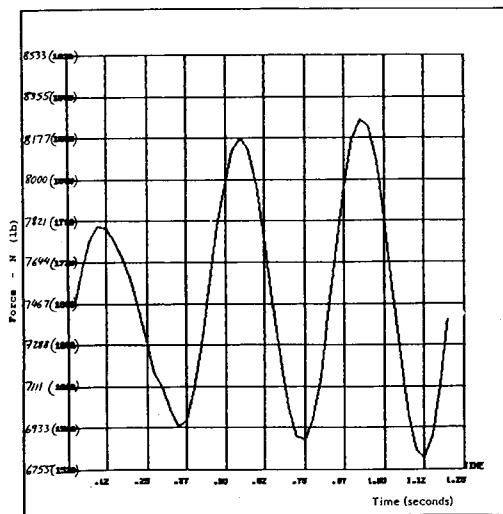
(E)     LATERAL FORCE (X) IN THE FORWARD END UNISTRUT
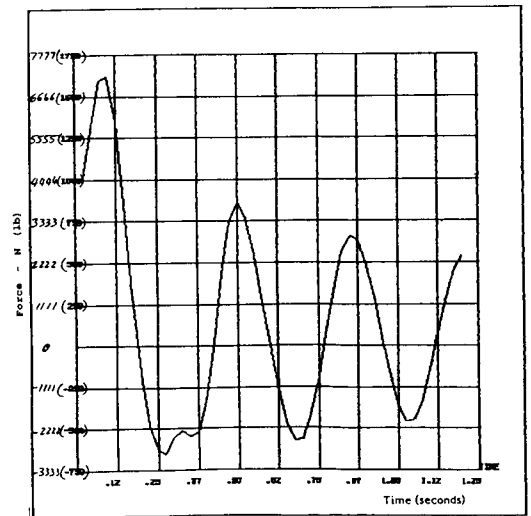
(F)     LATERAL FORCE (Z) IN THE FORWARD END UNISTRUT

FIGURE   11.     TIME   HISTORY   RESULTS   DUE   TO   THRUST   LOADS

352

# TEST STAND FOR TITAN 34D SRM STATIC FIRING

Vladimir Glozman
California Polytechnic University

George Shipway
Wyle Laboratories

## ABSTRACT

An existing liquid engine test stand at the AF Astronautics Laboratory has been refurbished and extensively modified to accommodate the static firing of the Titan 34D solid rocket motor (SRM) in the vertical nozzle down orientation. The main load restraint structure was designed and built to secure the SRM from lifting off during the firing. In addition the structure provided weather protection, temperature conditioning of the SRM, and positioning of the measurement and recording equipment. The structure was also used for stacking/de-stacking of SRM segments and other technological processes.

The existing stand, its foundation and anchorage were thoroughly examined and reanalyzed. Necessary stand modifications were carried out to comply with the requirements of the Titan 34D SRM static firing. A new superstructure was designed and erected on top of the modified test stand. The superstructure was a steel framework consisting of corner and side columns, horizontal mounting platforms, and cross bracing elements. Mounting platform elevations and superstructure height were designed for easy modification to facilitate stacking/de-stacking procedures and potential testing of different SRMs.

The superstructure and the test stand overall were analyzed by finite element methods utilizing IMAGES-3D, ANSYS, and NASTRAN codes. Critical joints, anchors and the environmental enclosure were evaluated by conventional methods. Analyses were performed for the specified loads transmitted to the structure from the SRM, as well as for wind loads, postulated seismic disturbances, and acoustic pressure. It was determined that the test stand exhibits a sufficient factor of safety under the most conservative combination of the applied loads. Stiffness of the test structure and its dynamic properties were found to be acceptable.

353

Specific attention was given to the SRM mounting structure, which includes a modified thrust pylon, a newly designed pylon adapter welded into the pylon, and an aft test skirt fixture connecting the SRM to the pylon through the adapter. Detailed finite element analysis of the mounting structure with and without the SRM was performed, and response of the mounting structure to the ignition transient and other loading conditions was thoroughly investigated. It was found that stress levels in all critical elements was below the yield strength of the selected materials with sufficient safety factor. The stiffness of the mounting structure and therefore dynamic response of the SRM during the static firing was shown to be also acceptable.

The modified test stand met all of the design criteria during the successful firing of the Titan 34D SRM.

## INTRODUCTION

The key element in the static firing of the Titan 34D SRM is the load restraint structure, which stabilizes the rocket and prevents it from lift-off during the test. The structure was designed and built utilizing an existing twenty year old liquid engine test stand at the AF Astronautics Laboratory. This allowed for the completion of all work for erecting a complex test facility in a timely, cost effective manner.

The existing stand was analyzed and design modifications were implemented to permit SRM testing. A new superstructure was erected on the top of the existing test stand. The superstructure consists of a steel beam framework with horizontal mounting platforms and environmental enclosure.

The ability of the existing pylon structure and its anchorage to withstand the static load prior to firing and the thrust load during firing was thoroughly investigated and necessary modifications have been implemented. A new thrust restraint fixture was designed to interface with the existing pylon structure, and to accommodate the SRM aft closure. Furthermore, the pylon and superstructure assembly were rigidly connected to provide additional stiffness for the SRM mounting. Each structure as well as the combined structure were evaluated for the specified restraint load transmitted from the SRM, as well as wind load, postulated seismic disturbances and acoustic pressure. Evaluations were performed by a combination of conventional and finite element methods using NASTRAN, ANSYS, IMAGES-3D and other structural codes. Furthermore, due to the time limitation and the critical importance of the design, evaluation of the combined structure was performed independently in two Wyle facilities (Norco, CA, and Huntsville, AL) using two different structural codes, ANSYS and NASTRAN. The results of these analyses compared favorably, and subsequent performance of the test facility during the static firing was the ultimate verification of the performed design and analytical work.

## SUPERSTRUCTURE

The 6.7 m x 6.7 m x 16.5 m superstructure (Figure 1) was erected on the top of the modified existing test stand (Figure 2). The design and analysis of the superstructure was performed using the IMAGES-3D finite element program.

The main structural elements of the superstructure are:

o  Four corner columns.
o  Four side columns.
o  Three permanent horizontal mounting platforms.
o  Two removable horizontal platforms at elevations of 3.2m and 14.5m for the side restraint of 2 segment and 5 1/2 segment specimens.
o  Side diagonal cross bars.

The finite element model of the superstructure (Figure 3) is comprised of the beam structural elements identified in Table 1.

The model consists of 112 nodes which are connected with a total of 264 beam structural elements at six different cross sections, based on the anticipated design. To account for the weight of stairways, handrails, the mounting platform grating, and other nonstructural elements, the density of the structural element material was increased by 20 percent. Weather protection is provided by side panels and a roof. Wind loading on the side panels was included; stiffness of the panels was assumed to be negligible. Because the superstructure is erected on top of the existing stand, the 36 spring elements were used to represent the stiffness of the stand. The spring stiffness was determined by finite element analysis of the existing stand.

The main load conditions as the front and side wind loads of 177 km/hr (110 mph), the postulated ultimate loads on the top of the superstructure from the attached SRM, and the potential seismic load were evaluated.

The wind load was represented as a static pressure on the projected area of the four sides of the superstructure. A pressure of 250 MPa (36 ksi) applied to the facing side and a negative pressure of 192 MPa (28 ksi) on the three other sides was assumed. Two wind directions were evaluated, a front wind (road to flame side) and a side wind.

The postulated ultimate forces applied by the SRM to the top of the superstructure were comprised of two elements: two forces for a total of 144 ton in road-to-flame direction (Z) and two forces for a total of 41 ton in side-to-side direction (X).

355

The effect of seismic excitation was conservatively analyzed by quasistatic method applying 0.5g load in three orthogonal directions simultaneously.

An operating load of 10.6 kN applied to the mounting platform at the 10 meter elevation and self-weight of the superstructure was considered in all load cases.

Maximum deflections on the top of the superstructure were calculated to be:

o due to front wind load;                        6.8 mm
o due to side wind load;                         6.3 mm
o due to ultimate side forces
    road-to-flame direction                15.2 mm
    side-to-side direction                 48.3 mm

Maximum stress due to wind load was 90 MPa which is below yield strength of A36 steel with a factor of safety of 2.8. The maximum stress caused by ultimate top forces of 180 MPa was below yield strength deflections and stresses caused by postulated seismic disturbance were substantially smaller of those due to the wind load.

In addition to the finite element analysis, conventional methods were used to address buckling of the frame elements and to evaluate joint connections. Results of these analysis conformed ability of the superstructure withstand the specified load with substantial factor of safety.

The environmental enclosure was analyzed by a combination of conventional and finite element methods and was shown to be capable of withstanding not only the specified wind load, but also the acoustic pressure during static firing of the SRM.

A dynamic analysis was performed to obtain dynamic properties of the superstructure, i.e. resonance frequencies and mode shapes, with and without the SRM. The main results of the analysis are summarized in Table 2.

EXISTING TEST STAND

The existing 1C test stand (Figure 4) was prepared by removing about 350 tons obsolete and surplus equipment including large propellant tanks, the liquid motor support and thrust measurement system, valves and piping, etc.

A preliminary analysis indicated the necessity of very limited modification of the stand main frame structure. The 12WF27 beams were changed to stronger 24WF76 beams at the superstructure interface to the stand and two other weak elements were replaced with stronger elements.

The stand was modeled as a framework (Figure 5) consisting of 321 beam elements supported at four points. The stand was analyzed for the same load conditions as the superstructure and interactive forces from the superstructure were applied to the finite element model of the stand. The minimum factor of safety for the wind load was calculated to be more than six against the yield strength of A36 steel.

The maximum stresses in the stand caused by the abnormal ultimate load applied to the top of the superstructure was calculated to be 345 MPa which was below ultimate strength of A36 steel.

The modified stand was also analyzed for a vertical downward load to determine its vertical load carrying capacity at the superstructure boundary. A factor of safety of 4.6 against ultimate strength was calculated for that load condition.

Stiffness properties of the existing stand also were calculated and subsequently used for a pylon-to-stand connection evaluation and for creating a general combined finite element model.

## MOTOR MOUNTING STRUCTURE

The attachment structure for the mounting of the motor (Figure 6) includes an existing pylon, newly designed pylon adapter welded into the pylon, and an aft test-skirt fixture connecting the motor to the pylon through the pylon adapter. A finite element analysis of the pylon structure, including a new pylon adapter, skirt, and a simple (stick) model of the SRM was performed using the IMAGES-3D and NASTRAN finite element programs. The model of the pylon is comprised entirely of beam elements. This assumes that cross sections, particularly those of the box beam at the top, do not warp. All beam connections are assumed to be rigid, as are the four support points. All section properties are based on the drawings of the original pylon structure.

The pylon adapter model is composed primarily of quadrilateral and triangular plate elements. The skirt model is basically a cylinder with a stiffening ring at the bottom. The SRM is modeled as a beam with section properties based on actual specimen geometry. The model was subjected to gravity loads in the three orthogonal directions. This served as a check of the structural soundness of the model, and also provided information for evaluating the structures' response to potential earthquake excitation.

The dynamic analysis of the mounting structure with and without the SRM was performed first in order to obtain the response of the structure to the ignition transient. The lowest resonance frequency of the SRM itself as a simple cantilever beam was computed at 1.96 Hz. The lowest resonance frequencies of the SRM installed are 1.22 Hz and 1.30 Hz in side-to-side and road-to-flame direction correspondingly. The dynamic response of the loaded structure to the ignition transient showed that there was no amplification of the vertical component of the motor displacement. However, the horizontal component was 1.7 times the static. The dynamic load factor was used to adjust the static force for a load combination calculation. Detailed static stress analysis showed that the only significant stress of 140 MPa occurs in the pylon adapter upper ring. Stresses in other parts of the pylon and the adapter were substantially lower. The maximum stress in the aft test skirt caused by the abnormal "ultimate" thrust of 10 million pounds canted at six degrees, was calculated to be 490 MPa. This is below the tensile strength of 620 MPa for normalized 4130 alloy steel.

## PYLON ANCHOR YIELD ANALYSIS

Pylon anchor yield analysis was critical. It preceded all other analyses, because the existing 40 steel anchors were imbedded in concrete and, therefore, could not be replaced. Each anchor is 57.1 mm (2.25 in.) in diameter and 11.6 m long and is made of quenched and tempered 4340 steel. Detailed analysis was performed taking into account anchor/concrete relative stiffness and the anchor/concrete interface. Even though the anchors can withstand the abnormal "ultimate" thrust of 10 million, maximum thrust force must be limited to 8.6 M based on yield of the anchors, and to only 7.2 M to maintain the joint. But even the smallest allowable thrust is substantially higher than that predicted and recorded during the SRM test.

## COMBINED MODEL ANALYSIS OF THE TEST STAND

After design and modification of the main elements of the test stand were completed, the finite element analyses of the stand were carried out. A combined finite element model of the superstructure, test stand, pylon assembly and SRM were developed on the NASTRAN and ANSYS finite element computer codes and carried out by two independent teams. These analyses were aimed to verify the design effort and also examine the stand-pylon-SRM interfaces. Therefore, the three following cases were analyzed:

1. Free standing pylon with the SRM without any attachment to the restraining structure.

2. Pylon with the SRM attached to the superstructure at the top level by means of struts.

3. Pylon attached to the stand at the second platform level with the SRM attached to the superstructure at the top level.

The analyses of the combined model were performed for different load conditions: thrust load, wind load, seismic disturbances, etc. The analyses took into account the transient nature of the thrust force and the SRM mass decay during the burnout.

The results of the combined model analyses gave additional information about static and dynamic behavior of the stand. They were in good agreement with the previously obtained data, and therefore, verified overall new design and modification of the test stand and the pylon.

Performance of the test stand during the SRM static firing was in good correlation with analytical predictions. No trace of damage, malfunction, or any structural problems have been noticed during the test. The measured stresses, eigenvalues, and eigenvectors were very close to those obtained during design and analytical activities. Overall the test stand performed exceptionally well and met all design criteria during the successful firing of the Titan 34D SRM.

## LIST OF FIGURES
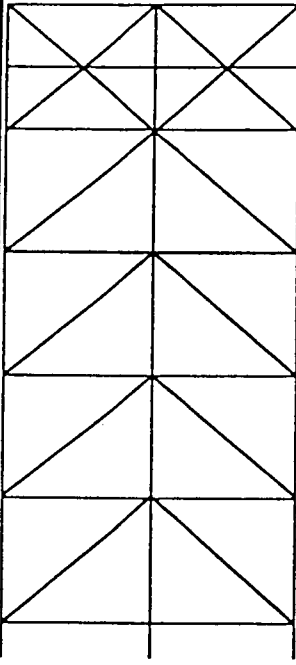
1. Superstructure framework.
2. Main structure of the test stand for Titan 34D SRM firing.
3. Finite element model of the superstructure.
4. Test stand 1C.
5. Finite element model of the modified test stand 1C.
6. Finite element model of motor mounting structure.

## LIST OF TABLES

1. Superstructure node and beam element summary.
2. Resonance frequencies of superstructure, Hz.

# TABLE 1

## SUPERSTRUCTURE NODE AND BEAM ELEMENT SUMMARY

| ELEV. M | VIEW | NODE NUMBER | COLUMN CORNER W12 X 58 | COLUMN SIDE W12 X 26 | PLATFORM W12 x 26 INNER | PLATFORM W12 x 26 OUTER | PLATFORM W12 x 26 CORNER | PLATFORM W12 x 26 CROSS | SIDE Two 6X4X1/2 |
|---|---|---|---|---|---|---|---|---|---|
| 16.2 | | 92-104 | 25-28 | 53-56 | —— | 185-192 | —— | —— | |
| 14.5 | | 79-91, 105-112 | 21-24 | 19-52 | 157-164 | 165-180 | 153-156 | 197-200 | 233-264 |
| 12.8 | | 66-78 | | | —— | 145-152 | —— | —— | |
| | | | 17-20 | 45-48 | | | | | 225-232 |
| 10.0 | | 53-65 | | | 117-124 | 125-132 | 133-136 | —— | |
| | | | 13-16 | 41-44 | | | | | 217-244 |
| 6.7 | | 40-52 | | | 97-104 | 105-112 | 113-116 | —— | |
| | | | 9-12 | 37-40 | | | | | 209-216 |
| 3.2 | | 27-39 | | | 77-84 | 85-92 | 93-96 | 192-196 | |
| | | | 5-8 | 33-36 | | | | | 201-208 |
| 0.1 | | 14-26 1-13 | | | 57-64* | 65-72* | —— | —— | |
| 0 | | | 1-4 | 29-32 | | | | | |

* SECTIONS W16 X 67

360

## TABLE 2

## RESONANCE FREQUENCIES OF SUPERSTRUCTURE, HZ

| Mode Description | Without Specimen | With Specimen |
|---|---|---|
| Global rocking side-to-side | 6.67 | 2.58 |
| Global rocking road-to-flame | 6.45 | 2.59 |
| Global torsion | | 7.41 |
| Local side column bending | 4.29 | 4.29 |
| Lower platform (local) | 8.66, 8.72 | 8.66, 8.71 |
| Upper platform (local) | 8.72, 8.73 | 8.71, 8.73, 8.75 |
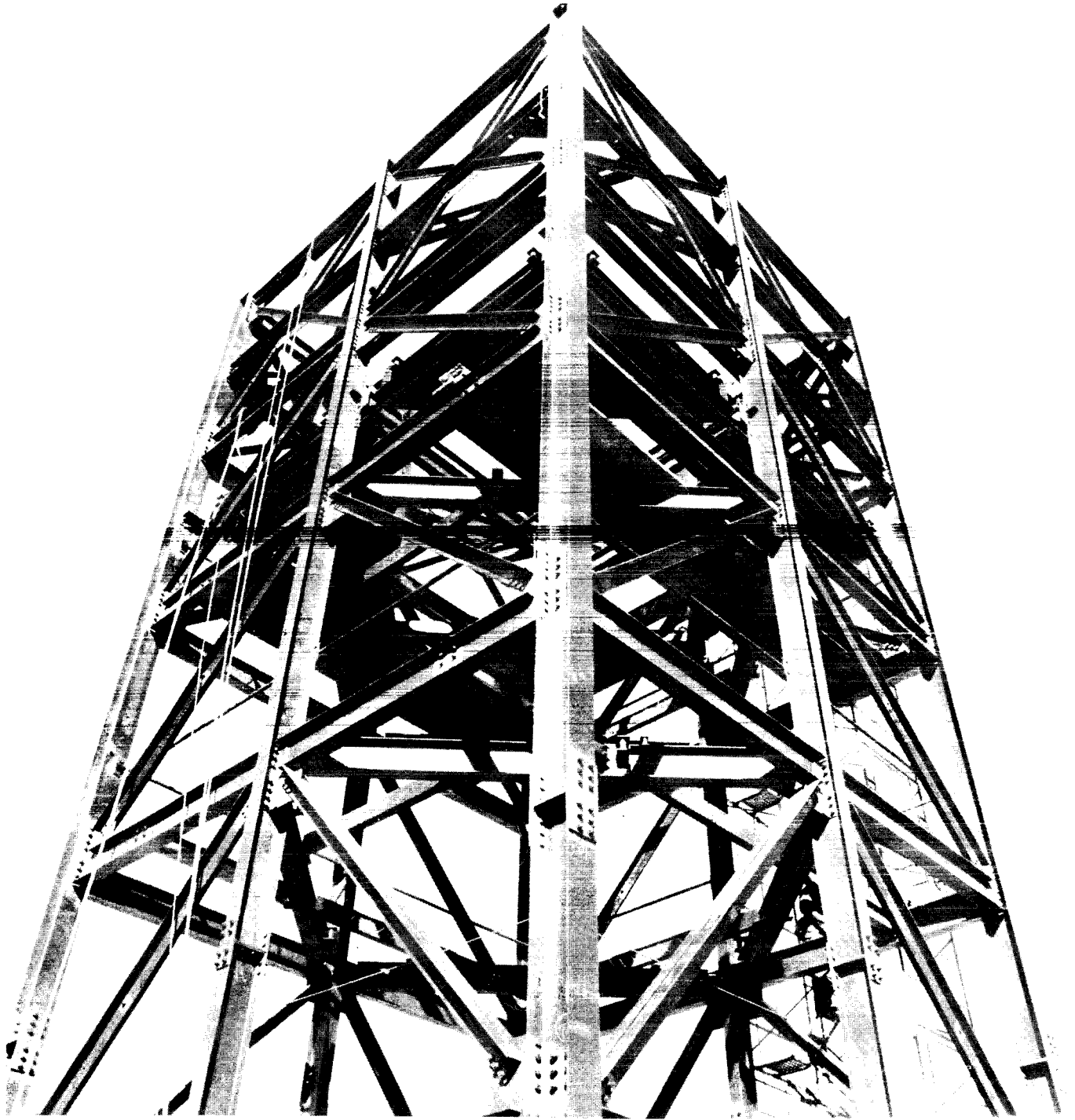
FIGURE 1

SUPERSTRUCTURE FRAMEWORK

362
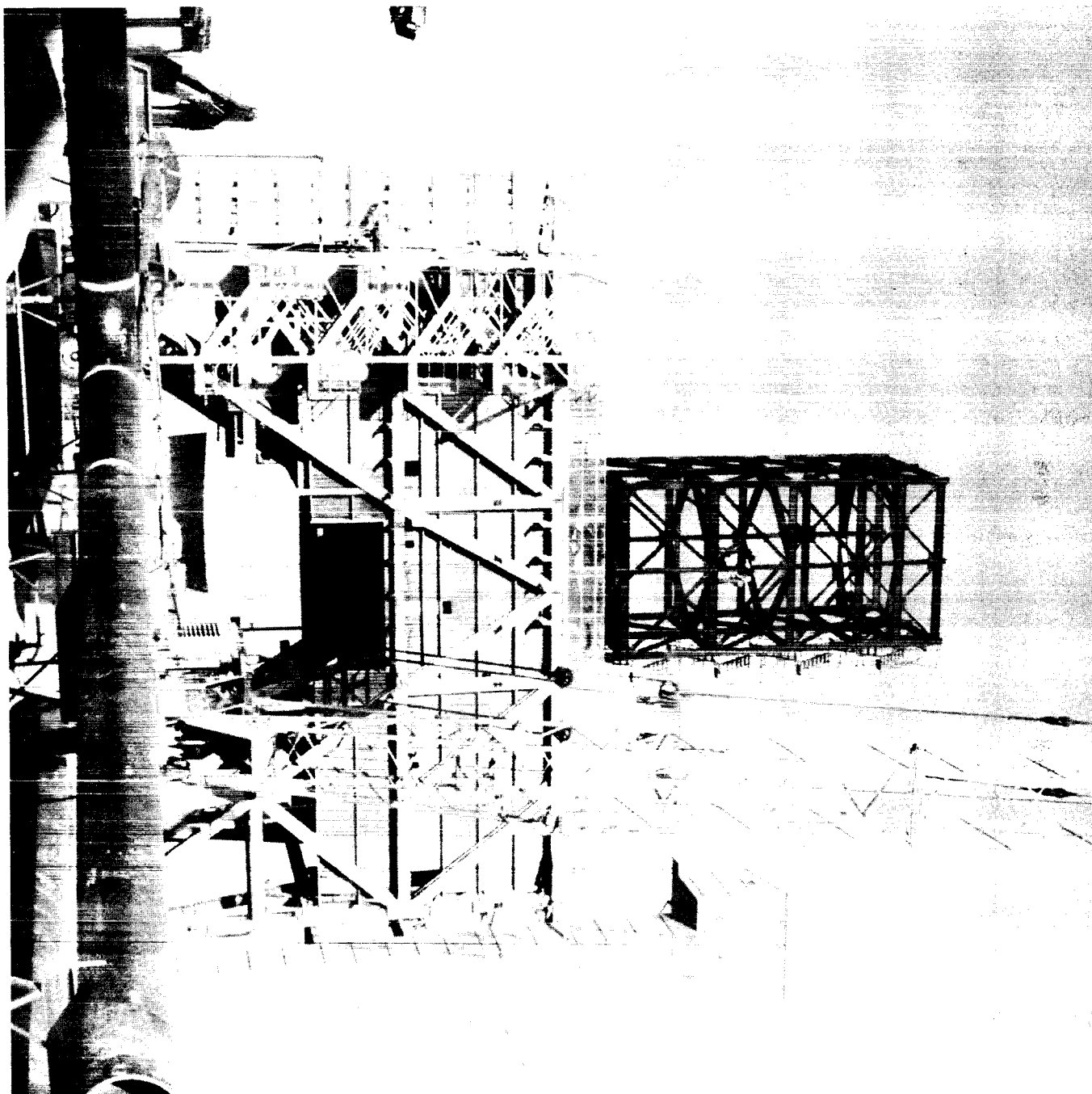
FIGURE 2

MAIN STRUCTURE OF THE TEST STAND FOR TITAN 34D SRM FIRING
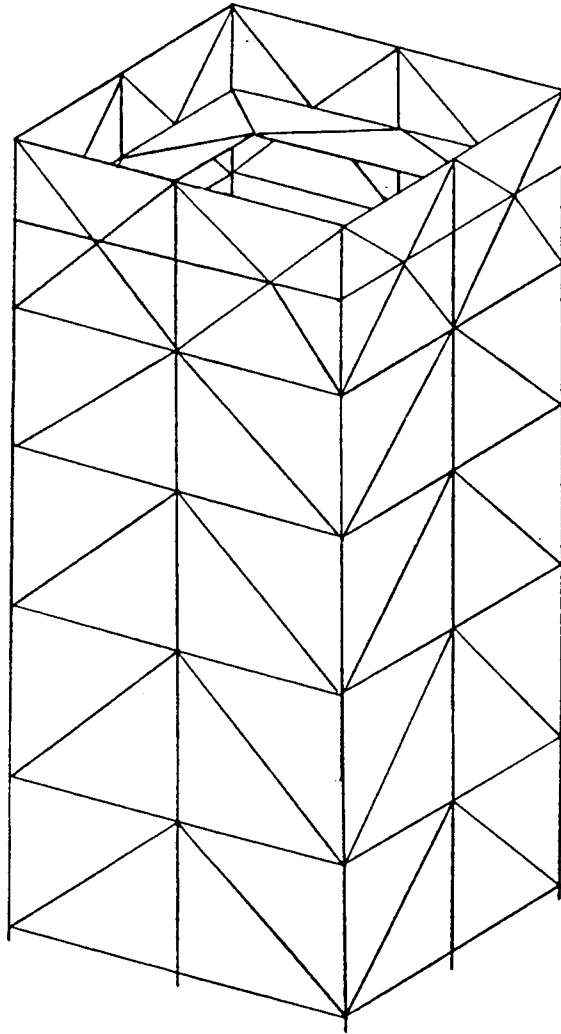
FIGURE 3

FINITE ELEMENT MODEL OF THE SUPERSTRUCTURE
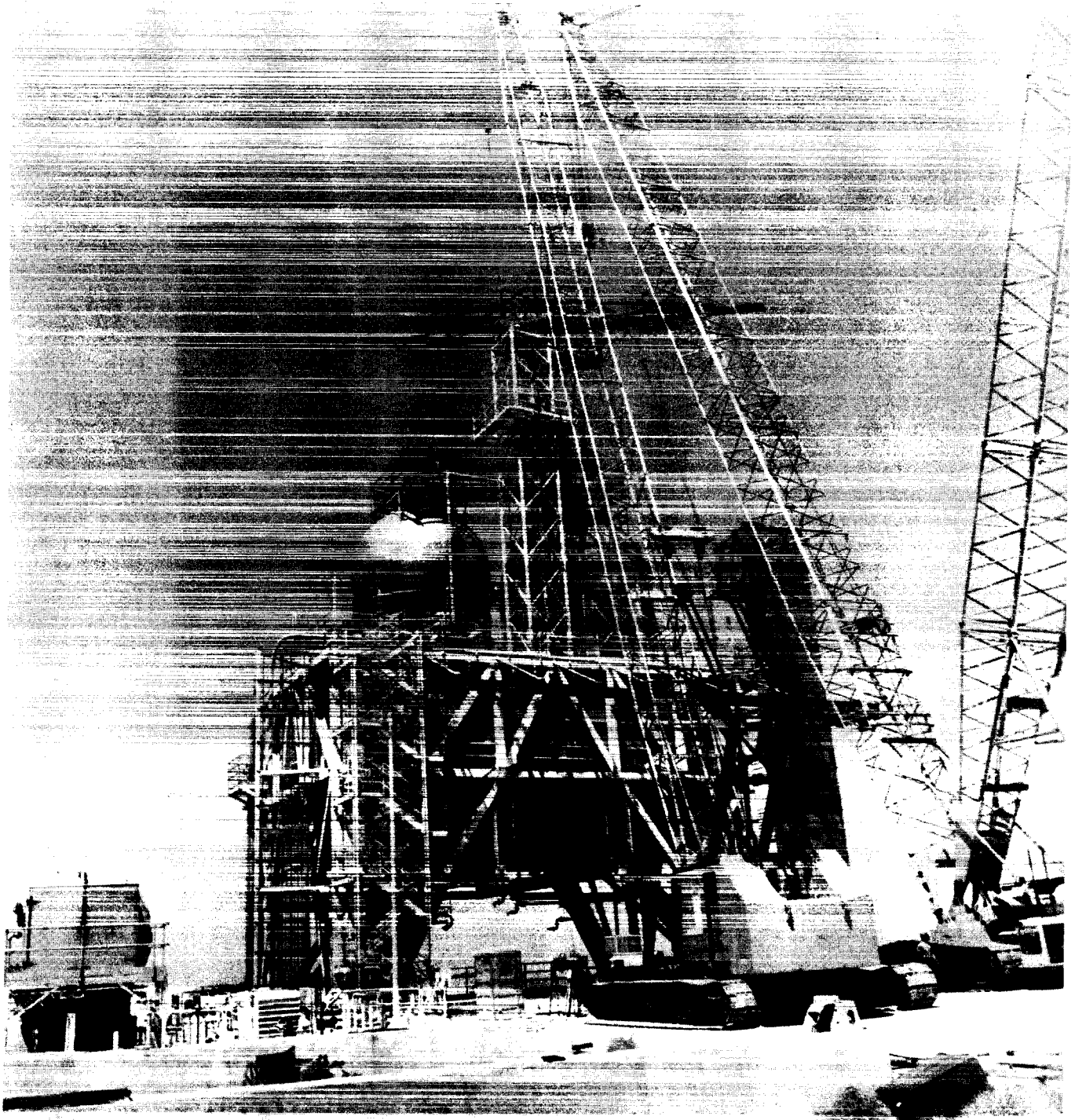
FIGURE 4

TEST STAND 1C
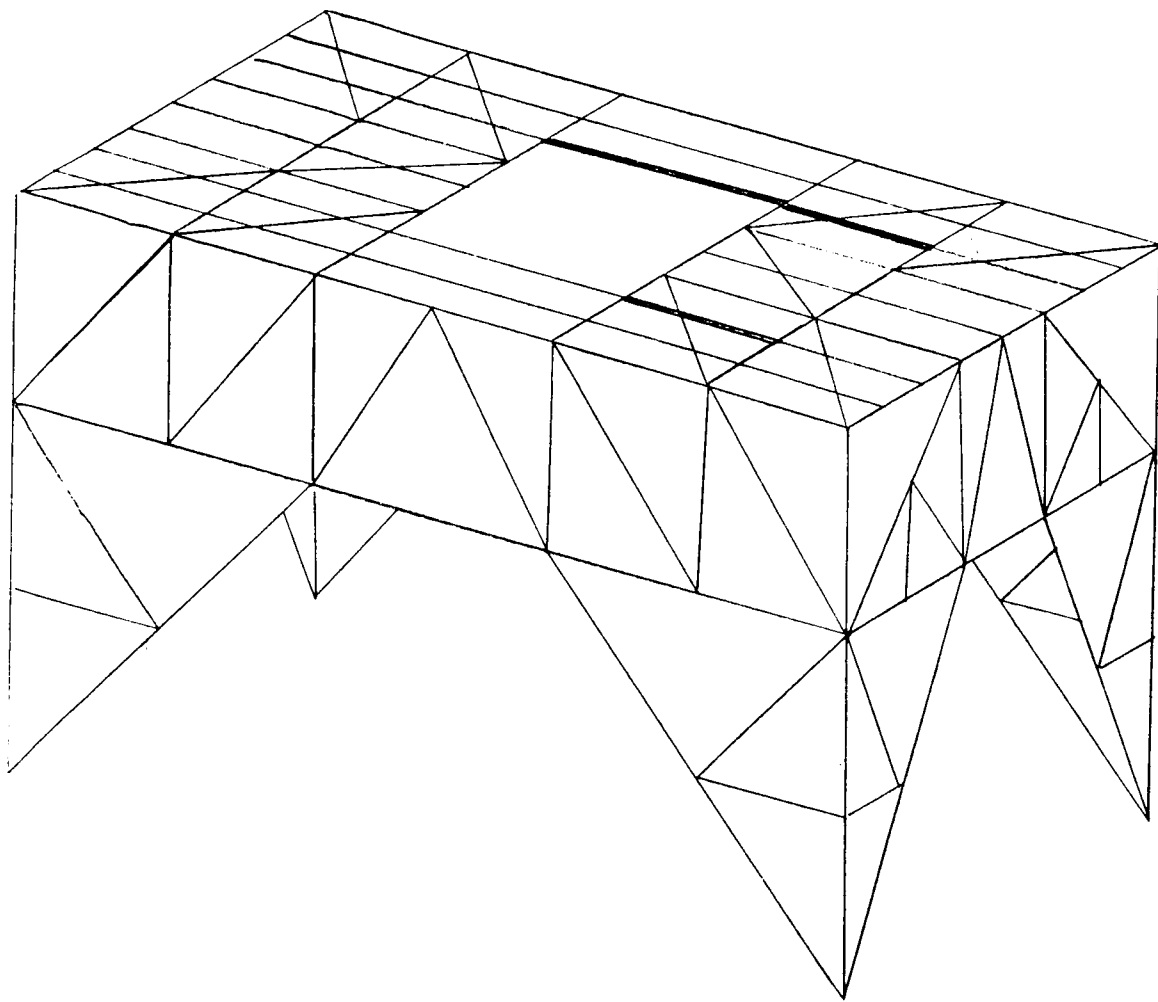
FIGURE 5

FINITE ELEMENT MODEL OF THE MODIFIED TEST STAND 1C

SRM

AFT SKIRT

PYLON ADAPTER

PYLON
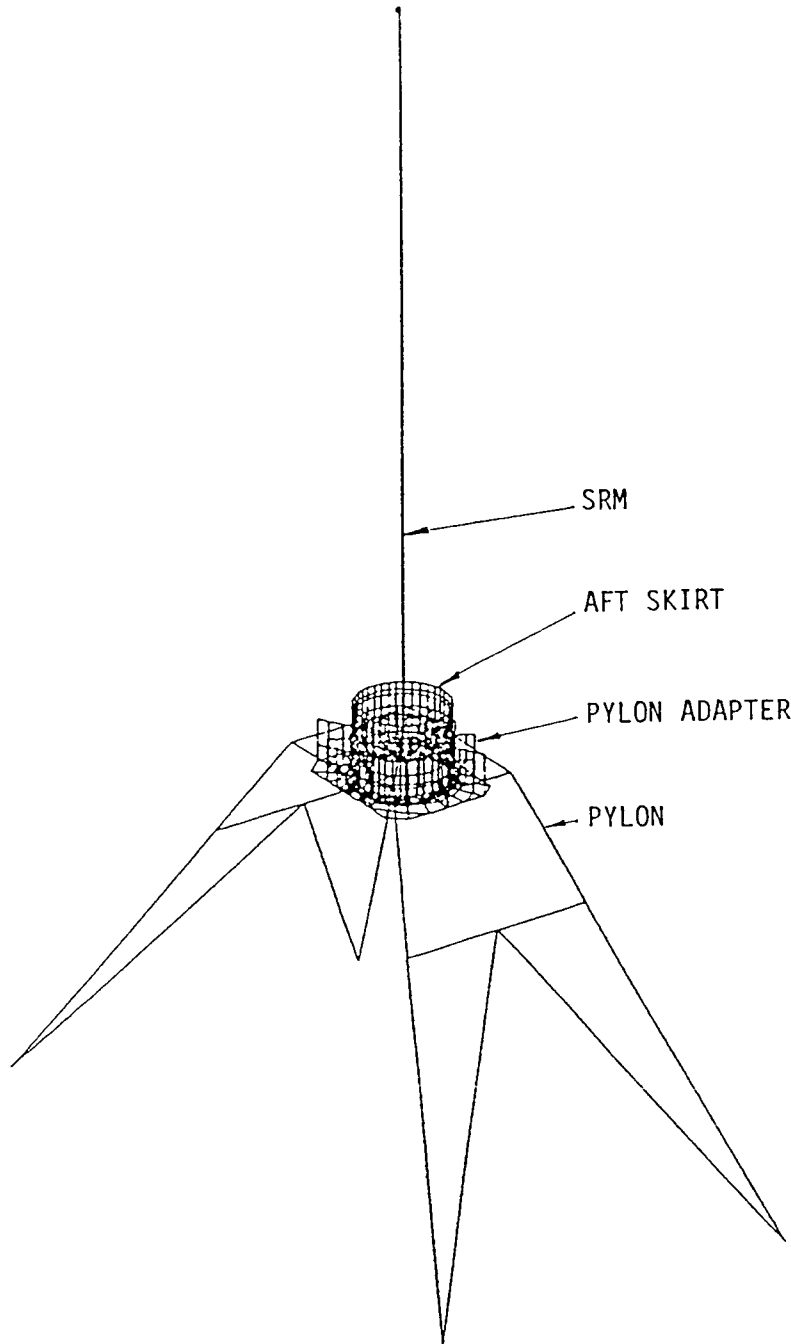
FIGURE 6

FINITE ELEMENT MODEL OF MOTOR MOUNTING STRUCTURE

367

# ARIANE 5 VERIFICATION AND ASSOCIATED TEST FACILITIES

M. Vedrenne and A. L. Gonzalez
ESA Headquarters – Paris

## ABSTRACT

The philosophy of verification tests of the Ariane 5 launcher programme is already established. It corresponds to the development and the ground and flight qualification phases for both unmanned and manned launches. The different types of test are outlined for the system, booster, main core and upper structures, allowing the identification of the associated test facilities which are then described.

## INTRODUCTION

The development of the Ariane 5 launcher is now beginning but a preliminary phase has been performed to establish the basis of both a sound configuration as well as its verification programme. A major part of this verification programme concerns testing and due to specific facilities foreseen and long delivery times, an early definition has been established.

In this paper, the test programme of the Ariane 5 is presented. First the tests classification is established to mention briefly the different tests proposed in each area and in a second part the test facilities are identified.

## ARIANE 5 TESTING

The launcher tests can be classified with respect to their programmatic objectives in the following categories:

- Environmental definition (external, internal)
- Development
- Qualification

Alternatively, tests can be classified in relation to the launcher assemblies, giving the following groups:

- System
- Booster
- Main core
- Upper stage and structures

This second classification is used in the following descriptions making reference to the programmatic objectives involved.

### SYSTEM TESTS

The following system tests are foreseen:

#### Reduced Scale Tests

The purpose of these tests is to define the external environment of the launcher: Aerodynamic, thermal and acoustic tests are included. They are performed with reduced models in appropriate existing facilities.

## Functional Tests in Europe

The main objectives are in the development and qualification of the launcher guidance and control functions. To run these tests a functional simulation installation (ISF: Installation de Simulation Fonctionnelle) will be set up at Les Mureaux near Paris.

## Structural Tests

They will include the dynamic testing of the booster, main core and upper structures. The dynamic tests of the booster will be performed in the French Guiana test installations (see booster testing below). For the dynamic testing of the main core a specific facility will be installed in Europe.

## Validation Tests in French Guiana

Mechanical integration of the launcher as well as electrical verifications will be performed in CSG (Centre Spatial Guyanais).

## BOOSTER TESTING

The booster testing comprises: Preliminary tests; Testing in nominal the configuration.

The preliminary tests will allow evaluation of the different technologies to be used, manufacturing process, functioning aspects like internal pressure build up behaviour, segment joints, etc. . . . Different types of models will be used, some of them being at reduced scale and using teststands.

Ten firing tests will be performed in nominal configuration in the test facilities prepared in CSG. Three types of tests arc to be distinguished.

## Tests B

The purpose of two tests is to evaluate the internal functioning with a reinforced structure to avoid the inherent risk of using a non fully developed structure.

## Tests M

These tests correspond to the development of the integrated booster. Four tests are foreseen, the first two will be used to verify the compatibility between the different elements of the booster. The other two will examine extreme environmental conditions.

## Tests Q

The functioning of the booster will be verified in four tests. The last two being associated in the same configuration as are the two flight units for the same launcher.

## MAIN CORE TESTING

Testing of this stage is broken down as follows:

    Tank
    Adjacent structures
    Engine
    Stage

The tank testing includes the usual verification of materials, technologies, manufacturing processes, functioning aspects of the anti-vortex, etc. . . .

369

For the adjacent structures, the tests are also the standard static and dynamic ones.

The engine in itself follows its own development sequence and a detailed description of its test plan is out of the scope of this communication. It should be mentioned in general terms that the engine testing started with the materials and processes verification followed by series of tests at components and subassemblies level to finally test the whole engine. A general description of the teststands will be found in the next section.

The complete stage will be tested in French Guiana, using the operational facilities: Launch integration building, transport platform and launch pad. It will be tested in launch configuration supported by two dummies representing the boosters.

## UPPER STAGE AND STRUCTURES TESTING

The upper stage follows at its level, the same testing logic as the main core: tank, structure, engine and stage testing. The teststands will be described below.

The upper structures comprise the vehicle equipment bay, the SPELTRA (Structure Porteuse Externe de Lancement Triple Ariane) (Structure allowing multiple launches) and the fairing. As for any structure, the main tests will be:

> Static Tests: stiffness, strength
> Dynamic Tests: vibrations, acoustic, separation


## ARIANE 5 TEST FACILITIES

It is too early in the programme to describe the test facilities, but the most important have already identified and a short description will be given in this section.

## BOOSTER TESTSTAND ZONE

This facility will comprise a test area with flues, a shelter structure including the technical premises and access facilities and mobile cover of the whole area; a mobile part made up of a pallet and the booster would be inserted in a solid metal structure integral with the foundations and having the handling facilities necessary for table/rail track levelling adjustments. A test monitoring zone about 700 m away, housing the monitoring and command facilities necessary for carrying out the tests and an access rail track linking the booster integration building to the teststand and enabling the whole mobile structure (pallet plus booster) to be transferred.

## MAIN CORE ENGINE TESTSTANDS

The engine testing involves many stands. Among them we can find the following ones:

Stand for testing components under high-pressure propellant (Vernon – France) to be used for characteristization of the generator injection elements, dynamic seals and bearings.

Stand for testing the generator and oxygen turbopump (Ottobrunn – W. Germany). Adaptation of an existing stand.

Turbopump teststand (Vernon). The corresponding tests will be made on the liquid oxygen and liquid hydrogen turbopumps fed either independently from a high-pressure gaseous hydrogen source or a gas generator fed by high-pressure tanks or coupled with the gas generator fed with propellants tapped at the pump outlets.

Chamber teststand (Lampoldshausen – W. Germany). This stand will allow characterization and qualification tests of the engine combustion chamber in a horisontal position to be carried out. The chamber will be fed from high-pressure cryogenic tanks.

Engine stands (Vernon and Lampoldshausen). Both stands will be identical. They will be designed to simulate as closely as possible propellant and fluid system of the stage and to carry out tests in "stage with battleship tanks" configuration.

## UPPER STAGE PROPULSION TEST FACILITIES

Tests on the engine and the propulsion unit will be done on the test site at Lampoldshausen. This site has various facilities where cold tests can be carried out for the purpose of tuning, pressure testing and functional testing on the components of the engine and the propulsion unit. The hot tests will be carried out on the following teststands:

- Stand to be used for short-duration chamber and engine tests under ground conditions. The tests could be performed with or without a supersonic diffuser.

- Stand to test the propulsion unit and the integrated stage under ground conditions.

- Stand fitted with a vacuum chamber and a stream ejector, thus making it possible to run engine tests under vacuum conditions.

## SUMMARY AND CONCLUSION

The Ariane 5 launcher development is starting. From the preliminary phase, the verification tests corresponding to the launcher system, booster, main core, upper stage and structures, have been identified, allowing the preliminary definition of the test facilities needed. Among them, the booster teststand in French Guiana and the stands for testing the main engine and the upper stage engine have been outlined.

# THE SEPARATION TEST IN VACUUM OF
# THE ARIANE 4 PAYLOAD FAIRING

J. R. Butcher
Contraves AG, Zurich

## ABSTRACT

This paper describes the separation tests performed during the qualification test programme of the ARIANE 4 Payload Fairing. As the first fairing structure to be developed using carbon-fibre technology, two separation tests of a flight standard fairing were performed under vacuum conditions. The primary objectives of these tests were to verify compliance with the vehicle imposed requirements and to establish the behavioural characteristics of the fairing structure itself.

## INTRODUCTION

ARIANE 4 is the latest increased lift version of the European family of launch vehicles. In order to optimise the volume to weight ratio of the correspondingly larger payload fairing, the structure was developed using carbon-fibre technology as opposed to the aluminium skin/stringer construction of previous ARIANE fairings.

Having protected the payload during ascent through the earth's atmosphere, the fairing is jettisoned from the launch vehicle, whilst still in the accelerated phase, at the end of 2nd stage burn. Separation is effected by means of releasing a tension band, (the Horizontal Separation System), which attaches the fairing to the vehicle's 3rd. stage. This is followed within milliseconds by the activation of a linear explosive device, (the Vertical Separation System), which acts along the longitudinal axis of the fairing, separating it into two halves and ejecting them laterally away from the launch vehicle, (and thus the payload).

In order to fulfill the clearance requirements, a detailed dynamic analysis determined that a relatively low radial stiffness was required for the fairing halves. The separation system therefore imparts a correspondingly high amplitude "flexing" motion into the fairing structure during separation. Precise evaluation of this behaviour was thus necessary to ensure that no part of the fairing structure impinges on the payload volume and launch vehicle structure after jettison, (and to verify the mathematical model used to predict the behaviour of all subsequent fairing configurations). It was therefore considered necessary to perform separation tests under conditions representing as far as possible, those in flight. To avoid any influence from aerodynamic drag during separation, it follows that such a test had to be performed under vacuum conditions.

The tests were also performed in a 1g. environment, (simulation of operational acceleration loads of approx 3g. not being possible), and at ambient temperature conditions as opposed to the elevated in-flight temperatures. The effect of the axial acceleration was subsequently analytically superimposed on the test results, and the effect of the lower test temperatures on the fairing structure represents worst case conditions with respect to the clearance achieved, due to the corresponding increase in structural stiffness.

Due to the size of the test object which has a diameter of 4m. (13ft) and a height of 9.6m. (31.5ft), the test was performed in the Dynamic Test Chamber at ESTEC in the Netherlands; currently the largest vacuum chamber available in Europe. Views of the fairing before and after separation are given in FIGS. 1 and 2 respectively.

In addition to verifying the various performance requirements, it was to be shown that no permanent deformation of the fairing structure occurred following two consecutive separation tests. As a result, two such separation tests were performed during August and October 1984.

## FAIRING DESCRIPTION

The test item consisted of the Qualification Model Fairing, which was a "medium length" version of the three design options. The overall height of this fairing is thus 9.6m. (31.5ft) with a diameter of 4.0m. (13.1ft).

The fairing takes the form of two symmetrical half shells, (designated T and TN), joined together in the vertical plane and attached to the launch vehicle at it's base.

The test item was built to the full flight standard configuration with the exception of some minor points mentioned in the following paragraphs.

A summary description of the various major subsystems of the fairing follows.

## STRUCTURE

The fairing structure consists essentially of a lower cylindrical section with a height of approx. 5.0m. (16.4ft), a Front Cone of height approx. 3.7m. (12.1ft), with a spherical section Nose Cap of height 0.9m (3ft) forming the apex of the fairing. The Cylinder and Front Cone sections are produced from an aluminium honeycomb core/Carbon Fibre Reinforced Plastic face sheets construction, whilst the Nose Cap is a more conventional aluminium skin/stringer design. An aluminium Separation Ring is attached to the base of the cylindrical section to provide the mating interface with the vehicle's upper stage.

A layer of cork is bonded to the outside surface of the Front Cone and Nose Cap sections to protect the payload and fairing from kinetic heating during launch.

The entire external surface is then coated with a white electrostatic paint. The test model was only painted on the TN-Half, the T-Half being left in order to observe any possible effects of separation on the surface of the structure itself.

## SEPARATION SYSTEMS

The fairing is connected to the launcher by means of a steel tension belt which maintains a circumferential tooth of the Separation Ring, in a corresponding groove at the vehicle interface. The steel belt is tensioned by means of two tension bolts located diametrically opposite each other. At the instant of separation, the two tension bolts are cut by pyrotechnic bolt cutters. This action effectively disconnects the fairing from the launcher and this assembly is thus known as the Horizontal Separation System (HSS).

Almost simultaneous with this release, (with less than 2msec. delay), the Vertical Separation System (VSS) is activated. During the launch phase, the VSS acts as the structural connection between the two fairing half shells. Upon detonation of the explosive device within the VSS, the two halves are separated and jettisoned laterally away from payload and launcher, (ref. FIG. 3).

As the fairing is ejected whilst the vehicle is still in an accelerated phase at the end of 2nd. stage burn, the VSS must impart sufficient separation energy to avoid any risk of impacting the payload or vehicle following separation.

Correct sequencing of the HSS and VSS activations is ensured by a pyrotechnic system initiated from a central distribution manifold from which Confined Detonating Fuses relay the detonation to the respective separation systems.

## FLIGHT INSTRUMENTATION

A full compliment of the normal flight instrumentation for operational launches was also installed and checked out during the separation tests. This comprises :

.   One displacement transducer per half fairing to record separation distance as a function of time.

.   Two linear potentiometers per half fairing to monitor the radial flexing motion of the structure during separation.

.   One Gyrometer per half fairing to measure the angular velocities of the separating structure about all three axes.

.   Pyrotechnic status signals to verify the instants of pyrotechnic ignition, bolt cutting and pyrotechnic connector separation.

.   One accelerometer was also installed at the base of the VSS on each half fairing to monitor acceleration levels. (Whilst not belonging to the definition of normal flight instrumentation, these are being flown on the initial technological launches and as such were also mounted during this test).

## SOFT TENSION BELT RELEASE SYSTEM

In order to reduce the shock levels imparted to the vehicle at fairing separation the Soft Tension Belt Release System was developed. This system consists essentially of one hydraulic actuator installed within each half HSS tension belt assembly.

Activation of this device some 5 secs. prior to fairing separation has the effect of reducing the HSS tension from the launch tension of 10 tonnes to 2 tonnes, thus reducing the stored energy in the HSS, (and Vehicle interface), at the instant of separation. This device was installed and tes-

ted prior to the second separation test for comparison purposes.

## CABLE STOWING SYSTEM

The function of the Cable Stowing System is to retain the deployable part of the instrumentation cable against the structure of the fairing halves during launch and ascent. It also has to resist the shock of separation but subsequently to gradually release the cable during separation, to enable instrumentation data from the fairing to be transmitted to the vehicle over a separation distance of approx. 6m (19.7ft).

As such a separation distance could not be achieved in these tests, a short section of cable was installed on the fairing, without the interface connectors, to verify that the method of fixation could withstand the separation shock.

## TEST OBJECTIVES

The objectives of the separation tests can be summarised as follows :

- Fulfilment of the clearance requirements with respect to payload volume and vehicle envelope during separation.

- Verification of the structural integrity of the fairing and its equipment, (including fixations), during separation.

- Correct functioning of the pyrotechnic as well as Horizontal and Vertical Separation Systems.

- Validation of the in-flight separation measurement plan.

- Validation of the finite element model to be used for fairing separation analysis.

## TEST CONFIGURATION

## FAIRING INSTALLATION

The fairing was installed in the Dynamic Test Chamber, (DTC), mounted to a structure which simulated the vehicle interface, known as the Adjacent Structure, (AS). The AS was

in turn mounted on the seismic structure of the DTC, at a location of 400mm. (16in.), from the chamber centreline, (ref. FIG. 4). This then enabled a free flying distance of at least 2m.(6.5ft) of one half (the TN-Half) fairing, which was required to ensure sufficient data was obtained to characterise the fairing's behaviour following separation.

## CATCHING SYSTEMS

In order to restrain the fairing halves following the separation and free-flight, fairing catching systems were installed in the DTC for each half fairing. These consisted of :

### Horizontal Fairing Catching System (HFCS)

This system consisted essentially of a catching net which was used to absorb the energy of the separated halves and prevented them from impacting with the wall of the DTC. The nets were attached to the chamber by means of hydraulic dampers and were tied back towards the wall to provide the required uninterrupted free-flying distance for each half fairing. The various catching systems were designed in such a way that it was the HFCS that first influenced the flight of the fairing halves, and was thus the limiting factor in determining this distance.

### Bounce Back Restraint Device (BBRD)

The aim of the BBRD was to retain the half fairing against the catching net after separation and to prevent them from bouncing back from the net and onto the mounting structures in the centre of the chamber. To achieve this, each device consisted essentially of four nylon cords attached near the corners of the cylindrial section of the half fairing.

These ropes passed through a jaw clamping mechanism before being attached to the DTC wall by means of elastic ropes and a pulley arrangement. The design of the BBRD was such that the nylon ropes passed freely through the clamp jaws during separation, without influencing the fairing behaviour, but could not be pulled back in the opposite direction after the fairing was caught in the net.

### Vertical Fairing Catching System (VFCS)

The VFCS consisted simply of two nylon cords for each half fairing, suspended from the underside of the DTC lid

and attached to the fairing at the bottom of the conical section. The lengths of the cords were determined to allow an unimpeded free flight but to avoid an excessive drop onto the chamber sub-floor and toppling of the separated half fairing.

## MEASUREMENT PLAN

In addition to the flight instrumentation mentioned above, a series of test instrumentation was added to the fairing to define its behaviour during separation. Due to the geometric constraints of the DTC, this instrumentation was concentrated on the TN-Half fairing, this being the half which was capable of sufficient free flying distance. The more important measurement systems can be summarised as follows :

## ELECTRO-OPTICAL CAMERAS

As the most critical aspect of the test was to define the precise motion of the fairing half-shell during separation, (in order to subsequently validate the mathematical model), an accurate, high speed, 3-Dimensional trajectory measurement system was required.

The SELSPOT Electro-Optical Camera, (EOC), system was developed and specially adapted for this purpose by SELCOM AB, Gothenburg, Sweden. This system consists of a number of Light Emitting Diodes, (LEDs), attached to the fairing structure; each one being measured by a pair of infra-red sensitive cameras, thus enabling the 3-Dimensional trajectory to be computed. The system operates on the principle of pulsing the LEDs at high frequency with a defined sequence, resulting in a number of discrete measurement points.

A total of 6 cameras were used for this test, to monitor 12 measurement points on the fairing. This combination results in a sampling rate of 833 HZ for each measurement point.

The LEDs are connected to LED Control Units, (LCU), which act as a distribution unit for pulsing the LEDs. The complete system is controlled and monitored by an Administration Unit, which in turn interfaces with a computer for command input and data storage.

A schematic of the measurement set up is shown in FIG. 5, whereby Cameras 1A and 3A were installed on a central tower structure inside the fairing and Cameras 2B and 4B were attached to the inside wall of the DTC. Cameras 1A and

2B thus acted as a pair viewing one quadrant of the cylindrical section of the fairing, whilst 3A and 4B monitored the other quadrant. These measurement points were achieved by mounting a "double" LED arrangement of which, one was installed on the inside surface and the other adjacent to, but on the outside surface of the fairing.

Pulsing this pair of LEDs simultaneously, enabled a measurement "point" on the fairing structure to be seen by a camera pair, one of which was installed inside and one outside the fairing. Cameras 5A and 6B were both attached to the underside of the DTC lid, monitoring LEDs attached to the outside surface of the fairing Front Cone.

## CINE CAMERAS

In order to obtain a general visual impression of the fairing behaviour during separation, four 16mm cine cameras, each equipped with a $94^{\circ}$ wide angle lens, were installed outside the DTC, viewing through optical view ports. The cameras had a film speed of 150 frames/sec. and were controlled by a single control unit providing synchronisation with each other and the ignition signal. For the second separation test, one of these cameras was relocated inside the DTC to improve its viewing angle. A special sealed container with outlets for the control and pressure lines to pass through feed throughs in the DTC wall, was produced to protect the camera from the vacuum conditions.

## BREAKWIRES

To establish the sequence of separation of the two halves, over the entire length of the fairing, at the instant of separation, a series of Breakwire assemblies were bonded across the joint between the two half shells. Each assembly provided timing information over displacements between the half fairings of 0,40 and 60mm, enabling accurate assessment of the separation sequence both along the fairing's length and comparison of the two separating joints.

## STRAIN GAUGES

In order to establish the stresses induced in the fairing structure as a result of separation and the subsequent flexing modes, 24 strain gauges were attached to the TN-Half fairing. The locations were selected as those areas indicated by the analysis as being the most critical, some of which were re-located for the second test based on the evaluation of the data from the first test.

379

## SHOCK ACCELEROMETERS

High frequency shock accelerometers were attached to the major interfaces of the pyrotechnic and separation systems; (i.e. pyrotechnic manifold, VSS detonator blocks, VSS end seals at the opposite ends to the detonators, and the bolt cutter housings). The purpose of these was to establish the event timings of the pyrotechnic system, to verify the correct sequence of operations.

Similar accelerometers were also installed on parts of the fairing catching systems to establish impact times and thus correlate the free-flying times established with other measurement systems.

## MEASUREMENT ACCELEROMETERS

In order to obtain an indication of the low frequency acceleration levels, a total of 15 measurement accelerometers were installed at various locations on the TN-Half fairing. Of primary interest were the areas of the VSS separation joints and the highest point on the Nose Cap.

## CLEARANCE DETECTORS

As a supplementary source of verifying the clearance requirement with respect to the vehicle interface, clearance detectors were bonded to the support structure onto which the fairing was mounted. These took the form of simple moulded polystyrene blocks extending to the limits of the forbidden volume, within which no part of the fairing structure may pass during separation. These would have provided immediate indication had this volume been breached.

## SHOCK MEASUREMENTS ON ADJACENT STRUCTURE

In addition to establishing the fairing behaviour, an indication of the shock levels induced into the vehicle, at the instant of separation, was also obtained.

A total of nine high frequency accelerometers were attached to the Adjacent Structure to monitor in particular the levels experienced close to the fairing mounting interface, around its complete circumference.

## IGNITION SYSTEM

The ignition of the pyrotechnic system was initiated by a start command entered on the computer keyboard of the EOC system, resulting in a trigger signal being sent to the Ignition Control Unit (ICU). This signal in turn closed power relays within the ICU which simultaneously provided the ignition current to the pyrotechnic detonators and recorded a "time zero" signal on each of the magnetic tape recorders of the data management system, as well as each cine film. This signal was thus used as a timing reference for subsequent data evaluation.

## TEST OBSERVATIONS

a)   A detailed visual inspection performed following the first separation test, indicated some anomalies. The TN-Half fairing structure, (inner face sheet and honeycomb core), had ruptured along a row of fixing inserts close to the axis of symmetry. The rupture extended along a length of approx. 1.5m (5ft) from the base of the fairing. Detailed evaluation of the instrumentation results revealed however, that the failure did not occur during the free-flight of the half-shell, but after being restrained by the catching nets. The position of the nets and stiffness of the support points were modified for the second test. The damaged area of the fairing was replaced and no such failure occurred during the second test.

b)   Three rivets from the lowest aluminium stiffener of the Nose Cap, adjacent to the VSS had broken loose. Localised shock loading due to separation was clearly higher than expected in this area. These rivets were subsequently replaced with steel bolts and again no such problems were observed during the second test.

c)   Some structural damage was observed in the area of the Bolt Cutter fixations which resulted in some parts becoming loose during separation. This area was also strengthened to avoid the possibility of any loose parts impinging the payload volume and this modification was successfully verified by the second test.

d)   Failures were encountered on both displacement transducers during the first test. The principle of operation of these transducers is of a thin cable attached to the vehicle interface. This is then extended from a pulley within the transducer which is attached to the fairing structure. As the cable extends up to 2m (6.5ft) during fairing separation, the resultant output of the potentiometer within the transducer provides an indication of displacement versus time.

The problem encountered during the first test was that both cables broke at the attachment interface with the vehicle, immediately on separation.

The geometry of the attachment point as well as that of the cable outlet and pulley arrangement was modified for the second test, resulting in successful functioning of both units.

e)    The fixations of the Cable Stowing System did not withstand the separation shock and the cables broke loose from the attachment points. Modifications were made for the second test but the cables again separated from the fixation brackets.

(Note: This system was subsequently redesigned and retested at sub-system level before becoming qualified for flight).


## TEST INSTRUMENTATION RESULTS


The results of the various methods of instrumentation are summarised below, with both separation tests being combined, as the measurements for both tests were essentially the same.

Measurement data has been quoted where it is considered meaningfull to do so. Much of the data however was used to validate the mathematical model to be used for the separation analysis of all subsequent ARIANE 4 launches. The results of this correlation are outside the scope of this paper.


## ELECTRO-OPTICAL CAMERAS

The 3-Dimensional trajectories of all measurement points were successfully obtained from both tests. Whilst all points were important to characterise the fairing's behaviour, the critical points are the bottom corners of the half-shell, at the HSS/VSS interface. It is in this area that the "flexing" motion of the fairing during separation is most extreme.

These measurement points are thus the most critical with respect to verifying that the clearance requirements of the payload and vehicle are satisfied. This flexing motion can be explained by considering FIG. 6 which indicates the forms taken by the circumference of the base of the fairing during separation. In addition to being jettisoned away from

the vehicle, the two sides of each fairing half-shell are also projected radially outwards by the force of the separation system. It thus follows that these points, having reached a maximum amplitude, will tend to return inwards. The relationship between separation velocity, flexing frequency and amplitude is thus clearly critical in determining the clearance margins during separation.

The plot of the trajectory of measurement point A of FIG. 6, in the horizontal separation plane, is indicated in FIG. 7 and is typical for both corners of the half-shell. A typical minimum clearance between these points and the payload volume was determined as approx. 350mm (14 in), which results in a satisfactory margin of safety when considered in a parametric separation analysis.

Measurement data was obtained over a horizontal free flight distance of 2m (6.5ft) within a time of 350msecs. before contacting with the catching system. As this corresponds to almost one complete cycle of the flexing motion, (Ref. FIG 7), confidence is achieved that the fairing motion can be fully characterised.

The trajectory traces of the measurement points also clearly indicated discontinuities at the instant of fairing rupture during the first test. These correspond to the instant of the second maximum amplitude of flexing, at which time the measurement points on the axis of symmetry of the half-shell are tending to be pushed back towards the centre of the DTC due to the resilience of the catching net. The failure therefore, did not occur during free-flight but as a combination of the flexing motion and the restraint of the catching system.

## BREAKWIRES

Data obtained from the Breakwire signals indicated that complete separation occurs between 2.5 and 4msecs. after ignition, with the base of the fairing tending to commence movement marginally before the upper part.

The results were consistent with those indicated by the EOC system and also the sense of rotation established by the gyrometers. Both sides of the fairing separated simultaneously as expected. These results applied to both separation tests.

## STRAIN GAUGES

All strain gauges yielded sufficient data to establish correlation with the dynamic analysis in all areas. Informa-

tion obtained from the strain gauges also assisted in verifying the cause of the structural failure experienced during the first separation test.

The time of an instantaneous discontinuity in the outputs of strain gauges located adjacent to the failure line, are identical with that obtained from the electro-optical system correlating to the moment of the second maximum displacement.

Data obtained from the second test, including the area repaired after the first test, indicated no abnormally high strain levels.

## SHOCK ACCELEROMETERS

The pyrotechnic timing sequence established from both tests, by means of the shock impulses, confirmed correct operation of this system. Activation of the two HSS Bolt Cutters and VSS detonation occurred simultaneously, (within 0.1msec.), approx. 0.5msec. after manifold ignition. An impulse on the VSS end seals at the opposite ends of the detonator blocks was recorded 1.3msec. later, which is consistent with an expected detonation velocity of the VSS of 6500m/sec. (21000ft/sec.).

Additional shock accelerometers attached to various parts of the catching systems confirmed that the impact occurred at the catching net before the vertical support ropes influenced fairing trajectory. The time of impact also agreed within 6msecs of that computed from the EOC system, when considering the available free-flight distance.

## MEASUREMENT ACCELEROMETERS

Sufficient information was obtained from the low frequency accelerometers to provide inputs to the dynamic analysis.

## CLEARANCE DETECTORS

Detailed visual inspection of the polystyrene clearance detectors revealed that no part had been touched during separation, thus confirming that the minimum clearance requirements with respect to the vehicle interface, had been satisfied.

# SHOCK MEASUREMENTS ON ADJACENT STRUCTURE

The high frequency accelerometers attached to the Adjacent Structure indicated peak levels of approx. 800g. in the area adjacent to the VSS, during the first test.

The effect of the reduction of the tension in the HSS for the second test, from 10 tonnes to 2 tonnes, as a result of the Soft Tension Belt Release Test, was to reduce the corresponding shock levels to approx. 400g.

## FLIGHT INSTRUMENTATION RESULTS

### DISPLACEMENT TRANSDUCERS

As discussed under Test Observations above, correct output data was obtained during the second test. This data agreed very closely with that obtained from the SELSPOT system.

### LINEAR POTENTIOMETERS

The linear potentiometer system, developed to monitor the flexing motion during separation, functioned correctly during both tests. Maximum amplitudes of 500-600mm (20-24in) were indicated, again correlating with values measured by the EOC system.

### GYROMETERS

Both gyrometers also functioned correctly yielding data compatible with that computed from the EOC system.

The ability of the unit itself, (as well as the fixation to the fairing structure), to withsland the separation shock, was thus also verified.

### EVENT STATUS SIGNALS

The status signals included as part of the Flight Instrumentation, assist in verifying that these events actually occur in flight and that the relative timing of the events are correct. The results again produced data compatible with other measurement systems by indicating Bolt Cutter functioning 0.5msecs after manifold ignition and pyrotechnic connector separation 20-30msecs later.

## ACCELEROMETERS

One of the accelerometers of the type proposed to be flown for supplementary information on the initial technological flights of ARIANE 4 was damaged during the first test, whilst the second unit functioned correctly. Following refurbishment by the manufacture, both units were again installed for the second test and both produced correct data.

## SOFT TENSION BELT RELEASE TEST

The Soft Tension Belt Release System was tested under vacuum conditions prior to the second separation test.

Instrumentation included additional strain gauges on the tension belts to monitor the tension, and shock accelerometers on the Adjacent Structure to measure the corresponding shock levels at actuation.

This system functioned satisfactorily, resulting in a final HSS tension of 2.5 tonnes and maximum shock levels recorded on the Adjacent Structure were approx. 180g. Following this test, the HSS tension was re-adjusted to the specification value of 2 tonnes for the actual separation test.

## CONCLUSIONS

The aim of this paper has been to describe the separation tests performed on the flight standard version of the ARIANE 4 payload fairing during it's formal qualification test programme. A total of two tests were successfully performed during August and October 1984, by the end of which all the main test objectives had been fulfilled. Correct functioning of all aspects of the fairing, including pyrotechnic and separation systems, were verified and sufficient measurement data obtained to enable validation of the mathematical model to be used for all subsequent flight predictions.

Prior to publication of this paper, the first launch of the ARIANE 4 vehicle was successfully achieved from the Guyana launch facility on 15 June 1988. On board instrumentation confirmed the predicted separation performance of the payload fairing.

## FUTURE OUTLOOK

The development programme of the payload fairing for the next generation of European launcher, the ARIANE 5, has already commenced. Due to signifiant design changes for this version, particularly in overall size, it is foreseen that similar separation tests will also have to be performed during this programme.

In order to be able to perform these tests without undue geometrical constraints from the test facility, studies have been initiated to investigate the availability of larger vacuum chambers; including those in the U.S.A.

Figure 2.  Fairing halves
after separation



Figure 1.  Fairing Installed
before separation
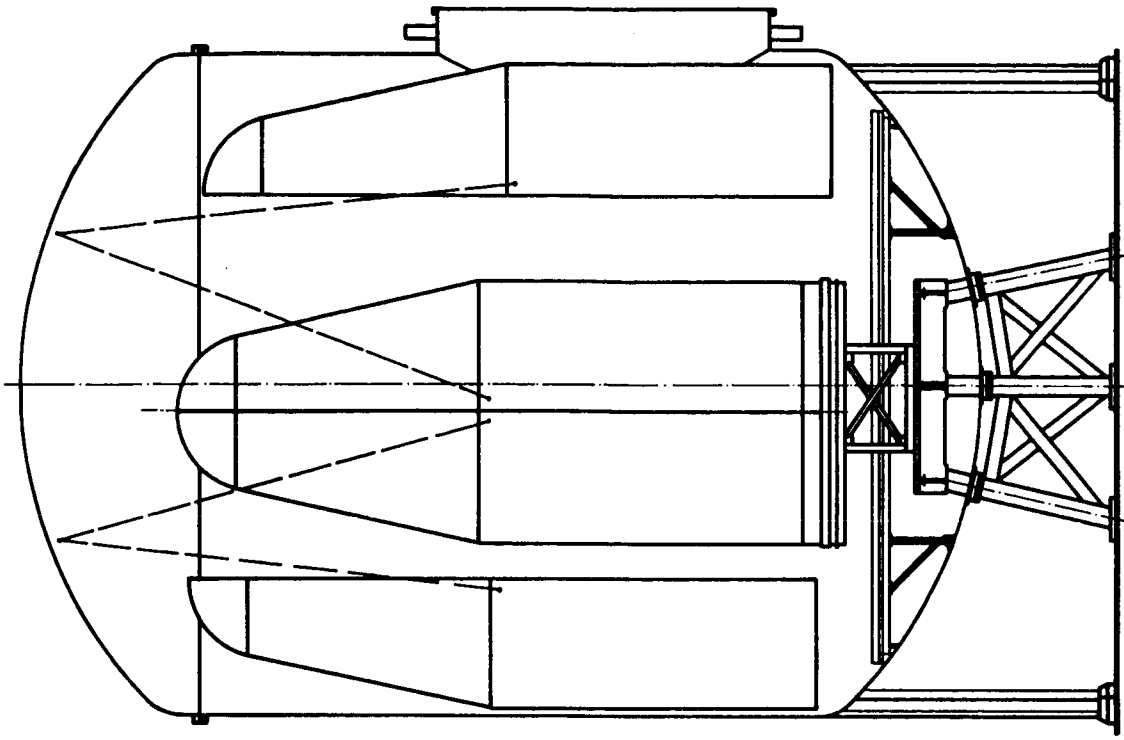
Figure 4.  Configuration of Fairing in DTC
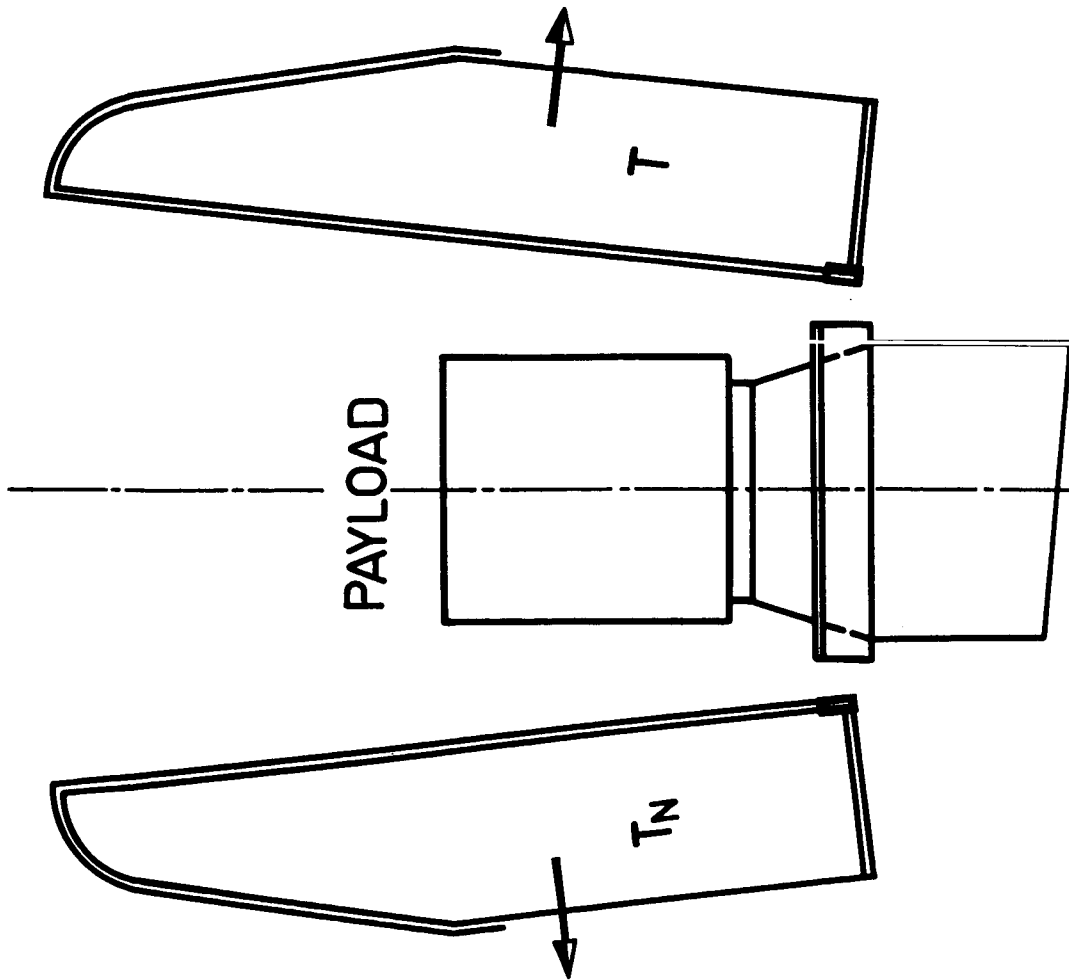


Figure 3.  Schematic of Fairing separation
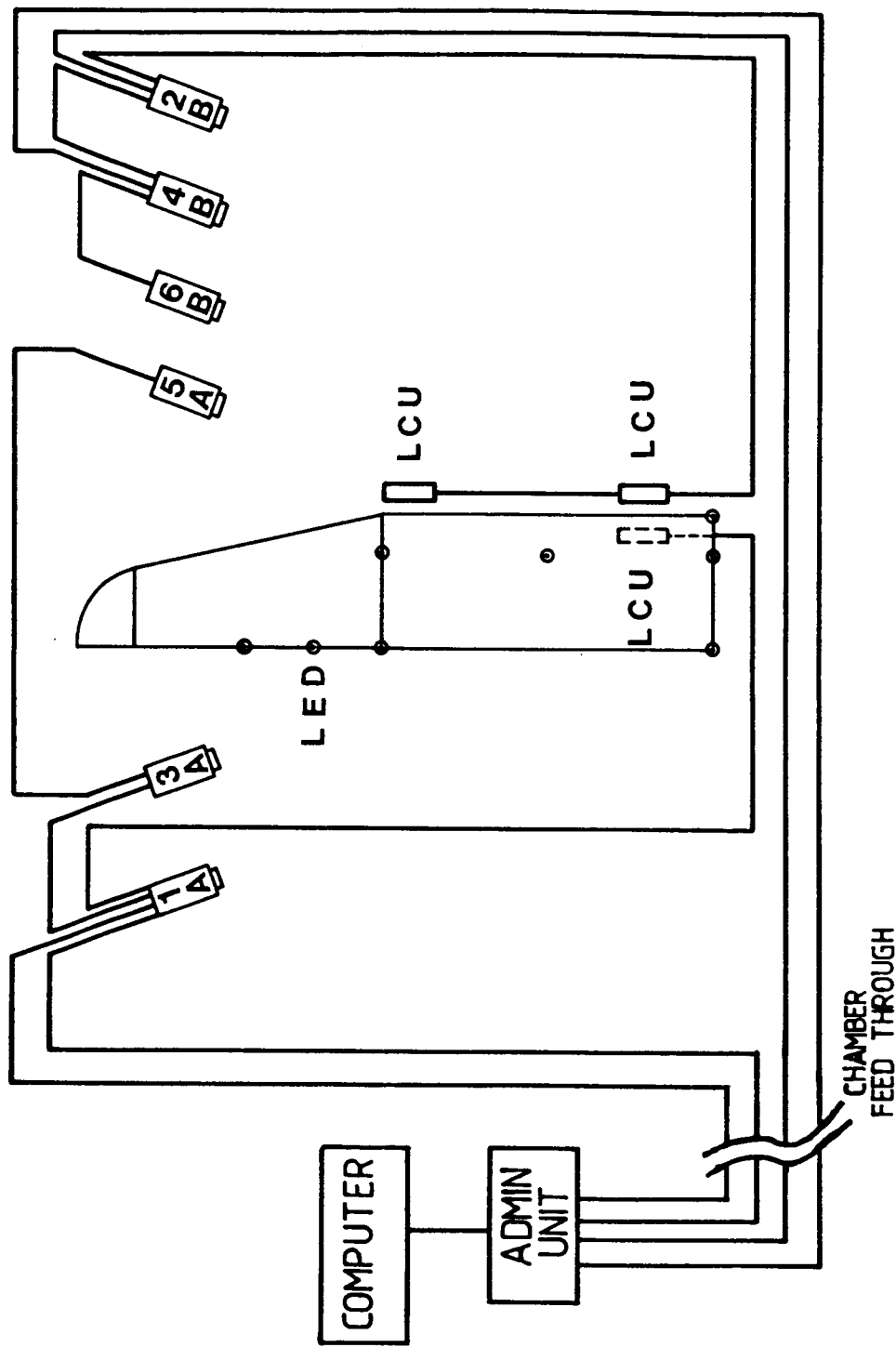
Figure 5. Electro-optical Camera system set-up
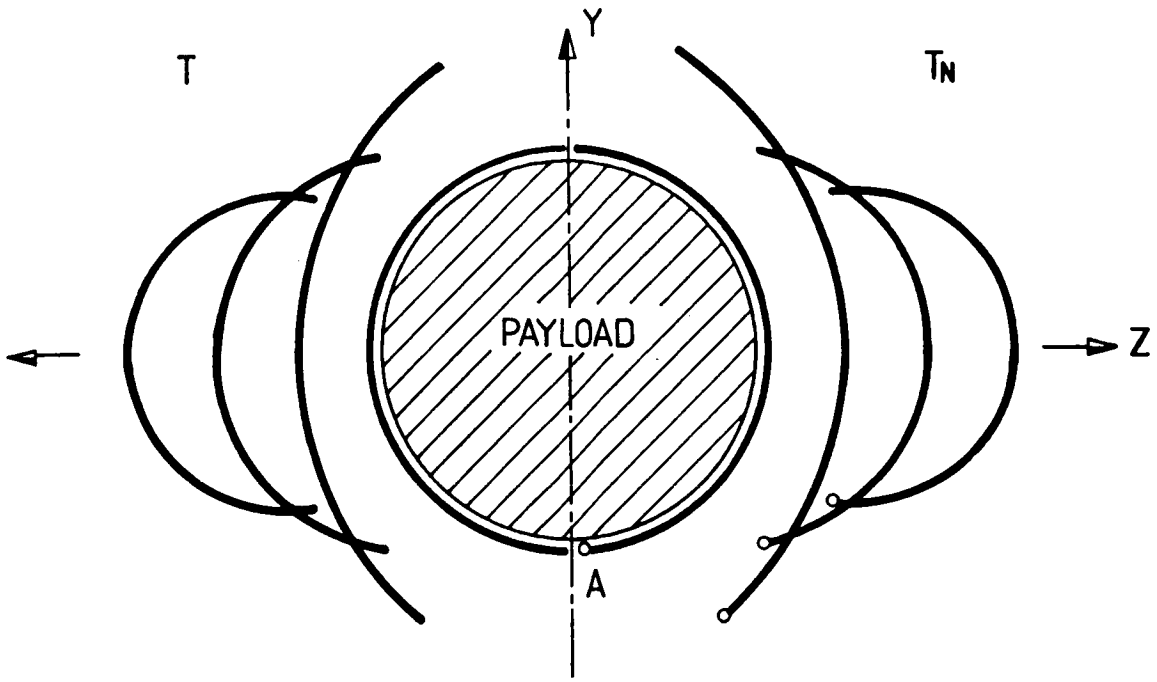
Figure 6. Fairing flexing motion
during separation
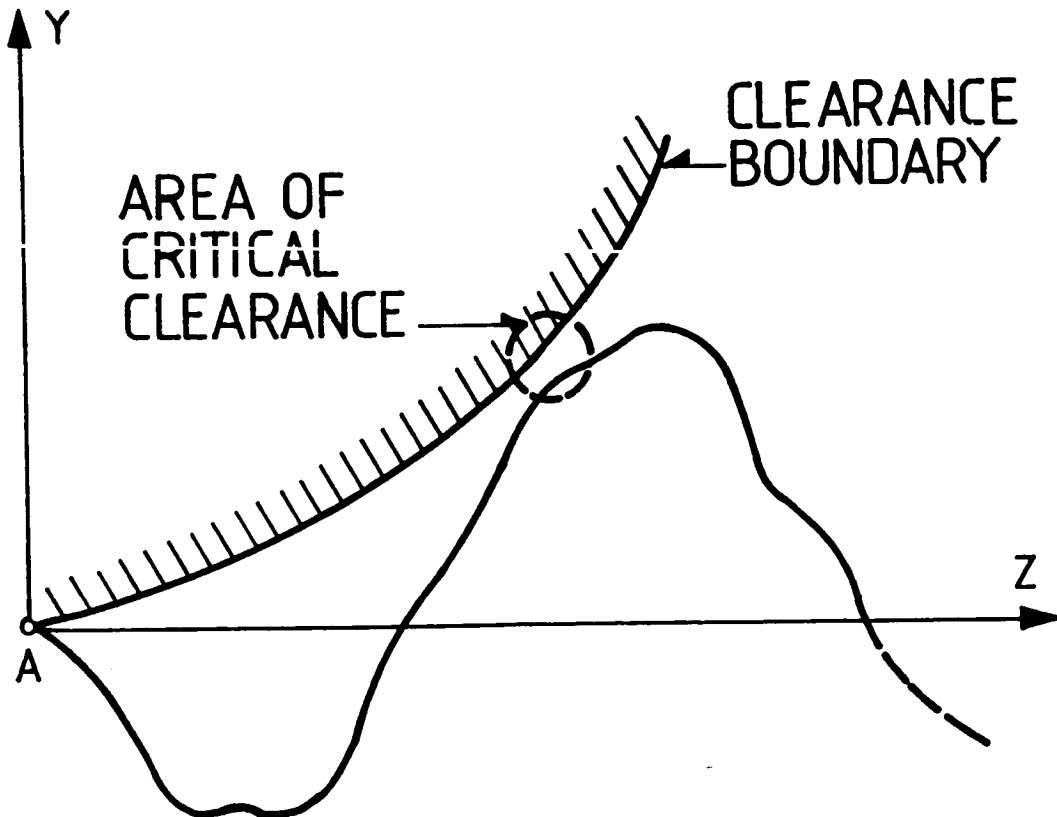


Figure 7. Trajectory of
critical point

391

Session VIII

# ANALYTICAL/EXPERIMENTAL HEAT TRANSFER

# THE SOLAR SIMULATION TEST OF THE
## ITALSAT THERMAL STRUCTURAL MODEL

M. Giommi, S. Liverani, and G. P. Santin
Selenia Spazio, Rome, Italy

## ABSTRACT

ITALSAT is a three axis stabilized communication satellite. It is the main program presently under development in Italy as part of the Italian Space Plan sponsored by the government through the National Research Council (CNR).

The spacecraft embarks three payloads: two for telecommunication at 20/30 GHz and one for a propagation experiment at 40/50 GHz. The antenna farm consists of five antennas: three of them are mounted on the earth facing platform while the other two are located on the east and west panels.

The overall spacecraft thermal design is SELENIA SPAZIO responsibility while the body thermal control has been subcontracted to AERITALIA.

The thermal control is achieved by means of the following techniques:

1. thermistors to control heaters located on the batteries and Antenna Pointing Mechanism (APM). The controls are achieved by a Thermal Control Unit (TCU) which processes the temperatures and commands the heaters;

2. thermostats to automatically control heaters located on the Reaction Control Thrusters (RCT) and earth sensors;

3. high dissipating units are located on the north and south radiators;

4. second surface mirrors (SSM) bonded on the external surface of radiator panels to minimize solar energy absorption and to increase the heat rejection;

5. all other spacecraft surfaces covered with thermal blankets to reduce the solar effects and to minimize thermal gradients.

The ITALSAT structural/thermal model (STM) has been submitted to a solar simulation test in order to verify the spacecraft thermal design and the thermal mathematical model which will be used to predict the "on orbit" temperatures. The test was performed, by SELENIA SPAZIO, in the INTESPACE SIMLES solar simulator (Toulouse, France) in November 1987.

The STM was representative of the flight model in terms of configuration, structure, appendages and thermal hardware; dissipating dummy units have been used to simulate the electronic units.

The test consisted of three main phases: on station (begin of life), on station (end of Life), transfer orbit.

The end of life condition has been simulated by applying a certain quantity of kapton tape on the north radiator SSM in order to increase its solar absorptance up to the end of life expected value.

Different seasonal conditions (i.e. solar fluxes cases) and diurnal transient have been properly simulated throughout the test in order to verify the spacecraft thermal control performances.

395

The STM was mounted on the SIMLES gymbal system via a test adaptor designed to minimize heat fluxes with the spacecraft. 436 thermocouples have been used to monitor the spacecraft temperatures during the test. 51 heater circuits provided the simulation of the heat dissipation in the various operative modes.

Test Results are currently under evaluation; on the basis of a preliminary analysis it is possible to say that:

- test performances have been satisfactory; test conditions had small and reckonable influence on the spacecraft temperatures;

- spacecraft measured temperatures were up to 15°C higher than the predicted ones. This imposes a careful correlation analysis in order to have a reliable flight temperature predictions.

The paper will describe the tested spacecraft model and the test approach. Finally test results, correlation with predicted temperatures as well as influences of test conditions on the spacecraft test temperatures will be extensively presented and discussed.

# DEVELOPMENT OF OPTIMIZED, GRADED–PERMEABILITY
# AXIAL GROOVE HEAT PIPES

Michael R. Kapolnek and H. Rolland Holmes
Lockheed Missiles and Space Company, Inc.

## ABSTRACT

Heat pipe performance can usually be improved by uniformly varying or "grading" wick permeability from end to end. This paper describes a unique and cost-effective method for grading the permeability of an axial groove heat pipe: selective chemical etching of the pipe casing. This method was developed and demonstrated on a proof-of-concept test article. The process improved the test article's performance by 50 percent. Further improvement is possible through the use of optimally etched grooves.

## INTRODUCTION

Grading the permeability of simple, nonarterial wicks has previously been shown to improve heat pipe performance. An axial groove heat pipe consisting of pipe segments with different groove geometries is one way in which this has been done (ref. 1). Graded porosity slab wicks (ref. 2 ) use the same principle but are more difficult and costly to fabricate than axial groove designs. This paper describes a new method for grading the permeability of an axial groove heat pipe.

The new method is based on variable chemical etching of the grooves so that the amount of material removed varies along the length of the pipe. Such a method is cost-effective and can substantially increase the heat pipe performance while slightly decreasing the weight. This improvement extends the weight-effective range of axial groove heat pipes to higher power applications, providing even more extensive usage of this flight-proven design.

## SYMBOLS

Values are given in both SI and U.S. Customary Units. The measurements and calculations were made in U.S. Customary Units.

| | |
|---|---|
| A | Area |
| $d_L$ | Liquid diameter |
| K | Permeability |
| $L_p$ | Length of the heat pipe |
| $\dot{m}$ | Mass flow rate |
| N | Number of calculation subintervals |
| $\Delta p_L$ | Liquid pressure loss |
| $\Delta p_v$ | Vapor pressure loss |

| r | Effective capillary radius |
|---|---|
| $r_c$ | Effective capillary radius at the heat pipe condenser end |
| $r_{min}$ | Minimum effective capillary radius |
| $R_t$ | Fin tip radius |
| $t_{etch}$ | Thickness reduction due to chemical etching |
| x | Distance along heat pipe measured from condenser end |
| $\mu$ | Liquid viscosity |
| $\rho$ | Liquid density |
| $\sigma$ | Surface tension |
| $\theta$ | Groove angle |

## CONCEPT

The thermal transport of axial groove heat pipes is generally limited by capillary pumping. The capillary transport limit is reached when the total of the liquid and vapor pressure losses at any location along the heat pipe length is equal to the local maximum available capillary pumping head (Figure 1). The capillary pressure head is created by the liquid/vapor meniscus at the groove slot and is inversely proportional to the radius of curvature of this meniscus. Figure 2 shows a cross-section of a typical groove, where this radius is specified as $r_{min}$. The maximum capillary head is, therefore, limited by the smallest capillary radius that can form in the given groove geometry. The performance of the pipe can be maximized by creating a small groove width at the liquid-vapor interface (which allows the formation of a meniscus with a small radius of curvature) and a large flow area in the groove.

This small groove width is not required over the entire pipe length to optimize performance. A small meniscus radius will only occur where large liquid/vapor pressure differences exist; small groove widths are only beneficial at these locations. A small meniscus radius generally occurs near the evaporator end of the pipe. Large liquid areas are desirable at all locations in order to minimize frictional flow losses. Since the groove area is directly related to the groove width, the performance of the pipe can be optimized by varying the groove size so that it is just small enough to support the meniscus that will form at any given point. In general, this will result in large open grooves in the condenser portion of the pipe and smaller grooves in the evaporator.

This new concept uses chemical etching to tailor the geometry of axial grooves along the heat pipe length. Chemical etching is a commonly used machining process. The amount of material etched is directly proportional to the time in the etchant as well as the concentration of etchant and its temperature. Of these three independent variables, exposure time is the easiest to control. The axial groove wick can be graded by controlling the exposure time of each axial location along the heat pipe.

This concept was developed as an alternative to the use of multiple cross sections for varying the groove geometry of axial groove heat pipes. The new process has two main advantages. With a well-controlled grading process, the groove profile can be optimized for any given application. Also, a single heat pipe casing is used, greatly simplifying the fabrication process.

## DESIGN ANALYSIS

A computer code (GGROOVE), capable of calculating the capillary transport limit of axial groove heat pipes with lengthwise-varying cross sections, was developed to analyze alternate grading profiles. The number and shape of the unetched axial grooves are input to the code, along with the equation that defines the etching profile. Input to GGROOVE also includes the vapor section shape, working fluid, operating temperature, and gravity constant. The code then iterates on the heat transport of the pipe until the total pressure drop (liquid and vapor) at any point in the pipe equals the available capillary head at that point. The working fluid charge quantity is also calculated by the code.

The code uses a bisection technique to iterate on heat transport until a local meniscus radius of curvature has been minimized at a point x within the heat pipe. By balancing local capillary pressure head with flow losses, an expression for the local meniscus radius of curvature, r(x), results:

$$\Delta p_L(x) + \Delta p_V(x) + 2\sigma \left( \frac{1}{r(x)} - \frac{1}{r_c} \right) = 0 \tag{1}$$

$$r(x) = 1 \bigg/ \left( \frac{1}{r_c} - \frac{\Delta p_L(x) + \Delta p_V(x)}{2\sigma} \right) \tag{2}$$

where $r_c$ is the effective capillary radius at the condenser end of the pipe. Gravity-induced flow losses have been neglected to simplify the discussion.

Viscous flow losses in the axial grooves are evaluated using Darcy's Law (ref. 3):

$$\frac{dp_L}{dx} = -\frac{\mu \dot{m}}{\rho K A} \tag{3}$$

The groove permeability, K, and total wick flow area, A, are dependent on the shape of the grooves. Since the groove shape varies with location, the permeability and flow area also depend on location. Because evaporation and condensation occur, the total mass flow through the grooves, $\dot{m}$, is location dependent. The mass flow rate is calculated using the heat transport and the latent heat of the working fluid.

Integrating both sides of Equation 3:

$$\Delta p_L = \int_0^L -\frac{\mu}{\rho} \frac{\dot{m}(x)}{K(x) A(x)} dx \tag{4}$$

the integral can be approximated by

$$\Delta p_L \approx -\frac{\mu}{\rho} \sum_{i=1}^N \frac{\dot{m}(w_i)}{K(w_i) A(w_i)} \Delta x \tag{5}$$

where $w_i$ is a number within the subinterval $[x_{i-1}, x_i]$. A(x), K(x) and $\dot{m}(x)$ are assumed to be constant within the subinterval, an assumption that improves as the subinterval size decreases. The GGROOVE

399

code evaluates $\dot{m}$, A, and K at the $x_j$ end of each subinterval. The number of subintervals, N, is input by the user and is typically about 1000. The viscous flow loss in the liquid wick from the condenser end of the pipe through subinterval j is then

$$\Delta p_L(x_j) = -\frac{\mu}{\rho} \sum_{i=1}^{j} \frac{\dot{m}(x_i)}{K(x_i) A(x_i)} \frac{L_P}{N}$$

(6)

Because the vapor pressure loss, $\Delta p_v(x_j)$, is typically 10 percent or less of the total pressure loss for an axial groove heat pipe, the effect of varying geometry on it is negligible. This allows the use of closed-form expressions for its calculation. These expressions are available in other sources (ref. 3) and are not discussed here.

The local meniscus radius, $r(x_j)$, is minimized when the geometry of the heat pipe can support no smaller value. For the axial groove geometry shown in Figure 2, the minimum effective capillary radius $r_{min}$ is:

$$r_{min} = d_L \sin\theta - 2R_t$$

(7)

The fin tip radius, $R_t$, will vary with the amount of material etched, so the expression for the local minimum capillary radius is:

$$r_{min}(x_j) = d_L \sin\theta - 2R_t(x_j)$$

(8)

The capillary transport limit found by GGROOVE is the maximum heat input at which a local meniscus radius is equal to the minimum effective capillary radius. The local meniscus radius is calculated using Equation 2; the minimum effective capillary radius is calculated using Equation 8. The meniscus radii are compared at each subinterval.

The performance of a proof-of-concept test article was predicted by GGROOVE for several proposed etching profiles (Figure 3). These profiles were chosen because they could be obtained with available equipment. The etching was limited to 0.127 mm (5 mils) to ensure that no part of any groove would be completely etched away. Profile A yielded the best performance improvement (Figure 4) and was chosen as the design profile for the proof-of-concept test article. The test article was a 27-groove heat pipe, 167.6 cm (66 in.) long and approximately 1.25 cm (0.5 in.) in diameter. The article was tested prior to groove grading to obtain a performance baseline.

Subsequent to fabrication of the test article, GGROOVE was modified to permit optimization of the grading profile for a given pipe configuration. The most significant change is that the etching profile is set by an optimization routine rather than input by the user. For each subinterval j, Equation 2 is used to find the capillary radius, $r(x_j)$, required to overcome the liquid pressure losses in subintervals 1 through j-1. The maximum thickness of material that can be removed while still supporting that radius is then found using Equation 8 and the variation of $R_t(x_j)$ with etching:

$$R_t(x_j) = R_t(L_P) - t_{etch}(x_j)$$

(9)

$$r(x_j) = d_L \sin\theta - 2(R_t(L_P) - t_{etch}(x_j))$$

(10)

$$t_{etch}(x_j) = \frac{r(x_j)}{2} + R_t(L_P) - \frac{d_L}{2} \sin\theta$$

(11)

The thickness of material etched, $t_{etch}(x_j)$, is then used to find the local groove shape as defined in Figure 2. The local permeability, $K(x_j)$, and flow area, $A(x_j)$, are calculated and used in Equation 6 to determine the liquid pressure drop $\Delta p_L(x_j)$. The capillary transport limit is found by the same method used in the original version. The code also outputs the optimum etching profile at that limit.

An optimized grading profile was found for the test article and is shown in Figure 5. It is very similar to the test article's design profile and yields a predicted performance that is the same (within the accuracy of the code).

## DEVELOPMENT ARTICLE FABRICATION

The fabrication of the proof-of-concept heat pipe followed standard Lockheed heat pipe manufacturing procedures except for the addition of the etching step. A standard, on-site chemical etching facility was used. The procedure included masking of the flange, exposure to 90° C (194°F) sodium hydroxide, and several rinse steps.

A number of trial runs were conducted before attempting to etch the proof-of-concept article. Initially, several 12.5 cm (5 in.) long extrusion samples were uniformly etched for varying times in order to calibrate the solution  and to assess the uniformity of the etched grooves. Examination of these samples showed the etching to occur uniformly throughout the cross section and at a rate of 0.015 mm/min (0.6 mils/min). The etched surfaces were no longer smooth but were covered with very small ripples. Because the liquid flow rate in axial groove heat pipes is highly laminar, this roughness was considered insignificant.

The next trial was on a 152 cm (60 in.)  long extrusion similar to the test article. The extrusion was mounted in a basket perpendicular to the etching solution surface. The basket and pipe were lowered into the bath so that half the pipe was rapidly immersed. The rate of descent was then slowed so that the remainder of the pipe would be etched to the desired grading profile.

Two problems occurred with this trial run. First, the reaction between the aluminum and sodium hydroxide was so violent that the reaction products forced unspent etching solution through the top of the extrusion. This resulted in etching above the surface of the bath. In fact, so much etchant was expelled that the extrusion was etched nearly uniformly throughout its length.

An associated problem was that the strength of the bath was higher than in earlier calibration runs, causing too much material to be etched from the pipe. Thereafter, the strength of the etchant bath was calibrated just before each subsequent run.

The first problem was more difficult to solve. Two approaches were taken. First, the temperature of the bath was lowered to 71° C (160°F). This reduced but did not eliminate the secondary etching. The bath temperature could not be lowered further because of facility restrictions.

The second solution was to insert a 0.64-cm (0.25-in.) solid, stainless steel rod in the vapor section of the pipe before etching. Its purpose was to block etchant from rising above the surface of the bath. This further reduced etching above the bath surface but did not totally stop it. Photomicrographs of sample heat pipe sections also indicated that the circumferential etching of the grooves was not uniform.

Considering the trial runs, we decided to grade the development test article with this procedure using a larger diameter rod. The procedure in detail was :

- After cutting the end caps off the test article, an 84 cm (33 in.) long, 0.79 cm (0.3125 in.) diameter stainless steel rod was inserted into the pipe and mechanically attached at the evaporator end. The flanges of the pipe were painted with a masking compound to prevent etching.

- The pipe was mounted in a basket perpendicular to the etchant bath surface with the evaporator end facing up. The basket was then quickly lowered into the bath until 84 cm (33 in.) of the pipe were submerged.

- The descent rate of the pipe was slowed to 15.3 cm/min (6 in./min). Descent continued until 10.2 cm (4 in.) of the pipe remained outside the bath. The pipe was then rapidly removed from the bath and put through the rinsing procedure.

- The masking paint was removed from the pipe flanges; the pipe was cleaned according to standard procedures, welded closed, and charged with ammonia. The heat pipe was then ready for performance testing.

## PERFORMANCE TESTING

The heat pipe evaporator and condenser configurations were the same as assumed for the design analysis. The pipe was mounted on a test stand and instrumented with 15 thermocouples. Nichrome heater tape was affixed to the pipe to heat the evaporator section. Cooling at the condenser end of the pipe was provided by 66 cm long axial groove extrusions supplied with tap water and clamped to the pipe. The test set-up is shown in Figure 6.

The heat pipe's transport limit was found with the pipe level and under four adverse tilts. The charge level was then changed and the variation of transport limit with adverse tilt redetermined. Testing was done for multiple-charge levels, because the optimum charge of the pipe could not be calculated until the exact grading profile was determined.

After testing was completed, the pipe was sectioned and photomicrographed in order to determine the actual grading profile. Sample photomicrographs are shown in Figure 7. The actual and desired profiles were then compared (Figure 8). A significant difference between them indicates that the etching procedure used did not adequately control the grading of the wick.

The actual grading profile was input to GGROOVE to determine the theoretical transport limit and optimum charge quantity. The performance of the test article at its optimum charge is compared with its theoretical performance and its performance before etching in Figure 9. Agreement between actual and theoretical performance is good. Most noteworthy, however, is the 50-percent performance improvement that resulted from the graded etching of the axial grooves.

## CONCLUSIONS

The work described in this paper shows the significant benefits of this graded axial groove heat pipe concept. A significant performance improvement was demonstrated even though the etching profile achieved deviated from the design profile. By starting with an extrusion shape that has been optimized for this concept and using a better controlled etching process, much higher improvements can be achieved.

## REFERENCES

1. Schlitt, K. R., "Development of an Axially Grooved Heat Pipe with Non-constant Groove Width," 3rd AIAA International Heat Pipe Conference, Paper No. 78-375, May, 1978.

2. Eninger, James, "Graded Porosity Heat Pipe Wicks," 11th AIAA Thermophysics Conference, Paper No. 76-480, July, 1976.

3. Brennan, Patrick J. and Kroliczek, Edward J., "Heat Pipe Design Handbook," NASA Contract NAS5-23406, June, 1979.

DISTANCE FROM CONDENSER END
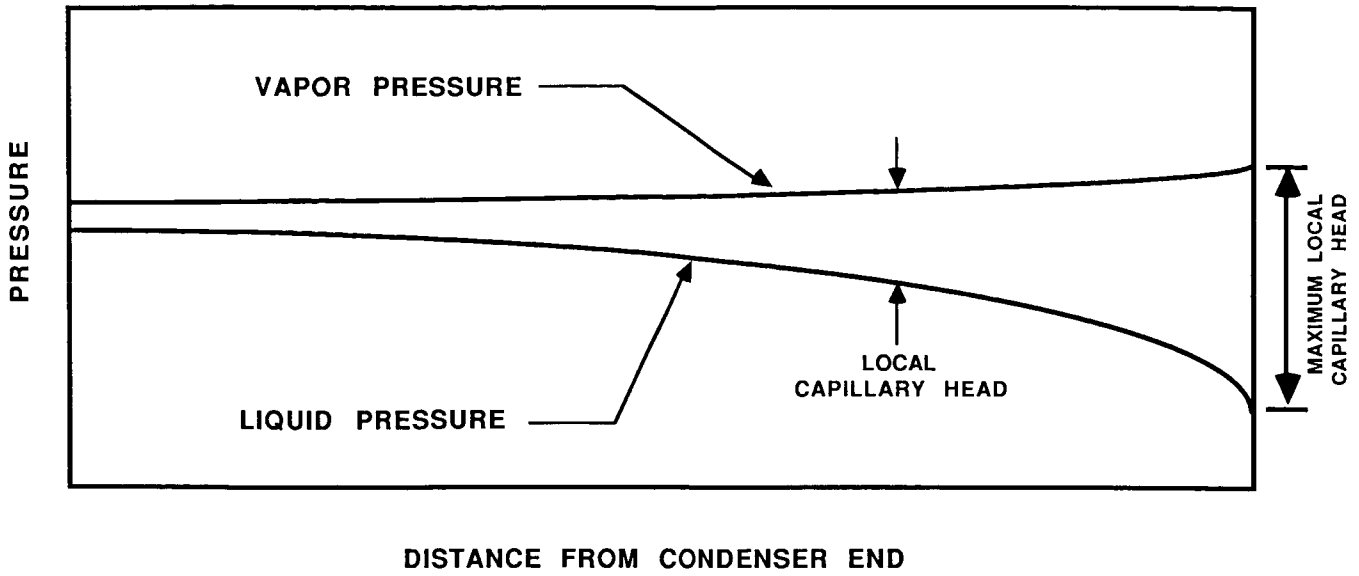
Figure 1 - Heat Pipe Pressure Distribution at Capillary Pumping Limit
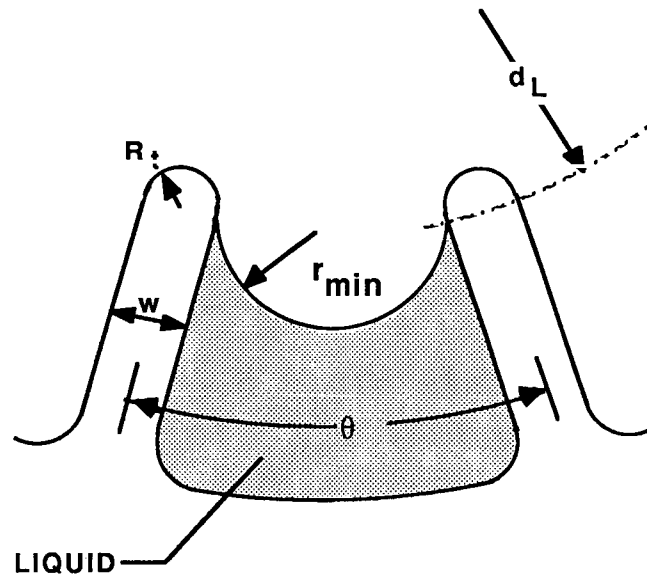


Figure 2 - Axial Groove Geometry
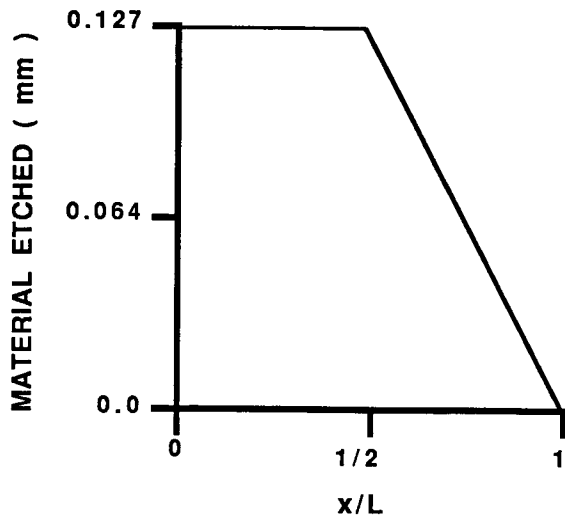
Profile A
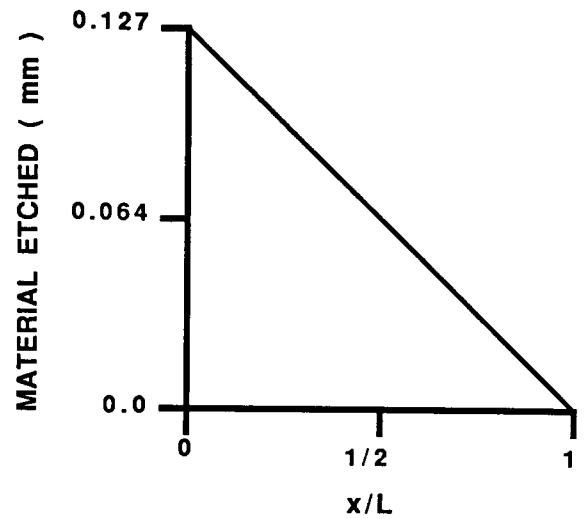
Profile B
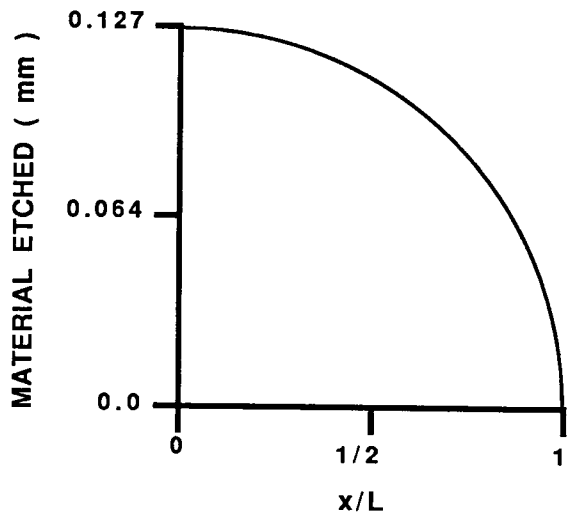
Profile C
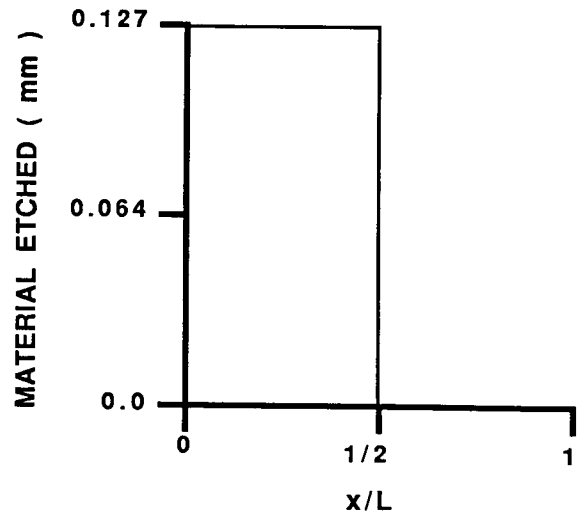
Profile D

Condenser End: x/L=0
Evaporator End: x/L=1

Figure 3 - Candidate Etching Profiles

| PROFILE | TRANSPORT LIMIT ( W ) |
|---------|----------------------|
| UNETCHED | 144 |
| A | 261 |
| B | 220 |
| C | 245 |
| D | 216 |

**ASSUMES:**
**0.0 cm TILT**
**AMMONIA WORKING FLUID**
**20 C OPERATING TEMPERATURE**
**81.3 cm EVAPORATOR**
**20.3 cm TRANSPORT SECTION**
**66.0 cm CONDENSER**

## Figure 4 - Etching Profile Analysis Results
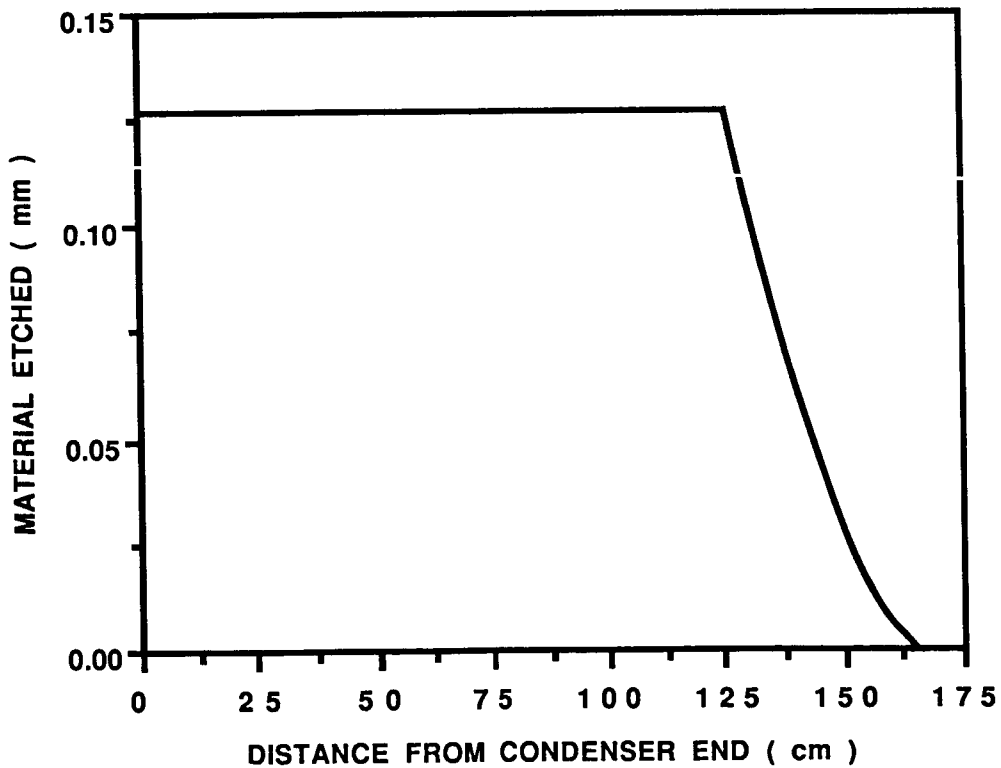


## Figure 5 - Optimum Etching Profile

INDICATES THERMOCOUPLE LOCATION

WATER COOLED CONDENSER ( 66 cm )

EVAPORATOR HEATERS ( 81.3 cm )

A-A
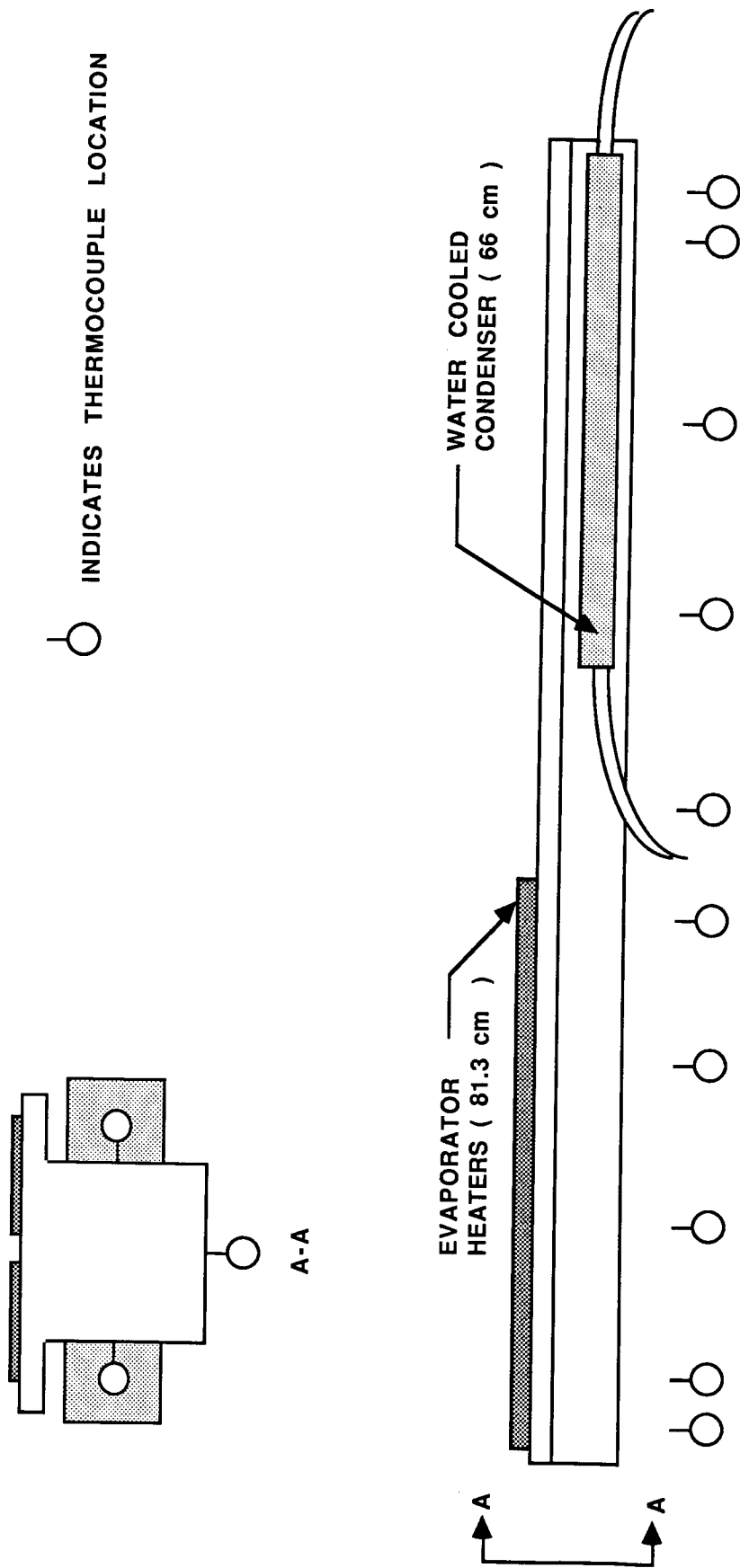
Figure 6 - Bench Test Set-up

406
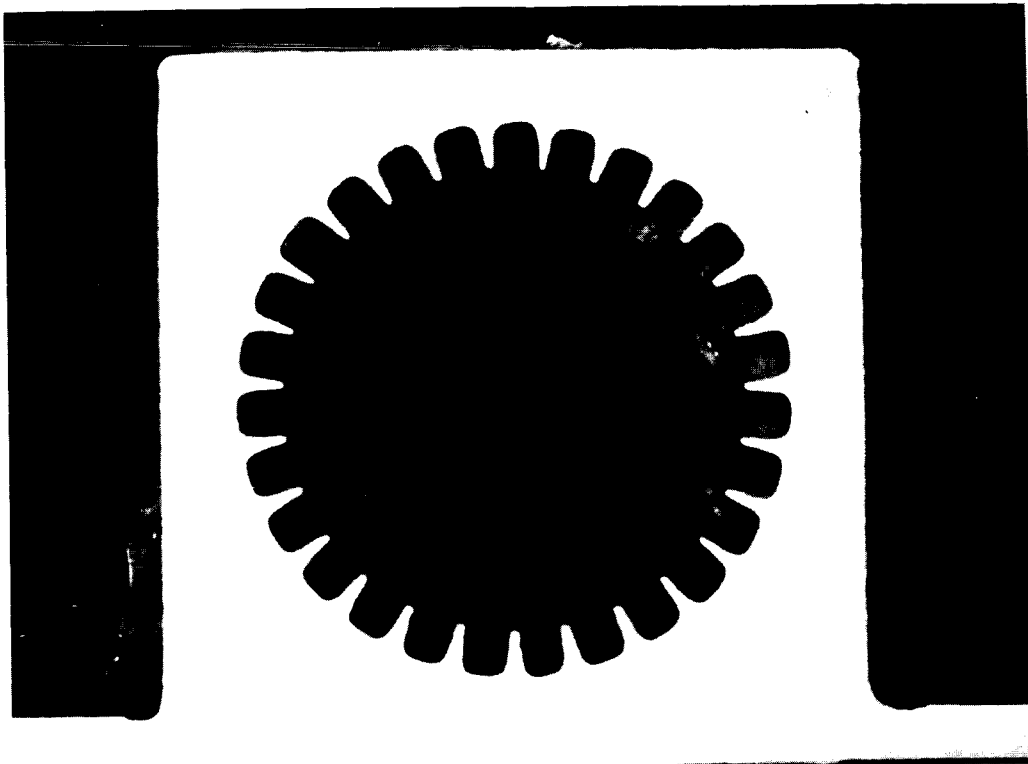
**Figure 7a - Sample Photomicrograph, Condenser End**
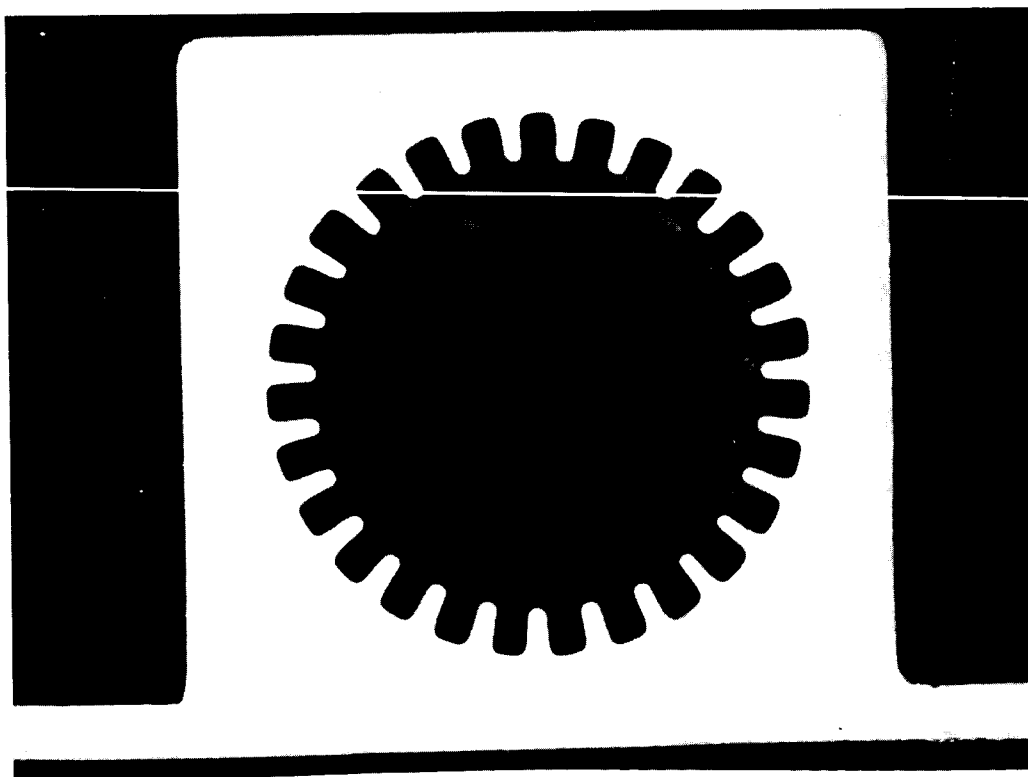


**Figure 7b - Sample Photomicrograph, Evaporator End**

407
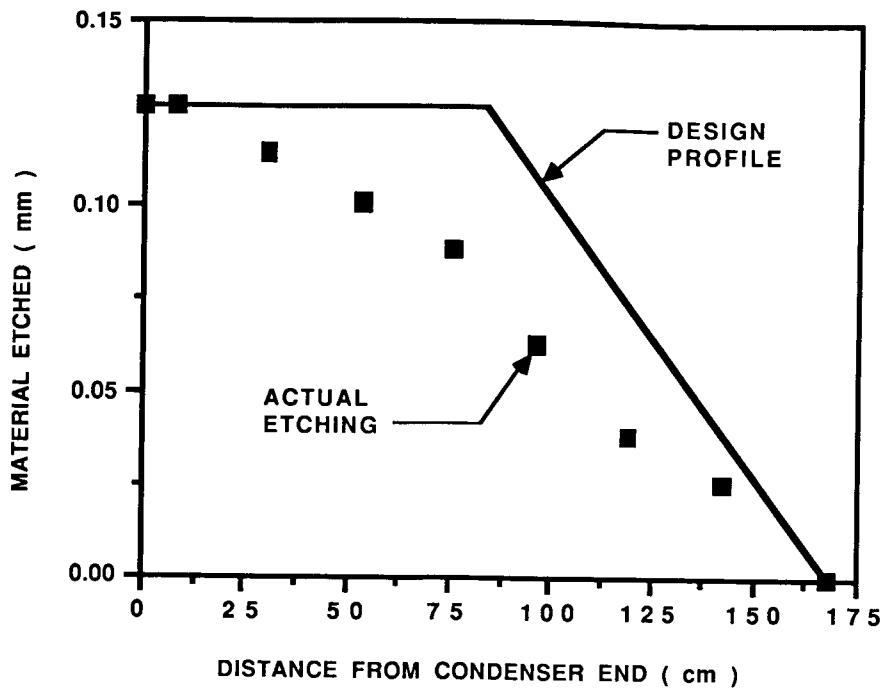
Figure 8 - Actual and Design Etching Profiles



■ ACTUAL FOR GRADED TEST ARTICLE
( AMMONIA CHARGE = 21.9 g )

◆ ACTUAL FOR UNGRADED TEST ARTICLE
( AMMONIA CHARGE = 17.5 g )

—— PREDICTION FOR GRADED TEST ARTICLE
( AMMONIA CHARGE = 21.3 g )
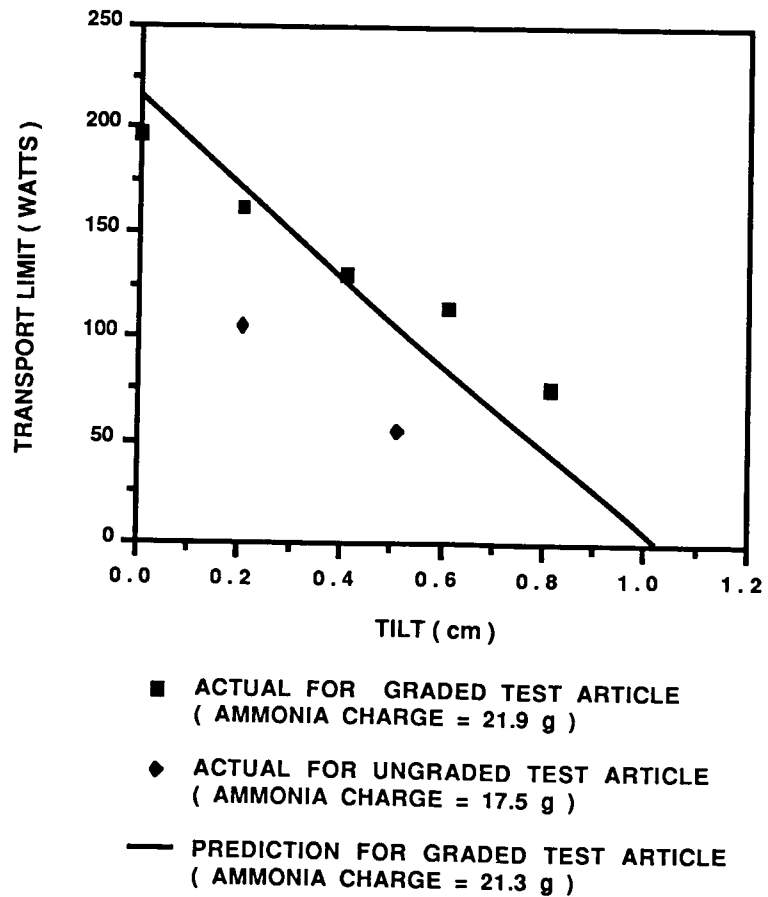
Figure 9 - Performance of the Test Article

408

# HEAT PIPE COOLING SYSTEM WITH SENSIBLE HEAT SINK*

Calvin C. Silverstein
CCS Associates

## INTRODUCTION

During hypersonic flight, the aerodynamic heat flux at uncooled stagnation regions can produce temperatures beyond the operational capability of virtually all structural materials. In such instances, the use of ablative materials may limit the temperature rise to acceptable levels. However, ablation can produce undesirable changes in the size and shape of affected stagnation regions.

If there is a suitable heat sink available, an alternate thermal protection approach is to utilize a heat pipe cooling system to transport heat from regions of high aerodynamic heating to the heat sink for ultimate disposal. The heat pipe approach is attractive because, in contrast to pumped cooling loops, heat transport is virtually isothermal and separate pumps and power supplies are not required.

Earlier studies have indicated the feasibility of heat pipe cooling for the leading edges of hypersonic aircraft wings (refs. 1,2,3). With this concept, a radiation heat sink is employed on the upper wing surface, where the aerodynamic heating rate is relatively low. A continuous heat pipe structure extends around the wing surface, from the regions of high aerodynamic heating to the radiation heat sink on the upper surface. Aerodynamic heat incident on the leading edge is then transported through the heat pipe structure to the upper surface, and dissipated by radiation to the environment.

This paper deals with a heat pipe cooling system which employs a sensible heat sink. With this type of system, incident aerodynamic heat is transported via a heat pipe from the stagnation region to the heat sink, and absorbed by raising the temperature of the heat sink material. The use of a sensible heat sink can be advantageous for situations where the total mission heat load is limited, as during re-entry, and a suitable radiation heat sink is not available.

## BASIC CONCEPT

The basic principle involved is illustrated in figure 1 for nose tip cooling. A cylindrical heat pipe occupies the central region of the nose cone. The hemispherical forward end of the heat pipe protrudes into the air stream, and serves as the nose tip. The heat pipe is surrounded by an appropriate heat

---

sink, which in turn is surrounded by ablative or temperature-resistant material. An optional heat shield limits heat transfer between the heat sink and the outer layer.

Aerodynamic heat incident on the nose tip is transported through the heat pipe and deposited in the adjacent heat sink. The cooling system thermal capacity is sufficient to absorb the total mission heat load on the nose tip, while limiting peak temperatures to levels consistent with the operational temperature capability of the heat pipe and heat sink materials. Heat incident on the lateral nose cone surface is generally of a much lower intensity than that experienced over the nose tip, and can be dissipated through the conventional ablative process or through sensible heating of a temperature-resistant layer.

With this cooling system, temperatures can be limited to levels permitting a metallic nose tip of fixed size and shape, even under exposure to stagnation heat fluxes on the order of thousands of $w/cm^2$.

## DESIGN CONSIDERATIONS

A preliminary investigation of a heat pipe nose tip cooling system of the type described has been carried out for a re-entry vehicle (ref. 4).

## COOLING SYSTEM GEOMETRY

The geometry of the heat pipe cooling system is shown in figure 2. In general, the axial cooled length $X_a$ must exceed the nose radius $R_n$ in order to maintain a nonzero ablator thickness between the cone surface and the heat sink. The heat sink may be mounted outside the heat pipe in a conical configuration, as shown in figures 1 and 2, in a cylindrical configuration, or as a combination of the two. Alternatively, the heat sink may be located inside the heat pipe by thickening the wick by an appropriate amount.

The conical heat sink configuration makes more effective use of the available volume within the nose cone than the cylindrical or internal configurations. The overall length required to accommodate the heat pipe cooling system can then be minimized.

To further reduce the heat load and hence cooling system size and weight, the heat pipe radius $R_c$ at the start of the heat sink section can be made smaller than the nose radius $R_n$. The axial cooled length $X_a$ is then smaller than if $R_c$ were equal to $R_n$.

## MATERIALS

Since sensible heat is the heat absorbing mechanism, the cooling system should be characterized by a high thermal capacity (i.e., heat absorption capability) per unit weight and volume. This requirement leads to the selection of heat pipe and heat sink materials with high mass and volumetric specific heats, and with high operational temperature capability. In addition, the heat pipe envelope should have high thermal conductivity to minimize the temperature grad-

ient and thermal stress in the stagnation region, as well as good strength at anticipated operating temperatures. Finally, the various heat pipe and heat sink materials must be chemically compatible.

For the application under consideration, lithium was selected as the heat pipe fluid and as the primary heat sink material. TZM molybdenum was selected as the heat pipe containment and wick material, and for containment of the lithium heat sink liquid. These materials satisfy cooling system operational requirements quite well. Additionally, lithium has the highest heat transport capability of the various heat pipe fluids, and its operational temperature range is quite compatible with thermal capacity requirements.

OPERATING TEMPERATURE

As previously stated, the highest feasible operating temperature is advisable for the heat pipe cooling system, in order to minimize system volume and weight. TZM is compatible with lithium to at least 1920°K (3000°F), and is probably adequate from the strength standpoint to at least 1810°K (2800°F). The principal limitation on temperature arises from the need to protect TZM from oxidation at temperatures above around 920°K (1200°F).

Data on the lifetime of TZM coated with molybdenum disilicide was obtained from reference 5. At the end-of-mission temperature of 1590°K (2400°F) which was selected as the basis for the design studies, a lifetime of 150-170 hr in still air is indicated. The actual coating lifetime will be determined by such additional factors as the influence of the pressure and velocity field over the nose cone, temperature gradients through the coating, and cyclic temperature operation.

COOLING SYSTEM DESIGN

A preliminary design of the heat pipe cooling system is shown in figure 3. The cooling system was designed for a peak cold wall heat flux of 3400 w/cm² (3000 Btu/ft²-sec), and a total heat load of 6640 kw-sec (6300 Btu). The system length is 61 cm (24 in.), and the half-angle of the lithium heat sink is 3.91 deg. The exposed surface of the TZM heat pipe is coated with molybdenum disilicide to prevent oxidation. The total cooling system weight is about 3.6 kg (8 lb).

The cooled surface extends beyond the nose tip to a small portion of the lateral nose cone surface, for a total axial cooled length of 3.28 cm (1.29 in.). This extension beyond the nose tip increases the heat load on the heat pipe cooling system, but is necessary to assure that the ablative layer will have a minimum thickness of 0.38 cm (0.15 in.) at its juncture with the forward end of the heat pipe.

The interior of the heat pipe is lined with a wire screen wick structure. The wick consists of two layers of different mesh TZM screen, of variable thickness. The wick is thinnest at the stagnation point, to minimize the temperature drop as heat flows through the wick thickness to vaporize the lithium in the wick pores at the inner wick surface. In the cooled region, the wick varies

411

from a thickness of 0.046 cm (0.018 in.) at the stagnation point to 0.091 cm (0.036 in.) at the beginning of the heat sink section. The outer layer, which serves as the lithium flow channel, is fabricated from 100 mesh screen. The inner layer, which provides the necessary capillary pressure for circulation of the lithium heat pipe fluid, is constructed from 400 mesh screen.

The wick is considerably thicker in the heat sink section of the heat pipe, with a total thickness of 0.254 cm (0.100 in.). Here, the outer liquid flow channel is fabricated from 50 mesh screen, and is covered by a 400 mesh capillary pumping layer. The thicker wick also makes a significant contribution to cooling system thermal capacity.

Heat pipe heat transport limits were evaluated at the most severe heating condition, which occurs when the cold wall stagnation heat flux has peaked at 3400 w/cm$^2$ (3000 Btu/ft$^2$-sec). At this time the hot heat pipe vapor has advanced about 36 cm (14 in.) into the heat sink section of the heat pipe. The calculations show that heat transport will not be constrained by limits imposed by: the attainment of sonic velocity in the heat pipe vapor, entrainment of the heat pipe liquid by its adjacent vapor, boiling of lithium in the heat pipe wick, or the maximum capillary pressure available in the wick pore structure.

During re-entry, the cooling system temperature reaches a peak of 1670°K (2550°F) at the stagnation point. The end-of-flight temperature is 2400°F. The internal cooling system pressure reaches a maximum value of 128,900 N/m$^2$ (18.7 psia), which is the vapor pressure of lithium at its maximum re-entry temperature of 1640°K (2500°F).

## CONCLUSIONS

Heat pipe cooling, in conjunction with an appropriate sensible heat sink, constitutes a simple, effective technique for the thermal protection of stagnation regions without compromising the size and shape of such regions. The technique is applicable to missions of limited duration for which moderate total heat loads are experienced.

REFERENCES

1. Silverstein, C.C., "A Feasibility Study of Heat-Pipe-Cooled Leading Edges for Hypersonic Cruise Aircraft," NASA CR-1857, NASA Langley Research Center, Hampton, VA, Nov. 1971.

2. Peeples, M.E., et al, "Thermostructural Applications of Heat Pipes," NASA Contractor Report 159096, NASA Langley Research Center, Hampton, VA, June 1979.

3. Camarda, C.J. & Masek, R.V., "Design, Analysis, and Tests of a Shuttle-Type Heat-Pipe-Cooled Leading Edge," J. Spacecraft & Rockets, Vol. 18, No. 1, Jan.-Feb. 1981, pp. 71-78.

4. Silverstein, C.C., "Preliminary Study of Nose Tip Heat Pipe," P.O. 33-0878, Sandia National Laboratories, Albuquerque, NM, March 1987.

5. Tuominen, S.M. & Dahl, J.M., "Cyclic Oxidation Testing of Molybdenum Protected by Silicide Coatings," J. Less Common Metals, Vol. 81, 1981, pp. 249-260.
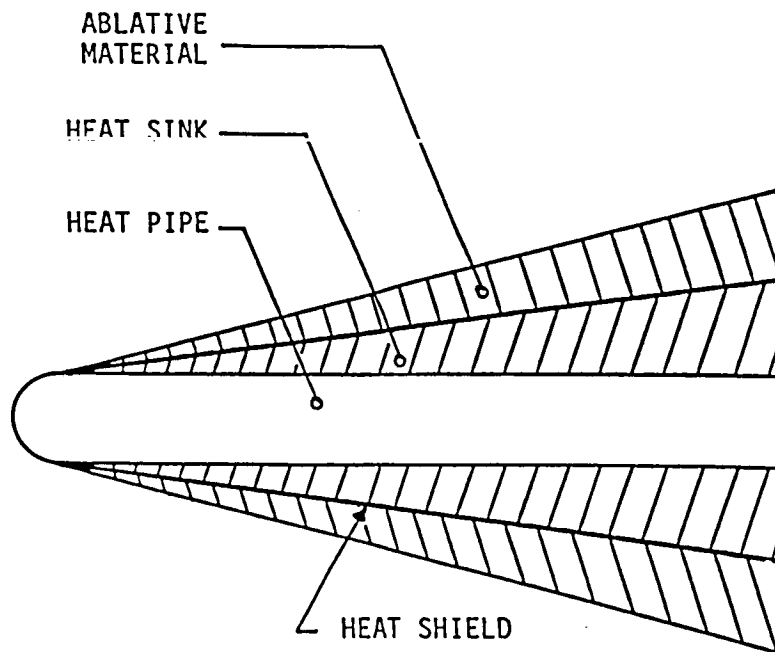
Figure 1. Basic Heat Pipe Cooling Concept for Nose Tip
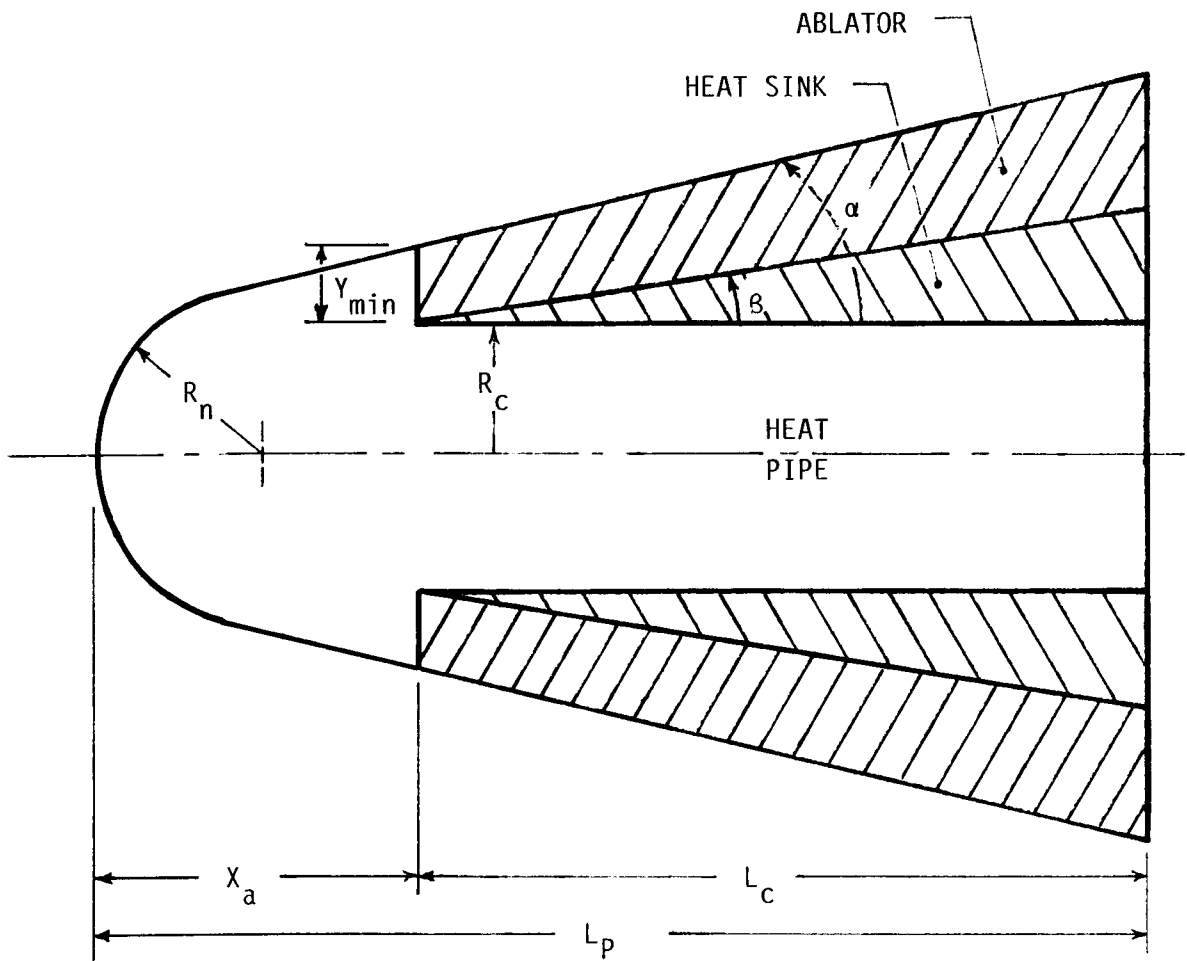
$R_n$ = nose radius

$R_c$ = heat pipe radius in heat sink section

$Y_{min}$ = minimum ablator thickness

$\alpha$ = nose cone half angle

$\beta$ = heat sink half angle

$X_a$ = axial cooled length

$L_c$ = heat sink length

$L_p$ = cooling system length

Figure 2. Geometry of Heat Pipe Cooling System

STRUCTURAL & WICK MATERIAL: TZM
HEAT PIPE & HEAT SINK FLUID: LITHIUM
WICK POROSITY: 0.65
EXPOSED TZM COATED WITH 0.008 MoSi$_2$.

DIMENSIONS IN CM.

1/3 SCALE

VIEW D-D

FULL SCALE

ABLATOR
RESERVOIR
HEAT PIPE WALL
WICK
VAPOR SPACE

VAPOR SPACE
0.025, 400 MESH WICK
0.229, 50 MESH WICK
0.127 HEAT PIPE WALL
0.127 RESERVOIR WALL
LITHIUM RESERVOIR

VAPOR SPACE
0.015, 400 MESH WICK
0.076, 100 MESH WICK,
TAPERS TO 0.0$\overline{\text{0}}$0 AT
STAGNATION POINT
0.051 HEAT PIPE WALL

HEAT PIPE
LITHIUM RESERVOIR

Figure 3. Preliminary Design of Reference Sensible Heat Pipe Cooling System

Session IX

# THERMAL CONTROL
# COATINGS AND MEASUREMENTS

# REQUIREMENTS AND TEST RESULTS FOR THE QUALIFICATION
# OF THERMAL CONTROL COATINGS

J. E. Brzuskiewicz and G. A. Zerlaut
DSET Laboratories, Inc.

K. Lauder and G. M. Miller
NASA/Goddard Space Flight Center

ABSTRACT

Paint type coatings are often used as engineering materials in critical satellite temperature control applications. The functional features of coatings used for temperature control purposes must remain stable throughout the satellite manufacturing process and the satellite mission. The selection of a particular coating depends on matching coating characteristics to mission requirements. The use of paint coatings on satellites, although having an extensive history, requires that the paint be qualified to each application on an individual basis. Thus, the qualification process through testing serves to ensure that paint coatings as engineering materials will fulfill design requirements.

## INTRODUCTION

The complexity and size of current and future spacecraft, the rigors of spacecraft manufacture and long mission life requirements impose increasing demands on paint type coatings used for spacecraft temperature control. Paint type coatings used on spacecraft hardware can be categorized into several general types. All of these coatings use inorganic pigments of a semiconductor or dielectric nature. The binder systems used are based on silicate, silicone or urethane chemistry. Coatings based on silicate binders, although among the most space stable, require absolute substrate cleanliness before coating application, are brittle, porous and are sensitive to environmental conditions during the coating process. Elastomeric silicone coatings are cleanable, flexible and relatively easy to apply, but are easily notched during routine assembly procedures. The silicone-alkyd and urethane coatings, while being durable, easily applied and easily maintained have unacceptable stability towards the space environment for long-term missions.

White thermal control coatings are used primarily for their properties of space stable, low solar absorptance, high emittance and relative ease of incorporation into hardware manufacturing processes. However, other coating properties are often considered during the coating selection and qualification procedure. As an example, the coating selection criteria for the Cosmic Background Explorer (COBE) satellite are generally more stringent than for other spacecraft due to added requirements for low surface particulates, high emittance at low temperature and a reasonable degree of conductivity for electrostatic discharge.

While none of the paints evaluated for COBE were found to meet all of the criteria, low outgassing elastomeric silicone paints, pigmented with silicate treated zinc oxide, were found to have the greatest combination of desirable features. Test data and an outline of the qualification test procedures followed are presented for one of these coatings. This coating, designated as TW-1300, was found to be acceptable for use on the COBE satellite.

## SYMBOLS

| | | |
|---|---|---|
| $\alpha_s$ | = | solar absorptance |
| $\Delta\alpha_s$ | = | change in solar absorptance |
| $\varepsilon_1$ | = | emittance of test specimen |
| $\varepsilon_2$ | = | emittance of standard |
| $\varepsilon_H$ | = | hemispherical emittance |
| $V_1$ | = | voltage output, specimen |
| $V_2$ | = | voltage output, standard |
| $C_p$ | = | heat capacity of block |
| m | = | mass of block |
| $\Delta T/\Delta t$ | = | rate of temperature change |
| $\sigma$ | = | Stefan-Boltzman Constant |
| T | = | temperature of the sample |
| $T_0$ | = | shroud temperature |
| $\dot{Q}_{tc}$ | = | heat loss due to thermocouple |
| $\dot{Q}_{gas}$ | = | heat loss due to residual gas |
| A | = | total area of block |

## COATING SELECTION CRITERIA

NASA Specification No. MSFC-PROC-1384 (Reference 1) outlines the basic requirements for a low outgassing, white silicone spacecraft temperature control coating. These requirements are dictated to ensure the quality and functionality of spacecraft temperature control coatings of this type. The requirements for low outgassing, solar absorptance, emittance, adhesion and ultraviolet stability are imposed to ensure that the coating, used as an engineering material to minimize solar load, meets all design and performance expectations. Paint type coatings used as engineering materials must also be incorporated into satellite manufacturing processes and schedules. Requirements for these practical realities include pot-life, shelf-life, sprayability and cure time. The basic requirements of MSFC-PROC-1384 apply to typical satellite requirements and are based on the experience of many satellite programs. Each program or mission however, contributes new demands on the performance of these coatings.

The selection of white paint for the exterior surface of the COBE satellite was based primarily on coating thermal properties. A liquid helium dewar and two instrument packages operate at a surface temperature between 140°K and 150°K. Paints can typically have an emittance in this temperature range which is 0.1 less than the emittance at room temperature. Therefore, a paint with the highest possible emittance was desired. Other important thermal properties include stable solar absorptance in a circumpolar orbit at 900km above the surface of the earth and good adhesion over varying thermal conditions.

Secondary selection criteria were low surface contamination and a high enough conductivity to minimize on-orbit surface charging and discharging to the satellite structure. A surface cleanliness rating of Level 300 or better was required in order that the coating would not produce particulate contamination. The cleanliness rating, as outlined in Reference 2, describes surface contaminant size, distribution and numbers. A rating for a typical silicate paint is 750, while urethane or silicone paints have ratings between 200 and 250. The coating conductivity requirement allowed a degree of latitude since the maximum electron flux and energy for satellites at the COBE altitude and inclination occur for only tens of seconds. The resulting peak differential charge, on the order of 200 volts, would therefore dissipate shortly after passing over the polar region.[1]

## TYPICAL PROPERTIES

The requirements and typical properties for the TW-1300 coating are summarized in Table 1. The specific test methods and detailed procedures followed to determine the properties listed in Table 1 may be found in References 3 through 7.

## SOLAR ABSORPTANCE AND REFLECTANCE

Solar absorptance was determined from absolute hemispherical spectral reflectance measurements performed in accordance with ASTM Standard Test Method E903-82. The measurements were performed using a Beckman DK-2A Spectrophotometer with a center mounted integrating sphere of the 'Edwards' type (Figure A1.2 of E903-82). Total reflectance measurements were obtained in the entire solar spectrum from 280 nm to 2400 nm wavelength at an incident angle of 7°. The measurements are properly denoted as being 'absolute hemispherical spectral reflectance'.

Air Mass Zero solar absorptance, $\alpha_s$, was determined using the solar spectral distribution from Johnson (Reference 8). Reflectance data for 48 selected equal energy ordinates, corresponding to 2% increments of the distribution, were averaged as a fraction and subtracted from unity. Measurement data between 295 nm and 2400 nm were used and account for 96% of total solar radiation. As seen in Figure 1, a nominal 8-10 mil coating thickness provides an optimal solar absorptance of less than 0.20.

---

[1] "Selection of White Thermal Paint for COBE Exterior Surfaces," COBE Systems Engineering Memorandum. October 20, 1987.

Hemispherical spectral reflectance measurements were also used to evaluate the effects of surface roughness and were conducted in accordance with ASTM Standard Test method E-903-82. The measurements were performed with a Beckman DK-2A Spectrophotometer using an integrating sphere as shown in Figure A1.3 of ASTM E-903-82. This detector-baffled, wall mounted sample integrating sphere precludes the necessity of using a reference standard, except when defining the instrument's 100% line. The reflectance measurements were obtained in the solar spectrum from 280nm to 2400 nm wavelength at an incident angle of 20°. The diffuse hemispherical reflectance measurements were made using a light trap as shown in Figure A1.3 of ASTM E-903-82. The total hemispherical spectral reflectance measurements were made using the integrating sphere with a continuous sphere coating by employing a sphere-completing segment.

The paint test panels used for the measurements were chosen on the basis of their having strikingly different visual surface texture while having approximately the same coating thickness. The test panel prepared from paint Lot No. 169-8 was produced by spray painting in such a way as to produce a pebble grained surface. The test panel prepared from paint Lot No. 1-0028 had a surface typical of the egg-shell finish resulting from normal spray painting procedures. The average total solar reflectance, and the average diffuse reflectance were calculated using the same 48 selected energy ordinates used to determine solar absorptance. Specular reflectance was calculated by taking the difference between the total reflectance and the diffuse reflectance. These data are shown in Table 2.

The reflectance data presented in Table 2 indicate that the surface roughness of the coating has little effect on diffuse reflectance. Indeed, the solar absorptance and average reflectance values exhibited in Table 2 suggest that the two coating samples are identical. It should be noted that the light trap used with the 8 in. diameter integrating sphere intercepts about 0.8% of the diffusely reflected flux from the sample. The 0.4% specular reflectance obtained for both samples is approximately equal to the uncertainty in the measurements, thus, the coatings are essentially as close to being perfectly diffusing surfaces as can be designed into organic coatings.

TOTAL EMITTANCE

Total emittance measurements were performed with a Devices and Services Company emissometer Model AE, Adaptor Model AE-AD1, equipped with a Model RD-1 scaling digital voltmeter. The detector portion of the emissometer is heated to 150°F so that the sample does not have to be heated. The detector responds only to radiation heat transfer and is designed to have an output linear with emittance. Being a differential thermopile with sensing elements of aluminum foil and black paint, the detector has a near-constant response to thermal wavelengths from 3 to 30 microns.

The test specimens and a flat black standard of known emittance (0.90) were placed on a heatsink and allowed to stabilize to ambient conditions. The detector was placed on the flat black standard for approximately one and one half minutes and the voltage output recorded. The detector was

then placed on the test specimen for approximately one and one half minutes and the voltage output recorded.

The total emittance was calculated as follows in Equation 1 and found to meet the requirements of 0.90 ±0.05 for nominal thickness.

$$\varepsilon_1 = \frac{V_1}{V_2} (\varepsilon_2) \tag{1}$$

In equation 1, where $\varepsilon_1$ = Emittance of test specimen,

$\varepsilon_2$ = Emittance of black standard,

$V_1$ = Voltage output for test specimen, and

$V_2$ = Voltage output for black standard.

ADHESION

Thermal shock tests were conducted using liquid nitrogen immersions, oven exposures and controlled rate temperature changes in an environmental chamber. The liquid nitrogen immersion temperature tests ranged between either 254°C or ambient temperature and liquid nitrogen temperature. An environmental chamber was used to cycle samples between 60°C and -70°C using a 0.5°C/min rate of temperature change. TW-1300 was evaluated on aluminum substrates primed with TW-1300 primer on both abraded and unabraded aluminum.

The aluminum substrates used for the 254°C - liquid nitrogen immersion tests were prepared by cleaning with Methyl Ethyl Ketone before applying TW-1300 primer and paint. Test samples were allowed to cure under ambient laboratory conditions for more than 40 hours before thermal cycling. After curing, the test samples were placed in a 254°C oven for 5 minutes. After 5 minutes the samples were immersed in liquid nitrogen until vigorous boiling ceased. At this point the samples were returned to the 254°C oven. This cycle was then repeated. None of the samples tested exhibited any change from their original appearance or condition.

The same cycles were used to test TW-1300 samples prepared on abraded and primed aluminum substrates. These substrates were prepared by scrubbing the substrate surface with a mixture of Comet cleanser, carborundum grit, and water. The substrates were thoroughly rinsed with water and allowed to air dry before applying primer and paint. These samples also did not exhibit changes from their original condition, after two cycles between 254°C and liquid nitrogen temperature.

TW-1300 was also evaluated on abraded and primed aluminum substrates, by cycling between ambient temperature and liquid nitrogen temperature. Test samples were allowed to "equilibrate" at each temperature before continuing the cycle. Samples tested in this manner exhibited no change from their original condition even after more than 40 such cycles.

TW-1300 applied to abraded and primed aluminum substrates with various thicknesses of primer were subjected to the liquid nitrogen immersion test and to a cyclic temperature test in an environmental chamber. Environmental chamber test samples were soaked for 6 hours at 24°C with 80% RH followed by another soak at 24°C with 50% RH for 1 hour prior to cycling temperature between 40°C with 50% RH and -70°C using a 0.5°C/min. temperature change rate. No adhesion loss, cracking or other signs of failure were noted after 100 cycles.

Additional test samples were subjected to thermal vacuum tests at $10^{-6}$ torr. 90 cycles with a 2°C/min. rate of temperature change were conducted between -130°C and 60°C and followed by a liquid nitrogen immersion. There was no apparent loss of adhesion after this testing.

COATING HANDLING PROPERTIES

The sprayability and resulting appearance of the TW-1300 coating are subject, in part, to paint preparation and spraying technique. The paint is applied using typical spray painting procedures and equipment in successive wet coats of uniform thickness, allowing just enough time between coats for solvent evaporation in order to avoid runs. The paint is air dried at room temperature generally for not less than 64 hrs. before conducting critical tests such as outgassing, ultraviolet degradation or thermal/vacuum tests. However, hardware or samples can be handled after 8 hrs. since nearly 100% of the mechanical strength of the film is developed in this time period.

The resulting paint coating is soft and subject to tearing when compared to polyurethane coatings. However, these characteristics are inherent to the coating material. Evaluation tests were conducted on the paint as a function of film thickness and as a function of temperature and humidity conditions during application and cure to determine optimum spray painting conditions. The results of this testing indicated that the greatest film strength is obtained with an 8-10 mil thick film cured at 70°F with relative humidity in the range between 25% and 45%. Softer paint films generally resulted when high humidity conditions were used during the cure time.

Other paint characteristics related to sprayability and handling include weight per gallon, shelf-life, pot-life and viscosity. Typical values for these characteristics are shown in Table 1 and are determined at the time of manufacture as part of quality assurance procedure.

SPACE STABILITY PROPERTIES

OUTGASSING PROPERTIES

Outgassing tests in accordance with ASTM E595 were conducted on paint samples which were applied to release films. The samples were allowed to cure under ambient conditions for a minimum of 5 days prior to the outgassing test. No elevated temperature cure or baking cycles were used. As shown in Table 1 Total Mass Loss (TML) averaged 0.35% and Collected Volatile Condensable Material (CVCM) averaged 0.01%.

## ULTRAVIOLET STABILITY

The ultraviolet stability of new spacecraft coatings with respect to changes in solar absorptance must be verified. Ultraviolet exposure and reflectance measurements must be performed invacuo and at nominal spacecraft operating temperature. Solar absorptance was determined in air prior ultraviolet exposure from reflectance measurements made in accordance with ASTM E-903 over the wavelength region between 290nm and 2400nm. Test samples were then mounted in a vacuum chamber and maintained at 25°C throughout the test. The samples were subjected to a total exposure of 1000 equivalent sun hours (ESH) at a one sun intensity using an X-25 airmass zero xenon source. The vacuum chamber was operated at $10^{-6}$ torr during the test and was not interrupted for reflectance measurements. Reflectance measurements were made in-situ through a quartz window at 0, 50, 100, 200, 500 and 1000 ESH. Although measurements made in this manner do not yield absolute solar absorptance values, relative changes in solar absorptance can be determined. Changes in solar absorptance using this technique can be determined within $\pm 0.02$.

Catalyst type, handling and storage effects on the ultraviolet stability of TW-1300 were determined during several ultraviolet degradation tests. The solar absorptance data shown in Table 3 indicates that the TW-1300 is quite stable to ultraviolet radiation when handled properly. The detrimental effects of surface contamination on reflectance, and thus solar absorptance, is shown by comparing the reflectance spectra in Figure 2 for an uncontaminated sample to the spectra in Figure 3 for a sample handled with latex rubber gloves.

## CHARGED PARTICLE STABILITY

The differential energy spectrum of electrons in the COBE mission environment exhibits two flux density peaks at relatively low energies. The lowest energy electrons occur between 6 and 30 eV and have a flux of approximately $2 \times 10^7$ electrons/$cm^2 \cdot sr \cdot eV \cdot s$. The higher energy electrons are typically on the order of 1 KeV but could be as high as 20 KeV. The 1 KeV electrons have a flux of approximately $5 \times 10^5$ electrons/$cm^2 \cdot sr \cdot eV \cdot s$.

Figure 4 presents data for separate but consecutive 1 MeV electron and proton exposures each with a total fluence of $10^{14}$ particles/$cm^2$. The results of the high energy electron irradiation indicates significant damage in the near infrared region and is not untypical. However, results obtained from tests conducted on a similar coating using more realistic energy levels were found to be considerably less dramatic (References 9 and 10). Further, a comparison of the effects of 20 KeV electrons to 80 KeV electrons also on a similar coating reported on in Reference 9 suggests that the electron energy dependent damage effects are generally less than the energy ratio. Therefore the $\Delta \alpha_s = 0.04$ measured after the 1 MeV exposure is not considered inordinate. This is especially true since the $10^{14}$ electron fluence is approximately two times greater than the total fluence predicted for the COBE mission.

The interpretation of the effects of the proton irradiation, conducted subsequent to the electron irradiation is less straight forward since both the electron and proton energy levels used exceed the threshold levels at which incipient damage can be observed in silicate treated zinc oxide systems. Therefore, the additional significant damage in the near infrared region occuring after the proton irradiation could be due to a synergistic effect of the prior damage caused by the electron irradiation. Low energy proton testing is planned for the very near future in order to further characterize the TW-1300 coating performance in the charged particle environment.

## LOW TEMPERATURE EMITTANCE

The hemispherical emittance of many materials is temperature dependent. Therefore, it was necessary to characterize the temperature dependency of emittance for the coatings used on COBE. Coating samples were evaluated using a transient calorimetric technique where a metallic block of known mass and heat capacity was coated with the test material and suspended in a liquid nitrogen cooled shroud inside a vacuum chamber (Reference 11). Sample temperature was monitored while the sample radiatively cooled under these conditions. Heat loss by conduction in the vacuum chamber was minimized by maintaining a pressure less than $10^{-6}$ torr. Heat loss through the thermocouple lead was calculated and accounted for in each temperature interval.

The thermal balance of the test chamber is described by Equation 2, where:

$m$ = mass of block

$C_p$ = heat capacity of the block

$\Delta T/\Delta t$ = rate of temperature change

$A$ = total area of the block

$\varepsilon_H$ = hemispherical emittance

$T$ = sample temperature

$T_o$ = shroud temperature

$\dot{Q}_{tc}$ = heat loss from the thermocouple

$\dot{Q}_{gas}$ = heat loss due to residual gases

$\sigma$ = Stefan-Boltzman Constant

$$-mC_p(\Delta T/\Delta t) = A\sigma\varepsilon (T-T_o) + \dot{Q}_{tc} + \dot{Q}_{gas} \qquad (2)$$

Hemispherical emittance was calculated using Equation 3 by rearranging Equation 2 and neglecting the heat loss to the chamber, $Q_{gas}$.

$$\varepsilon_H = \frac{-mCp(\Delta T/\Delta t)-\dot{Q}_{tc}}{A\sigma (T-T_o)} \qquad (3)$$

This technique has been found to be reliable for determining hemispherical emittance as a function of temperature for temperatures as low as 120°K with an accuracy of ± 2%. Emittance data for the TW-1300 coating is shown in Figure 5 and ranges from 0.90 at +363°K to 0.75 at -123°K.

## SUMMARY

The results of qualification tests conducted on a white thermal control coating have been presented. The test results show that this coating is acceptable for use on the exterior surfaces of the COBE satellite. The coating meets specific requirements for low solar abosrptance, emittance, cleanliness and space stability. The physical features and handling characteristics of the coating tested were also found to meet requirements for sprayability, adhesion, pot-life and storage-life, thus allowing the coating to be easily incorporated into the satellite manufacturing and assembly process. The resistance of this particular coating to degradation by the effects of ultraviolet, electron and proton bombardment was found to be not unlike similar coatings that have been well characterized and which have a long history of use in satellite temperature control applications. The analysis of NASA Specification MSFC-PROC-1384 and the specific requirements of the COBE satellite clearly suggests the suitability of the TW-1300 coating investigated for many satellite applications in addition to the COBE mission.

## REFERENCES

1.  "Application of S-13G/LO-1 Thermal Control Coating." Marshall Space Flight Center Specification: MSFC-PROC-1384.

2.  "Product Cleanliness Levels and Contamination Control Program." Military Standard Number: MIL-STD-1246A.

3.  "Total Normal Emittance of Surfaces using Inspection Meter Techniques." ASTM Number: E 408.

4.  "Total Mass Loss and Collected Volatile Condensible Material from Outgassing in a Vacuum Environment." ASTM Number: E 595.

5.  "Elongation of Attached Organic Coatings with Conical Mandrel Apparatus." ASTM Number: D 522.

6.  "Test Method for Solar Absorptance, Reflectance and Transmittance of Materials Using Integrating Spheres." ASTM Number: E 903.

7.  "General Specification – Vacuum Stability Requirements of Polymeric Materials for Spacecraft Applications." Johnson Space Center Specification: SP-R-0022A.

8.  Johnson, F. S., "The Solar Constant", J. Met., Vol. 11, No. 6, 1954, pp. 431-439.

9.  Fogdall, L.B., Cannaday, S.S., and Brown, R.R., "Electron Energy Dependence for In-Vacuum Degradation and Recovery in Thermal Control Surfaces." AIAA Paper No. 69-643 Progress in Astronautics and Aeronautics Vol. 23. Academic Press. 1970.

10. Mell, R.J., Harada, Y., "Space Stable Thermal Control Coatings." AFWAL-TR-87-4010. May 1987.

11. Fussel, W.B., Triolo, J.J. and Henniger, J.H., "A Dynamic Thermal Vacuum Technique for Measuring the Solar Absorption and Thermal Emittance of Spacecraft Coatings." Measurement of Thermal Radiation Properties of Solids-NASA Publication No. SP-31. 1963.

TABLE 1
Summary of Coating Properties and Test Results

| Test | Requirement | Result |
|------|-------------|--------|
| Total Emittance ($\varepsilon_1$) | $0.90 \pm 0.05$ | 0.93 |
| Emittance vs. Temperature ($\varepsilon_H$) | 123°K to 363°K Stability | 0.75 - 0.90 |
| Solar Absorptance ($\alpha_s$) | Less than 0.22 | 0.18 |
| Ultraviolet Stability ($\Delta\alpha_s$) | Less than 0.02 after 500 ESH | Less than 0.02 after 1000 ESH |
| Adhesion | | |
|   - Thermal Shock | No loss of adhesion | No loss of adhesion |
|   - Conical Mandrel | No loss of adhesion | No loss of adhesion |
|   - Thermal/Vacuum | No loss of adhesion | No loss of adhesion |
| Coating Weight | | |
|   - As Manufactured | 11.3 to 12.5 lbs./gal. | 11.8 lbs./gal. |
|   - Dry Film | Not specified | $0.03 g/mil-in.^2$ |
| Pot-Life | 45 minutes minimum | Greater than 45 minutes |
| Paint Shelf-Life | 6 month minimum when refrigerated | Greater than 6 months when refrigerated |
| Catalyst Shelf-life | 6 month minimum when refrigerated | Greater than 6 months when refrigerated |
| Viscosity at Time of Manufacture | 25 to 31 seconds No. 4 Ford Cup | 25 to 31 seconds No. 4 Ford Cup |
| Outgassing-No Oven Cure or Bake | TML - 1.0% CVCM - 0.1% | TML - 0.35% CVCM - 0.01% |
| Self-Generated Particulate Contamination | Not Specified | Better than Level 300 |

Table 2

Solar Reflectance and Solar Absorptance
of TW-1300 Samples Having
Different Surface Roughness

| Sample | $\alpha_s$ | Total Reflectance (%) | Diffuse Reflectance (%) | Specular Reflectance (%) |
|--------|------------|-----------------------|-------------------------|--------------------------|
| 169-8  | 0.190      | 81.0                  | 80.6                    | 0.4                      |
| 1-0028 | 0.190      | 81.0                  | 80.6                    | 0.4                      |

430

TABLE 3

TW-1300 ULTRAVIOLET/VACUUM EXPOSURE TEST RESULTS

| Sample Description | Initial $\alpha_s$ In Air | Initial $\alpha_s$ In Vacuum | $\alpha_s$ After 50 ESH | $\alpha_s$ After 100 ESH | $\alpha_s$ After 200 ESH | $\alpha_s$ After 1000 ESH | $\Delta\alpha$ After 1000 ESH |
|---|---|---|---|---|---|---|---|
| TW-1300 | 0.19 | 0.19 | 0.19 | 0.19 | 0.19 | 0.19 | Less than 0.02 |
| TW-1300 After Storage in Clean Room Bag | 0.18 | 0.18 | 0.18 | 0.18 | 0.18 | 0.18 | Less than 0.02 |
| TW-1300 Contaminated After Handling with Latex Rubber Gloves | 0.20 | 0.21 | 0.22 | 0.22 | 0.21 | 0.23 | 0.03 |
| TW-1301 (Organometallic Catalyst) | 0.20 | 0.20 | 0.20 | 0.20 | 0.20 | 0.20 | Less than 0.02 |
| TW-1301 (Organometallic Catalyst) | 0.19 | 0.19 | 0.19 | 0.19 | 0.19 | 0.19 | Less than 0.02 |
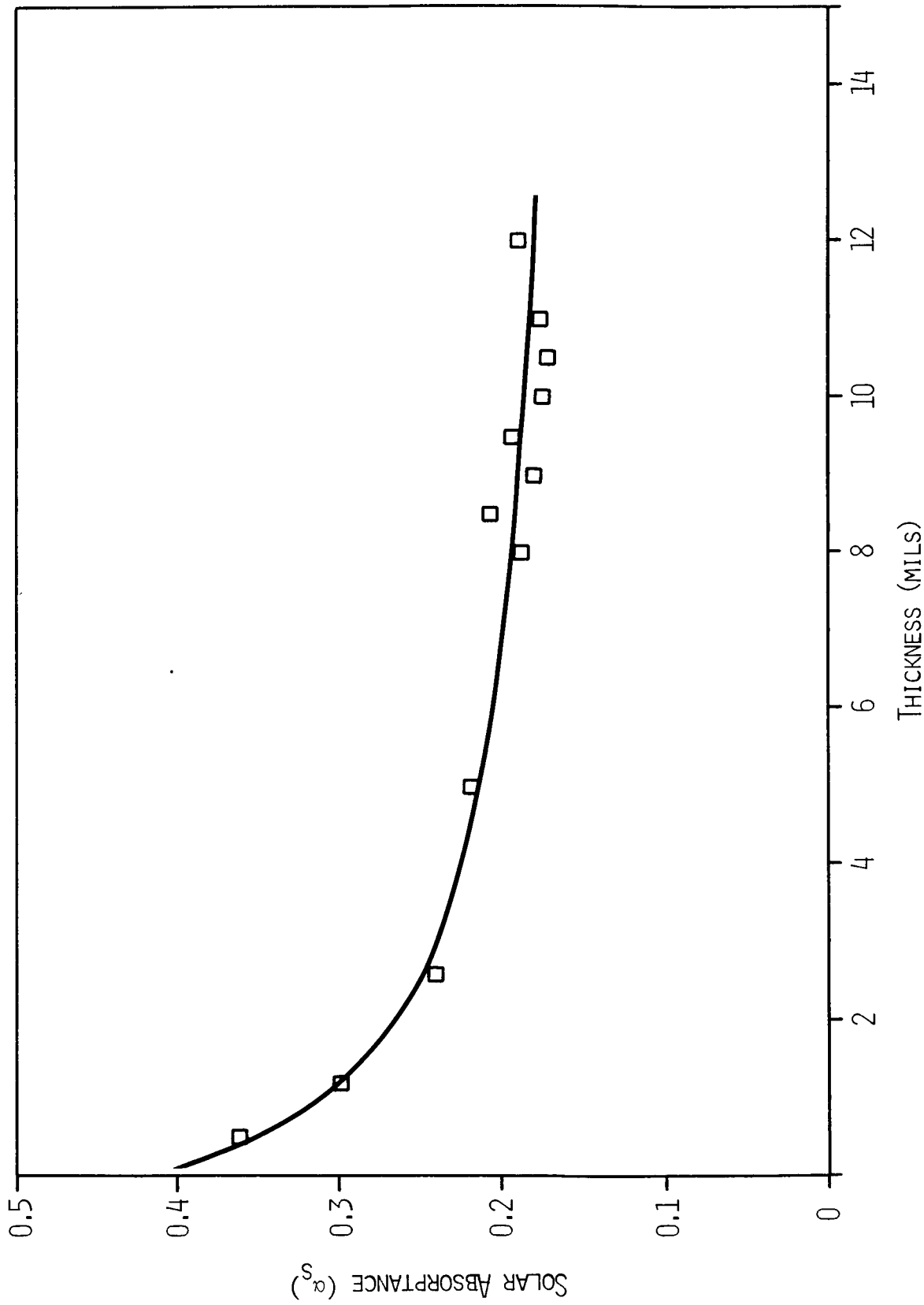
Figure 1. TW-1300 Solar Absorptance vs. Thickness
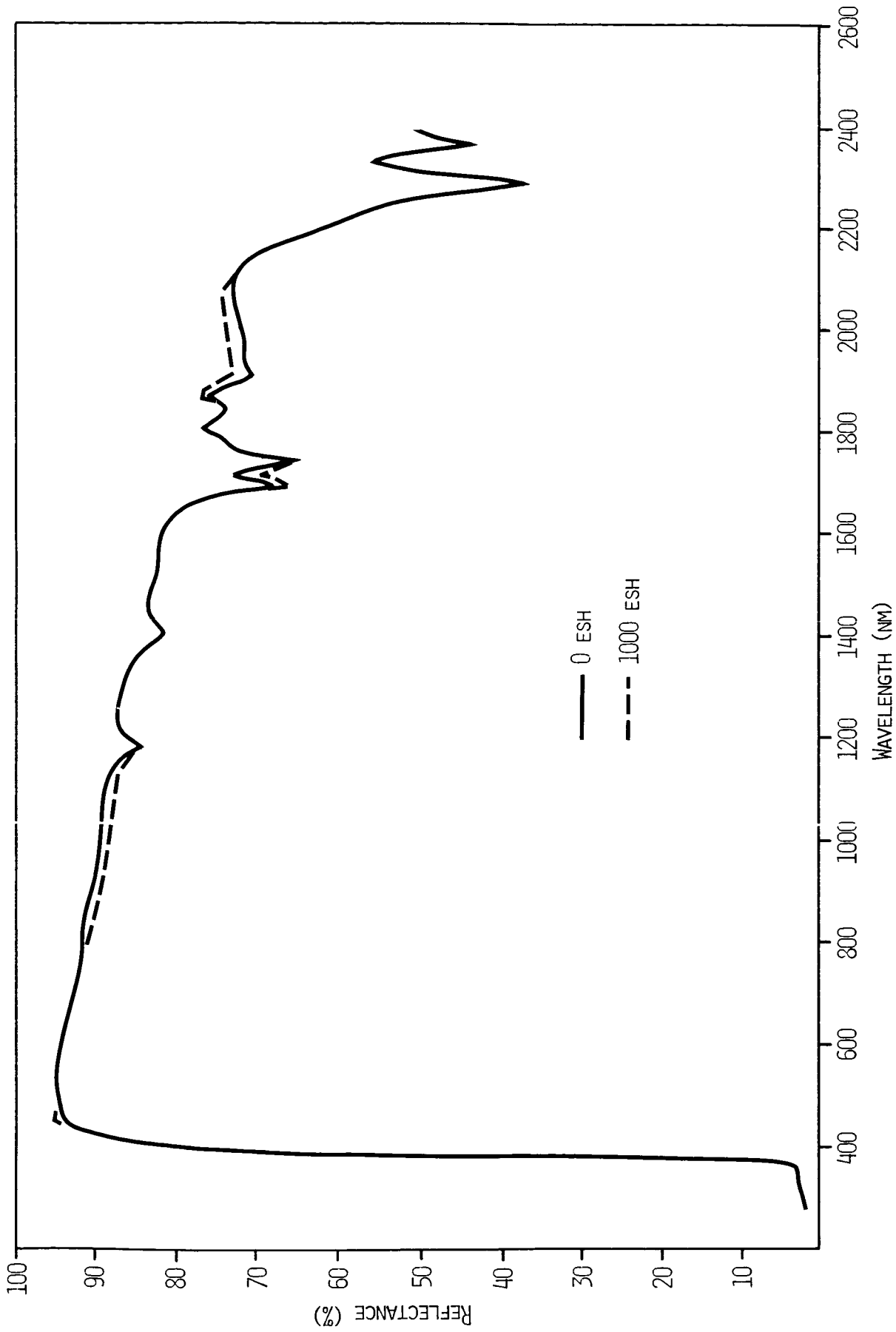
Figure 2. Ultraviolet Stability Test Results – Uncontaminated Sample

433
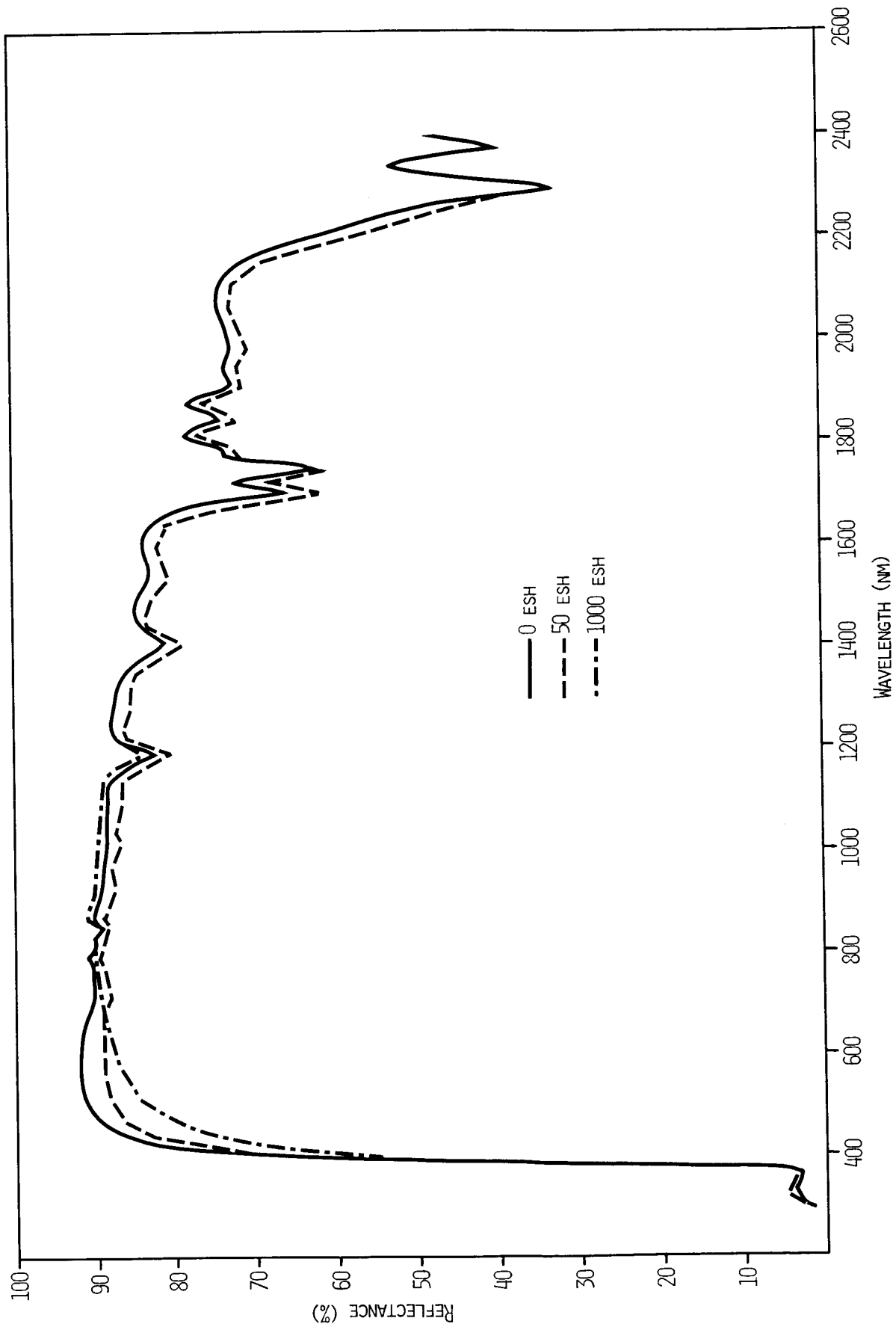
Figure 3. Ultraviolet Stability Test Results – Contaminated Sample
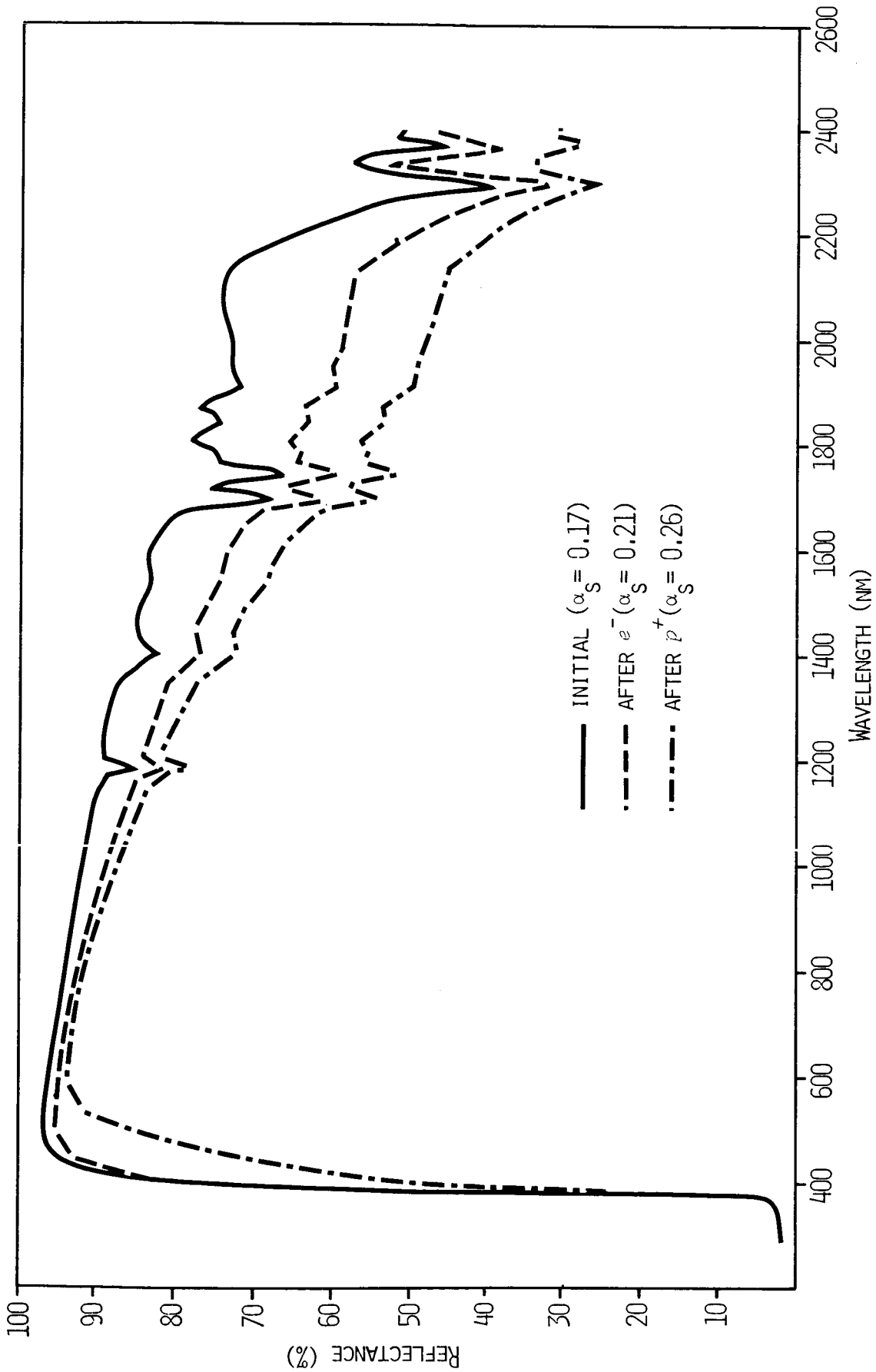
Figure 4. Charged Particle Stability Test Results

435
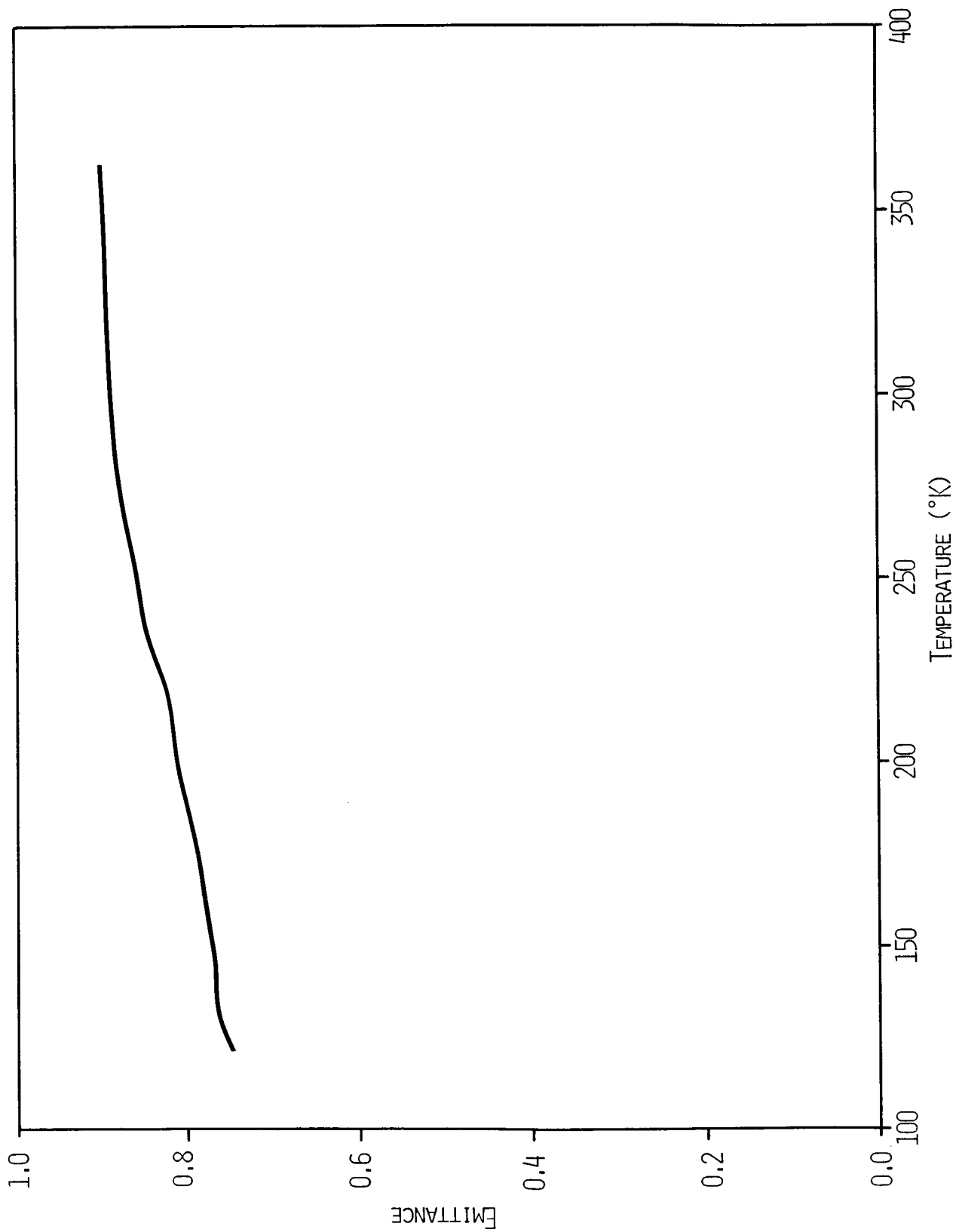
Figure 5. TW-1300 Emittance vs. Temperature

# COMPARISON OF SULFURIC AND OXALIC ACID ANODIZING FOR PREPARATION OF THERMAL CONTROL COATINGS FOR SPACECRAFT*

Huong G. Le, John M. Watcher, and Charles A. Smith
McDonnell Douglas Corporation

ABSTRACT

The development of thermal control surfaces, which maintain stable solar absorptivity and infrared emissivity over long periods, is challenging due to the severe conditions in low-Earth orbit (LEO). These conditions include ultraviolet radiation, atomic oxygen, and thermal cycling as the spacecraft passes into and out of the Earth's shadow. Some candidate coatings are second-surface silver-coated Teflon; second-surface, silvered optical solar reflectors made of glass or quartz; and anodized aluminum. We have evaluated sulfuric acid anodized and oxalic acid anodized aluminum under simulated LEO conditions. Oxalic acid anodizing shows promise of greater stability in LEO over long missions, such as the 30 years planned for the Space Station. Sulfuric acid anodizing; however, shows lower solar absorptivity.

# INTRODUCTION

Thermal control systems are needed on spacecraft to maintain temperatures in the range required for effective operation. These systems have a surface which is exposed to space and has a range of acceptable values for solar absorptivity ($\alpha$) and for infrared emissivity ($\epsilon$). Usually, the surfaces are chosen to have the lowest possible absorptivity and the highest possible emissivity, for the minimum $\alpha/\epsilon$ ratio. One material used for these surfaces is FEP Teflon film with a silver-coated second surface. However, samples of this material which were returned from the Solar Max satellite after repair showed significant degradation after only four years.[1] Although the degradation may be due to exposure conditions and temperatures that were more severe than those expected, there is concern that this material will degrade during the extremely long periods of time planned for spacecraft; such as the Space Station. Another surface used on satellites is thin glass or quartz with a second-surface silver coating. These surfaces show good stability; however, they are expensive to make and attach to a radiator or other structures. There is also insufficient data on their stability or the stability of the adhesives used to attach them for many years in orbit.

Anodizing, which is the process of electrochemically forming a coating of aluminum oxide on an aluminum surface, has been investigated for more than 20 years for thermal control coatings for low $\alpha$, high $\epsilon$ applications[2]. Large areas can be anodized in a relatively short period of time; the surface is much harder and more resistant to damage than other thermal control coatings. The three most common types of anodizing are produced using chromic, phosphoric, and sulfuric acid. Of these, only sulfuric acid anodizing has a sufficiently low $\alpha$ to be a candidate for spacecraft radiators. Depending on the alloy and the anodizing process conditions, $\alpha$ can be as low as 0.1, and $\epsilon$ can be as high as 0.9. However, sulfuric acid anodizing is not stable to the ultraviolet radiation in space and the $\alpha$ tends to increase with time in orbit, possibly due to the formation of defects in the lattice which increase scattering of the solar radiation[2]. One theory for the susceptibility of sulfuric acid anodizing to ultraviolet radiation is that it is sensitized by sulfur or sulfate anions occluded in the

lattice. Sulfuric acid anodized coating contains about 13% to 18% of sulfate $(Al_2(SO_4)_3)$.

We investigated oxalic acid for thermal control surfaces because there are no inorganic ions occluded in the aluminum oxide that may sensitize the anodizing to ultraviolet radiation. Although oxalic acid is not commonly used in the United States, it is more popular in Japan where it was first developed. Oxalic acid anodized coating has about 3% of oxalic acid in the form of aluminum oxalate[3] $(Al_2(C_2O_4)_3$, indicating that it may be less susceptible to changes due to UV. Also, faying surface corrosion of anodized components due to oxalic acid residues is not a problem, in contrast to chromic and sulfuric acid residues, since neutralization with dilute ammonia or sodium bicarbonate is adequate to avoid corrosion.

## EXPERIMENTAL PROCEDURE

### SAMPLE PREPARATION

Previously anodized 5657 aluminum/magnesium alloy with the trade name Coilzak was selected as our test material since bare 5657 alloy was unavailable at the time this work was performed. This alloy was first studied for spacecraft thermal control coatings by D. Duffy[4]. Coilzak is extensively used in the automotive industry; it is preanodized by Alcoa, and has a high specular reflectivity. The test samples were fabricated from a 0.081 cm (0.032 in.) thick Coilzak sheet into 8 x 25 cm specimens.

In the anodizing sequence the test specimens were stripped with a phosphoric/chromic acid stripper to remove the preanodized coating (Figure 1). The test specimens were bright dipped in a phosphoric/nitric acid solution at temperatures from 95°C to 100°C for 45 seconds. After anodizing, the test specimen was wiped with a clean cloth to remove smut. (Smut is a thin layer of unwanted material formed during processing.)

We performed the anodizing process in the Chemistry Laboratory pilot process line at our facility. Anodizing was accomplished in a temperature controlled lead tank with a volume of 11 L. Power was supplied by a Trygon 40-volt, 8-amp power source using the lead tank as the cathode.

We performed a series of experiments to determine the optimum electrolyte concentration, current density, anodizing time, and bath temperature for oxalic acid anodizing. Our preliminary results indicate that an electrolyte concentration of 15% oxalic acid at a current density of 10 amperes per square foot (A/sq ft) yields the most suitable anodic coating. To produce the best $\alpha/\epsilon$ ratio of 0.20 for oxalic acid anodizing, we first selected a $50^o$C electrolyte temperature (Figure 2). However, Taber abrasion and ultraviolet test results showed that the coating prepared at this temperature is mechanically weak and unstable to ultraviolet radiation in vacuum. At $0^o$C to $20^o$C the coatings exhibit good abrasion resistance but poor optical properties. The best combination of results is obtained at $30^o$C. These results show that higher electrolyte temperatures yield better optical properties (lower $\alpha/\epsilon$ ratio) but softer coatings.

The optical properties of coatings prepared at different current densities and anodizing times at $30^o$C show that sulfuric acid anodized aluminum yields a better $\alpha/\epsilon$ ratio (0.20) than that of oxalic acid anodizing (0.25) and its emissivity increases more rapidly with increasing coating thickness.

ULTRAVIOLET RADIATION EXPOSURE

Test samples of candidate coatings were subjected to an ultraviolet flux equivalent to two and three solar constants intensity at NASA Langley Research Center (NASA-LaRC) and the TRW Thermophysical Laboratory, respectively.

At NASA-LaRC, a modular ultraviolet exposure system consisting of six high vacuum chambers surrounding a 1 KW xenon arc lamp source was used for ultraviolet exposure of anodized aluminum specimens over the wavelength region of 0.18 to 0.40 microns. Quartz optics were used to transmit the ultraviolet radiation incident on the 1-in. square specimens in these individual vacuum chambers. Typical vacuum in each chamber was $1 \times 10^{-8}$ torr. Each test specimen was mounted on a water cooled plate and the test temperature was less than $43^o$C.

Reflectance was measured in-situ using a Beckman DK2A spectrophotometer with an integrating sphere reflectometer. Measurements were made over a wavelength range of 0.25 to 2.5 microns. Reflectance data was recorded by a computer at 0.015 micron intervals and integrated over an air mass 0 solar spectrum to obtain the solar absorptance. Values of normal emittance at room temperature were determined ex-situ using a Gier-Dunkle Instrument DB-100 Emissometer[5].

At TRW, a similar ultraviolet exposure system was employed for exposure of anodized aluminum specimens. A 5 KW xenon arc lamp was used as the ultraviolet radiation source over the wavelength region of 0.18 to 0.40 microns. The 1-in. square specimens were mounted on a water cooled plate which was then enclosed in a quartz tube and pumped down to a vacuum of $1 \times 10^{-6}$ torr. The exposure temperature was approximately $66^{\circ}C$.

The solar absorptance and normal emittance at room temperature of the test specimens were measured using a technique similar to that used at NASA-LaRC. Spectral directional reflectance was measured in-situ using a Beckman DK2A spectrophotometer with an Edwards type integrating sphere reflectometer. Measurements were made over a wavelength region from 0.28 to 2.5 microns. Solar absorptance was determined by first finding the average reflectance of the specimen at a number of wavelength bands. An overall average solar reflectance was then calculated; subtracting this value from unity gives solar absorptance for an opaque specimen. The normal emittances at room temperature were determined using a Gier-Dunkle Instrument Model DB-100 Infrared Reflectometer.

## RESULTS AND DISCUSSION

## ULTRAVIOLET RADIATION

After 1000 equivalent sun hours (ESH) exposure at two solar constants at NASA-LaRC, both oxalic and sulfuric acid anodized aluminum samples developed a yellowish color with increased solar absorptivity. In all cases, emittance was unaffected by ultraviolet radiation.

Oxalic acid anodized samples produced at 50°C electrolyte temperature degraded significantly compared to those produced at 30°C (Table 1). However, the oxalic acid anodized coatings produced at the lower temperature were more stable to the ultraviolet radiation than the control sulfuric acid anodized samples produced at the same temperature. For example, the change in solar absorptance ($\Delta\alpha$) of the oxalic acid anodized sample is 0.023 after 1000 ESH, while the sulfuric acid anodized sample with a similar coating thickness exhibited $\Delta\alpha$ of 0.063. The change in absorptance as a function of exposure hours at two solar constants of oxalic acid anodized aluminum (Figure 3) indicates that the degradation increased gradually from 300 to 1000 ESH. Long-term exposure (5000 ESH) testing is needed to determine whether the degradation will be stable with time.

We also subjected the anodized aluminum to ultraviolet radiation at three solar constants at TRW Thermophysical Laboratory to determine if there is a direct correlation between different levels of accelerated ultraviolet testing. After ultraviolet exposure at three solar constants for 1000 ESH, oxalic acid anodizing produced at 50°C showed severe degradation similar to that at two solar constants (at NASA-LaRC). Both oxalic and sulfuric acid anodized samples produced at 30°C exhibited a similar change in absorptance (0.04) (Table 2). However, both of the sample surfaces cracked after 1000 ESH. The cracks on the oxalic acid anodizing radiated from several edge locations and appeared to be caused by mechanical handling. The sulfuric acid anodizing had many uniformly distributed short cracks, indicating a different cause. Possibly differential expansion during ultraviolet exposure combined with the residual stress in the anodize layer to produce these cracks. It was hypothesized that the exposure temperature was much higher than the anticipated 27°C. Thus, identical samples were resubjected to ultraviolet exposure. The exposure temperature was measured by attaching a thermocouple directly to the exposure surface. It was observed that at only two solar constants the test temperature was elevated to 43°C. To avoid damaging the anodized samples, the ultraviolet exposure was conducted at two solar constants for 1000 ESH. One interesting note was that the sulfuric acid anodized sample started to craze under vacuum prior to ultraviolet exposure. The oxalic acid anodized crazed after 500 ESH. However, the change in absorptance of oxalic acid anodizing after 1000 ESH (0.03) was significantly

less than that of sulfuric acid anodizing (0.08)(Table 3). Thus, ultraviolet test results obtained at two solar constants at both test facilities (TRW and NASA-LaRC) indicate that oxalic acid anodizing is more stable to ultraviolet radiation than sulfuric acid anodizing.

Further investigation is being conducted to solve the crazing problem which occurs on the anodized samples during ultraviolet exposure at TRW.

We also investigated the phenomenon of "bleaching", which has been observed with white paints[5,6], to determine if there is a lowering of absorptance for clear anodized aluminum on exposure to atmospheric oxygen after ultraviolet exposure. Solar absorptance was measured both ex-situ and in-situ. Although the mechanism of bleaching has not been fully explained, a likely explanation is that color centers formed within the film under ultraviolet radiation are partly destroyed in the presence of oxygen in air. Our results showed that bleaching occurs and the ultraviolet degradation is reversed in both oxalic and sulfuric acid anodized coatings (Table 4). However, only a small portion of the solar absorptance gain is reversed, indicating that bleaching with molecular oxygen is not a feasible approach for reconditioning anodized coatings.

THERMAL CYCLING

The clear anodized aluminum samples were subjected to thermal cycling from -73°C to 38°C in a nitrogen environment. After 4000 cycles, neither oxalic nor sulfuric acid anodized coatings of various thicknesses (0.012 to 0.0203 cm) exhibited cracking or spalling and their emissivity remained unchanged.

SALT SPRAY CORROSION RESISTANCE

Both types of clear anodizing passed the salt spray testing, conducted under conditions specified in ASTM method B117-73, indicating that corrosion resistance satisfies Military Specification 8625, Anodizing of Aluminum Alloys. This also indicated that no corrosion problems would occur with either type through production, transportation, or prelaunch storage.

## ABRASION RESISTANCE

Taber Abraser tests on oxalic and sulfuric acid anodized aluminum (Table 5) showed that oxalic acid anodizing produced at a low temperature (30°C) was somewhat more resistant to abrasion than sulfuric acid anodizing produced at the same temperature, and that the oxalic acid coating produced at 50°C eroded rapidly. These results are probably due to the porous structure of the anodic surface, as observed in the scanning electron micrographs (Figures 4 and 5).

## SCANNING ELECTRON MICROSCOPY

Using scanning electron microscopy, we examined the surface morphology of the oxalic acid anodized coatings produced at 30°C and 50°C electrolyte temperatures (Figures 4 and 5). The surface produced at 50°C is significantly more porous than that produced at 30°C, indicating that more contaminants can be trapped inside the pores, lowering its ultraviolet stability.

We also examined the anodizing produced at 30°C by sulfuric acid, and by oxalic acid using the scanning electron microscope. No significant differences were observed.

## CONCLUSION

The properties of the oxalic acid anodized thermal control coating prepared at 30°C are similar to the sulfuric acid anodized coating. Our current data obtained at two solar constants indicates that oxalic acid anodized coating exhibits significantly less degradation to ultraviolet radiation than sulfuric acid anodized coating. The most noteworthy observation is that our and Acurex' anodizing studies[4] show much less degradation than was reported in earlier work.[2] Further testing is in progress. Additional ultraviolet testing, which includes the shorter wavelength region (0.14 - 0.18 microns) and longer term exposure, is essential to ascertain the stability of both anodizing systems to be used as thermal control coatings in the LEO environment.

We will include selected oxalic and sulfuric acid anodized aluminum samples identical to those tested at our ground-based accelerated test facilities on

the FOIM-III (Evaluation of Oxygen Interactions with Materials-III) flight experiment[7]. The samples will be exposed for 40 hours in the LEO and will be retrieved for examination. These flight results will enable us to compare our simulated test results with those obtained in a real space environment.

## REFERENCES

1. Whittaker, A. F., et. al.: Orbital Atomic Oxygen Effects on Thermal Control and Optical Materials-STS 8 Results, AIAA-85-04146, AIAA 23rd Aerospace Sciences Meeting, January, 1985.

2. Weaver, J. H.: Effects of Vacuum Ultraviolet Environment on Optical Properties of Bright Anodized Aluminum, Technical Report No. AFML TR 64-355, January, 1965.

3. Wernick, S.; Pinner, R.; and Sheaby, P. G.: The Surface Treatment and Finishing of Aluminum and Its Alloys, ASM International Finishing Publications Ltd., 5th Edition, 1, pp 298-301.

4. Duffy, D.: Final Report on Development of Durable/Long Life Radiator Coatings, Acurex Technical Report FR-88-100/ESO, Acurex Corp., Environmental Systems Div., 485 Clyde Ave., P. O. Box 7044, Mountain View, CA 94039.

5. Dursch, H. W. and Slemp, W. S.: Evaluation of Chromic Acid Anodized Aluminum Foil Coated Composite Tube for the Space Station Truss Structure, International SAMPE Conference, March 1988.

6. Harada, Y. and Wilkes, D. R.: Inorganic $Zn_2TiO_4$ Thermal Control Coatings, SAMPE paper, 1979.

7. Cull, R. A., et. al.: Requalification of S13G/LO, AIAA 19th Thermophysics Conference, June, 1984.

8. Visentine, J. T., and Leger, L. J.: Materials Interactions with the Low Earth Orbital Environment: Accurate Reaction Rate Measurements, AIAA-85-7019, AIAA Shuttle Environment & Operations II Conference, November, 1985.

Huong G. Le attended the University of California at Los Angeles where she
received her BS in chemistry in 1982. She is currently working towards an MS
in Materials Science Engineering at California State University-Long Beach.
She is currently a technology engineer in the chemistry laboratories at
McDonnell Douglas Astronautics Company Huntington Beach, where she is working
on the research and development of thermal control coatings for the Space
Station Program. She is a member of the Society for the Advancement of
Material and Process Engineering, the Material Research Society, and the
Society of Automotive Engineers.

John M. Watcher attended California State University at Long Beach where he
received his BS in chemistry in 1985. His interests include surface finishing
such as anodizing, electroplating, chemical milling, and environmental effects
related to the degradation of surface finishes. He is currently a technology
engineer in the chemistry laboratories at McDonnell Douglas Astronautics
Company -- Huntington Beach. He is a member of the American Society of Testing
Materials.

Charles A. Smith is the manager of the chemistry laboratories in the
Materials, Processes, and Producibility department at McDonnell Douglas
Astronautics Company - Huntington Beach. He received his BS in chemistry at
St. Thomas College, St. Paul, Minnesota in 1961 and his PhD in analytical
chemistry from Kansas State University in 1966. His interests include
spacecraft contamination and the natural and induced space environment. He is
a member of American Chemical Society, American Society for the Testing of
Materials, the American Society for Mass Spectrometry, and the Society of
Material and Process Engineering.

Dudley L. O'Brien, after 25 years of service, has returned in a consulting capacity for the Materials, Processes, and Producibility department at McDonnell Douglas Astronautics Company - Huntington Beach. He joined the Air Force in 1943 and received his BS in chemistry and mathematics from Case Western Reserve University in 1950. His expertise in the field of metal finishing and processing include development of brighteners and low-temperature cleaners for electroplating, electropolishing, anodizing and chemical milling. His most recent interests are the development of thermal control chemical conversion coatings and electroplated coatings for aerospace applications and solar energy collectors.

**Table 1. Effects of UV Exposure at Two Solar Constants for 1000 ESH on the Optical Properties of Oxalic and Sulfuric Acid Anodized Aluminum***

| Anodized electrolyte (temperature) | Coating thickness (mil) | Solar absorptance ($\alpha$) | | |
|---|---|---|---|---|
| | | Before exposure | After exposure | $\Delta\alpha$ |
| Oxalic acid (50°C) | 0.50 | 0.199 | 0.365 | 0.166 |
| Oxalic acid (30°C) | 0.65 | 0.250 | 0.249 | 0.024 |
| Oxalic acid (35°C) | 1.00 | 0.231 | 0.254 | 0.023 |
| Sulfuric acid (30°C) | 0.80 | 0.242 | 0.307 | 0.065 |

*Test performed at NASA-LaRC

**Table 2. Effects of UV Exposure at Three Solar Constants on the Optical Properties of Oxalic Acid Anodized Aluminum***

| Anodized electrolyte (temperature) | Coating thickness (mil) | Exposure time (ESH) | Solar absorptance ($\alpha$) | |
|---|---|---|---|---|
| | | | After exposure | $\Delta\alpha$ |
| Oxalic acid (50°C) | 0.50 | 0 | 0.22 | — |
| | | 100 | 0.28 | 0.06 |
| | | 300 | 0.33 | 0.10 |
| | | 500 | 0.36 | 0.13 |
| | | 1000 | 0.38 | 0.16 |
| Oxalic acid (30°C) | 0.51 | 0 | 0.22 | — |
| | | 300 | 0.25 | 0.03 |
| | | 500 | 0.26 | 0.04 |
| | | 700 | 0.26 | 0.04 |
| | | 1000 | 0.26 | 0.04 |
| Sulfuric acid (30°C) | 0.55 | 0 | 0.17 | — |
| | | 300 | 0.19 | 0.02 |
| | | 500 | 0.21 | 0.04 |
| | | 700 | 0.22 | 0.05 |
| | | 1000 | 0.21 | 0.03 |

*Test performed at TRW Thermophysical Laboratory

**Table 3. Effects of UV Exposure at Two Solar Constants on the Optical Properties of Oxalic Acid Anodized Aluminum***

| Anodized electrolyte (temperature) | Coating thickness (mil) | Exposure time (ESH) | Solar absorptance ($\alpha$) | |
|---|---|---|---|---|
| | | | After exposure | $\Delta\alpha$ |
| Oxalic acid (30°C) | 0.51 | 0 | 0.22 | — |
| | | 250 | 0.25 | 0.03 |
| | | 500 | 0.25 | 0.03 |
| | | 1000 | 0.25 | 0.03 |
| Sulfuric acid (30°C) | 0.55 | 0 | 0.16 | — |
| | | 250 | 0.22 | 0.06 |
| | | 500 | 0.24 | 0.08 |
| | | 1000 | 0.24 | 0.08 |

*Test performed at TRW Thermophysical Laboratory

**Table 4. Effect of Bleaching on Oxalic and Sulfuric Acid Anodized Aluminum**

| Anodized electrolyte (temperature) | Exposure time (ESH) | Solar absorptance | |
|---|---|---|---|
| | | In vacuum | In air |
| Oxalic acid (30°C) | 0 | 0.225 | 0.228 |
| | 1000 | 0.249 | 0.240 |
| Oxalic acid (50°C) | 0 | 0.199 | 0.201 |
| | 1000 | 0.365 | 0.351 |
| Surfuric acid (30°C) | 0 | 0.242 | 0.238 |
| | 1000 | 0.307 | 0.291 |

Note: Exposing samples to air after they were exposed to UV radiation in vacuum

**Table 5. Abrasion Resistance of Oxalic and Sulfuric Acid Anodized Aluminum**

| Wheel revolutions | Sulfuric acid anodized Al (30°C) weight loss (g) | Oxalic acid anodized Al (30°C) weight loss (g) | Oxalic acid anodized Al (50°C) weight loss (g) |
|---|---|---|---|
| 0 | 0.0000 | 0.0000 | 0.0000 |
| 200 | 0.0015 | 0.0044 | 0.1542 |
| 450 | 0.0020 | 0.0050 | 0.1548 |
| 600 | 0.0030 | 0.0053 | 0.1624 |
| 3000 | 0.0174 | 0.0075 | Bare metal |

Note: Coating thickness of 0.40 mil; Teledyne Taber abraser conditions: load of 1 kg, CS17 wheel, 70 rpm

449

```
┌─────────────────────────────┐
│ Vapor Degrease              │
│ 1, 1, 1 — Trichloroethane   │
└─────────────────────────────┘
              ↓
┌─────────────────────────────┐
│      Anodic Strip           │
│      H₃PO₄/CrO₃             │
└─────────────────────────────┘
              ↓
┌─────────────────────────────┐
│          Rinse*             │
└─────────────────────────────┘
              ↓
┌─────────────────────────────┐
│       Bright Dip            │
│       H₃PO₄/HNO₃           │
└─────────────────────────────┘
              ↓
┌─────────────────────────────┐    ┌──────────────────┐
│          Rinse*             │◄───│  1N HNO₃         │
└─────────────────────────────┘    │  (Desmutting)    │
                                   └──────────────────┘
```

Figure 1. Flow Chart of Anodizing Steps

┌──────────────────────────┐     ┌──────────────────────────┐
│ Sulfuric Acid Anodize     │     │ Oxalic Acid Anodize       │
│ 15% Solution, 30 °C       │     │ 15% Solution, 30 °C       │
└──────────────────────────┘     └──────────────────────────┘

┌─────────────────────────────┐
│          Rinse*             │
└─────────────────────────────┘

*With Deionized Water

┌─────────────────────────────┐
│      Water Seal*            │
│      at 100 °C, 15'         │
└─────────────────────────────┘

┌─────────────────────────────┐
│    Air Dry at Ambient       │
└─────────────────────────────┘
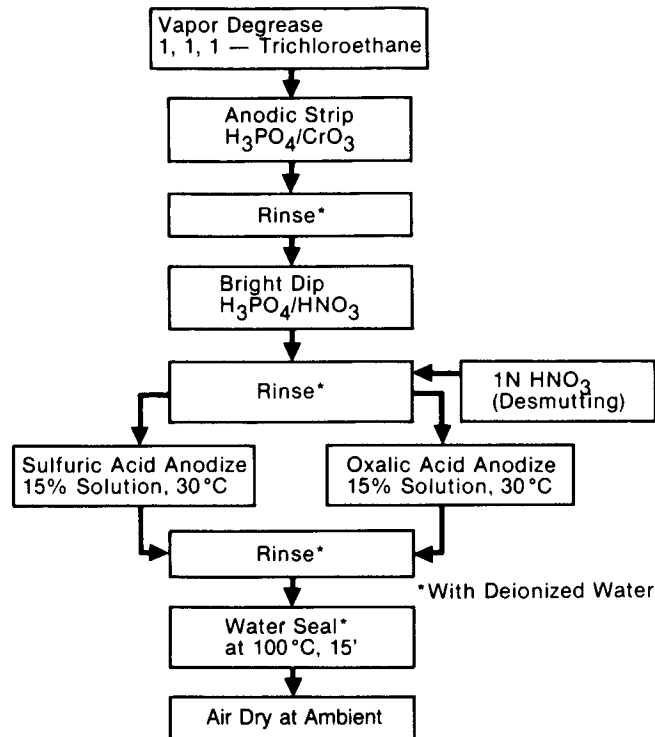
**Figure 1. Flow Chart of Anodizing Steps**

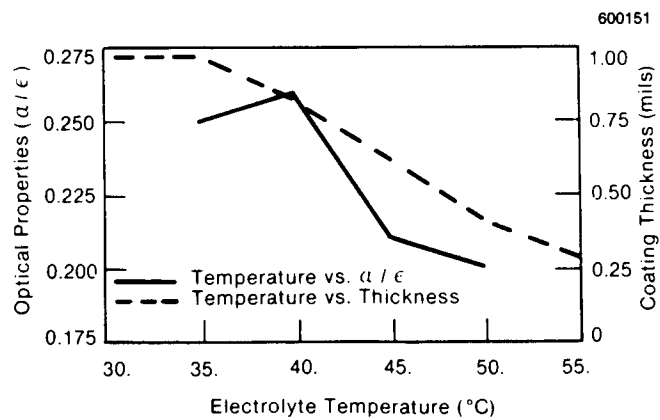Figure 2. Effects of Electrolyte Temperature on the Optical Properties and Maximum Coating Thickness of Oxalic Acid Anodizing (at 15% Oxalic Acid and 10 A/sq ft)
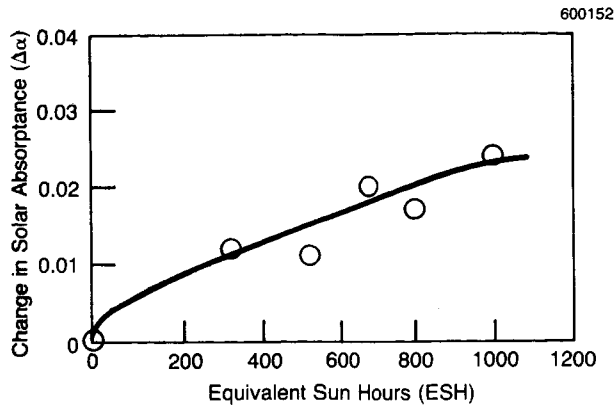
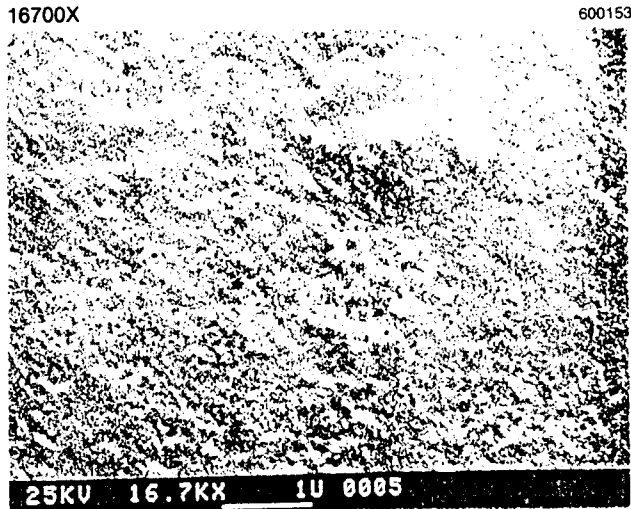Figure 3. Change in Solar Absorptance vs Equivalent Sun Hours Exposed for Oxalic Acid Anodized Sample

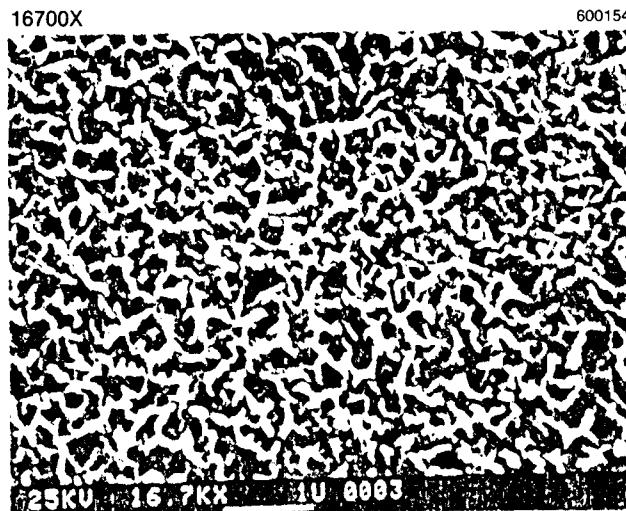Figure 4. Surface Morphology of Oxalic Acid Anodized Coating Produced at 30°C

Figure 5. Surface Morphology of Oxalic Acid Anodized Coating Produced at 50°C

451

# MOISTURE INTERACTION AND STABILITY OF
# ZOT THERMAL CONTROL SPACECRAFT COATING*

Gordon R. Mon, Charles C. Gonzalez, Ronald G. Ross, Jr.,
Liang C. Wen, and Timothy O'Donnell
Jet Propulsion Laboratory

## ABSTRACT

Two of many performance requirements of the zinc orthotitanate (ZOT) ceramic thermal control paint covering parts of the Jupiter-bound Galileo spacecraft are that it be sufficiently electrically conductive so as to prevent electrostatic discharge (ESD) damage to onboard electronics and that it adhere to and protect the substrate from corrosion in terrestrial environments. The bulk electrical resistivity of ZOT on an aluminum substrate was measured over the ranges $22^{\circ}C$ - $90^{\circ}C$ and 0%RH - 100%RH and also in soft ($10^{-2}$ Torr) and hard ($10^{-7}$ Torr) vacuums. No significant temperature dependence was evident, but measured resistivity values ranged over 9 orders of magnitude: $10^5$ ohm-cm @ 100%RH; $10^{10}$ ohm-cm @ 0%RH; > $10^{12}$ ohm-cm in a hard vacuum. This latter value violates the ESD criterion for a typical 0.019 cm. thick coating. The corrosion study involved exposing typical ZOT/substrate combinations to two moisture environments--$30^{\circ}C$/85%RH and $85^{\circ}C$/85%RH--for 2000 hours, during which time the samples were periodically removed for front-to-back electrical resistance and scratch/peel test measurements. It was determined that ZOT/AL and ZOT/MG systems are stable (no ZOT delamination) although some corrosion (oxide formation) and resistivity increases observed among the ZOT/MG samples warrant that exposure of such parts to humid environments be minimized.

## INTRODUCTION

Two important in-flight performance functions of spacecraft paints and coatings are (1) to passively control spacecraft temperatures (requiring low and stable solar absorptance to emittance ratios) and (2) to maintain external surfaces at $\pm$ 10 volts equipotential in order to (a) prevent electronics-disrupting static discharge events and (b) minimize the effects of spacecraft surfaces on the charged particle environment. The Galileo Project ESD criterion is as follows:

$$\rho_V * t < 2 \times 10^{10} \text{ ohm-cm}^2 \tag{1}$$

where $\rho_V$ is the paint bulk resistivity and t is the paint thickness.

Because of launch delays following the Challenger tragedy, another property of the paint has recently received considerable attention--namely, the effects on it of long-term exposure to terrestrial storage environments: will the paint protect the substrate from corrosion without itself delaminating and will the paint maintain its desirous electrical conduction properties until launch and, indeed, for the duration of the mission? To answer these questions and to test the ESD criterion for ZOT paint, we first measured the bulk electrical resistivity of ZOT paint on an aluminum substrate and then determined the effects on the ZOT paint of long-term exposure to a moist environment.

## MATERIAL DESCRIPTION

In the 1970's IITRI reported on the development of an inorganic thermal control coating, formulation designation YB-71, which uses a zinc orthotitanate pigment with a potassium silicate binder (designated PS7 by Sylvania Electric Products Corporation) (refs. 1, 2). This coating is herein referred to as ZOT paint, or ZOT. Further details on ZOT processing and material characteristics can be found in a paper by Harada and Mell (ref. 3). ZOT resistivity has been reported (refs. 2-4) as being nominally $10^8$ ohm-cm. However, test details and test environments are generally lacking. Lockerby, et al. (ref. 4), measured nominal resistivity values of $10^{12}$ ohm-cm for ZOT on aluminum but discounted the validity of this measurement in favor of a measured $10^7$ ohm-cm value for ZOT on fiberglass.

## ZOT RESISTIVITY MEASUREMENTS

In this section we report measured bulk resistivity values of ZOT paint in humid air and in vacuum. We also establish that lateral ionic conduction through ZOT paint can be explained in terms of bulk conduction--i.e., using measured bulk conductivity values to calculate lateral conductance yields lateral conductance values of the same order of magnitude as was observed by direct measurement.

All JPL ZOT samples were prepared in accordance with an internal Fabrication Specification FS511315.

### Bulk Resistivity

Bulk electrical resistivity of ZOT paint was measured for eight samples consisting of 0.019 cm of ZOT paint applied to 5 cm x 10 cm x 0.16 cm aluminum (6061-T6) substrates. Resistivity measurements were sequentially made in the following nominal environments:

     (1) $30^\circ C/50\%RH$;
     (2) $30^\circ C/85\%RH$;
     (3) $85^\circ C/50\%RH$;
     (4) $85^\circ C/85\%RH$;
     (5) $20^\circ C$ and $60^\circ C$ "soft" vacuum ($3 \times 10^{-2}$ Torr); and
         $20^\circ C$ - $50^\circ C$ "hard" vacuum ($10^{-7}$ Torr).

Chamber equilibrium was achieved within two hours of initiation of the environment. Achievement of sample equilibrium with the environment may require considerably more time. Accordingly, samples were measured in the same environment over a period of at least 26 hours and, in some cases, longer. Every 30 minutes data were acquired over two minute intervals.

The bulk resistivity of ZOT paint was determined by establishing a uniform electrical field across the ZOT paint in the direction of its thickness. This was achieved by applying voltage to the sample aluminum substrate, serving as the positive electrode, and collecting the measurement current at the ZOT surface by means of a cylinder-and-guard-ring electrode system consisting of a conductive elastomeric rubber mounted at the end of a moveable core of a pneumatic solenoid that can be forced into intimate contact with the ZOT surface when it is desired to make a measurement. The applied voltage and the voltage drop across a known precision resistor in series with the sample are measured and the sample resistance and its bulk resistivity are determined from the following formulas:

$$R_{ZOT} = R_k*(V_P - V)/V \tag{2}$$

$$pV = R_{ZOT}*(PI*r^2/t) \tag{3}$$

where

$$t = \text{paint thickness, 0.019 cm}$$
$$r = \text{electrode radius, 0.333 cm}$$
$$R_k = \text{precision resistance, ohm}$$
$$V_p = \text{applied voltage, volts}$$
$$V = \text{voltage across } R_k, \text{ volts}$$
$$R_{ZOT} = \text{bulk resistance of ZOT, ohm}$$
$$P_V = \text{bulk resistivity of ZOT, ohm-cm}$$

A schematic of the measurement set-up is depicted in figure 1.

## Lateral Resistance

In order to measure lateral resistance through ZOT paint, samples were fabricated consisting of a concentric metal electrode system (0.03 um Ti/0.30 um Al) vacuum evaporated onto a borosilicate glass (Pyrex 7740) surface to which 0.019 cm of ZOT paint was then applied. Glass-only samples (no ZOT) were first measured to quantify contributions from the glass (ref. 5); then the ZOT/glass samples were measured. A schematic of the measurement set-up is depicted in figure 2.

Measurements were made at essentially the same nominal environments following essentially the same measurement procedures as for the bulk measurements but with the exception that voltage was continuously applied to these samples. Positive polarity voltage was applied to the large central interfacial electrode; current was collected at the concentric ring electrode. The lateral resistance is determined from the measured applied voltage and the measured voltage drop across the precision resistor using

$$R_T = R_k*(V_p - V)/V \tag{4}$$

where $R_T$ is the lateral interelectrode resistance; it is composed of several terms including:

(1) ZOT/glass lateral interface resistance; (2) ZOT lateral bulk resistance; (3) interface-to-surface ZOT bulk resistance; and (4) ZOT surface resistance terms. Determining surface and interface resistance from lateral and bulk resistance measurement data requires complex analytical models. Rather, we shall compare the measured lateral interelectrode resistance $R_T$ with the lateral resistance calculated using bulk resistivity values obtained from the "bulk measurement" data, using

$$R_c = p_V * \ln(r_2/r_1)/2 * PI * t \qquad (5)$$

where

$$
\begin{aligned}
r_1 &= \text{electrode radius, 3.651 cm} \\
r_2 &= \text{guard ring radius, 3.810 cm} \\
R_c &= \text{calculated lateral resistance,} \\
&\quad \text{ohms.}
\end{aligned}
$$

See figure 2 for measurement details.


**Test Results**


ZOT paint bulk resistivity data, obtained from the measurements on four samples at several oven temperature/humidity setpoints, are presented in figure 3, together with the best linear regression line through the data. Note that ZOT bulk resistivity varies by five orders of magnitude over the full range of relative humidity; little or no temperature sensitivity was observed. In other words, the bulk resistivity of ZOT paint exhibits almost no sensitivity to temperature variation in the range of the measurements ($20^\circ C$ to $85^\circ C$) but exhibits enormous sensitivity to moisture in the ambient air.

ZOT bulk resistivity data obtained in vacuum are also presented in figure 3. As a result of a 100hr/$100^\circ C$ bakeout the ZOT bulk resistivity in a $10^{-2}$ Torr vacuum increased from $3.5 \times 10^{10}$ ohm-cm at $22^\circ C$ and $1.6 \times 10^{11}$ ohm-cm at $60^\circ C$ to about $3 \times 10^{12}$ ohm-cm. ZOT bulk resistivity data gathered in a $10^{-7}$ Torr vacuum are also presented in figure 3; values as high as $10^{14}$ ohm-cm were measured.

The ESD acceptability criterion, equation (1), is violated for 0.019 cm thick ZOT if $p_V > 1 \times 10^{12}$ ohm-cm. The hard vacuum measurements flag possible concerns that ZOT paint may not be sufficiently conductive to provide its intended ESD function in the hard vacuum of space; the plasma (ionizing radiation) environment of Jupiter, however, is expected to provide compensation.

Lateral ("surface") resistivity of the ZOT/glass samples, determined from measurement data on three samples, is presented in figure 4 together with the lateral resistivity calculated using bulk resistivity values determined from the "bulk measurement" data. The values determined from the bulk data agree quite well with the directly measured values. We infer from this that lateral conduction in ZOT paint is bulk-dominated, i.e., surface and inter-

face resistances are of the same or larger order of magnitude than the lateral bulk resistance.

As a point of information, the bulk resistance data was obtained 3 - 10 minutes after the application of sample voltage; this interval between the application of the voltage and acquisition of the data may not have been sufficiently long in some cases to allow current transients to dissipate. Two typical cases are presented in figure 5, showing that at 22°C/40%RH the 10-minute reading may differ from the equilibrium value by more than a factor of 5; whereas at 85°C/5%RH the variation between the 10- and 1000-minute readings is less than a factor of 2. This effect is less pronounced at lower sample moisture content levels and is typically less than the measurement scatter noted in figure 3.

## AGING STUDIES ON ZOT PAINT

In this section we present the results of investigating the effects on coating/substrate combinations of long term exposure to moist environments. ZOT/AL, ZOT/MG, and ZOT/SIKKENS/GOLD-PLATE/MG (ZSGM - "SIKKENS" is a black thermal control paint) samples were aged, i.e., exposed for long periods of time to constant temperature/humidity environments--30°C/85%RH and 85°C/85%RH--as indicated in table 1. The samples were periodically removed from the exposure environments for scratch/peel testing, visual observations of degradation, and total front-to-back electrical resistivity (effective bulk resistivity of the ZOT coating) measurements.

### Scratch/Peel Test Results

The scratch/peel tests were conducted in conformance with ASTM test standards (ref. 6):
"An X-cut is made in the film to the substrate, pressure-sensitive tape is applied over the cut and then removed, and adhesion is assessed qualitatively on the 0 to 5 scale...

5A  No peeling or removal
4A  Trace peeling or removal along incisions
3A  Jagged removal along incisions up to 1/16 in. on either side
2A  Jagged removal along most of incisions up to 1/8 in. on either side
1A  Removal from most of the area of the X under the tape
0A  Removal beyond the area of the X"

Observed post-exposure degradation and pre- and post-exposure scratch/peel test results are listed in the last two columns of table 1.

### Visual Observations

The ZOT/AL samples exhibited only minor visible degradation and no loss of adhesion of the ZOT to the aluminum. The same is essentially true for the ZOT/MG samples, although for these samples some limited edge delamination of

456

the ZOT coating and the formation of an interface oxide layer was observed. The ZSGM samples faired poorly--samples exposed to the 30°C/85%RH environment exhibited localized spots of ZOT delamination, while those samples in the 85°C/85%RH environment degraded so much that they were removed from the aging chamber after only 95.5 hours of exposure. The ZOT surfaces on these samples were extensively pock-marked with what appeared to be oxide bits of the magnesium substrate that had upwelled through the coating at many locations, a phenomenon known as "magnesium flowering", figure 6. In addition, delamination of the coating at the Sikkens/gold interface was common.

## Electrical Resistance Measurements: Substrate Corrosion

Electrical resistance data were acquired at room ambient conditions. The resistance measured was that between the exposed ZOT surface and the underside of the substrate. The measured resistance values include contributions from the ZOT paint layer and interfacial oxide (corrosion product) layers, if any; we refer to the measured value as the effective coating resistance. Effective coating resistivity (calculated using the thickness of the ZOT paint) is plotted against time-of-exposure for ZOT/AL, ZOT/MG, and ZSGM, respectively, in figure 7.

The ZSGM system is comparatively the most resistive. The rate of corrosion of ZSGM in an 85°C/85%RH environment is significantly greater than in a 30°C/85%RH environment. The ZOT/AL and ZOT/MG systems are initially equally resistive, but upon exposure to steady temperature/humidity environments, the ZOT/AL systems become somewhat less resistive, while the ZOT/MG systems become somewhat more resistive. When account is taken of the large variation of ZOT resistivity with moisture content (five orders of magnitude: figure 3), the spread of the 2000-hr data and the relatively small changes in resistivity with aging (about one order of magnitude or less: figure 7), it is not unreasonable to conclude that the ZOT/AL systems exhibit essentially no resistivity change after 2000 exposure hours, but that the ZOT/MG systems do exhibit an increase in effective resistivity. The actually observed small decrease in resistivity of the ZOT/AL systems is attributed to excess moisture in the ZOT paint: the time between removal of the samples from the environments and measurement of their resistances--about 24 hours--was perhaps insufficient to allow the samples to achieve moisture equilibrium with the room ambient. On the other hand, the increase in resistance of the ZOT/MG samples has been confirmed as due to the formation of high resistance magnesium oxides at the ZOT/MG interface.

Aluminum forms a thin protective oxide layer which we believe retards the formation and build-up of reaction product. The magnesium substrate, on the other hand, is chemically less stable when in contact with moisture (sorbed in the ZOT)--the build-up of resistive reaction product dominates the resistance properties of the ZOT/MG system.

Additional post-exposure resistance measurements were made on selected samples to determine which layers were dominating the overall front-to-back resistance measurement. This was done by scraping away the ZOT and exposing the substrate at a corner of the samples. Thus resistance measurements between the ZOT surface and the corroded and freshly exposed substrate could be made. For the ZOT/AL samples, the measured resistances were those of the bulk ZOT. It was verified that the increasing resistance of the ZOT/MG sys-

tems is attributable to the formation and growth of a magnesium oxide layer between the ZOT and the magnesium substrate. The curious fact that the effective resistivity of the ZSGM systems was almost two orders of magnitude higher than that of the other systems was also verified by this means.

The ZOT in the ZSGM systems actually measured higher for resistivity than did the ZOT in the other systems--irrespective of substrate materials. This may suggest a different coating morphology for ZOT on Sikkens/Au-plate/Mg than for ZOT on aluminum or even on magnesium by itself.


## MOISTURE DESORPTION


The moisture desorption behavior of ZOT paint in a soft vacuum ($3 \times 10^{-2}$ Torr) at room temperature has been measured using a Cahn Electrobalance. The procedure followed was to first determine the desorption behavior of ZOT/GLASS samples and then of GLASS samples alone. By subtraction, the desorption behavior of ZOT paint was deduced. The data indicate that ZOT paint will lose most of its physically sorbed moisture within an hour after injection into space.

Figure 8 exhibits typical weight-time response to forepump vacuum application. There is an initial jump in weight due to buoyancy--a mass weighs more in vacuum than it does in air--followed by an approximately exponential loss of weight due to desorption of volatiles, assumed to be moisture. Also plotted in figure 8 is the pressure vs. time profile as measured in the Cahn Balance chamber during a typical data acquisition run. Most of the air is lost almost immediately, but the sample weight loss is a more gradual exponentially decreasing function of time. Figure 8, therefore, approximates the sample weight response to a step change in ambient pressure.

The buoyancy, $B_e$, is obtained from experimentally measured data using the equation $B_e = W_1 - W_o$, where $W_1$ is the initial weight after forepump vacuum is achieved, and $W_o$ is the initial weight in air.


## Desorption


The large loss of sample weight upon initial vacuum application (approximately the first minute) is due to desorption of loosely (physically) bonded surface moisture. The remainder is due in small part to some desorption of chem-adsorbed moisture and in larger part to the diffusion to the surface and desorption of loosely sorbed moisture.

The total weight of desorbed moisture, $W_m$, is given by the equation $W_m = W_1 - W_2$, where $W_2$ is the equilibrium vacuum weight. The sample dry weight, $W_d$, is determined from the equation $W_d = W_2 - B$. The desorption D, as reported in table 2 is given, in mg/gm, by $D = W_m/W_d$.

## Data and Results

Sorption data and results for ZOT paint are presented in table 2. Each gram of ZOT loses at least 13 mg of moisture in the vacuum of space; or in terms of area, each $cm^2$ of ZOT surface loses at least 0.4 mg of moisture (for a 0.019 cm coating thickness).

As can be seen from figure 8, most of the moisture desorbed from the ZOT is freed within a few minutes after vacuum application. Very little desorption occurs after just a few hours. Therefore, we conclude that ZOT paint will lose most of its physically sorbed moisture content shortly after being injected into the space environment, and will experience a corresponding increase in resistivity.

As a final note, it was observed that the moisture sorption process was reversible--i.e., after testing, the test samples fully recovered the moisture that had been desorbed.


## SUMMARY AND CONCLUSIONS


The important bulk resistivity measurement data are summarized as follows: the bulk resistivity of ZOT paint exponentially increases by five orders--of-magnitude as the ambient relative humidity decreases from 100%RH to 0%RH; in vacuum, the bulk resistivity of ZOT paint continues to rapidly increase as its moisture content decreases, from $10^{10}$ - $10^{11}$ ohm-cm @ $3x10^{-2}$ Torr up to $10^{12}$ - $10^{14}$ ohm-cm @ $10^{-7}$ Torr. ZOT paint is hygroscopic and its low resistivity in ambient conditions is due to moisture-induced ionic conductivity (not unlike the behavior of classical humidity sensors).

ZOT/AL was observed to be a chemically stable system--the ZOT appears to be tenaciously attached to the aluminum substrate. In ZOT/MG systems, the substrate magnesium exhibits a greater tendency to corrode than does the substrate aluminum in ZOT/AL systems, but ZOT/MG is substantially more durable than the ZSGM systems tested. The ZSGM system is questionable on two accounts: (1) in humid terrestrial environments, the substrate corrodes and disrupts the ZOT surface layer (the galvanic Au-Mg couple may contribute substantially to the corrosion of this system); and (2) in a space vacuum environment, its resistivity, like that of ZOT on aluminum, may be too high to satisfy the Galileo mission ESD constraint.

## REFERENCES

1. G. Zerlaut, J. Gilligan, N. Ashford, "Space Radiation Environmental Effects in Reactively Encapsulated Zinc Orthotitanates and their Paints", Paper No. 71-449, **AIAA 6th Thermophysics Conference**, Tullahoma, TN, April 1971.

2. Y. Harada, D. Wilkes, "Inorganic $Zn_2TiO_4$ Thermal-Control Coatings", 24/2, **24th National SAMPE Symposium**, p. 936, 1979.

3. Y. Harada, R. Mell, "Inorganic Thermal Control Coatings - A Review", Paper No. 83-0074, **21st Am. Inst. Aero. & Astro. Aerospace Sciences Meeting**, Reno, NV, Jan 1983.

4. S. Lockerby, M. Barsh, D. Mossman, "ZOT - A White Thermal Control Coating for Space Environment: Considerations", **Proceedings of the 14th National SAMPE Technical Conference.**, Atlanta, GA, Oct. 1982, pp. 49-57.

5. G. Mon, L. Wen, R. Ross, Jr., "Encapsulant Free-Surfaces and Interfaces: Critical Parameters in Controlling Cell Corrosion", **Proceedings of the 19th IEEE Photovoltaic Specialists Conference**, May 1987.

6. ASTM D 3359-83: Standard Methods for Measuring Adhesion by Tape Test.

```
-----------------------------------------------------------------
                            Table 1
                     Aging Data, ZOT Paint
_____

                                                        Scratch
                                                        Test
SAMPLE    Time @          Time @          Observed      Results
          30°C/85%RH      85°C/85%RH      Degradation   (1)   (2)
          (hr)            (hr)
_____

ZOT/AL    1969                            None.         4A    3A

ZOT/AL                    1969            Some dis-      4A    3A
                                          coloration,
                                          yellowish
                                          blotches.
          - - - - - - - - - - - - - - - - - - - - - - - - - -
ZOT/MG    1994                            A few          3A    3A
                                          yellowish
                                          spots.

ZOT/MG                    2012            Yellowing.     4A    3A
                                          ZOT delam
                                          along edges.
                                          Blackened Mg.
          - - - - - - - - - - - - - - - - - - - - - - - - - -
ZSGM      1994                            Yellowing.     4A    3A
                                          Localized
                                          delams.

ZSGM                      95.5            Extensive      4A    0A
                                          yellowing.
                                          Mg "flowers"
                                          protruding
                                          thru coating.
          - - - - - - - - - - - - - - - - - - - - - - - - - -
(1) pre-exposure
(2) post-exposure
```

```
--------------------------------------------------------------------
                            Table 2

                   Desorption Data, ZOT Paint
_____

SAMPLE      W0      W1      W2      Be      Wm      Wd       D
           (gm)    (gm)    (gm)    (mg)    (mg)    (gm)   (mg/gm)
_____


ZOT/GLASS  4.5308  4.5341  4.5306  3.3     3.5     4.5273   .77

GLASS      5.7496  5.7522  5.7508  2.6     1.4     5.7482   .24

ZOT                                                         13.0
--------------------------------------------------------------------
```
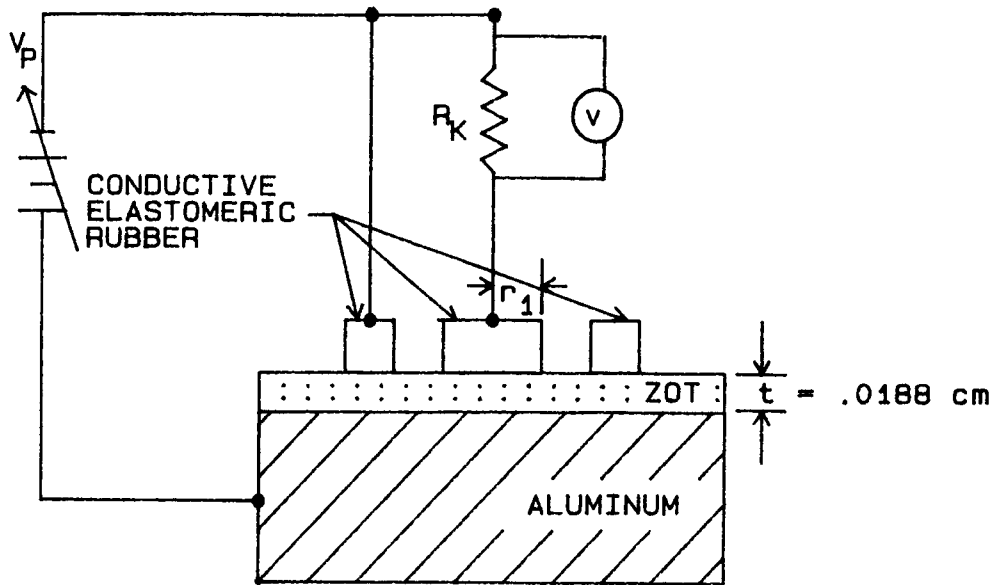
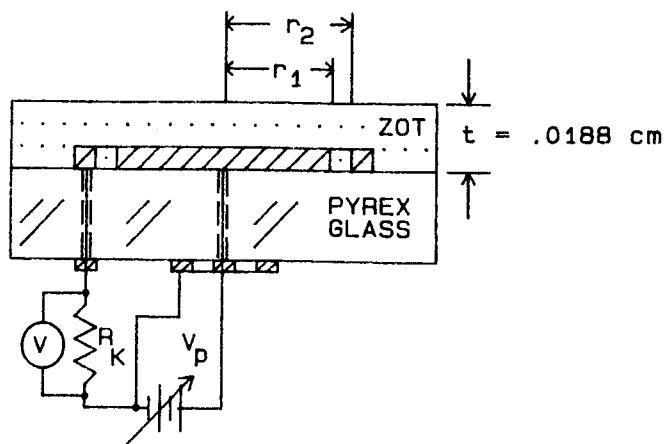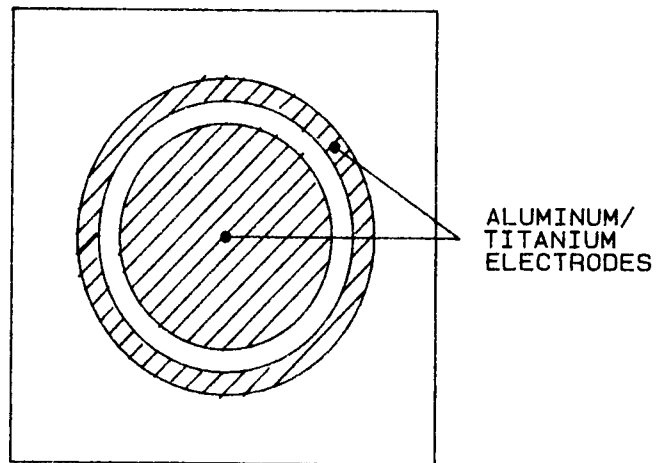Figure 1. Bulk Resistivity Measurement Schematic



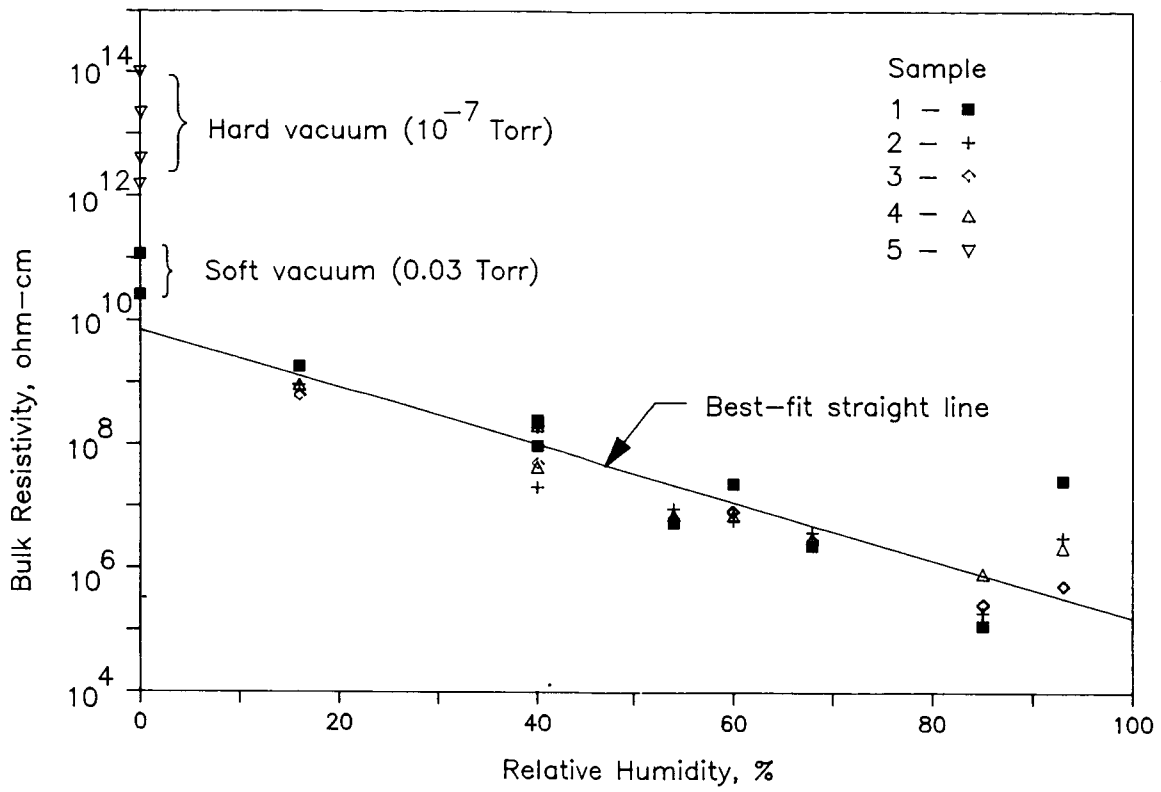Figure 2. Lateral Resistance Measurement Schematic
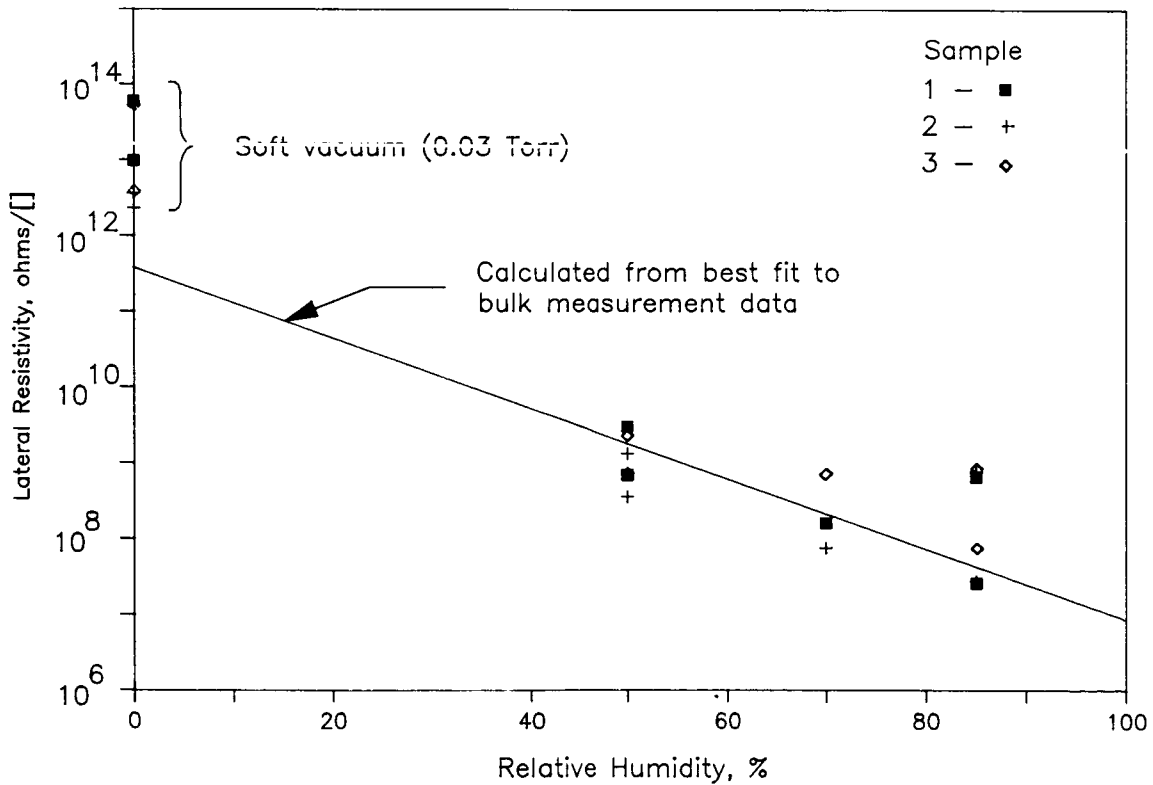
462

Figure 3. Bulk Resistivity of ZOT Paint



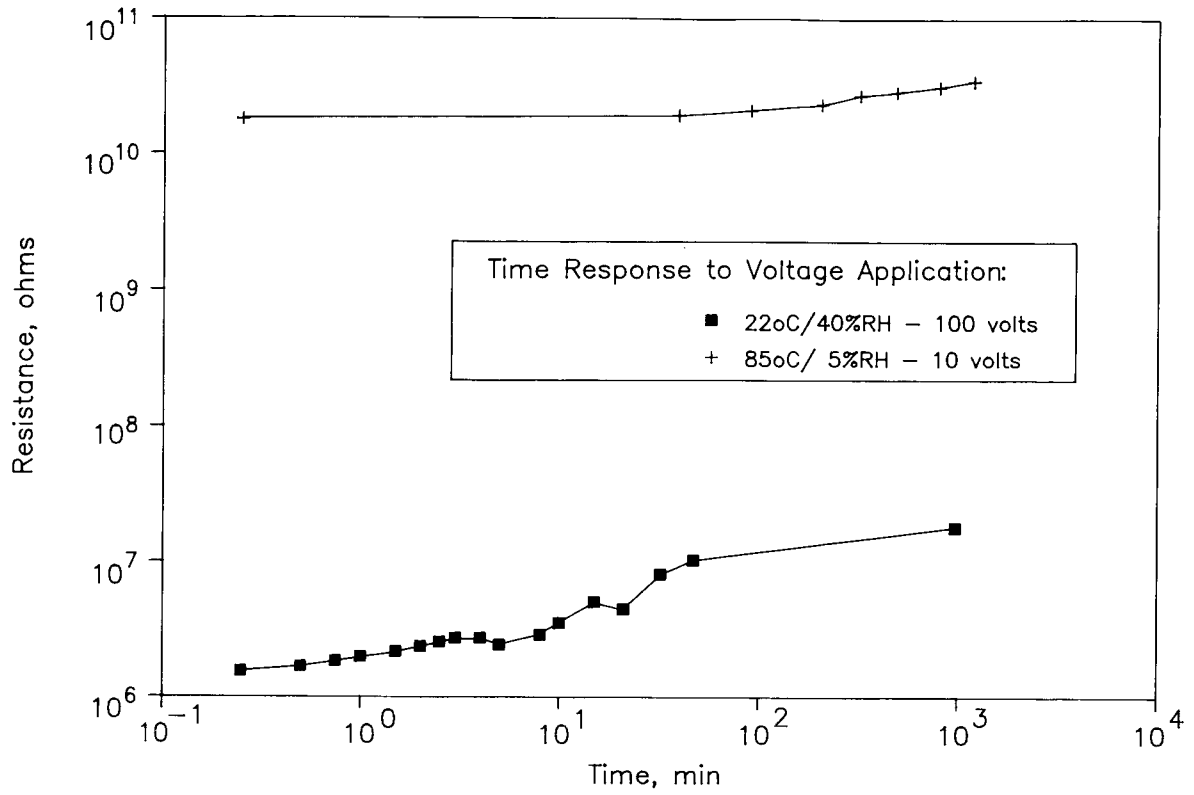Figure 4. ZOT Lateral Resistivity – Measured, and Calculated from Bulk Data

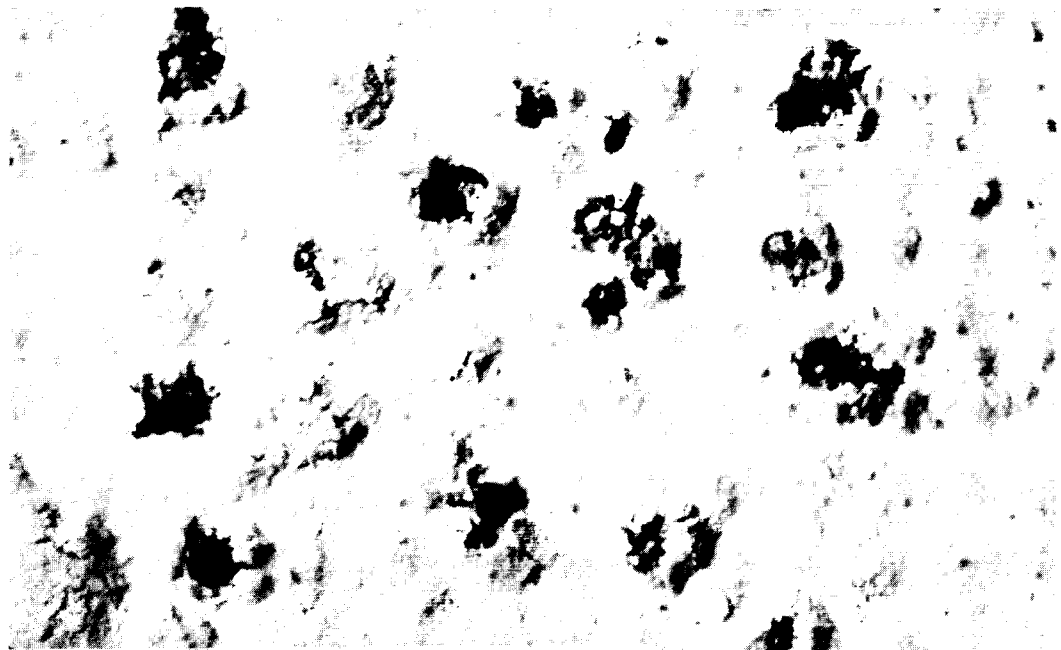Figure 5. Resistance Measurement Time Response of ZOT Paint



Figure 6. Magnesium "Flowers" Forming at Substrate and Upwelling through the ZOT Paint
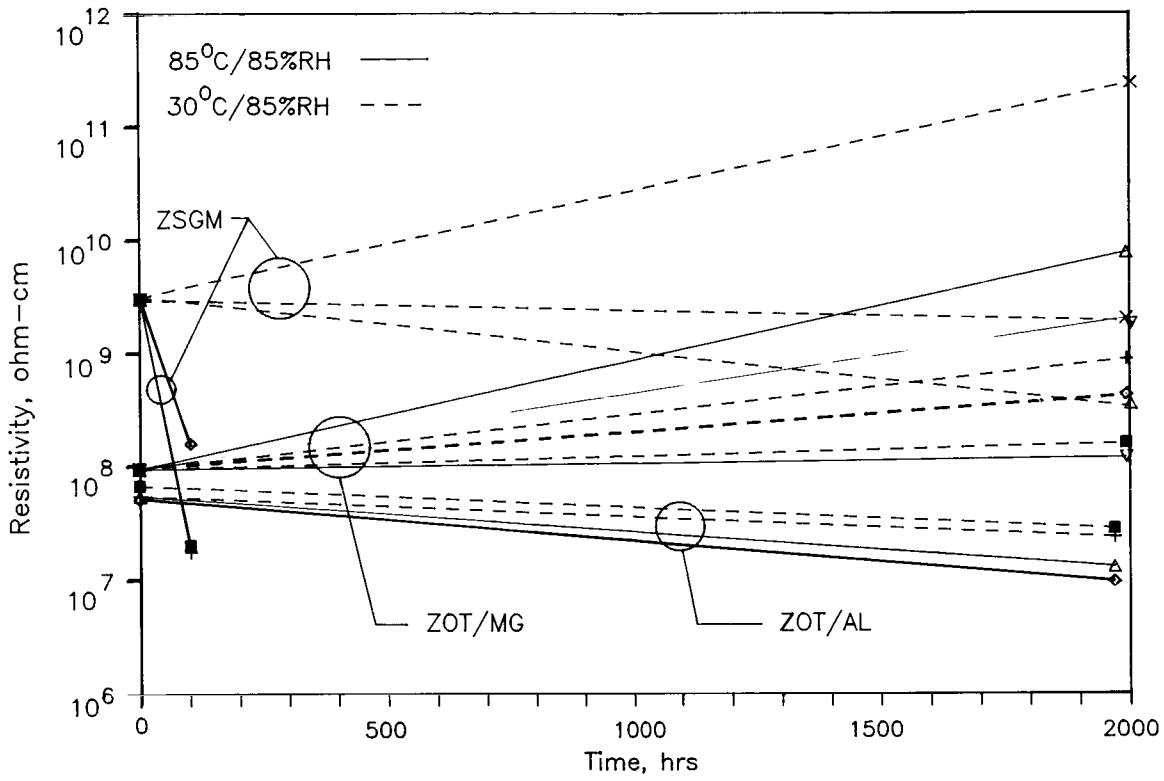
464

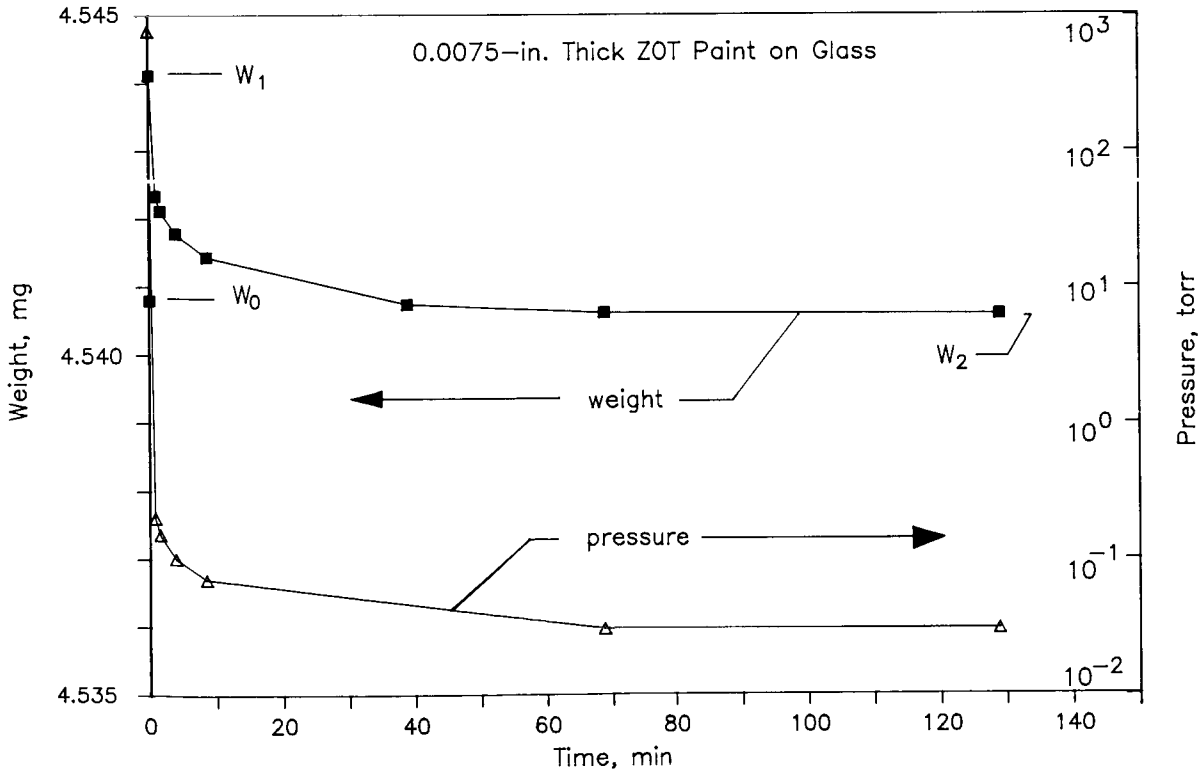Figure 7. Effective Coating Resistivity vs. Exposure Time



Figure 8. Weight Response to Vacuum Application

465

# COST EFFECTIVE ALTERNATIVE TO LOW IRRADIANCE MEASUREMENTS

Scott T. O'Leary
Martin Marietta Astronautics Group
Space Systems Company

ABSTRACT:

Martin Marietta's Space Simulation Laboratory (SSL) has a Thermal Environment Simulator (TES) with 56 individually controlled heater zones. The TES has a temperature range of approximately -129°C to +149°C (-200°F to +300°F). Because of the ability of the TES to provide complex irradiance distributions, it is necessary to be able to measure a wide range of irradiance levels. SSL currently uses ambient temperature controlled radiometers with the capability to measure sink irradiance levels of approximately 42.6 mw/cm$^2$ (135 Btu's/ft$^2$hr), sink temperature =21°C (70°F), and up. These radiometers could not be used to accurately measure the lower irradiance levels of the TES, therefore it was necessary to obtain a radiometer or develop techniques which could be used to measure lower irradiance levels.

## INTRODUCTION:

There are a number of low irradiance measurement devices available, but they are complicated and very expensive. An alternative was to use the existing radiometers by cooling them to liquid nitrogen (LN$_2$) temperatures and establishing a new output (mv) vs. irradiance mw/cm$^2$ (Btu/ft$^2$hr) curve. This was done by developing a black body source which could be used in the calibration process and a method for modeling the characteristics of the radiometer at LN$_2$ temperatures. A method for obtaining an output (mv) vs. irradiance (Btu/ft$^2$hr) calibration curve was established as well as a model of the radiometer's response to temperature fluctuations. The following information was obtained for each radiometer:

1.) An output vs. irradiance curve was generated with a maximum error of ±1.26mw/cm$^2$ (±4 Btu/ft$^2$hr) at the upper end of the irradiance curve(69.4mw/cm$^2$ (220 Btu/ft$^2$hr)) .

2.) A model of how each radiometer responds to temperature fluctuations at three fixed sink temperatures; -129°C, -20°C, 60°C (-200°F, -4°F, and 140°F).

The results demonstrate the ability to measure low irradiance levels with an acceptable error, and at a fraction of the cost of other low irradiance measurement devices.

## TEST PLAN:

A test was developed to ascertain the ability of the radiometers to measure low irradiance levels.

The test had four primary objectives:

1.) Obtain the irradiance vs. output data for fourteen P-8400 and two P-8410 radiometers, at liquid nitrogen temperatures. The black body cells were cycled between -129°C and 60°C (-200°F and 140°F). Temperatures of the black body source, the radiometer, and the radiometer's mv signal data was collected to establish the new calibration curve for the liquid nitrogen cooled radiometers.

2.) Obtain data on the response of each radiometer to temperature fluctuations. The radiometer temperature was varied between -193°C and -162°C (145°R and 200°R) at three fixed black body cell temperatures, -129°C, -20°C and 60°C (-200°F, -4°F and 140°F). Due to the difficulty of maintaining the radiometer at a constant temperature during an actual test, this information could be used to adjust the data if necessary.

3.) Compare the black body calibrated radiometer to the vendor calibrated ambient temperature radiometer data to evaluate the quality of the black body source. It was necessary to control the black body calibrated radiometer at ambient temperature while cycling the black body source. The radiometer was maintained at 26.7°C ± 3°C (80°F ± 5°F) with GN$_2$, while the sink temperature was cycled between 24°C (75°F) and 93.5°C (200°F). The data obtained from this test compared favorably to the vendor's calibration data.

4.) Three cycles were run to demonstrate repeatability and to establish confidence in the test methods used to obtain the irradiance data. The data from these cycles compared favorably.

## BLACK BODY SOURCE FIXTURE DESCRIPTION:

An ideal black body has a very simple relationship between temperature and radiated energy, $I=e(Sig)T^4$. The value of the emissivity (e) is 1, Sig is Stefan-Boltzmann's constant $0.57 \times 10^{-8} W/m^2 \cdot K (1.714 \times 10^{-7} (btu/ft^2hr)/°R^4)$, and T is the temperature of the black body source.

The black body source was built using a cylindrical body with a large length to diameter ratio. This inherently gives a high value for the emissivity. Individual cells were constructed of 0.635 cm (1/4") wall aluminum tube, 4.76 cm (1 7/8") inner diameter by 30.48 cm (12") long, (see figure #1 for sketch of black body cell). This gave the black body source a length to diameter ratio of approximately 6.4. The thickness of the tube allowed the heat being applied to the external surface of the cell to be distributed evenly on the internal radiating surface. The inside of the cells were painted with Cat-A-Lack-Black which has a published emissivity of 0.92.

This geometry inherently contibutes to a good temperature uniformity on the internal radiating surface. The walls in the cavity radiate energy to each other and therfore have a tendency to wash out any local temperature gradients on the inside of the cell.

The black body cells were mounted on a temperature controlled base plate. The base plate was used to add or remove heat from the bottom portion of the cell to reduce the temperature gradient from top to bottom of the cell. The resulting black body fixture consisted of 16 individually controlled black body cells and a temperature controlled base plate. The external fixture was painted black for effective heat radiation. Cells were individually controlled, using a Variac power supply, manually controlled. This was done to eliminate the use of contact relays which could introduce noise in the radiometer output signal.

Heaters were spiraled up the external portion of the cell with the heater tape laid edge to edge in such a way as to prevent overlapping (hot spots) or gapping (cold spots) of the heating element.

To minimize the error in the reading due to the gradient, the temperature sensors were imbedded in the body of the cell as close as possible to the internal radiating surface.

RADIOMETER INSTALLATION AND INSTRUMENTATION CALIBRATION:

A number of actions were taken to ensure proper radiometer installation:

1.) The radiometers had a view of 180°. Therefore, care was taken to ensure the receiver surface was perpendicular to the cell so that it would view only the cell. Since the receiver surface was placed 0.635 cm (1/4") into the opening of the cell, care was taken to ensure that the radiometer did not come in contact with the sides. See figure #2.

2.) An indium sheet was used as an interface between the radiometer and the tubing to provide good conduction between the radiometer and the liquid nitrogen cooled line.

3.) Each radiometer and all liquid nitrogen lines were wrapped with multi-layer insulation (MLI) to limit losses.

4.) The thermocouples used to monitor the black body fixture and radiometer temperatures were calibrated end-to-end to reduce temperature measurement error. The calibration showed that the thermocouples were within ±0.2°C for the majority of the temperature ranges in which the black body cells were cycled.

5.) A thermocouple was imbedded approximately 0.635 cm (1/4") into the surface of the radiometer, and the wire wrapped twice around the body of the radiometer and down the $LN_2$ plumbing to reduce the thermal gradients which might exist along the wire.

RESULTS:

Results are best explained graphically:

PLOT #1: Calibration Curve: This curve plots the radiometer's output against a calculated irradiance level. The irradiance was calculated using the equation $I=e(Sig)T^4$. The data was compiled and a Least Squares Fit calculated to obtain the best fit line. One can see from the high correlation coefficient and the low value for three standard deviations, that the data is linear and has a small degree of error.

PLOT #2: Calibration Curve With Error Boundaries: This curve plots the calibration curve as well as three standard deviations of the data and the largest additional error due to the recorders. The curves indicate that the maximum error expected is approximately ±1.26 mw/cm$^2$ (±4 Btu/ft$^2$hr). This is a fairly small error for the higher irradiance ranges, but leads to a large percentage error for the lower irradiance ranges. The error in the lower ranges is exaggerated because the three standard deviation calculations take into account the entire temperature range tested.

PLOT #3, #4 and #5: Millivolt Signal Fluctuations at Fixed Sink Temperatures -129°C, -20°C and 60°C (262°R, 455°R and 600°R): These curves plot the radiomater's output against its temperature, in degrees Rankine, for a fixed sink. The sink temperature was held constant while the radiometers were cycled between -195°C and -162°C (140°R and 200°R). For a given sink temperature, the different runs compared favorably.

PLOT #6: Comparison Curves: This curve compares the black body calibrated radiometer against the vendor's calibration data. The lower curve represents the calibration curve, supplied by the vendor, for an ambient temperature controlled radiometer. The higher curve represents data obtained using the black body source and a radiometer maintained at ambient temperature. These curves compare favorably. If the black body source had a poor emissivity or poorly represented an ideal black body source, the line woukd have fallen below the vendor's calibration curve. Recently, a comparison test was run using a Kendall Cavity Radiometer (considered a standard), and two of the P-8400 radiometers. In this comparison test, the same type of curve shift was noted.

ERROR SOURCES:

There are a number of factors invloved in this test which impact the data.

When cycling the sink temperature, the radiometer temperature varied. At the lower sink temperatures the radiometers had a tendency to drift cold. This may have caused the data points in the lower irradiance ranges to be on the higher mv side of the curve. For this test, the temperature of the radiometer varied approximately 5.5°C (10°R).

The mv output for a given sink temperature while ramping cold is slightly different than the mv output at the same sink temperature while ramping hot. This is caused by the radiometer's slow response to sink temperature changes. This introduces a small error in the results. Also, the inability to sample mv and temperature data at precisely the same moment introduced a small error into the results.

The mv signal introduced an error of ± 0.03% of the reading + ±0.012% of the range. This is the published maximum error of the recorder.

CONCLUSION:

The test could be refined to reduce the error in the results, but the results of this test were adequate for the needs of most program requirements. The maximum error in the irradiance vs. output curves for the radiometers was ±1.26 mw/cm$^2$ (±4 Btu's/ft$^2$hr).

An NBS traceable calibration is not available at this time. Martin Marietta plans to obtain NBS approval using this calibration method.

LESSONS LEARNED:

For future radiometer calibration tests, three changes could be implemented to improve results:

1.) A temperature sensor could be used which is more accurate in the lower temperature ranges.

2.) A pressure controlled liquid nitrogen dewar could be used to precisely control the temperature of the radiometer, thus limiting temperature fluctuations during test.

3.) Increase data point collection by stabilizing the sink temperature every 5.6°C (10°F) during temperature transitions.

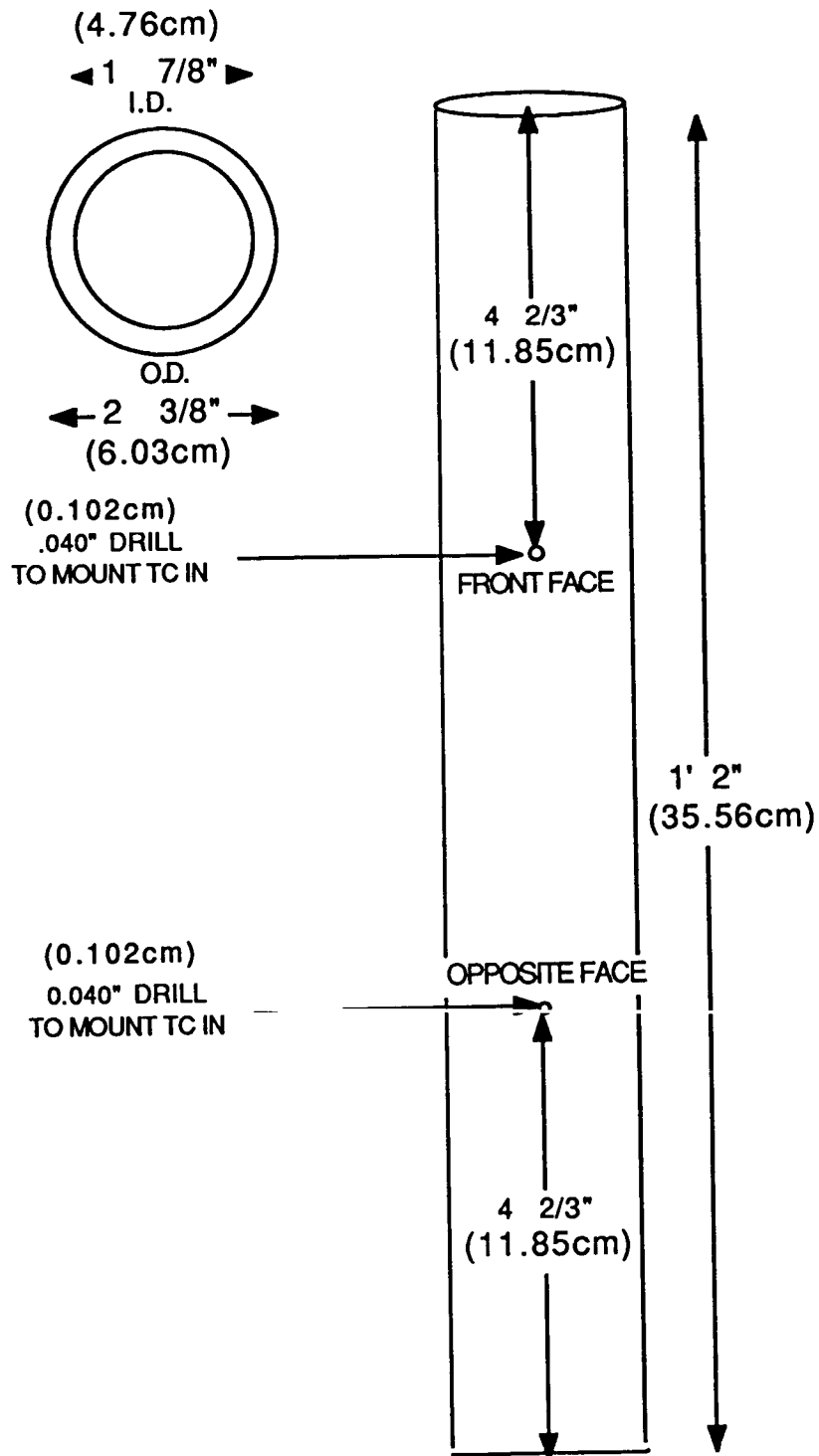(4.76cm)

◄ 1   7/8" ►
I.D.

O.D.

◄ 2   3/8" ►
(6.03cm)

(0.102cm)
.040" DRILL
TO MOUNT TC IN

FRONT FACE

4   2/3"
(11.85cm)

1' 2"
(35.56cm)

(0.102cm)
0.040" DRILL
TO MOUNT TC IN

OPPOSITE FACE

4   2/3"
(11.85cm)

FIGURE 1. BLACK BODY CELL

OFFSET X2

OFFSET XI

PERFECTLY PERPENDICULAR
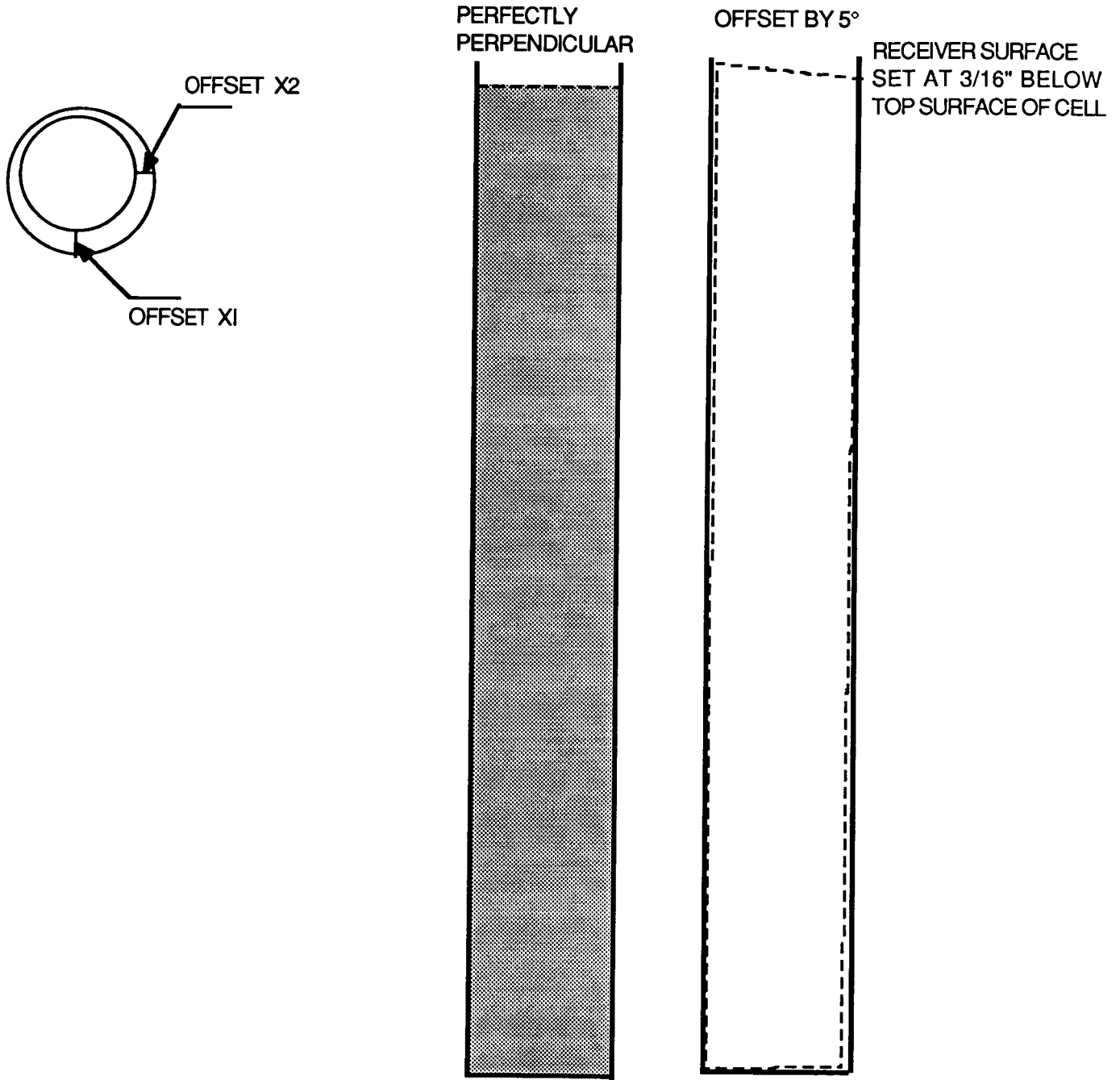
OFFSET BY 5°

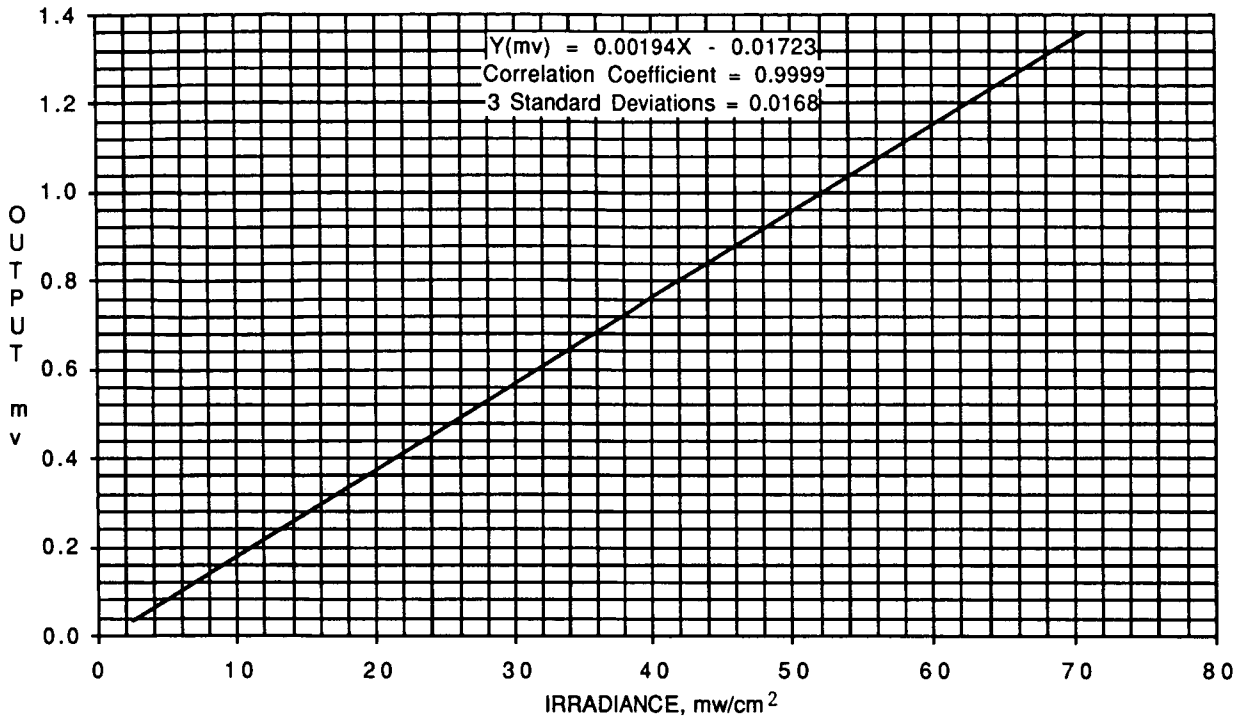RECEIVER SURFACE SET AT 3/16" BELOW TOP SURFACE OF CELL

FOR RADIOMETER WITH NO WINDOW AND A 180° VIEW ANGLE

OFFSET ANGLES OF MORE THAN 5° COULD DISTORT THE DATA DUE TO THE RADIOMETER VIEWING THE COLD WALL.

FIGURE 2. RADIOMETER TILT AND ORIENTATION

PLOT #1
CALIBRATION CURVE

Y(mv) = 0.00194X - 0.01723
Correlation Coefficient = 0.9999
3 Standard Deviations = 0.0168

OUTPUT mv

IRRADIANCE, mw/cm$^2$

PLOT #2
CALIBRATION CURVE
AND ERROR BOUNDARIES

Y(mv) = 0.00194X - 0.01723
Correlation Coefficient = 0.9999
3 Standard Deviations = 0.0168

OUTPUT mv

CALIBRATION CURVE
ERROR LOW
ERROR HIGH

IRRADIANCE, mw/cm$^2$

473
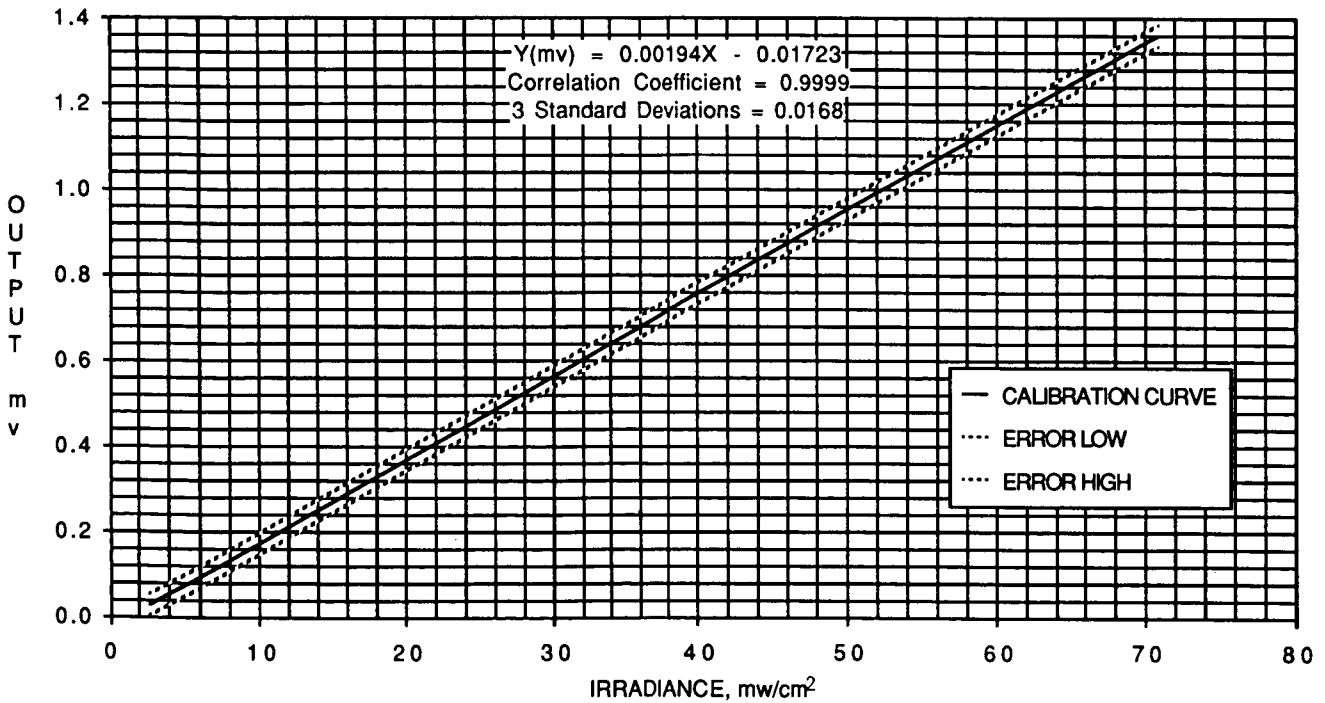
PLOT #3
COLD CASE
RADIOMETER CYCLE

SINK TEMPERATURE AT 262±6 R

- ● - 256±1 °R SINK, CYCLE 2
- ○ - 269±1 °R SINK, CYCLE 5
- ■ - 259.5±1 °R SINK, CYCLE 3

MILLIVOLTS mv

RADIOMETER TEMPERATURE, °R
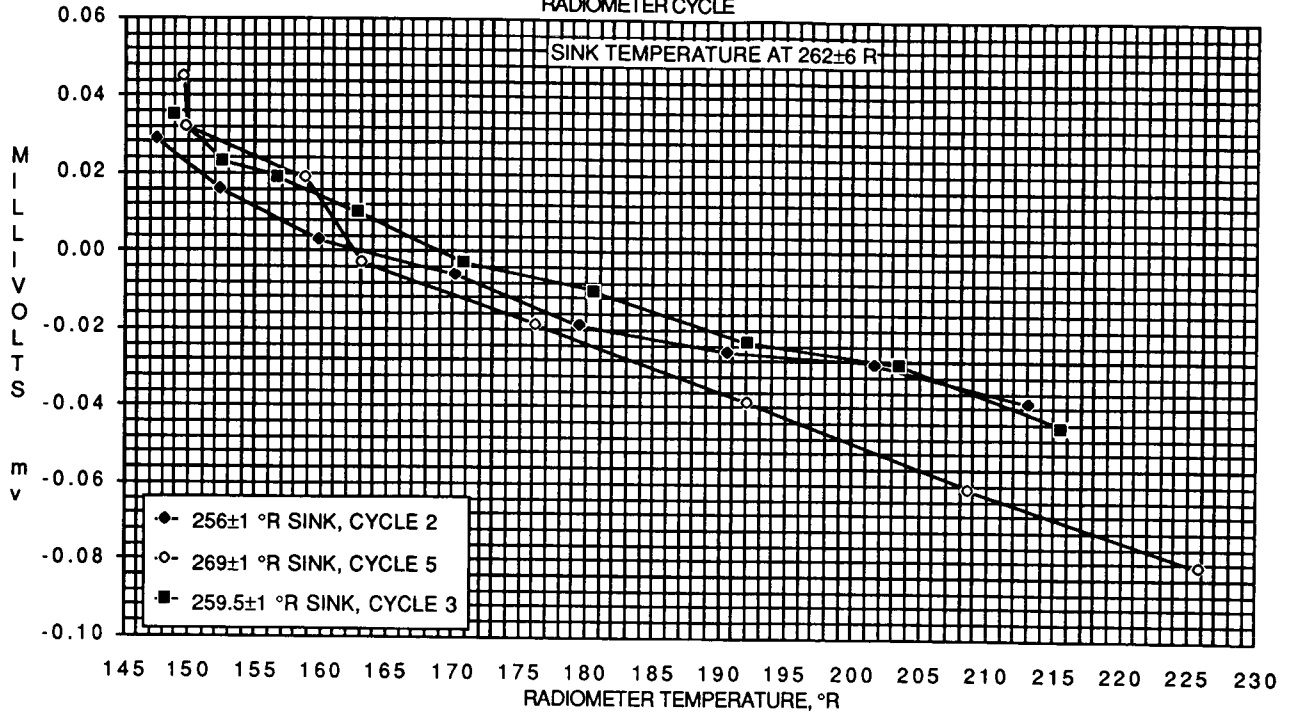
PLOT #4
MID CASE
RADIOMETER CYCLE

SINK TEMPERATURE AT 455 R ±3 R

- ● - 456 ± 1 °R SINK, CYCLE 1
- ○ - 457.5±1 °R SINK, CYCLE 2
- ■ - 456.5±1.5 °R SINK, CYCLE 3
- □ - 454 ± 1 °R SINK, CYCLE 4

MILLIVOLTS mv

RADIOMETER TEMPERATURE, °R

474
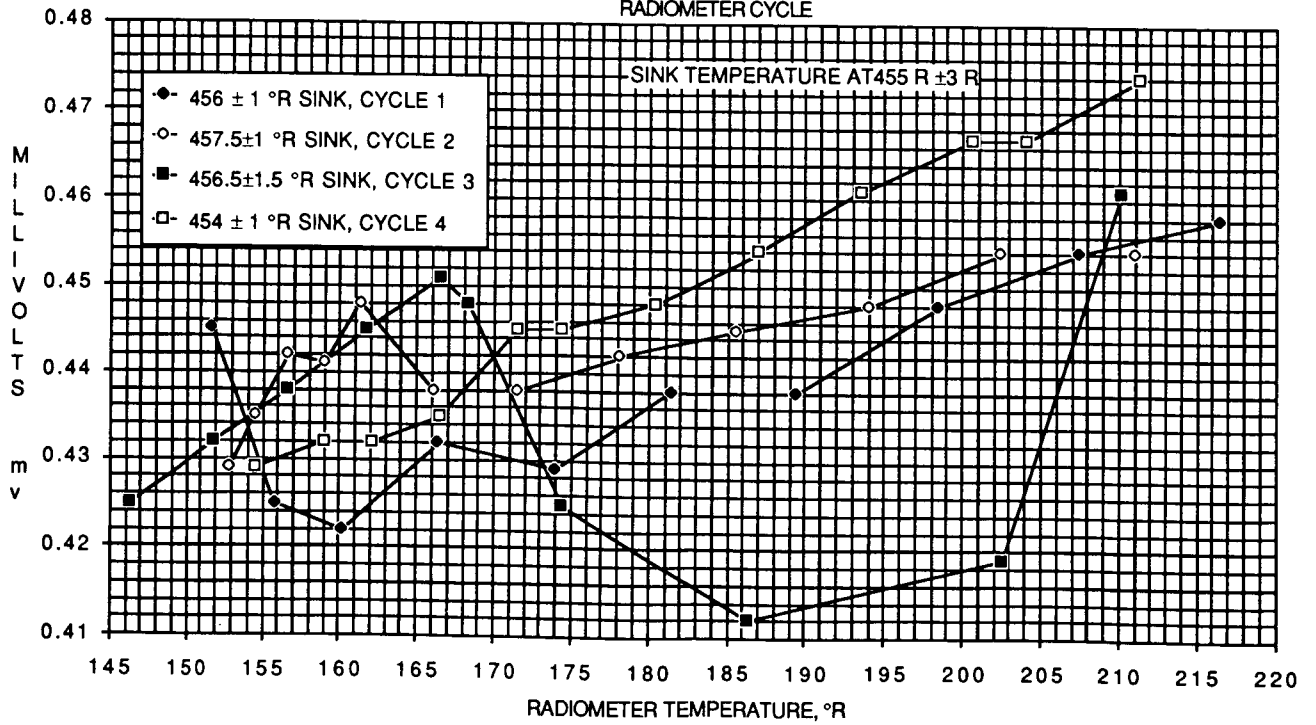
PLOT #5
HOT CASE
RADIOMETER CYCLE

SINK TEMPERATURE AT 600.5±1 °R

- ●- 600.5±0.5 °R SINK, CYCLE 1
- ○- 601±0.5° R SINK, CYCLE 2
- ■- 600±0.5 °R SINK, CYCLE 3
- □- 601±0.5 °R SINK, CYCLE 4

RADIOMETER TEMPERATURE, °R



PLOT #6
COMPARISON CURVE

Y(mv) = 0.00424X + 0.01776
Correlation Coefficient = 0.9998
3 Standard Deviations = 0.04533

-·- CALIBRATION CURVE
— BLACK BODY CURVE

IRRADIANCE, mw/cm$^2$

475
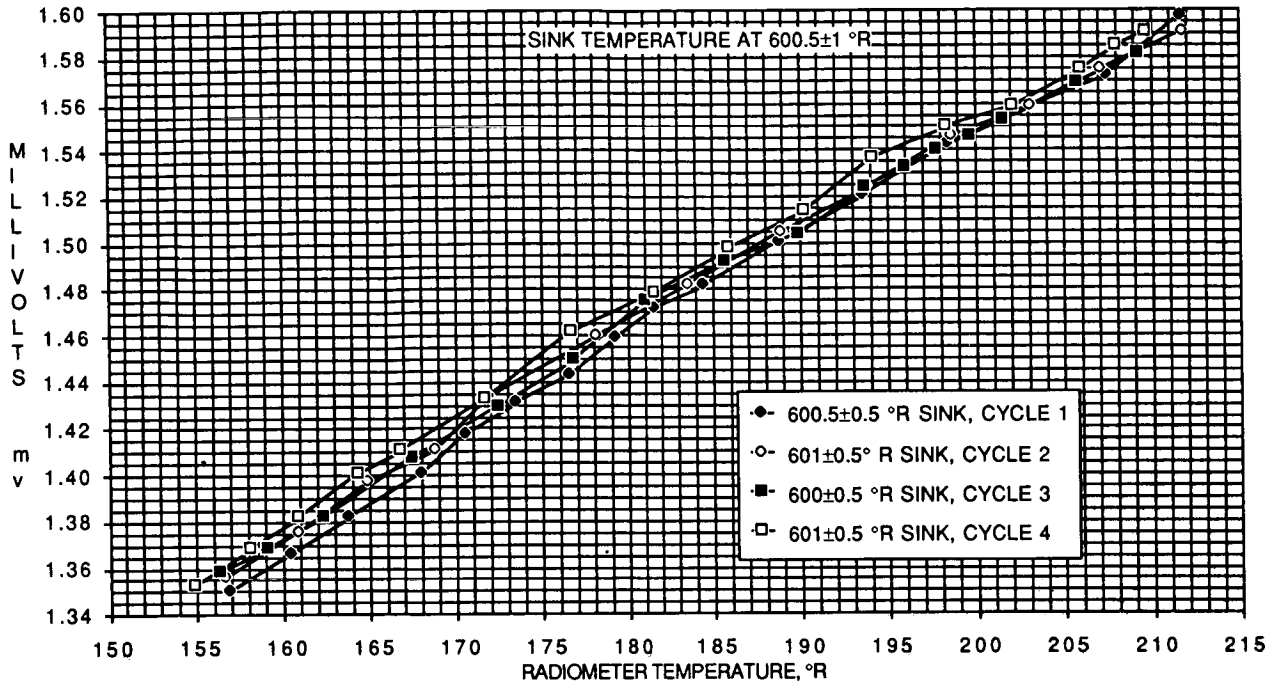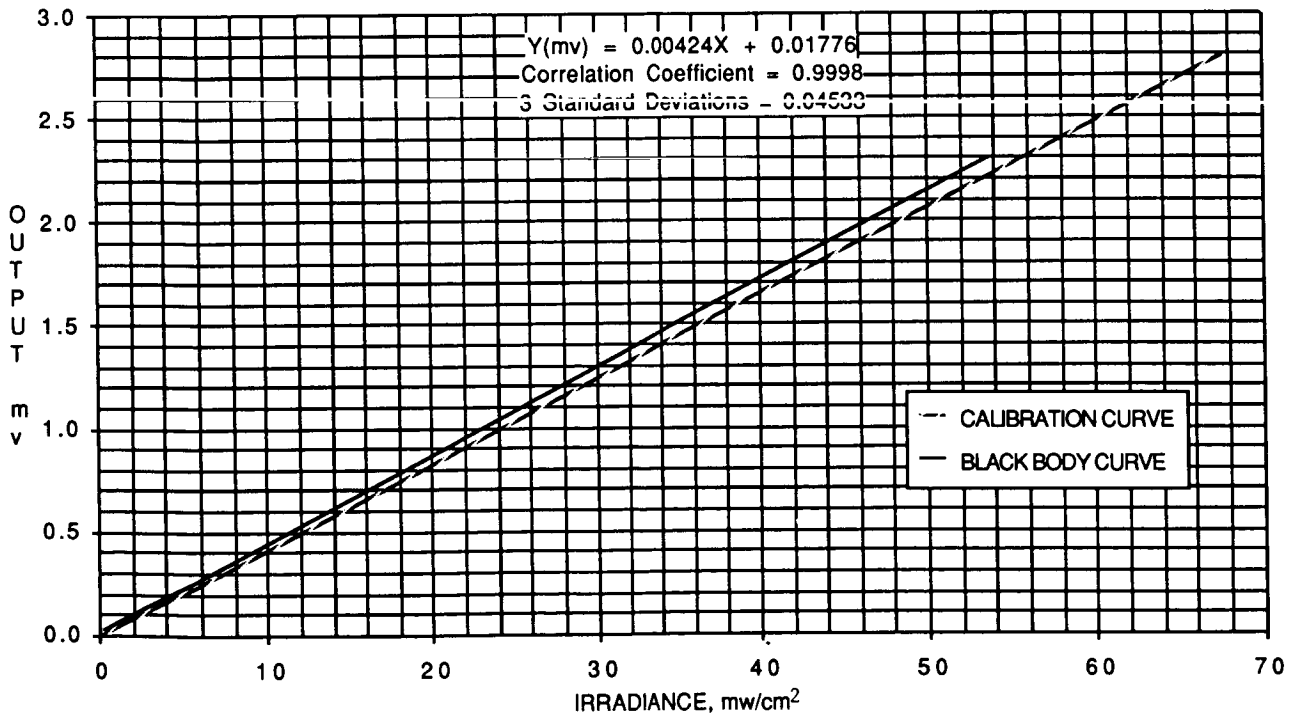
# TEST DATA ACQUISITION SYSTEM FOR THE ESTEC
# LARGE SOLAR SIMULATOR AT ESA/ESTEC

G. Buroni
Carlo Gavazzi Space, Milano, Italy

L. Zucconi
ESA/ESTEC, Noordwijk, The Netherlands

## ABSTRACT

ESA has placed a contract to Carlo Gavazzi Space for the study of a new data acquisition system for the ESA Large Space Simulator and for the implementation of the prototype. The program has been completed successfully, the prototype tested and its performance demonstrated by ESTEC. The paper describes the device characteristics, its performances and the system aspects connected to the integration into the space simulator instrumentation and environment. The data acquisition system has modular architecture and manifold configuration capability. The input characteristics feature high resolution and accuracy/stability for the measurement of low level (thermocouple originated) analog signals, even in presence of high common mode and S/N figures. The output is serial digital, compatible with ESA data handling standards. The device is designed to be installed in particularly hostile environment, such as that of a solar simulator, and saves in this way large amount of harness and the formerly used slip ring coupling. The implemented prototype is described in details in the paper, which provides also the results of the unit's characterization tests.

## INTRODUCTION

To face the increasing demand of testing large systems in space simulating environment, ESTEC has endeavoured enhancement of their 10 metre Dynamic Test Chamber (DTC) to convert it into a Solar Simulator Facility, with a 6 metre diameter beam (LSS = Large Solar Simulator). Large systems under test mean also a large amount of sensor data to be transferred to the Control Centre of the DTC; successful use of the chamber for IRIS and Hipparcos has proved recently that the background concepts are correct and adequate, while the means should be prepared on time to upgrade the data acquisition capability to meet the requirements of such programmes as Columbus and Hermes.

The increased capability however should not cause electrical problems neither at the level of acquisition (e.g. noise, common mode) nor at the level of data transmission to the control room (e.g. number of slip-rings and cable bundles), while reliability shall possibly be improved, along with a simplified maintenance scheme.

The Data Acquisition and Encoding System for thermocouple signals presented in this paper has been successfully tested and designated as candidate for being used in the LSS in the near future.


## INFRASTRUCTURE ENVIRONMENT

New instrumentation to upgrade the LSS has to be conceived as an extension to the existing facilities, to satisfy the growth capability of the original system design and to optimize the overall project costs which have to stay in the boundaries of a very tight budget. The structure where the new data acquisition instrumentation has to be integrated has the following main characteristics:

- test articles to be tested are supported by a platform isolated from chamber and building motions

- test types in the same chamber are: dynamic, infrared, vacuum thermal cycles and solar simulation

- test operations, under vacuum conditions, are: deployments, separations, dynamic balancing, spin performance, determination of MOI (Moment of Inertia)

- large infrared test rig and control equipment is available

- the LSS is linked to all other environmental test facilities of ESTEC, namely vibration equipment, optical alignment and checkout equipment, customer's EGSE, acoustic chamber, antenna test (EMC) facility, etc.

- the simulated solar light beam is horizontal and is very stable in time (although not necessarily uniform in space and spectrum)

- the light energy density in the reference plane is 1.6 kW/m.

# THE THERMOCOUPLE DATA ACQUISITION DESIGN CONCEPT

The amount of sensors on a sample and the level of thermocouple signals impose the main design drives to the Data Acquisition System:

- modularity and expansibility

- common mode rejection

- noise immunity

- digital processing of signals and data concentration

- digital transmission link, with facility of error correction codes.

As test samples are often moved during the test with respect to the LSS structures, data have to be fetched from it to the Control Room through slip rings (or radio link) this leading to the requirements of:

- having the maximum number of data on minimum number of output lines

- providing for peripheral collection of data, to be gathered into a central unit

- designing the Data Collection Structure in such a way that it can withstand the same thermal vacuum and environmental conditions as the test sample

- assembling the unit into sturdy compact box, mounted close to the test sample with minimum impact with physical test set up.

Modularity shall be such that more than one autonomous unit can deliver serialized data to a master module (CPU and formatter) for further concentration and serialization, to reduce the number of output lines, therefore of slip-rings, compatibly however with the required sampling rate.

## GENERAL CHARACTERISTICS OF THE DATA ACQUISITION UNIT

The unit conceived by Carlo Gavazzi Space to fulfil the above tasks is mainly based on the modular concept and on the facility to electrically decoupling all its interfaces. A sketch of a 4 unit configuration system is in fig. 1.
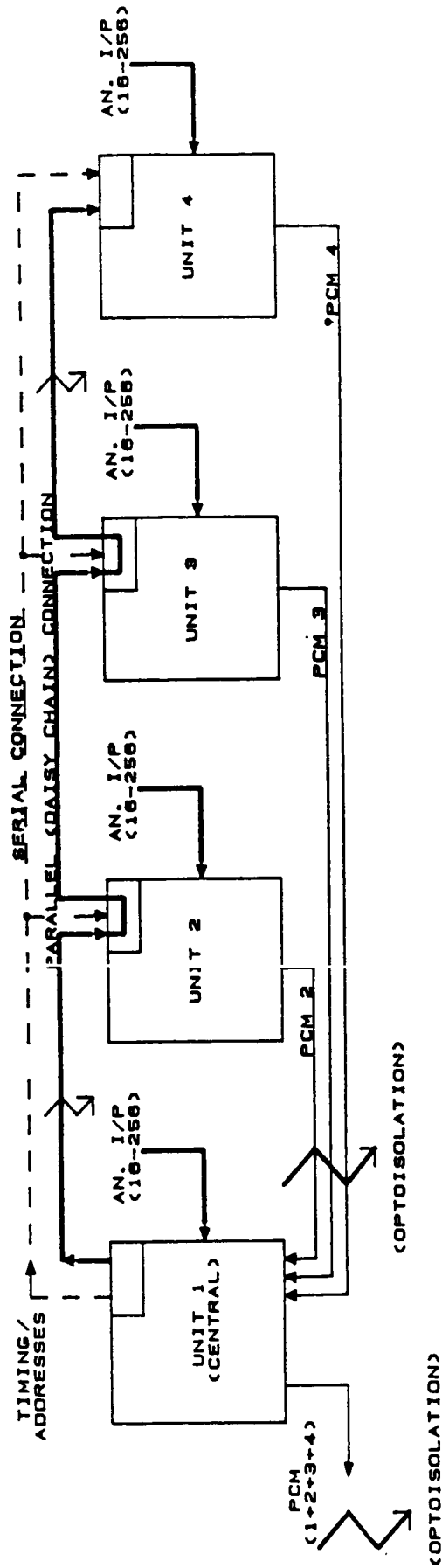
NOTES : — SERIAL CONNECTION MAY REPLACE PARALLEL LINK FOR DIGITAL TIMING/ADDRESS DATA
        — OPTOCOUPLING IS POSSIBLE IN ALL INTERFACES
        — EXPANSIBILITY ALLOWS FOR UP TO 1024 CHANNELS ALLOCATED TO 4 TO 64 UNITS.
          DEPENDING ON THE CHOSEN MODULARITY

Figure 1. Example of System Containing Four Data Acquisition Units (Flexible Capability)

The individual unit is an acquisition device, which conditions and digitally converts low voltage analog data, namely temperatures, which are measured with characteristics of high resolution and accuracy in hostile environment (-30°C through +50°C, 10 EXP-7 torr). It shall be capable of multiplexing up to 256 analog (low level, differential) channels and of issuing the necessary timing and addressing signals to permit synchronization with other identical units and reporting to a master unit. In the same standard unit is housed the 12 bit plus sign (double integration) A/D converter and possibly the programmable PCM formatter, which yields an organized stream of digital bits out of the collected analog data. While the data output is definitely a serial stream, the timing/addressing signals are in parallel form for the normal version used to handle fairly low number of users. Provision is made for serialized organization also for the timing/addressing signals, to minimize the amount of interconnecting wires, depending on the application: in this latter case the serial output of these signals can be used like a bus.

The unit has been designed to handle low level signals (namely from thermocouples) affected by up to ±16V common mode which is automatically compensated. It features very high accuracy and linearity of response in the whole range of operating temperature (the actual specifications and verified performances are in the next sections). The modularity in the unit is at level of 16 channels, expansible to 256 by means of 16 identical modules. Four to 16 units can be used simultaneously to collect up to 1024 low level signals which could generate a single PCM stream issued by that unit, which has been selected to contain the final stage of multiplexing and the PCM formatter. The possible architectures of the system have been conceived to cope with signals affected by either identical or different common modes. Namely, every single module has floating power supply, while coupling between modules and with the programmer is by optocouplers, to allow for acquisition of input signal blocks whose common modes differ by more than 250V.

In this way the recurring problem has been solved of having low level signal sources with different common modes, all the way through offering the facility of centralized processing, therefore a single output line carrying the resulting PCM stream.

Current organization of the unit is the following:

- Power Supply, floating and based on either DC/DC converter (28V DC) or AC-DC converter (110V-400 Hz).

- Central Processing Unit, with output timing and address generation and settable to become either central or peripheral in a system.

- Multiplexer (modular 16 or 64), for low level differential input.

- A/D converter (12 bit + sign, double integration).

- Formatter and serial digital output, issuing 12 bit words and synch codes, with selectable frame and subframe length.

- Optoisolated interfaces (serial and parallel, as applicable).

One module per type can be assembled into an autonomous unit, whose acquisition capability ranges from 16 or 64 (one only multiplexer module; 2 channels may be used for autocalibration) to 256 thermocouple channels (4 to 16 multiplexer modules).

Typical system level possible architectures are shown in fig. 2 for the 3 cases of:

. groups of signal sources with different range and common mode characteristics
. signal sources with homogeneous characteristics
. more than 3 groups of signal sources, with peripheral units connected through a bus.

Extra development has been carried out subsequently by Carlo Gavazzi Space to employ the basic unit into all the envisaged configurations and to make units programmability more flexible. Use of several units communicating through a bus has been taken into consideration and the development is currently ready for different types of application and requirements, both commercial and project dedicated.


## MAIN IMPROVEMENTS WITH RESPECT TO THE EXISTING SYSTEM

The functional and performance requirements have been met by the successfully qualified prototype, which has proved to be capable of:

- handling bigger amount of low voltage channels (from few hundreds to almost unlimited, but certainly more than one thousand), by expansion of modular connections
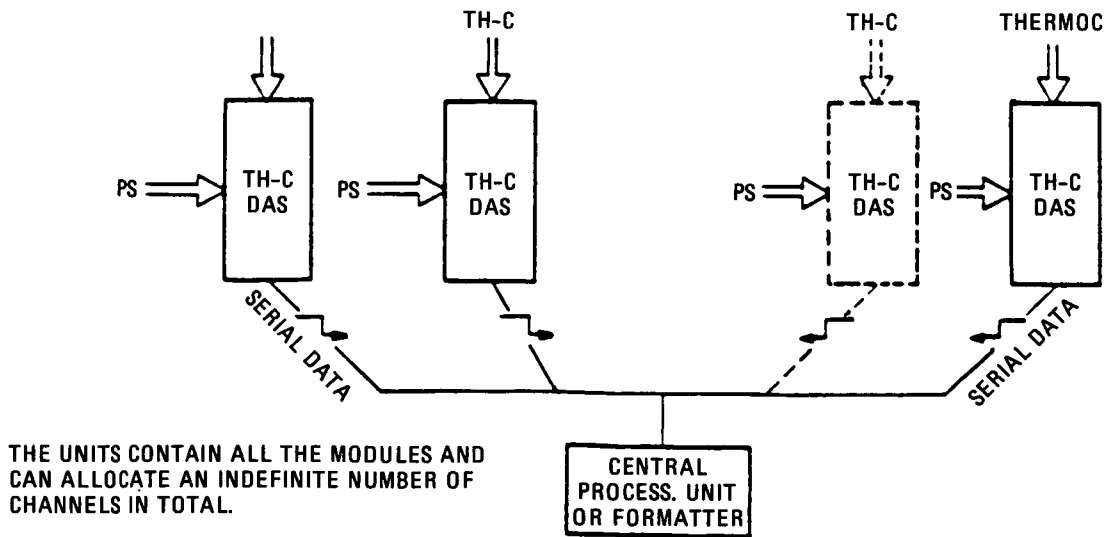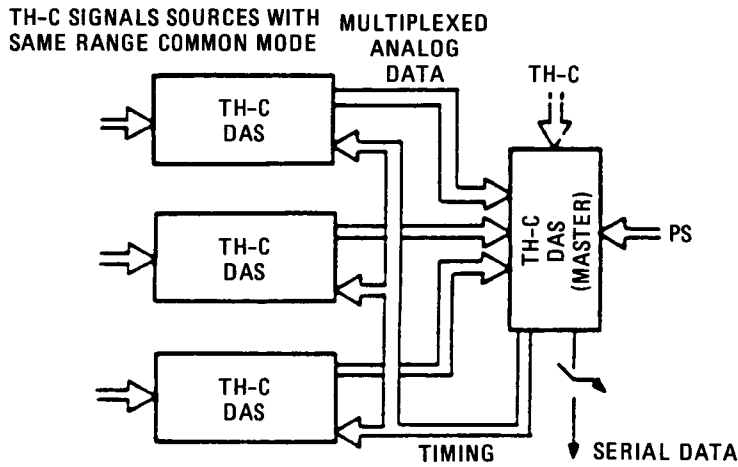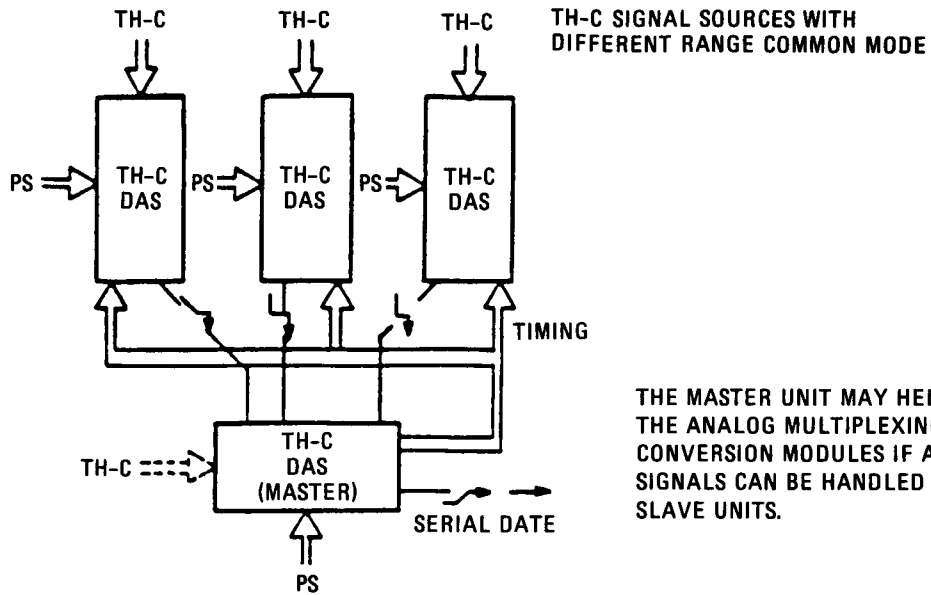
TH-C SIGNAL SOURCES WITH
DIFFERENT RANGE COMMON MODE

THE MASTER UNIT MAY HELP WITHOUT
THE ANALOG MULTIPLEXING AND A/O
CONVERSION MODULES IF ALL THE TH-C
SIGNALS CAN BE HANDLED BY THE 3
SLAVE UNITS.

TH-C SIGNALS SOURCES WITH MULTIPLEXED
SAME RANGE COMMON MODE ANALOG DATA

THE MASTER UNIT MAY HELP WITHOUT THE FIRST
TWO LEVEL ANALOG MULTIPLEXING MODULES IF
ALL THE TH-C SIGNALS CAN BE HANDLED BY THE
3 SLAVE UNIT.

THE UNITS CONTAIN ALL THE MODULES AND
CAN ALLOCATE AN INDEFINITE NUMBER OF
CHANNELS IN TOTAL.

Figure 2. Use of TH-C DAS Unit at System Level

482

- increasing measurement accuracy, thanks to the built in 12 bit plus sign A/D converter (formerly, the analog data were processed outside the system, in the control centre where they arrived through long length, disturbance sensitive cables)

- tolerating very high common mode levels, without degrading measurement accuracy and noise rejection

- improving electromagnetic interference tolerance, especially on the long cables beyond the slip-rings, thanks to the digital technique used for transmission (formerly, the analog signals running in the cables where seriously affected by the electrical disturbance inducted by the facility service equipment); the digital technique itself may be improved by adding error correction algorithms

- permitting decentralized collection of data, thus:

  . reducing the path of analog signal prior to reaching the nearest collection unit (with improved immunity to noise)
  . optimizing harness length and routing, with improvement of plant cleanliness and accessibility for maintenance
  . improving reliability by multiple levels of multiplexing (a failure in a peripheral unit should not affect more than 16-64 neighbour channels on a single module)
  . decoupling groups of thermocouple signal sources which can be handled homogeneously by the decentralized collection unit; a failure in one group shall not affect any other group of channels
  . easing maintainability, by local interventions in turn on peripheral units and optimization of facility downtime (modularity is such that any peripheral unit might even replace the master unit, if this one fails, thus providing for a set of immediately available spare modules)

- reducing quite drastically the need for slip-ring contacts (only the lines carrying PCM, clock and safety signals have to be transmitted to the steady part of the facility)

- reducing the amount of harness carrying the thermocouple measurement information outside the facility.

    Reliability and maintainability improvement deserves further clarification: in fact the new data acquisition unit is conceived to suit architectures with space type characteristics, with the further advantage of immediate accessibility in case of preventive or corrective maintenance.

The selection of components, which shall withstand simulated space environment, makes the unit reliability figure definitely higher than the commercial equipment's used so far. Moreover interchangeability of modules, as already mentioned, permits to replace immediately those units which may have failed in a critical area of the facility. The only critical item is the central multiplexing and formatting unit gathering all data from the peripheral multiplexers: should the need arise, this unit could be made redundant like in the usual space electronics practice.

Along with reliability, maintainability is improved, not only due to the intrinsic lower probability of failure, but also thanks to the new architecture. In the previous facility, in fact, data could only be processed in the control room, a few hundred metres apart, and the operator in the facility could only communicate with the control room by telephone link. Local digital processing of data allows for a central computer terminal to be placed in the facility where the operator gets an immediate replica of the data displayed in the control room. Moreover, by means of a simple telemetry decommutator, the operator himself has straightforward access to anyone of the Data Acquisition Units (either peripheral or central) thanks to their serial digital output; this saves testing time and prevents misinterpretation of data. Especially in those configurations where redundant processing unit is available, maintenance interventions are possible without stopping data processing by the facility, except for only those parts which are maintained.

This aspect of improved maintainability has been stressed because current experience demonstrates that facility down time has critical cost impacts on any affected program and re-organization of the maintenance approach becomes absolutely necessary for cost effectiveness.

Finally, in can be stressed that installation of systems of any complexity is sensibly easier than for the current architecture, with reduction of harness, simplification of documentation, improved flexibility of application, smaller size of equipment and easier access to interfaces.

# SUMMARY OF THE UNIT SPECIFICATIONS

## General Features

The basic unit functional block diagram is shown in fig. 3. The general features are summarized hereinafter:

- modular 16-64 differential analog input multiplexing (up to 4-16 modules per unit, maximum unit capability 256 channels)

- up to 3 additional units connectable to a central unit performing A/D conversion, serialization and electrical decoupling

- facility for electrically decoupling all interfaces

- more than 100 dbDC and AC (more than 500 Hz) common mode rejection ratio on thermocouple generated signals, in the electrically decoupled architecture

- 12 bit plus sign A/D conversion, double integration, followed by a programmable amplifier with maximum gain of 1000

- high linearity and low gain error (see performance below)

- 12 bit plus sign and overrange parallel digital output

- PCM serial digital output, plus synchronization and timing signals

- parallel digital input (ON/OFF) capability

- facility for autocalibration and for autocompensation in the operational temperature range (-30°C +50°C)

- compact package for aerospace application

- decoupled built-in DC voltage supply distribution

- internal staus monitoring channels (2 in each unit).

## Optional Features

On request the following extra options are available on the baseline unit.

- 19 inch crate mounting architecture

- stabilized (protected) DC voltage lines for slave units

- DC power inputs from master unit ($\pm$19V, +12V, +8,5V, -6V)

- programmable size and format of serial PCM (to accommodate all collected channels)

- additional digital or analog inputs and outputs to permit connection of more than 3 units to a master unit

- facility for polling interrogation by a central data processing unit (computer bus protocol interface).


## Specifications

Power input          : 20 kHz sinewave 500 mV p/p ($\pm$10%) 28 VDC ($\pm$10%)

Power consumption     : less than 4 W (basic unit)

Input                 : $\pm$5 mV differential thermocouple signals (62-254 channels max, optoisolated), impedance higher than 100 MOhm

Digital output        : optically isolated PCM NRZL (TTL compatible)

Connectors (prototype): CANNON, type D*

Size (prototype)      : 183x225x157 (h)

Weight (prototype)    : about 2.5 Kg. with power supply transformers

Sampling rate         : programmable, typically 60 sec. for 1000 channels.


## SUMMARY OF VERIFIED PERFORMANCE

The figures recorded here below have been measured in conditions of vacuum and in the whole range of temperature, with input signals

from -5 mV to -5 mV.

Operational temperature on baseplate : -30°C...+50°C.

Vacuum conditions : 10 EXP-7 torr.

Input resolution at maximum gain : ±1.25 microV.

Maximum linearity error : ±0.2% of full scale = ±11.2 mV full scale, conventionally taken as ±5.6 microV.

System accuracy (as referred to input): ±4 microV in the range 75°K to 425°K, with measurement repetitivity better than 0.1°K.

Standard deviation (±3 sigma) : ±8.02 microV max.

Gain error : ±0.04% (±2.3 microV) max.

Offset error : -1.7 microV max

Thermal drifts : Offset : 5.8 ppm FS/°C
Gain : -19.8 ppm FS/°C
Linearity: ±17.5 ppm FS/°C

Common mode rejection ratio (CMRR) : DC -137 db
AC -106 db
DCCOMP -124 db

Common mode voltage : ±250V between channels of different units or with respect to ground.

±16V between channels of the same unit.

## TECHNIQUES AND DESIGN APPROACH

The study phase trade-offs have led to choosing the following techniques to meet the project main targets (all other functions not covered under this section have to be considered as satisfactorily met by current state of the art of commercial components application).
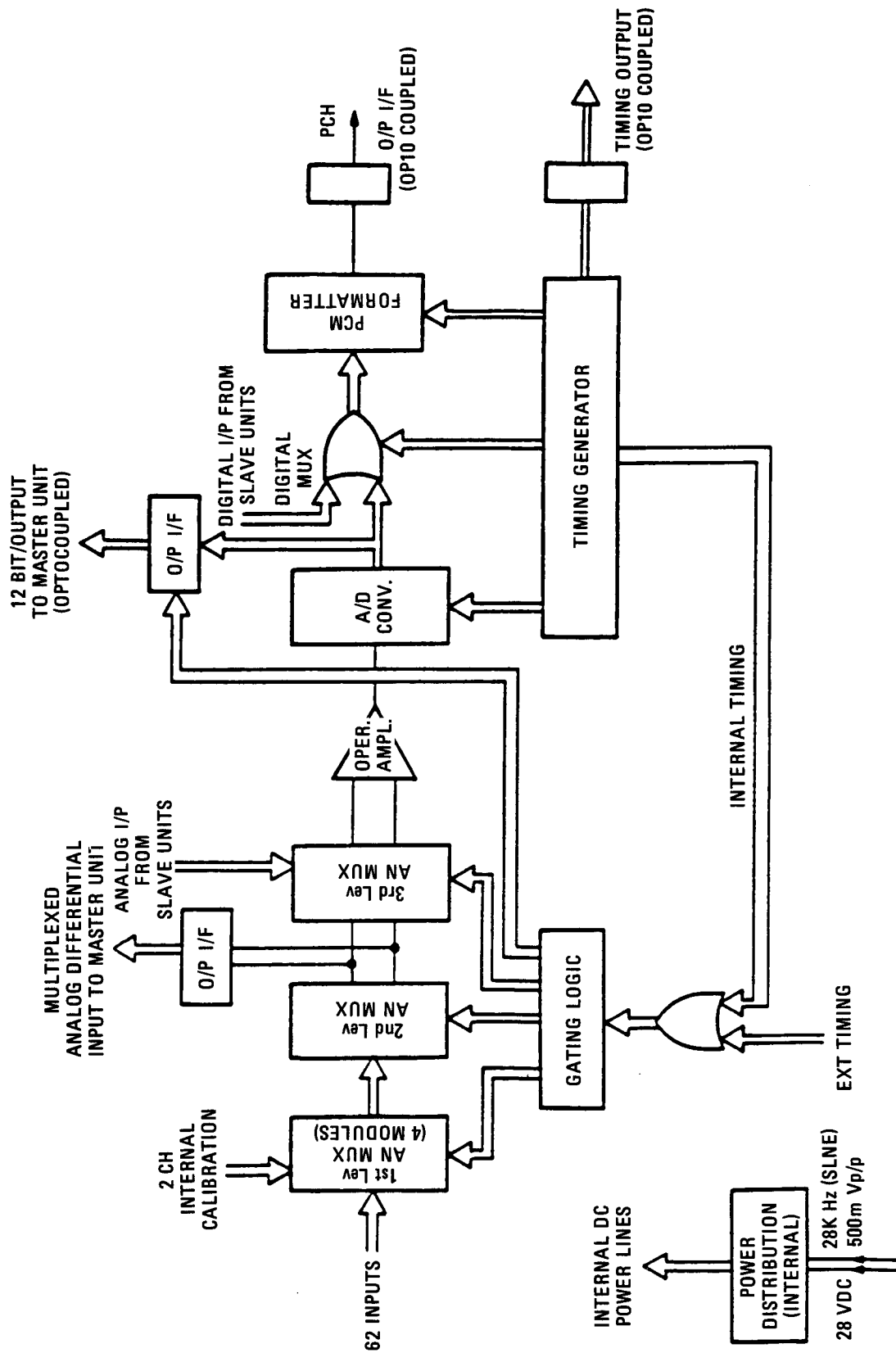
Figure 3. Functional Block Diagram

488

**Effects of set-up errors on gain**

Design characteristics are such that set-up errors have systematic effects over the gain, therefore correctable off-line by software. In particular, gain set up is done by means of discrete resistors, thus preventing instability and ageing effects of trimmers.


**Causes of gain drifts**

The following causes of gain drifts due to temperature sensitive components have been identified:

a) drift of the resistor network defining the differential gain

b) drift of open loop gain of op-amp's

c) drift of over voltage protection resistors and connection resistance (due to non-infinite value of input resistance of instrum.amplifier)

d) drift of ADC reference voltage.

Note that temperature effects on offset are compensated by the selected design techniques. Fig. 4 shows the resistor network layout.

A) Drift of the resistor network defining the differential gain.
   Overall theoretical drift with 20 ppm/°C resistors with temperature range of 80°C is better than 40 ppm/°C, which can be reduced to about 20 ppm/°C by proper matching of selected resistor value.

B) Effects of open loop gain drift on overall gain. On the assumption that Common Mode Rejection Rate (CMRR) is very high and the signal source impedance is low, a clever selection of the two operational amplifier stages open loop gain leads to a maximum gain drift better than 10 EXP-8 in the temperature range of 80°C.

C) Effects of source and series resistor. On the assumption of instrument amplifier input resistance higher than 2 MOhm and of 2 kOhm total series resistance, the resulting gain drift is better than 10 EXP-4 in the temperature range of 80°C.

D) Effects of Analog to Digital Converter (ADC) voltage reference (VREF). With suitable optimization of VREF stability in the temperature range -50°C to 100°C, the effect on gain drift is better than 10 EXP-3.

489
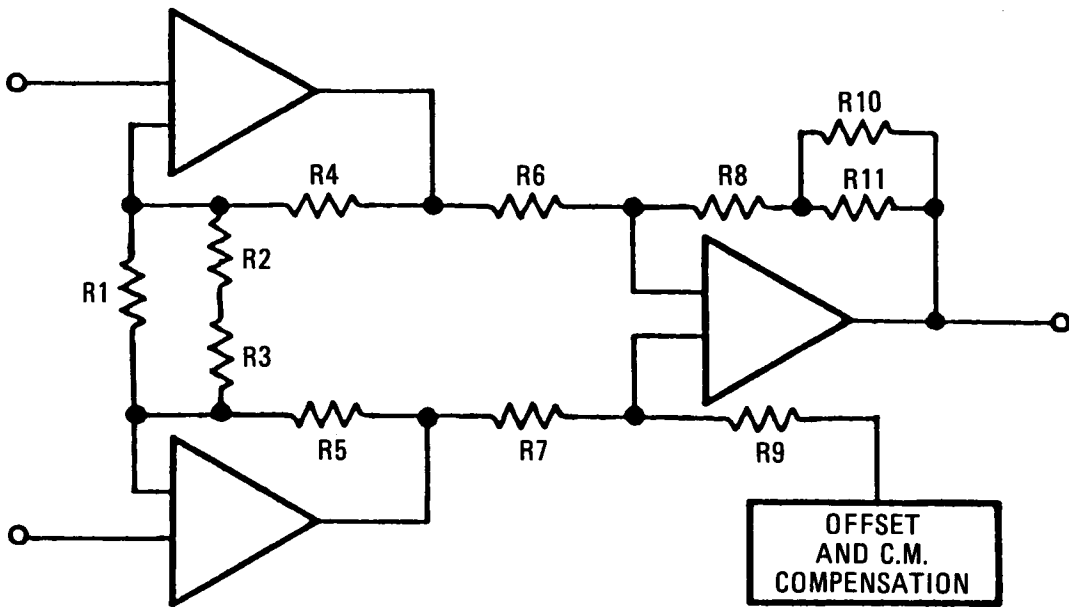
- GAIN DRIFT MAINLY AFFECTED BY $R_3$, $R_4$ AND $R_5$ DRIFT DUE TO:
  - FIRST STAGE DIFFERENTIAL GAIN OF ABOUT 10
  - VERY HIGH VALUE OF ADJUSTMENT RESISTORS $R_1$
  - VERY LOW VALUE OF ADJUSTMENT RESISTORS $R_2$

Figure 4.  Gain Drift due to Drift of Resistor Network

## Gain Calibration Approach by Software

The approach consists of mapping into the operator work station the absolute gain error data, observed during a system calibration phase, with respect to the gain calibration performed at ambient temperature during final factory tests; the gain setting accuracy in the calibration phase is 0.2% of full scale. The work station shall therefore correct in real time the received data against the map stored in the system calibration phase (target environment).

The data delivered to the operator are only affected by temperature drift errors, which have been proved to be negligible. Further software correction of temperature effects on gain drift is still possible with the same method, provided the mapping of gain errors in the work station is extended from ambient temperature to a significant number of temperatures in the range $-30°C$ to $50°C$; additional information is needed in this case about the actual Acquisition Unit temperature, which needs to be fairly accurate and derived from one of the channels of the acquisition unit itself. Hardware compensation of the thermal gain drift is not recommended due to the insufficient accuracy of the analysed methods. Advantages of software calibration approach are:

- No criticality during initial factory gain calibration phase performed by selection of gain setting resistors.

- No requirements of data acquisition system removal from the target environment (LSS).

- No requirement of hardware modification to data acquisition system.

- Off line preset of calibration data (manual or automatic) and real time gain correction performed automatically in operator workstation, without performing any physical action on data acquisition system.

- Periodic system verification and calibration procedures performed directly by the personnel normally in charge of LSS operations.


## Calibration Philosophy

The proposed philosophy is a direct consequence of conclusions of gain error analysis. No action is performed on data acquisition system but its behaviour is analyzed and deviation with respect to theoretical characteristics is recorded for further use during LSS operations, in order to correct actual data from systematic error.

Calibration is performed by personnel normally involved in LSS operations in accordance with a user oriented procedure, with no need for hardware or software specialists. No overhead nor change of current acquisition procedure in the data handling centre:

- data acquisition system correction data are obtained during workstation off line operations
- during LSS operations, temperature data cycles are sent from workstation over HP-IB to data handling centre, on request
- LSS is the master of the data acquisition cycle.

Calibration is performed automatically, therefore reducing possibilities of errors. Calibration is not a time consuming activitty. Calibration is executed:

- on a periodical basis at regular time intervals in order to take control over the accuracy of the system
- on a random basis during the installation of a new spacecraft in LSS or after a corrective maintenance intervention.

Between successive calibrations the operator workstation uses the same calibration data for the correction of the actual samplings from data acquisition system, which are affected by errors determined during calibration phase. Different sets of calibration data can be maintained in the operator workstation, displayed and used during LSS operations under full operator control.


## Calibration Procedure for Systematic gain errors

It is executed off line and at ambient temperature. Involved items are:

- a calibration source
- the actual LSS harness
- the thermocouple data acquisition system installed in LSS
- the operator workstation connected to the data acquisition system by the operational links (power and data).

Systematic gain error data are obtained by:

- acquiring data from data acquisition system into operator workstation as during normal LSS operations
- comparing acquired data against the theoretical ones associated to the value of the calibration signal used in the procedure

. determining the correction factor to be used during normal operation in order to eliminate the gain systematic error.

The gain correction factor is stored into the operator workstation and used during normal LSS operations to fetch data already corrected from systematic gain error. The gain correction factor can be displayed by the operator and overwritten if so deemed necessary. The workstation can store a catalogue of gain correction factors, each one associated to a given and well identified (date, S/C...) calibration procedure execution. The operator may use the most recent calibration data or select among the calibration data available in the catalogue.

## Grounding and Shielding

Optimum grounding and shielding performance is normally obtained by tailoring to the target system the most suitable philosophy derived from theoretical rules. This design choice however is affected by the uncertainty of several project dedicated requirements, such as:

- thermocouples floating or referred to ground

- location of common mode voltage (CMV) source, whether it is concentrated on the differential low level signal source or distributed over the signal cable (or both)

- EMC environment of the installed thermocouple data acquisition system

- amplitude and frequency of the AC common mode voltage sources concentrated on the L.L. (low level) signals sources

- amplitude and frequency of the noise signal induced in the L.L. signal lines due to the effect of the electric field coupling.

Moreover:

- each thermocouple channel can have in principle AC common mode voltage characteristics different from all the other channels, i.e. the channels, if tightly coupled, can influence each other

- because the acquisition system handles multiple channels with low level multiplexing and centralized signal conditioning, it is not possible to implement a conventional "guarding" approach as on

systems with individual signal conditioners and with guard terminals associated to each individual channel.

The selected approach, implemented in the prototype is the following:

- twisted pairs shall carry thermocouple channel signals to affect both lines of a channel by the same coupling

- each twisted pair is protected by individual shield (guard) connected to the low impedance terminal of the low level signal source. This shield, unconnected on the data acquisition system side, closes the loop of the induced AC C.M. currents without affecting the signal lines

- a shield protects a bundle of twisted shielded pairs. This outer shield is connected on one side to the data acquisition system star ground point and on the other side to the system ground via the VTR box structure. Figs. 5., 6., 7., show the preferred grounding concept.
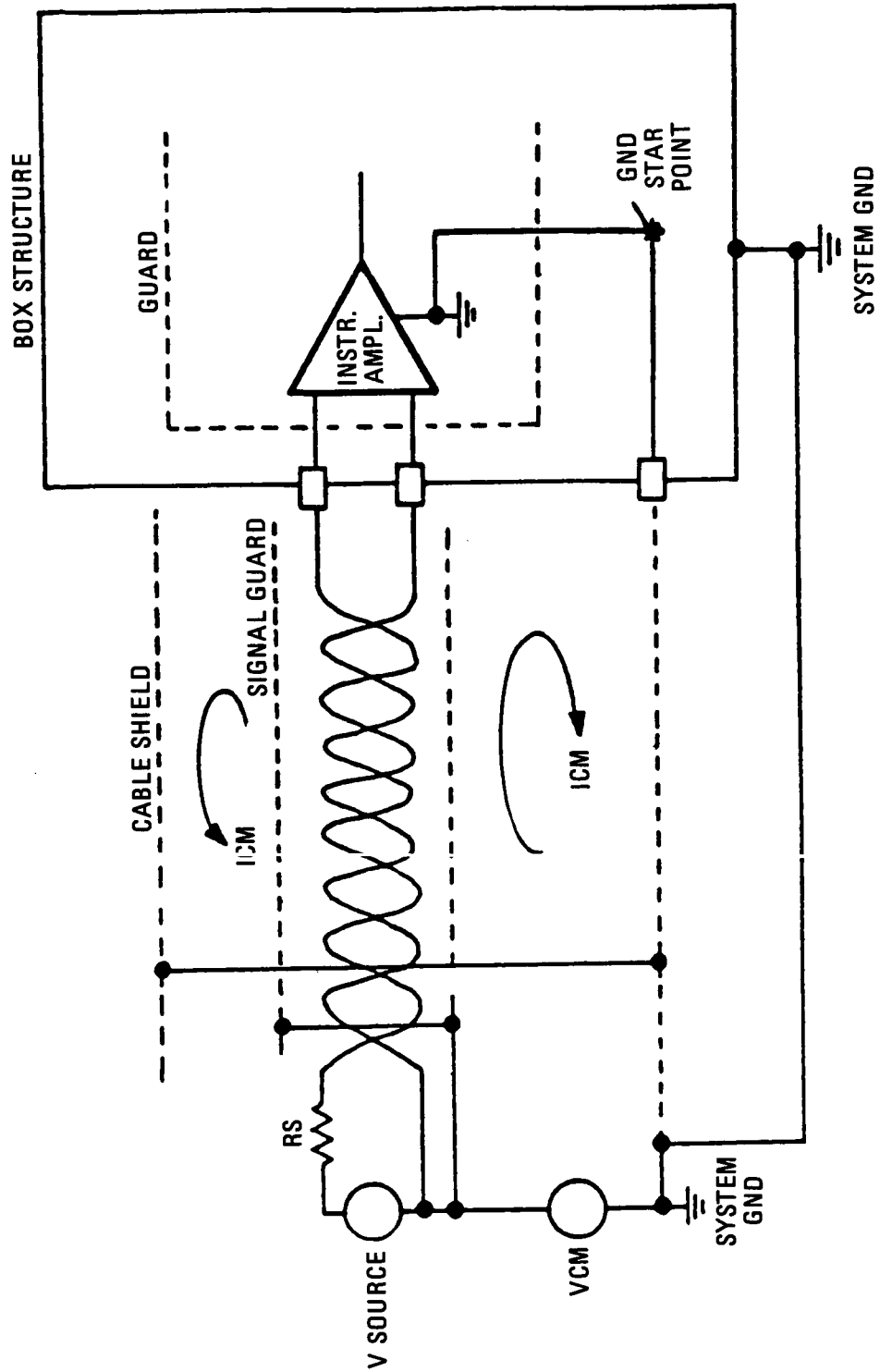
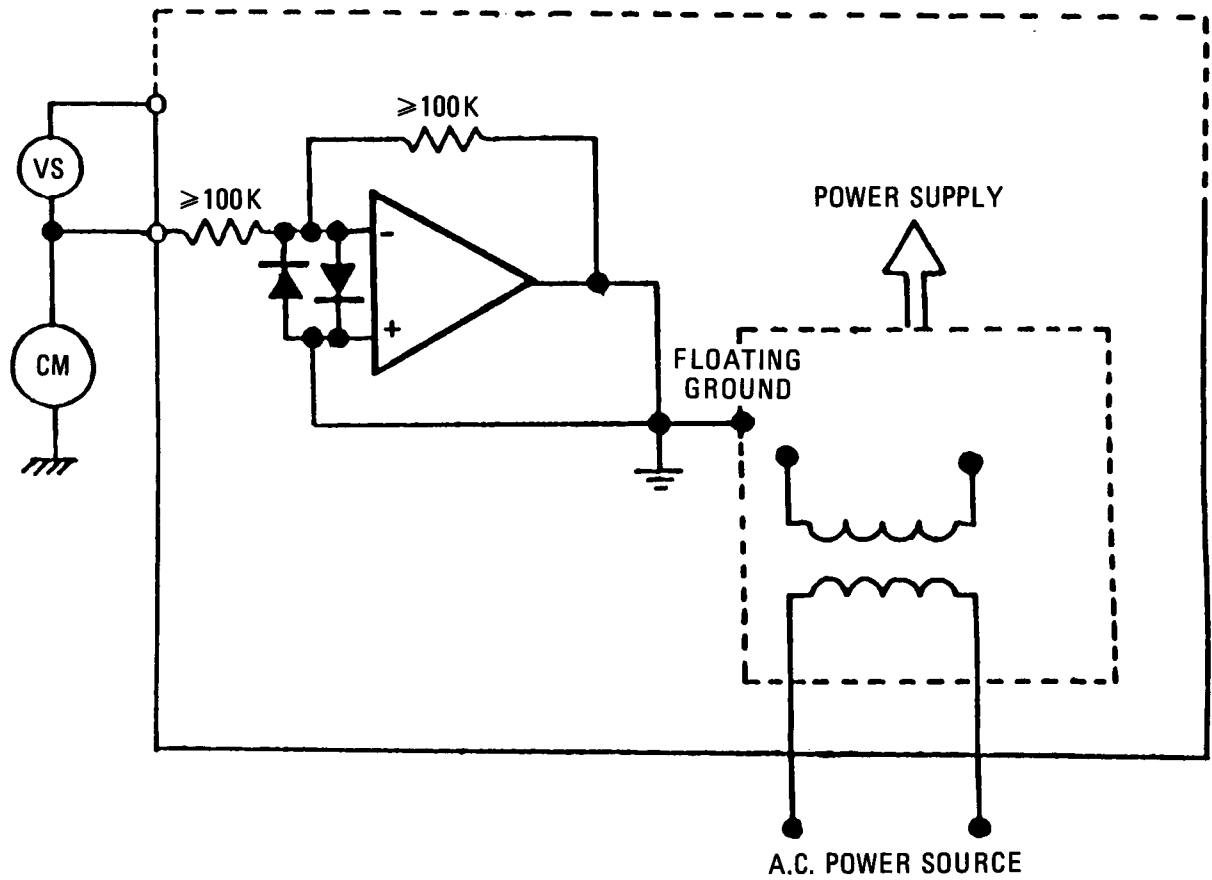Figure 5. Proposed Ground and Shielding Approach
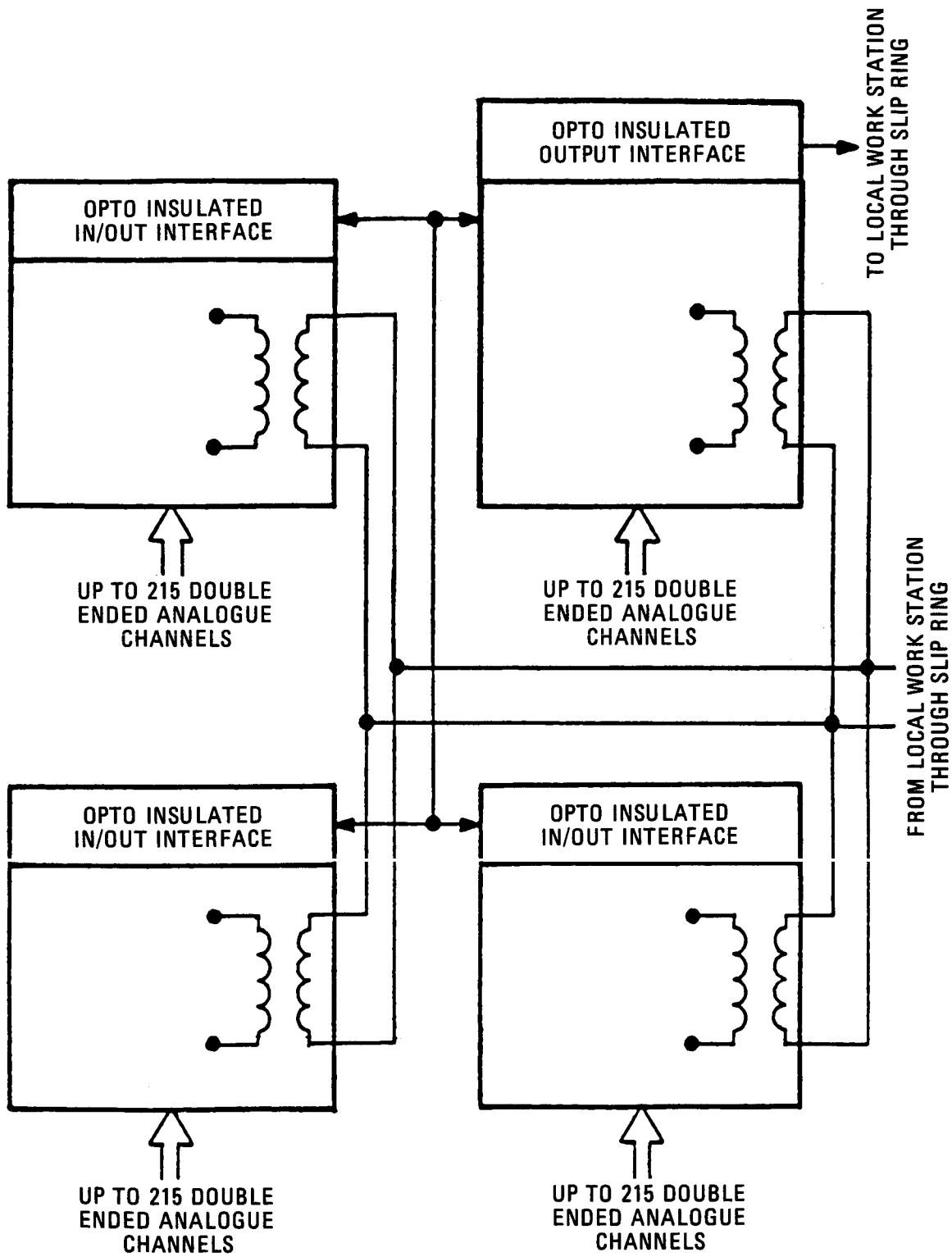
Figure 6.  Foating Ground Approach

Figure 7. Complete Data Acquisition System Grounding Block Diagram

# REFERENCES

Classen E., May 1984, New Integration and Test Facilities at ESTEC, ESA Bulletin N. 38, May 1984.

Bonnot P., Brinkmann P.W., June 1982, Large Infrared Test Rig for Vacuum Temperature Cycling Tests in the ESTEC "DTC", ESA SP-173, June 1982.

P.W. Brinkmann, 1985, Main Characteristics of the Large Space Simulator (LSS) at ESA/ESTEC.

P.W. Brinkmann, The European Large Space Simulator Comes into Operation, ESA Bulletin N. 50, May 1987.

# NASA
National Aeronautics and
Space Administration

# Report Documentation Page

| 1. Report No. NASA CP-3015 | 2. Government Accession No. | 3. Recipient's Catalog No. |
|---|---|---|

| 4. Title and Subtitle | 5. Report Date |
|---|---|
| 15th Space Simulation Conference: Support the Highway to Space Through Testing | June 1988 |
| | 6. Performing Organization Code Code 750 |

| 7. Author(s) Joseph Stecher, Editor | 8. Performing Organization Report No. 88B0253 |
|---|---|
| | 10. Work Unit No. |

| 9. Performing Organization Name and Address Goddard Space Flight Center Greenbelt, MD 20771 | 11. Contract or Grant No. |
|---|---|
| | 13. Type of Report and Period Covered |
| 12. Sponsoring Agency Name and Address National Aeronautics and Space Administration Washington, D.C. 20546-0001 | Conference Proceedings Oct. 31 - Nov. 3, 1988 |
| | 14. Sponsoring Agency Code |

**15. Supplementary Notes**

**16. Abstract**

The Institute of Environmental Sciences' "15th Space Simulation Conference: Support the Highway to Space Through Testing" provided participants a forum to acquire and exchange information on the state-of-the-art in space simulation, test technology, thermal simulation and protection, contamination, and techniques of test measurements. The papers presented at this conference and the resulting discussions carried out the conference theme of "Support the Highway to Space Through Testing."

| 17. Key Words (Suggested by Author(s)) Space Simulation Thermal Simulation Contamination Control Dynamic Testing | 18. Distribution Statement Unclassified - Unlimited Subject Category 18 |
|---|---|

| 19. Security Classif. (of this report) Unclassified | 20. Security Classif. (of this page) Unclassified | 21. No. of pages 512 | 22. Price A22 |
|---|---|---|---|

**NASA FORM 1626** OCT 86

National Aeronautics and
Space Administration
Code NTT-4

Washington, D.C.
20546-0001

# NASA

POSTMASTER:    If Undeliverable (Section 158
Postal Manual) Do Not Return